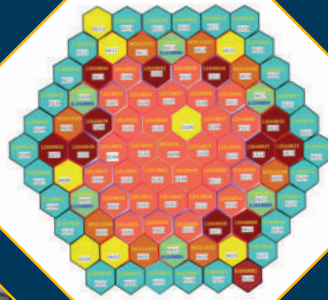




Indira Gandhi Centre for Atomic Research



Annual Report 2021



Government of India
Department of Atomic Energy
Indira Gandhi Centre for Atomic Research
Kalpakkam - 603 102

IGCAR

2021

INDIRA GANDHI CENTRE FOR ATOMIC RESEARCH

ANNUAL REPORT



Government of India
Department of Atomic Energy
Indira Gandhi Centre for
Atomic Research
Kalpakkam 603 102

Editorial Committee**Chairman**

Ms. S. Rajeswari

Members

Dr. John Philip

Dr. T. R. Ravindran

Dr. C. V. S. Brahmananda Rao

Shri A. Suriyanarayanan

Shri M. S. Bhagat

Shri G. Venkat Kishore

Dr. Girija Suresh

Shri M. Rajendra Kumar

Shri S. Kishore

Shri Biswanath Sen

Dr. N. Desigan

Shri Gaddam Pentaiah

Shri K. Varathan

Member-Secretary

Dr. V. S. Srinivasan

CONTENTS

Foreword

Editorial

Articles at a Glance

I. Fast Breeder Test Reactor & Kalpakkam Mini Reactor	1
II. Prototype Fast Breeder Reactor	11
III. R&D for Fast Breeder Reactors	49
IV. Fuel Cycle	81
V. Basic Research	137
VI. Directed Basic Research	165
VII. Infrastructure, Resource Management & Biodiversity	183
VIII. Awards/Publications/Events/Organisation	205

Address for Correspondence

Ms. S. Rajeswari

Chairman, Editorial Committee

Head, Scientific Information Resource Division

Indira Gandhi Centre for Atomic Research

Kalpakkam - 603 102

Phone : +91-44-27480281

Email : raj@igcar.gov.in

e-Copy available at: <http://www.igcar.gov.in>

Published by

Scientific Information Resource Division, SQ&RMG,
Indira Gandhi Centre for Atomic Research, Kalpakkam - 603 102

Foreword



Dear Colleagues,

I am delighted to release the IGCAR Annual report of 2021. The report highlights accomplishments in R&D pertaining to fast reactor and associated fuel cycle technologies as well as in the frontier areas of basic and applied research.

The Fast Breeder Test Reactor (FBTR), the flagship reactor of second stage of the Indian Nuclear Power Programme continues to serve as the irradiation test bed for advanced fuels and structural materials. Efforts are put to raise FBTR to its rated power. The prerequisite tasks such as reactor vessel internal inspection, qualification of steam generators, regulatory clearances and full revamping of cooling tower in progress are discussed in detail.

Reprocessing is an important step in closing the nuclear fuel cycle. The 17th campaign of reprocessing at Compact Reprocessing of Advanced fuels in Lead shielded cells (CORAL), after relicensing is under advanced stage of completion. By application of dose-control measures and good operating practices, huge reduction in cumulative dose expenditure was achieved.

Demonstration Fast Reactor fuel reprocessing Plant (DFRP) is in an advanced stage of commissioning. Development of various systems and processes include large diameter annular centrifugal extractor, indigenously made shrouded probe and air-sparged mixer settler, to name a few.

The Prototype Fast Breeder Reactor (PFBR) is in an advanced stage of integrated commissioning with successive milestones: In-house manufactured four 170 m³/hour capacity Annual Linear Induction Pump of modified design was developed. This resulted in substantial savings in both time and cost. Other

significant activities include development and testing of main vessel-safety vessel interspace crawler system and filling of sodium in purification circuit of safety grade decay heat removal system.

It is heartening to note that the R&D efforts towards future fast breeder reactors is actively pursued. This include sizing of reactor assembly for 500 MWe FBRs meeting the revised safety criteria, constructing the Sodium Technology Complex to test full-scale components of future FBRs, to develop and manufacture special valves, evaluating the performance of reactor structural materials and inspection of irradiated fuel pins.

Basic research provided valuable insights and laid the foundation for development of new technologies. Investigations during the reporting period covered physical, mechanical and chemical characterization of novel materials and accelerator based materials research. Some of the accomplishments as I see in application oriented research are, recovery of boron from spent radioactive control rods by the pyrohydrolysis method, boric acid as converter material for semiconductor neutron detector, development of portable room temperature Cadmium Zinc Telluride based Gamma Radiation Detector and nanomaterials for various other applications. In addition, NDE techniques were developed for mapping of defects, inspection of large diameter bearings etc.

It is commendable to note that infrastructure and services have been added to support R&D activities of the centre. In this period, Central Water Chilling Plant-II was established to augment the central air-conditioning infrastructure of IGCAR.

Other infrastructure facilities reported are the Indigenous development of portable whole body counters to be used during radiological emergency, a private cloud, and a water quality monitoring system for the water bodies in DAE campus, Kalpakkam.

The programmes of HBNI, BARC Training school and UGC-CSIR node at IGCAR continue to progress with full vigour. Relevant information resources and literacy services for high-impact research are available to scientists and engineers round the clock. The rich biodiversity within the DAE-Kalpakkam complex is continuously documented and a book is published on the exotic birds of Kalpakkam in 2021. The Incubation Centre of IGCAR has successfully transferred Technologies, viz., "Portable High Volume Air Sampler" and "Autonomous Gamma Dose Logger, " to the industries.

I congratulate the scientists and engineers for their excellent contributions to IGCAR Annual Report - 2021. I appreciate the publication team in bringing out the report with rich technical content and a pleasing layout.

In all our endeavour, we have been well supported by BARC, NFC, NPCIL, RRCAT, VECC, HWB, DPS and other units of DAE. With the continued support and cooperation we hope to accomplish the milestone activity pertaining to BHAVINI and also the vision & mission of the Centre.



(B. Venkatraman)
Distinguished Scientist &
Director, IGCAR

Our Primary Mission

To conduct a broad based multidisciplinary programme of scientific research and advanced engineering development, directed towards the establishment of the technology of Sodium Cooled Fast Breeder Reactors (FBR) and associated fuel cycle facilities in the Country. The mission includes the development and applications of new and improved materials, techniques, equipment and systems for FBRs, pursue basic research to achieve breakthroughs in Fast Reactor technology.

Editor's Desk



Dear Reader,

I am pleased to present the Annual Report of IGCAR for 2021 as the Editorial Committee Chairman.

This year, the annual report has 143 technical articles. A significant portion of this report reflects the progress in mission-specific activities of IGCAR concerning FBTR, PFBR, R&D on future Fast Reactors, and the Fuel Cycle. The rest of the chapters indicate the basic research essential for sustained growth in research and development, technology transfers and societal benefit programs. Other supporting development activities are part of the chapter on infrastructure, resource management and biodiversity.

The articles have gone through multiple editing stages to ensure accuracy and readability. I convey my sincere thanks to the Editorial Committee for their dedicated efforts in successfully bringing out the Annual Report.

Chapter-I on Fast Breeder Test Reactor has a few articles that focus on the design and development carried out to raise the power of FBTR to 40 MWt / 13.2 MWe. A few other articles focus on irradiation of Yttrium pins for radioisotope production and seismic studies.

Chapter-II on Prototype Fast Breeder Reactor highlights the current status of PFBR. The articles on novel crawlers for reactor vessel inspections, models to simulate transients, manufacturing and evaluation of the components indicate the significant contribution of the Centre towards the commissioning of PFBR.

Chapter-III on R&D for FBR has articles about the Centre's efforts to develop indigenous technology for future nuclear reactor programs. There are various articles on the sizing of reactor assembly for 500 MWe FBRs to meet the revised safety criteria, DHDYN code enhancement, high-temperature mechanical behavior, and studies on manufacturing, characterization and quality assurance programs.

Chapter-IV on Fuel Cycle has the highest number of articles, including studies related to commissioning of various sub-systems in DFRP, Pyroprocess R & D facility, reprocessing of high burn-up fuel in CORAL, simulation studies, ultrasonic evaluation and other developments.

Chapter-V on Basic Research contains articles covering the atomistic simulations, studies on optical properties, development of NDE tools, physical characterization techniques and analysis. Chapter-VI on Directed Basic Research refers to the outcome of activities and technologies developed that have immediate applications. It includes developing materials for various applications such as anti-fouling and self-cleaning, organic dye removal, etc., and ultrasonic testing methods for inspection of large diameter bearings.

Chapter-VII on Infrastructure, Resource Management, and Biodiversity is a chapter that highlights the efforts & augmentation of essential services, public awareness, biodiversity documentation, and infrastructure management. Chapter-VIII has details on the publications, the events, awards, organization, and a summary of the activities of the various groups.

We welcome feedback from readers concerning the quality of the presentation and the technical content therein. We thank the Group Directors for their support and the enthusiastic authors for providing quality articles in the stipulated time.

The committee sincerely thanks Dr. B. Venkatraman, Director, IGCAR, for his keen interest, continued guidance and support towards bringing out the publication in its present form.

S. Rajeswari
Chairman, Editorial Committee &
Head, Scientific Information Resource Division

I. Fast Breeder Test Reactor		
Sl.No	Title	Page No
1.01	Design & Development of Nuclear Fuel Management System	02
1.02	Estimation of Life of Poison Subassembly for FBTR 40 MWt Core	04
1.03	Estimation of Pressure Drop and Temperature Distribution in Large Bore Subassembly Intended for Yttria Capsule Irradiation	05
1.04	Reactor Vessel Internal Inspection before Raising FBTR Power to the Target Power	06
1.05	Seismic Qualification of Class-I Power Supply Chargers	08
1.06	Normalization and Qualification of Steam Generators for Full Power Operation	09
1.07	Revamping of the FBTR Cooling Tower of 50 MWt Capacity	10

II. Prototype Fast Breeder Reactor		
2.01	PFBR Commissioning Status	12
2.02	Development and Testing of Main Vessel - Safety Vessel Interspace Crawler System for Inspection	13
2.03	Development of Advanced Position Drive System for Failed Fuel Localization Module	14
2.04	Development of In-Situ Joining Technology for Back-Up Seal and its Demonstration	16
2.05	Development of Models for Simulating Operation Grade Decay Heat Removal System Transients in DYANA-P Code	17
2.06	Design Modifications of Guard Pipes of Intermediate and Decay Heat exChangers to Improve the Gap Between the Inlet/Outlet Nozzle and the Guard Pipe	19
2.07	Deployment of Reactor Core Viewing System and Inspection of Grid Plate Top and Core Sub-Assemblies	21
2.08	Evaluation of response delay for PFBR Core Temperature probe under flow transients	23
2.09	Quality Assurance and Inspection during Fabrication of Nickel Detector Assembly	24
2.10	Miscellaneous Manufacturing activities at Central Workshop Division for PFBR Commissioning	26
2.11	An Application of Level-1 Probabilistic Safety Analysis to PFBR Safety	29
2.12	Testing and Qualification of Selected High Temperature Grease for Gripper Screw in CSRDM	30
2.13	Manufacturing of Annular Linear Induction Pump Components for PFBR	32
2.14	Performance Evaluation of Modified 170m ³ /h Annular Linear Induction Pump in Sodium Loop	35
2.15	Vibration Measurements on Annular Linear Induction Pump of Primary Sodium Purification Circuit in Sodium Facility for Component Testing	37
2.16	Vibration Analysis of Primary Sodium Purification Circuit - Annular Linear Induction Pump	39
2.17	Experimental investigation on Sodium leak through Roof Slab-Large Rotatable Plug Gap under Hypothetical Core Disruptive Accident	40
2.18	Radiography Examination of Annular Joints in Inner Duct of Annular Linear Induction Pump using Special Tool Arrangement	42
2.19	Visual and Dimensional Inspection with Geometric Features of Critical Components	43
2.20	Seismic Analysis of Inclined Fuel Transfer Machine Shielding Door	44

2.21	Experimental Demonstration of Carbonation Method for Neutralisation of Alkaline Solution in a Pilot Scale Test Setup	46
2.22	Performance and Safety Evaluation of Network Components used in Distributed Digital Control Systems	48

III. R&D for Fast Breeder Reactors		
3.01	Sizing of Reactor Assembly for 500 MWe FBRs Meeting the Revised Safety Criteria	50
3.02	Fabrication of Pressurized Capsules of IFAC-1 SS Clad Tube & SS 316LN Plug using Laser Welding for Biaxial Creep Tests	52
3.03	Enhancement of Capability of DHDYN Code for Analysis of Transients in Sodium Decay Heat Removal System	53
3.04	Development of Multi-Coil Eddy Current Probes for Automated Inspection of Irradiated Fuel Pins	55
3.05	Characterization of High Temperature Fracture Behavior of Grade 91 Steel	56
3.06	Measurement of Creep Strain Gradient in U-notched Specimens of Boron added P91 Steel using Video Extensometer	57
3.07	Studies on Carbon Activity Measurement of D9, IFAC-1SS and T91 by Foil Equilibration Method in Liquid Sodium	58
3.08	Synthesis and Characterization of Zeolite and Geopolymer for the Immobilization of Zr, Cr-Constituents of T91 Cladded Metallic Fuel	60
3.09	Measurement of Activity of Irradiated Materials using Hot Cell Gamma Scanning System	61
3.10	Studies on Effect of Pump Inclination on Performance of Active Magnetic Bearing	62
3.11	Indigenous Development of Sodium Service Frozen Seal Gate Valves	63
3.12	Fabrication, Installation and Quality Control of Sodium Piping System in Sodium Technology Complex	65
3.13	In-situ Regeneration of Cold Trap of HEXAMINI Bench Top Sodium Loop	66
3.14	Upgradation of SGTF Sodium Distributed Digital Control System	67
3.15	Studies on Sodium Jet Fragmentation for Determination of Droplet Size Distribution	68
3.16	Hydraulic Studies to Characterise Pore Size of Sintered Micro Filters	69
3.17	Evaluation of Fission Gas-Fuel Particle Unsteady Flow in a Voided Channel under Design Extension Conditions in Sodium cooled Fast Reactors	71
3.18	Laser Surface Remelting of Ytria-Stabilized Zirconia Thermal Barrier Coating for Sacrificial Core Catcher	72
3.19	Ventilation Systems for a Radioactive Micro Analytical Characterization Facility	73
3.20	Structural Modification in Nanocrystalline Ytria During High-Energy Ball-Milling	75
3.21	Thermal Properties of Natural B ₄ C and the Effect of ¹⁰ B Enrichment	76
3.22	A Space Time Kinetics Benchmark Study with Doppler Feedback	77
3.23	Safety Studies Including In-Pin Motion Feedbacks Their Impact on Unprotected Transient Over Power Accident	78
3.24	Numerical Modeling of Ignition and Burning of Cables Exposed to External Heat Source	80

IV. Fuel Cycle		
4.01	Conceptual Design & Development of a Fuel Pin Retrieval System to Retrieval of the Fuel Pins	82
4.02	Sodium Removal using Vacuum Distillation Technique from Sodium Bonded Simulated Metallic Fuel Pins Prior to Reprocessing and from Spent Absorber subassemblies of PFBR	83
4.03	Shield Requirement Analysis for Fuel Pin Gamma Scanner in Fast Reactor Fuel Cycle Facility	85
4.04	Mock up Study of Remote Replacement of Components in a Multiple Pin Chopper for PFBR Fuel	86
4.05	Design, Fire Test Finite Element Simulation of Fire Proof Air Tight Door and its Validation	88
4.06	Design and Development of Wireless Overhead Tank Level Control System for Demonstration Fast Reactor fuel reprocessing Plant`	90
4.07	Development of Air-Sparged Mixer Settlerfor the Treatment of Lean Organic Phase at DFRP	92
4.08	Modification of Centrifugal Extractor Banks of DFRP and Performance Assessment	93
4.09	Flow Sheet Simulation and Optimization of DFRP HC Bank	95
4.10	Reprocessing of High Burn-up Fuel Discharged from FBTR at CORAL	96
4.11	Development of Specialized Remote Handling Tools for Pyro Process R&D Facility	97
4.12	Air and Steam Oxidation Behaviour of Pyrolytic Graphite for Pyrochemical Reprocessing Applications	98
4.13	Design, Fabrication and Commissioning of Precipitator Column for Ammonium Diuranate Precipitation	99
4.14	Development of Remote Handling Equipment for Fuel Reprocessing	100
4.15	Development of Analytical Methods and Processes For Fast Reactor Fuel Reprocessing	101
4.16	Development of a Novel Speed Sensor for the Centrifuges in Fast Reactor Fuel Reprocessing	103
4.17	Development of Vacuum Control System for Vacuum Based Liquid Transfer System in Reconversion	104
4.18	Design, Installation and Commissioning of Averaging Pitot Tube Flow Meters with Wireless Communication for the Exhaust Ducts	105
4.19	Experimental Determination of Phase Equilibria in the system $U_{1-x}Cr_x$ (x=0-55 at.% Cr) by using DTA	106
4.20	Nd(III) Hypersensitive Peak as an Optical Absorption Probe for Determining Nitric Acid in Aqueous Solution: An Application to Aqueous Raffinate Solutions in Nuclear Reprocessing	107
4.21	Pulsating Dielectric based Approach To Determine Tributyl Phosphate in Mixtures Containing TBP and Dodecane	108
4.22	Modeling and Validation of Solidification of Molten Salts	109
4.23	Conversion of 500 m ³ Containment Box from Air to Nitrogen Environment and Achieving Required Purity using Purification System under Negative Pressure	111
4.24	Synthesis of Isorecticular Metal Organic Frame work-3 for Recovery of Uranium from Aqueous Solutions	113
4.25	Interaction of Uranium Ions with Moisture in LiCl-KCl Eutectic Melts	114
4.26	Direct Preparation of Uranium – Titanium (U ₂ Ti) Intermetallic Compound by Direct Oxide Electrochemical Reduction Method	115
4.27	Extraction and Monitoring of Uranyl Ions in Aqueous Solutions using Gel Immobilized Microgel Photonic Crystals	116

4.28	High Temperature Corrosion Evaluation of 2.25Cr-1Mo in LiCl-KCl Molten Salt by Electrochemical Technique	117
4.29	High Temperature Mass Spectrometric Studies on $\langle \text{GdAl}_2(\text{cr}) + \text{GdAl}(\text{cr}) \rangle$ Two Phase Region of Gd-Al System	118
4.30	Design and Development of Machine Vision based Slug Inspection System	119
4.31	Seismic Integrity Assessment of Free-Standing Lead Wall Assembly using a Shake Table Facility	120
4.32	Confirmatory Leak Testing and Qualification of Containment Boxes	121
4.33	Ultrasonic De-Choking Studies on Centrifugal Extractor Bowls	122
4.34	Radiolytic Degradation Behavior of Tri-Iso-Amyl Phosphate/N-Dodecane System Upon Cyclic Irradiation	123
4.35	Performance Assessment of Some In-Cell Equipment for Reprocessing	125
4.36	Testing of Grease for In-cell Application	127
4.37	Development of a Novel Hydroxyacetamide based Extractant for The Preferential Separation of Zirconium from Simulated High Level Liquid Waste Through Liquid-Liquid Extraction and Extraction Chromatography Methods	128
4.38	Design and Structural Analysis of Large Capacity High Level Liquid Waste Storage Tank and Aid on Components for its Handling, Safe Transportation and Installation at the Underground Farms	130
4.39	Catalytic Denitration Process for Treatment of High Level Liquid Waste in Fuel Reprocessing	132
4.40	Quality Assurance and Non-destructive Examination for Rotating Bowl of Centrifugal Extractor used in Reprocessing Plant	133
4.41	Feasibility Studies on use of Single Piece Bottom Closure for geometrically Safe Annular Tanks for Reprocessing Plants	135
4.42	Establishment of Fabrication Sequence during Manufacturing of Jacketed Cylindrical Tanks for Back End Fuel Cycle Facility	136

V. Basic Research

5.01	Development of Portable Cadmium Zinc Telluride based Gamma Radiation Detector	138
5.02	Understanding the Darkening of White Amorphous TiO_2 under X-ray Irradiation	139
5.03	Damage and Recovery by Ion Irradiation in 3C-SiC	140
5.04	Atomistic Simulations of Grain boundary Effects on the Crack Growth Behavior in BCC Fe	141
5.05	Bandgap Opening in Monolayer Graphene by Low Energy Argon Ion Impacts	142
5.06	First Report on Growth of 2D Van der Waals Bonded Bi-layer V_2O_5	143
5.07	Pnictogen Bonding with Nitrogen: Matrix Isolation Infrared Spectroscopic and Computational Studies	144
5.08	Phonon Instabilities and Symmetry Breaking in Uranium Intermetallics: U, U_2Ti and U_2Mo	146
5.09	Tailoring the Polarization and Complex Amplitudes of Light Beams	147
5.10	Virtual Instrument Automation of Ion Beam Analysis and Ion Implantation Experiments for Accelerator Based Materials Research	149
5.11	Evaluation of Spatial Resolution of Gamma Ray Computed Tomography System	150
5.12	The Role of Alkyl Chain Length in Phosphoryl Oxygen Basicity	151
5.13	Correlation Between Anion Related Defects and Ion Beam Induced Luminescence in $\text{Y}_4\text{Zr}_3\text{O}_{12}$	152
5.14	Colorimetric Detection of Nano-molar Oxalic acid at Room Temperature	154
5.15	Investigation of Magnetic and Magnetocaloric Properties of DySe_2	155

5.16	Metal Oxide / Vertical Graphene Nanosheets Hybrid Electrodes for Energy Storage Applications	156
5.17	Effect of Electric Dipolar Interaction on Inter-Droplet Force Profiles in Magnetically Polarizable Pickering Nanoemulsions	158
5.18	Depth-resolved Microstructural Response in He-ion Implanted FeCrCoNi	159
5.19	Structural, and Mechanical Properties of $Y_2Ti_2O_7$ Single Crystal	160
5.20	Blue Luminescence of SnO ₂ Quantum Dots for Selective Trace Ammonia Detection	161
5.21	Structure–Compressibility Correlation among MoB _x	162

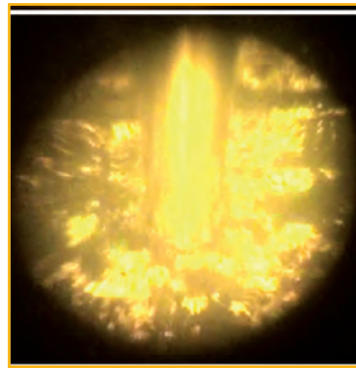
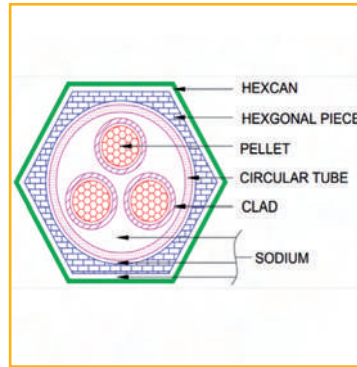
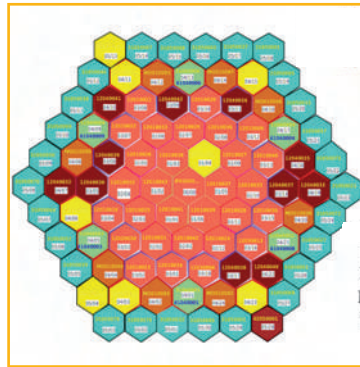
VI. Directed Basic Research		
6.01	Quantitative Recovery of Boron as Boric acid from Enriched Boron Carbide by Pyrohydrolysis	166
6.02	Boric acid as Converter Material for Semiconductor Neutron Detector - A GEANT4 Simulation	167
6.03	Comprehensive Analysis of Evolving Serrated Hysteresis Loops of Alloy 617M in low Cycle Fatigue Under Dynamic Strain Ageing Range	168
6.04	Development of Tools for Enhanced Detection of Flaws in Metallic Materials using Pulse Phase Thermography	169
6.05	Synthesis of Silicon Carbide Capped Cobalt Ferrite Nanoparticles for Organic Dye Removal	170
6.06	New Ways of Fabrication of Superhydrophobic Titanium and Aluminum Surfaces with Superior Antibiofouling and Self Cleaning Abilities	171
6.07	Development of Multi-Mode Plane Wave Imaging Methodology for Mapping of Planar Defects	174
6.08	Efficient Degradation of Organic Effluents using Core-Shell Iron Oxide-MnO _x Nanoparticles via Advance Oxidation Process	175
6.09	Determination of Carbon in Primary Sodium by Distillation-Combustion Followed by Infrared Spectroscopic method: A Feasibility Study	177
6.10	Enhanced Magnetic Fluid Hyperthermia in Copper Ferrite Nanoparticles due to Near-Resonant Relaxation Dynamics	179
6.11	A Novel Method for Thickness Measurement in Conducting Materials by Apparent Conductivity Calculations Through Transient Eddy Current NDE	180
6.12	Depth Measurement of Surface Discontinuities by Ultrasonic Testing Technique in Diaphragm compressor of Additional Up-Gradation Facility	181
6.13	Ultrasonic Testing Methods for Inspection of Large Diameter Bearing Balls	182

VII. Infrastructure, Resource Management & Biodiversity		
7.01	Development and commissioning of an In-Situ Heating System for Elevated Temperature Impact Testing	184
7.02	Design and Development of Standing Wholebody Monitor	185
7.03	Health Physics Surveillance at IGCAR during Special Operations	186
7.04	Safety Management During COVID-19 Pandemic- Prevention of Virus Spread	187
7.05	Water Quality Monitoring System using Pulsating Sensors for Applications in Various Water Reservoirs in IGCAR	188
7.06	Development of Face Recognition Based Attendance Recording System	190
7.07	Commissioning of Private Cloud for providing On-demand Computing and Storage Services at IGCAR	191
7.08	Development USB Access Control System for Desktops	193

7.09	Analysis of Intze Type of Overhead Water Tank for Hydrodynamic Effect	194
7.10	Infrastructure Development at DAE Nodal Center, Chennai	197
7.11	Establishment of Central Water Chilling Plant – II	199
7.12	Green Cover and Biodiversity at Kalpakkam	200
7.13	Digitally Transformed Research Library	204

VIII. Awards/Publications/Events/Organisation

8.01	Awards & Honours	206
8.02	Publications	209
8.03	Events	210
8.04	IGC Council	221
8.05	Activities of Various Groups	224
8.06	Organisation Chart	237
8.07	List of Important Abbreviations	243
8.08	Annual Report Editorial Team	244



Fast Breeder Test Reactor

CHAPTER I

I.01 Design & Development of Nuclear Fuel Management System

Fast Breeder Test Reactor is a 40 MWt / 13.2 MWe mixed carbide fuelled, sodium cooled breeder reactor. FBTR core consists of 745 locations with fuel at the centre surrounded by Nickel reflectors, Thoria blankets and Steel reflectors. Fuel handling (FH) is carried out during reactor shutdown state using charging, discharging and special flasks. FH operations include charging of fresh subassemblies (SAs) into the reactor, transfer of SAs within the reactor, relocation of irradiated SAs from the reactor and storing them in spent fuel storage area.

In FBTR, fuel pins are received in a container called 'cassette' and these cassettes are stored in Fresh Element Storage Area (FESA). Each cassette contains 61 fuel pins and these pins are fabricated into Fuel Sub-assemblies (FSA) in the Fuel Assembly shop. Fabricated FSAs are stored in FESA after inspection and alcohol washing.

Charging of fresh SAs into reactor involves a sequence of operations. Based on Fuel Handling Campaign (FHC) agenda, fresh SAs are ensured to be free from any flow blockage and their foot profile is in accordance with the specified flow zoning. These SAs loaded into a Fresh Fuel Transfer Chamber (FFTC) are transported to the Reactor Containment Building (RCB) and loaded into the reactor using Charging flask.

In-pile transfer operations are done in order to (i) shift fuel SAs from the core position to storage positions for cooling prior to discharging or (ii) interchange fuel SAs within the core to obtain optimum power output or (iii) alter the core configuration as and when need arises to carry out test irradiation/experiments, identification of failed fuel, etc.

Handling of irradiated SAs involves discharging of irradiated SAs from the reactor, their storage in Irradiated Element Storage Area (IESA) and transportation to RML/RDL/CWMF.

The movement of SAs between various work posts is shown in Figure 1.

To have an inventory record of fresh and irradiated SAs as well as to track the movement of SAs from one position to another position within the reactor core and outside the core, a PC based stand alone system, namely Nuclear Fuel Management System (NFMS) was designed and developed.

NFMS system was developing Net Beans IDE 8.2 with MySQL as back ended database. NFMS system shall provide user interface to enter/edit the data and also to view the information. Figure 2 shows the user interface to enter the data at various stages of fuel movement.

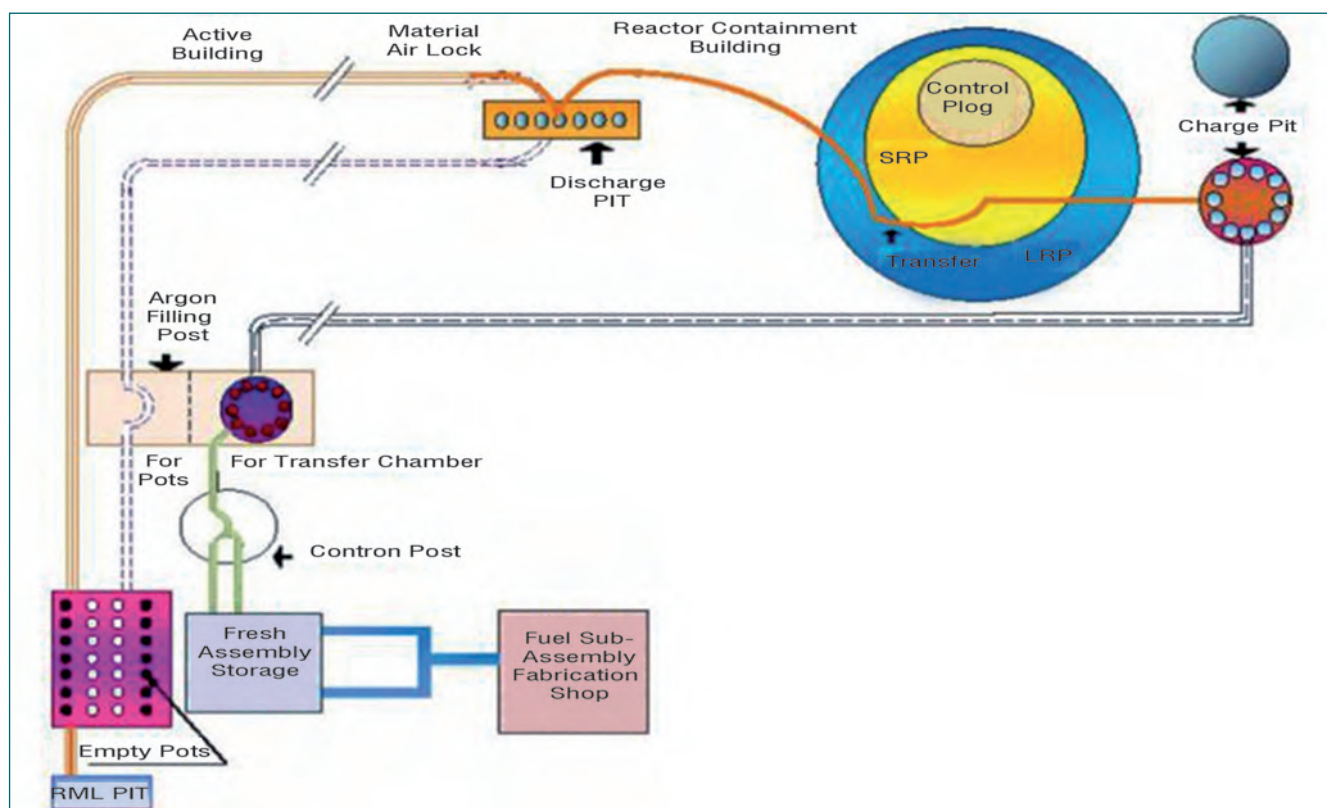


Fig. 1 Movement of SAs in various work posts

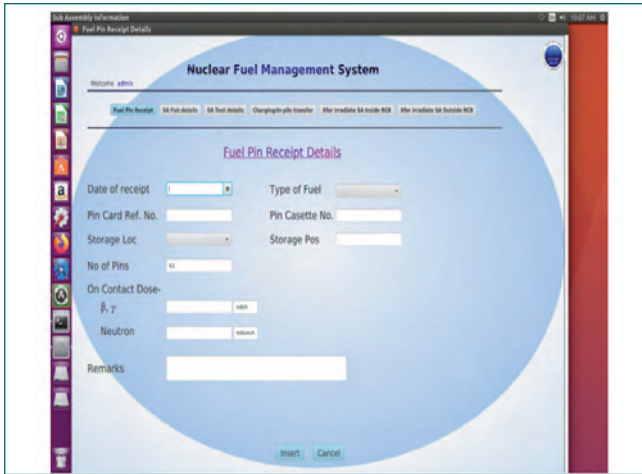


Fig. 2 User interface to enter data

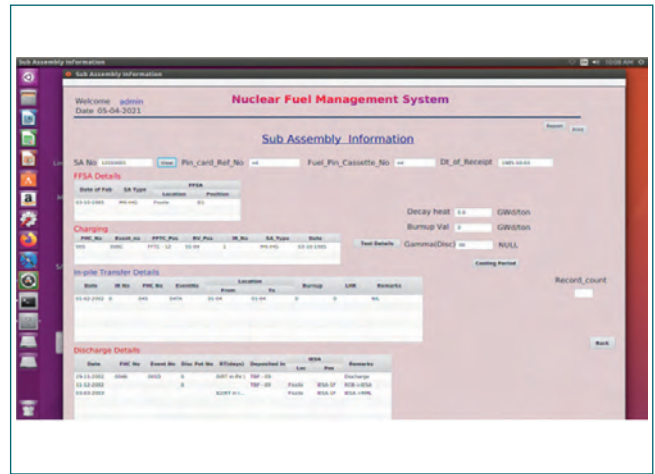


Fig. 3 SA information

Major functions performed by NFMS are

- Track the movement of different types of SAs from one work post to another before loading into reactor
- Track the movement of different types of SAs within the reactor during different fuel handling campaigns
- Display reactor core configuration for each irradiation campaign(IRC)
- Inventory of fuel pin cassettes, fissile and non- fissile SAs in Reactor, FFSA, IESA and details of the SAs which were sent to RML/CWMF

Entered data will be stored in database and enables the user to view details such as Inventory Information, Irradiation & FHC information, Core Configuration, Core Position, SA Test Details & SA Tracking Information.

SA Tracking information will provide the complete details about the movement of selected SA in FFSA

before loading into reactor, movement within the reactor during different irradiations, movement in Transfer block position and in IESA etc. Figure 3 shows the SA information display.

User can view the core configuration for a particular IRC along with total number of fuel SAs as shown in Figure 4.

NFMS is a standalone system and as it deals with vital information related to special nuclear material (SNM), only privileged users as per plant policy are allowed to have access to this system. Since sensitive data are stored in the database, internet access to the server system is disabled. Only authorized persons with appropriate privileged level are allowed to enter or edit the data through GUI. The inventory and tracking information is made available only to the authenticated users.

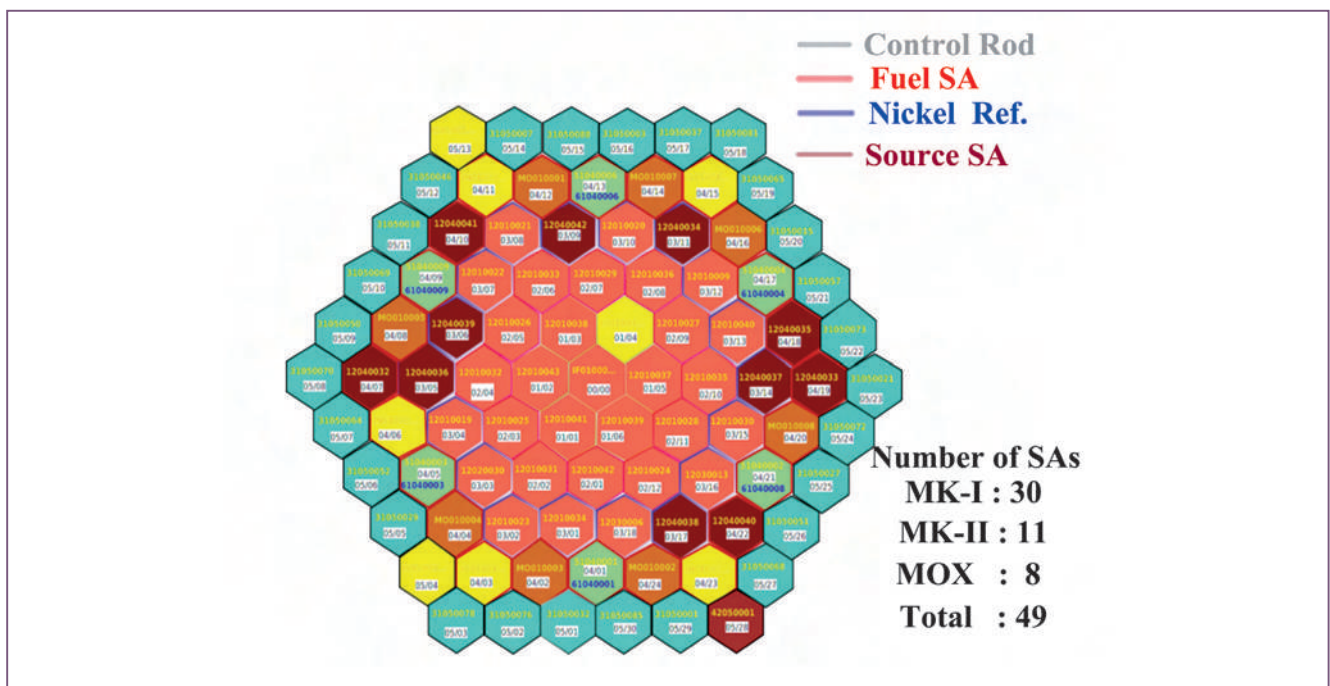


Fig. 4 Core configuration

I.02 Estimation of Life of Poison Subassembly for FBTR 40 MWt Core

For maintaining the shutdown margin, four number of poison subassemblies (SAs) are to be loaded in the second ring of FBTR core. The schematics of poison SA are indicated in Figure 1. The maximum power in poison SA is 35.73 kW corresponding to peak LHR of 1140 W/cm. The designed flow through poison SA is 0.409 kg/s with which Design Safety Limits (DSL) for nominal and 16% overpower conditions are met. The neutron flux at the poison SA region is 2.6×10^{15} n/cm²/s. Due to the hostile environment of the reactor core in terms of higher neutron flux and temperature, the structural material of the SA would undergo degradation and deformation due to irradiation swelling and creep, limiting the life of the poison SA in the reactor. The various parameters which govern the life of poison SA (apart from ¹⁰B depletion) are:

1. Closure of inter SA gap from hexcan dilation
2. Pellet-clad mechanical interaction (PCMI)
3. Ductility exhaustion limit of wrapper
4. Ductility exhaustion limit of clad
5. Flow reduction in the SA
6. Respecting the DSL limits

The life of the poison SA worked out based on the first four parameters are given in Table 1 while the last two parameters are checked for the computed dose limit. It is inferred from the table that the life of poison SA is limited from inter SA gap closure due to hexcan dilation. The gap closure occurs at a fluence of 8.83×10^{22} n/cm² (63 dpa).

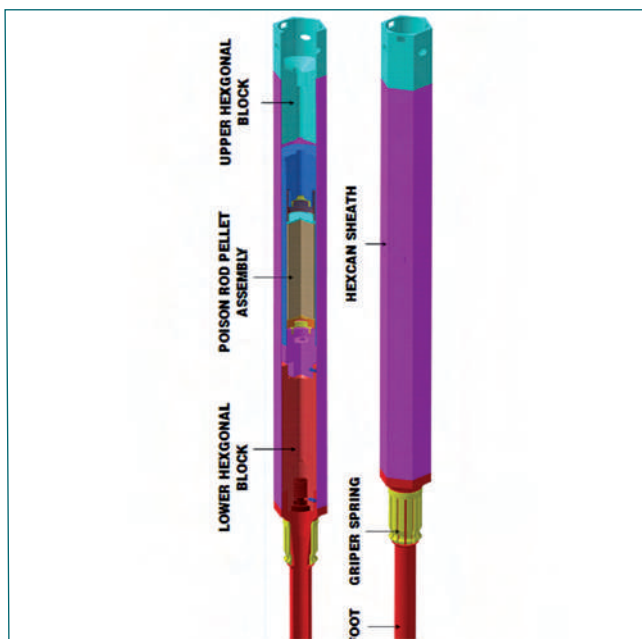


Fig. 1 Schematics of Poison sub-assembly

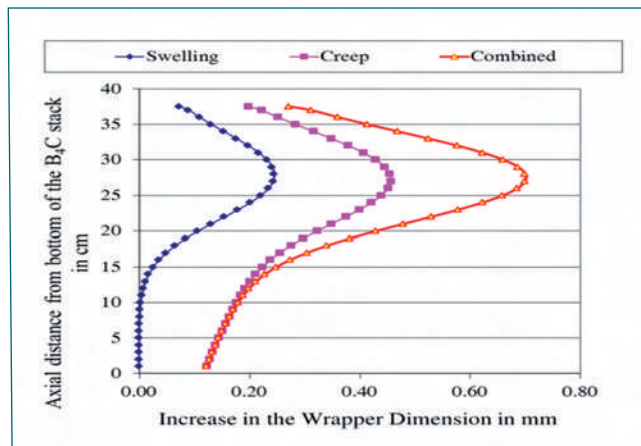


Fig. 2 Swelling and creep components in dilation of hexcan

The axial variation of swelling and creep components in dilation of hexcan is shown in Figure 2.

At 63 dpa, the change in flow rate due to swelling is found to be negligible (< 0.1 %). Since there is no change in flow rate of the SA up to a target 63 dpa, clad and wrapper temperature remains same as initial design. For the estimation of temperature of poison pellet, reduced thermal conductivity (50 %) was considered in the initial design itself. Further, with sodium infiltration into the pellet, the thermal conductivity will increase, which is conservatively ignored in the present analysis. Hence, no increase in the centerline temperature is expected from the design value.

From the above analysis, the life of the poison SA is fixed as 1.39 years of full power operation equivalent to 63 dpa for the initial target. With subsequent Post Irradiation Examination after the target dose, the limit will be re-confirmed.

Table 1: The limits for SA life based on the various parameters			
S. No.	Parameter	Poison SA life	
		Years of full power operation	dpa for steel
1	Dilation of hexcan	1.39	63
2	Pellet-clad mechanical interaction	5.97	269.9
3	Ductility exhaustion of wrapper	2.28	103.2
4	Ductility exhaustion of clad	2.55	115.1

1.03 Estimation of Pressure Drop and Temperature Distribution in Large Bore Subassembly Intended for Yttria Capsule Irradiation

Large Bore Subassembly (LBSA (Sr-89)) was designed and developed to irradiate a capsule containing three numbers of Yttria (also known as yttrium oxide, Y_2O_3) pins in FBTR core for the production of strontium-89 isotope. It is planned to be loaded at 5th ring of FBTR 40 MWt core. Pressure drop calculations are carried out for different regions of the LBSA (Sr-89) to estimate flow through the SA. The minimum flow required to meet Design Safety Limits (DSL) on temperature of LBSA and corresponding temperature distribution is estimated using CFD simulations.

SA Description

The SA houses three Yttria pins of length 530 mm each at the center. The pin has Yttria stack of length 440 mm which is enclosed in clad and closed by steel end plugs. The three pins of Yttria in a triangular pitch are enclosed by circular tube. The circular tube (irradiation capsule) is surrounded by hexagonal piece and hexcan wrapper. The sodium flows through the capsule, capsule-hexagonal block gap and hexagonal block-hexcan gap. A typical cross section of LBSA (Sr-89) in active core region is shown in Figure 1.

Flow Distribution

Pressure drop in different regions of LBSA (Sr-89) is calculated using empirical correlations from literature and with loss coefficients determined using CFD. The schematic of the flow resistance path is as shown in Figure 2. Coolant flow enters the foot region axially. Coolant from the foot region splits into three paths above the SA foot region- flow through the irradiation capsule (Path-1), flow through the annular gap between irradiation capsule and hexagonal block inner surface

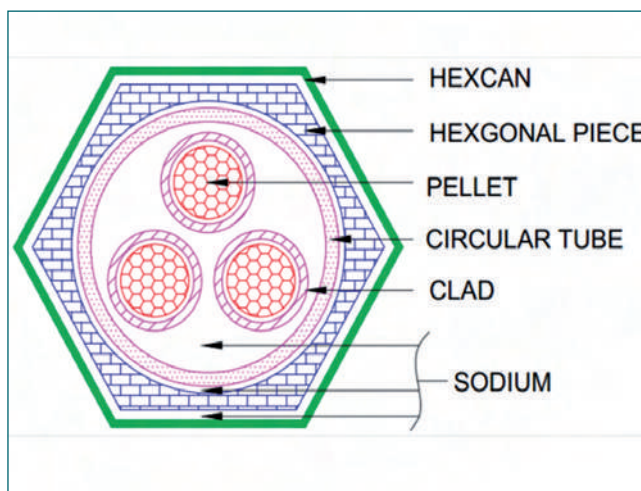


Fig. 1 Cross section LBSA at active core region

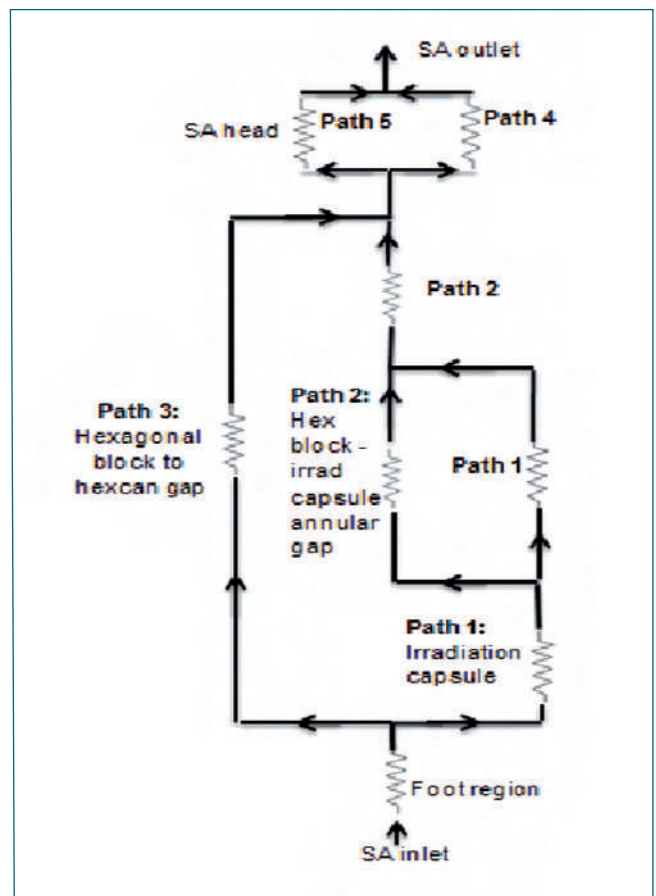


Fig. 2 Flow resistance path of LBSA (Sr-89)

(Path-2) and flow through the annular gap between the hexagonal block and hexcan (Path-3). The subassembly head consists of two flow paths for the coolant- flow through the central part of head (path-4) and flow through the peripheral gap between head components (path-5). These two flow streams exit to the coolant pool above the subassembly. For a FBTR core pressure drop of 33 m of sodium, total flow through subassembly is 0.46 kg/s.

Temperature Distribution

Heat generated in yttria pellet stack and other steel structural components is extracted by the liquid sodium flowing in three paths by conduction and convection. The minimum flow through SA to satisfy the temperature DSL is estimated using 3D CFD simulations. It is found that as the flow is reduced, the DSL corresponding to hotspot clad midwall temperature is reached earlier than the rest of the DSLs. The minimum flow satisfying all DSL is 0.074 kg/s for the irradiation of LBSA in 5th ring of 40 MWt FBTR core. But as the LBSA is designed for different irradiation programs in the core, the flow through SA is retained as 0.46 kg/s.

I.04 Reactor Vessel Internal Inspection before Raising FBTR Power to the Target Power

The internal of the Reactor Vessel (RV) have to be visually inspected by the periscope using the lighting provided by the projector. Non-plugging of Siphon Break Pipe (SBP), which prevents complete draining of RV in case of sodium leak outside RV and Emergency Injection Pipe (EIP) were to be verified once in two years by this visual inspection. This is a mandatory requirement as per FBTR technical specification. Projector and periscope were tested for its healthiness prior to installation (Figure 1).

Previous RV internal inspection was carried out in 2019 and reactor was operated for 1696 hours at 32 MWt subsequently. This inspection was carried out as pre-requisite before raising the reactor to its full power of 40 MWt. The data obtained from the present



Fig. 1 Periscope and projector as installed in the pile

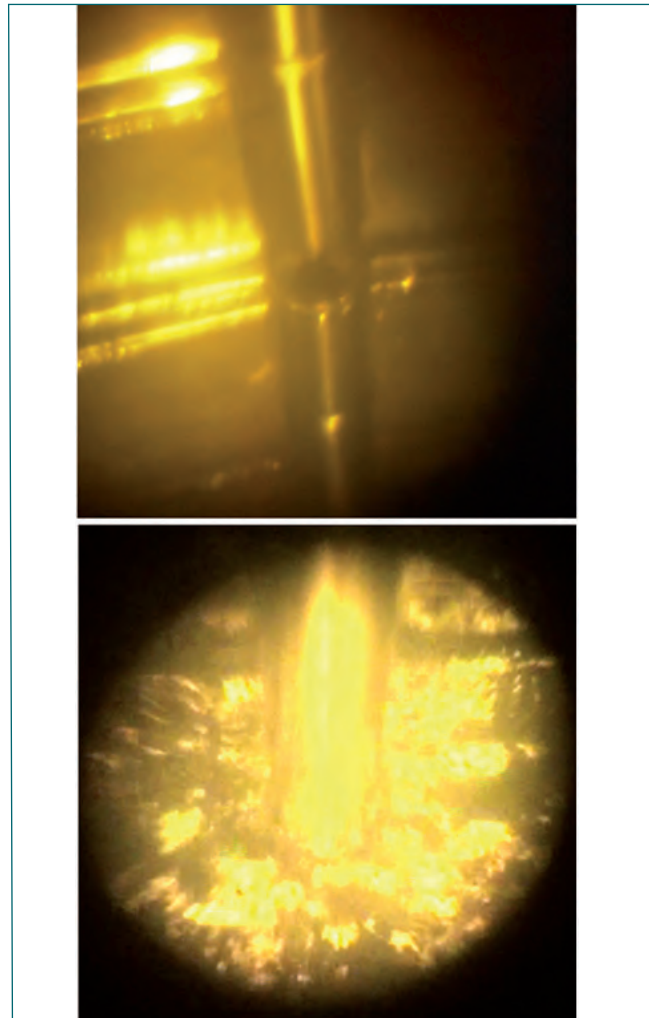


Fig. 2 Gap between SBP and its reflection and sodium flow through SBP in sodium

inspection campaign will also form the base line data for further high power operations.

Internal inspection of RV was carried out both in the partial sodium drained condition and as well as in sodium filled condition by rotating the rotating plugs and swiveling the objective prism of the periscope. Observations during the inspection are mentioned below.

SBP and its reflection in sodium are very clear (Figure 2). Flow through SBP was established by running one primary sodium pump at low speed to verify the non-plugging of SBP. Sodium flow was found to be smooth and clear.

Flow through EIP by injecting sodium from flooding tanks was observed through periscope after normalizing sodium level in the reactor. Clear, shining, smooth sodium flow was seen covering the entire cross section

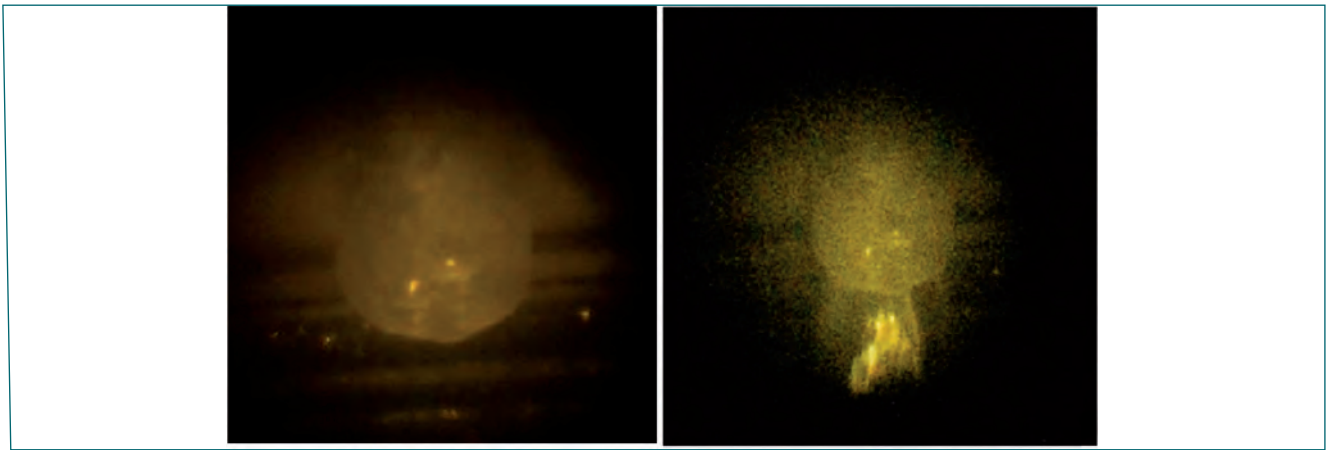


Fig. 3 EIP before flooding and flow through EIP

of the pipe (Figure 3). Sodium flow was comparable with the earlier inspection campaigns. More sodium oxide deposits were observed on the edges of the free end of EIP. Visual inspection was also utilized for ensuring non-plugging conditions of other pipes like Sodium Purification Return Pipe (SPRP), Over Flow Pipe (OFP), Argon pipe, healthiness of bolting of the flow restriction shell on outlet pipe and observing deposits of sodium and sodium oxides on the vessel wall. In the partial drained condition, SPRP free end

along with reflection in sodium was clearly seen. Pipe opening was clear with no plugging. OFP was also seen with no sodium deposits and clear vortex sodium flow through OFP was also observed in sodium filled condition. Argon pipe opening was clear with no sodium deposits (Figure 4).

Both continuous and discontinuous level probes were seen intact and intermediate vibrations were observed in one of the discontinuous level probes similar to the earlier inspection campaigns and was within the acceptable level. The gaps between the thermal shields were seen more clearly, except observation of non uniform gaps between the thermal shields in some segments as observed in earlier inspection campaigns (Figure 5). The support pins for the thermal shields were seen intact during partial drain condition. Sodium deposits were observed in RV flange and on adjoining RV vessel surfaces and on surfaces of thermal shields, which may be due to long shutdown of the reactor.

No other abnormalities were noticed during the inspection. The data obtained during the present visual inspection also gives us further confidence for operation of reactor at its full power of 40 MWt.

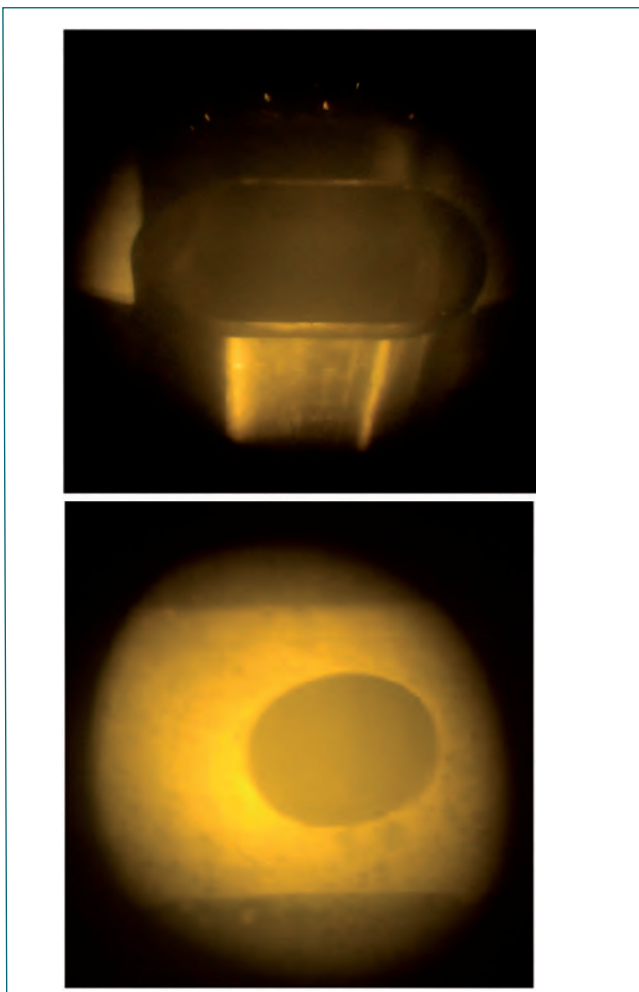


Fig. 4 OFP in partial drained condition and argon pipe



Fig. 5 Thermal shields

I.05 Seismic Qualification of Class-I Power Supply Chargers

The class-I power supply system of FBTR consists of 24 V, 48 V and 220 V DC station battery banks and their respective chargers which cater the needs of control power supply of the plant. In addition to this, each primary sodium pump drive system consists of 2 numbers. of dedicated 48 V DC battery banks and their chargers for field and armature circuits of DC motors of the pumps. These battery banks are required to run the pumps for decay heat removal during the station blackout condition.

These chargers were in continuous service for the past 35 years. As a part of ageing management and post-Fukushima retrofit, it was planned to replace the old chargers with state-of-the-art seismically qualified chargers.

In the first phase, the retrofitting work of 48 V DC chargers of sodium pump drive system was taken up. The system consists of 4 numbers. of 48 V, 30 A rated chargers. Initially one prototype charger was seismically qualified in Structural Mechanics Laboratory (Figure 1). The test was conducted as per the approved test procedure based on the IEEE Standard for Seismic Qualification of Equipment for Nuclear Power Generating Stations, IEEE Std 344-2013.

The structural integrity and functional operability of the battery charger was confirmed using Review Based Ground Motion (RBGM) spectra with 5% damping ratio taken as Required Response Spectra (RRS). The test matrix consisted of resonance search tests followed by one Safe Shutdown Earthquake (SSE) test for the floor response spectra (Figure 2).



Fig. 1 Prototype 48 V DC charger in shake table

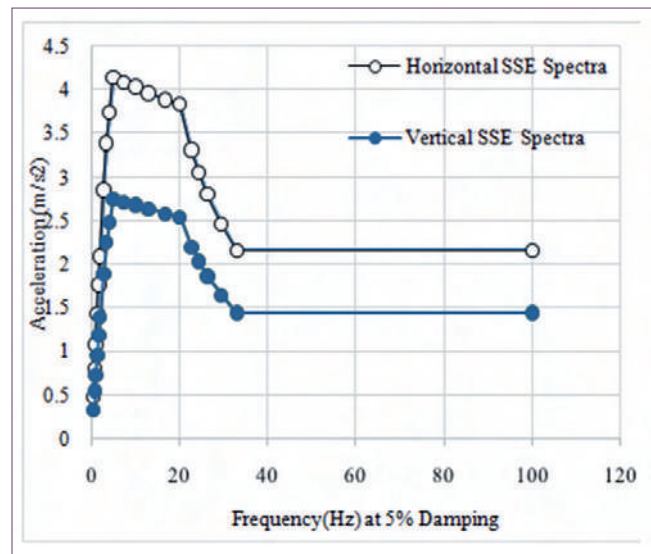


Fig. 2 Floor response spectra for SSE

To measure the acceleration responses, four tri-axial accelerometers were used. To measure the structural damage of the panel, three bi-axial strain gauges and four uni-axial strain gauges were installed at critical locations.

In the second phase, the retrofitting work of 24 V DC, 110 A rated chargers of control power supply system was taken up. The system consists of 3 main chargers and one standby charger. One prototype charger was seismically qualified using similar procedure (Figure 3).

Both the chargers have been qualified successfully in the seismic test. Retrofitting of the other chargers is in progress.



Fig. 3 Prototype 24 V DC charger in shake table

I.06 Normalization and Qualification of Steam Generators for Full Power Operation

Steam Generator (SG) of FBTR is an once through shell and tube type counter flow heat exchanger which generates superheated steam at 125 kg/cm² and 480°C. There are two SG modules in each east and west secondary sodium loops. Out of the total 4 modules, three are made of 2.25Cr-1Mo-Nb Stabilized ferritic steel and one of 9Cr-1Mo-Nb Stabilized ferritic steel. In the SG module, sodium flows through shell side and water/steam through the tube side. In order to operate the reactor near or its design temperature at reactor power lesser than the design power, 3 out of the 7 tubes in each SG module were blanked in 2008. The Reactor was operated with partially blanked SG tubes till 29th irradiation campaign (Figure 1).

From 30th irradiation campaign onwards, it is planned to operate the reactor at design power level. This necessitated the normalization of the blanked tubes of SG modules.

Before starting the normalization work, welding procedure sequence and welder performance qualification were carried out for meeting the FBTR specifications. As FBTR Steam Generator modules were fabricated with different materials for Steam Header and Water Header of individual modules, separate procedure and performance qualifications were carried out.

After successfully completing the qualification requirement, mock-up trials were made for the weld

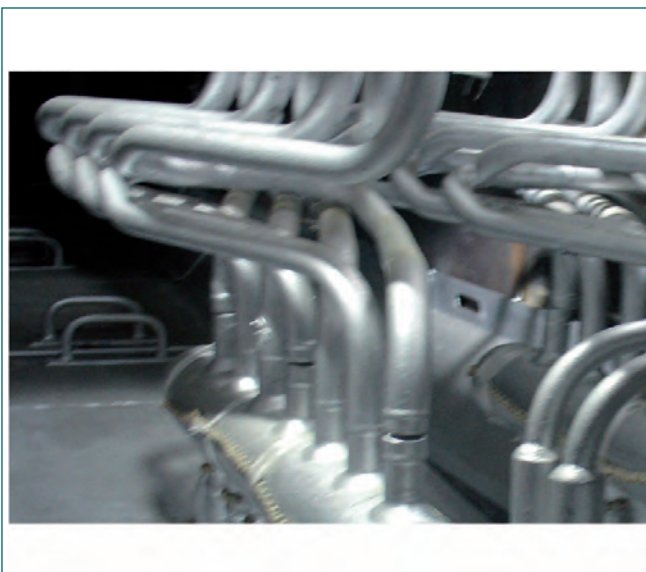


Fig. 1 Tubes of SG in blanked condition

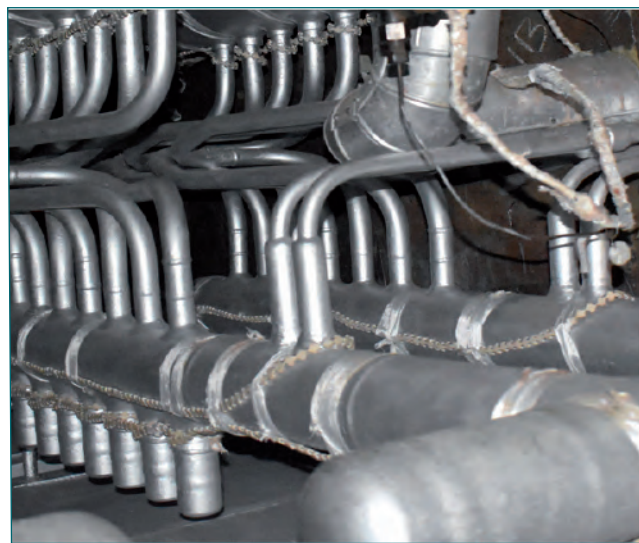


Fig. 2 Tubes of SG after normalisation

configurations simulating the site constraints to train the working personnel as the entire welding work has to be performed in the highly congested SG cabin. Difficulties were faced in the internal grinding of SG tubes. To overcome this, a special purpose ID grinding tool was fabricated for SG tubes. For normalization, 12 blanked portions in each SG modules were to be cut and normalized.

After gaining sufficient confidence from the mock-up trials, caps of blanked tubes were cut suitably, spool tube piece was introduced between the open ends and welded. Gas Tungsten Arc Welding (GTAW) process with argon gas purging was used for welding. Every day, before commencing the actual job, trial pieces were welded to establish the consistent performance of welders. Tube internal areas were visually inspected with videoscope before fit-up. Weld edges were also visually inspected to avoid any abnormalities before fit-up. Liquid Penetrant Test (LPT) was carried out on weld edges to detect any surface defects. Spool material was tested for its conformability to the joining tube material before making the weld joint with X-ray fluorescence spectroscopy.

After successful completion of all the welding works (Figure 2), Post Weld Heat Treatment (PWHT), Liquid Penetrant Test (LPT), Radiographic Test (RT) and Helium Leak Test (HLT) were carried out for all the weld joints. Finally, SG was subjected to hydro test at 135 bar. SG was normalized. Water and sodium were valved in and is kept in service.

I.07 Revamping of FBTR Cooling Tower of 50 MWt Capacity

The ultimate heat sink for FBTR is a 50 MWt evaporative Cooling Tower (CT) located at the Northern side of FBTR. It is an induced draft, cross flow and wet type one. There are four cells and each cell is provided with an induced draft fan at the top. Hot water from the plant sprayed from the top of the cells through distributor channels over the fills. Air is drawn from the bottom of the CT. The water is cooled mainly by evaporative cooling. The cold water collected at the CT bottom is brought back to the cooling water pit in the plant through an underground concrete channel.

The cooling tower was revamped in 2000-2001 earlier. Over the years, the performance was getting gradually affected due to ageing of components. Hence, it was decided to completely revamp the CT with fresh fill materials, drift eliminators, etc.

Specifications of the cooling towers are given below:

- Cooling tower model: WHP-1004
- Type: Induced draft wet type cooling tower
- Design cooling tower capacity: 50 MWt
- Total cooling water flow rate: 4200 m³/h
- Total dry air flow: 2,423,822 kg/h
- L/G: 1.7228
- Range: 9.22°C
- Approach: 6.67°C

Material Specifications

- The Splash Bars are of “V” section and perforated made from PVC for excellent resistance to corrosion and give maximum wet area
- Splash bars are supported on SS - 304 grids for positive and permanent positioning
- Drift Eliminators: UV resistant rigid PVC designed to remove entrained particles from air stream efficiently with minimum pressure drop thereby reducing the fan power requirement when the air passes through the Drift Eliminator.

- Synthetic resin bonded glass fiber sheets are used on air inlet louvers of cooling tower
- Wooden components: Fabricated from Douglas fir timber, “Grade-II” as per CTI STD-114

Acceptance Criteria of Materials

The design, manufacturing and testing of all the materials conform to the relevant standards.

- Cooling tower timber components - Physical and Mechanical tests as per IS: 1708-1986 and Chemical Treatment tests as per IS: 401-2001.
- Marine grade Plywood - Physical & Mechanical tests as per IS 710: 2010.
- Synthetic resin bonded glass fiber Sheets - Physical, Electrical, Mechanical and Thermal properties tests were tested as per IS 10192: 1982.
- PVC items material (PVC V-bar, PVC Drift Eliminator) physical properties, burning properties and recommended testing procedures employed to determine the defined values are confirmed as per CTI STD-136.
- SS hardware: IS 1367
- SS 304 Grid wire: IS 6528

Revamping of Cooling Tower

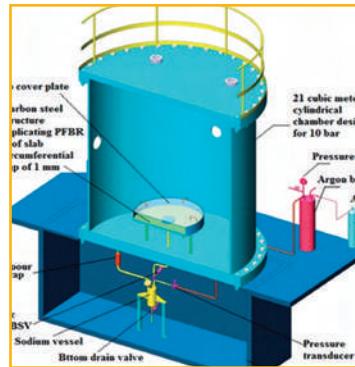
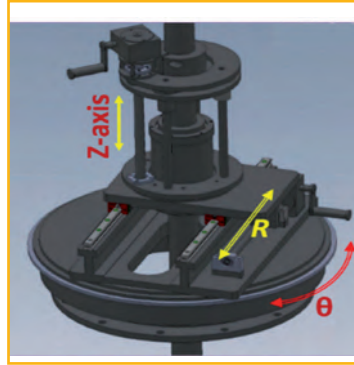
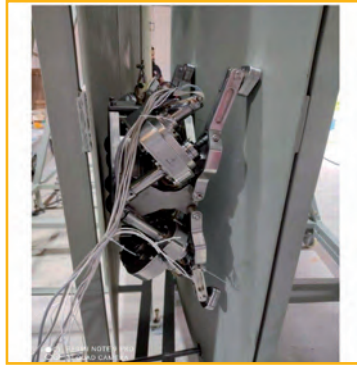
Cooling tower internals were completely dismantled and refurbished. The exiting cooling tower splash box and cover assembly on water distribution system, PVC ‘V’ type splash bars, Splash bars support grid system, PVC drift eliminators and GI corrugated louver sheets were dismantled completely. The fresh splash box and cover assembly on water distribution system, PVC ‘V’ type splash bars, splash bars support grid system, PVC drift eliminators, air inlet louver synthetic resin bonded glass fiber sheets were erected. The refurbished cooling tower was put into service. The structural stability of all the internal materials were checked and found to be satisfactory.



Fig. 1 FBTR 50 MWt cooling tower before revamping



Fig. 2 FBTR 50 MWt cooling tower after revamping



Prototype Fast Breeder Reactor

CHAPTER II

II.01 PFBR Commissioning Status

Prototype Fast Breeder Reactor (PFBR) at Kalpakkam is a 500 MWe (1250 MWt) liquid sodium cooled, pool type fast reactor using mixed oxide of uranium and plutonium as fuel. The plant is located 500 m south of the existing Madras Atomic Power Station. After completion of construction, manufacture & erection of all the structures, systems & components of PFBR, commissioning of the individual systems, the integrated commissioning is in progress. Figure 1 shows the overall view of PFBR. The major works that have been completed during the year 2021 are as follows:

Modification of guard pipe nitrogen circuit pipe lines of decay heat exchanger & intermediate heat exchanger lines were completed towards design improvement which is based on detailed analysis. As part of refurbishment activity, replacement of balls in the Small Rotatable Plug (SRP) ball bearing has been taken up. The performance of both Large Rotatable Plug (LRP) and SRP bearings during testing was found to be satisfactory. During refurbishment activity, inflatable seals integrity was also checked and backup seal was replaced.

Trailing cable system connection was carried out to facilitate in-situ inflatable seal replacement in future. Commissioning of fuel handling systems is in progress in parallel.

In order to carry out internal inspection of reactor hot pool, reactor core viewing system was deployed. Another important activity taken up was the refurbishment of control and safety rod drive mechanisms. Filling of sodium in purification circuit 1 of safety grade decay heat removal system was completed and it was put into service. Rectification, design validation and functional testing at room temperature as well as elevated temperature of In service inspection vehicle DISHA was carried out at site assembly shop. In addition, functional testing of multi-purpose flask at site assembly shop was completed.

Presently all the preparatory works for carrying out preheating of main vessel after completing the modification on dummy subassembly and filling of sodium in main vessel are in progress.



Fig. 1 Overall view of turbine and nuclear island connected building

II.02 Development and Testing of Main Vessel - Safety Vessel Interspace Crawler System for Inspection

Periodic inspection of the Main vessel (MV) and Safety Vessel (SV) of PFBR is important to assess their structural integrity and to take remedial measures, whenever needed. As the MV of PFBR is inaccessible from the inside, its inspection can only be performed from outside. The MV is surrounded by SV forming the annular MV-SV inter-space gap of 300 ± 50 mm, which has to be utilized for deploying remotely operated devices for the inspection of both vessels. Six access chutes are provided on the reactor vault through which the inspection device(s) will have to be deployed into the MV-SV annular inter-space, for the inspection of the MV and SV. In view of the above requirements, a Main-Vessel Safety Vessel Inter-space Crawler (MSISC) (Figure 1) is designed.

The design of the MSISC crawler was conceived in-house and exhaustive feasibility studies were conducted using 3D CAD models for refinement. The crawler system envisages friction gripping to cling to MV/SV walls. The crawler enters into the annular inter-space in collapsed conditions and expands to adapt to the MV/SV inter-space gap of 300 ± 50 mm. The crawler consists of seven dedicated modules viz. (a) Friction Actuator Module (FAM) (Figure 2): for friction gripping and inter-space gap adaptation. (b) Steering Assembly Module (SAM): for steering the crawler along the desired directions. (c) Traction Actuator Module (TAM): for providing traction to the crawler. (d) Drive System Module (DSM): for protecting the motor drives. (e) Emergency Recovery Module (ERM) for emergency handling. (f) Crawler Control Module (CCM): a distributed control system and communication architecture for operation (g) Soft Intelligent System Module (SIM): a bundle of firmware/ software for the intelligent

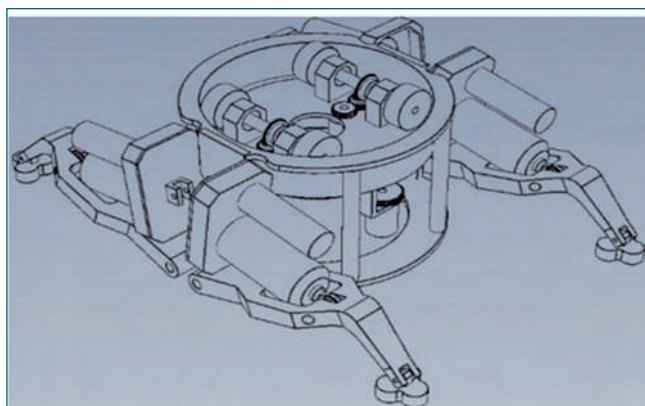


Fig. 1 Main-vessel safety vessel inter-space crawler

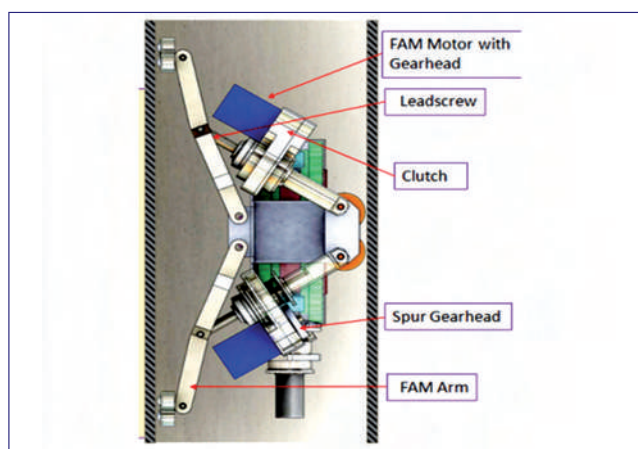


Fig. 2 CAD model of FAM of Main-vessel safety vessel inter-space crawler

operation of the system considering safety and reliability. The design is completed in all aspects and the actuator sizing & the system geometry is fixed. The kinematic analysis of various links in FAM has been done to meet the required motion of 300 ± 50 mm annular space. After completing the kinematic analysis for various friction coefficients, the torque requirement has been estimated & the actuator has been selected accordingly. A mock test setup is also designed to perform stage-wise testing and validation of the design. Figure 3 shows the test setup in which MSISC system (for concept validation & room temperature trials) gripping the walls and balancing the system weight. Motor tuning of all 7 motors was done for simultaneous operation of various modules. Further, each component was integrated and inspected to meet specification requirements. Various trial of MSISC was carried out at the supplier site at room temperature in the mock test set up and all modules were found to be working effectively. The same system has been commissioned at the IGCAR site and further trials are underway.



Fig. 3 MSISC system gripping on the wall

II.03 Development of Advanced Position Drive System for Failed Fuel Localization Module

Function of Failed Fuel Localization Module (FFLM) in PFBR is to locate the fuel subassembly (FSA) with failed pin after getting indication from global Delayed Neutron Detector (DND) system. The mode of detection is by monitoring the presence of delayed neutrons in the sampled sodium issuing out of FSA. There are 3 identical FFLMs housed in Control Plug, each one for monitoring 66 FSA positions. The FFLMs are housed in the control plug. FFLM selector valve housing is an integral part of the control plug. The top plate of FFLM is fastened with the flange of the selector valve housing. Each FFLM is taking care of sampling from 66 fuel sub-assemblies (FSA). The sodium flow diagram of FFLM is shown in Figure 1. Sodium sampling tubes, concentric over each thermocouple passage tube, are positioned above the top of each FSA (except the central FSA). The other ends of the sampling tubes are connected with the base plate of the selector valve of FFLM.

Advanced Position Drive System (APDS), shown in Figure 2 is the main control system to position the selector valve. Fuel Subassembly sampling tubes in the user interface are placed in two concentric circles, inner circle and outer circle. Each circle has thirty three representative sub assemblies sampling positions. Outer circle subassemblies are numbered from A1 to A33 as shown in Figure 3. Inner circle sub assemblies are

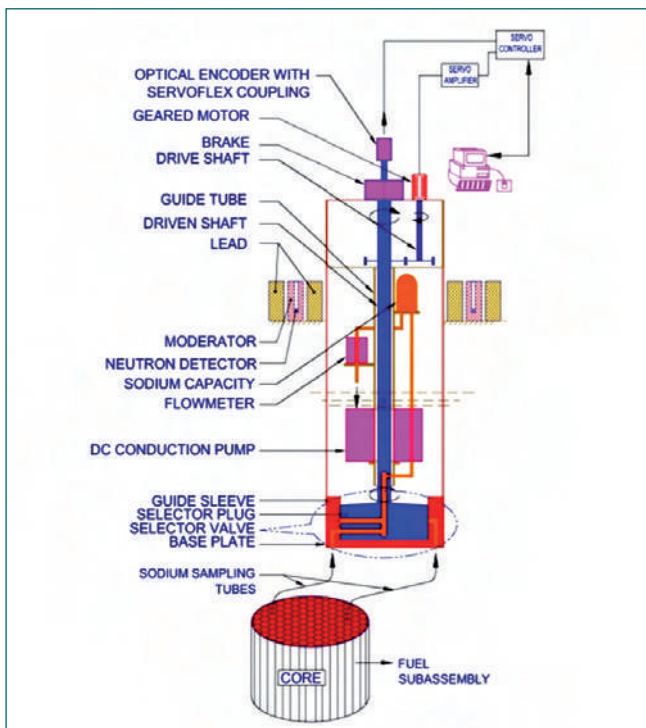


Fig. 1 FFLM sodium flow diagram

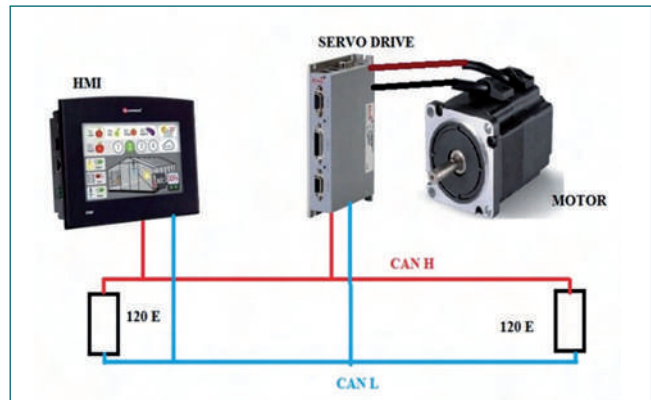


Fig. 2 APDS control block diagram

represented by numbers A34 to A66. For any FFLM, A1 is taken as the reference tube with position as zero reference with angle theta equal to zero degrees. The purpose of APDS is to align the sampling point precisely over the selected subassembly sampling point. It consists of Controller Area Network (CAN) communication network interconnecting a DC Servo Drive, Human Machine Interface (HMI) and motor. The HMI sends the commands over the reliable CAN network through interconnecting CANopen protocol and Servo Drive decodes the commands and moves the motor. The brushless DC Motor is connected to the FFLM mechanical assembly to make the selector valve move to collect the samples of sodium for the delayed neutrons. APDS support different modes of operation Auto and Manual for inspection in which it has cyclic and acyclic mode of operation for optimizing minimum backlash and minimum time. APDS supports advanced initialization in which different homing procedures are feasible. Manual mode of homing is a man in loop operation where APDS drives to match the ref position A1 and position reach is

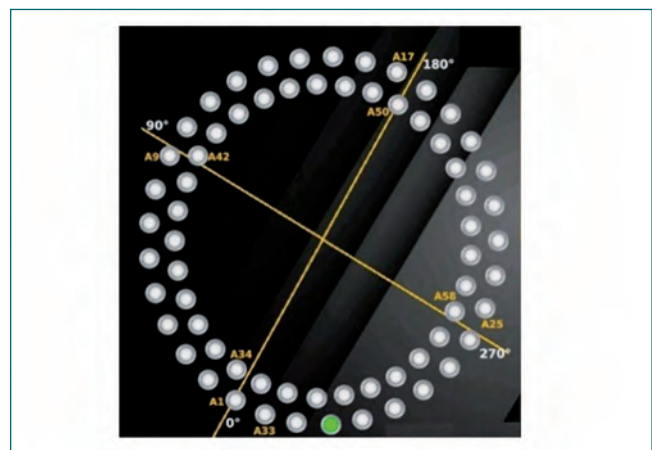


Fig. 3 APDS user interface showing SA position

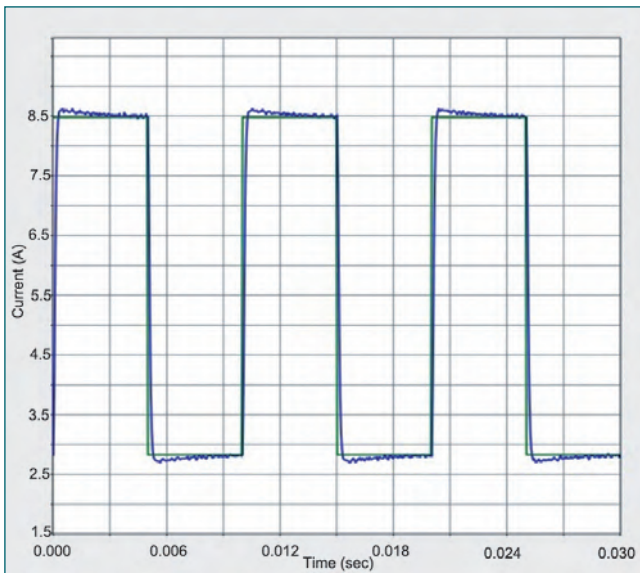


Fig. 4 Time response plot during dual loop tuning

checked and verified manually. In Auto Mode of Homing, automatic Homing is done with the help of optical non contact type limit switch placed on the reference position. In advanced Auto Homing, limit switch is placed in an arbitrary position and system computes the offset with respect to reference position and on the fly correction for each tube position reach is carried out. This provides an advantage of placing limit switch anywhere in the rotating plate. The generic formula for computing the position of SA has been derived, and this will avoid the need for storing the values in the lookup table. In this calculation, the absolute angle values of position of each subassembly with reference to the reference position is calculated.

Processor in the Loop (PIL) Tuning methodology has been used for tuning of FFLM. The open loop system characterization is obtained by exciting the plant with standard input signals and system response is measured. The Plant transfer function is derived and closed loop system behavior is predicted for various gain parameters. This provides insight to various parameters like Gain Margin, Phase Margin, Gain crossover

frequency, Phase cross over frequency and plant stability. By carefully choosing the gain parameters, the best stable system is designed. The best gain parameter which suits for the optimum operation is designed and programmed into the servo controller in dual loop mode. Dual loop tuning removes the backlashes in the gearboxes and by providing the feedback at the load end. This scheme improves the accuracy in positioning. Figure 4 shows time response plot during the dual loop tuning.

HMI graphics user interface(GUI) has been developed and programmed using IEC 61131-3 standards to interface with Servo Drive. GUI has been divided into many screens as per the functionality like settings, initialization, operation, diagnosis and reports. Figure 5 shows the operation page of APDS where any tube can be selected for sampling. It also features provisions for auto scanning of tubes with user defined delay time. In house design of solid state relay board for brake control of FFLM has been carried out. The Relay board was designed, fabricated and integrated to Servo Drive for synchronized operation and also integrated with HMI with a manual overriding feature for any maintenance activity.

APDS is tested and qualified using a test setup as shown in the Figure 6. Using the test setup, all the sub-assembly positions are tested and qualified. Motion control system is tuned and gain parameters are set. Tests for repeatability and accuracy are also carried out. Various modes of operation of the device are also tested and verified. The functionality testing which includes initialization, calibration, sampling operations are carried out. The APDS empowers the plant personnel for conducting the Failed Fuel Localization in an effective way. Preparatory activities for sodium testing and qualification in Hall 3 test setup are underway. APDS will be integrated with control panel and will be used in the operation of the FFLM module of PFBR after the in-sodium qualification test.

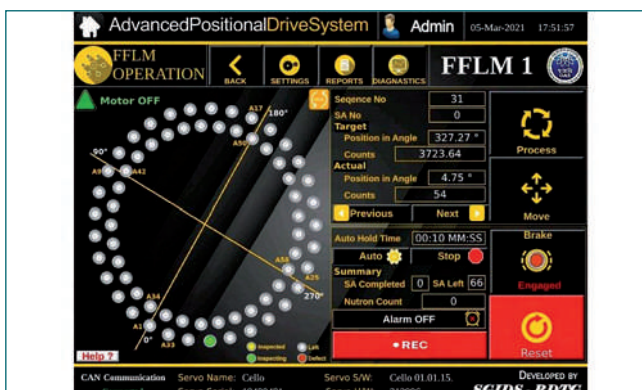


Fig. 5 APDS operation HMI screen

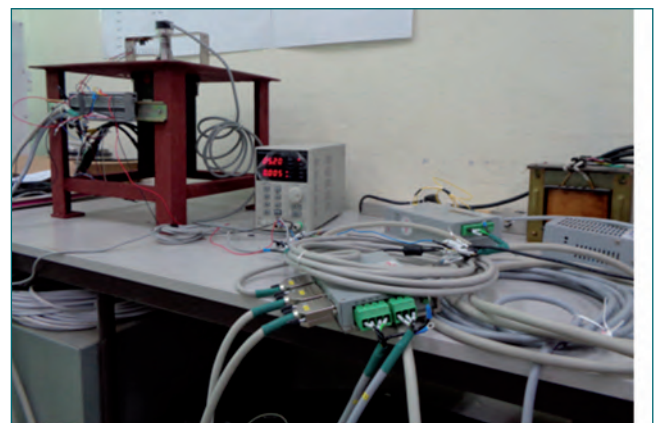


Fig. 6 APDS test setup

II.04 Development of In-Situ Joining Technology for Back-Up Seal and its Demonstration

Rotatable plugs are provided in PFBR to facilitate fuel handling operation through rotation of plugs. The annular gap between the stationary and rotating parts are sealed with elastomeric seals (Figure 1). During rotation, two inflatable seals are used for sealing the gap whereas a combination of one inflatable seal and one back-up seal is used during normal operation of the reactor. Back-up seal is an elastomeric seal of customized shape. The seal is fixed to the seal holder and the sealing is achieved by pressing the seal holder to the required amount, which in turn presses the seal. These are extruded seals and normally, the seal ends are joined at shop to form a ring, which is inserted from the bottom of top & middle ring so that the same can get fixed to seal holder. However, this call for several time consuming activities like disconnection of large number of cables, shifting of trailing cable posts etc. on top of pile in reactor. If the seal could be joined in-situ to form the rings, these activities can be avoided. Though seals can have multiple joints, except for the final one, other joints can be carried out at supplier's premises.

Shop joint vs in-situ joint

During the previous development as well as for presently fitted seals, the joints were made at supplier's shop in

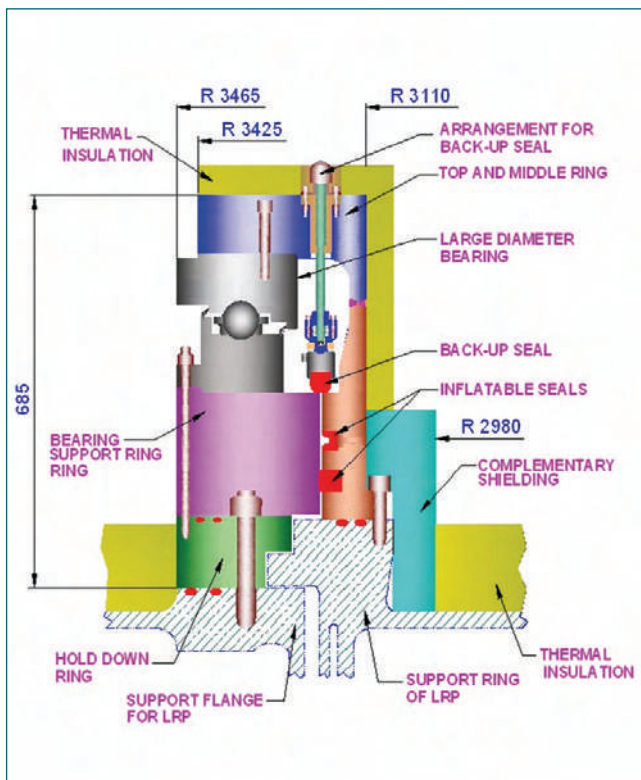


Fig. 1 Sealing arrangement for rotatable plugs



Fig. 2 Test seal with in-situ joint

semi-cured state and then cured in an autoclave. Due to large size of the seals, the autoclave size is quite large. Since, the present seal needs to be joined in-situ prior to fixing the same in the seal holder at site, the in-situ joining activity was taken-up as a development effort. A splice strength of ~ 5 MPa was defined as target for the development.

Development of in-situ joining technology

A special mould was used and the joint was cured at 150-160°C for 30 minutes and at room temperature for 24 hours. Joint were made in both 2 mm thick standard slab sample as well as 4.6 mm thick extruded samples and splice strength was checked and found to be 4.43 & 4.86 MPa, respectively.

Demonstration of in-situ joining technology and Performance Qualification of Seal

A $\Phi 1$ m test seal was made for qualification under simulated operating conditions (Figure 2). One more test joint was carried out as production test coupon and the joint was tested to obtain the splice strength, which was found to be 4.58 MPa, which is closer to the required splice strength. Performance qualification of the seal included compressing the seal by 5 +/-1 mm and testing at a temperature of 110°C for 15 days. During testing, the leak-tightness of the inter-space between two sealing lips was monitored. At the end of 15 days, the rig was cooled down, opened and seal was inspected for any physical damage and compression set. This test was repeated several times to qualify the seal for a longer duration. With the seal and joint are intact and leak-tightness maintained, the in-situ joining technology was successfully demonstrated and cleared for its implantation at PFBR site.

II.05 Development of Models for Simulating Operation Grade Decay Heat Removal System Transients in DYANA-P Code

There are two decay heat removal (DHR) systems in PFBR, viz., (1) Operation Grade Decay Heat Removal System (OGDHR) is an active system, and (2) Safety Grade Decay Heat Removal System (SGDHR) is a passive system. When all the dependent systems and offsite power are available, decay heat is removed by OGDHR. Otherwise, it is removed by SGDHR. It is essential to study the dynamics of the DHR systems to ensure stable operation during planned & unplanned transients and to establish reactor safety. It is also helpful in the conceptual design of the DHR systems. In addition, simplified operating procedures can be devised based on these studies. In the present study, development of models for OGDHR system in PFBR has been carried out and incorporated into the in-house plant dynamics code DYANA-P. SGDHR system models were already incorporated into DYANA-P.

The schematic of OGDHR system of PFBR is shown in Figure 1. A bypass line from the main steam lines is connected to a moisture separator tank (MST) which in turn is connected to main feedwater lines through a recirculation pump (RCP). During reactor shutdown, when two-phase steam comes out of the steam generators (SGs), it is passed to MST, where steam is separated from the water. Steam is sent to Decay Heat Removal Condensers (DHRCs), where steam condensation occurs. There is also a connection to send steam to the main condenser via turbine bypass lines. In DHRCs, air under forced circulation is used to remove the heat from the steam. The condensate water is sent

back to the MST. Water from the MST is circulated to the SGs by RCPs. There is also a connection to send water directly from the MST to the deaerator/main condenser. DHRC air flow rate is adjusted to control the reactor's cooling rate and maintain the systems at required temperatures.

New models for OGDHR system of PFBR were developed and incorporated in the DYANA-P code. One-dimensional mass, momentum and energy conservation equations in single-phase were used in the DYANA-P code for modeling primary and secondary circuit components. Similar equations for two-phase fluids (with homogeneous flow assumption) are used to develop new system models in the present study. Cool Prop database has been used to evaluate two-phase properties. Mass and energy conservation equations are solved in nodes/plenums, while momentum conservation equation is solved in branches. The flow rate in the DHRC circuit is obtained from integral momentum balance applied for the loop. MST has been modeled as a lumped volume using the conservation equations and the equation of state. In addition, whenever two phase mixture is present in the tank, it is assumed that the mixture is at saturated conditions with water separated at the bottom of the tank. A single representative tube has been modeled in DHRC with water/steam inside and the air outside and axially discretized into several control volumes. It is assumed that the cross flow streams passing over the tubes are equally distributed from the total flow, and there is no intermixing of flow streams. The total fin area is used for heat transfer calculations on the air side.

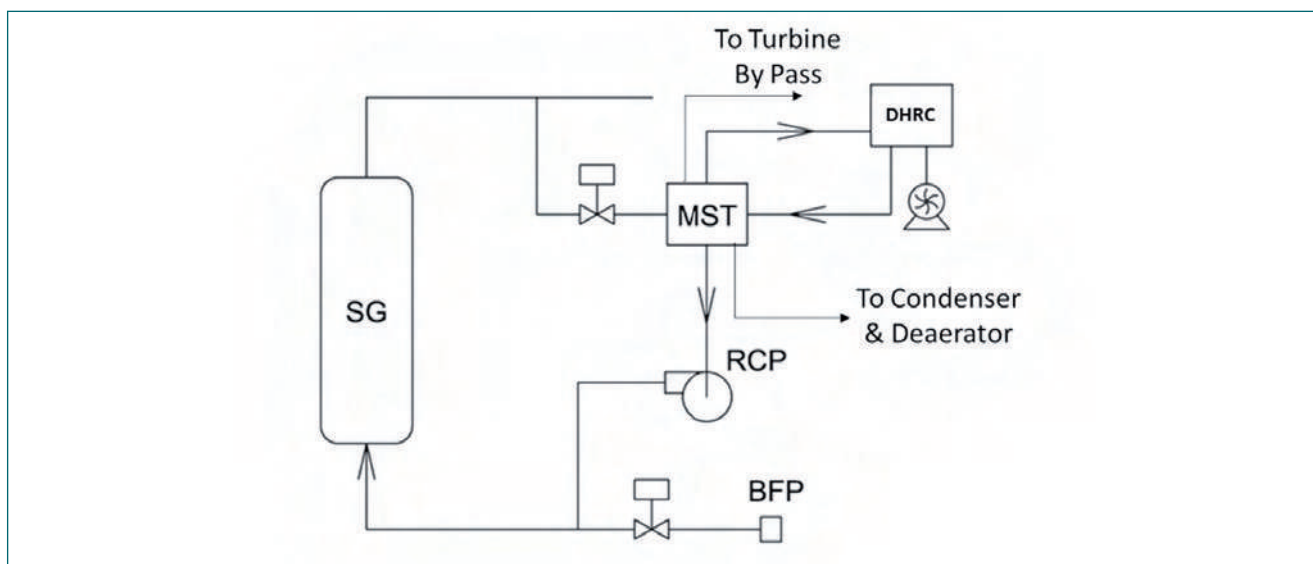


Fig. 1 Schematic of OGDHR system in PFBR

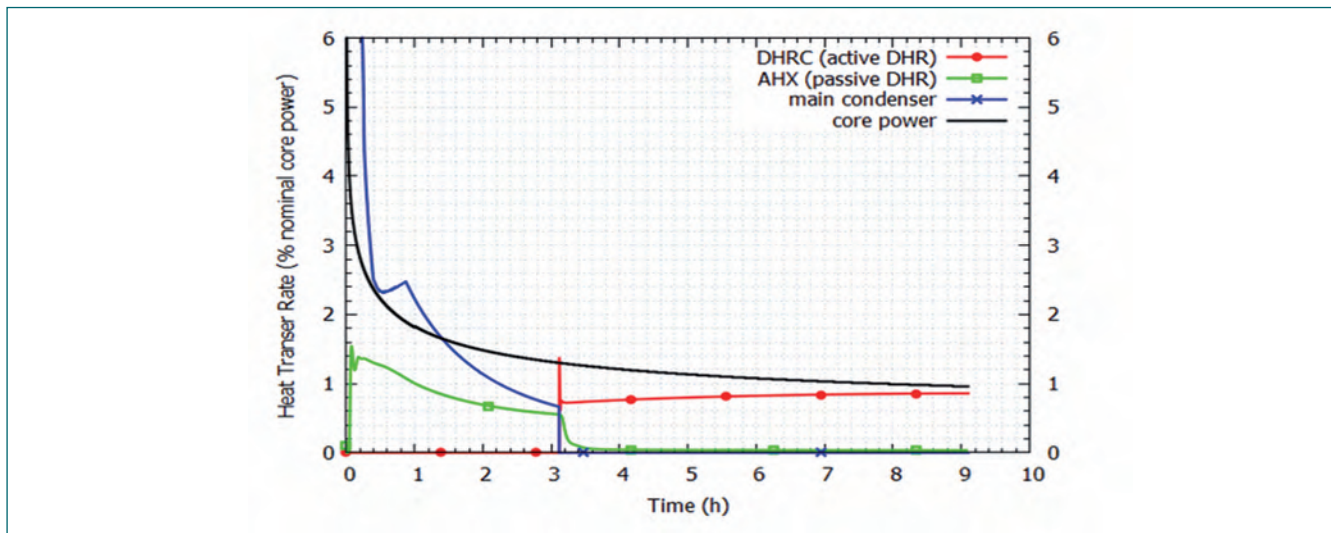


Fig. 2 Evolution of heat sources and sinks

In order to demonstrate the application of the new code, the event of spurious SCRAM has been simulated using the modified code. Following SCRAM, fission power reduces to zero rapidly. Primary and secondary sodium pump speeds coast down to 20 % due to Sympathetic Safety Action (SSA), and their flow rates become close to 20 %. The feed water water flow rate is manipulated to maintain the SG sodium outlet temperature, reaching a minimum value of 15 %. SGDHR system air dampers also open automatically following SCRAM. The steam temperature reduces and reaches near saturation temperature (~350 °C) at ~15 min, after which steam is fed to the MST. During this initial filling period, steam in the MST is continuously removed in the turbine bypass line, and only water is stored in the MST. When MST is filled with water (~24min), the water is fed into the main condenser and de aerator. During the transient, due to loss of feed water heating, the de aerator temperature

reduces from its nominal value (235 °C) to 150 °C. It is maintained at this value by manipulating water split up from MST to condenser and de aerator. MST temperature reaches 200 °C (cold shutdown) at ~3 h, following which the MST outlet to the main condenser/ de aerator is stopped, RCP is deployed and SGDHR air dampers are closed. The evolution of major heat sources and sinks during the transient is shown in Figure 2. The evolution of hot and cold pool temperatures is shown in Figure 3. The net heat sink is less than the core power shortly after 3 h. Hence, there is a slight increase in the pool temperature. Eventually, core power decreases, and reactor temperatures can be maintained at cold shutdown conditions by manipulating OGDHRS fan speed. In the first ~30 min, the reactor temperature reduced at a rate of ~400 K/h. Later, it is reduced at a rate of ~60 K/h.

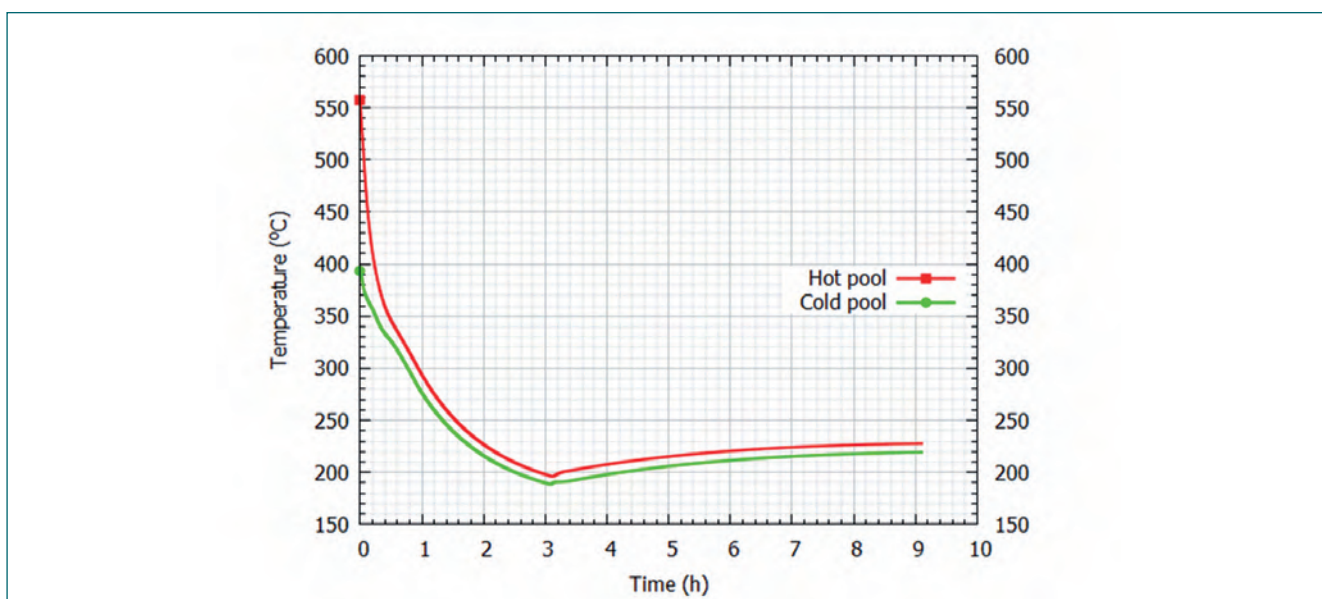


Fig. 3 Evolution of hot pool temperature

II.06 Design Modifications of Guard Pipes of Intermediate and Decay Heat exchangers to Improve the Gap between the Inlet/Outlet Nozzle and the Guard Pipe

Liquid sodium when exposed to air/water, reacts exothermically, resulting in sodium fires. As per PFBR design philosophy, sodium fire has to be avoided inside Reactor Containment Building (RCB). To meet the requirement, components carrying sodium are provided with second physical boundary inside RCB and inter space is filled with nitrogen or argon to maintain inert atmosphere. Portions of Intermediate Heat exchangers (IHXs) and Decay Heat exchangers (DHXs) above the roof slab have a guard shell and their connected sodium piping inside RCB has a guard pipe.

Intermediate Heat exchanger

The schematic of IHX along with guard pipe is shown in Figure 1. The IHX is subjected to various temperature transients during its lifetime. The responses of various shells to these transients vary based on the geometry and the boundary conditions viz., insulation, restricted/free for thermal expansion and exposure to the ambient. The differential thermal expansions of the shells result in secondary stresses if they are restricted. The IHX inlet/outlet nozzles are provided with respective nozzles in the guard shell. Both the guard shell nozzles and the guard pipe nozzles are welded to the main pipe close to the IHX as shown in Figure 1. Since the IHX is long and slender

component, the differential thermal expansions between shells in its axial direction result in relative movement of inlet/outlet nozzles w.r.t. to their guard shell. The IHX was designed with an assumption that the main nozzles expand freely without being restricted by the weld between the guard shell nozzle and the main pipe. Since the weld at the inlet/outlet nozzle restricts free thermal expansions, the weld is subjected to large thermal stresses.

Free thermal expansions of IHX shells and nozzle movements are estimated for enveloping operating conditions experienced by the IHX. With the nominal clearance of 24.6 mm, the net maximum interference between the guard pipe and the IHX nozzles at inlet and outlet are estimated as 23.3 mm and 10.3 mm respectively. Adding the geometric and concentricity tolerances (14.3 mm), the minimum clearance required becomes 61.9 mm at the top of inlet nozzle and 48.9 mm at the top of the outlet nozzle. The nozzles also grow in the radial direction. The maximum net radial thermal movement in the inlet and outlet nozzles is 10.8 mm and 11.6 mm respectively. There are no bellows between the main and guard shell nozzles to absorb these differential thermal expansions. Since the introduction of a new bellows requires major modifications in IHX/sodium piping, existing bellows in sodium piping is

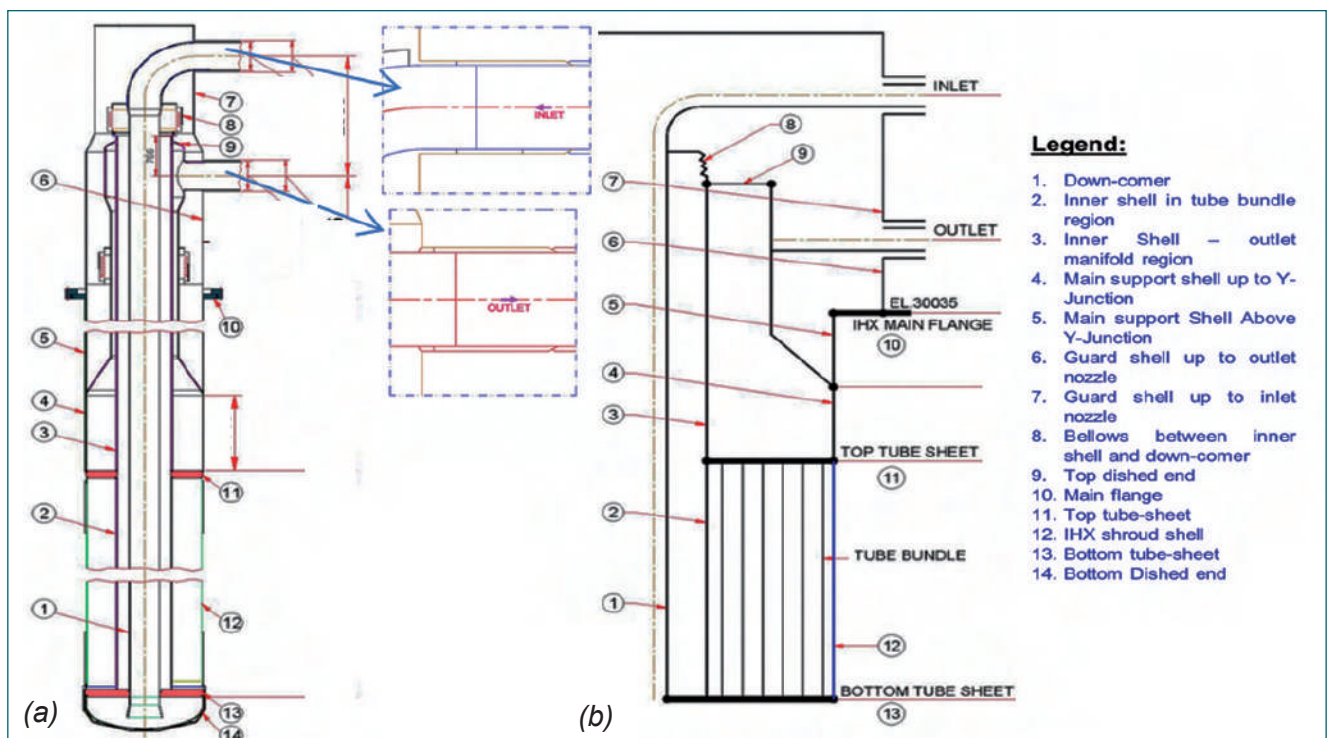


Fig. 1 Schematic arrangement of intermediate heat exchanger (a) major shells and (b) line diagram for explaining the thermal expansions in IHX

The schematic of the initial arrangement and the modified design of the guard pipe near inlet nozzle of a typical DHX are shown in Figure 3. The modifications carried out are, (i) merger of the first and second compartments, (ii) introduction of transition arrangement near the bellows and offset the bellows downward by ~20 mm, (iii) offset of bottom half of guard pipe by 35 mm downward and

connect with top half by straight vertical plates and (iv) introduction of box structure near the downcomer bend to connect mitre bend with guard shell / pipe in order to have leak tight boundary.

The necessary changes were successfully implemented at site and qualified for all the four IHXs and DHXs.

II.07 Deployment of Reactor Core Viewing System and Inspection of Grid Plate Top and Core Sub-Assemblies

During commissioning of PFBR, it was decided to carry out remote visual inspection of the top of grid plate and core sub-assemblies. A Reactor Core Viewing System for Room Temperature (RCVS-RT) was developed in-house which was deployed through the Observation Port (OP) on the roof slab of the reactor. Viewing of the core internals has been accessed remotely. The RCVS-RT consists of camera probe to the core top, which is about 11.5 m below from the OP and negotiate through a extracted sub-assembly(SA) slot to reach down to the Grid Plate(GP) top level for inspection for visual inspection.

Figure 1 shows the RCVS-RT system which has radial motion, R (range: 200 mm), rotary motion, Θ (range: 360°) and precision camera vertical motion, Z (range: 100 mm) and azimuth motion to localize the visual inspection(VI) probe camera to target position. The camera module which has extender pipes, reaches up to the GP top position from the observation port.

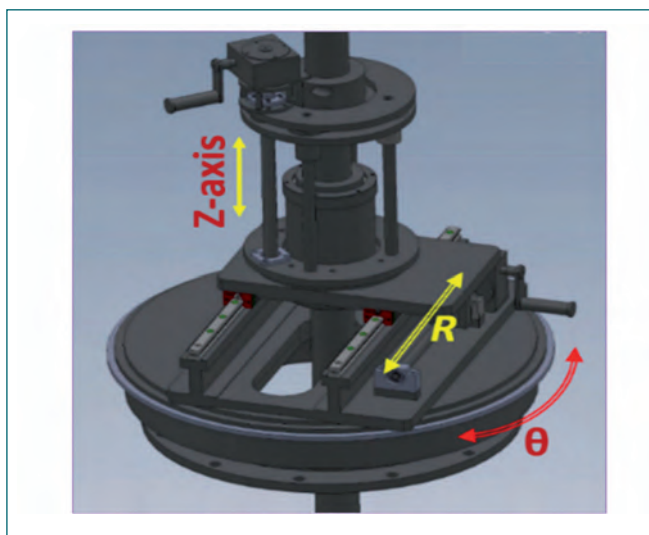


Fig. 1 R , θ and Z motion for the RCVS



Fig. 2 View of PFBR reactor core through global camera of RCVS

The base module of the RCVS-RT below the OP enables a global view of the reactor internals and the camera extender pipes, facilitated by a camera and



Fig. 3 Inspection of grid plate region using RCVS



Fig. 4 RCVS control panel with images

illumination module. Two pinhole cameras are mounted at the end of the tube facilitate a combined radial and axial viewing during deployment of RCVS through a vacant SA slot for the purpose of navigation. The VI probe camera is attached with the suction hose, which is actuated through a linear actuator mechanism. The movement of the linear actuator provides a swing to the hose-camera combination w.r.t. to the RCVS centre-line. This swing (0° to 30°) facilitates the visual inspection by providing the required orientation of camera once the camera module reaches the grid plate top surface. The VI probe camera is designed to have direct and lateral viewing to view the required target position with LED lighting. The entire system is specially sealed for all the R, Θ and Z motions to mitigate leaks through the RCVS-RT system during inspection. The RCVS-RT system has been deployed into the reactor core through OP. Images



Fig. 5 Extracted SA slot

of the global view of the reactor core, top surface of the GP, lateral view of the adjacent six SA outer surface from SA top to GP top surface have been obtained. Figure 2 shows the view of PFBR reactor core internals & Figure 3 shows the view of grid plate using RCVS camera.

Images of the reactor core internals, GP & SA surfaces are stored and viewed in the control panel as shown in Figure 4. Images of extracted SA slot is shown in Figure 5. Figure 6 shows the schematic of the SA locations for visual inspection. From the images taken by the pinhole cameras of the RCVS, it could be observed the subassembly reference number as shown in Figure 7. Clear images of the SA and clear visibilities of the grid plate top surfaces are seen by the movement of linear actuator attached to the pinhole cameras. From the top of the grid plate, it was observed the inside view of the sleeve up to grid plate bottom surface.

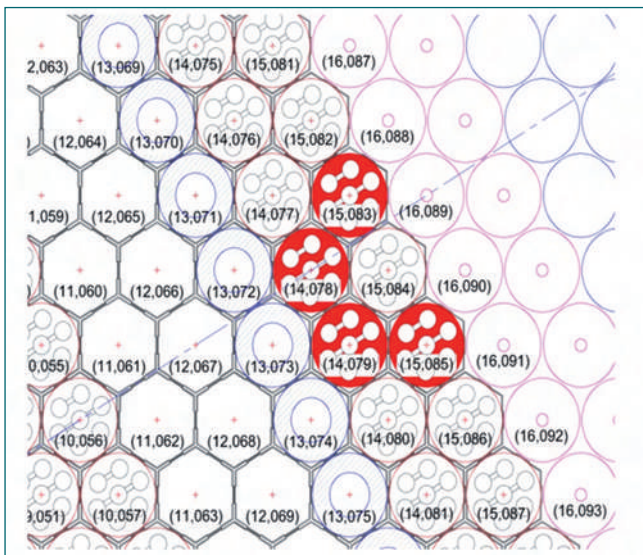


Fig. 6 Schematic of SA for inspection



Fig. 7 Image of showing SA number

II.08 Evaluation of response delay for PFBR Core Temperature probe under flow transients

In PFBR, sodium temperature at outlet of each Fuel Sub Assembly (FSA) is continuously monitored. Deviation from the estimated value by $+10^{\circ}\text{C}$ is one of the SCRAM parameter. All FSAs (except the central FSA) are provided with duplex thermocouple probe (2 nos. of 1 mm diameter K-type SS sheathed ungrounded thermocouples) inserted in thermowell, which is positioned at 125 mm above the FSA outlet. The specified response time of TC probe is $6 \pm 2\text{s}$, when the duplex TCs are in contact with tip of the thermowell. However, the possibility of gap between the TC probe and thermowell tip cannot be ruled out due to various uncertainties. On other hand, response of the TC probe under temperature transients in flowing sodium is to be verified. Hence, an experimental facility has been designed and commissioned to evaluate response time delay of TC probe under simulated sodium flow and temperature transients envisaged in PFBR.

The experimental facility consists of two test vessels (TV-1 & TV-2) connected to a sodium dump tank and sodium valves. The sodium system is integrated with argon cover gas system containing two individual buffer tanks for each test vessels (Figure 1). Test vessel-2 (TV-2) is meant for housing TC probe to be tested. The test vessel-1 (TV-1) acts as a source from which sodium at relatively high temperature is made to flow into TV-2 through interconnected pipe. Two pre-calibrated K-type thermocouples (FTC-1, FTC-2) were positioned at outside the thermowell as reference temperature measuring device. A permanent magnet type flow meter is integrated in the sodium loop for measuring sodium flow rate during the experiment (Figure 2). The sodium system is designed for a pressure of 5 bar at 600°C .



Fig. 1 Experimental facility

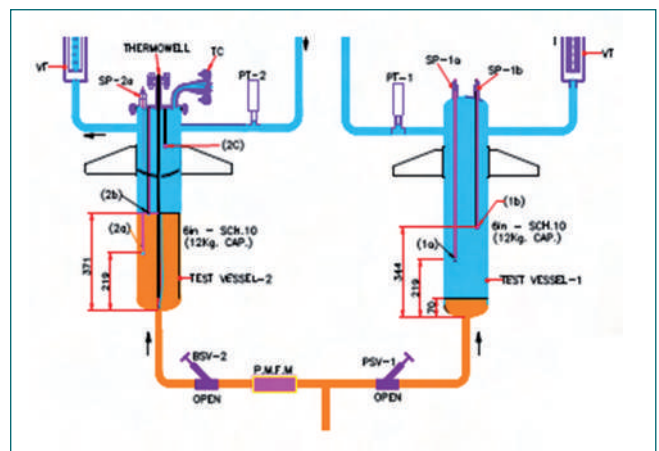


Fig. 2 Simulated sodium flow from TV-1 to TV-2

Sodium filling in TV-1 and TV-2 from the dump tank and sodium transfer from TV-1 to TV-2 are carried out by using differential pressure technique. The driving pressure required for sodium transfer was estimated for simulating the sodium velocity at FSA outlet ($\sim 3\text{ m/s}$). Sodium flow control was achieved by using timer based solenoid valve in the cover gas circuit. Experiments were carried out by positioning the TC probe in full insertion mode (i.e. full contact with thermowell tip). Sodium flow was induced at required velocity for about 45 seconds, maintaining a temperature difference of $\sim 30^{\circ}\text{C}$ between the two sodium vessels, with TV-2 at 550°C . The recorded temperature rise in duplex TC probe was compared with the reference TC. The response delay of TC probe for 10°C temperature rise above 550°C was found to be $\sim 9\text{ s}$ (Figure 3). Experimental to studies on the effect of gap between thermocouple probe and thermowell bulb on response of TC probe during a step champ/ ramp in the sodium temperature are in progress.

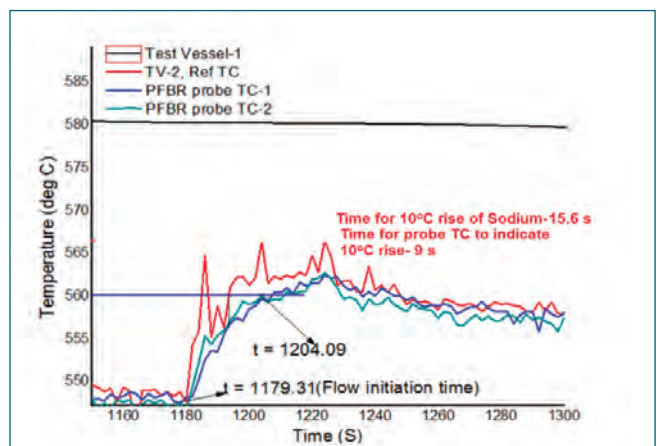


Fig. 3 Response of TC probe

II.09 Quality Assurance and Inspection during Fabrication of Nickel Detector Assembly

In sodium heated steam generators, in case of water/steam leak into sodium, there will be exothermic reaction between sodium & water and in the process, hydrogen will be liberated. This hydrogen reacts with sodium and increases Hydrogen concentration in sodium. This increase can be detected to find leak of water/steam into sodium.

Hydrogen in Sodium Detection Circuit (HSDC) is provided in each Steam Generator (SG) sodium outlet line and one at common outlet in the secondary sodium main circuit. Each HSDC is provided with Electro Chemical Hydrogen Meter (ECHM) which uses the principle of concentration cell and Nickel detector. Shell side of Nickel detector is maintained with vacuum by Sputter Ion Pump (SIP) which measures Hydrogen concentration in Sodium.

The nickel tubes are manufactured at NFC as an import substitute and nickel detectors are fabricated by IGCAR. Nickel detector (Figure 1) consists of four nickel tube of 6.6/7.2 mm size, formed as 90° bend and inserted to a 32 NB SS 304LN pipe which acts as shell. Sodium is circulated in tube side and shell side is put under vacuum.

Inspection of Raw Materials

Seamless Nickel tubes conforming to ASTM B 161 Grade 201(Ni:99.5%Purity) manufactured as per approved QAP and supplied by Nuclear Fuel Complex (NFC) are inspected for Chemical analysis (Table 1), mechanical tests, Hardness tests, Grain size, Ultrasonic examination (UT), Eddy Current examination (ET), Helium leak tests (HLT). Specific reference blocks for UT with 60° longitudinal 'V' notch of 0.1 mm depth

	Result	R/N
Carbon (C)	0.006	0.02 Max
Manganese (Mn)	0.110	0.35 Max
Silicon (Si)	0.008	0.35 Max
Sulfur (S)	0.004	0.01 Max
Iron (Fe)	0.019	0.40 Max
Copper (Cu)	0.006	0.25 Max
Nickel (Ni)	99.80	99.0 Min

& 12.6 mm long on inner and outer surface of tube, for ET with 0.8 mm through wall hole and leak rate of 10^{-8} Std. CC/ Sec are used for acceptance of tubes.

Visual and dimensions are inspected and found within the tolerance of +0.1 / -0.05 mm for diameter 7.2 mm and $\pm 10\%$ for thickness of 0.3 mm. Other than Nickel tubes, SS 304LN pipe of 32 NB, Plates and rounds are ensured for heat number link ability with Manufacturer's Test certificates and cleared.

Quality Assurance of Nickel Detector

Detailed Quality assurance Plan with sequence of operations is prepared and approved before execution of the fabrication. Pneumatic test procedure to ensure integrity and leak tightness of shell and tube side of detector is prepared and approved.

Bending of Pipes and tubes

Nickel tubes having 7.2 mm diameter are bent to radius of 150 mm with angle of 90° are inspected for corrugations at bent portion, ovality, angle and thinning at outer race of bent tubes and found within approved drawing tolerances. Liquid Penetrant examination is

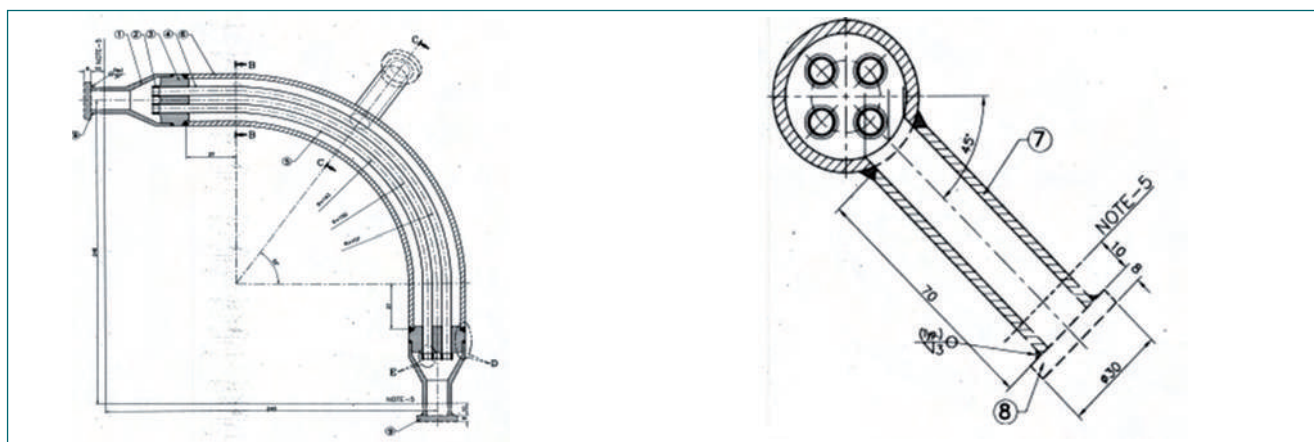


Fig. 1 Nickel detector



Fig. 2 Bent pipes

also carried out on bent surfaces to ensure free of micro cracks. Inspection reports are prepared and issued (Figure 2).

Lip seal welding qualification

Four numbers of Ni tubes are joined to a tube sheet (27 mm thick) (Figure 3) at both the ends by lip seal welding (Figure 4). A mock up test coupon was welded to standardize the welding parameters and macro examination was carried out to ensure soundness of the joint.

Stage inspections during welding and assembly

Tube sheet to shell side pipe and shell pipe to nozzle pipe was inspected for fit up dimensions such as root gap, included angle, mismatch and cleared for welding.



Fig. 3 Tube sheet

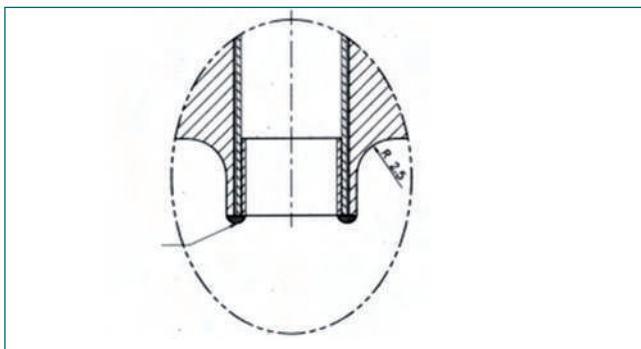


Fig. 4 Lip seal joint

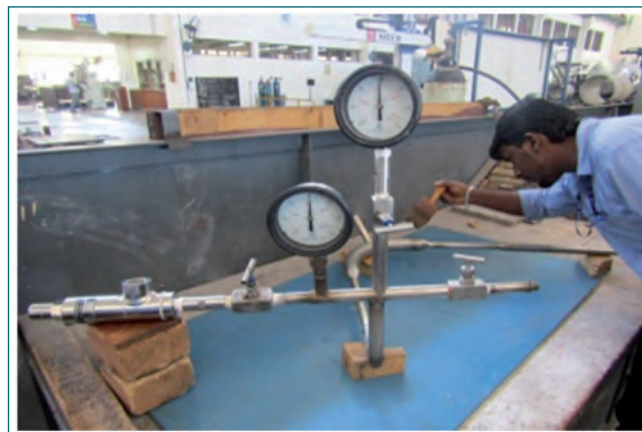


Fig. 5 Pneumatic test setup

Qualified welders are permitted to perform the welding using approved welding procedure specification as per ASME Section X. Each weld passes were examined for visual and solvent removable visible liquid penetrant examination

Pneumatic tests

After final dimensional inspection of nickel detector assembly, pneumatic integrity tests at 32 Kgf/cm²(g) using calibrated pressure gauges and soap bubble leak tests are carried out as per approved procedures and cleared. Before test, safety valve at 1.1 times of test pressure was checked for its functionality and installed with the test setup (Figure 5).

Helium leak tests

Nickel detector (Figure 6) is evacuated to vacuum and examined using mass spectrometer (Helium) leak detector as per ASME Section V Article 10 and found no detectable leak of the order of 1×10^{-7} Std. CC/Sec. Quality requirements of Nickel detector is ensured during its fabrication through effective implementation of QA practises. All quality documents and records are issued for records.



Fig. 6 Nickel detector assembly

II.10 Miscellaneous Manufacturing activities at Central Workshop Division for PFBR Commissioning

Central Workshop Division (CWD) is a design and manufacturing facility of IGCAR under Technical Services Group (TSG) of Engineering Services Group (ESG). CWD primarily specializes in machining, fabrication and inspection and caters to the needs of various manufacturing activities towards Prototype Fast Breeder Reactor (PFBR), Fast Breeder Test Reactor (FBTR), Kalpakkam Mini Reactor (KAMINI), Reprocessing Facilities, Post-Irradiation Examination Facilities, R&D Projects and Infrastructure Development apart from operation and maintenance requirements. CWD maintains the highest quality standards to meet the stringent specifications and requirements under various codes, viz. ASME, ASTM, RCC-MR and ISO.

This article highlights miscellaneous manufacturing activities carried out by CWD in 2021 towards commissioning of PFBR. Major such activities including turn-key manufacturing and modifications of components/systems are as follows:

- Sodium Duct Assemblies for 170m³/hr Annular Linear Induction Pump.
- Anti Convection Barrier Plug for in-service inspection.
- Mechanism for simultaneous lifting of three sub-assemblies from reactor core.
- Setup for forced air cleaning of sub-assemblies.
- Modification of Labyrinth, Ratchet Cover Plate and Ratchet Support Flange of Primary Sodium Pump.
- Buffing setup, procedure and debris collection-retrieval setup for hard-faced Grid Plate Sleeves.
- Radius Gauges for inspection of corners and edges of subassemblies.



Fig. 1 Photos show radius is being formed in DSA adopting traditional method using filing and hand Grinding techniques



Fig. 2 Photos show radius formed DFSA ends, Discriminator guide portion and completed DFSAs

- Modification of dummy sub-assemblies
- Leak-tight Flask for Absorber Rod Drive Mechanism.
- Assistance for indigenous development and qualification of large bearing balls for LRP & SRP through machining of qualification specimens and inspection.
- Spacers and Space Lifting Tool for fuel container handling.
- Clamps for RCVS systems deployed for reactor core visual examination.
- Mechanical stopper for PFBR Cell Transfer Machine.
- Modification of dummy containers for SSTM, CTM and UWT systems.
- Welding and brazing of ESP type leak detector arrangement for main vessel sodium leak detection.



Fig. 3 Photos show machined gauges and their usage on the DSAs



Fig. 4 Fabricated DSA cleaning setup

Hexagonal clamps for rotation of sub-assemblies.

- Welding and brazing of Aluminum pipe setup for visual inspection of Grid Plate top and debris collection.
- Taper machining of inner Lip surface and height reduction of outer lip of back up seal ring.
- Sodium Leak Detector for SSP Argon balance line.
- Back-up seal position sensor actuating rods and inflatable seal connector for LRP & SRP.
- Guard Pipes and Support Structure for IHX & DHX.

Majority of the above activities involved high precision modifications in heavy, slender, intricate as well as miniature jobs. Accordingly there were challenges in handling, machining/ welding/ inspection process plans, selection of equipment, work holding devices to achieve Critical to Quality (CTQ) in the existing fabricated components as per applicable codes. A few challenging critical jobs are highlighted in the following sections.

Modification of Dummy Sub-Assemblies (DSA)

CWD is entrusted to carry out modification of the DSAs of PFBR before final installation. The modification works are very challenging as it involves high precision hand grinding of numerous sharp corners and edges in the handling head, guide lugs and discriminator and micro-machining of the discriminator having alternating

cylindrical-flat faces. Detailed measurement procedures were developed and demonstrated for the DSAs using Co-ordinate Measuring Machine (CMM), digital vernier & micrometer before commencing the modifications. Process plans were developed and implemented for grinding and micro-machining of the DSAs and 15 nos. of DSAs have been modified so far and functionally tested. Figures 1 and 2 depict the process in action and corrected DSAs.

Manufacturing of radius gauges for inspection of PFBR DSAs

CWD manufactured multiple sets of high precision radius gauges to inspect radius of curvature at the edges and corners of the DSA. To obtain the required radius profile accuracy, gauges were made using CNC wire EDM process. All gauges were found satisfactory and used in inspection of the modified DSAs as shown in Figure 3.

Manufacturing of setup for forced air cleaning of Dummy Sub-Assemblies

The modified DSAs of PFBR would need internal cleaning before final installation prior to sodium filling in the main vessel. CWD manufactured a setup made up of SS304/ SS316 material for forced air (7 bar) cleaning of the DSAs at PFBR site. The setup of overall size 345 mm Dia x 800 mm Height consists of sleeve, chamber with two nozzles for air entry/exit, blind flange, slip-on flange and support Ribs (Figure 4). Precision machining of the sleeve of ID 78.8 mm with H7 tolerance to a depth of 380 mm was successfully achieved. The precision machined sleeve was welded with minimum/nil distortion into the chamber within specified straightness tolerances.

Manufacturing of Mechanism for Simultaneous Lifting of Three Sub-Assemblies from PFBR Core

CWD manufactured a lifting mechanism for PFBR, which would enable simultaneous lifting of three sub-assemblies from the reactor core to speed up DSA removal process. The mechanism consists of two major assemblies namely



Fig. 5 Parts of lifting mechanism



Fig. 6 Finger holder assembly



Fig. 7 Labyrinth machining in VTL Machine



Fig. 8 Ratchet support flange machining in Radial Drilling Machine

Finger Holder Assembly and Main Frame Lifting Assembly. Overall Height of the mechanism is 1627 mm and the assemblies consist of 18 components of stainless steel. Major components are finger holder, conical guide, spacers, fingers, locking plate & block, main lifting frame etc. and have very intricate profiles with stringent tight tolerances necessitating multiple precision machining processes, welding and assembly. Machining was carried out using CNC Lathe, Horizontal Machining Centre, CNC Spark Erosion and CNC Wire Cut EDM. Challenging and critical task of maintaining close tolerances while using multiple machine tools was accomplished and the mechanism was successfully assembled followed by satisfactory functional testing. Figure 5 shows the precision machined and welded parts and Figure 6 shows one finger holder assembly.

Modification of Labyrinth, Ratchet Cover Plate and Ratchet Support Flange of Primary Sodium Pump (PSP)

CWD carried out modifications on the PFBR PSP parts within stringent tolerances. The components are heavy in structure and it was challenging to accurately measure, align, position and clamp the jobs on the available machines

to carry out the required modifications. Overall size of the Ratchet Support Flange and Labyrinth are 2100 mm Dia x 60 mm Thick and 810 mm Dia x 200 mm Height respectively. Increasing the inner diameter of the labyrinth by 2 mm and providing camber at both edges of each groove was very critical and it was successfully machined in the heavy duty Vertical Turret Lathe (VTL) using unique grooving tool developed in-house as shown in Figure 7. Two radial slotted holes of 110 mm Dia on 1670 mm PCD were drilled in the machined ratchet support flange using the Radial Drilling Machine as shown in Figure 8.

Leak-tight Flask for Absorber Rod Drive Mechanism (ARDM)

CWD was entrusted to fabricate the ARDM Flask, which is a leak-tight 402 mm OD x 3 mm Thick x 14200 mm Length cylindrical shell. It was challenging to manufacture such long, slender and thin leak-tight shell within stringent perpendicularity and cylindricity tolerances of 5 mm. The shell was fabricated in four segments and joined axially by bolted flanges and gaskets as shown in Figure 9. Necessary leak tightness of the complete ARDM flask was achieved at specified 10 m bars (g) positive pressure.



Fig. 9 ARDM flask

II.11 An Application of Level-1 Probabilistic Safety Analysis to PFBR Safety

Level-1 Probabilistic Safety Analysis for PFBR assesses core damage frequency against a wide range of design basis and beyond design basis events. The scope of present analysis is limited to full power operating state of the reactor with internal initiating events including loss of offsite power. The study adheres to the available probabilistic safety analysis (PSA) standards of AERB, IAEA and ASME/USNRC. The necessary technical elements of PSA such as initiating events analysis, accident sequence analysis, success criteria formulation and system analysis, human reliability analysis, dependent failure analysis, core damage frequency quantification, sensitivity and uncertainty analysis have been addressed in this study.

This study considers 94 initiating events grouped into 25 initiating event groups. The total initiating event frequency considered in this analysis is ~10.3 / ry. Three frontline safety systems and eight support systems have been considered. The front line safety systems considered are Shut Down System (SDS), Safety Grade Decay Heat Removal System (SGDHRS) and Operational Grade Decay Heat Removal System (OGDHRS). Quantifying the unavailability of highly redundant / partially diverse SDS and passive SGDHRS are the main challenges. Small event tree large fault tree approach is used for modeling. Data from FBTR operational experience and generic sources applicable to FBR specific components are used. The safety critical human actions are identified and appropriate

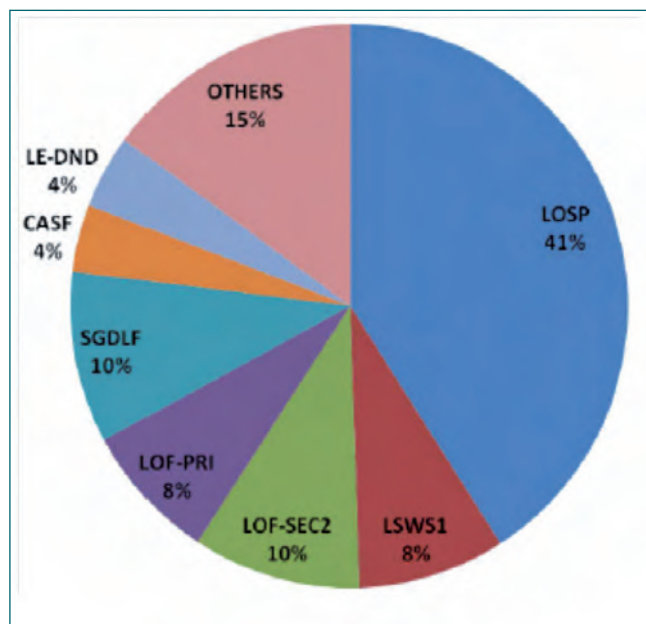


Fig. 1 Initiating event groups contribution to core damage frequency

Sl. No	System	Unavailability
1.	Shutdown System	
	a. Global Fault	7.4E-08
	b. Local Fault	6.1E-09
	c. Manual Scram	2.4E-10
2.	SGDHRS (Mission Time = 720 Hrs)	8.5E-07
3.	OGDHRS (Mission Time = 24 Hrs)	0.058

performance shaping factors, stress level / available time window for operator actions are considered in human reliability analysis. While the explicit dependence between redundant components / systems is modeled in logic models, the implicit dependence is modeled through common cause failure models.

The unavailability of safety systems are evaluated through fault trees. For SDS, separate fault trees are developed for events which have an impact on whole core, events affecting few sub assemblies and events which require manual scram. For SGDHRS, the fault trees are quantified for different mission times depending on the nature of initiating events. The change in hardware configuration of safety systems with respect to initiating events is also considered. The unavailability of front line safety systems are listed in Table 1. The dominant contributors to the unavailability of safety systems are identified using Fussell-Vesely importance measure. The quantification of core damage frequency necessitates the definition of core damage categories which are one of the end states of event sequence models. The core

Sl. No	Core damage category	Frequency (/ry)
1.	A1 - Large Early Core Damage	1.0E-07
2.	A2 - Large Late Core Damage	3.0E-07
3.	A3 - Non-energetic Late Core Damage	1.24E-06
4.	B1 - Sub Assembly Failure	4.6E-11
5.	B2 - Pin Failure	3.2E-08
6.	C - Reduced Safety Margin	5.7E-07

damage categories are classified based on severity, time delay and potential for large release. The identified core damage categories with their identification labels are listed in Table 2.

The estimated total core damage frequency (including core damage categories A & B1) is $\sim 1.7E-06/ry$ (5% lower bound is $\sim 3.9E-08 / ry$ and 95% upper bound is $\sim 4.8E-06/ry$). The core damage frequency corresponding to significant release of radioactivity due to energetic CDA (core damage categories A1, A2) is $\sim 0.4E-06 / ry$. The contribution to total core damage frequency from different initiating event groups is shown in Figure 1.

Loss of offsite power contributes $\sim 41\%$ to the total core damage frequency. In Figure 1, the core damage frequency contribution from 18 initiating event groups which does not explicitly appear in the pie chart are shown as others category. The dominant event sequences which contribute to total core damage frequency are identified. Sensitivity studies on the critical assumptions are also performed. Significant observations have been made to reduce core damage frequency, to improve system reliability and to improve quality and utility of the analysis.

II.12 Testing and Qualification of Selected High Temperature Grease for Gripper Screw in CSRDM

Control & Safety Rod Drive Mechanism (CSRDM) forms part of the first shutdown system. Nine CSRDMs were used to control and safe shut down the PFBR. During a routine test on the pile, noise was observed during the gripping / de-gripping operation in CSRDM-7. A root cause study was done, and drying of lubricant in the trapezoidal screw of the gripper operating tube was identified as the reason for the noise. To address the issue, it was decided to lubricate the gripper screw with high temperature grease. The Balmer & Lawrie

made Hytec EP2 grease was chosen for lubricating the gripper screw. Gripper operating mechanism consists of a gripper operating shaft, gripper operating tube sheath, gripper operating tube, gripper rod, fork, gripper body and gripper fingers. Figure 1 shows the part of the gripper operating mechanism in the translation tube upper. The translation tube houses the Gripper operating tube sheath on a needle thrust bearing. The needle thrust bearing supports the gripper operating tube sheath. The gripper operating tube is featured with a trapezoidal thread Tr 33 x 6 (P2). The screw is made of SS316LN, and the nut is made of aluminium bronze. The noise has been observed in this screw nut pair. These items are housed in CSRDM lower part and are in remote location hence in-situ lubrication is not possible. For application of grease, the CSRDM lower part needs to be partially dismantled.

To qualify the selected grease before actual application in CSRDM, a mock-up gripper screw mechanism was manufactured simulating the mechanical configurations and load. The test setup is also provided with a heating provision to simulate the reactor condition of $\sim 100^{\circ}C$ at the gripper screw location. Figures 2 and 3 shows the schematic and the photograph of the gripper test setup. The mock-up gripper screw was coated with a fine layer of high-temperature grease and assembled in the test setup. The grease on the mock-up screw was found intact even after the high-temperature exposure

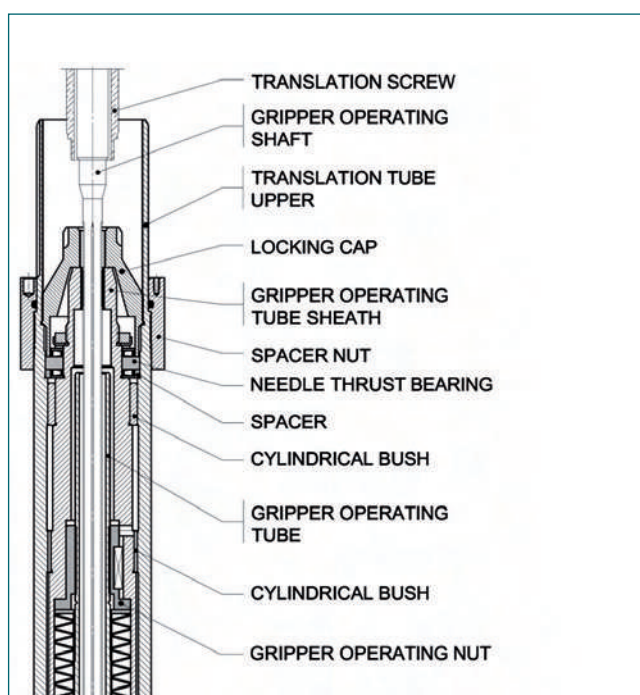


Fig. 1 Schematic of gripper operating

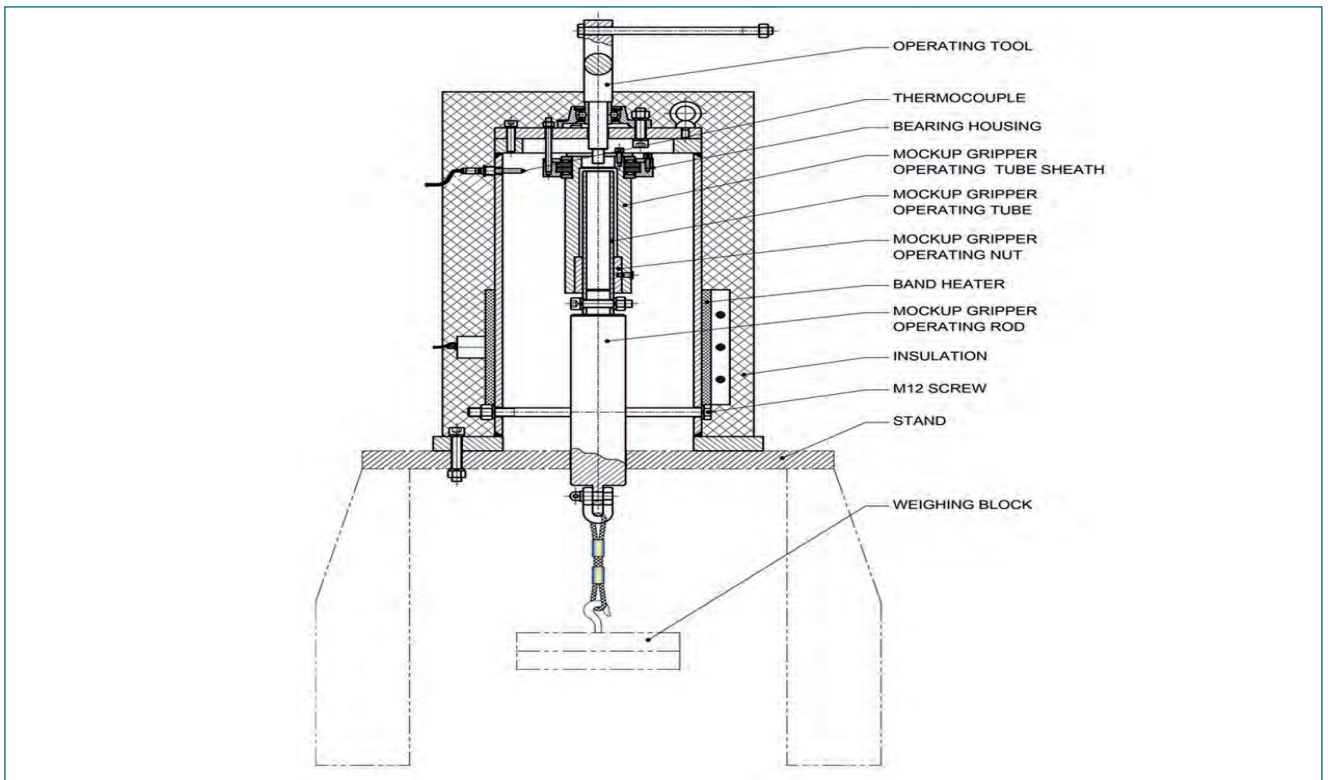


Fig. 2 CSRDM gripper screw test setup

test for 160 hours. Subsequent to high temperature exposure test, performance testing has been carried out, gripper operation was smooth during the rising and lowering operation with no load and 95 kg axial load at room temperature. The nominal torque values of 5 Nm and 2 Nm for rising and lowering of gripper screw matched with the previously measured torque values at PFBR. The nominal gripper rising and lowering torque with 95 kg axial load at 120°C temperature was measured as 5 Nm and 1.5 Nm, respectively.

The nominal gripper rising and lowering torque with 945 kg axial load at 120°C temperature was measured as 30 Nm and 10 Nm, respectively. The gripper operation was smooth, and torques values were almost constant throughout the testing. 120 cycles of gripper operation with simulated load cycles were completed successfully and the grease was qualified for reactor use. Figure 4. Shows the photograph of gripper screw lubricated with high-temperature grease after performing all the qualification tests.



Fig. 3 Photograph of CSRDM gripper screw test setup



Fig. 4 Grease lubricated mock-up gripper operating tube (screw) after testing

II.13 Manufacturing of Annular Linear Induction Pump Components for PFBR

Annular Linear Induction Pump (ALIP), working on electromagnetic principle is used for pumping liquid metal sodium in the Secondary Sodium Fill and Drain Circuit of PFBR. It is a reflux type pump having both inlet and outlet on the same end and used at maximum operating temperature of 450°C. Central Workshop Division (CWD) was entrusted to manufacture four sets of inner and outer duct assemblies for the 170 m³/h capacity ALIP.

These duct assemblies are critical components of the ALIP and demand a robust and repeatable manufacturing process to achieve the required precision dimensional & geometrical tolerances and specified leak tightness. Systematic machining, hard-facing and assembly process plans were established, quality assurance plan (QAP) was prepared and followed during the manufacturing of these duct assemblies in order to achieve high quality and reliability.

Machining of ALIP Components

Each 170 m³/h capacity ALIP has total 47 precision machined parts. The parts, as shown in Figure 1, were precision machined using both conventional and CNC machines within the specified tolerances.

The outer ducts were machined from 1170 mm long ASTM A312 TP 316L 200NB x Sch.120 austenitic stainless steel pipes of 18.36 mm wall thickness. The outer duct was pre machined to 6 mm thickness from 18.36 mm which is about 67.5% material removal in wall thickness and had further radial machining allowance of 1.5 mm. Intermediate dimensional stabilization heat treatment was done at 550 °C for 1 hour to relieve the peak stresses developed due to heavy material removal. A 30 mm thickness support flange was integrated with the pre-machined outer duct adopting sequence welding technique to minimize distortion. Figure 2 shows pre machined outer ducts.

The stress relieved outer duct was machined on internal diameter (ID) side with sufficient grinding allowance for internal boring and external grinding operations. During outside diameter (OD) turning (Figure 3) and cylindrical grinding (Figure 4) operations, the ID was taken as



Fig. 1 Machined parts of ALIP



Fig. 2 Pre-machined outer duct



Fig. 3 OD machining of outer duct

reference using a precision mandrel assembled into the ID. Taking OD as reference internal grinding, boring (Figure 5) and vertical honing (Figure 6) were carried out to achieve the specified wall thickness of 3 mm, perpendicularity of 0.5mm and concentricity of 0.1 mm with reference to the supporting flange and surface finish of 0.4µm in the outer duct.

The inner duct components viz. return pipe, pipe connector, diffuser cone, core support ring, round nut M109 x 1.5P were precisely machined within stringent dimensional tolerances and surface finish. Being thin walled components, meticulous care was taken during machining to achieve specified dimensions and tolerances. The other parts of ALIP like diffuser cone (Figure 7) were also precision machined to achieve specified dimensions and tolerances.

Hard-facing of ALIP Components

To minimise wear and tear of contacting surfaces, the outer periphery of the porous shell, centering pads and spacers, as shown in Figures 8 and 9, were hard-faced to minimum 50 HRc using Plasma Transferred Arc Welding (PTAW) process with Nickel base Colmonoy -5 (NiCr-B) powder and qualified as per nuclear industry standards. All hard-faced parts passed non destructive testing (NDT). Microstructure and hardness profiles of the hard-faced porous shell are shown in Figures 10 - 12. Machining of hard-faced parts was done using Cubic Boron Nitride (CBN) tools and final required profiles were cut by CNC wire EDM process.

Forming of Dished End

Torispherical dished ends of 3 mm wall thickness for ALIP ducts were formed by progressive cold pressing method.



Fig. 4 Cylindrical grinding on OD of outer duct



Fig. 5 ID boring of outer duct



Fig. 6 Vertical honing of outer duct



Fig. 7 Machining of diffuser cone



Fig. 9 Hardfaced spacers

Solution annealing heat treatment of the formed dished ends was carried out at 1050°C cooled by furnace cooling to 900°C followed by rapid quenching in water. Solution annealing of the formed dished ends ensured achieving single phase microstructure and stress-free product with uniform mechanical properties, improved corrosion resistance and ductility.

Close packing of inner duct with Cold Rolled Grain Oriented Steel Lamination Sheets

All machined parts of the inner duct were joined by welding in the defined sequence for enabling packing and to have access for NDT of the weld joints. Cold Rolled Grain Oriented (CRGO) steel lamination sheets of 25.9 mm width x 0.27 mm thickness were stacked together as specified using a set of special fixtures developed in-house to overcome the difficulty faced during insertion of stacked sheets into the annulus between the inner duct and the precisely machined sodium return pipe. Packing density of 96.3% was achieved as against minimum specified 95%. The inner duct was subjected to pneumatic pressure testing (external) at 2 MPa (g) to establish integrity of the weld joints. Helium leak testing of the inner duct under vacuum was carried out separately as well as in assembled condition in accordance with ASME code requirements.

Final Assembly and Testing of ALIP

The outer duct and the inner duct assemblies were integrated ensuring concentricity through the hard faced

front centering pads as well as spacers. One cold formed torispherical dished end was connected to the delivery side of the outer duct along with the inlet branch pipe. The hard-faced porous shell was connected to the other dished end, which was welded in the other end of the outer duct. Three butt welds for fixing the dished end and inlet branch pipe to the outer duct were carried out simultaneously by gas tungsten arc welding process to ensure dimensional accuracy. All weld joints were subjected to non-destructive testing viz. LPT, RT and UT as per ASME Section V. To check the integrity of the weld joints, pneumatic testing was carried out in accordance with UG-100 of ASME

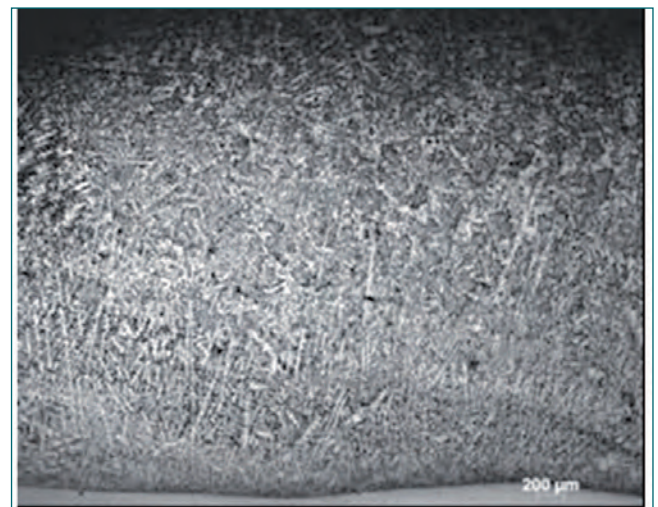


Fig. 10 Microstructure of hardfaced porous shell

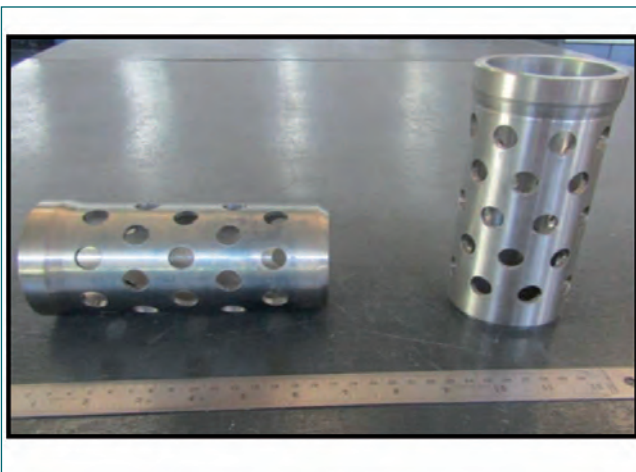


Fig. 8 Hardfaced porous shell and spacers

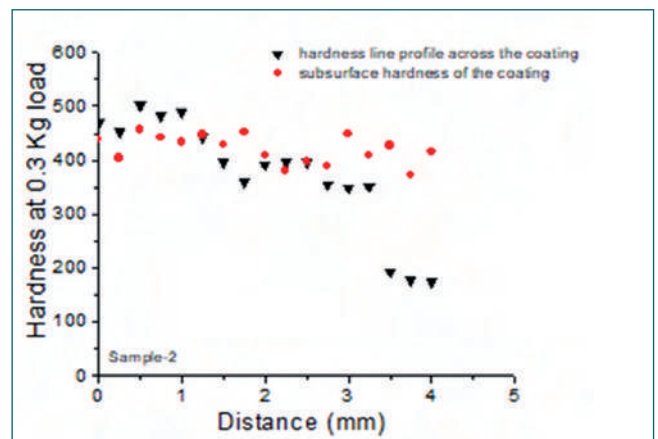


Fig. 11 Hardness profiles of of hardfaced porous shell across coating



Fig. 12 Microstructure of hardfaced porous shell across coating

section VIII division-1 to a pressure of 2 MPa (g) as shown in Figure 13. Thorough quality checks including external dimensions of the ALIP were carried out after pneumatic testing as shown in Figure 14. The assembled ALIP duct assemblies were finally subjected to Helium Leak Testing in accordance with ASME Section VIII Division 1

and achieved leak tightness less than 1×10^{-8} std.cc/s meeting the specification.

The ALIP duct assemblies as shown in Figure 15 manufactured at CWD were delivered to BHAVINI for final installation in PFBR.



Fig. 13 Pneumatic testing of ALIP



Fig. 14 Quality checks after pneumatic testing



Fig. 15 Inner and outer duct assemblies of PFBR annular linear induction pumps of $170 \text{ m}^3/\text{h}$ capacity

II.14 Performance Evaluation of Modified 170m³/h Annular Linear Induction Pump in Sodium Loop

The secondary sodium fill and drain circuit (SSFDC) of PFBR has an Annular Linear Induction Pump (ALIP) for circulating sodium. Some design modifications were carried out in this pump to make this pump more robust to withstand vibration load and to take care of differential thermal expansion during transient conditions. The modified sodium duct was manufactured in-house. After assembly of the modified duct with its electrical winding assembly, the pump was installed in Sodium Facility for Component Testing (SFCT) for its performance evaluation. The schematic of ALIP is shown in Figure 1. It is a reflux type of ALIP where the inlet and outlet lines are at one end. The photograph of ALIP installed in the SFCT sodium loop is depicted in Figure 2.

The performance of an ALIP was evaluated in terms of various characteristics like the head vs flow characteristics and input power vs flow characteristics. Characterisation of annular linear induction pump (ALIP) is required to ascertain its behaviour in the actual reactor system. For measurement of pressure developed by ALIP, cover-gas pressure balancing technique was utilized. In this technique, pressure at pump suction

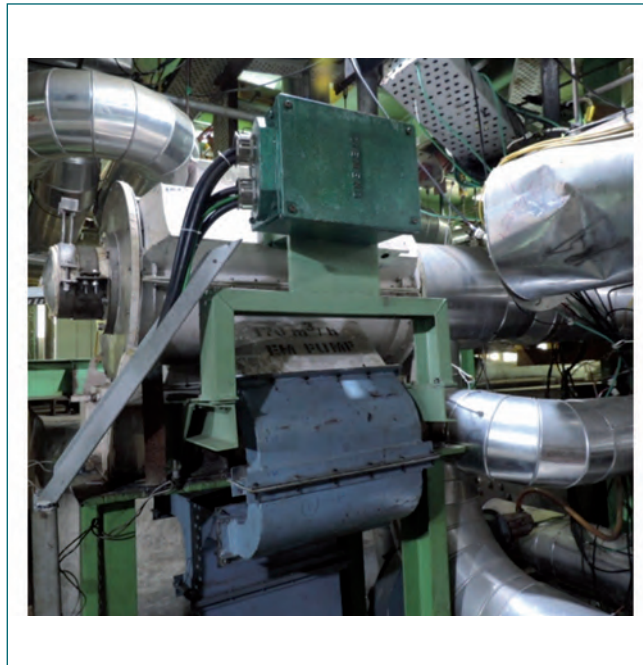


Fig. 2 Modified ALIP installed in SFCT

and discharge was measured by means of two sodium pressure pots with argon as cover gas which were at the same height. The levels of sodium in the two pressure pots were maintained at the same value by suitably adjusting the pressure of argon as per pressure

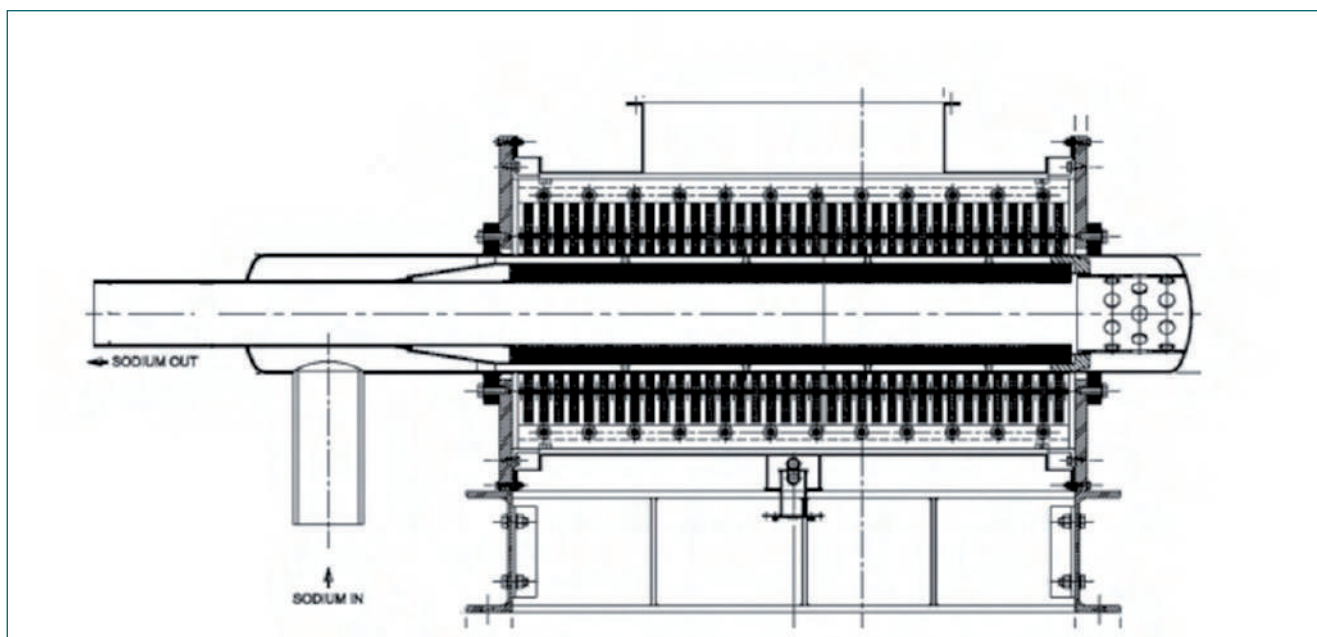


Fig. 1 Schematic of modified SSFDC Annular Linear Induction

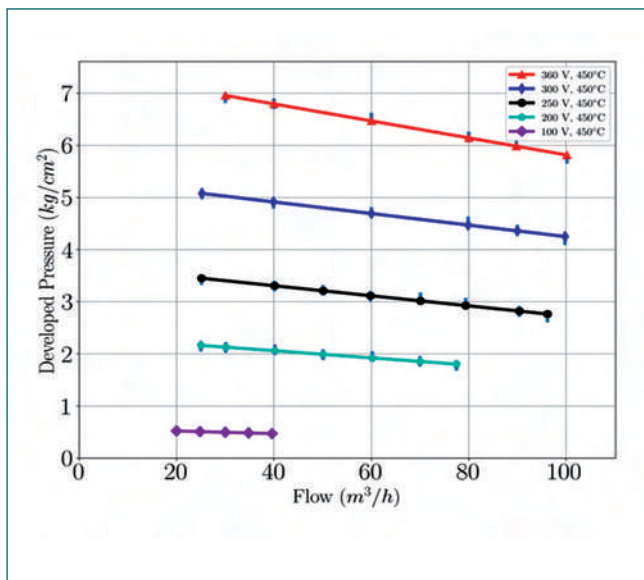


Fig. 3 Experimental head vs flow characteristic of ALIP

developed by ALIP. Thus, the difference of cover gas pressures in the two pressure pots provided the pressure developed by ALIP. The input power drawn by the pump was measured by means of a power analyzer. The sodium flow rate was measured using a permanent magnet flowmeter. The vibration was measured using high-temperature piezoelectric transducers.

The performance of the pump was evaluated at various terminal voltages, temperatures, and flow rates. At a given terminal voltage and temperature, different flow rates were obtained by throttling the valve at the pump discharge. At each flow rate, various pump parameters like differential pressure, input power were measured. The variation of developed pressure with flow rate (i.e. pressure (ΔP) vs flow (Q) characteristics) at sodium temperature of 450 °C is shown in Figure 3. The maximum pressure required to be developed in the reactor system is 4 kg/cm² at 120 m³/h sodium flow rate. From the ΔP - Q curve shown in Figure 3, it is observed that the pump develops a pressure of around 5.75 kg/cm² at a flow rate of 100 m³/h when the pump terminal voltage is 360 V. Thus, the modified pump will be able to meet the requirement of the reactor system. Moreover, the ALIP has drooping or descending ΔP - Q characteristics which show that the pump is operating in the hydrodynamically stable zone.

The input power variation with flow rate is depicted in Figure 4. The input power decreases linearly with an increase in sodium flow rate. As the pump

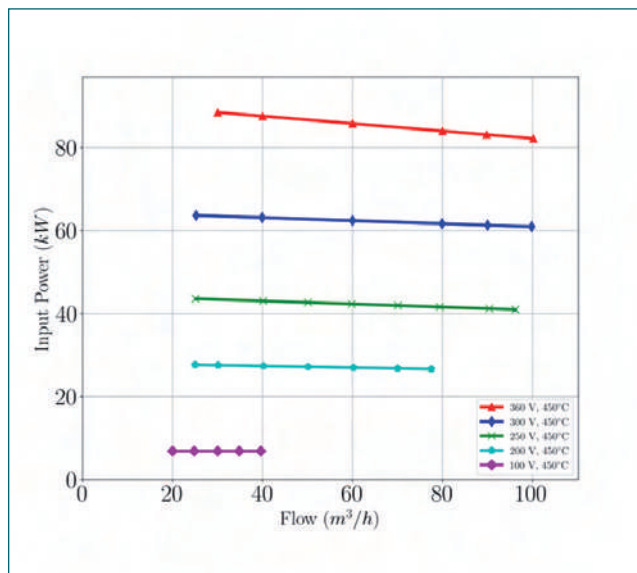


Fig. 4 Input power vs flow characteristic of ALIP

terminal voltage increases, the input power as well as the pressure developed by the ALIP increases. The efficiency of ALIP is defined as the ratio of output hydraulic power to input electrical power and is plotted in Figure 5. The maximum efficiency obtained is 19 %. Vibration measurements were also performed during this experimental performance evaluation and were found to be within limits. The vibration spectrum did not contain any low frequency (<10Hz) component which indicated the absence of magneto-hydrodynamic (MHD) instability. The experimental performance evaluation in sodium loop at various voltages and flow rates has established that the modified design of the pump has the capability to meet the requirements of SSFDC in PFBR.

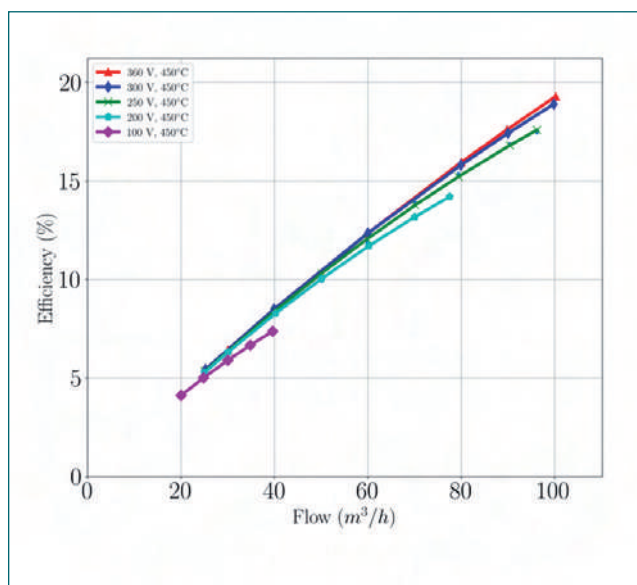


Fig. 5 Variation of efficiency with flow rate

II.15 Vibration Measurements on Annular Linear Induction Pump of Primary Sodium Purification Circuit in Sodium Facility for Component Testing

Testing of PFBR spare Annular Linear Induction Pump (ALIP) 50 m³/h capacity of Primary Sodium Purification Circuit (PSPC) was carried out in Sodium Facility for Component Testing (SFCT) in Engineering Hall-I, IGCAR. Performance tests were carried out on ALIP at sodium temperature of 200°C, 450°C and also after endurance testing of 250 hrs, 1000 hrs, 1500 hrs and 2000 hrs at 450°C. ALIP was operated at different voltages ranging from 100V to 380V and sodium flow was varied 5 m³/h to a maximum of 55 m³/h at various input voltages. Vibration on ALIP was recorded at 8 different locations for each experimental condition.

Piezoelectric accelerometers were installed on ALIP as shown in Figure 1. Clamps with sensor adaptors are welded on the pump similar to PFBR ALIP and sensors are mounted on this adaptor (Figure 2). This arrangement keeps the temperature of the sensors within the prescribed limit of 125°C. Vibration data during the experiment was acquired at 1kS/s and stored for a period of 2 minutes for each condition using DEWESOFT SIRIUS data acquisition system.

During the measurements on ALIP at sodium temperature of 450°C, ALIP was supplied different voltages; 0V, 100V, 150V, 200V, 250V, 300V, 360V and 380V. For each supplied voltage, ALIP was operated at various flow rates from 5 m³/h to 55m³/h. For each sodium flow rate, vibration spectra on ALIP were recorded and analysed. The overall vibration amplitude (RMS velocity in mm/s) in the frequency range of 2 Hz to 400 Hz was recorded. Figure 3 show the variation in vibration amplitude at the 8 sensor locations for different flow rates at 380V



Fig. 2 Photograph of sensor locations at dish end on ALIP

and 450°C. The eight sensor locations are as follows :

- A1: ALIP Dish end-Horizontal (H)
- A2: ALIP Dish end-Vertical (V)
- A3: ALIP Dish end-Axial (A)
- A4: ALIP Discharge-Horizontal (H)
- A5: ALIP Discharge-Vertical (V)
- A6: ALIP Discharge-Axial (A)
- A7: ALIP Suction- Horizontal (H)
- A8: ALIP Suction- Axial (A)

Similar measurements on ALIP were carried out After completion of 1000 hrs of endurance testing at 450°C and 50 m³/h, ΔP-Q curve was again obtained experimentally.

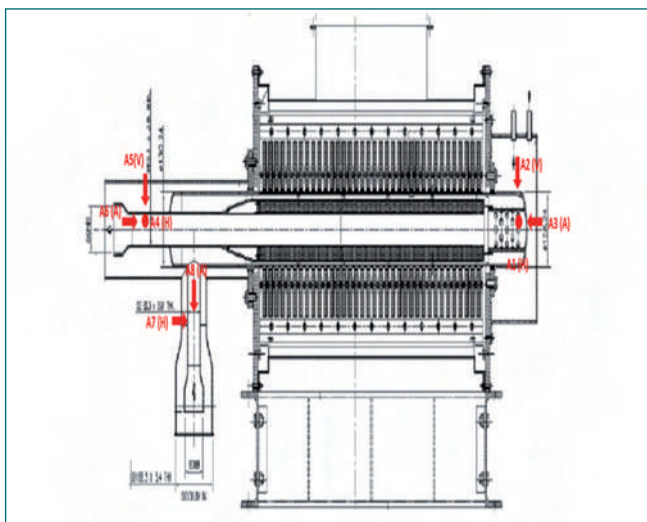


Fig. 1 Schematic view of ALIP with vibration sensor locations

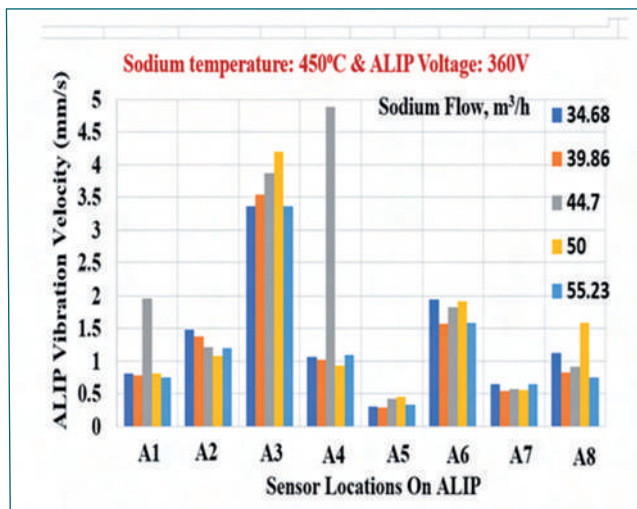


Fig. 3 ALIP vibration amplitude at sodium temperature of 450°C and ALIP voltage of 360 V

During this ΔP -Q curve measurement, vibration measurements were also taken on ALIP. Net Positive Suction Head Available (NPSHA) - A at pump suction when ALIP was operating at 50 m³/h of flow rate after 1000 hours of operation was 1.70 kg/cm². Similarly, vibration measurements were carried out after endurance testing of 1500 hrs and 2000 hrs at 450°C. ALIP vibration amplitude at sodium temperature of 200°C and ALIP voltage of 360 V is shown in Figure 4.

In order to evaluate the pump performance under different available NPSHA, cavitation testing of the pump was carried out. The testing was performed in two modes. In first mode, the pump was put in closed circulation mode from TV-3 to TV-3; whereas in second mode the pump suction was from the sodium storage tank and sodium discharged to TV-3. In first mode, the pressure in pump suction was reduced by throttling the pump suction valve. In second mode, pressure at pump suction was reduced by reducing the pressure in sodium storage tank and flow increased by increasing the voltage of pump. The pressure at pump suction was measured by argon pressure balancing technique in suction pressure pot. The pressure in the pump suction was varied by throttling valve till the point cavitation was observed. Vibration spectrum of ALIP was recorded during these cavitation studies also.

The important observations of vibration measurements are:

1. Major frequency components observed in the spectra are ALIP Double supply frequency (DSF)-

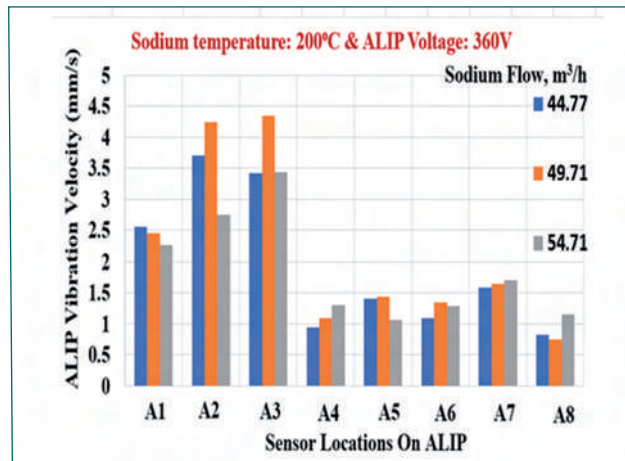


Fig. 4 ALIP vibration amplitude at sodium temperature of 200°C and ALIP voltage of 360 V

100 Hz and its harmonics (Figure 5). This DSF is due to the end effects present in an ALIP.

2. No low frequency components (< 10 Hz), indicative of MHD instability, are observed.
3. Maximum overall vibration amplitude was observed in dished end location and contribution of which was mainly from 100Hz component. No side bands are observed around DSF.
4. Overall amplitude of vibration is found to be less than 5 mm/s even after 2000 h of endurance run at 450°C and 360 V (corresponding to a flow rate of 50m³/h.).
5. It is seen that there is significant increase in RMS value of vibration signals (acceleration/velocity) as well as flow oscillation under cavitation condition.

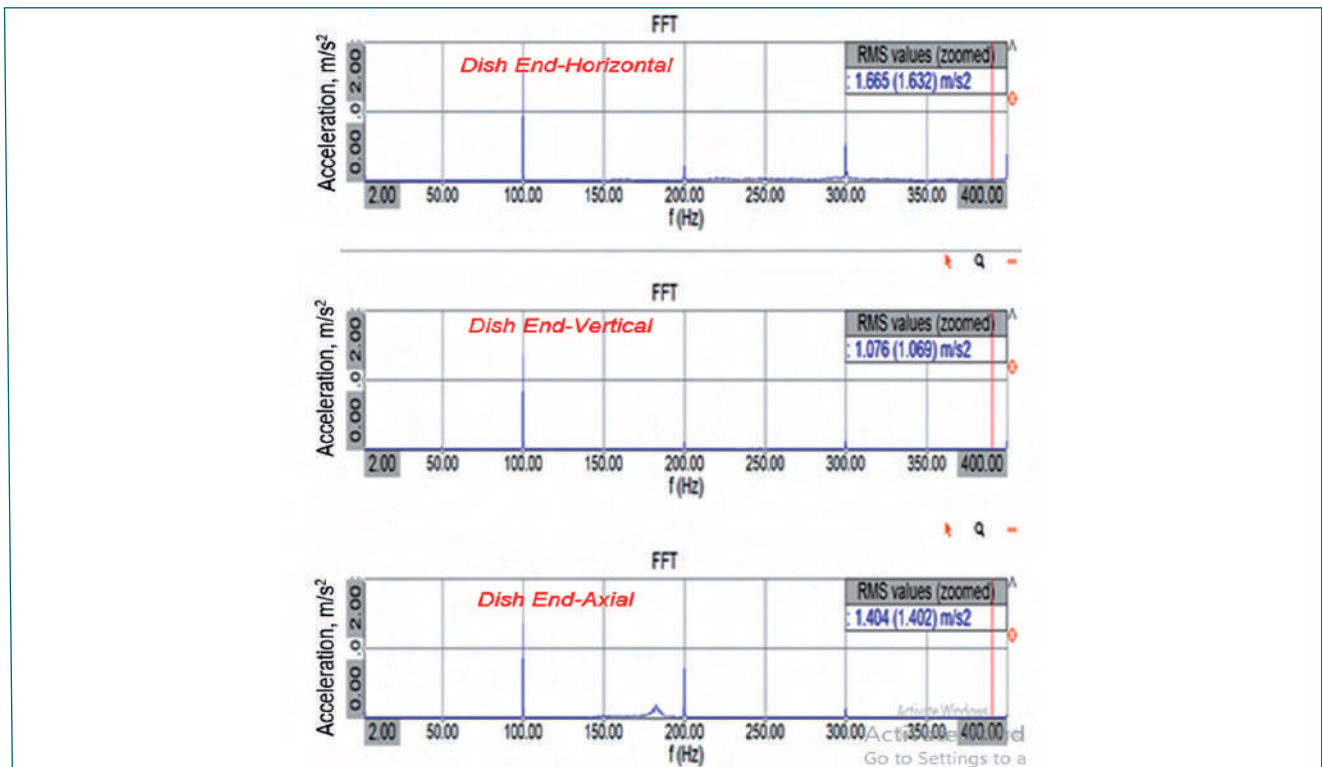


Fig. 5 Typical vibration spectra from ALIP at rated operating parameters; temperature of 450°C, voltage of 360V and sodium flow of 50m³/h.

II.16 Vibration Analysis of Primary Sodium Purification Circuit - Annular Linear Induction Pump

Annular Linear Induction Pump (ALIP) of 50 m³/h capacity and made of SS304 LN is used for pumping sodium in primary sodium purification circuit (PSPC). The part of the PSPC loop containing ALIP is shown in Figure 1. High cycle fatigue due to flow induced vibration and electromagnetic induced forces at the stress concentration zones in ALIP is the main concern for the smooth operation and integrity of the ALIP. A methodology has been developed to estimate the peak stresses induced due to high cycle fatigue during normal operation based on data obtained from experiments and finite element analysis. Acceleration time histories at different locations of ALIP, e.g., inlet nozzle, outlet nozzle dished end etc. are measured during vibration experiments at 450°C in Sodium Facility for Component Testing (SFCT) of Engineering-Hall-I, IGCAR. The main challenge here is to find the unknown forcing function (frequency, amplitude) and the location and distribution of the forcing function. A methodology has been adopted based on Finite Element Analysis using ABAQUS FE software to predict the forcing function and it is applied to the inner-duct region to simulate the vibration and compared with experimental measured data at critical locations.

Evolution of forcing data

To understand the response of the model with forces in different directions, a forcing data (pressure vs. time) has been assumed with frequency and amplitude variation similar to that of the measured acceleration with the scaling factor taken randomly. Implicit dynamic analysis has been performed to estimate the accelerations at critical locations from these force time histories. The assumed forcing data have been applied at different locations of inner part of ALIP in three perpendicular directions viz. horizontal, vertical and axial directions. Accelerations vs. time at

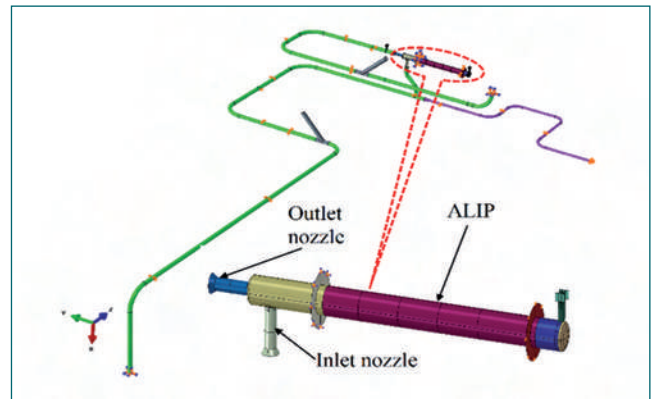


Fig. 1 ALIP with piping layout

the dished end location in all three directions for each of forcing excitation are estimated and relative contribution of each direction excitation on acceleration response in given a direction has been estimated. The final FEA acceleration has been achieved by the suitably scaling each direction forcing functions so that the response acceleration envelops the experimentally measured acceleration data. The FEA and experimental acceleration responses in horizontal direction is compared in Figure 2. The dominant mode with natural frequency 52 Hz (natural period = ~0.02 sec) produces deformation in ALIP.

Fatigue damage

The maximum alternating stress is found to be 20 MPa (with stress concentration effect) at the inlet nozzle junction of ALIP. The fatigue damage is calculated as per ASME SEC III NB. The fatigue endurance limit in the design fatigue curve, for temperature not exceeding 425°C, as per ASME appendix-I (FIG. I-9.2M) for Austenitic steels is 100 MPa. Since the stress is well below the endurance limit, there is no concern of fatigue damage due to high cycle fatigue.

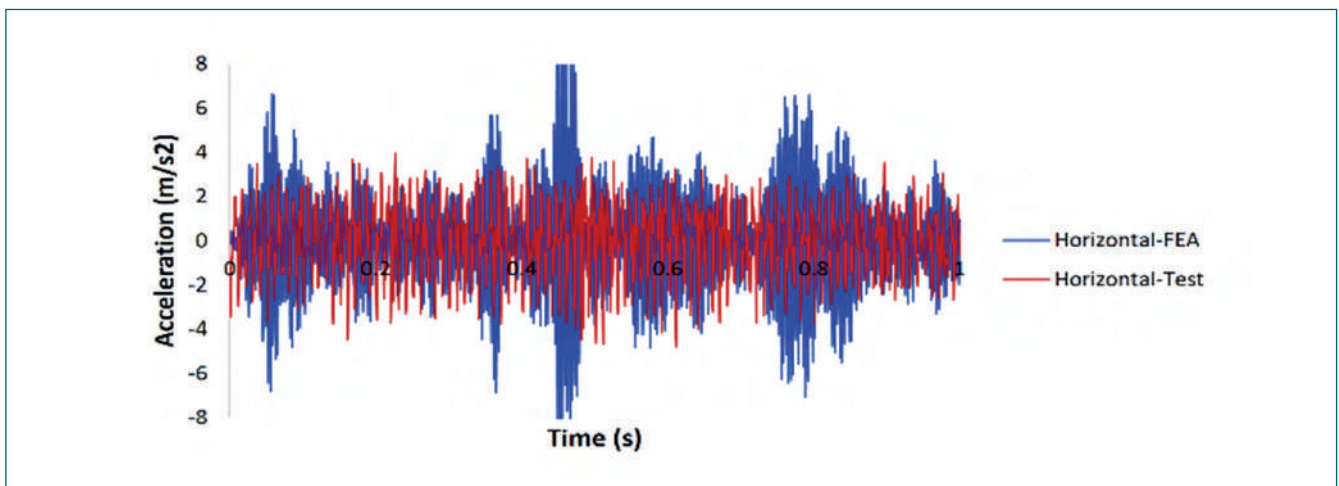


Fig. 2 Comparison of horizontal acceleration from FEM and test at dished end

II.17 Experimental investigation on Sodium leak through Roof Slab-Large Rotatable Plug Gap under Hypothetical Core Disruptive Accident

PFBR consists of large sodium inventory (~1150 t) in main vessel. No sodium leaks are envisaged in the Reactor Containment Building (RCB) during normal operating condition. However, in case of a hypothetical core disruptive accident (HCDA), sodium slug impact on the bottom of the roof slab can result in sodium leak into RCB through penetrations in the roof slab (Large and small rotatable plugs) subject to failure of elastomer seals. One of the probable leak paths is assumed to be created due to extension of hold down bolts of LRP support rings leading to a gap of 1 mm between the roof slab and LRP with opening area of 213 cm². Theoretically, a sodium leak of 39 kg was predicted within a time span of 0.6 s. However, the actual amount

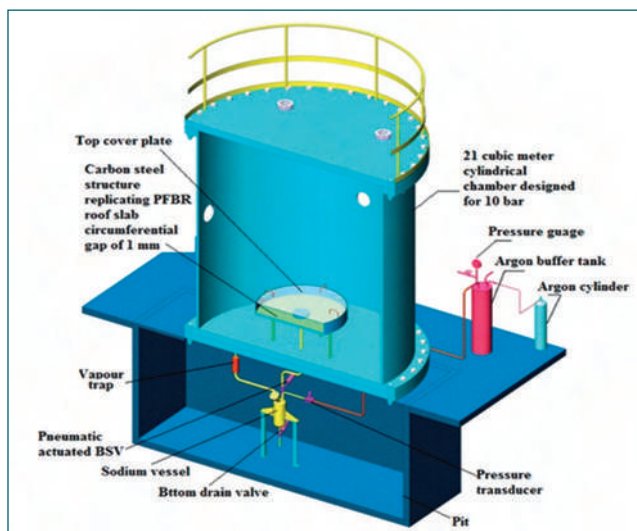


Fig. 1 3D Schematic of experimental setup



Fig. 2 Sodium leak scenario in (A) with insulation, (B) with 10 mm gap and (C) without insulation

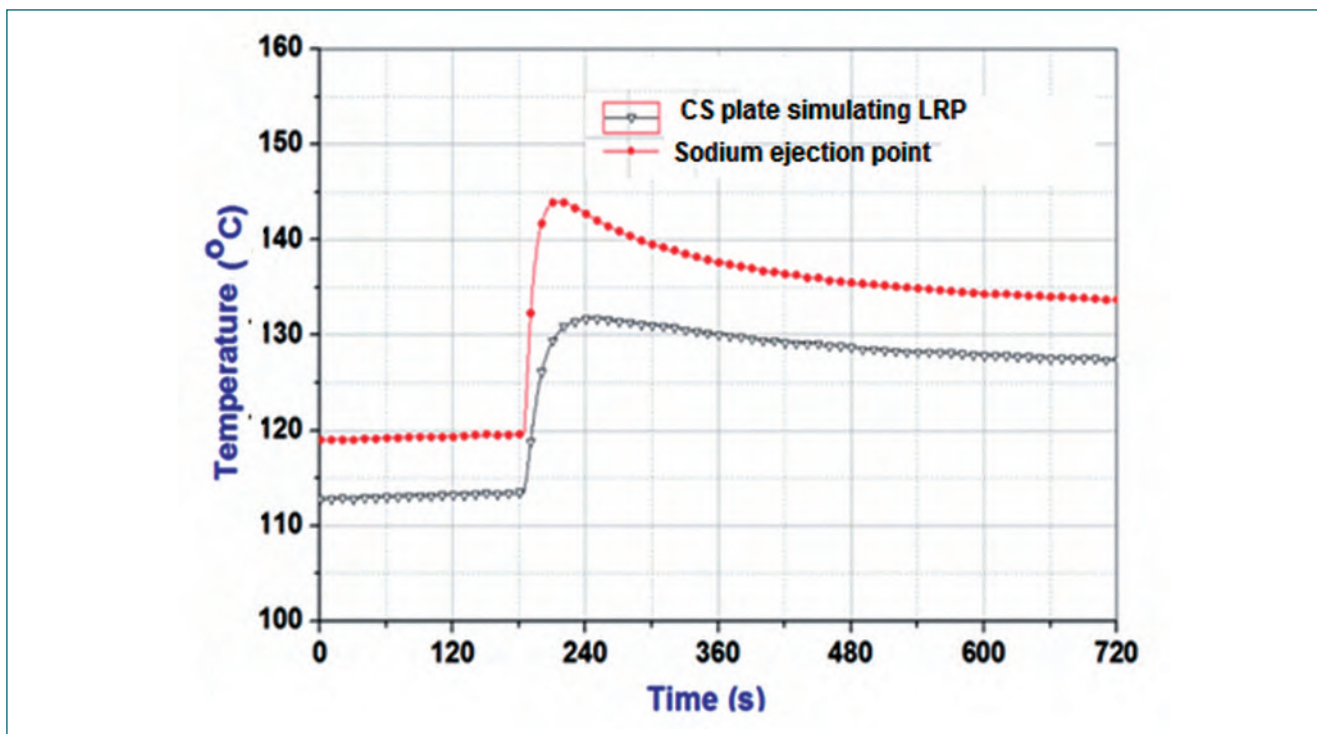


Fig. 3 Temperature profile at leak path

of sodium leak into RCB and its consequences are essential inputs for estimating pressure rise in RCB and radioactive source term. Hence, an experimental study has been taken up to determine sodium release into RCB and its potential to undergo combustion.

An experimental setup consisting of a scaled model top shield platform simulating roof slab-LRP leak path was fabricated and installed at SOCA facility. The experimental setup was integrated to a sodium supply system through a pneumatically operated bellow seal valve as shown in Figure 1. The valve actuator was connected to a timer circuit for controlling valve opening/closing precisely. The sodium system, structure and transfer pipe are mounted with surface heaters for preheating to the desired temperatures.

Preliminary experiments were carried out with water to calibrate the valve actuation mechanism and to estimate the driving pressure required for achieving the targeted sodium leak rate of 2.5 kg/s. The water leak scenarios were analyzed through high speed video images.

Subsequently, sodium leak experiments were conducted in air ambience with three geometrical configurations such as (i) Leak path fully covered with thermal insulation (ii) A radial gap of 10 mm between thermal insulation & ejection path and (iii) Without any insulation on the structure (Figure 2). In all the experiments, pure

sodium at 550°C was ejected through 1 mm gap of roof-slab structure model in 0.6 s. The model roof slab temperature was maintained at 110°C as in realistic case. Thermocouples were mounted at sodium transfer line, leak path, interspaces between insulation-leak path and roof slab structure. Temperatures were recorded during ejection. After each experiment, the ejected sodium was retrieved and weighed.

Maximum temperature of ejected sodium was found to be ~144°C and no sodium fire was observed (Figure 3). The temperature of roof slab was observed to be ~120°C. The reduction of sodium temperature from 550°C to 144°C was mainly due to heat transfer from sodium to steel structure. Maximum amount of sodium ejected through the gap was measured to be ~ 300 g against predicted 1.5 kg. Flow resistance offered by the gap coupled with transient variation in flow properties were major contributing factors for reduction in ejected sodium quantity.

Based on the results, by considering geometrical scale ratio, the possible sodium ejection through the leak path in top shield platform of PFBR would be ~13 kg, which is much less than the theoretical estimate. Due to reduction in sodium temperature below ignition temperature, no instantaneous combustion of sodium is possible. Thus, the experimental results indicate a conservative margin in design of RCB.

II.18 Radiography Examination of Annular Joints in Inner Duct of Annular Linear Induction Pump using Special Tool Arrangement

In PFBR, 170 m³/h Reflux type Annular Linear Induction Pump (ALIP) is used in the fill and drain circuit for filling sodium and maintaining the required sodium level in the Secondary Sodium Main circuit during operation. The inner duct of ALIP consists of two concentric pipes connected to each other by diffuser cone and core support ring. The joint between core support ring and two concentric pipes of inner duct as shown in Figure 1. can not be examined due to joint layout and inaccessibility. The outer pipe of inner duct is 6" sch. 10 (OD 168.3 mm) of AISI 316L material having thickness 3.4 mm. The annular gap between the concentric pipes is 56.5 mm and length of duct is 918 mm. The radiographic film cannot be placed inside the annular gap to carry out radiography testing. The complex nature of the weld joint calls for development of some special technique. To overcome the geometric constraints, a tool has been designed and developed to keep the radiographic film inside the annular gap for achieving quality radiographs with 2% sensitivity.

A special tool arrangement has been designed and developed by the QAD and CWD team, to assist the radiographer in placing the radiography film inside the annular gap. A wooden piece machined into a cylinder of ID 110mm X OD 143mm as shown in Figure 2 for holding



Fig. 1 Inner duct during fabrication

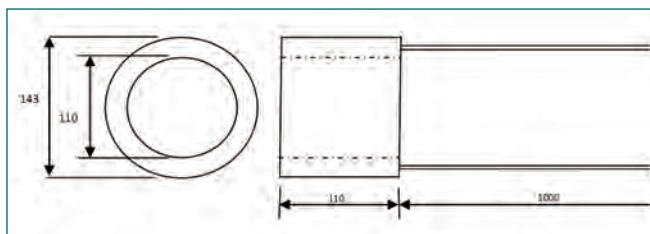


Fig. 2 Sketch of film insertion tool with dimensions



Fig. 3 Radiography film insertion and placement tool



Fig. 4 Sequence of operation (a) Placement of film on the tool (b) Marking and IQI placement (c) Insertion of film cassette inside the annular gap

the flexible vinyl film cassette. The dimensions of the wooden cylinder have been calculated by considering the thickness of film cassette plus lead sheets and available annular gap of 56.5 mm to ensure absence of any air gap between film and weld joint. A proper figment of film with weld joint has been ensured and achieved. Two steel tie rods were connected to the wooden cylinder to facilitate insertion and removal of film as shown in Figures 3 and 4.

A reliable radiography examination procedure has been designed and developed to qualify the weld joint between core support ring and outer shell of inner duct of ALIP. This tool facilitated the placement of film cassette inside the narrow annular gap which in turn resulted in better quality radiographs, faster operation and higher productivity.

II.19 Visual and Dimensional Inspection with Geometric Features of Critical Components

Most of the components in PFBR are large in size and requires close tolerance in dimensions with geometric features for functional requirements. All those components are erected and being checked for its performance during commissioning activities. Compared to fabrication stage inspections, inspection of dimensions of large size components always imposes challenges, especially in site conditions. With recent technological advancements, Coordinate Measuring Machine that precisely measures the three dimension measurement with one micron accuracy are being utilised. But these measurements could be made only inside laboratories and other constraint such as limitation in size of the part. Here we shared our experiences gained during dimensional inspection of large size components of PFBR like Secondary sodium pump wear ring, Labyrinth ring, CRDM lower part components, etc. and also comparative study was done to estimate uncertainty in manual and CMM measurement.

Dimensional Inspection of Wear rings for suction & discharge sides of Secondary Sodium Pumps

In parts such as Wear rings of Secondary Sodium Pump assembly of PFBR, clearance between the mating parts is stringent. Large size wear ring having diameter $\varnothing 750$ H7 with stringent dimensional tolerance requirement like H7 and g6, were measured with measuring instruments (Figure 1) like Vernier caliper (0-750mm), Stick Micrometer (0-1500mm) and slip gauge sets. Procedure for measurement was made with check points such as zero error of the Instrument, holding of Vernier shall be kept straight and both the jaw at same height, both end of the instrument shall touch the centre point of the component, equal application of Pressure, One end shall be kept stationary and other shall be rotated to get the exact values. Manual error is minimized by adopting standard methodology.

During measurement, Vernier Caliper of Large size like (0-750 mm, 0-1000 mm) for outer diameter measurement (Figure 2) and Inside stick micro meter (0-1500 mm) for inner diameter (Figure 3) and slip gauge set were used.

The repeatability of these manual measurements at shop floor conditions is found within the 20 microns as per Table 1 and the actual values meets the specified tolerances. Large



Fig. 1 Concentricity measurement



Fig. 2 Outer diameter measurement

diameter measurement at different stages such as before machining, after Colmonoy deposition to check the required thickness of overlay and after machining.

Inspection of Geometric features of CRDM sub assembly

Measurement of geometric features of slender assemblies of control rod drive mechanism, FBTR poses challenges. Among those, stringent tolerances such as +0.4 mm for the length of 5165 mm and 0.06 mm for concentricity (Figure 1) of the sub assembly of Control Rod Drive Mechanism (CRDM) of FBTR was measured at CWD and reported.

Uncertainty in Measurements

In order to estimate the uncertainties involved in Manual measurement for large diameters, we have selected



Fig. 3 Inner diameter measurement

Sl. no.	Description	Required Dimension as per drawing	Observed (mm)
1	Suction Casing Subassembly	Ø750 H7 (+0.08)	750.059
			750.070
			750.078
2	Casing Ring	Ø 749 g6 (-0.024, -0.074),	748.951
			748.965
			748.949
3	Impeller Ring Suction side	Ø264+ 0.05	263.988
			263.972
			263.981

Sl.No.	Measurements in mm	
	Manual	CMM
1	528.90	528.86
2	528.96	528.96
3	529.15	529.09
Std deviation	0.106	0.094
uA	0.061	0.054
Uexpanded	0.074	0.068

machined ring of diameter 529 mm with allowable tolerance of H7. Initially, Inner diameter of the ring was measured manually using stick micrometer at three different locations and same ring ID was measured using CMM at the same locations. Both the measured values were compared and uncertainty was estimated in both the case (Table 2).

Large size components with stringent tolerance requirement like H7 and g6, were measured with instruments like Vernier caliper (0- 750 mm), Stick Micrometer

(0-1500 mm) and slip gauge set. Though manual error can not be eliminated totally, but it was minimized by adopting standard methodology. The testimony is the repeatability of the measurement and uncertainty measurement shows minor variation between the manual and CMM measurement.

Visual and dimensional Inspection including geometric features of large components such as Secondary sodium pump wear ring, Labyrinth rings, CRDM lower part components, FFLM components. labyrinths, wear rings, etc. are performed effectively and efficiently by standardizing measurement methods using advance instruments such as coordinate measuring machines.

II.20 Seismic Analysis of Inclined Fuel Transfer Machine Shielding Door

Inclined fuel transfer machine is provided with a movable shielding door to allow inspection and servicing. Shielding door is connected to a supporting frame with studs, locking plates and nuts. Studs are welded to both shielding door as well as I-sections by fillet weld. Supporting frame consists of I-sections and stacked plates. A detailed seismic analysis of shielding door along with supporting frame is carried out to assess realistic responses under seismic conditions.

Shielding door and stacking plates are made of Fe 410W material. Finite element model consisting of shielding door, studs and locking plates along with the supporting frame is created using appropriate type of finite elements. Modal analysis is carried out by considering embedded plate and vertical I-section adjacent to wall as fixed supports. Fundamental frequency of the structure is above 33 Hz, viz. structure is behaving as rigid body. Mode shape corresponding to first natural frequency is shown in Figure 1.

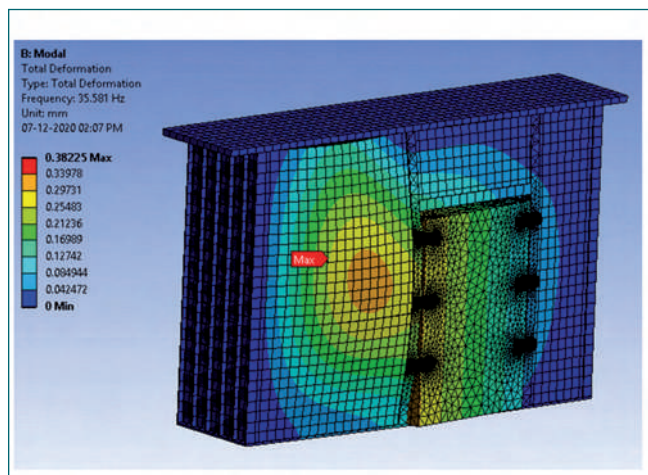


Fig. 1 First mode shape of Shielding door along with support structure corresponding to 35.9 Hz

Response spectrum analysis is carried out by including missing mass and rigid body effects. The stress distributions obtained at locking plate and I-sections for all cases are shown in Figures 2 and 3 having maximum primary stresses as 36.7 MPa and 11.8 MPa

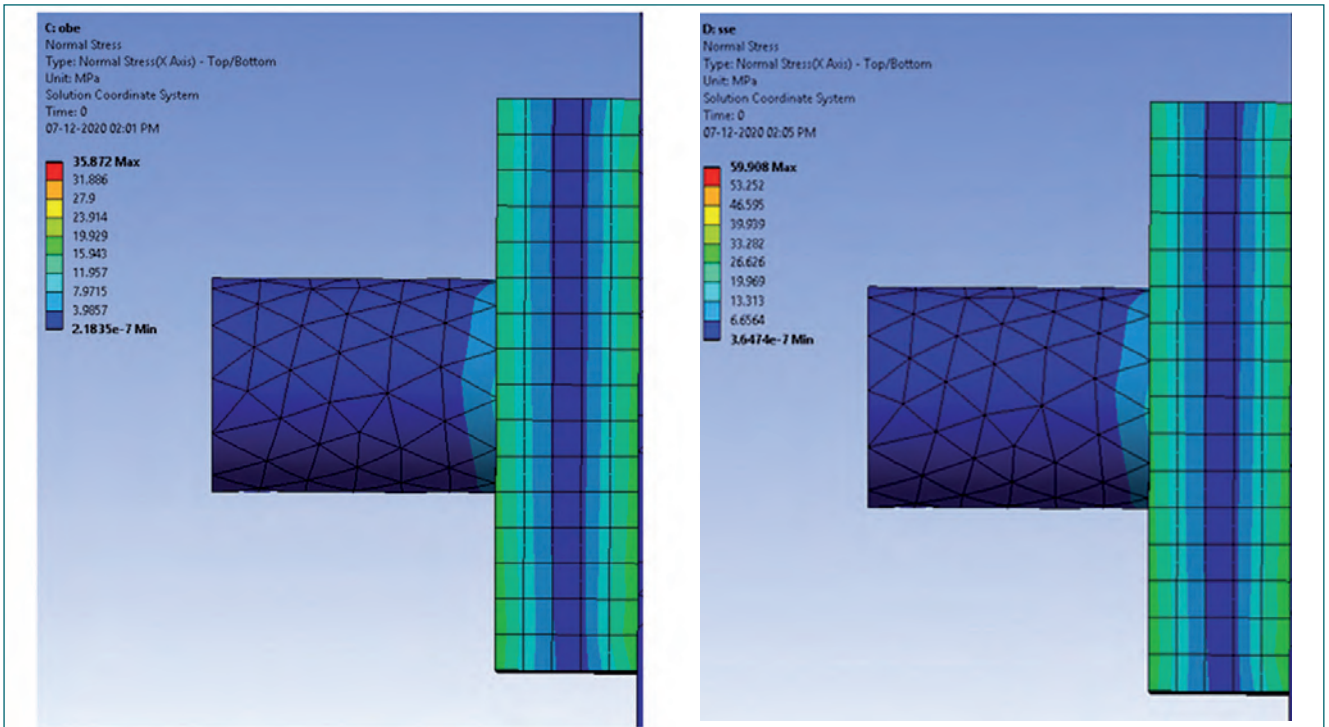


Fig. 2 Stress distribution across locking plate for OBE and SSE loading respectively

respectively. Equivalent static method is used for stress calculation in fillet weld between stud and I-section as the structure is rigid. For equivalent static analysis, Zero Period Acceleration (ZPA) is considered for shielding door as the fundamental frequency is above the rigid frequency range of response spectrum. The forces considered for equivalent static analysis are given in Table 1.

The maximum stresses at weld location are 113.4 MPa and 187.3 MPa in case of OBE and SSE respectively. The shielding door along with support structure corresponds to seismic category-1. ASME Division III Section I (subsection NF) has been followed for qualification of supports. Stresses in locking plate and I-sections are well below the allowable limits. Stresses in the fillet weld between studs and I-section were more than the allowable limits. A pair of studs were additionally added to reduce the stresses within limits.

Table 1: Shear force, normal force and bending moment on each stud for OBE and SSE		
	OBE	SSE
Shear force (kN)	2.6	4.4
Normal force (kN)	2.2	3.7
Bending moment (N.m)	270	450

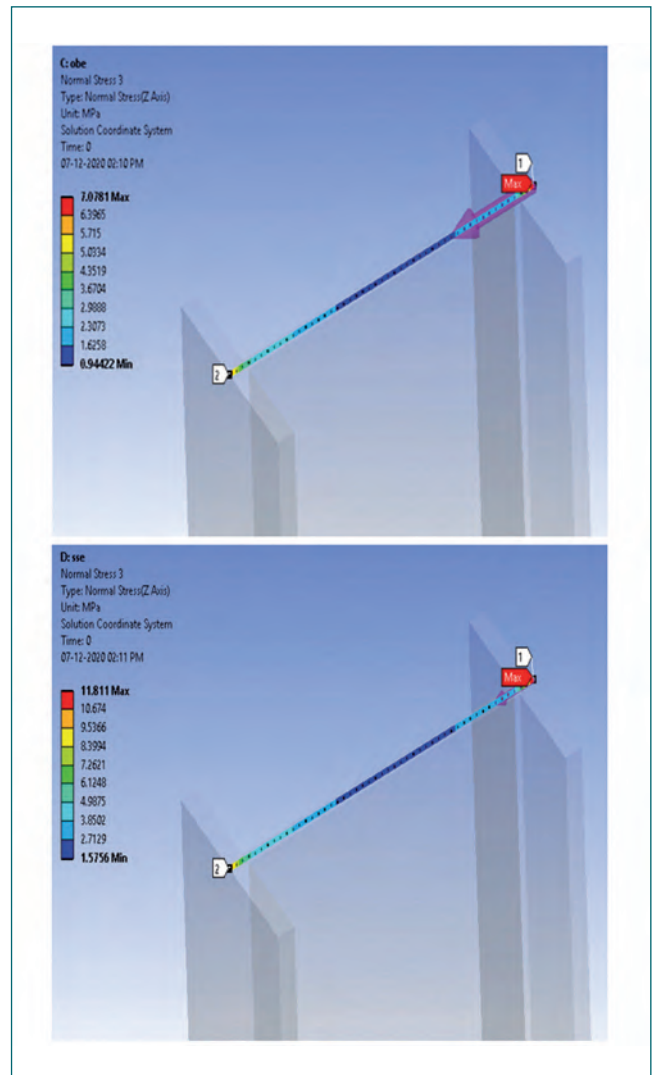


Fig. 3 Normal stress distribution in I-section channels for OBE and SSE loading respectively

II.21 Experimental Demonstration of Carbonation Method for Neutralisation of Alkaline Solution in a Pilot Scale Test Setup

During initial fuel loading of PFBR, washing of sodium wetted dummy sub-assemblies by Steam-Nitrogen process and subsequent rinsing at Spent Sub-assembly Washing Facility (SSWF) generates alkaline liquid effluent of chemical composition viz; 0.12 M NaOH and pH 13. Around 725 liters of alkaline effluent gets generated per subassembly during this process, considering 2 kg of sodium is sticking to each SA. The total amount of 220 m³ of alkaline liquid effluent is generated considering the existing dummy subassemblies (SA) in the core are replaced with Blanket SA (120 nos.) and Fuel SA (181 nos.). The alkaline liquid effluent generated is categorized as potentially active liquid waste (Category-B₁) due to the possibility of contamination from Blanket and Fuel SA loaded during the initial fuel loading. The low-level liquid effluents (Category B₁ and Category B₂) can be treated and discharged from PFBR site into sea through Liquid Waste Management Plant (LWMP). But discharge of the effluents into sea with a pH value greater than 9 is not permissible as per the Central Pollution Control Board discharge limits (CPCB pH discharge limit is 6.0-9.0 in marine coastal areas). These alkaline effluent generated during non-continuous process at SSWF is characterised to be outside the allowable range for direct discharge into sea and will have to undergo onsite treatment. Hence, a Mechanically Agitated gas-liquid Contactor (MAC) was designed and it is being envisaged to be installed at Liquid Waste Management Plant (LWMP) dyke area.

The lowering of the pH inside MAC is achieved through carbonation method. In this process, carbon dioxide gas is supplied through sparger and mixed further by rotating agitator assembly provided inside the MAC. Carbonation for neutralisation of caustic effluents resulting from sodium cleaning is attempted first time. The process parameters of carbonation method needed to be experimentally demonstrated at pilot scale before making the changes at plant site. The experimental demonstration of the process was carried out by using existing facilities at SGTF DM water plant. The components for conducting pilot scale experimental demonstration of neutralising the alkaline solution (concentration 0.12 M as that of effluents coming out of SSWF) are discussed below:

The process parameters of carbonation method needed to be experimentally demonstrated at pilot scale before making the changes at plant site. The experimental demonstration of the process was carried out by using existing facilities at SGTF DM water plant. The components for conducting pilot scale experimental demonstration of neutralising the alkaline solution (concentration 0.12 M as that of effluents coming out of SSWF) are discussed below:

- A tank for preparing required quantity of dilute caustic soda solution of known concentration of 0.12 M.
- A CO₂ gas supply system with all accessories like a CO₂ cylinder, pressure regulator and a flow metering device for quantifying the CO₂ gas going into the mixing tank.
- Mixing tank for allowing the prepared caustic/alkaline solution to react with CO₂ in an effective manner by

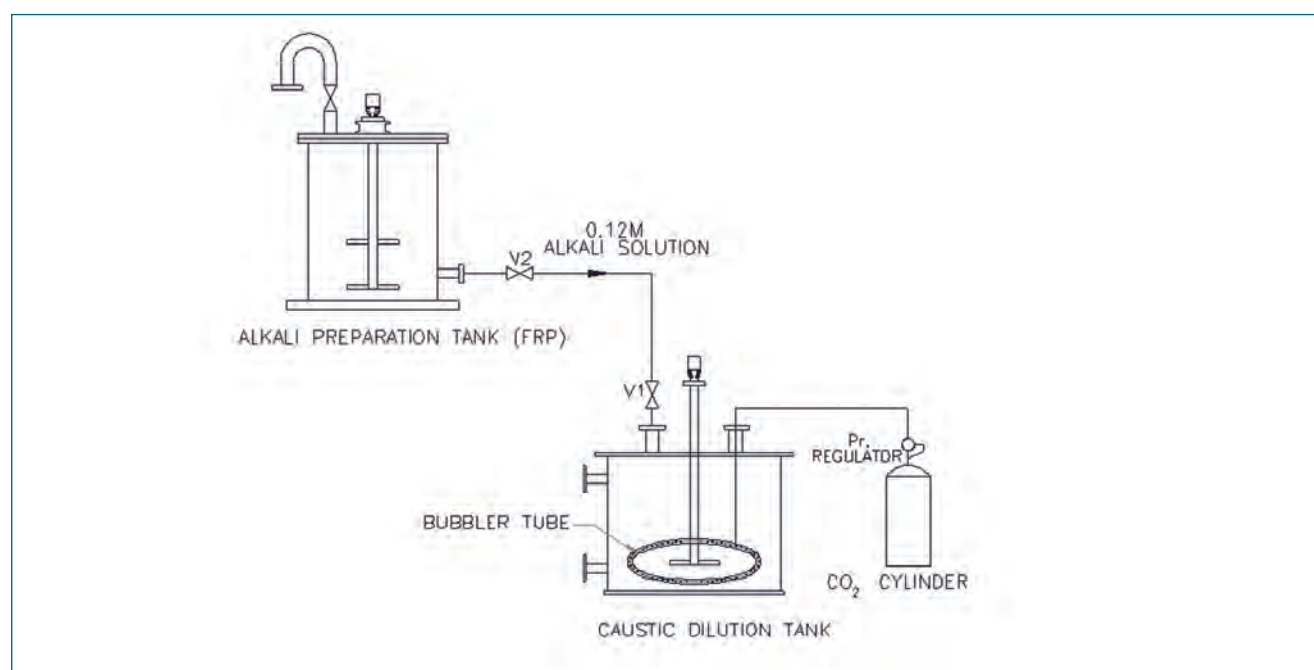


Fig. 1 Schematic of the experimental test setup

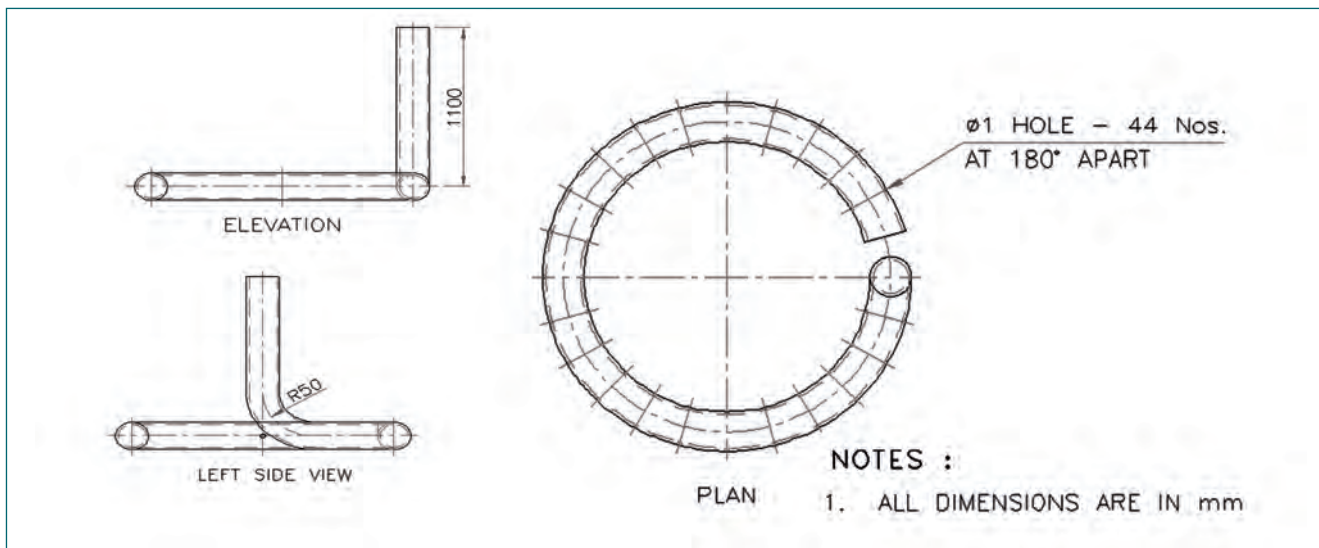


Fig. 2 Schematic of ring-shaped sparger for CO₂ gas bubbling

ensuring proper dispersion of CO₂ gas bubbles. Also, the mixing tank is provided with ring-shaped sparger just above the bottom head of the mixing tank, such that it is located just below the impeller blades. The CO₂ gas enters into the mixing tank through the perforations provided in the sparger and is dispersed into the solution by the shearing action of the rotating impeller blades.

The schematic showing experimental test setup used for the pilot study is shown in Figure 1. The details of the ring-shaped sparger which is installed inside the mixing tank is shown in Figure 2.

The steps involved in carrying out the experimental run are discussed below:

- i. Preparation of 0.12 M alkaline solution: It is achieved by dissolution of 720 grams of pure solid sodium hydroxide flakes in 150 liters of DM water inside preparation tank. The preparation tank is provided with low-speed agitator which ensures complete dissolution of the flakes and homogeneity of the solution. The pH of the solution is in the order of 12.6 as expected and thus confirmed the strength of prepared solution. The prepared solution is then transferred from alkali preparation tank to mixing tank by gravity head available in the system.
- ii. Experimental run: After the complete transfer of the prepared solution, the agitator system of the mixing tank is started. The CO₂ gas from the cylinder is admitted at a regulated pressure to achieve a bubbling flow rate of 4-5 litre/min (NTP) as measured by the rotameter. The CO₂ gas is dispersed thoroughly within the alkaline solution by the high-speed propeller type impeller system. At regular intervals, all important process parameters like CO₂ supply pressure, CO₂ gas flow rate, pH of the reacting solution are noted down and log sheet of the process is prepared. The recorded data of pH versus time from the log sheet is plotted and shown in Figure 3.

From the Figure 3, it can be seen that pH of the solution start decreasing gradually as the alkaline solution is getting neutralised by carbon dioxide gas. The pH of the alkaline solution finally stabilizes at around 7.7. When pH value of the two successive samples collected showed identical values with no further decrease, the neutralization reaction is declared complete. It took nearly five hours of operation to bring down the pH value from 12.6 to 7.7. Total CO₂ gas consumption was around 5 kg at the end of the experimental run.

Thus, a pilot scale demonstration of neutralization of alkaline solution (made up to concentration 0.12 M as that of effluents coming out of SSWF) using carbonation method was successfully carried out. The process parameters were validated and the proposed method was successfully demonstrated. The final pH of the solution obtained was 7.7 which is below the upper discharge limit of pH 9.0 set by Central Pollution Control Board (CPCB) for disposal of effluents into the sea. This process now validated is useful in treating the caustic effluents from reactor as well as from sodium facilities.

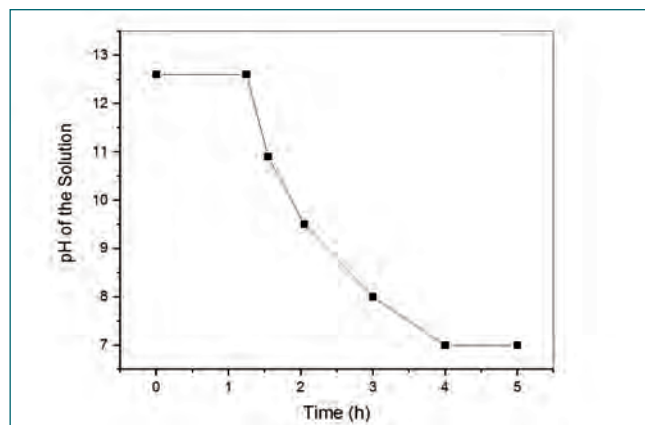


Fig. 3 Change in pH of prepared 0.12 M alkaline solution with time (h) as carbon dioxide gas is added

II.22 Performance and Safety Evaluation of Network Components used in Distributed Digital Control Systems

Distributed control systems are being used in PFBR where in-house designed I&C systems control the final control elements based on the process logics performed on acquired data & commands. The data acquired from analog/digital sensors are digitized by Real Time Computer (RTC) systems and sent to centralized fault tolerant servers and various display stations for logging & display purposes. Similarly, commands received from operator's desk are again routed through network switches to the final control element via RTC systems. TCP/IP communication over Ethernet network forms the backbone of Distributed Digital Control System (DDCS) architecture. Data communication in RTC system is taken care by dual redundant TCP/IP offload network modules present in each CPU card which in turn are connected to layer edge switches followed by core switches that are finally connected to the centralized server i.e., Process Computer. The aim of this project is to characterize the entire plant communication network in view of ethernet data corruption, packet losses, unexpected delays, denial-of-service attacks, data flooding, network latency and throughput in bespoke hardware & software components used for plant safety applications.

Test set-up was done to emulate PFBR DDCS architecture, where VME systems are connected to

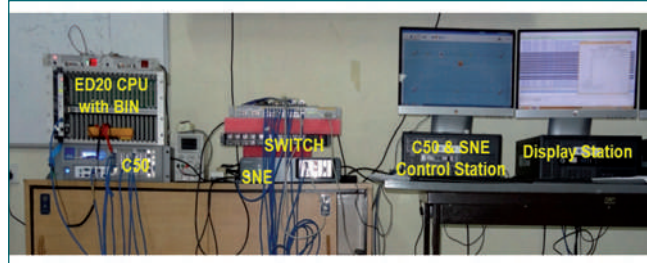


Fig. 2 Test setup in Lab

display stations/server over switched local area network, as shown in Figure 1a. RTC system software and display station diagnostic software were developed to keep track of TCP packet transactions and record anomalies. Network impairment & Load generator tools were used to test the behavior of RTC system & Ethernet switches (Figure 1a). Impairment tool was used to inject faults like packet corruption, packet delays, packet drops, accumulated packets, and is also generates background traffic. Load generator tool was used to characterize the routing latencies of ethernet switches as per RFC2544-Benchmarking Methodology. Denial-of-Service attacks were also carried out manually as well as with tools; and the RTC response was recorded. Security features of switches like rate limiting, MAC/IP binding, and port disabling were also tested. RTC communication was validated as per IEEE802.3 MAC protocols and TCP/IP RFC-791, 792 & 793. The detailed connectivity diagram is shown in Figure 1b. Lab setup is shown in Figure 2. Similar test setup (Figure 3) was established at PFBR site, and actual DDCS network characterization was done for a representative SC-2 RTC system, as per the test methodology described earlier. Based on the results obtained, the suitability analysis of network components were done, and further safety/security recommendations were provided.

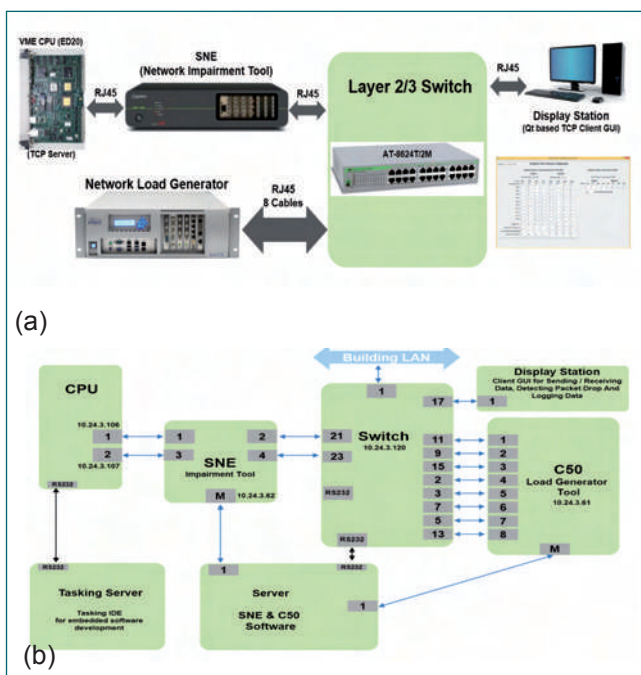
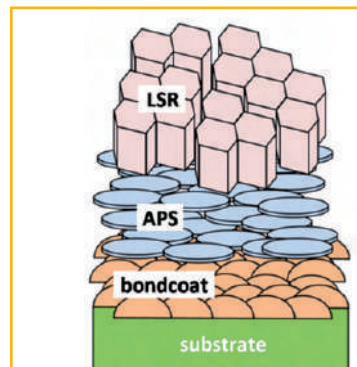
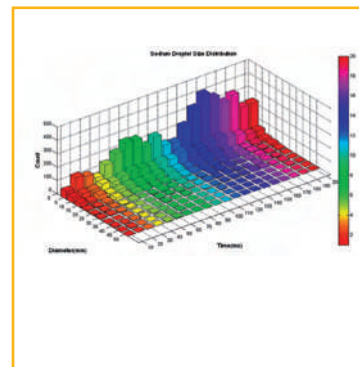
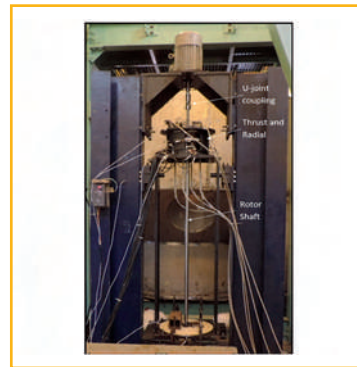
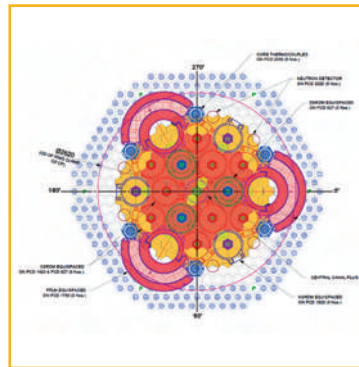


Fig. 1 (a) Configuration and (b) network connectivity diagram of test setup



Fig. 3 Test setup at PFBR site



R&D for Fast Breeder Reactors

CHAPTER III

III.01 Sizing of Reactor Assembly for 500 MWe FBRs Meeting the Revised Safety Criteria

After PFBR, a road-map to construct six more MOX fuelled sodium-cooled fast breeder reactors with improved safety and economy, meeting the revised AERB safety criteria has been worked out. The first twin unit (FBR 1&2) will be located at Kalpakkam. The design of FBR 1&2 will be improved by incorporating the experiences from design, R&D, safety review, construction and commissioning of PFBR. Towards this objective, the conceptual design of a 600 MWe FBR core with reduced sodium void coefficient was initially made. During detailed review of proposed changes in consultation with all the stake holders, it is observed that the changes to static components like reactor assembly components (an increase of dia. 1 m to accommodate the larger core) and intermediate heat exchangers (an increase of ~1 m in height to meet the additional heat removal requirements) can be implemented without much difficulty and without losing the experiences gained. However, the changes to dynamic components like pumps, shutdown & handling mechanisms calls for fresh developmental effort and testing before deploying them in reactor. Also, major changes to core & fuel design calls for detailed safety reviews, afresh. Based on the above considerations, necessity of further study of conceptual design of future FBRs with 500 MWe for implementing the revised safety criteria was identified with an aim to minimise the design changes w.r.t. PFBR and restricting changes to only bare essential, which are required based on feedback from PFBR construction & commissioning.

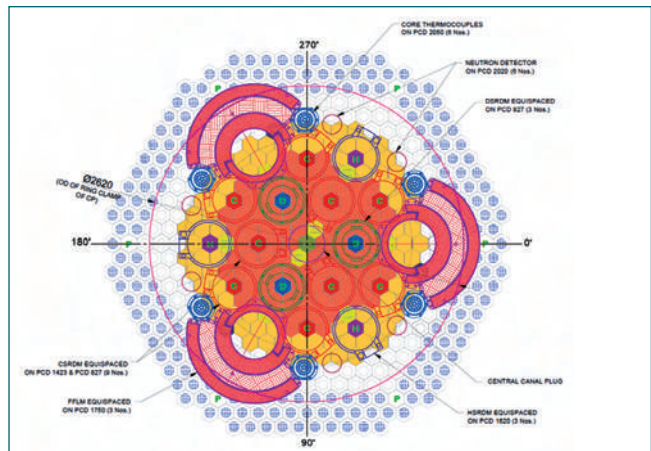


Fig. 2 Layout of Items in control plug

Reactor Physics Design

Physics design of a 500 MWe core was carried out by taking the PFBR core design itself as reference design. Several core configurations were studied to incorporate the additional safety provision of Hydraulically Suspended Absorber Rods (HSAR) of 76% enriched B₄C (ref. Figure 1). Due to the presence of HSAR and Stroke Limiting Device (SLD) in CSRDM, both Unprotected Transient Over Power Accident & Unprotected Loss of Flow Accident are avoided, thereby practically eliminating the core disruptive accident. The beginning of life (BOL) core has a sodium void coefficient of 2.3\$. Breeding ratio for the BOL core is 1.14 and ~ 1.07 in the equilibrium core. Three rows of reflectors are provided to facilitate provision for increasing radial blanket in future for achieving higher breeding.

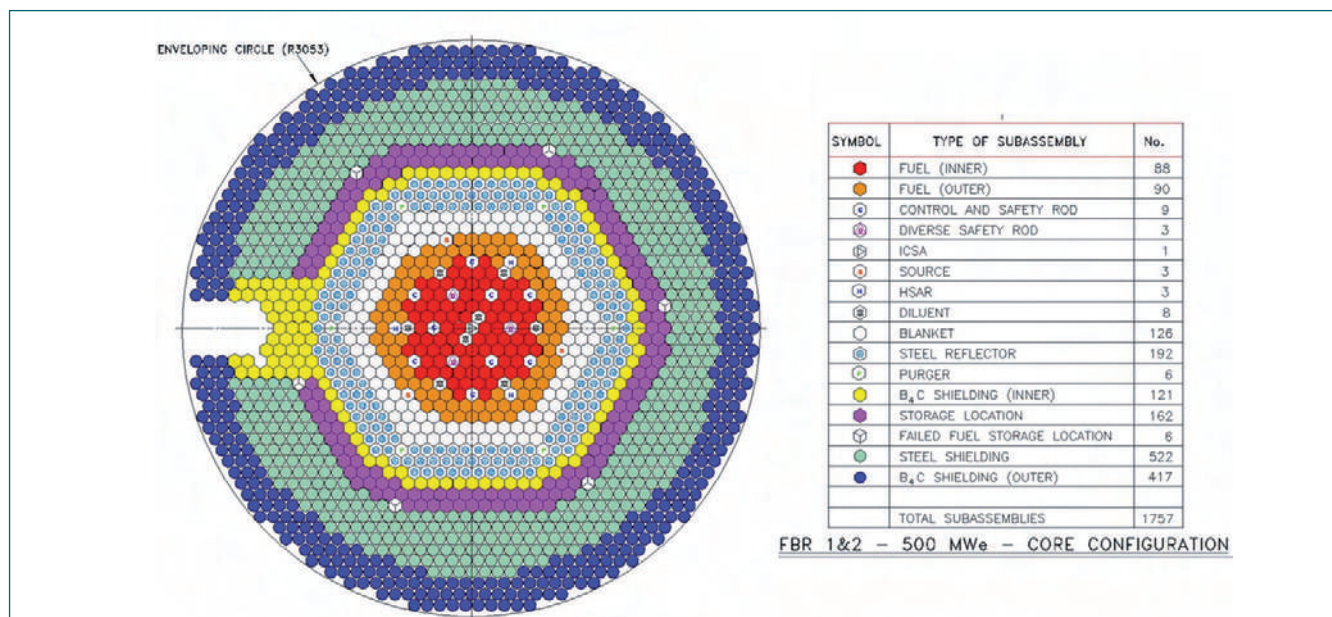


Fig. 1 Core configuration for optimised 500 MWe FBR 1&2

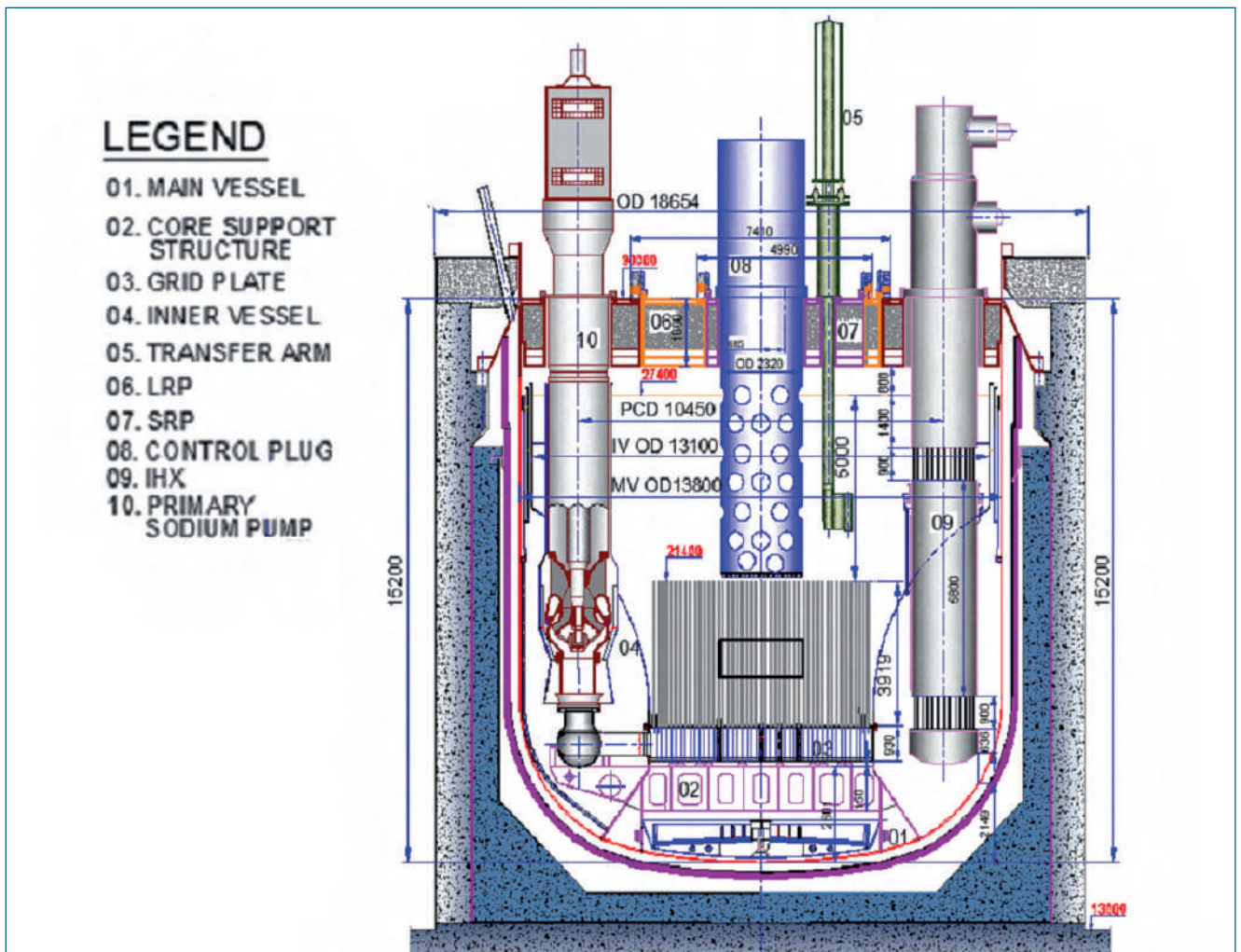


Fig. 3 Vertical section of reactor assembly

Control Plug Layout

For the recommended core configuration, layout of components supported over control plug (CP) was finalized considering various engineering and physics constraints. This includes 9 CSRDMs, 3 DSRDMs, 3 HSRDMs, 3 FFLMs, 219 thermocouples in six groups, 6 neutron detectors & one Central Canal Plug / SNDHM. Since thermocouples are provided in 12 additional locations, diameter of CP is increased by 70 mm w.r.t. PFBR. The skirt shell diameter of CP is 2320 mm and the OD of the ring clamp fixing CP to SRP support flange is 2620 mm. Layout of components over CP top is shown in Figure 2.

Sizing of Reactor Assembly

Subsequent to finalization of layout of items in control plug, sizing of reactor assembly (RA) was taken-up. Based on the control plug shell diameter, an eccentricity of 685 mm between SRP & LRP was arrived at. Considering offset arm handling machine same as in PFBR, the SRP and LRP diameters were worked out to be 4990 mm & 7420 mm, respectively. One of the important feedback from PFBR is need to increase the gaps between

control plug - SRP and SRP - LRP for installation of complementary shield blocks as well as carrying out decoupling / coupling of rotatable plugs with top & middle ring for replacement of seals and maintenance of bearing. Hence, various gaps like CP-SRP, SRP-LRP, LRP-IHX and IHX-RS Support shell are increased by 50 - 105 mm so that sufficient free space will be available for carrying out maintenance activities smoothly. Since, the maximum diameter of indigenous ring forgings are limited to $\varnothing 5$ m, efforts were made to restrict the SRP diameter to less than 5 m so that ring forgings for SRP including bearing could be sourced within the country.

Based on the layout of pump and intermediate heat exchangers, the mean PCD of major equipment location is worked out to be 10450 mm based on top shield level layout considerations. The height of the reactor assembly was also worked out from both the IHX height considerations as well as height of sodium column and RA internals along the RA centre axis and a height of 15200 mm is found to be adequate against 15000 mm in PFBR. The cross section details of reactor assembly finalised for FBR1&2 is shown in Figure 3.

III.02 Fabrication of Pressurized Capsules of IFAC-1 SS Clad Tube & SS 316LN Plug using Laser Welding for Biaxial Creep Tests

Fast Breeder Test Reactor (FBTR) serves as an irradiation test bed for the development of improved and advanced versions of core materials for Fast Breeder Reactors (FBRs). IFAC-1 SS (D9I) as material for clad tube and SS 316LN as material for end plug are planned to be used for the fabrication of fuel pins in future fast breeder reactors. The swelling and irradiation creep resistance properties of IFAC-1 SS are better than that of alloy D9. Extensive laser welding trials with varied weld parameters have been carried out on IFAC-1 SS & SS 316LN joints to find out the feasibility of obtaining solidification crack free welds. For the development of fuel pins using IFAC-1 SS as a clad tube material, there is need to generate irradiation creep and swelling data. Also, pressurised capsules are widely used all over the world to simulate the biaxial stress, which will be developed in the clad tube of the fuel pin due to fission gas pressure. Towards that, components (Figure 1a) of the pressurised capsule is fabricated from the clad tube, which is having outer diameter of 6.6 mm and 0.45 mm wall thickness (dimensions of clad tube of PFBR fuel pin). The overall length of pressurised capsule is around 70 mm. The clad tube is welded with end plugs made of SS 316LN on either side using laser welding. The bottom plug serves as a closure and the top plug has a passage of dia 0.3 mm for pressurization by keeping it in the high pressure chamber (Figure 1b). Two numbers of pressure gauges (one analog and another digital) are connected in the high pressure chamber to determine the pressure of gas inside the capsule.

After desired pressurization, the passage is fused using laser. LASER welding setup for sealing of pressurized capsule inside the pressure chamber is shown in Figure 2. Subsequently, a disk is welded over it to complete the



Fig. 2 LASER welding setup for sealing of pressurized capsule inside the pressure chamber

fabrication of pressurised capsule (Total: 9 nos.) (Figure 3). The weight of the pressurised capsules are measured before and after pressurization, and the weight of the gas filled in is calculated. From the weight of the gas, gas volume and filling temperature, the pressure in the capsule is determined using gas laws. Due to the argon gas filled at RT (30°C) at the pressure of 5.0 MPa, the corresponding pressure and the hoop stress (average) arising in the wall of pressurized capsule is calculated. The pressurised capsules will be encapsulated in quartz tubes with a low-pressure argon environment. The quartz tubes containing the individual pressurised capsules will be kept in a microprocessor controlled electrical furnace to expose them at the temperature of 750°C to carry out the biaxial creep tests. This study can also be extended further to carry out accelerated creep & thermal fatigue tests.

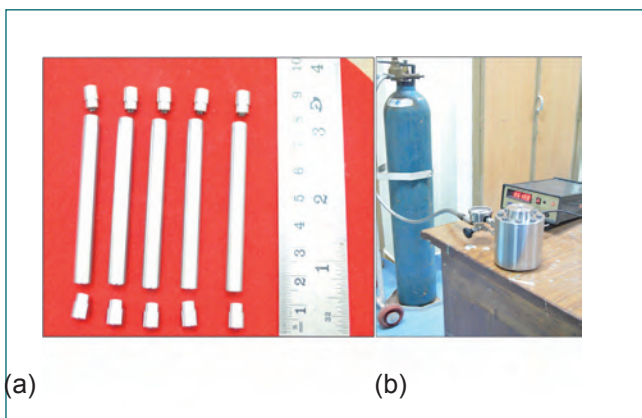


Fig. 1 (a) Components of pressurized capsules
(b) Pressure chamber with gas filling set up



Fig. 3 Fabricated pressurized capsules of IFAC-1 SS (clad tube) & SS 316LN (plug) using laser welding and ready for biaxial creep tests

III.03 Enhancement of Capability of DHDYN Code for Analysis of Transients in Sodium Decay Heat Removal System

Decay heat removal (DHR) through Secondary Sodium Decay Heat Removal System (SSDHRS) is envisaged in future FBRs, in addition to Safety Grade Decay Heat Removal System (SGDHR). SSDHRS is envisaged to (a) reduce the demand on SGDHR and (b) to demonstrate that failure of DHR function is highly unlikely to be regarded as practically eliminated. Towards achieving these objectives, SSDHRS of capacity 15 MW/ per secondary sodium loop is designed for future FBRs. Detailed analysis of SSDHRS is carried out in DHDYN code to assess its performance towards meeting the temperatures limits during various design basis events. DHDYN is an in-house developed plant dynamics code for DHR study through SGDHR. To cater to the DHR simulation requirement of future FBRs, this code is modified to improve its capability to study DHR through SSDHRS. Off-site power failure (OSPF) event is analyzed using this modified code.

The design configuration of SSDHRS is shown in Figure 1. In this system, the decay heat received by primary sodium from the core is transferred to the secondary sodium flowing in the tube side of IHX. From IHX, heat is transported to sodium flowing in air heat exchanger

(AHX) which in turn is removed by ambient air flowing through the shell side of AHX. SSDHRS is designed to operate on forced circulation mode to remove the required decay heat. Secondary sodium pump (SSP) and blower in air circuit are provided with Class-III power supply, so that DHR can be achieved even when class-IV power is not available.

The secondary sodium circuit thermal hydraulics model of the DHDYN code is modified to incorporate SSDHRS model. Two new segments are modeled in the secondary hydraulics model. These are bypass line connecting IHX inlet T-junction to SG outlet header (providing a recirculation path for pump flow) and AHX line connecting surge tank (ST) and SG outlet header (Figure 2). A T-junction is modeled at the IHX inlet, which connects the bypass circuit. Continuity and momentum equations are solved to estimate various parameters in the secondary circuit, viz., four flow rates (SSP outlet flow rate in pipe connecting SSP outlet to T-junction, IHX secondary flow rate (connecting T-junction to ST inlet), bypass flow rate (connecting T-junction to SG outlet header), and AHX flow rate (connecting ST to SG outlet header)), three pressures, viz., ST, Pump inlet and T-junction.

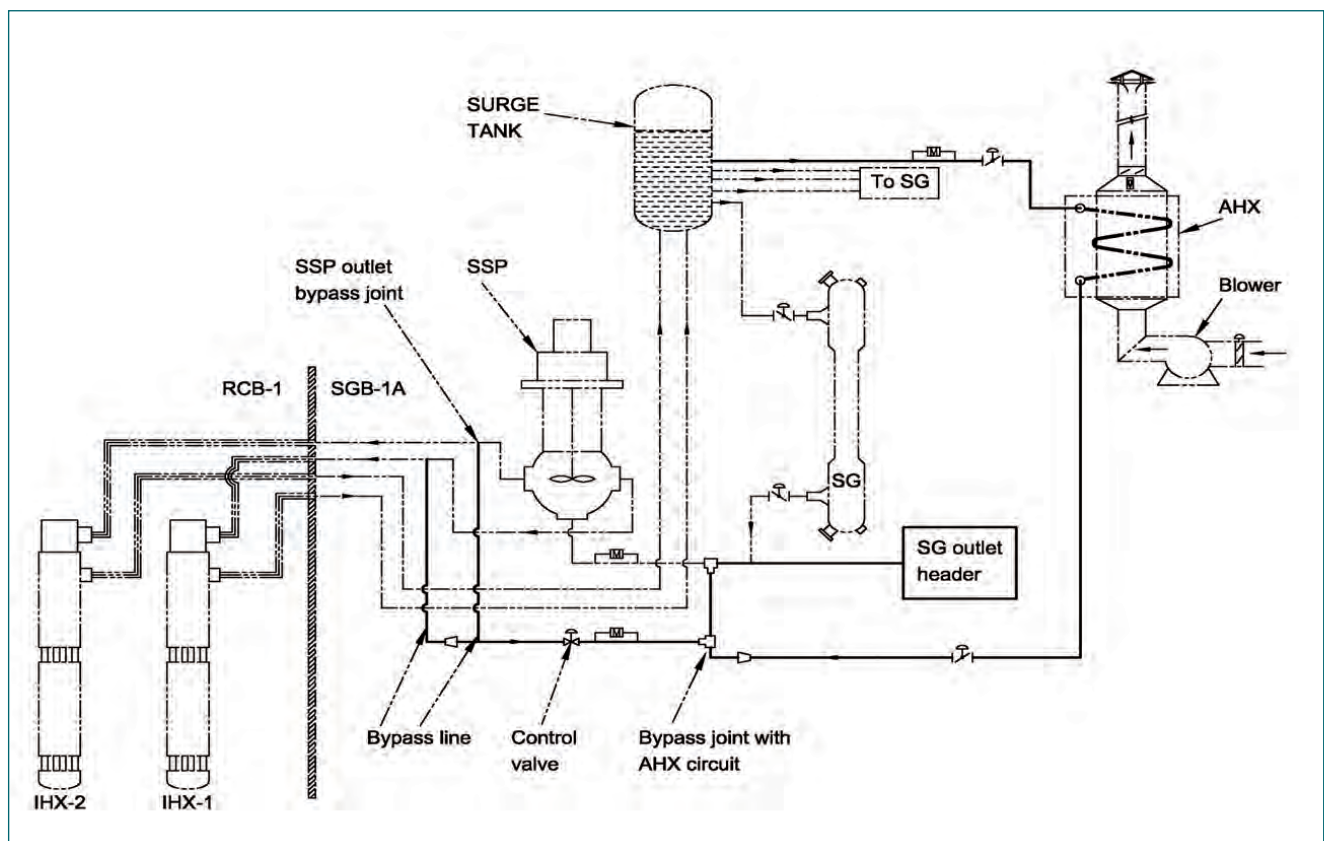


Fig. 1 Process flow sheet for secondary sodium decay heat removal system

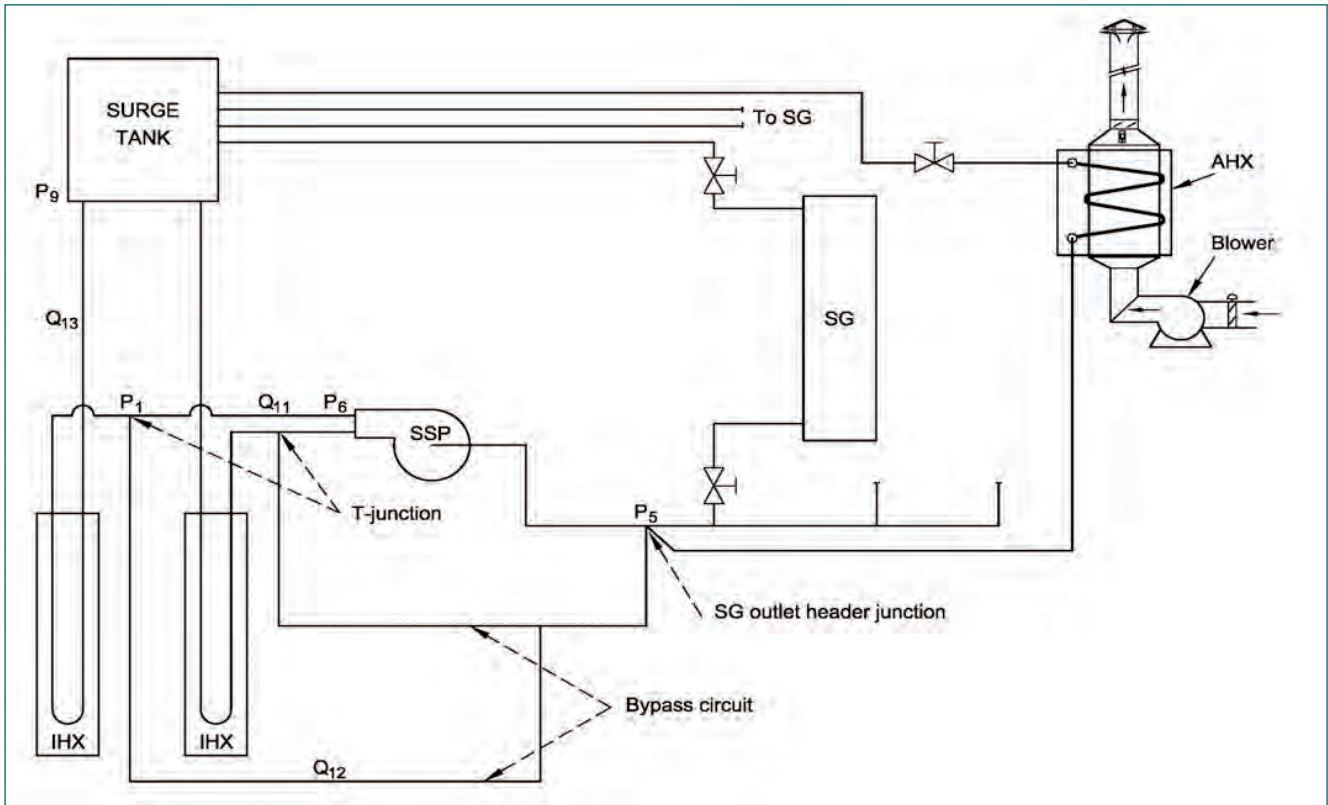


Fig. 2 Schematic of SSDHRS model in DHDYN

A transient thermal model is developed for analysis of AHX. Thermal mixing of AHX outlet sodium with the bypass flow is considered at the SG outlet header junction. Air flow developed by the blower is considered as constant flow rate boundary condition.

Following the deployment of SSDHRS, both the sodium and air flow rate are established within 30 s. The design heat removal capacity is attained within 1 min of starting of blower. Hot pool and cold pool temperature evolutions following OSPF are shown in Figure 3. Hot pool temperature reduces sharply post shutdown. Afterwards, it rises, reaches a second peak, and reduces gradually

due to heat removal by SSDHRS. Cold pool temperature increases following the shutdown, reaches a peak value and decreases afterwards. Maximum magnitude of hot pool and cold pool temperatures post shutdown are observed as 545 °C and 520 °C respectively. Evolutions of fuel Subassembly (SA), storage subassembly and blanket subassembly clad hotspot temperatures (CHST) are shown in Figure 4 and the maximum temperatures are found to be 561 °C, 574 °C and 533 °C respectively. Thus, the maximum temperatures are within category 2 design safety limit (DSL).

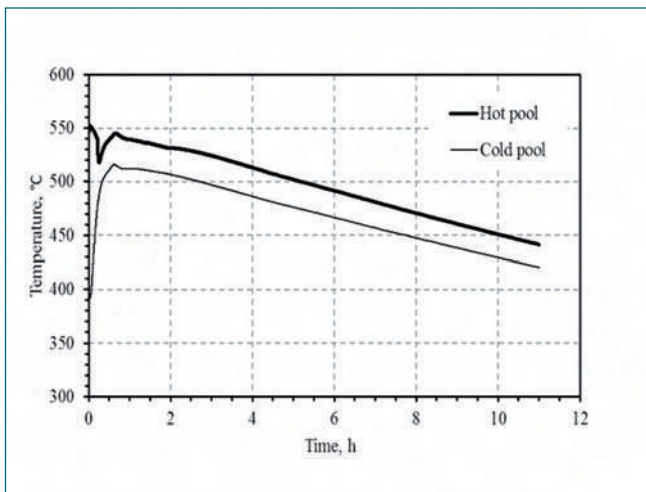


Fig. 3 Evolution of hot pool and cold pool temperature following OSPF

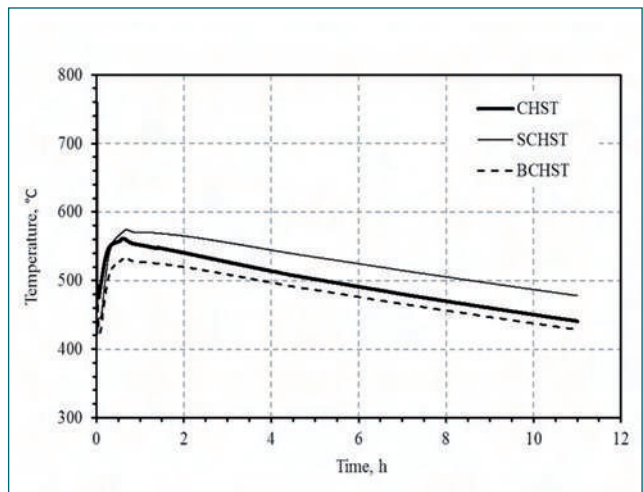


Fig. 4 Evolution of fuel, storage and blanket SA CHST following OSPF

III.04 Development of Multi-Coil Eddy Current Probes for Automated Inspection of Irradiated Fuel Pins

Eddy current (EC) technique is routinely employed for structural integrity assessment of irradiated carbide fuel pins (OD 5.1 mm and thickness 0.3 mm). In general EC testing of such small diameter tubes is carried out by employing an encircling differential probe as per standard. However, this technique suffers from limitations such as reduced sensitivity to circumferential flaws and inability of localisation of flaws in the circumferential direction. In this regard, a multicoil segmented EC probe has been developed for enhanced detection and localization of flaws.

The developed multi-coil EC probe comprises of four surface differential segmented miniaturized (3.0 mm diameter) coils positioned along the circumference of the tube at 90° interval. In addition, an encircling differential probe has also been housed along with the segmented coil in a single araldite mould. For effective focusing and shielding of magnetic fields to achieve higher spatial resolution, a 0.75 mm ferrite core has been used as a core and thin copper wire (48 SWG) has been used to have higher turn density for enhanced sensitivity. The photograph of the EC probe is shown in Figure 1.

A dedicated z-θ scanner and data acquisition system has been designed and developed for automated imaging of fuel pins. The scanner and the EC data acquisition has been interfaced using an inhouse developed LabVIEW software. The photograph of the experimental setup for automated imaging is shown in Figure 2.

The detection performance of the developed probe has been tested on machined artificial flaws such as shallow axial and circumferential notches of 0.07 mm and through holes as small as 0.3 mm. The schematic of the reference flaws and the corresponding typical



Fig. 2 Photograph of the experimental setup

EC signals from encircling differential probe are shown in Figure 3a.

The reference flaws could be successfully detected with a signal to noise ratio greater than 12 dB (Figure 4a). Imaging of the artificial flaws has also been carried out at 9° pitch along the circumference to study the circumferential coverage of the segmented probes. The images of the flaws obtained by individual segmented probes and the composite image (the sum of the four images) in normalized scale shown in Figure 4b demonstrate that the individual segmented probes have coverage of slightly more than 1/4th of the circumference. Hence, a localized defect anywhere in the circumference of a fuel pin can be detected and located.

This in-house developed probe and data acquisition system have been deployed in RML hot cell for testing of 105 GWd/t burnup carbide fuel pins with linear heat rating of 450 W/cm. The developed system of high sensitivity is expected to improve the technique for enhanced characterization of irradiated fuel pins.

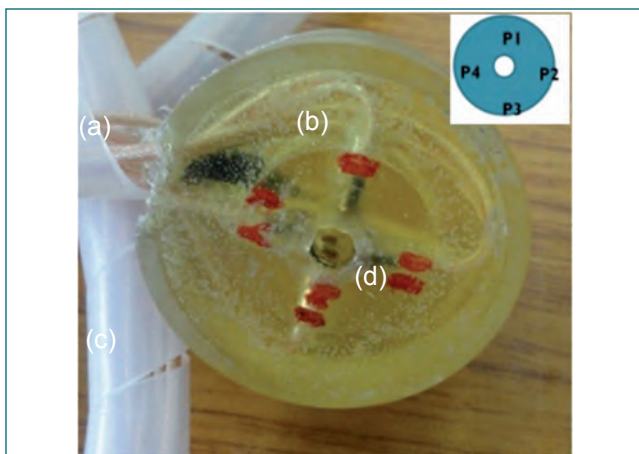


Fig. 1 Photograph of multi-coil segmented EC probe

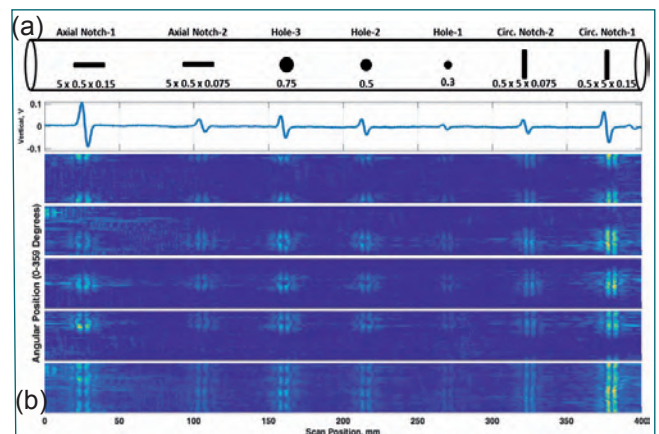


Fig. 3 (a) Reference flaws and typical EC signals from encircling differential probe and (b) imaging of the flaws using four segmented probes and the composite image showing full circumferential coverage by the combination of four segmented probes

III.05 Characterization of High Temperature Fracture Behavior of Grade 91 Steel

Modified 9Cr-1Mo (or Grade 91 steel) is the material for steam generator (SG) components of Prototype Fast Breeder Reactor and these components operate at temperatures of 370 -550°C. It is also a candidate material for cladding of metal fuel fast reactors. The evaluation of fracture toughness (J_{1c}) at elevated temperatures is essential for understanding fracture behavior of Grade 91 steels at operating conditions. In earlier studies, it was observed that for this steel, dynamic strain aging (DSA) influences the flow properties in the operating temperature range (370-550°C). Similarly, fracture behavior at elevated temperature is also expected to be influenced by DSA. Thus, a study was undertaken to characterize the fracture behavior of this steel in the temperature range 300-550 °C.

The Grade 91 steel was subjected to tensile testing at test temperatures 300, 350, 400, 450, 500 and 550 °C and as per ASTM E8 standard. The J-R curves were determined for the above mentioned test temperatures and at different loading rates and as per ASTM E1820. From the J-R curves, initiation fracture toughness (J_{1c}) and tearing modulus values were determined.

From tensile test results, it was observed that yield

strength and tensile strength (Figure 1a) values decreased with test temperatures. A minimum in ductility (Figure 1b) was observed in the temperature range 400-450°C. The initiation fracture resistance (J_{1c}) values at various temperatures and different loading rates are shown in Figure 2a. The minimum in fracture toughness was observed in the temperature range 400-450°C. Similarly a decrease in tearing modulus values (Figure 2b) was observed in this temperature range.

The mechanism responsible for DSA was identified by correlating the crack tip strain rate as function of temperature. The crack tip strain rates were estimated for minimum values of fracture toughness in the temperature range 350-450°C and plotted against inverse of temperature (T^{-1}). The activation energy of ~67 kJ/mol obtained from the slope of the plot, corresponds to diffusion of interstitial atoms which is reported in the range of 55-80 kJ/mol for this class of steels.

It can be summarized that the fracture toughness and tearing modulus values of Grade 91 steel exhibit minima around 450°C confirming that fracture properties, like tensile properties, are also influenced by DSA.

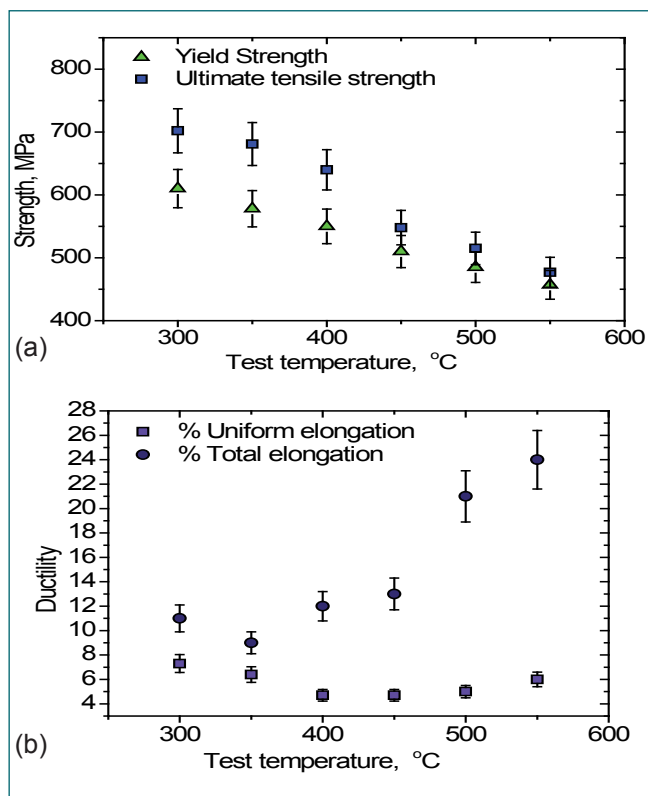


Fig. 1 Tensile properties at various temperatures (a) strength and (b) ductility

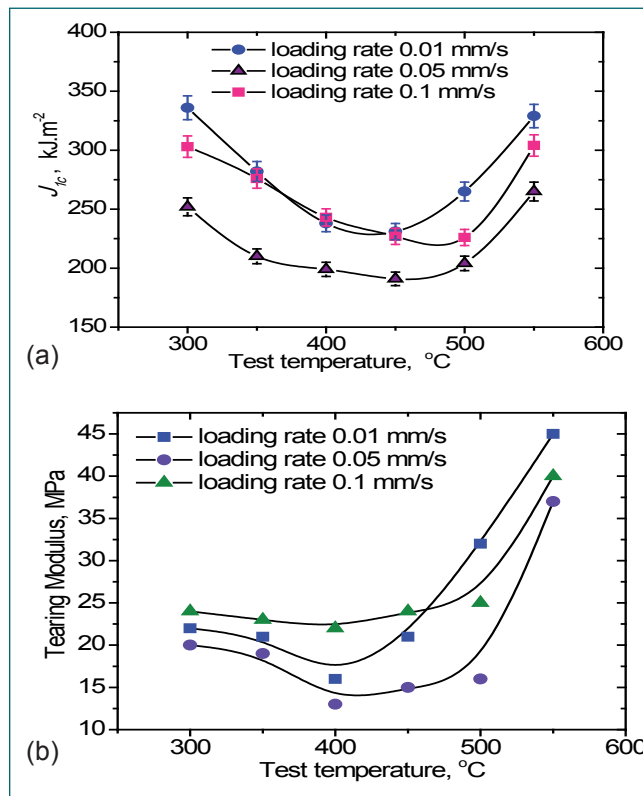


Fig. 2 Fracture results at different temperatures and loading rates (a) fracture toughness; (b) tearing modulus

III.06 Measurement of Creep Strain Gradient in U-notched Specimens of Boron added P91 Steel using Video Extensometer

Boron added modified 9Cr-1Mo (P91B) steel is being considered as an alternate candidate material for the steam generators of sodium cooled fast reactors. As stress concentration is inevitable for the components in service, the multiaxial creep behavior of P91B steel is investigated at 923 K by including discontinuity in the form of U-notch. In the current study, a non-contact type video extensometer was used to measure the creep strain, as it enables to obtain vital information on the strain partitioning between notch and the plain sections. For this, speckle pattern is first produced on the notched specimen using alumina powder following which, predefined targets (set at desired locations as in Figure 1) are used to measure the elongation. In view of the difficulty to map the creep strain along the varying notch profile, the average strain across the entire notch region is measured in the longitudinal direction.

The gross and net diameters of the notched specimen are 8.35 and 5 mm respectively. Specimens with different values of notch root radius (r : 0.25, 1.25 and 2.5 mm) were studied, and in all the specimens the notch depth (h) is 1.675 mm. Creep tests were conducted at the nominal applied stresses of 240 and 260 MPa, which were estimated based on the notch root cross-section. It may be noted that the stress developed in plain sections is much lower than the corresponding nominal stress applied in the notch region. The creep strain is calculated in the different regions by taking corresponding initial length as their gauge length. For example, the average strain across the entire notch region is measured by taking the gauge length of each notch region between the plain regions.

The strain measurements clearly revealed the differences in creep strain evolution from the notched regions and plain sections of the notched specimens (Figure 2). In general, creep curve would consist of three stages, viz., Primary, Secondary and Tertiary. It may be noted from Figure 2 (shown for 1.25 mm notch radius) that only the notch regions exhibit three stages of creep, while plain sections remain in primary creep as they

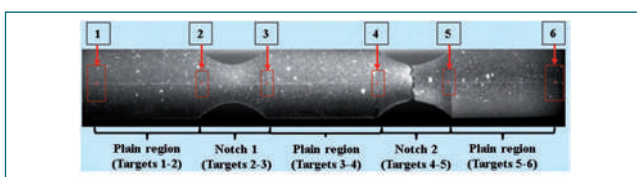


Fig. 1 Double-U notched creep specimen marked with speckle pattern and pre-defined targets

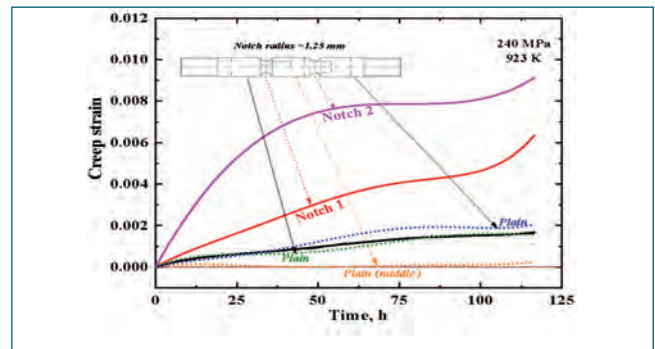


Fig. 2 Average creep strain evolution from notch and plain regions of P91B U-notched specimen

experience relatively lower stresses. Further, though both notches in a test specimen are geometrically similar, the accumulation of creep strain at the two notches is different in all the three stages of creep. The failure occurred at one of the notches in all the test conditions. Similar observations were noticed at all the above notch root radii. The creep rate curves calculated for the plain and notched regions are shown in Figure 3. Ignoring minor anomalies in plain sections, the primary creep with decreasing strain rate, steady state creep (with slightly varying creep rate) and accelerating creep rate in the tertiary stage have been clearly observed at the notch regions (Figure 3). Specimen thus fails at a location wherein one of the notches accommodates creep strain and damage at a faster rate, eventually leading to failure. The creep rupture life increased with decrease in the notch root radius and the increase is up to 1.5 times.

The current study demonstrates the creep strain measurement from the notched regions in creep specimens for the first time at IGCAR. The measured average creep strain at notch is 5-15 times higher than that at the plain regions under the investigated test conditions.

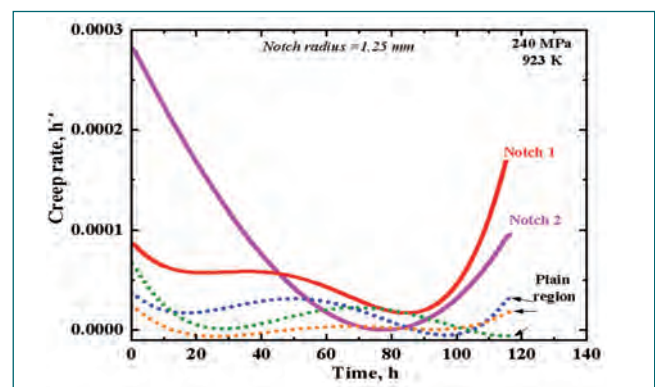


Fig. 3 Average creep rate curves derived for the different regions of notched specimen

III.07 Studies on Carbon Activity Measurement of D9, IFAC-1SS and T91 by Foil Equilibration Method in Liquid Sodium

Austenitic stainless steel D9 is used as fuel clad and wrapper material in PFBR. Modified version of alloy D9, IFAC-1 SS and T91 are candidate clad material for future FBRs. Carbon is an important constituent of steels. The difference in carbon activity between the structural steel and sodium would result in carburization or decarburization of structural steels which would be detrimental to their mechanical properties. Carbon activity measurements of D9, IFAC-1SS and T91 were carried out as a function of carbon content by foil equilibration method in liquid sodium with nickel as the reference foil.

The foils of D9, IFAC-1SS and T91 alloys of thickness 150 to 200 μm along with high pure Ni foils were equilibrated in distilled sodium containing known amount of graphite powder and SS 410 taken as carbon source. The foils were heated at 873 and 948 K for 360 h in a high temperature furnace. Figure 1 shows the schematic diagram of the experimental assembly.

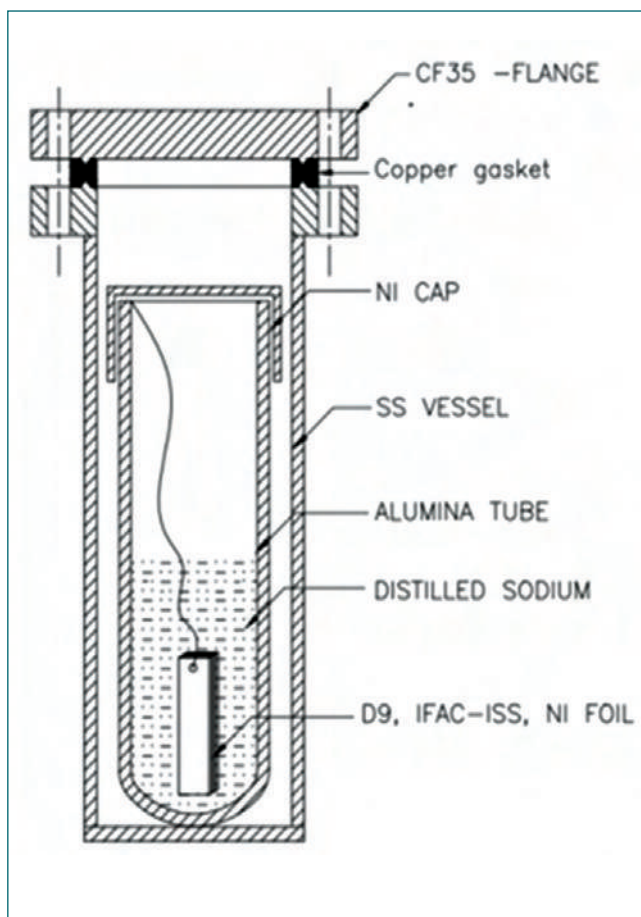


Fig. 1 Schematic diagram of the experimental assembly used for foil equilibration

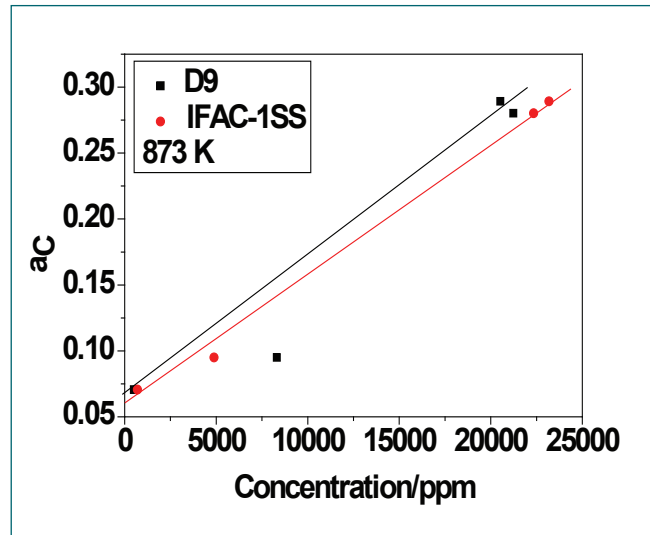


Fig. 2 Activity vs composition for D9, IFAC-1SS at 873 K

After the equilibration, the vessel was quenched in ice cold water. The foils were thoroughly cleaned with alcohol followed by distilled water and dried. The foils were characterized using XRD, SEM/EDX analysis. The carbon content of these foils was analysed by carbon analyser before and after equilibration. At equilibrium, the chemical activities of carbon in sodium and foils would be same, i.e., $a_{C_{Na}} = a_{C_{foil}}$. From the activity, composition relationship for nickel reference foil, activity of D9, IFAC-1SS and T91 foils were determined.

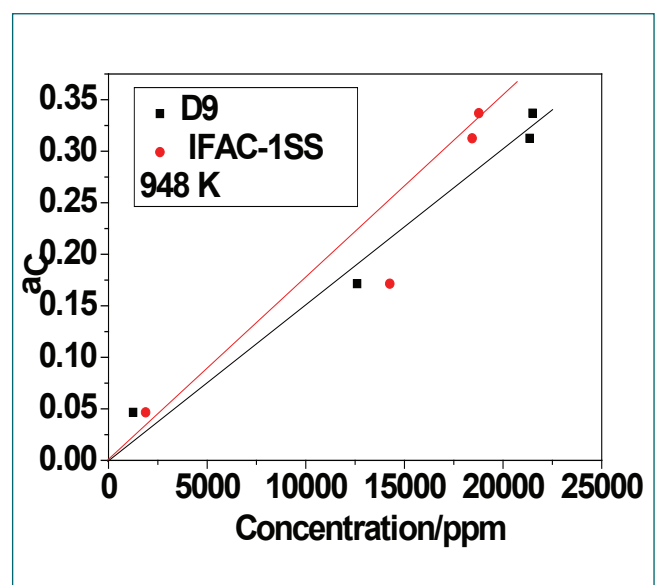


Fig. 3 Activity vs composition for D9, IFAC-1SS at 948 K

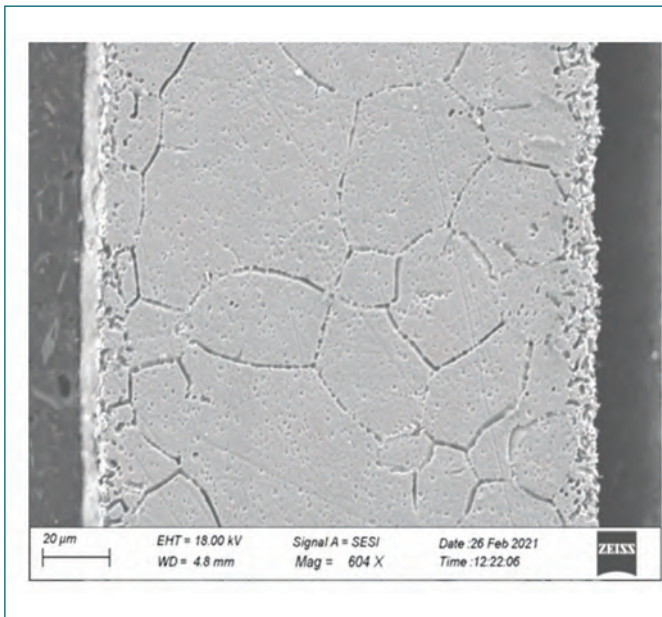


Fig. 4 SEM images of cross-section of D9 after equilibration at 948 K

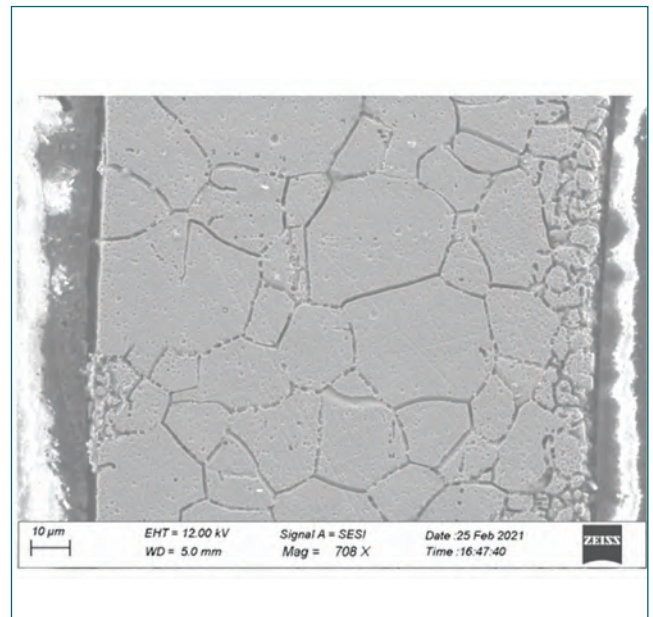


Fig. 5 SEM image of cross-section of IFAC-1SS after equilibration at 948 K

XRD pattern of the foils before and after equilibration was identical and showed austenite single phase indicating diffusion of carbon into the matrix forming interstitial solid solution. From the carbon content measurement and activity vs. composition relationship of nickel standard, the carbon activities of D9, IFAC-1SS and T91 foils were determined for different carbon contents. The initial and final carbon contents of D9, IFAC-1SS and T91 alloys at 873 K and 948 K before and after foil equilibration are shown in Table 1. A plot of activity of carbon versus carbon concentration of D9 and IFAC-1SS at 873 K and 948 K are shown in Figures 2 and 3 respectively. Further experiments for determining the carbon activity for the change in carbon contents are being conducted for T91 alloys at different temperatures. The results show

that increased carbon content in sodium carburises D9, IFAC1-SS and T91 alloys. The extent of carburisation is marginally higher in T91 compared to D9 and IFAC1-SS. Typical SEM images of D9 and IFAC1-SS samples after equilibration experiments are shown in Figures 4 and 5. The SEM/EDS analysis of both D9 and IFAC-1SS foils revealed that the carbon concentration increased in both the foils after equilibration. The EDS and carbon analysis using carbon analyser indicates carburization of the alloys.

The carbon activities of D9, IFAC-1SS and T91 for different carbon concentrations were determined for the first time by foil equilibration method at 873 K and 948 K.

Table: 1 Initial and final carbon contents of D9, IFAC-1SS and T91 alloys at 873 K and 948 K before and after foil equilibration

S.No..	Alloy	Initial Carbon content(%)	Carbon source	Final carbon content at 873 K (%)	Final carbon content at 948 K (%)
1.	D9	0.0415	SS410	0.094	0.125
			Graphite powder	0.831	1.260
2.	IFAC-1SS	0.0515	SS410	0.144	0.187
			Graphite powder	0.488	1.450
3.	T91	0.0765	SS410	0.112	0.448
			Graphite powder	1.705	1.274

III.08 Synthesis and Characterization of Zeolite and Geopolymer for the Immobilization of Zr, Cr-Constituents of T91 Cladded Metallic Fuel

Zeolites ($M_{n/p}[Al_pSi_qO_{2(p+q)}] \cdot nH_2O$) are frame work structured crystalline materials made of silicon (Si), aluminum(Al) and oxygen with cavities and channels inside which cations, water and/or small molecules would be absorbed/occluded. They are also often referred to as molecular sieves. Whereas geopolymers are inorganic, typically ceramic, alumino-silicates forming covalently bonded non-crystalline (amorphous) networks. These materials were synthesized from coal fly ash / kaolin by hydrothermal technique and characterized by XRD, SEM, FTIR and various other techniques. The HLW generated from the aqueous reprocessing of metallic fuel would be rich in Cr, Zr and Fe because of partial dissolution of the T91 clad (9Cr-1MoVNb ferritic-martensitic alloy steel) used in metallic fuel. Attempts were made to explore the immobilization behavior of Cr and Zr in zeolite and geopolymer in the context of aqueous reprocessing of metallic fuel waste.

Zeolite-A was ($Zt-A: Na_{12}Al_{12}Si_{12}O_{48} \cdot 27H_2O$) explored as a probable host matrix for the immobilization of Cr or Zr. Loading of Cr or Zr in Zt-A were carried out by equilibration in solution with zeolite solid powders at ambient conditions. In equilibration approach, a fixed quantity of Zt-A (1g) was equilibrated in batches for 4 hrs with 10 mL of solution containing varying concentrations of Cr or Zr. After equilibration the Cr or Zr loaded Zt-A of each batch was separated by filtration and the solution was analysed by ICP-OES. Figure 1 shows typical images of the Cr or Zr loaded Zt-A obtained after equilibration.

XRD patterns of Cr or Zr loaded Zt-A indicates the equilibration of Zt-A with higher concentration of Cr or Zr solution (started with minimum 1000ppm i.e 10mg of Cr^{3+} /1g of Zt-A) leading to structural changes in the Zt-A. A typical XRD pattern of Cr loaded Zt-A is shown in



Fig. 1 Equilibration experiment of Zr & Cr with Zt-A

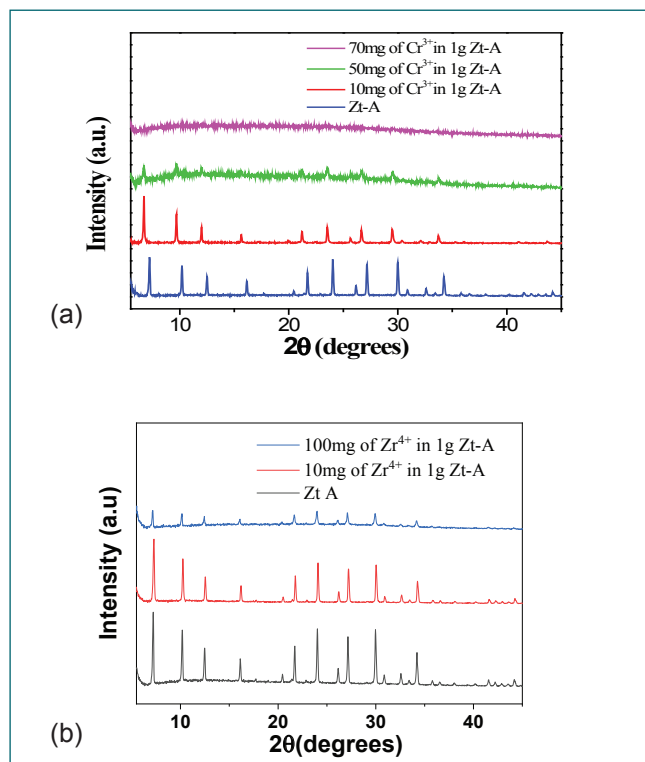


Fig. 2 XRD pattern of (a) Cr loaded (b) Zr loaded Zt-A

Figure 2a for reference. Analysis of the XRD results of the products indicates that a maximum of 10 wt% of Zr or 5 wt% of Cr can be safely loaded into Zt-A matrix. A typical XRD pattern of Zr loaded Zt-A is shown in Figure 2b for reference.

Similarly, the immobilization of Cr and Zr in geopolymer was found to be 15 and 25 wt %, respectively under ambient conditions. It was observed that up to 15 wt.% of Cr or 20 wt.% of Zr-loading is feasible without any phase separation as shown in the XRD pattern (Figure 3), beyond which, separation of crystalline nitratine ($NaNO_3$) phase was detected by XRD.

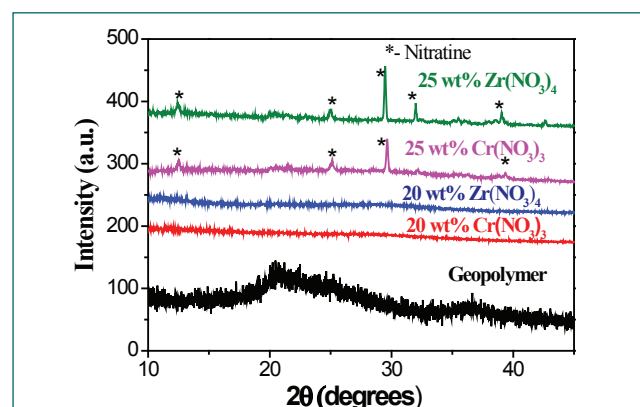


Fig. 3 XRD pattern of Cr or Zr loaded geopolymer

III.09 Measurement of Activity of Irradiated Materials using Hot Cell Gamma Scanning System

Knowledge of the radioisotopes and their activities is essential for estimation of the neutron fluence experienced by materials during irradiation. Gamma spectrometry is a valuable non-destructive tool for this purpose. However, highly irradiated specimens require proper collimation to limit the count rate and thereby reduce the dead time of gamma detectors. Radio Metallurgy Laboratory (RML) hot-cells are equipped with a gamma scanning system for axial and radial scanning of irradiated fuel pins and sections, and other irradiated structural materials for evaluating the distribution of fission products and their yield. It consists of primary and secondary collimators made of tungsten alloy and lead incorporated in a turret established in the hot cell front wall, a HPGe based gamma spectrometry system installed in the hot cell operating area, and an automated four axis gamma scanning bench inside the hot cell for precise positioning of the sample in front of the collimator.

Recently, surveillance coupon samples of Calandria Side Tube Sheet material of end shield (ASTM A203 Grade D 3.5%Ni ferritic steel) irradiated in Unit – 1 of Madras Atomic Power Station (MAPS) was received in RML for evaluating the changes in mechanical properties due to neutron irradiation. The estimated value of fluence seen by these Charpy V-Notch (CVN) impact test specimens (55 mm x 10 mm x 5 mm) during their 36 years of reactor operation is 1.13×10^{21} n/cm² (E > 1 MeV). One of the broken halves of impact tested CVN specimen was subjected to gamma spectrometry for identification of activation products produced during irradiation and a measurement of their activity. Due to the high dose rate on the sample (~0.1 Sv/h), spectrometry was carried out with the sample in the hot-cell, requiring a custom-built fixture for the gamma scanning bench. The fixture is designed such that the 10 mm width of the sample faces the collimator turret assembly. The coaxial, p-type HPGe detector used for spectrometry has a relative efficiency

of 30% and energy resolutions of 0.875 keV at 122 keV and 1.8 keV at 1332 keV.

Quantification of radioactivity requires precise knowledge of the efficiency of the detector for the measurement geometry adopted during gamma spectrometry. Since the gamma spectrometry is carried out in the hot cell collimated geometry, detector efficiency for this geometry was measured prior to the specimen analysis. The absolute efficiency of the detector was estimated for the primary collimator dimension of 1 mm (W) x 10 mm (H) x 320 mm (L) using a spacer wire section from an irradiated carbide fuel pin. The source term for efficiency measurements was determined using the activity of the spacer wire computed by chemical dissolution and gamma spectrometry.

Detector efficiency was measured for gamma energies of 843.81 keV, 1173.23 keV and 1332.51 keV present in the gamma spectrum of irradiated spacer wire using the following equation.

$$\epsilon = \frac{\frac{N_s}{t_s} - \frac{N_b}{t_b}}{P_\gamma * A * K_{SC} * K_{SA} * K_{DC}}$$

where A (Bq) is the activity of radionuclide, N_s and N_b are gamma counts for sample and background respectively, t_s and t_b are counting duration in seconds for sample and background respectively. ϵ is the full energy peak efficiency, P_γ is the emission probability, K_{SC} the cascade summing correction, K_{SA} the correction factor for self-attenuation and K_{DC} the decay correction factor for radionuclide. The log-log plot of efficiency vs. gamma energy is shown in the figure.

The dimension of the collimator selected for acquiring gamma spectrum from the surveillance specimen of MAPS was 1 mm (W) x 10mm (H) for which the detector efficiency was previously measured. To obtain better counting statistics the sample was counted for 2×10^6 s (~ 23 days). The radiation decay of the activation products during the counting time was also considered and was applied for activity calculation. The volume of the specimen exposed to the detector during the measurement is 0.05 cc. The total activity of the specimen is computed from the total volume of the specimen (2.77cc) which is calculated from the measured dimensional data.

The gamma spectroscopy of MAPS end shield surveillance coupon specimen using the hot cell gamma scanning system indicated neutron activation products of ⁵⁴Mn and ⁶⁰Co. The measured activity of ⁵⁴Mn is 0.11 mCi and that of ⁶⁰Co is 9.69 mCi for one impact test specimen. The uncertainties in the measurements are ± 5.01% and ± 2.34% for ⁵⁴Mn and ⁶⁰Co respectively.

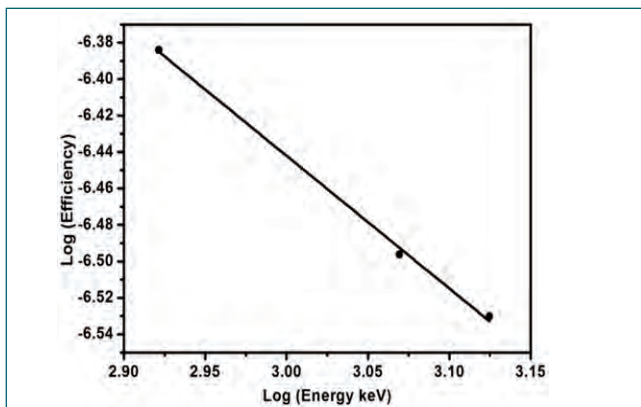


Fig. 1 Efficiency of HPGe detector for the collimated geometry

III.10 Studies on Effect of Pump Inclination on Performance of Active Magnetic Bearing

Centrifugal sodium pumps are used to circulate liquid sodium coolant in the primary and secondary circuits of fast reactors. The pump rotor is supported by conventional oil lubricated bearings at the top and by hydrostatic sodium pressurised bearing inside sodium. Active Magnetic Bearings (AMB) are oil free substitute for the top oil lubricated bearings as they eliminate the risk of oil leak into the primary sodium.

As part of the ongoing work on developing oil free bearings and seals for main coolant pumps of future FBR's, collaborative work was done with M/s CSIR-NAL, Bangalore to study the effect of pump inclination on AMB performance. A scaled-down model of the primary pump rotor was designed and fabricated, and operated at the expected inclination to study the effect of pump rotor inclination on the performance of AMB.

The AMB test rig (Figure 1) consists of the dynamic scaled-down rotor supported by thrust and radial AMB at the top and a radial roller bearing at the bottom. The scaled down rotor assembly weighs 14 kg and is 1.8m in length.

The AMB test rig is supported on a base plate and vertical columns. The thrust AMB consists of four independent actuator pairs, one per quadrant of the thrust disk. The radial AMB consists of an 8 pole heteropolar stator arrangement. AMB components are housed in AMB

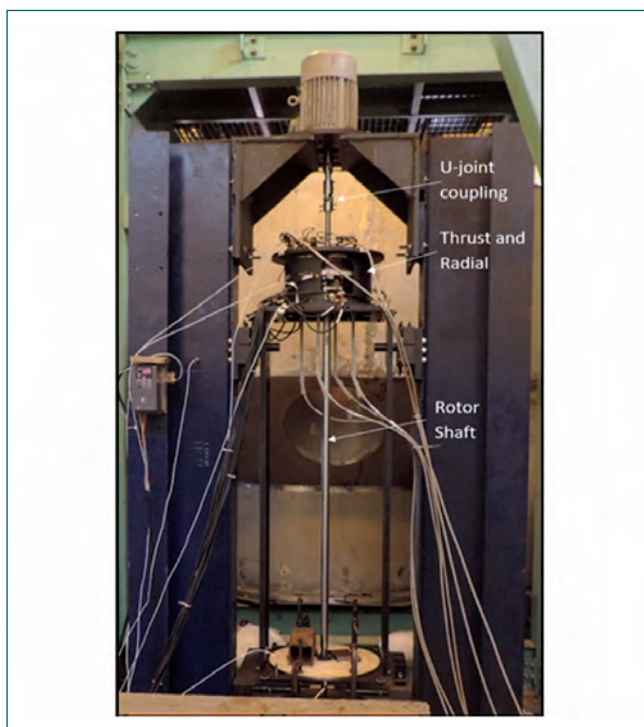


Fig. 1 AMB test rig

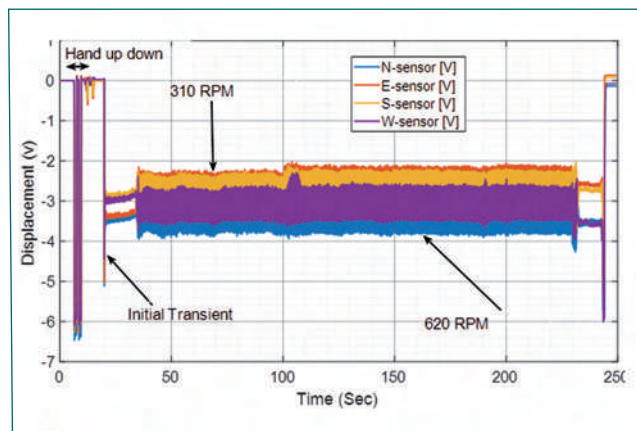


Fig. 2 Vibration in thrust direction at 0.40 tilted shaft (590 rpm)

casing, consisting of stator components of both the thrust and radial AMB, auxiliary bearings, and sensor mounts. Top AMB casing and bottom bearing assembly are connected through vertical plates hinged on the columns. This arrangement simulates the inclination of pump rotor and the tilting of the AMB assembly during operation. The impeller disk is fixed at the bottom of the shaft with the help of a lock nut and the shaft is connected to the motor through a U-joint coupling. Analog PID controller is used for controlling AMB.

The AMB performance was satisfactory under static levitation and during full speed rotation (590 rpm) both in vertical and 0.4 degree tilted shaft condition. The shaft's maximum vibratory displacement (Figures 2 & 3) measured at full speed is below 40% of the nominal gap between actuators, indicating satisfactory performance in compliance with ISO 14839.

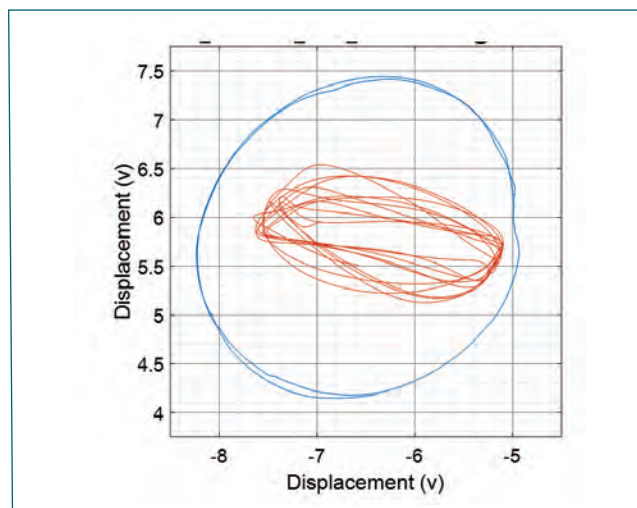


Fig. 3 Radial direction orbit plot at 0.40 tilted shaft (590 rpm)

III.11 Indigenous Development of Sodium Service Frozen Seal Gate Valves

Sodium service Frozen Seal Gate Valves (FSGVs) with backup gland packing are widely used in the sodium circuits of FBRs. The application of these valves is mostly for isolation purpose. All the valves of this type used in Prototype Fast Breeder Reactor (PFBR) were imported. To reduce the import dependency, initiatives were taken to indigenously design, develop and manufacture FSGVs for future FBRs and experimental facilities dedicated to fast reactor program. Sodium service valves are different from conventional valves, sodium being highly reactive with air and moisture, leakage prevention to external environment is most important design feature. In frozen seal valves, leakage of sodium to external environment is prevented by a sodium frozen seal itself, which is formed in the tiny annular gap between valve bonnet and stem. Fins are provided externally on the bonnet to enhance the heat transfer from sodium to exterior and promote formation of frozen seal. In case sodium rises to unsafe level in valve bonnet, a contact type sodium leak detector is provided to detect sodium and give indication to the plant operator. A secondary seal by graphite- asbestos based gland packing is provided on top of the bonnet to serve

as additional safety feature. Cover gas line is provided on valve bonnet to supply/vent argon cover gas on demand to support sodium level rise in annular gap which helps in formation of frozen seal.

Development of frozen seal valves in India was first of its kind activity; several experienced valve manufacturers in India were approached to explore the feasibility of manufacturing FSGVs in India. Finding a suitable supplier for developmental work, fabrication difficulties of finned bonnet, valve forgings and parts suitable for sodium applications were some of the few challenges encountered during valve development. Two sizes of valves such as 100 NB and 200 NB were taken up for the developmental activity. Material of construction of the valves in PFBR is 316 LN as per ASTM A182F, but the indigenous valves were manufactured in SS-316 L due to ease of availability. During the course of indigenization, the design of FSGV was optimized without compromising the functional features of existing FSGV. The valve was designed with compact size, lesser weight and better thermal hydraulics. The mode of actuation for newly designed valve was changed to motorized actuator from pneumatic actuator.

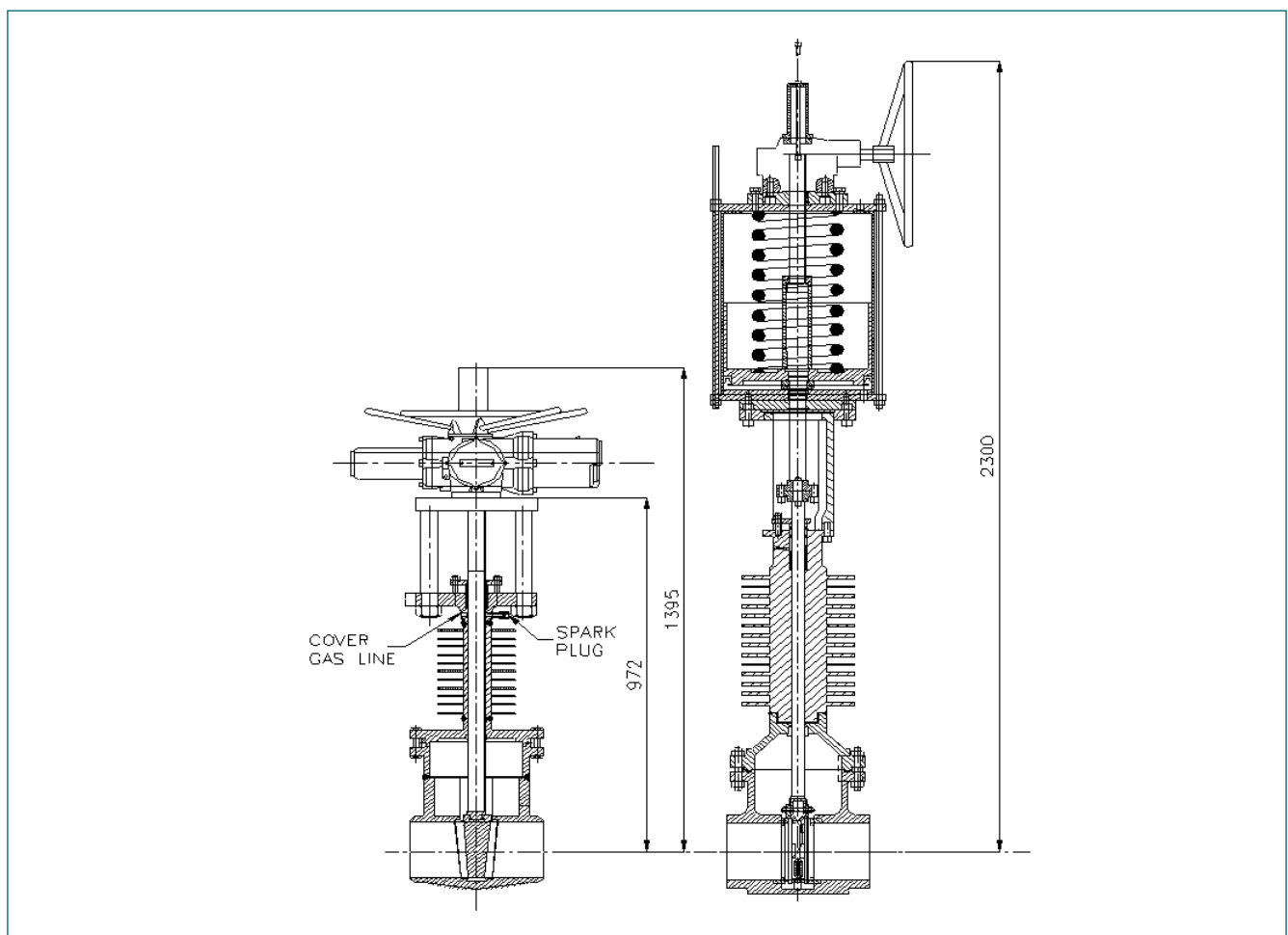


Fig. 1 100 NB FSGV indigenously developed (left) and imported for PFBR (right)



Fig. 2 Photograph of indigenously manufactured FSGV of size 100 NB & 200 NB

Usage of motorized actuator helped in ~40% reduction of overall height and space occupied by the valve. This reduces weight and height of mass center from support location, hence leads to a better resistance to seismic events. Figure 1 shows the schematic drawing of indigenously developed valve as well as imported valve of same size for comparison.

Manufacturing of finned bonnet was one of the critical tasks in the process of manufacturing of these valves. Fins are provided on bonnet to cool the sodium present inside the annular gap of bonnet and stem. Imported valves were equipped with finned bonnet machined from single stainless steel bar. This requires complex machining processes which increases the cost of the valve. Machined type finned bonnet was replaced with welded type for easiness in manufacturing and thus reduce cost. The welding of fins over the bonnet was a vital operation and several mock up were made prior to final bonnet assembly to achieve the required parameters. Wall thickness of bonnet is important parameter in deciding the frozen seal height. Wall thickness was optimized to an optimum value, such that the resistance for heat transfer and participating thermal mass is reduced considerably. Number of fins was also optimized to achieve comfortable freezing against a design basis ambient air temperature as 60°C. Analysis indicates that, establishment of frozen seal is ensured for events like local fire, which increases the surrounding air

temperature up to 80°C. Furthermore, provision of cover gas port was introduced as additional design feature in the new FSGV. An argon communication line is connected to bonnet assembly which is maintained at same pressure as the overall cover gas pressure of system. Sodium filling inside the annular gap will be independent of argon back pressure.

FSGVs were designed as per technical requirements of sodium service valve for reactor applications. Valve body was made as per ASME B16.34 special class 300. Inspection & testing plans were followed as per the standard to ensure proper functionality. Valve forgings and all the pressure retaining welds were qualified by NDT techniques i.e. Ultrasonic testing/ Radiography. Valve body was qualified by conducting hydro test at 63 bar(g). Final assembly was qualified by seat leak test at 13.5 bar(g) and proof test at 18 bar(g). Integrity of pressure boundaries after the proof test was confirmed by helium leak test in vacuum condition with allowable leak rate of 10⁻⁸ Pa m³/s. Functionality check was also carried out at manufacturer's site by performing 100 ON-OFF cycles to ensure smooth operation. The final picture of manufactured valves are shown in Figure 2.

Both the valves are received at site and are being erected in the sodium test facility for its mandatory functional testing in sodium at operating conditions.

III.12 Fabrication, Installation and Quality Control of Sodium Piping System in Sodium Technology Complex

The Sodium Technology Complex (STC), a large sodium test facility with high bay space, is under construction to test full-scale components of future FBR's. It consists of two sodium storage tanks, three test vessels, EM Pump, purification circuit, heating system, cooling system, and connecting piping. The sodium piping system consists of three different pipe sizes: NPS 1", 2" and 4" of schedule 40. SS 316LN is the material of construction of the piping. A detailed Quality Assurance Plan (QAP) was prepared in consultation with QAD, IGCAR before starting the piping erection. The initial isometric piping spools for the fabrication were generated from AUTOCAD 3D isometric piping layout. The spool drawings were prepared with the number of weld joints kept to a minimum. Before taking up the spool fabrication, surface treatment of pipes and the fabrication of pipe bends were completed based on approved procedures. The welding of sodium piping joints was carried out by Gas Tungsten Arc Welding (GTAW) process. Pipe bends are of minimum 5D bend radius. Before taking up the welding work, Welding Procedure Specification (WPS), Performance



Fig. 2 Dump lines of piping system



Fig. 1 Overflow and outlet pipe lines

Qualification Record (PQR), and Welder Performance Qualifications (WPQ) were qualified as per ASME Sec IX.

The pipelines are erected with a 2% slope towards the sodium storage tank to ensure complete sodium draining under gravity. The locations and ratings of the tie rods and hangers are decided based on the flexibility/seismic analysis of the system. Typical pipelines are shown in Figure 1 and 2. Since leak tightness is the primary requirement in sodium systems, all butt weld joints were inspected with 100% X-ray radiography in addition to visual and LP examinations. After the weld joints qualification, the complete integrated piping system was subjected to pneumatic test followed by leak tightness test consisting of soap bubble leak test and helium leak test.

III.13 In-situ Regeneration of Cold Trap of HEXAMINI Bench Top Sodium Loop

A bench-top mini sodium loop with six ports called HEXAMINI sodium loop (HSL) used for testing and calibration of Electrochemical Hydrogen Meters (ECHM). HSL has a Cold Trap (CT) which controls the hydrogen and oxygen impurities in the HSL by trapping the impurities as hydrides and oxides. Continuous operation of HSL, injection of H₂ for testing and frequent opening of HSL for various purposes has led to the saturation of CT and it needed regeneration for further usage. In-situ CT regeneration was carried out by thermo-vacuum process in which the NaH decomposed to sodium and hydrogen according to the following equation:



Since, hydrogen forms explosive mixture with air beyond 4%, hydrogen mitigation (HM) during the process is the key concern. HM was carried out by online hydrogen monitoring and maintaining below 2% during the process. In-house developed H₂ sensors like ECHM, Polymer electrolyte membrane based hydrogen sensor (PEMHS) and semiconducting metal oxide based hydrogen sensors (SMOHS) deployed simultaneously for the first time during the process of regeneration. Schematic of experimental set-up for CTR is shown Figure 1. CTR set-up was made by integrating of i) Gas purging system to cover gas space of HSL, ii) vacuum pumping system and iii) online hydrogen sensors.

UHP argon was purged in to HSL using mass flow controller (MFC-2) and needle valve (NV1). Diaphragm vacuum pump was used to maintain the vacuum level of cover gas volume and the same was measured by digital pressure transmitter. The sample gas from pump outlet was passed through MFC-3 to the sensors after

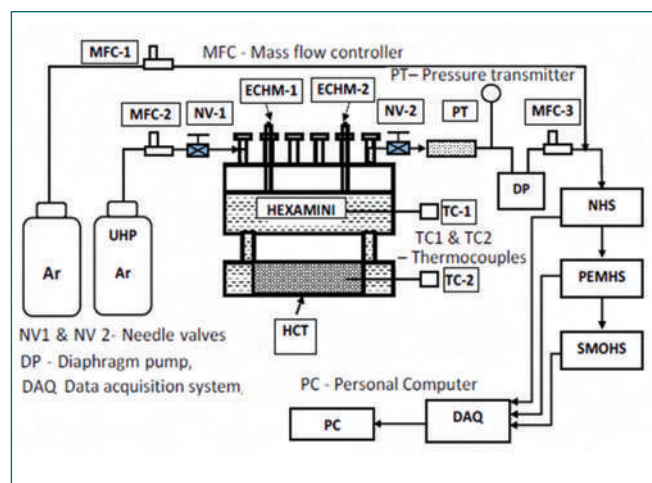


Fig. 1 Experimental set-up for CT regeneration

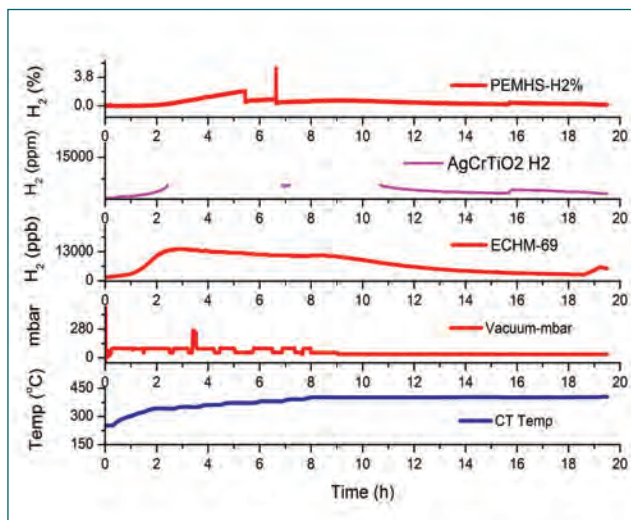


Fig. 2 Hydrogen concentration measured by sensors ECHM, SMOHS and PEMHS during CT regeneration

diluting with Ar using MFC1. The regeneration process was carried out by heating of CT from 250 to 400°C in steps with cover gas space vacuum level of 50 mbar.

Figure 2 shows the hydrogen release profile measured by the sensors. ECHM measured the [H]_{Na} in liquid Na in ppb range; SMOHS and PEMHS measured H₂ gas released to cover gas phase in ppm and percentage levels, respectively. For the CT temperature 250 to 300°C at 50 mbar vacuum, the marginal raise in hydrogen concentration was observed in both in both liq. Na and cover gas phases. ECHM value increased from 2000 to 3000 ppb and 800 ppm to 1500 ppm in SMOHS while no hydrogen was detected in PEMHS. However, for CT temperature from 300 to 340°C, significant raise of hydrogen in both liq. Na and cover gas phase was observed. ECHM value attained maximum of 14000 ppb and H₂ in gas phase also increased from 1400 to 5000 ppm when PEMHS value changed from 0.01 to 0.42%. Beyond 340°C, ECHM and SMOHS sensors were saturated and H₂ conc. in PEMHS increased faster and attained 2%. The hydrogen was diluted with argon and its conc. was maintained less than 2% throughout the experiment.

CT regeneration was carried out successfully by deploying in-house developed online H₂ sensors in both liquid Na and cover gas phases. The H₂ sensors profiles facilitated to determine the decomposition rate of NaH, the H₂ distribution in liquid sodium and cover gas phases as function of time. The total quantity of decomposed NaH and hydrogen released were determined accurately.

III.14 Upgradation of SGTF Sodium Distributed Digital Control System

Steam Generator Test Facility (SGTF) was constructed in 2004 and many experiments related to PFBR steam generator have been successfully completed. Due to obsolescence, the instrumentation system was upgraded with state-of-the-art indigenously developed Programmable Logic Controller (PLC) based system developed by ECIL. The main advantages of the new PLC system are customized leak detector modules and analog modules (mV) for flow signals which are not available in commercial systems.

The three sub systems namely Interlock system, Data Acquisition cum heater Control System (DACS) and Leak Detection system (LD) form part of Distributed Digital Control System (DDCS). The PLC uses master/slave configuration and data display through server/client architecture. Out of 2 servers one server is acting as cold stand by. The Architecture is shown in Figure 1.

The Interlock system has redundant CPU and power supply, whereas DACS and LD are standalone systems. The salient features of PLCs are increased input /output(I/O) capability with Remote I/O (RIO)

configuration and integrated signal conditioning functionality in I/O modules. The features provided in DACS are configurable ON/OFF capability, fail safe operation of heaters and display of heater/thermocouple layout in MIMIC. The innovative method of leak detection system was implemented to detect leak with contact resistance up to 2 Kohms. The system has provision to configure and assign leak channels to digital outputs through Man Machine Interface (MMI).

All the CPU racks/panels are placed in the same location for easy maintenance. To achieve this, sodium instrumentation electronics was repositioned. The architectural capability was effectively utilised in heater control system by providing the remote digital output module in the main control room thereby minimizing the cable utilization.

The installation and commissioning activities of the newly augmented I&C system has been completed. After successful commissioning, the system is handed over for operation.

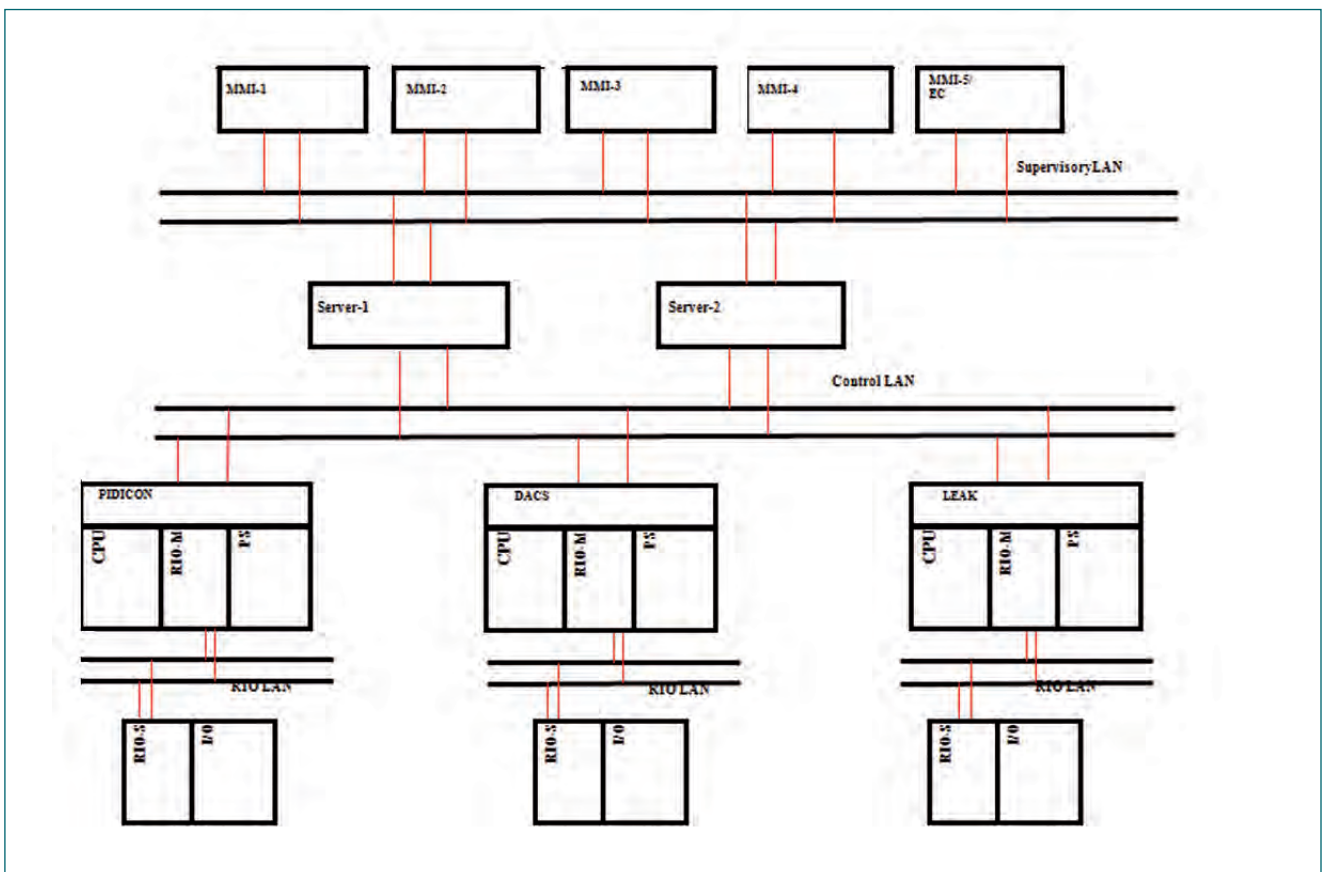


Fig. 1 Architecture of DDCS system in SGTF

III.15 Studies on Sodium Jet Fragmentation for Determination of Droplet Size Distribution

In Sodium cooled Fast Reactors, sodium leaks can't be ruled out completely despite of sound design, fabrication, stringent quality control and safe operating procedures. In air, the leaked sodium burns vigorously in spray form and rate of combustion is directly related to interfacial surface area between sodium droplet and air. Modeling of sodium spray fire is based on initial size distribution of sodium droplets. A dedicated experimental facility was designed and commissioned to study fragmentation of sodium spray for obtaining sodium droplet size distribution required for assessment of sodium combustion and its consequences.

The experimental facility consists of a sodium system and a 6 m long test chamber. The sodium tank (10 kg capacity) is provided with argon circuit and an argon buffer tank for ejection of sodium at constant jet velocity. The sodium system is provided with two bellow sealed valves installed before and after the electro magnetic flow meter (Figure 1). The test chamber is provided with toughened glass windows on sides as well as on top for video imaging the spray fragmentation process. Test chamber (6 m³ volume) is also provided with argon purification circuit for inerting the chamber and pressure relief valve for over pressure protection (Figure 1). The sodium tank is integrated to the test chamber.

Preliminary experiments were conducted with water as simulant of sodium at ~2 bar driving pressure through a nozzle of 5 mm diameter. The spray fragmentation at 1 m away from the nozzle was captured by using high speed video camera. Subsequently, experiments were conducted with 2 kg sodium at 350 °C and 500 °C in inert ambience (oxygen concentration <100 ppm) at 2 bar pressure. In each run, the sodium jet was tracked by high speed camera at 500 fps. Total duration of experiment was about 8 s. The sodium jet was observed

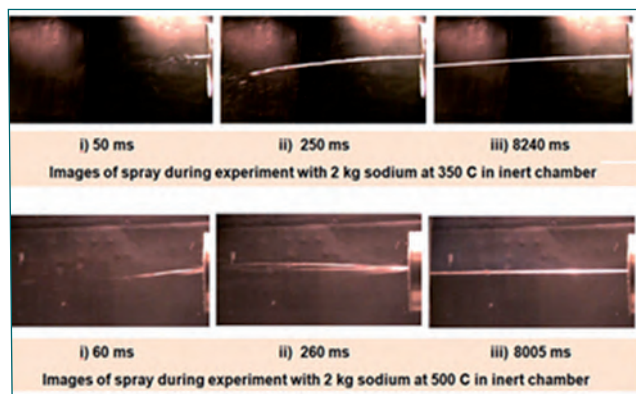


Fig. 2 Sodium jet scenario in inert test chamber from nozzle

to undergo fragmentation at about 2 m away from the release nozzle. The captured images of sodium jet from nozzle are shown in Figure 2. The fragmented sodium jet at 2 m distance from the nozzle is shown in Figure 3. The captured frames were subjected to image analysis and particle size distribution with respect to time was obtained successfully (Figure 4). Further experiments are planned with sodium inventories upto 5 kg for different nozzle diameters.



Fig. 3 Fragmented sodium jet at 2 m distance from nozzle



Fig. 1 Experimental setup with and sodium system

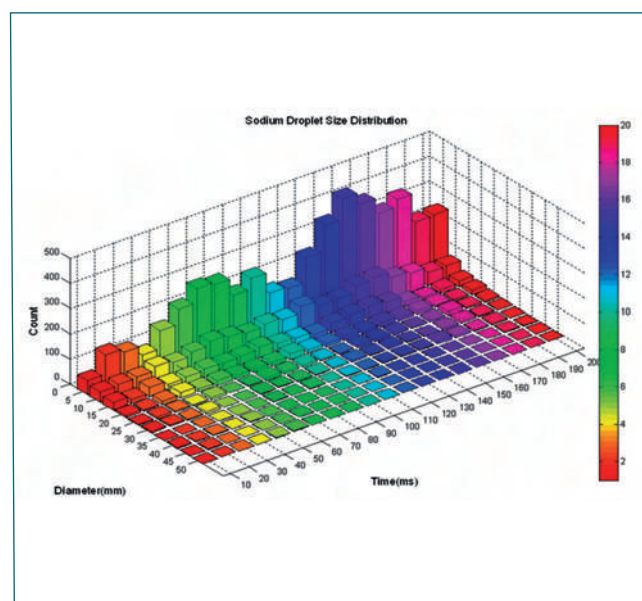


Fig. 4 Size distribution of fragmented sodium droplets

III.16 Hydraulic Studies to Characterise Pore Size of Sintered Micro Filters

Sodium is manufactured by electrolysis of molten sodium chloride in a Downs's cell. The process uses a graphite anode and an iron cathode. Carbon enters into sodium as a result of erosion of the graphite anode. In sodium cooled FBRs, majority of sodium components are made up of low carbon-austenitic stainless steels to minimize failures due to stress corrosion cracking. The higher carbon content in sodium also leads to carburization/decarburisation of austenitic stainless steels. Operating temperature of sodium in FBRs is 550°C. Studies indicate that decarburization occurs in sodium-stainless-steel system at temperatures above 425°C and carburisation at lower temperatures. As the carburisation of stainless steel takes place, it becomes brittle and its hardness increases. Detrimental effects of carbon on structural material demands limiting the activity of carbon in sodium. Upper limit for carbon content in nuclear grade sodium is less than 30 ppm. Solubility of carbon in sodium is 2.5 ppm at 550°C, whereas, higher carbon content is often found in commercial sodium. Undissolved or particulate form of carbon in sodium appears to be the major part. Undissolved carbon can be removed from sodium by microfiltration process. The efficiency of microfiltration process depends upon the pore size of micro filter against the size of carbon particles present in sodium. Characterization of pore size in the filter is important in the selection and design

of microfilters. To characterize the pore size of sintered micro filters, pore size of the filter was estimated by pressure drop studies which were conducted using water at room temperature which has nearly similar hydraulic properties of sodium at operating temperature. This article details the methodology adopted and results obtained from the studies performed to characterize the pore size of carbon microfilters.

Sintered porous filter element, manufactured through powder metallurgy, is used for this study. In fact, the structure of sintered porous filters is complex. Pores of different sizes could be randomly distributed. However, theoretical studies were performed by normalizing the porous structure into a series of pores of identical diameter, equivalent with the nominal size of pore designated by the manufacturer. It is assumed to be consisting of cylindrical pores with constant diameter and length equal to porous filter thickness. Hagen-Poiseuille model is used to estimate the pressure drop through a porous media. The model considers the fluid as incompressible, Newtonian and the flow is laminar through pores of uniform circular cross-section that is substantially longer than its diameter. The flow of fluid through the pores, given by Hagen-Poiseuille law is as follows:

$$G = \frac{\pi r^4 \Delta P N_p}{8 \mu l}$$

Pressure drop through the microfilter can be estimated by rearranging the above equation as follows:

$$\Delta P = \frac{8 \mu G}{\pi r^4 N_p}$$

Where,

G= Flow rate of fluid, m³/s

ΔP = Pressure drop, Pa

l= Thickness of porous medium, m

N_p= Number of pores

r= Pore radius, m

μ=Viscosity of the fluid, kg/m/s

Number of pores in the porous element depends upon its porosity. Porosity is fraction of total volume occupied by pores. Porosity of the porous disk was calculated from the ratio of pore volume to total bulk volume. The pores are actually not straight through but have convoluted paths with non-uniform cross section. Practically the length of the convoluted pore would be longer than the straight

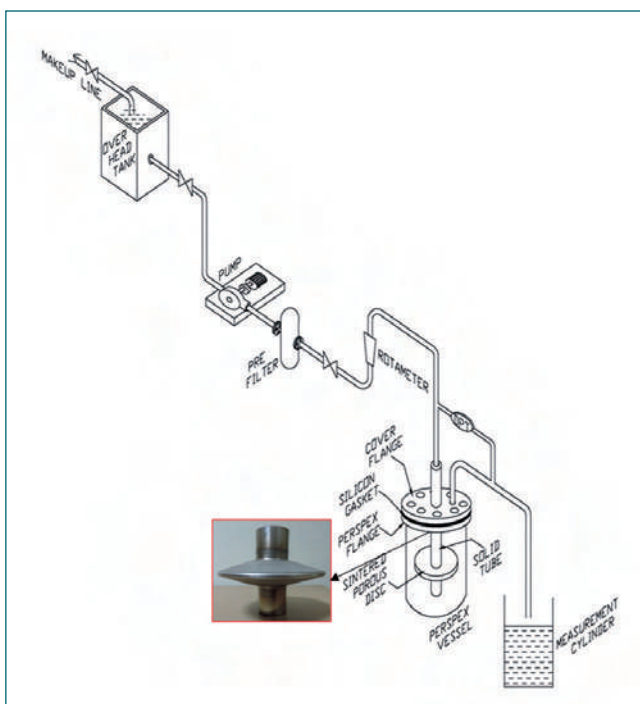


Fig. 1 Experimental setup

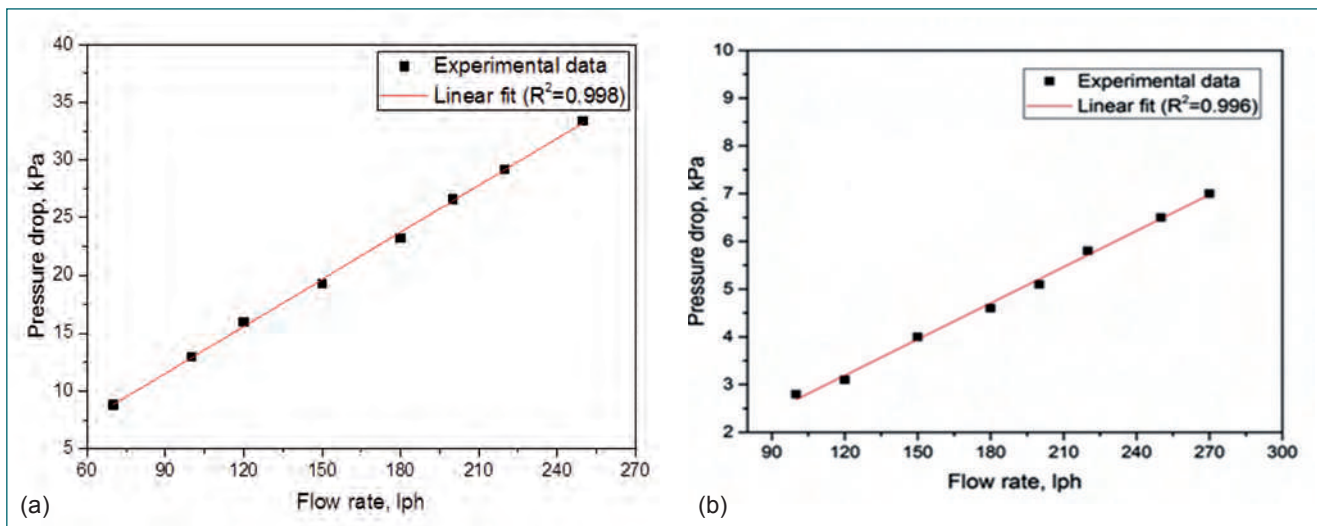


Fig. 2 Curve fitting of experimental results :(a) Type A disk; (b) Type B disk

through thickness i.e. the tortuosity of the channel would be greater than one. Tortuosity is a measure of the extent to which the path traversed by fluid elements deviates from a straight-line in the direction of overall flow and may be defined as the ratio of the average length of the flow paths to the distance travelled in the direction of flow. Tortuosity-porosity relation given in literature is used to calculate correction factor for tortuosity of the porous media.

Two types of micro filter elements in the form of a hollow porous disk were tested. Physical properties of the sintered porous disks are given in Table 1. The nominal size of pores indicated by the manufacturer for type A and type B discs are 5 µm and 15 µm. Experimental setup to establish the pressure drop characteristics is shown in Figure 1. To avoid difficulties associated with sodium experiments, the pressure drop studies were conducted using water as a stimulant fluid in a perspex vessel. The experimental setup consists of the porous disk inside a Perspex shell fixed in a process water line. The casing of the setup is made of Perspex, for better visualization of water flow coming out of the porous disk. The inlet of the porous disk was connected to an overhead water tank. Ultra pure water (particles size < 10 nm) was filled in the water tank. Pre-filter was connected before the setup as additional protection in order to prevent sediments entering into the pores of sintered disk. A Differential Pressure Transmitter (DPT) with a pressure range of 0-100 kPa calibrated to full scale was connected to measure pressure drop across the porous disk. A rotameter with a flow range of 0-500 lph was connected at the inlet to measure the flow rate of water. Filtration takes place when sodium flows from inside to outside through the disk. The filtered off particles would be held within the disk. Micro filter is designed for flow entry at the top to avoid carryover of filtered particles

during draining of sodium from micro filters. The flow pattern of water through the disk in the experimental setup was similar to carbon microfilter planned in sodium system.

At first, Type A disk was installed in the Perspex shell. Rotameter was calibrated by volume collection method before conducting the experiment. Flow rate of water to the setup was varied using a control valve. Pressure drop across the porous disk was recorded at different flow rates. Experiment was repeated with Type B disk. The experiments on Type A and Type B disks were repeated to establish the repeatability of experimental results.

Pressure drop values are plotted against flow rate and a curve of best fit are found. Experimental results shown in figure 2 (a) and 2 (b) shows that pressure drop have a linear relationship with flow rate which is in agreement with the Hagen–Poiseuille model. This shows that the contribution of the viscous forces to the pressure gradient is greater than the inertial forces. Experimental results were compared with theoretical calculations. For Type A disk, the experimental results are in good agreement with the theoretical calculations corresponding to 5 µm pore size disk. But in the case of Type B disk, the experimental results match with estimation corresponding to 10 µm pore size disk. This experiment provides an effective and simple methodology to characterize complex flow paths of stainless steel sintered disks.

Table 1: Physical properties of sintered porous disk

S.No.	Physical properties	Type A	Type B
1	Nominal pore diameter	5 µm	15 µm
2	Material	SS316L	SS316L
3	Thickness	2 mm	2 mm
4	Weight of sintered disk	390 g	320 g
5	Porosity	36%	45.4%

III.17 Evaluation of Fission Gas-Fuel Particle Unsteady Flow in a Voided Channel under Design Extension Conditions in Sodium cooled Fast Reactors

During the Design Extension Condition (DEC) such as unprotected loss of flow, rapid release of high pressure fission gas -fragmented fuel particle mixture into the coolant channel can take place within few hundred milliseconds of clad rupture. Subsequent dispersion behavior of gas-particle mixture in the coolant channel significantly influences the event progression path. Figure 1 shows the schematic of a fission gas-fuel particle mixture release from the failed pin following clad rupture under DEC. The gas-particle flow in the coolant channel involves complex interaction between the gas and particle phases, and influences dispersal behavior of core materials in the disrupted core. The gas - particle mixture flow resistance in a channel reduces significantly compared to a clean gas flow due to the presence of particles, which suppress turbulent dissipation. In this regard, an analytical model for gas-particle mixture flow through a circular channel (Figure 2) under the influence of fission gas pressure gradient is developed.

A parametric analysis is carried out to evaluate the gas-particle mixture flow in a channel of 4 mm diameter following the fuel pellet disruption and clad rupture. The pressure gradient in the channel due to fission gas release is defined using an exponentially decaying function. Figure 3 shows the variation of particle relaxation time with particle diameter for 10 μm to 1 mm diameter range. Result shows that the particle relaxation time varies from few milliseconds to few tens of seconds. Also, the particle relaxation time decreases significantly

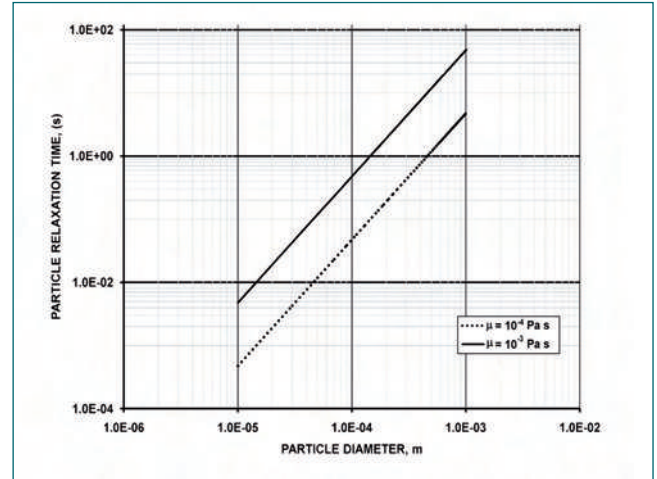


Fig. 3 Variation of fuel particle relaxation time with particle diameter and fission gas viscosity

with increase in gas viscosity due to effective momentum transfer. Figure 4 shows the unsteady velocity distribution of particles of diameter 10 μm along with the carrier phase (fission gas) velocity for an exponentially decaying pressure gradient with the characteristic time constant of 0.3 s and an initial acceleration of 100 ms⁻². The results bring out the behavior of gas-particle mixture flow under exponentially decaying pressure gradient and will be used in the validation of gas-particle two phase flow numerical model developed for the analysis of core material release and dispersive characteristics under DEC in Sodium cooled Fast Reactors.

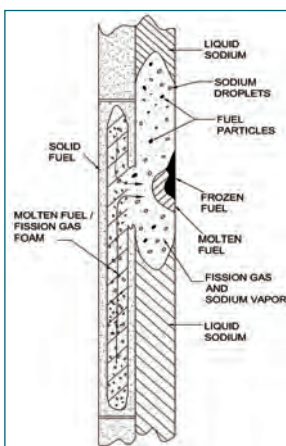


Fig. 1 Schematic of fission gas - fuel particle flow in coolant channel

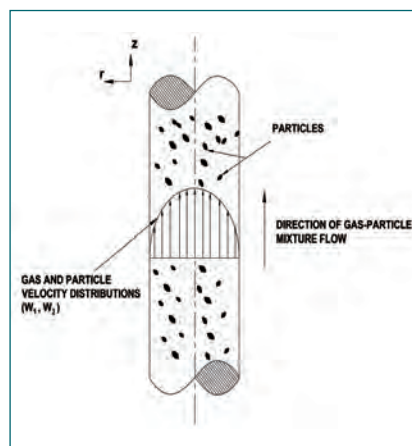


Fig. 2 Geometry of gas - particle flow in the circular channel

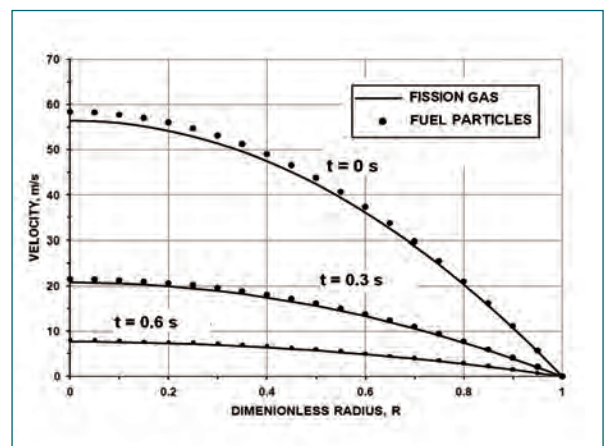


Fig. 4 Fuel particle and fission gas velocity distribution in a circular channel for 10 μm diameter particle

III.18 Laser Surface Remelting of Yttria-Stabilized Zirconia Thermal Barrier Coating for Sacrificial Core Catcher

Sacrificial core catcher with thermal barrier coatings (TBC) are proposed for future fast reactor to collect and retain the corium in a subcritical and coolable configuration during a hypothetical core melt situation. The molten sodium environment inside the fast breeder reactors necessitates long term resistance to liquid sodium-induced failure for the TBCs. Thus, it is essential to study the effect of molten sodium exposure on the properties of different TBCs towards qualifying as a sacrificial layer for core catcher applications.

Liquid-metal corrosion in molten sodium is a significant issue to porous TBCs proposed for in-core fast breeder reactor applications. In this work, the viability of controlling molten sodium corrosion of plasma-sprayed yttria-stabilized zirconia (YSZ) TBCs is investigated by microstructure re-engineering using Laser Surface Remelting (LSR). Additionally, the molten sodium corrosion behavior of laser-remelted YSZ TBCs is explored and compared to that of the plasma-sprayed. Comparing to the as-sprayed microstructure, LSR TBCs showed notably the following changes, i.e., smooth surface (Figure 1a), segmented vertical cracks (Figure 1b and 1c), and columnar grains (Figure 1d). The laser-remelted zone suffer inter-columnar and inter-granular attack along with the extension of segmented cracks almost up to the bond coat after 1 h of molten sodium exposure (Figure 2a). Further, the open vertical cracks allowed infiltration of molten sodium causing severe damage to the underneath lamellar splat layers. This leads to the spallation of the laser-remelted layer, exposing the underneath non-remelted layers. Further disintegration is accompanied by decohesion and

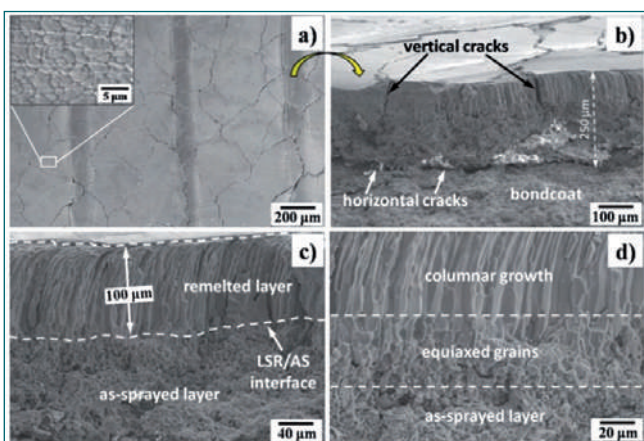


Fig. 1 a) Surface and (b, c, d) fracture cross-section of laser-remelted coating. The LSR induced changes are obvious in the SEM images provided

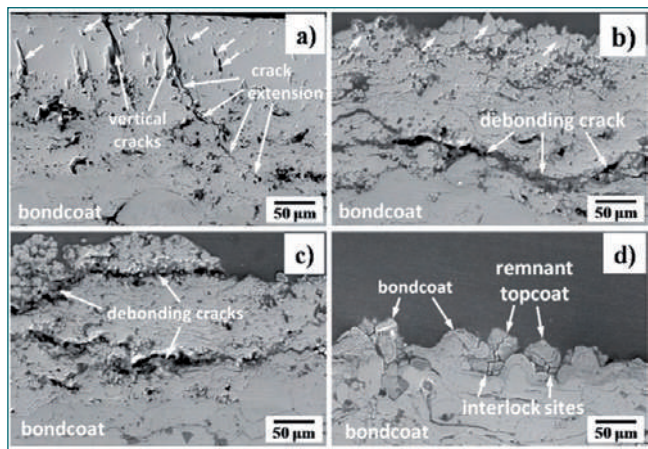


Fig. 2 Cross-sectional SEM micrograph of laser-remelted samples exposed for a) 1h, b) 10h, c) 100h, and d) 1000h in molten sodium

debonding between inter-splat layers (Figure 2b and 2c). The retention of the structural integrity of LSR up to 1h of exposure is attributed to the reduction in the specific reactive area resulting from densification with smoothing of the coating. However, the advantages offered by the above features are deluge by the columnar grain boundaries and segmented vertical cracks that allow easy molten sodium infiltration because of least tortuosity and thereby gradual degradation of the TBC on prolonged exposure (Figure 2d). The schematic of the microstructural degradation mechanism driving the molten sodium attack on LSR YSZ TBC is shown in (Figure 3).

Thus, laser-remelting of YSZ TBCs in the present case is not very efficient in minimizing the molten sodium corrosion unless a novel and innovative microstructure is evolve to completely arrest the molten sodium infiltration in the coating thickness direction.

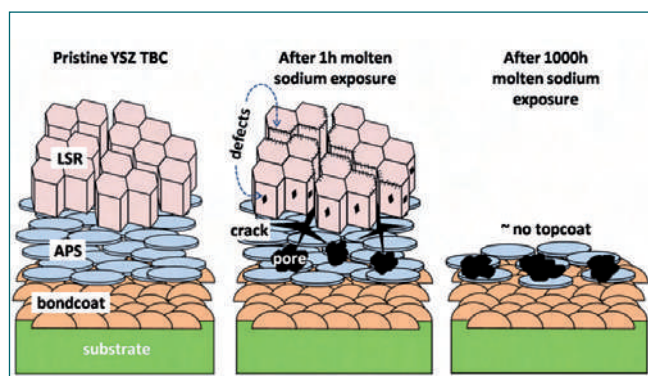


Fig. 3 Schematic of molten sodium attack in LSR YSZ TBC's

III.19 Ventilation Systems for a Radioactive Micro Analytical Characterization Facility

A laboratory for micro-characterization of irradiated fuel and structural materials up to 100 mCi of γ activity has been commissioned. A scanning electron microscope (SEM) with glove box interface (Figure 1) and an X-ray diffraction (XRD) machine are commissioned in laboratory for micro-structural examination of irradiated specimens. Stringent ambient conditions have to be maintained in the glove box to avoid degradation of surfaces of metallographic specimens and efficient trouble free operation of the machines in the laboratory area. Another major objective of the ventilation systems is the prevention of build-up of radio-activity and heat in the respective areas by providing adequate number of air/nitrogen changes.

There are three once-through ventilation systems in the laboratory to meet the above requirements. They are:

- Air-conditioning & ventilation system for the laboratory area.
- SEM hood ventilation system.
- Nitrogen/air ventilation system for the glove box.

Air-conditioning & ventilation of the laboratory area

Volume of the laboratory area is 150 m³. The total heat load expected inside the room is 4.2 kW, which includes internally generated heat from the equipment, occupants, lighting, and solar heat conducted inside through the walls and roof. Approximately five air changes are required to prevent the build-up of activity and heat in the room. Temperature and relative humidity requirements in the room are 24 ± 1°C and 50 ± 5% respectively.

A dedicated air supply system consisting of an air

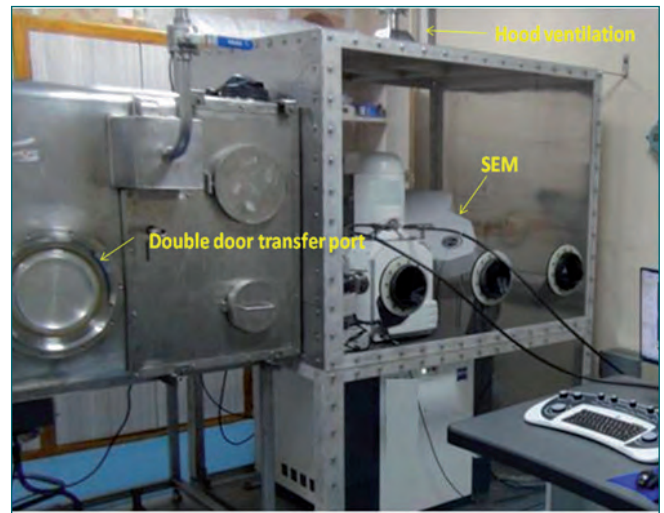


Fig. 1 SEM with glove box interface

handling unit (AHU) of capacity 1000 m³/hr, 6 nos. of 1 kW heaters for humidity control, a 10 TR water chilling plant, water tanks, re-circulating pumps, ducting, dampers, valves, pressure gauges and control & instrumentation system are provided to supply filtered conditioned air to the laboratory area. There are 100% capacity stand-by units for AHU, water chilling unit and pumps to ensure 24x7 availability of the system. For redundancy, the system has provision for operating AHU using chilled water supply from an independent source. A schematic of the air supply system is shown in Figure 2. The room exhaust is connected to the RML Phase-I Exhaust System-I to establish once-through ventilation. Exhaust System-II exhausts the air from the room to the environment via the 60m stack after filtration through HEPA filters. The pressure in the laboratory area is

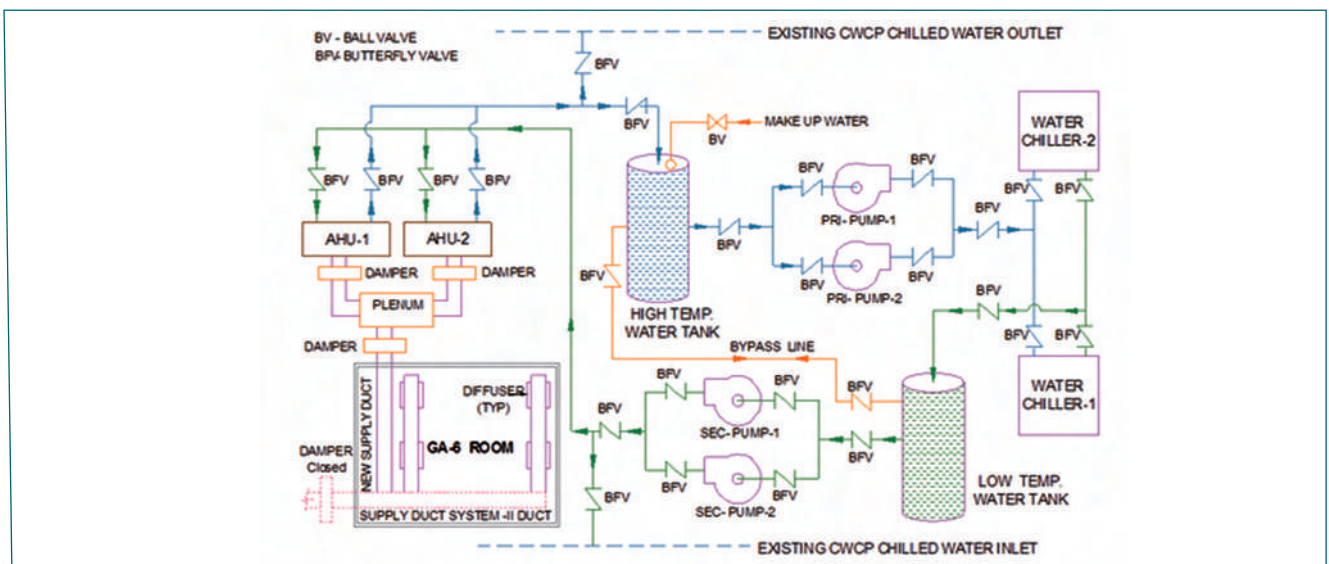


Fig. 2 GA 6 laboratory ventilation supply system

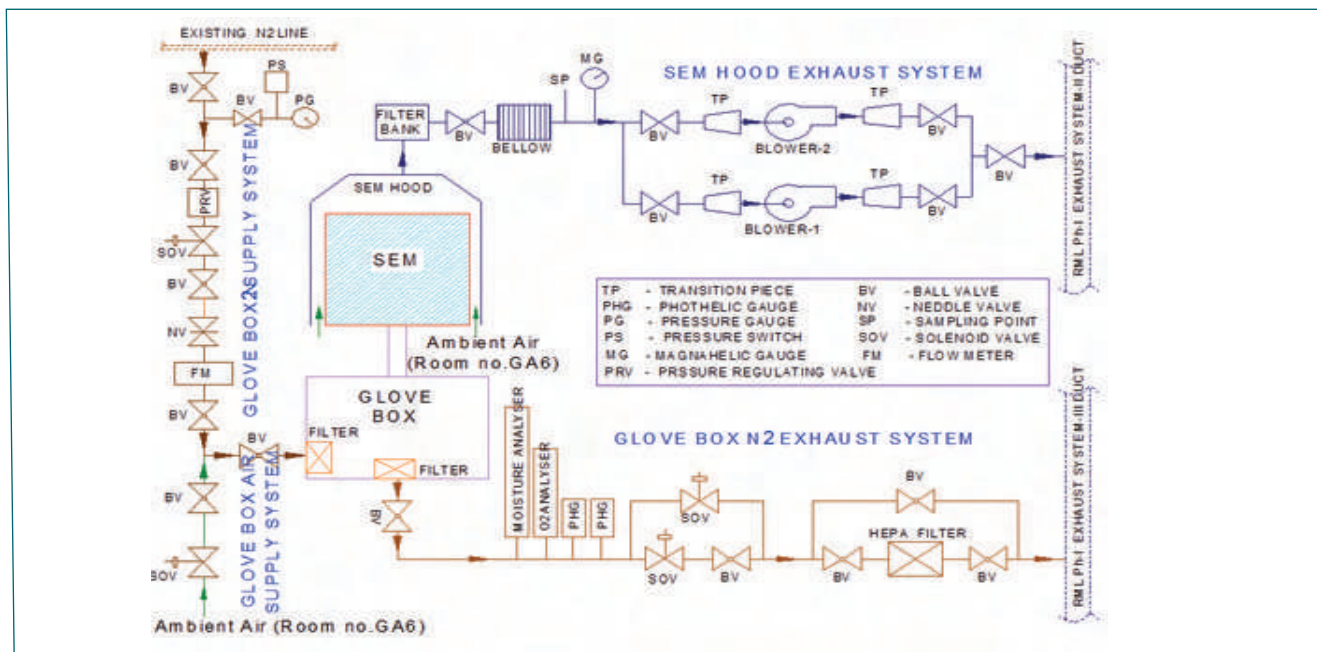


Fig. 3 Glove box & SEM hood ventilation

maintained between -3mm to -5mm WC with respect to the lower warm work area by adjusting the air supply and exhaust side dampers.

SEM hood ventilation system

A hood with once-through ventilation enshrouding the SEM is provided to avoid the SEM specimen chamber environment come in direct contact with laboratory environment during the opening of specimen chamber for maintenance and thereby preventing the spread of contamination to the laboratory area. The SEM hood ventilation line consists of a centrifugal blower, valves and associated piping. It draws air through the hood from the laboratory area and exhausts it to the RML phase-I exhaust system-II. A schematic of the SEM hood ventilation system is shown in Figure 3.

Nitrogen/air ventilation of glove box

Fast reactor irradiated fuel specimens have to be handled in α-tight manner under inert environment during their examination. The glove box interfaced with the specimen chamber of SEM satisfies this requirement. A double door transfer port is provided in the glove box for the transfer of irradiated specimens. Remote handling tools and a transfer device enables handling of irradiated specimen in the glove box and its transfer to SEM through a tunnel between the glove box and specimen chamber of SEM. Volume of the glove box is 1.10 m³. Considering the quantity of fuel handled and heat load, the required number of air changes is 2. Operating temperature of the glove box is required to be 20°C to 35°C.

The glove box is maintained under high purity nitrogen (> 99.9%) environment when fuel specimens are being

handled. Its exhaust is connected to RML phase-I exhaust system-III through a HEPA filter. Exhaust system-III vents air / nitrogen from the glove box to the environment via the 60m stack after filtration through HEPA filters. The ventilation system draws nitrogen from the RML phase-I nitrogen PSA plant. The nitrogen ventilation system (Figure 3) consists of manual/automatic valves, pressure/flow regulators, HEPA filters, stainless steel piping and control system. The control system maintains the pressure inside the glove box in the range -15mm to -25mm WC with respect to the laboratory area by operation of nitrogen feed and bleed valves. It has provision to bottle-up the glove box in case of failure of exhaust system, power source, or in the event of breakage of viewing glass, etc.

Whenever fuel specimens are not handled in glove box, nitrogen supply to the glove box is stopped and the glove box is maintained in air environment by drawing air from the laboratory area through a HEPA filter.

Procurement of raw materials and standard components, fabrication, welding, erection, and inspection were carried out as per work quality plan. After installation, piping / ducting segments of the systems were tested for leaks. During hold-up tests for 24 hours with initial pressure 1kg/cm², pressure drops in pipe/duct segments were found to be less than 0.05kg/cm². Subsequently the instrumentation and control systems were integrated with the piping and duct systems and extensive functional tests were carried out by simulating normal and accidental operational conditions. The system has been commissioned after successful completion of the tests.

III.20 Structural Modification in Nanocrystalline Yttria During High-Energy Ball-Milling

Advancement in development of novel structural materials requires tailoring of microstructure with careful choice of alloying elements and also ceramic oxide addition. Oxide dispersion strengthened (ODS) alloys are promising candidate materials for core applications of future FBRs, with excellent high temperature mechanical properties. Nanocrystalline yttria (Y_2O_3) stands out among all other ceramic oxides considering its high thermal stability up to $\sim 2327^\circ C$ and low coefficient of thermal expansion. Mechanical milling of steel and the ceramic oxide is an important step in the powder metallurgical synthesis of advanced ODS materials, which involves severe plastic deformation and fragmentation of particles, repeated cycles of cold welding and fracture. Along with other parameters, milling duration needs to be optimised for narrow grain size distribution. The methodology of achieving narrow size distribution may induce intrinsic defects beyond the critical defect density, which can lead to structural rearrangements resulting in the formation of disordered structures under atmospheric conditions. Detailed study of structural changes in nanocrystalline Y_2O_3 as a function of milling duration is vital to understand the mechanism of the phase transformation dictated by the extent of deformation during mechanical milling, which can influence the microstructural characteristics of the ODS alloys.

The structural evolution of nano crystalline Y_2O_3 powder is investigated using high energy ball milling for various durations up to 30h maintaining other optimized milling parameters. Figure 1 shows the XRD pattern obtained after different durations of milling. It is observed that, Y_2O_3

initially with a cubic structure gets refined and gradually transforms to the monoclinic structure as the milling duration increases. Results show the complete structural modification after 30 h of milling. The co-existence of both cubic and monoclinic phases at the intermediate stage of milling (8-15 h) indicates the progress of transformation being assisted by the accumulation of strain induced by the ball milling process. Peak broadening and peak intensity reduction with increasing milling duration also suggests increase in structural defect formation due to strain introduced during mechanical deformation accompanied by crystallite size reduction. TEM results given in Figure 2 (a-d) show the SAED pattern and the dark field images of Y_2O_3 powder before and after 30 h of milling, that confirms the monoclinic phase formation at 30 h of milling. Spotted ring patterns confirms the polycrystalline nature of material before (0 h) and after 30 h milling. Crystallite size distribution obtained from the dark field images of cubic and monoclinic Y_2O_3 before and after 30h of milling is given in Figure 2(e). It is apparent that at finer size of Y_2O_3 , monoclinic phase is preferred over the cubic one. The critical crystallite size for the monoclinic phase to stabilize can be determined to be ~ 15 nm from the analysis of the distribution, which confirms that the structural transformation from cubic to monoclinic- Y_2O_3 is influenced by crystallite size. The transformation sequence is established to be cubic- $Y_2O_3 \rightarrow$ (cubic- $Y_2O_3 +$ monoclinic- Y_2O_3) \rightarrow monoclinic- Y_2O_3 . The mechanism involved in the crystallite size dependent transformation could be also be due to strain induced during milling and thus it is hybrid of displacive and diffusional transformation.

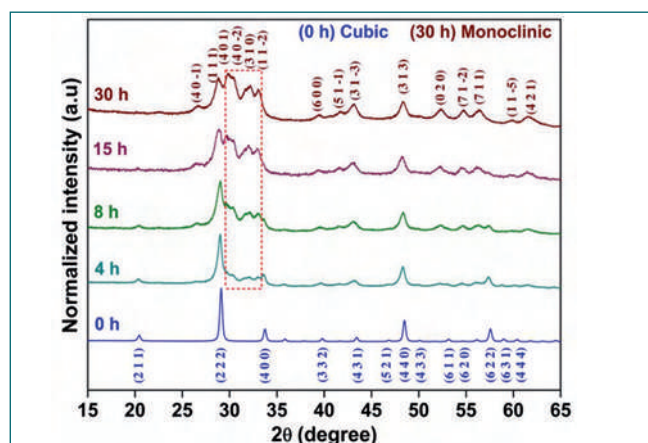


Fig. 1 XRD pattern of Y_2O_3 powder as a function of milling duration. Gradual phase transformation is observed beyond 4 h of milling and complete phase transformation from cubic to monoclinic after 30 h of milling

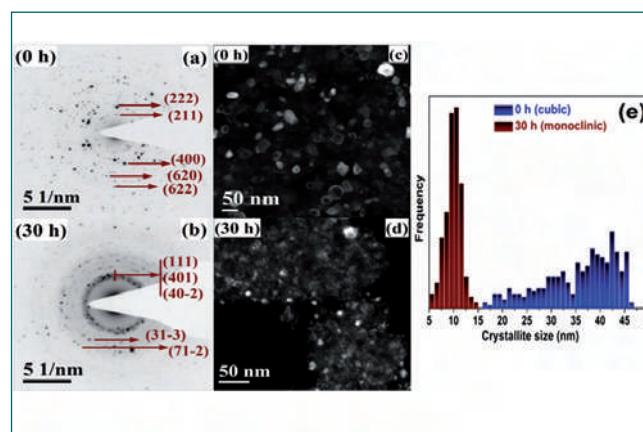


Fig. 2 (a-d) SAED pattern and dark field micrographs taken using (222) reflection of 0 h and spotty band of 30 h milled Y_2O_3 powder to illustrate the formation of monoclinic phase during milling. (e) crystallite size distribution of Y_2O_3 powder before and after 30h of milling

III.21 Thermal Properties of Natural B₄C and the Effect of ¹⁰B Enrichment

Boron carbide (B₄C) has attracted much attention in the nuclear industry due to its excellent neutron absorption cross section due to the presence of ¹⁰B isotope. Natural B₄C containing 14.7% of ¹⁰B has limited absorption cross section for fast neutrons and further the absorption cross section decreases with increase in neutron energy. Therefore B₄C with adequate ¹⁰B enrichment has to be used in Fast Breeder Reactors (FBRs) as a crucial safety component not only to control the core reactivity but also for the emergency shutdown systems. In addition, ¹⁰B enriched B₄C is also employed as a burnable poison in order to reduce the excess core reactivity and enhance the life of fuel subassemblies in small modular reactors. In the design of 500 MWe Prototype Fast Breeder Reactor (PFBR), 57% and 65% ¹⁰B enriched B₄C is being proposed for the absorber rod application. In order to achieve higher burn up in FBTR, 90% enriched B₄C (90 E B₄C) and 50% enriched B₄C (50 E B₄C) have been proposed for absorber rod and poison rod applications respectively. In this regard, the high temperature thermophysical properties of indigenously prepared hot pressed Natural B₄C (N B₄C), 90 E B₄C and 50 E B₄C have been estimated precisely from room temperature up to 1262 K to qualify these materials under reactor operating conditions. A critical analysis has been carried out to identify the effect of ¹⁰B isotope on the thermophysical properties of B₄C.

The measurements of heat capacity (C_p), temperature induced dilation Δl(T) (i.e. l_T-l₂₉₈) and thermal diffusivity (a) were carried out on hot pressed polycrystalline B₄C specimens as a function of temperature using dynamic scanning calorimetry (DSC), push rod dilatometry and laser flash method respectively, following appropriate ASTM standards. The temperature dependence of mean coefficient of thermal expansion (CTE) i.e. α_{mean} was estimated from measured Δl(T) and the bulk density (ρ) is estimated from the α_{mean} assuming isotropic expansion. From the measured values of C_p, ρ and a, the thermal conductivity (k) was calculated as per the equation $k = \rho a C_p$. Measured values of isobaric heat capacity (C_p), CTE (α_{mean}), thermal diffusivity (a) and thermal conductivity (k) of N B₄C, 90 E B₄C and 50 E B₄C are shown in Figure 1(a)-(d) respectively. These values are also reported in Table 1 at select temperatures. A systematic change in the Cp and CTE has been observed for B₄C as a function of ¹⁰B enrichment. However the thermal conductivity values for N B₄C is

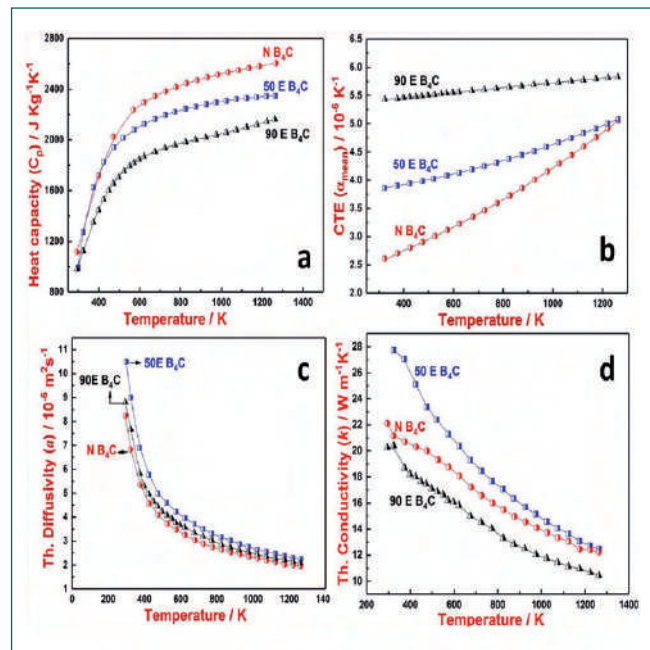


Fig. 1 A comparison of measured (a) heat capacity (C_p); (b) mean coefficient of thermal expansion (CTE, α_{mean}); (c) thermal diffusivity (a); and (d) thermal conductivity (k) for N B₄C, 90 E B₄C and 50 E B₄C with temperature

found to be intermediate between 90 E B₄C and 50 E B₄C for the entire temperature range of measurement.

Table 1 : Values reported at select temperatures

T (K)	Material	Cp (J/kgK)	α _{mean} (10 ⁻⁶ /K)	a (10 ⁻⁶ m ² /s)	k (W / mK)
294	N B ₄ C	1113	2.61	8.23	22.11
	50 E B ₄ C	993	3.82	10.5	27.2
	90 E B ₄ C	981	5.40	8.81	20.26
573	N B ₄ C	2237	3.11	3.74	18.75
	50 E B ₄ C	1825	4.08	4.23	21.31
	90 E B ₄ C	1450	5.49	4.45	16.21
773	N B ₄ C	2416	3.59	2.75	15.99
	50 E B ₄ C	2126	4.30	3.31	17.68
	90 E B ₄ C	1707	5.53	3.78	14.03
973	N B ₄ C	2505	4.15	2.35	14.04
	50 E B ₄ C	2240	4.58	2.76	15.13
	90 E B ₄ C	1840	5.60	3.19	12.04
1173	N B ₄ C	2580	4.75	2.01	12.45
	50 E B ₄ C	2307	4.91	2.37	13.07
	90 E B ₄ C	1955	5.69	2.63	10.97

III.22 A Space Time Kinetics Benchmark Study with Doppler Feedback

In nuclear reactor kinetics, the space time kinetics (STK) model is favoured over the point kinetics approximation in cases involving deforming core geometry, fuel slumping, asymmetric control rod withdrawal etc. It is planned to incorporate STK model into the future core disassembly accident (CDA) studies. A FORTRAN code is written to solve the complete space time kinetics equations in multi-group using five point difference equation for spatial discretization and implicit methods for time integration. The Gauss-Seidel method is used for solving the linear system of equations occurring in implicit methods. An adaptive time step scheme is also adopted to speed up the computational time. A Doppler feedback model along with an adiabatic fuel heat-up thermal model is also included. This code is accompanied by another indigenous code for solving the diffusion equation which provides the initial flux shape. The current code can handle both 2-D rectangular (x-y) as well as 2-D cylindrical (r-z) geometries. A benchmark problem known as the LRA-BWR problem, is used for a sample study. It is a 2-D rectangular BWR model of 330 x 330 cm size and containing 312 fuel subassemblies. A homogenised model of quarter of the core is shown in Figure 1. The homogenised macroscopic cross-sections for five material mixtures and other kinetics parameters are given as input. There are two delayed neutron precursor groups and two energy groups. Zero flux boundary conditions are used and the transient starts with steady state initial conditions.

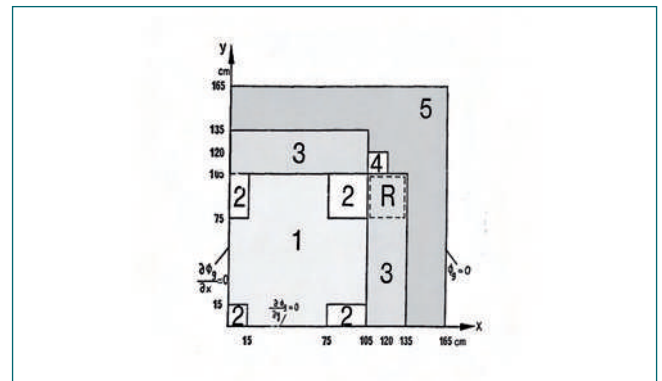


Fig. 1 Homogenized model of quarter of LRA-BWR core

Mesh size of $\Delta x = \Delta y = 2.5$ cm is used, giving a 132 x 132 mesh. The maximum eigen value of the initial flux distribution is found to be $k_{eff} = 0.99669$ compared to the reference value $k_{eff} = 0.99633$ (deviation of 36 pcm). Initially, the reactor is made critical by dividing the fission cross sections by k_{eff} . The transient is a control rod withdrawal incident in which control rods at the four corners of the core is withdrawn in 2 seconds. It is simulated by linearly reducing the thermal absorption cross-section in those regions for 2 seconds. The transient was followed for 3 seconds.

The initial flux is normalized such that the core average power density, $P = 1 \times 10^{-6} \text{W/cm}^3$. The core average power density verses time and the core average temperature verses time plots are given in Figure 3 and 4 respectively. Both power density and temperature

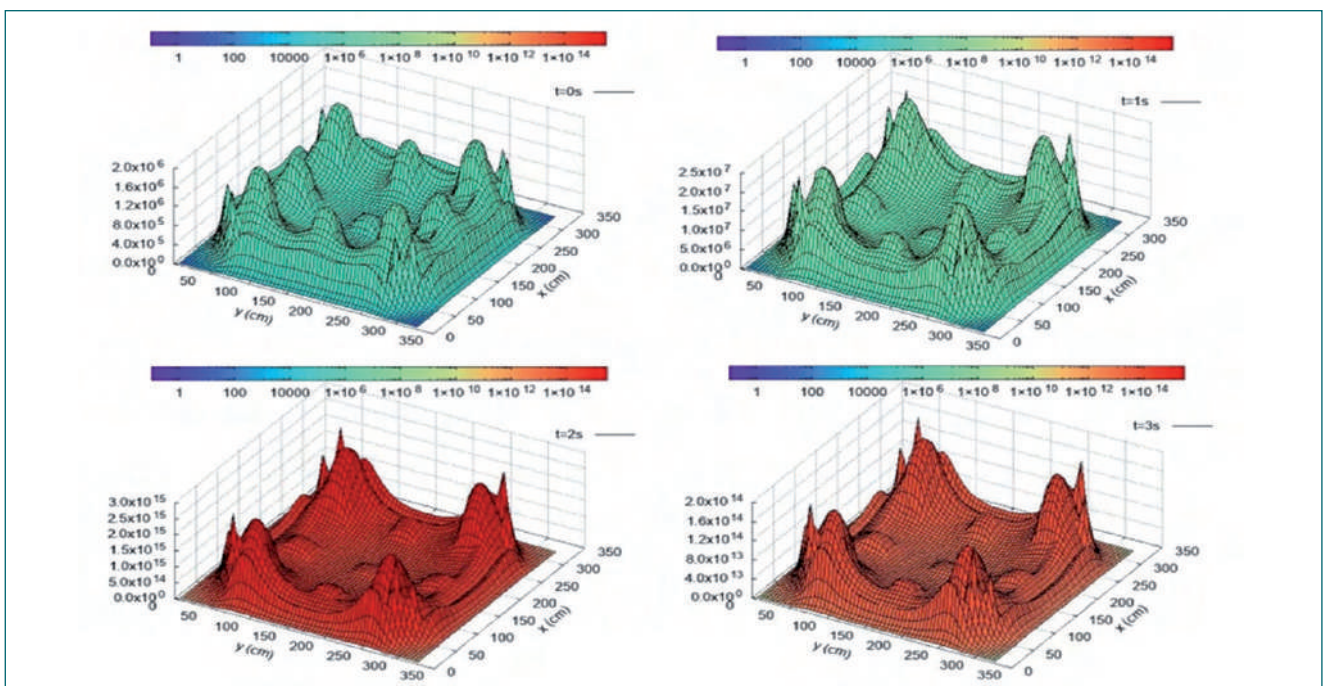


Fig. 2 Thermal flux at t = 0, 1, 2 & 3 s

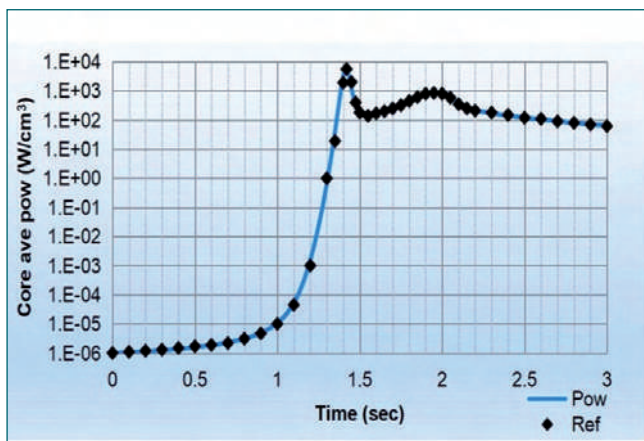


Fig. 3 Core average power vs. time

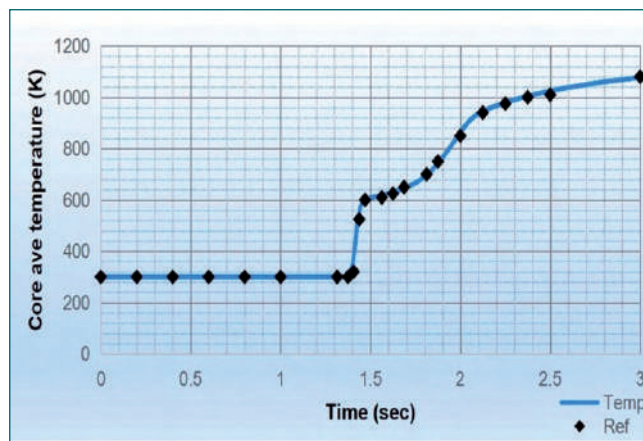


Fig. 4 Core average temperature vs. time

matches satisfactorily ($< 2\%$ relative error) with the reference values. The thermal flux at times $t = 0$ s, 1 s, 2 s & 3 s are plotted in Figure 2. It is observed that the thermal flux is peaking at and near the corners where the control rod was withdrawn instead of uniformly peaking (preserving the initial shape) as would be assumed by the point kinetics model. This also speaks towards the spatial decoupling of the BWR core. The normalised power densities of individual subassemblies were also given in the reference for comparison, from which a maximum deviation of 7% was observed in the present study. This is due to the different spatial discretization methods used (nodal method vs. finite difference)

resulting in a small variation of the initial flux shape. The computational time for this study with 132×132 mesh size, 2 energy groups and 2 precursor groups with a transient time of 3 sec, was about 4 hrs. The large computational time may be explained by the fine mesh size (2.5 cm) (which was needed to reduce the error in k_{eff} to about 30 pcm at $t = 0.0$ s) and having to solve a large linear system (whose condition number might have been reduced by the fine meshing) at every time step. Apart from the large computational time, the benchmark study agreed satisfactorily with the reference. This STK model with Doppler feedback can be confidently incorporated in the future CDA analyses.

III.23 Safety Studies Including In-Pin Motion Feedbacks Their Impact on Unprotected Transient Over Power Accident

Unprotected Transient Over Power Accident (UTOPA) is one of the beyond design basis events (BDBE), in which uncontrolled withdrawal of one control rod results in rise in power and fuel temperature. Upon rise in fuel temperature, it is possible for the fuel to melt and undergo in-pin fuel motion through the available central hole. Consequently, a multi-phase flow occurs inside the pellet cavity, with several hydrodynamic effects influencing the fluid motion. The relocation of molten fuel from high fuel worth to low fuel worth region necessitate the dynamic studies of molten fuel within the fuel pin and also to study its associated reactivity feedback appropriately.

When fuel melts, it is initiated at the site of peak power, closer to the core mid-plane. Initially, it tends

to move downwards under the effect of gravity, while continuously remaining in contact with the pellet inner surface. Upon encountering a relatively cooler surface, it begins to freeze. The freezing begins close to the site of melting. With further rise in power, the frozen fuel re-melts, leading to further downward relocation due to gravity, followed again by freezing at a relatively cooler pellet inner surface. Due to the continuous rise in heat generation, there is significant thermal expansion inside the melt column. This expansion results in outward growth of the melt column, whereas the freezing and re-melting confine the melt motion in both the top and bottom regions. Therefore, the melt column appears to grow simultaneously in both the upward and downward directions, as a function of the melt fraction. The initial

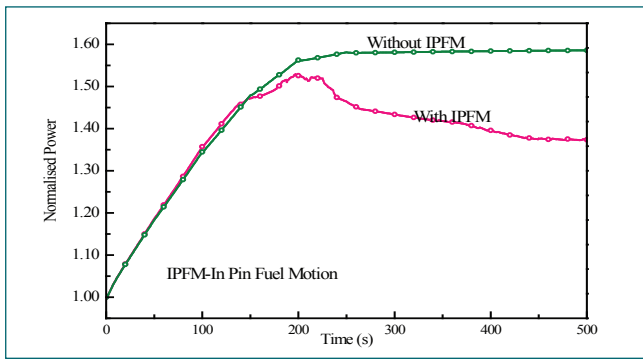


Fig. 1 Comparison of UTOPA Results with and without In Pin Fuel Motion Feedback

downward motion driven by gravity, along with the significant thermal expansion of molten fuel near the core mid-plane, decreases the fuel mass near the high neutron density regions, and increases it in the top and bottom regions of the fuel column. Consequently, an advantageous negative reactivity feedback is derived from in-pin fuel motion. A first order perturbation mass worth analysis is used to predict the resultant feedback due to In Pin Fuel Motion (IPFM).

With uncontrolled withdrawal of one control rod, there is positive external reactivity which results in power rise. It goes to a maximum of 58 % (Figure 1) over-power on a typical medium sized reactor of 600 MWe FBR 1&2. With power, fuel clad and coolant temperatures also increase. With the change in power and temperature, the important reactivity feedback contribution such as the Doppler, fuel axial expansion, core radial expansion, expansion of CSRDM and vessel expansion feedbacks becomes effective. Combinations of all these feedback reactivities could balance the external reactivity and makes the net reactivity almost closer to zero. However, initiation of fuel melting occurs and it goes up to 28 % of melting. It is observed that there is melting in four

axial nodes and four radial nodes up to the time of complete CSR withdrawal. The peak clad and coolant temperatures are 741 and 739°C respectively. Peak hot-spot clad and coolant temperatures are 788 and 780°C respectively. From the above results, it is understood that the possibility of clad failure is exceedingly small for an uncontrolled withdrawal of CSR, as the fuel melting is less than 50 % and the clad temperature is far away from its melting point. Even though there is melting, the outer part of the fuel is found to be in solid state. Hence, it is concluded that, there is no direct contact between molten fuel and clad.

When the above said UTOPA analyses is carried out with considering negative In Pin Fuel Motion(IPFM) reactivity feedback, the reactor power drops and finally it is stabilized at 137 % of nominal power, as opposed to 158 % without IPFM. IPFM reactivity contribution is found to be about -0.441 \$ (Figure 2). The peak clad temperature is 729°C as compared to 741°C without IPFM feedback. Similarly, the peak coolant temperature is 727°C as compared to 739°C without fuel IPFM feedback. Peak hot-spot clad and coolant temperatures are 774 °C and 766°C respectively as compared to 788 °C and 780°C without IPFM feedback. From the above analyses, it is learnt that the IPFM feedback not only reduces the power at the end of the transient, but it also reduces the hot spot clad and coolant temperatures.

From the study, it is concluded that UTOPA without considering IPFM feedback gives the most conservative results. If the transients converge to a safe state without considering IPFM feedback then, the transients are expected to settle down to a safe state with IPFM feedback. Thus, it is concluded that, UTOPA does not leads to CDA and the in-pin fuel motion reactivity feedback adds to the inherent safety of a reactor.

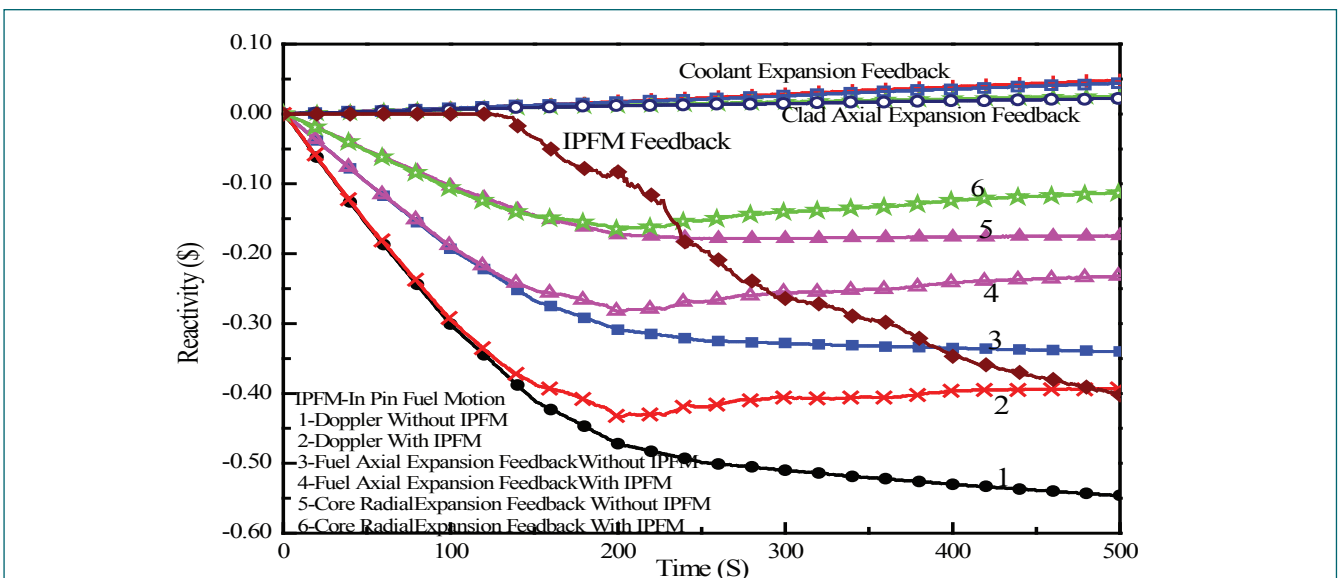


Fig. 2 Feedback reactivities of FBR-600 under UTOPA with and without in pin fuel motion feedback

III.24 Numerical Modeling of Ignition and Burning of Cables Exposed to External Heat Source

Cables are important components of Nuclear Power Plants (NPP) as they transmit the electrical power, control and instrumentation signals to different equipment and instruments of the reactor systems. The safety of reactor could be jeopardized by the loss in functionality of the cables due to damage caused by the heat source like fire. Moreover, the cables can be a source of fire in NPP, exist in large quantity and contain different combustible materials like PVC, XLPE, PE etc. as insulation and filler materials. The cables are generally hard to ignite, as the insulation and filler materials are not highly flammable. Moreover, the metallic core acts as a heat sink due to its large thermal inertia and causes heat loss along the cable length. However, the cable ignition can occur from the consistent external heat source like flame or hot smoke from other fires. Once ignited, cables may continue to burn generating heat, smoke and toxic gases.

A 1-D heat transfer model has been developed to analyze the ignition of cable wires subjected to external heating conditions. The model evaluates the transient temperature distribution along the cable based on external heat flux in the heating zone, considering axial heat conduction and convective heat loss from the cable surface. Using this model, the thermal behaviour of cables has been analyzed under various heating conditions and based on this the effect of heat loss through core material on ignition and burning process of cables has been brought out. The typical configuration of single core cable used for the analysis is shown in Figure 1. The model predictions have been validated with experimental results in the literature for the thin cables of ~ 1 mm overall diameter and 0.15 to 0.3 mm insulation thickness exposed to various external heating conditions. Two types of core materials (Copper and Nickel-Chromium) are used and the insulation material is PVC. The Biot number of the chosen cable configuration is $\ll 0.1$, and hence uniform temperature throughout the cross section can be assumed.

The ignition behaviour of cables has been evaluated by varying the parameters like external heat flux, heating length, insulation thickness and core material. The results show that possibility of cable reaching the ignition condition increases with the increase in heating

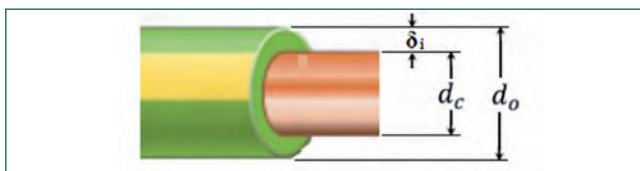


Fig. 1 Schematic of the cable configuration

length, decrease in conductivity of core material and its cross-sectional area due to reduction in heat loss through the cable core. The time varying temperature profiles estimated for the cables with copper and Ni-Cr cores are shown figure 2. The model predicted that for a cable with high conductivity core material (i.e., copper) the ignition becomes difficult due to large conductive heat loss along the core. On the other hand, for cable with Ni-Cr core (having one order of magnitude lower thermal conductivity than copper) the ignition can be easily achieved and the model predicted relatively less time scales for the ignition due to negligible heat loss along the core.

During steady state burning, the cable surface is surrounded by the hot flame zone and part of the combustion heat generated at the flame zone is transferred to the cable surface to sustain the burning process. The presence of metal core can change the burning rate of cable due to heat sink effect, as it reduces the heat energy available for the evaporation of insulation material. This heat sink effect is higher for copper core cables due to their high thermal conductivity. However, the reduction in cable burning rate is not appreciable for the Ni-Cr cables due to its lower thermal conductivity and lower heat loss through the core.

The model predicted trends of ignition delay time and cable burning rates were found to be in good agreement with the experimental results reported in the literature. The model will be used in the evaluation of postulated cable fire scenario in SFR systems.

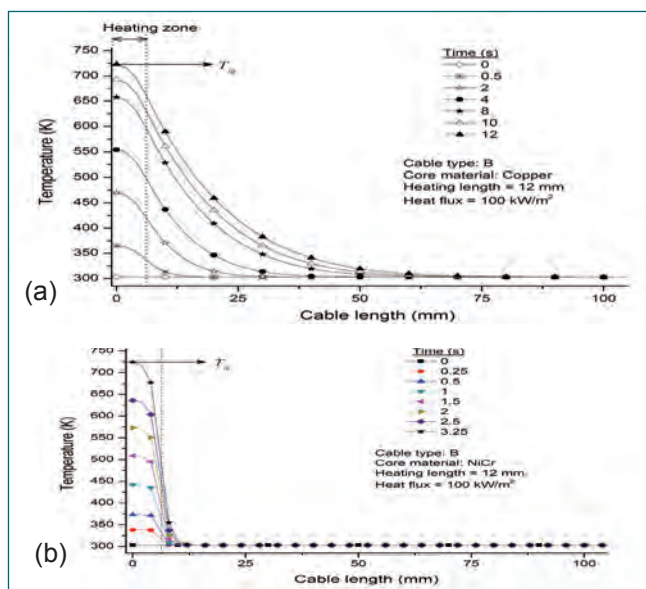
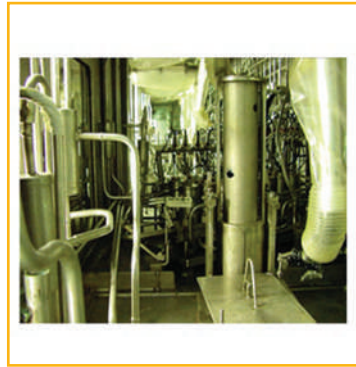
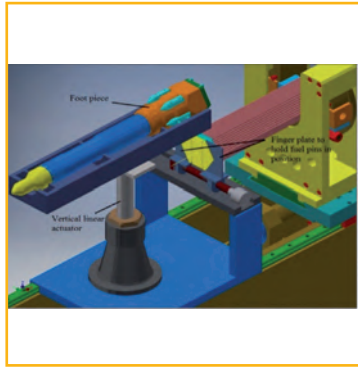


Fig. 2 Time varying temperature profiles of (a) copper and (b) Ni-Cr core



Fuel Cycle

IV.01 Conceptual Design & Development of a Fuel Pin Retrieval System to Retrieval of the Fuel Pins

The spent Fuel Sub-Assemblies (FSA) from the Prototype Fast Breeder Reactor (PFBR) need to be dismantled and the pins will have to be retrieved from them before reprocessing the used fuel. In order to cut open the hex-wrapper of sub-assembly for dimensional measurements-cum-laser dismantling (DMLDM), a machine has been developed. Each FSA contain 217 fuel pins, arranged in triangular pitch housed in a hexagonal sheath called wrapper. A schematic of the FSA along with sectional view showing the stacking of these fuel pins is shown in Figure 1. The bottom plug of each fuel pin has a recess in the shape of a key-notch for positioning. The fuel pins are positioned precisely by using 17 numbers of Guide Rails (GRs) having key shaped cross section, placed in parallel. These GRs are supported with two Support Rails (SRs) placed perpendicular to the guide rails. The GRs have a matching key shaped notch to get interlocked with SRs. The SRs are in turn fastened to the upper part of the foot of the FSA by four dowel pins. The details of the above arrangement is shown in Figure 2.

A mechanism has developed for retrieval of fuel pins from the fuel bundle & loading them into the Fuel Pin Can (FPC) that could hold 80 fuel pins in an array of 8

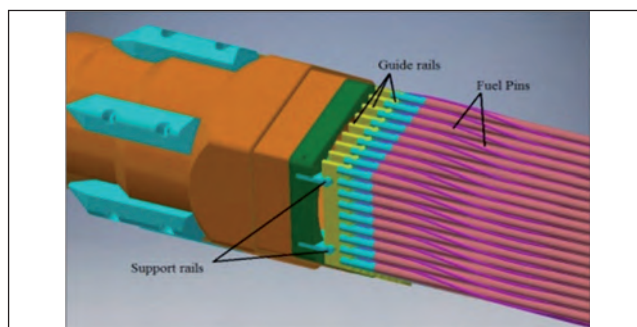


Fig.2: Positioning of fuel pins with foot piece using support rails & guide rails

x10 matrix. The sequence of operations involved in the transfer of fuel pins are described below.

Step 1: Removal of wrapper, followed by holding the fuel bundle in the horizontal orientation with the help of the DMLDM chuck. Removal of the foot piece by holding all the 17 GRs parallel with the help of a guide rail gripper. The foot piece is held horizontally with the help of a fixture provided with counter profile baffles that match with the foot piece contour. A vertical linear actuator is placed exactly below the centre of gravity of the foot piece, the actuation of which facilitates an upward movement of the foot piece along with the SRs and helps the disengagement of the foot piece (Figure 3).

Step 2: Transfer of the fuel pin bundle on to a platform equipped with four sets of grippers, by using an in-cell crane, shown in Figure 4. Each hexagonal gripper consists of a pair of fixed jaws at the bottom and a pair of moveable jaws at the top. These moveable jaws of all the four hexagonal grippers are operated by a single point drive by using a differential gear mechanism that ensures synchronized motion. The retractable moveable jaw is operated through a rack and pinion

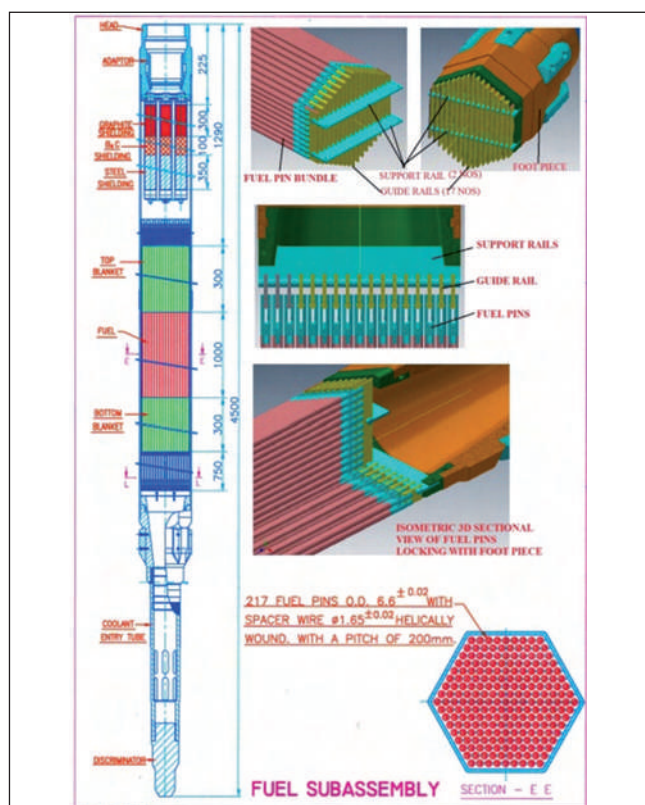


Fig.1: FSA with fuel pin stacking

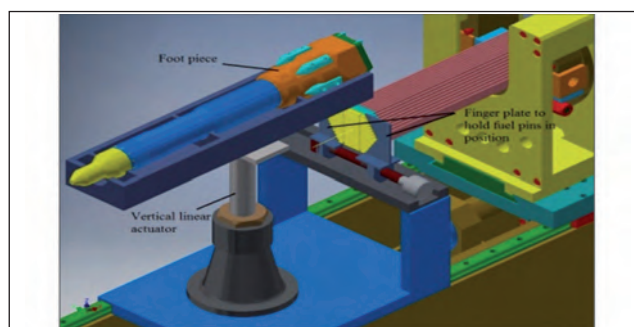


Fig.3: Removal of foot piece from fuel pin bundle by using foot piece fixture

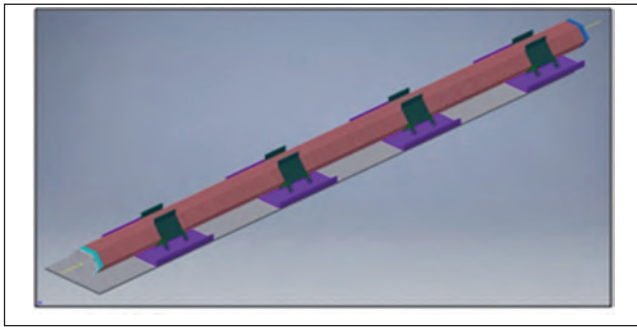


Fig.4: Platform with hexagonal gripper holding the fuel pin bundle

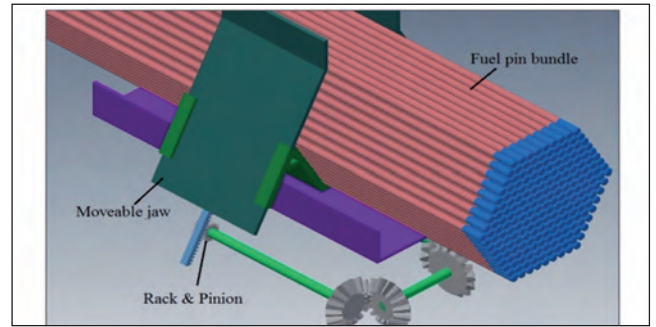


Fig.5: Isometric view of hexagonal gripper

mechanism as shown in Figure 5.

Step 3: The movable jaw is guided downwards so as to provide sufficient clearance for the removal of the top row of the fuel pins in the dismantled bundle (Figure 5). Then, this set of the top pins are along with their GR, pulled outward and are lifted up with a pair of tongs. These tongs attached to a roller gripper. One of these tongs hold on to the pins in the top row at one end (where the GRs are present) while the other holds and lifts the pins at the other and facilitates the removal of

this entire set from the remaining rows of pins.

Step 4: The freed top row of fuel pins are picked and placed into the fuel pin can (FPC) by using a special mechanism. The tongs of the pick and place mechanism are provided with a rotary actuator to facilitate reorientation of the array of fuel pins from the horizontal to vertical sense. The above steps 3 & 4 are repeated until the FPC is completely filled to its full capacity to hold 80 pins in a matrix form by transferring subsequent rows of fuel pins from the fuel pin bundle.

IV.02 Sodium Removal using Vacuum Distillation Technique from Sodium Bonded Simulated Metallic Fuel Pins Prior to Reprocessing and from Spent Absorber subassemblies of PFBR

Metallic fuels offering high breeding ratio, chemical compatibility with sodium and thermal conductivity etc. therefore are preferred for the next generation breeder reactors. While the development of molten salt reprocessing route is at the advanced stage, the most widely used PUREX process is also under consideration as a fallback option. However, sodium removal from sodium bonded U-6%Zr-Pu alloy is mandatory for applying PUREX process to avoid runaway reaction during dissolution of sodium bonded metallic fuel in aqueous nitric acid. Removal of sodium by wet chemical processes leads to possible Pu contamination in the effluent with radioactive burden for handling and recovery. Therefore, alternate physical methods are suggested. Similarly, absorber pins (control rod) of PFBR are of vented type wherein liquid sodium is continuously flowing through the annular gap between clad and B₄C pellets during reactor operation. It is estimated that about 2.8 kg of sodium remains in each subassembly (SA) and their periodic removal from the reactor (once

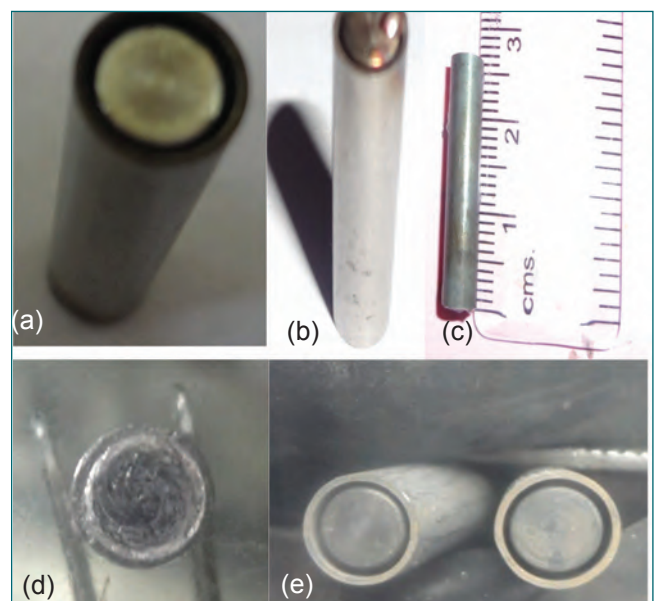


Fig. 1 Photographs of simulated chopped fuel pin showing (a) concentricity maintained, (b) the tig weld, (c) the length of a chopped pin, (d) the sodium bonded between the clad and the fuel rod and (e) sodium free pin after distillation

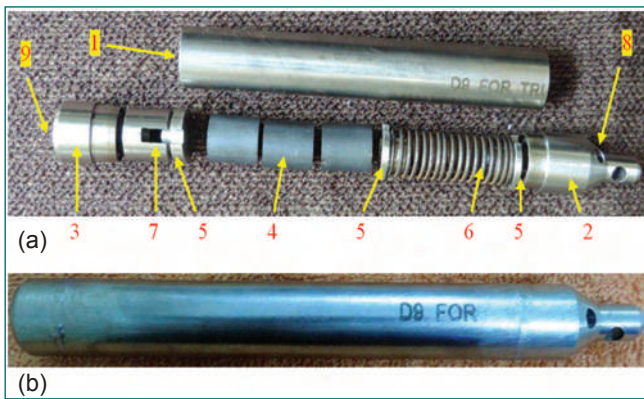


Fig. 2 Photographs of (a) components used for making absorber pin [1. D9 clad, 2. bottom plug, 3. top plug, 4. B₄C pellets, 5. support disc, 6. spring, 7. support sleeve, 8. sodium entry and 9. sodium exit] and (b) assembled view

in 2 year) requires removal of sodium from them prior to safe disposal/recycle.

Simulated chopped fuel pins were made of SS tube (OD 6.6 mm, wall thickness 0.49 mm & length 25 mm) as clad and SS rod (4.9 mm dia and 25 mm long) as fuel and were fabricated as per the proposed design. The SS rod was spot welded with tube so as to maintain the concentricity as shown in Figures 1a & 1b. The chopped fuel pin (Figure 1c) containing sodium in the annular region is shown in Figure 1d. Simulated absorber pin of length 200 mm instead of ~1100 mm provided by RDTG was taken up for sodium filling and cleaning. Figures 2a & 2b shows the photograph of the typical absorber pin. The SS vessel containing the fuel pins was filled with liquid sodium heated to 773 K for 10 days for sodium wetting and bonding. Sodium is clearly seen in the annular gap between the SS rod and SS tube and the increase in weight of 160 mg of fuel pin matches with that of the theoretical weight of sodium in the annular region of volume 0.17 cc which confirms the filling is complete as seen from Figure 1d.

Similarly, leak tight SS vessel containing simulated absorber pin was filled with liquid sodium and heated to 473 K at 63 kPa argon pressure for 17 days as recommended by RDTG for confirmation of sodium filling in the annular space of the absorber subassembly of PFBR. The increase in weight of the absorber pin by about 25 g matches with that of theoretical estimate of 26 cc and confirms that the sodium filling in the annular space. Filling of sodium was checked for 5 times for confirmation and was shown that the absorber pin gets completely filled with sodium under PFBR conditions.

An experimental set up used for distillation of sodium is shown in Figure 3. It consists of a distillation vessel,

collection vessel, bellow sealed valves for sodium and gas applications, level probe for monitoring sodium level in the collection vessel and a rotary vacuum pump as marked in the Figure 3. Temperature of the distillation vessel and collection vessel were maintained at 723 and 423 K respectively. 40 Nos. of chopped sodium bonded pins each containing 160 mg of sodium amounting to 6.5 g of sodium were taken in the distillation vessel and heated at 723 K under dynamic vacuum of about 10⁻² torr. Completion of the sodium removal is probed by the collective signal from the rise in vacuum along with the reading from the sodium level probe. The pins were taken out and examined. Photograph of the fuel pins after sodium cleaning by distillation are shown in Figure 1e.

The efficiency of sodium cleaning is observed to be greater than 98% and the remaining ~2% could be due to presence of sodium oxide may be formed during handling which cannot be removed by distillation at 723 K. Similar procedure was followed for the cleaning of sodium filled absorber pin and is successfully demonstrated at MC&MFCG.

It is concluded that sodium can be removed completely and safely from the annular regions of the fuel/absorber pins by vacuum distillation method. Optimization of the experimental setup, pumping capacity, addressing the flow characteristics and FPs trap configuration certainly offers the scope to improve the efficiency of the process.



Fig. 3 photograph of the experimental setup used for cleaning sodium by vacuum distillation. (1) distillation vessel kept in a furnace, (2) sodium collection vessel with insulation, (3) SS bellow sealed valves for sodium, (4) bellow sealed valves for argon gas, (5) level probe, and (6) rotary vacuum pump

IV.03 Shield Requirement Analysis for Fuel Pin Gamma Scanner in Fast Reactor Fuel Cycle Facility

Fast Reactor Fuel Cycle Facility (FRFCF) is an upcoming facility in Kalpakkam, to reprocess the spent fuel discharged from Prototype Fast Breeder Reactor and to fabricate fresh fuel assemblies. During various stages of fuel fabrication, quality of fuel has to be ensured. Passive gamma scanning is one of the non-destructive assay technique used to estimate the PuO_2 content in MOX fuel at pin stage. In passive gamma scanning, fuel pin is allowed to pass through a detector at uniform speed. The signature peaks of Pu^{239} nuclide are counted. The spatial distribution of gamma activity along the length of the fuel pin is inferred from the recorded activity profile.

The fuel pin gamma scanner in FRFCF is shown in Figure 1. During scanning, the fuel pins from a fuel pin tray containing 8 pins will be picked up one by one and scanned by NaI detector sequentially. While scanning a fuel pin, to reduce the background radiation from the other 7 pins, the detector has to be shielded. Shield requirement for the detector has been estimated using 3D transport code. The gamma scanner consists of 4"x4" NaI(Tl) detector with a side through hole of diameter 2.5 cm. Two annular Lead collimator assemblies of length 21.4 cm and OD/ID 2.5/0.7 cm each are fitted inside the detector with 0.35 cm gap in between them. During scanning the fuel pins are made to move through the collimator. The detector is kept inside SS housing.

PFBR fuel is a MOX ($\text{PuO}_2 + \text{UO}_2$) fuel. The fuel pin contains annular MOX fuel pellets and solid depleted UO_2 blanket pellets, which are stacked and loaded into



Fig. 1 Gamma scanning system

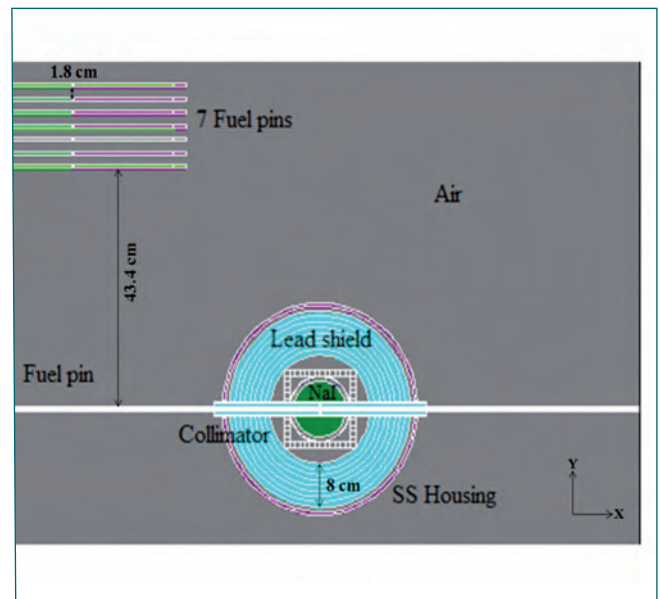


Fig. 2 Detector with shield - plan view (Geometry for Monte Carlo Simulation)

the clad tubes and sealed at both ends by end plugs. Fresh fuel pin contains both neutron and gamma ray sources. Neutron sources come from spontaneous fission and (a,n) reaction. Major sources of gamma radiations are actinides and fission product impurities of the reprocessed mixed oxide fuel. The neutron source strength per pin is $3.68\text{E}+4$ n/s/pin. Gamma source strength of the fuel and blanket pins are $9.68\text{E}+10$ g/s/pin and $1.52\text{E}+7$ g/s/pin respectively.

Detailed models of the helium bonded annular fuel pin and blanket pin are prepared. The plan view of the detector and the collimator simulated using Monte Carlo codes is shown in Figure 2. Keeping the 'pin under scanning' inside the detector, neutron and gamma transport calculations are carried out separately to estimate the total dose rate due to other pins on the surface of the NaI detector. For the purpose of dose estimation 1 cm^3 meshes are created virtually around the detector as shown in Figure 2 (as white boxes). Dose rate due to neutron, gamma and capture gamma are estimated at all mesh points.

During gamma scanning of the fuel pin, the dose contribution from surrounding fuel pins should not affect the ability to detect the actual gamma radiation emitted by the fuel pin under scanning. For that purpose, shield is designed surrounding the detector in such a way that dose due to other pins on the surface of the detector is less than one tenth of the blanket pin dose. Keeping the

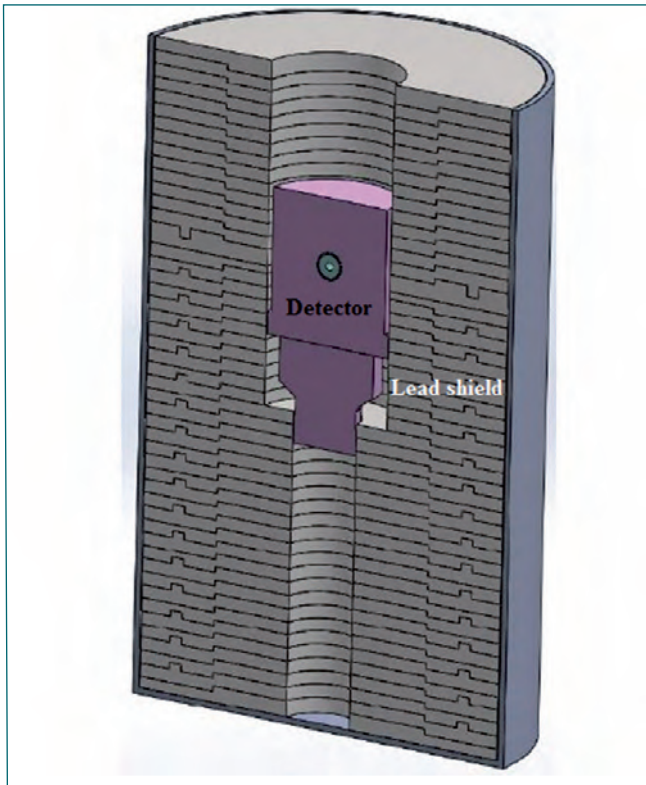


Fig. 3 Schematic of the layout of shielding around the detector

blanket pin inside the detector, the peak total dose rate on the detector surface is estimated. It is found to be 57 $\mu\text{Sv/h}$. Major contribution is from gamma radiations.

Neutron and capture gamma dose rates are negligible. Total dose rate due to surrounding fuel pins is 79.3 $\mu\text{Sv/h}$, corresponding neutron and gamma dose rates are 1.6 $\mu\text{Sv/h}$ and 77.7 $\mu\text{Sv/h}$ respectively. Since the dose rate due to near by fuel pins is more than one tenth of the dose rate due to blanket pin, detector has to be shielded. Shield optimisation calculations are carried out using Lead and mild steel as shield material. Streaming contribution due to the cable duct that pass through the bottom shield is accounted by introducing an one inch dia hole in the bottom shield. Schematic of the shield around the detector is shown in Figure 3. Totally 10^9 histories are analysed. Calculations show that, either 15 cm thick mild steel shield or 8 cm Lead shield is required all around the detector, including the top and bottom. It is seen that with 15 cm steel shield around detector, the maximum total dose rate on the surface of the detector is 1.7 $\mu\text{Sv/h}$, corresponding neutron and gamma dose rates are 1.4 $\mu\text{Sv/h}$ and 0.3 $\mu\text{Sv/h}$ respectively. With 8 cm Lead, the estimated peak total dose rate on the surface of the detector is 2.4 $\mu\text{Sv/h}$, corresponding neutron and gamma dose rates are 1.8 and 0.5 $\mu\text{Sv/h}$ respectively. Safety factor two has been considered in the calculation. Hence, to reduce the dose contribution from nearby 7 fuel pins on the detector surface to one tenth of the dose contribution from blanket pin, either 15 cm thick mild steel or 8 cm Lead shield is required around the cylindrical detector assembly.

IV.04 Mock up Study of Remote Replacement of Components in a Multiple Pin Chopper for PFBR Fuel

The first step in fast reactor fuel reprocessing is the chopping of the retrieved spent fuel rods. Since the fuel bundles similar to the ones used in the Prototype Fast Breeder Reactor (PFBR) has not been used in the other reactors, there is a need to develop a special and unique shearing machine for chopping PFBR spent fuel pins. It is a vertical shearing machine which is capable of chopping multiple pins in one stroke. The design had been so optimized as to last for 40 years. But some of its components would need to be replaced remotely from time to time due to wear and tear. These include the linear actuators, gripper block, cutting tool and the pneumatic cylinder. In order to test the viability of this design a mock equipment had been fabricated and trials on its remote maintenance had been completed.

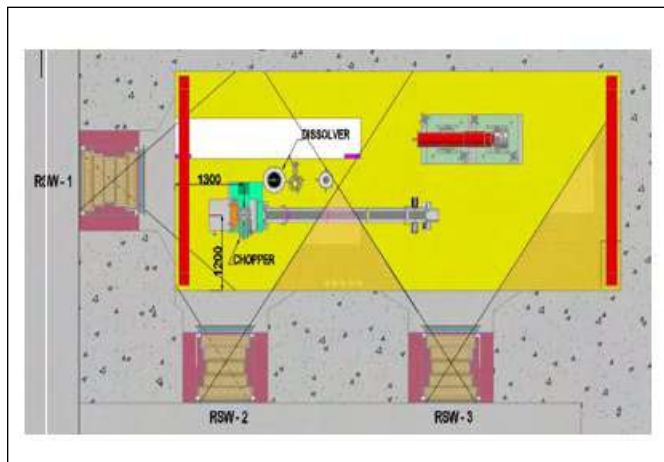


Fig.1: Chopper location in B92 cell

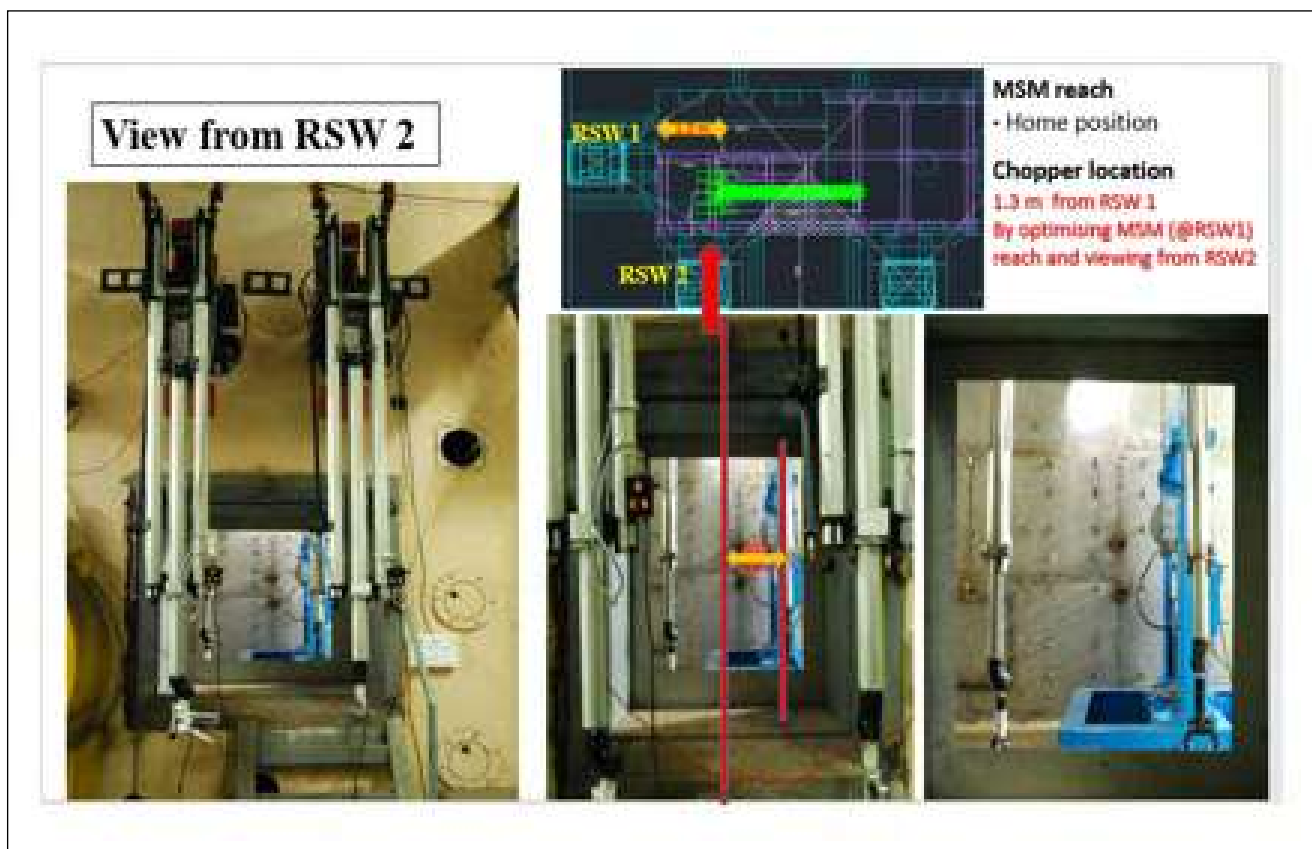


Fig. 2: Chopper visibility and MSM reach from RSW2

Challenges involved in finalisation of chopper location

- MSM reach
- Visibility of chopping operation
- Remote maintenance
- Crane reach
- Dissolver operation

- Fuel pin magazine transfer

Chopper has been installed in an inactive cell to simulate the field conditions as shown in Figure 2. The assessment of MSM reach and the visibility of the chopper have been carried out and shown in Figure 2 and 3. The functional requirements have been studied towards remote operation and maintenance of chopper with its associated systems.

The following modifications were incorporated to improve the design and make it more amenable for remote maintenance and operation.



Fig.3: Chopper visibility and MSM reach from RSW1

The radiation Shielding Window (RSW) has been chamfered to increase the visibility of chopper. Pillar towards window side in present design of chopper structure has been removed for better visibility of chopping operation. Distance between centre line of chopper and pillar (away from RSW) has been reduced for better visibility of dissolver operations. Base height has been reduced to increase MSM reach at anchoring point of actuator. Weight of the gripper blocks were reduced by reducing height of block which enable them for remote maintenance. The direction of motor has been changed towards window for better MSM reach. A new multi-pin chopper has been designed by incorporating the above features.

IV.05 Design, Fire Test Finite Element Simulation of Fire Proof Air Tight Door and its Validation

The fire proof leak tight doors are to be deployed for the HEPA filter bank & exhaust room of spent fuel reprocessing plant. HEPA filter bank room houses the filter bank. Each filter is made up of glass wool. The inventory is quite large and could sustain a fire. In case of any accidental fire hazard, the radioactivity lodged in the HEPA filter should not be released due to breach of the containment. Hence it is imperative that the doors of this containment need to be fire proof apart from being leak tight. A mock-up door designed by the design consultancy was fabricated and subjected to fire test by gradually increasing temperatures as per IS 3614 (part 2). The schematic of the door and fire test setup at the start, i.e. time, T=0 is shown in Figure 1.

At time T=120 min from the commencement of the fire test, it was observed that, the door could not meet the qualification criteria which stipulates integrity check, insulation and stability of the door. The failed door is shown in Figure 2. To evaluate the root cause of this failure, the FE simulation of the fire test carried and the FE results shown in Figure 3 at time, T = 120 min are validated with test results thereby the FE methodology established. The root cause of failure was found out to be direct metal to metal contact of the inner and outer sheet through an intermediate channel and the lack of use of an appropriate insulation material within the locking mechanism.

The design of the locking mechanism was modified with the insulation in place in order to isolate the inner and outer sheet of the door. The destructive testing of fire



Fig. 2: Door at time, T=120 min

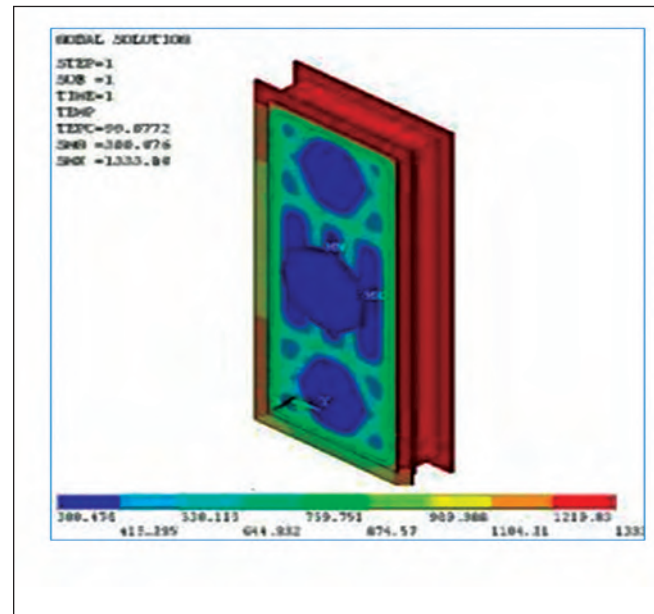


Fig. 3: Fire test FE simulation

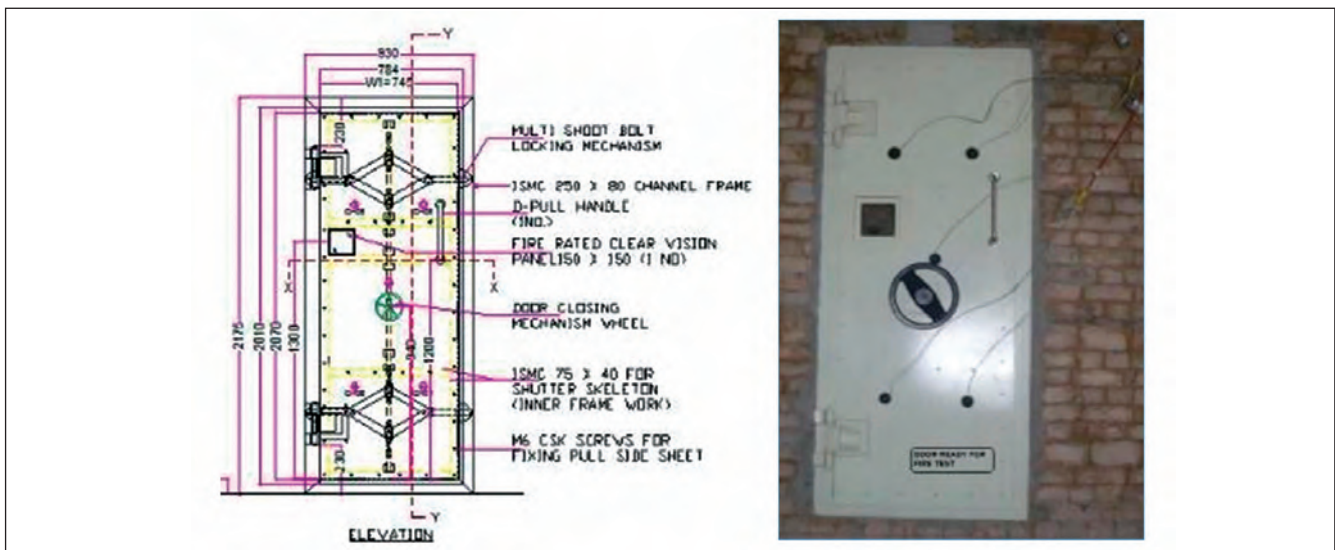


Fig.1: Schematic of door and fire test setup at time, T=0

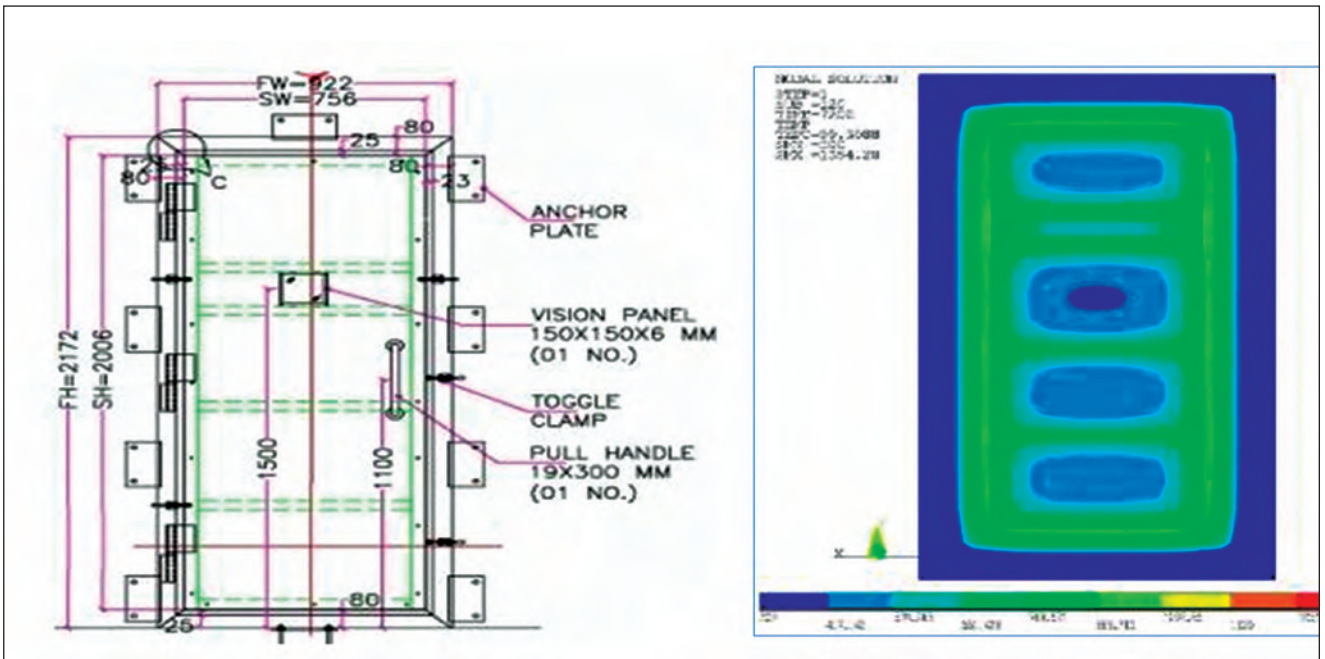


Fig.4: Schematic of modified door & its fire test FE simulation at T=120 min

door consumes a lot of resources and time. In order to access the insulation requirement, material thickness and to ensure that the door qualifies the fire test, finite element (FE) analysis simulating the fire test was carried out prior to the clearance for mock-up fabrication of door for conducting the fire test. The schematic of the modified door and its fire test FE simulation at time, T=120 min. is shown in Figure 4

The temperature-time curve of the outer sheet of the door is shown in Figure 5. The FE simulation of fire test ensured that adequate insulation has been provided and

the structural rigidity of the door is retained at the end of the test. Thus the modified door was found to qualify the fire test. Based on the FE outcome, clearance was given for the fabrication of the mock-up door for conducting the destructive fire test. Subsequently the fire test was conducted. The appearance of the fire proof door at time, T=120 min from the commencement of test is shown in Figure 6. The actual simulation of the fire test also concluded that the modified design qualified the fire test. Based on this clearance for mass production was given, fabricated and the same are being installed at site.

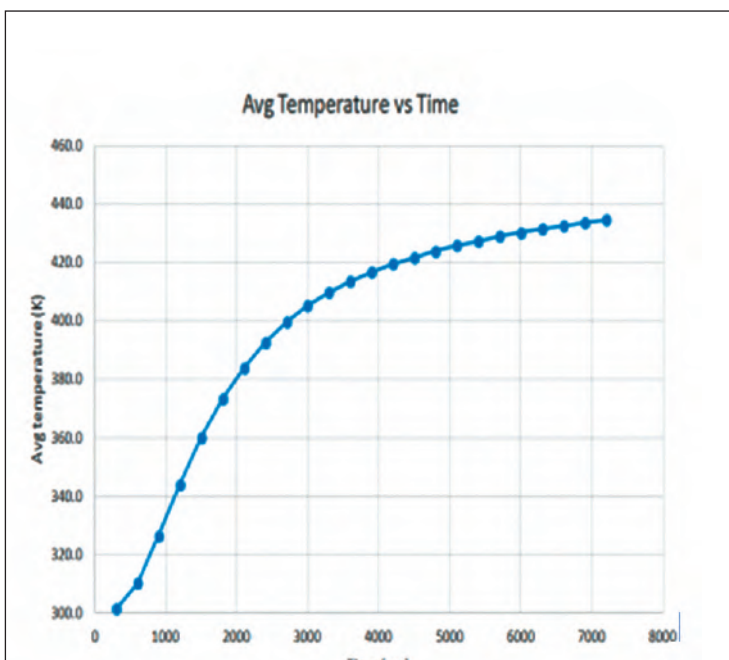


Fig. 5: Temp.-Time plot

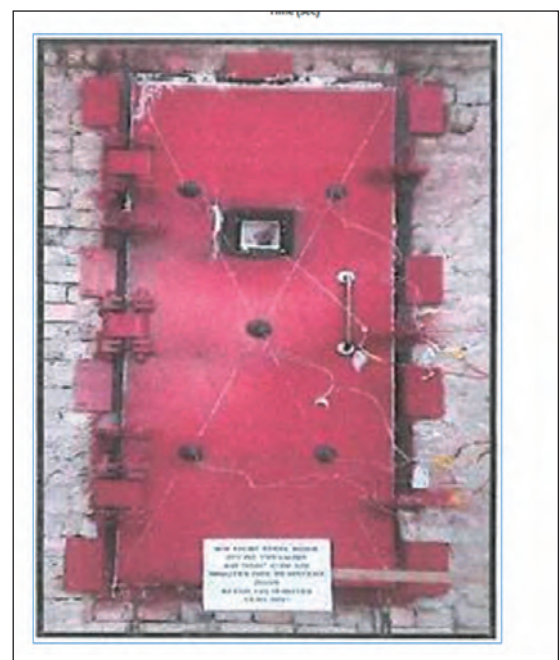


Fig.6: Fire test door at T=120 min

IV.06 Design and Development of Wireless Overhead Tank Level Control System for Demonstration Fast Reactor fuel reprocessing Plant

Monitoring and ensuring the availability of adequate quantity of the general use water and emergency use water is an important pre-requisite for the operation of a reprocessing plant. At this Centre a reprocessing facility viz., Compact Reprocessing of Advanced fuels in Lead shielded cells (CORAL) is in operation, viz., another viz., the Demonstration Fast Reactor fuel reprocessing Plant (DFRP) is in an advanced stage of commissioning. The water is pumped from the underground sump located at the Reprocessing Development Laboratory (RDL) to the two Over-Head Tanks (OHT) located at DFRP, depending on the water levels in both the sump and the receiving tanks (Figure 1). This pumping was being carried out manually. As an additional safety feature an automatic pump control system that would pump water as and when required by sensing the water level in both the sump and the tanks was designed, installed and commissioned. Considering that the Line of Sight (LOS) distance between the two locations is about 400 metres, it was decided to implement this control by using a system that would use a wireless communication. In order to accomplish this a wireless Network has been established. This had significantly brought down both the cost and time by avoiding cabling.

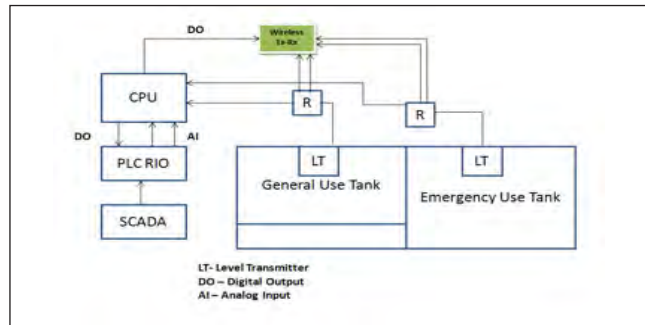


Fig.2: Level transmitter interfaced with WSN node and PLC

Wireless Sensor Network (WSN) nodes developed in-house by the Computer Division (CD), EIG, IGCAR were used for this deployment. Two different signal conditioner boards have been designed for this application. Ultrasonic level transmitters were installed at the OHTs to measure the tank levels. Level based interlocks were implemented at the PLC and the pump control output signal is communicated using this wireless network.

WSN nodes contain Zigbee System-In-Module and ARM7 controller. These nodes are equipped with IP54 rated enclosure and are EMI / EMC qualified. Two different Signal Conditioner Boards (SCB) have been

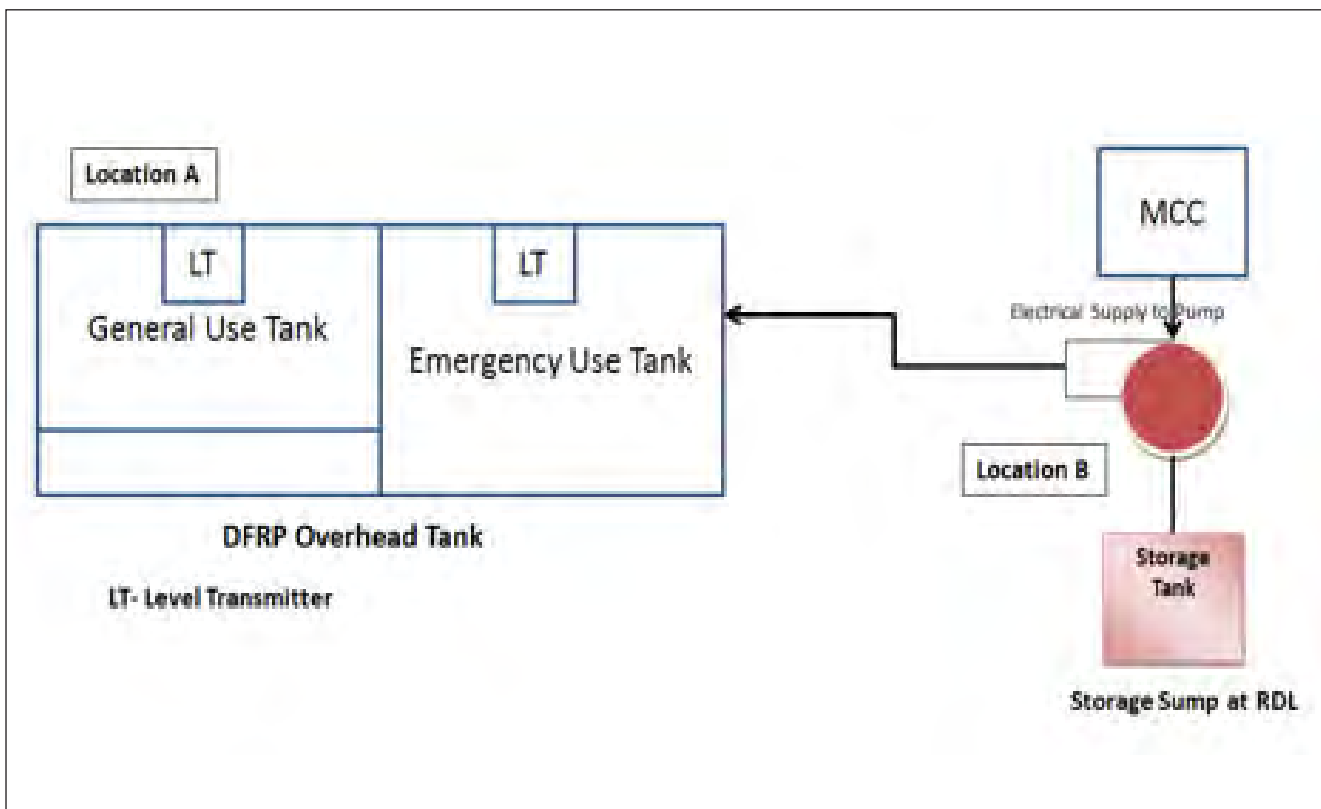


Fig. 1: Level control system schematic

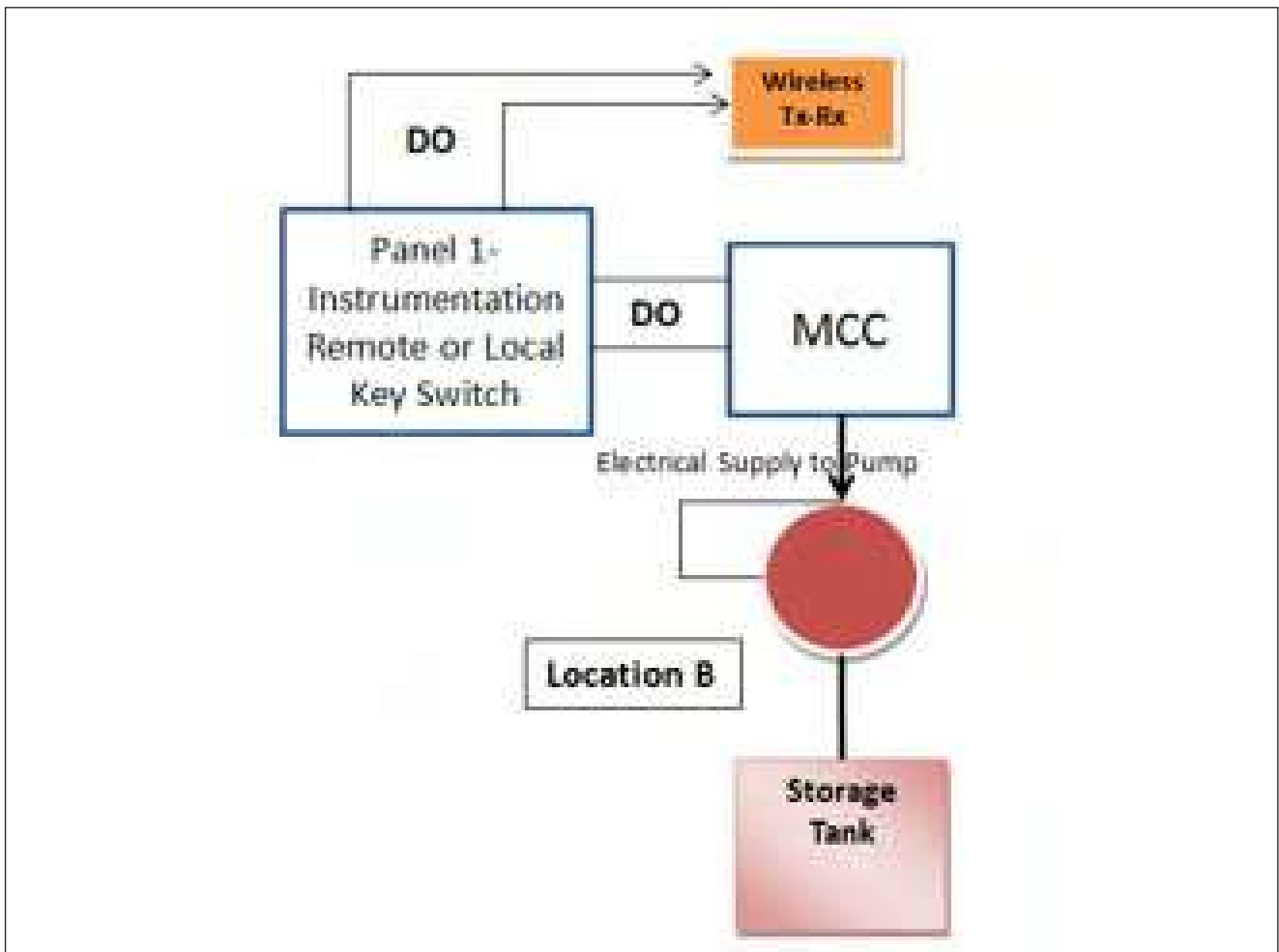


Fig.3: WSN at RDL water sump

designed for this application. The first SCB contains two analog (4-20 mA) inputs and one digital input. Other SCB has one digital input and one digital output.

The OHT Level transmitters were interfaced with the PLC and the WSN node. The schematic of the system is shown in Figure 2. The system has been so programmed as to start the pump when the level in any of these tanks falls below 40% and eventually the pumping would stop when the levels in both the two OHTs at DFRP reach 80%. Digital output (DO) signal for pump ON/OFF has been interfaced with the WSN sensor node by using the first SCB. Level sensor data and corresponding control input has been sent wirelessly to the WSN sensor node located in Location B. The DO signal from WSN node 'B' actuates a potential free relay which in turn actuates a contactor to control START/STOP of the pump

At location "B", the operator selector switch for local and remote operation is connected via the Instrumentation Panel. In the local mode, start and stop are done manually and in remote mode, start is done manually and stop is automatic (based on level interlock).

WSN node firmware for level sensor signal acquisition,

transmission and reception has been developed and tested by the Computer Division (CD) of this Centre. SCBs were calibrated with the level sensor. This firmware is also capable of receiving and parsing the frame and actuating the control action based on frame data. Data packets containing the level sensor data and digital pump ON/OFF output are sent wirelessly every 2 seconds. Packet retries at application layer are also implemented along with lower layer packet retries to ensure successful packet transmission.

A detailed site survey was carried out by CD in assessing the radio frequency (RF) strength and interference at various locations between CORAL & DFRP before finalizing the optimal number and locations of router nodes required for Wireless Network has been commissioned to control the pump operation of OHTs. Two sensor nodes were deployed and communication has been tested. Level Interlocks were generated at PLC and pump control signal has been transferred wirelessly using this network Based on operation of network, this application could be extended to other controls in future. This is a first of its kind implementation carried out in our Centre.

IV.07 Development of Air-Sparged Mixer Settler for the Treatment of Lean Organic Phase at DFRP

The PUREX process is based on liquid-liquid extraction of uranium and plutonium from the spent nuclear fuel using a solvent phase composed of 30% (v/v) Tri-Butyl Phosphate (TBP) and n-Dodecane (nDD). During this process, both TBP and nDD undergoes degradation due to radiolysis and acid hydrolysis, producing a large number of degradation products. Presence of these degradation products results in inefficient recovery of uranium/plutonium, and significantly alters the physicochemical properties of the solvent causing increased phase separation time, formation of interfacial crud etc. All these factors significantly reduce the performance of the solvent. Solvent degradation is more severe during reprocessing of the fast reactor spent fuel due to high burnup in comparison to that of thermal reactor spent fuel. This results in generation of large amounts of organic waste. Hence, a reliable solvent purification system is essential for the sustained operation of a reprocessing plant.

Most commonly the degraded solvent is washed using an alkali solution in a suitable contactor, since majority of the degradation products are acidic. Due to various limitations of existing/available liquid-liquid contactors such as ejector mixer settlers, impeller driven mixer settlers, pulsed column etc., a new continuous equipment was designed and developed. Figure 1 shows the photograph and solvent treatment scheme by using this new equipment which is a continuous, cross current, three-stage air sparged mixer settler. This new equipment is amenable for remote operation, less likely to choke, and requires less headroom. The entire work had gone through multiple stages of development

starting with small scale batch experiments using actual spent solvent from 60th campaign of FBTR fuel at CORAL for the selection of right chemical reagent for solvent treatment. This was followed by investigating the kinetics of solvent treatment and phase disengagement behavior that helped in designing a continuous process equipment and fabricating the prototype of the same. Performance of the prototype was investigated in every aspect by performing full scale experiments, on site and off site, before freezing the design of the solvent treatment equipment. As shown in Figure 1, the equipment consists of three stages in which the first two stages are used for washing the solvent using 1.5 M hydrazine carbonate followed by washing with 3 M nitric acid in the 3rd stage. Performance evaluation of the prototype had shown that the new equipment can remove nearly complete amount of the primary degradation products from the organic phase even from the highest level of concentration so far observed in the history of CORAL, and the equipment can satisfactorily process the organic phase at four times the processing capacity required for DFRP. Solvent extraction flow sheet of DFRP consists of two co-decontamination cycles followed by one U/Pu partitioning/stripping cycle. Each cycle would be provided with a dedicated three-stage air sparged mixer-settler solvent wash unit for treating the corresponding lean organic phase. Three such units were fabricated in compliance with ASME Section III Division 1 Subsection NC for installing at different contactor cells of DFRP. Each unit was independently tested and qualified for functionality and commissioning of the all the units are in progress.

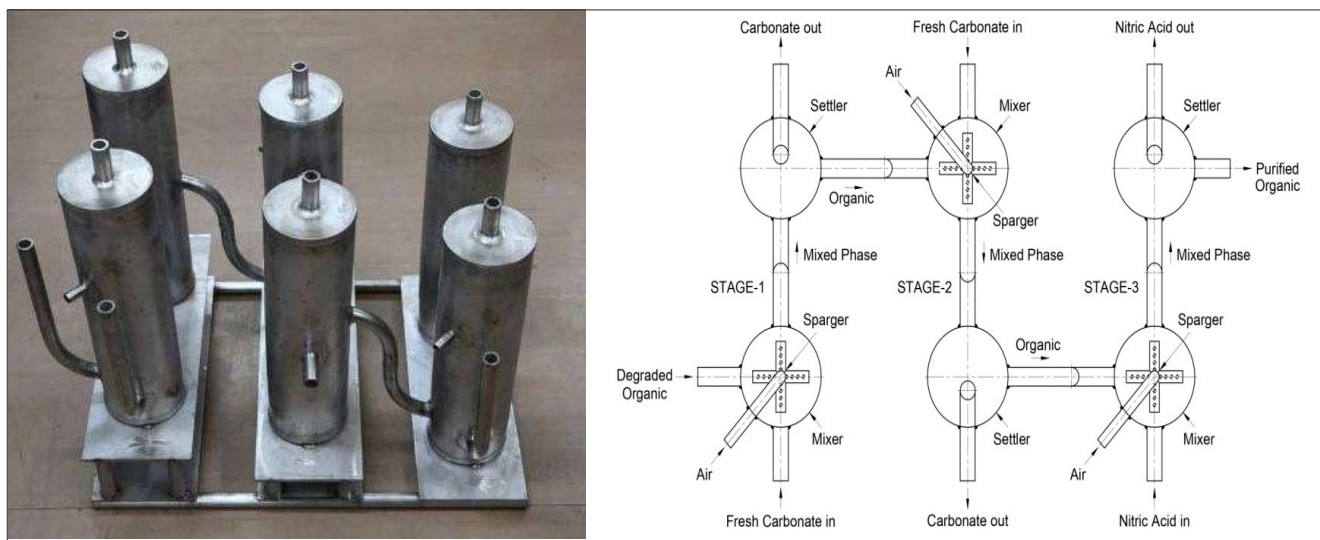


Fig. 1: 3-stage, cross current, air sparged mixer settler for solvent wash at DFRP

IV.08 Modification of Centrifugal Extractor Banks of DFRP and Performance Assessment

An annular centrifugal extractor (ACE) is one of the high efficient stage-wise solvent extraction equipment, and it has been widely used in the different process industries. It is selected for fast reactor nuclear reprocessing application due to its high throughput and short residence time which is in the order of seconds for reducing the solvent/diluent degradation during reprocessing. A larger diameter annular centrifugal extractor has been developed and deployed in the DFRP plant to meet the process requirements for reprocessing of the spent nuclear fuel from FBTR and PFBR. In total eight numbers of the larger diameter bowl ACE banks were deployed to meet the DFRP process requirements. These banks were designated as: (i) HA, (ii) HC, (iii) 1A, (iv) 1C, (v) 2B, (vi) 2C, (vii) RA and (viii) RC banks to suit various process requirements.

Initial design of ACE bank installed in the DFRP

The centrifugal extractor banks installed at DFRP were designed such a way that half of the extractors (back row, Figure 1) were kept slightly at a raised elevation as compared to the front row of ACE to facilitate clear visibility of the motor/bowl (back row) during remote maintenance. Two types of ACE banks consisting of 20 and 22 stages were installed in the DFRP as per the process requirements. The organic feed at the 2nd stage of ACE is in the front row and comes out from the 20th or 22nd stage in the back row. Similarly, the aqueous phase is fed at the 19th or 21st stage of ACE in the back row and comes out from the 1st stage.



Fig.2: View of the modified inter-stage organic and aqueous pipe lines connected in-between 10th (Right) and 11th (Left) stages

The inter-stage organic airlift pump was connected between front rows to back row to transfer organic from the lower elevation stage to the higher elevation stage. The flow of the aqueous (heavy) phase from the higher to the lower elevation stage is by gravity.

Modified ACE bank in the DFRP

Organic airlift pumps are prone to choke due to the sludges generated by solvent/diluent degradation due to radiation.

Chocking leads to the stoppage of the entire operation in that ACE bank. In order to mitigate these difficulties, it was decided to bring down the back row in the cascade to the same elevation as the front row with a suitable

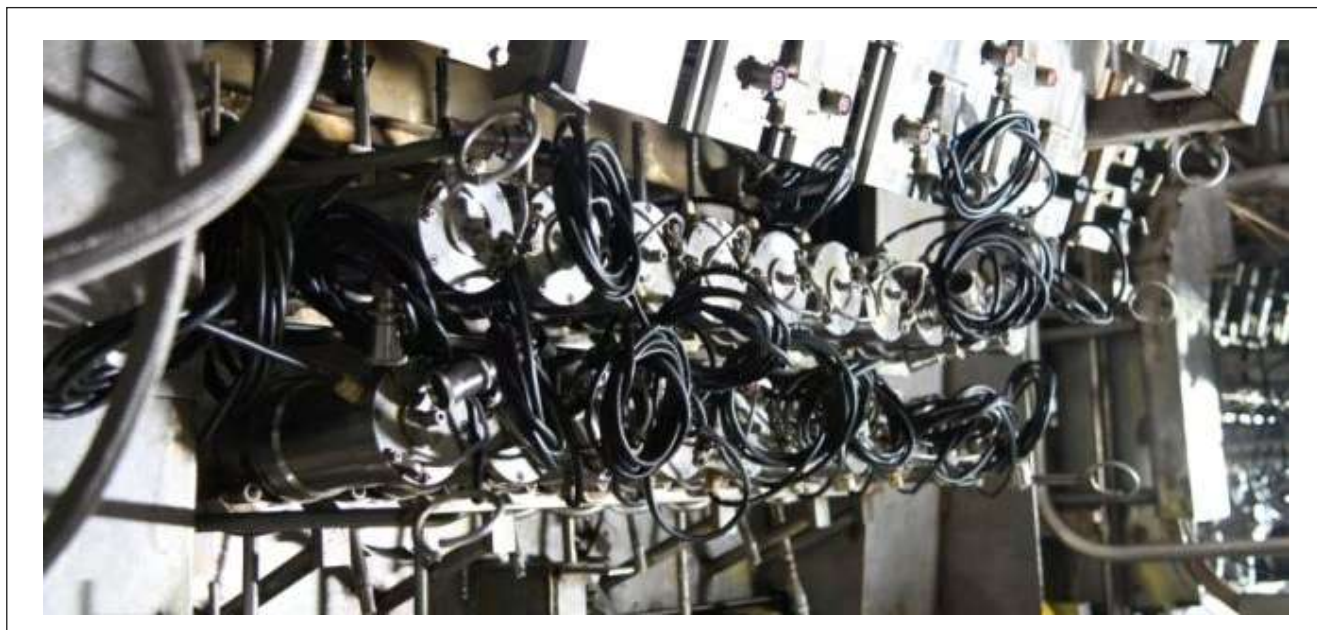


Fig.1: Photographic view of 20 stages larger dia ACE bank inside cell before modification



Fig.3: View of the modified 20 stages larger dia ACE bank

modification in the aqueous and organic inter-stage pipe connections Figure 2 and eliminate the inter stage air lift. A view of the modified 20 stages ACE bank is shown in Figure 3 and after installation inside the DFRP cell is shown in Figure 4.

Challenges due to modification

Compared to single-stage ACE, multistage ACE bank flooding throughput is less. The aqueous and organic outlets are open to atmospheric pressure for a single-stage ACE. In multi stage ACE bank; inter-stage pipeline diameter, length, orientation and hydraulic head available for aqueous and organic streams in-between stages decides the flooding capacity of ACE bank. To understand the effect of modified pipe lines, flooding experiments were conducted to evaluate the hydrodynamic (flooding capacity) performance.

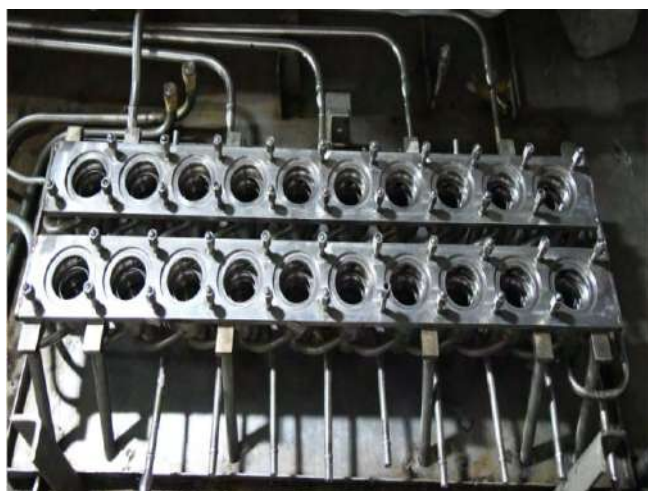


Fig.4: Photographic view of modified 20 stages larger dia ACE stationary bank inside the DFRP cell

Flooding experiments

The flooding experiments were conducted in all the modified ACE banks in the non-mass transfer region. During these flooding experiments, 1.1M TBP in n-DD pre-equilibrated with nitric acid was used as the organic phase, and nitric acid pre-equilibrated with 1.1M TBP in n-DD was used as the aqueous phase. The nitric acid concentration was so selected as to suit the conditioning pertaining to the actual process. The ACE bowls were operated at 3600 rpm, and the A/O ratio was fixed to match the actual process. These flooding experiments show that the flooding capacity of larger bowl diameter ACE banks installed in the DFRP varies in the range of 50 to 77 L/h, which is much higher than the flow rate compare to actual process.

Mass transfer experiments

The mass transfer experiments were conducted in all the modified ACE banks. During these mass transfer experiments, 1.1M TBP in n-DD pre-equilibrated with nitric acid was used as the organic phase, and nitric acid was used as the aqueous phase. The nitric acid concentration, the flow rate of the aqueous phase, the flow rate of the organic phase, aqueous feed points in the ACE cascade, and organic feed points in the ACE cascade were selected to suit the conditioning pertaining to the actual process. The ACE bowls were operated at 3600 rpm, and other parameters were fixed to match the actual process. The aqueous and organic samples were collected with respect to time. After reaching the steady-state condition, the aqueous and organic stage samples were collected. The acid concentration stage profiles in aqueous and organic phases were generated, and the results will be used as base-line data for the DFRP plant.

IV.09 Flow Sheet Simulation and Optimization of DFRP HC Bank

The 1st cycle stripping operation of the PUREX process (HC) in DFRP is carried out in a 22 stage centrifugal extractor (CE) bank as shown in Figure 1. During the processing of FBR spent fuel, due to the presence of significant quantities of DBP, generated by the radiolytic and hydrolytic degradation of TBP, the retention of Pu in the organic phase is higher. The near complete stripping of Pu from DBP containing organic phase can be accomplished only by the addition of U(IV). The presence of U(IV) in organic phase reduces Pu(IV) to Pu(III) which is inextractable in organic phase. The computer aided simulation was carried out for determining the optimum location in the CE bank for U(IV) addition for minimizing the requirement of U(IV). In addition, the operating envelope for the near complete stripping of U and Pu from the organic phase is estimated. By simple factorial design of experiments about 10,000 simulations were carried out for estimating the combined effect of the flow rates of organic feed, aqueous strip 1&2 and U(IV) streams. Based on the simulation results, the desired operating envelope (green) for the organic and aqueous strip 1 flow rate at the constant U(IV) and aqueous strip 2 flow rate of 0.3 L/hr is shown in Figure 2. Figure 2a shows that the stripping of U(VI) from the organic phase decides the minimum requirement of aq strip 1 flow rate, since U(VI) has higher distribution coefficient as compared to Pu(IV). From simulation results, the U(IV) requirement for the stripping of Pu complexes with the DBP decreases for the feed location away from the organic phase inlet. However 15th stage is found to be the optimum feed location for U(IV) since feeding at 18th stage increases the HNO₃ concentration from 0.01 to 0.1M which reduces the U(VI) stripping efficiency. The concentration and flow rate of U(IV) required for the near complete stripping of Pu is shown in Figure 3a.

The condition for the Pu polymerization must be avoided in the stripping cycle especially during Pu rich FBR spent

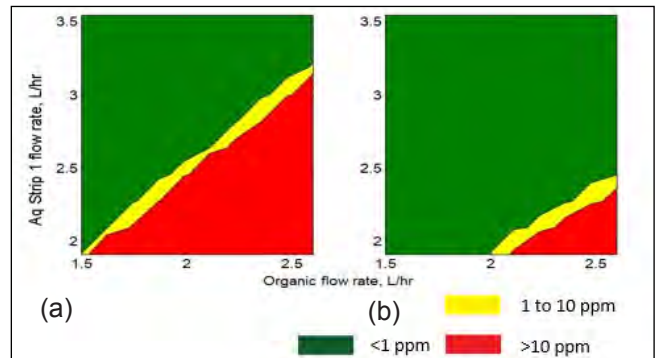


Fig. 2: The lean organic phase concentration of metal ion (a) U(VI) and (b) Pu(IV)

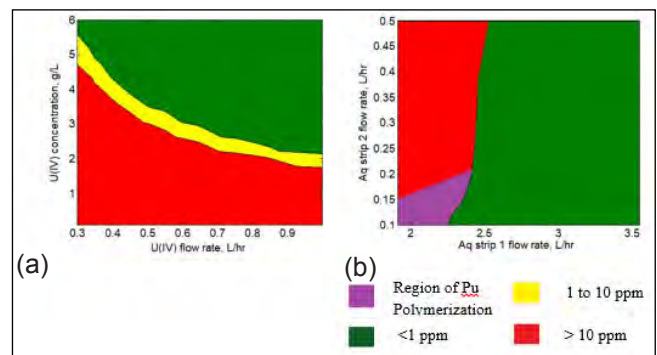


Fig. 3: (a) The concentration of Pu in the lean organic, (b) The aqueous phase concentration of Pu from 13th -22nd stage

fuel reprocessing. To aid this, dual stripping was provided where aqueous strip 2 with 4M HNO₃ concentration is provided at 12th stage. This results in the minimum HNO₃ concentration of 0.45M in the stages from 1 to 12 where majority of the Pu is stripped and comes along with the aqueous product stream in the 1st stage. However the condition which leads to the Pu leakage to the lower HNO₃ concentration region (13th to 22nd stage) is shown in Figure 3b. The purple color region in Figure 3b is the Pu polymerization zone which must be avoided during normal operation. From Figure 3b, the minimum aqueous strip 2 flow rate required for avoiding Pu polymerization is 0.2 L/hr for the organic feed flow rate of 2 L/hr.

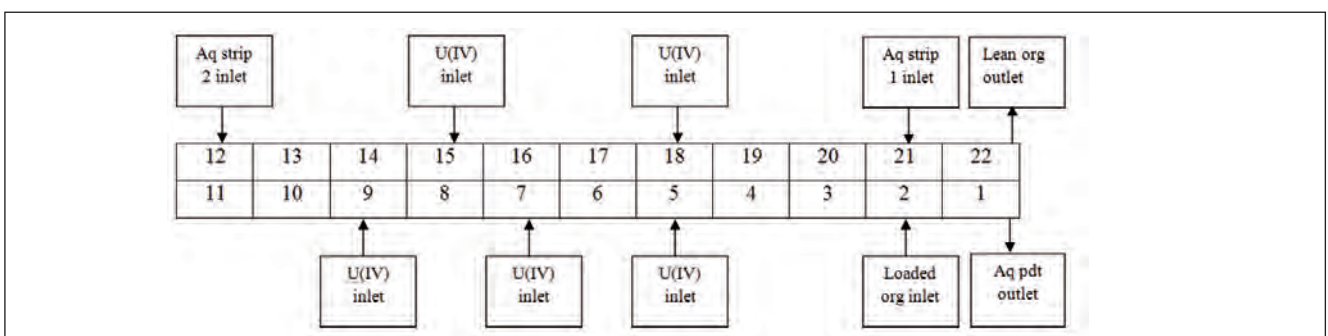


Fig. 1: Flow sheet of DFRP 1st cycle stripping

IV.10 Reprocessing of High Burn-up Fuel Discharged from FBTR at CORAL

CORAL (COmpact Reprocessing of Advanced fuels in Lead cells, earlier known as Lead mini cells) located at the Reprocessing Development Laboratory houses the equipment and systems for the demonstration of reprocessing of FBTR fuel. The primary objective of CORAL operation was to process the irradiated mixed carbide fuels with varying degrees of specific activities so as to gain operating experience with Pu-rich carbide fuels through aqueous reprocessing. It is a unique facility dedicated to innovative research, design, development and deployment of closely guarded reprocessing technology required for higher capacity plants like DFRP for demonstration of recycling mixed-oxide FBR fuels and the FRP of FRFCF. CORAL is actually a hotbed for evolutionary technology and related equipment for fast breeder fuel reprocessing. Figure 1-4 show different perspectives of CORAL.

Since 2003, CORAL facility had operated as a pilot plant facility initially seeking clearances from the regulatory authorities at required intervals for campaign or sub-assembly basis initially till enough confidence was acquired and later on annual basis. CORAL had carried out some changes for improvements in process, equipment and operating procedure to meet the desired objective of developing spent fast reactor fuel reprocessing technology for future plants such as DFRP and FRP etc. These operations had given vital design inputs, and valuable operating experience for future plants. Fine tuning of some of the process parameters/equipments are required primarily to minimize ultimate radioactive waste generation with minimum down time in the future plants viz. DFRP and FRP. CORAL is the only plant which can carry out such studies with optimum inventory and to follow the variations closely. At present, CORAL is the only operating plant for FBR fuel reprocessing to provide the necessary operator training that would be required for licensing.



Fig. 1: A view of CORAL operating area



Fig. 2: A view of CORAL fuel charging area



Fig. 3: A view of equipment inside CORAL hot cell

During CORAL operation in 2003, initially discharged FBTR fuel with low burnup was reprocessed. Progressively higher burnup fuel was taken in accordance with necessary regulatory approvals from AERB. Discharged FBTR fuels of 25, 50 100 and 150 GWd/t burnup were reprocessed and currently 155 GWd/t burn up highly-active Pu-rich mixed carbide fuel is being reprocessed as per approved technical specifications and license conditions.

CORAL completed its initial design mandate of reprocessing 14 subassemblies of FBTR in February 2017 over an extensive run of 44 campaigns. After extensive deliberations at IGCAR safety committee, intensive refurbishment as per ageing management plan, detailed in-service inspections and regulatory inspections, CORAL was relicensed for five years since September 2018. Since then 16 campaigns have been successfully completed and 17th campaign after relicensing is under advanced stage of completion.

Another feature of CORAL operation post relicensing is drastic reduction in cumulative dose expenditure. By extreme application of ALARA, dose-control measures and good operating practices, about 72% reduction in cumulative dose expenditure is achieved in the current operations as compared to operation prior to re-licensing.



Fig. 4: A view of centrifugal extractors installed in CORAL

IV.11 Development of Specialized Remote Handling Tools for Pyro Process R&D Facility

A pyrochemical process based on molten salt electrorefining, commonly called pyroprocess, is considered as a promising option for reprocessing metal fuels. IGCAR is pursuing the development of pyroprocess technology as part of its metal fuel cycle program. As all major process steps of pyroprocess are executed in batch mode, developing suitable remote handling mechanisms and tools, required for remote handling/transfer of material between the process equipments, is vital for the success of pyroprocess technology. Evaluating the suitability of remote handling equipments like power manipulator and in-cell cranes and developing & demonstrating the functionality of specialized remotely operable tools, is one of the major objectives of Pyro Process R&D Facility (PPRDF), an engineering scale facility being set up in IGCAR. The facility consists of a 500 m³ (18.5m length, 3.5m width, 6.0m height) argon atmosphere containment box (CB), in which the process equipments are housed. A 5 Ton crane, 2 Ton monorail hoist and a power manipulator (25 kg capacity) are the general purpose remote handling equipments provided inside CB of PPRDF. In addition, dedicated mechanisms are also provided for specific tasks like Crucible Transfer Mechanism for handling of graphite crucible. All heavy process equipments are designed so that these can be directly handled by general purpose remote handling equipments.

Certain equipments like electrodes required special purpose remote handling tools that act as interfaces between general purpose remote handling equipments and the equipment to be handled. These tools have to be designed for easy and reliable operation. Customized tools were therefore designed based on the specific requirement. Photograph of mechanically operated grippers developed for lifting of electrodes, used in the electrorefining step of the pyroprocess, are shown in Figure 1. These are used with the in-cell

crane for lifting the electrodes. The grippers provide positive locking during transfer. Fingers of the gripper are actuated by an actuator rod which can be locked in finger open/close positions by a lock plate. Power manipulator is used for the operation of the lock plate. The design of gripper is in such a way that fingers cannot be opened during handling of electrodes, which prevents accidental fall of electrode. Similarly, specialized tool has been developed for handling of reference electrode. This tool can be used for remote removal of nozzle plug and insertion of reference electrode in to high temperature electrorefiner using in-cell crane. During insertion electrical signal connectors are engaged and leak tight nozzle flange connection is established. Figure 2 shows the remote transfer operation of reference electrode into electrorefining vessel.

For any maintenance work the electrorefining vessel may be required to be taken out from CB remotely. Therefore, all connections to vessel such as electrical and pipeline connections are to be removed remotely for taking out the vessel for maintenance. One such example is the argon inlet to the vessel. A special remote connector is designed for this application (Figure 3). It is a flanged connection which gets engaged based on self-weight of the vessel, sliding seal and spring supports are provided for achieving leak tight connection. Similarly, the molten salt transfer pipeline to the vessel is provided with remotely removable connectors (Figure 4) with metal seals, which have been successfully tested at site for high temperature operation. Metal C-rings used in these connector can be compressed by operating single bolt provided at the top of connector. All electrical connections to the process equipments are through remotely removable electrical connectors. All these tools have been successfully tested and introduced in the operation of PPRDF.



Fig. 1 Electrode grippers



Fig. 2 Reference electrode handling tool



Fig. 3 Argon line connector



Fig. 4 High temperature pipeline connector

IV.12 Air and Steam Oxidation Behaviour of Pyrolytic Graphite for Pyrochemical Reprocessing Applications

The pyrolytic graphite (PyG) is a chemically pure, highly crystalline, and synthetic form of graphite obtained by pyrolysis of hydrocarbon precursor on heated graphite substrates by chemical vapour deposition (CVD). The exceptional properties of CVD grown PyG, such as the nearer theoretical density (~2.2 g/cm³), zero porosity and defect free, turbostratic stacking exhibiting a high degree of anisotropy in its thermal and electrical properties, makes it an exotic member among conventional graphite materials. Accidental air and water/steam ingress into the containment box of pyrochemical reprocessing can be detrimental to the integrity of high-density graphite (HDG) nuclear components. Commercial HDG undergoes active oxidation at temperatures above 500 °C. To enhance the performance, durability, efficiency, and cleanliness of batch processes pyrochemical reprocessing, sealing of surface pores and defects on HDG by depositing dense oxidation resistance PyG coatings is recommended. PyG coating on HDG crucibles and containers are being pursued for applications in pyrochemical involving highly corrosive molten salts and molten metals. Furthermore, the Generation IV reactors like high temperature gas cooled reactors with both pebble and prismatic fuel form design and the molten salt reactor design use graphite for in-core applications where PyG sealing is of primary importance. In the present study simulated air and steam oxidation kinetics of PyG synthesized at 2400 °C pyrolysis were studied by thermogravimetry analysis (TGA).

The dynamic oxidation of PyG synthesized at 2400 °C from ambient to 1500 °C under simulated air atmosphere are shown (Figure 1a). The PyG exhibited higher thermal stability and superior oxidation resistance with maximum

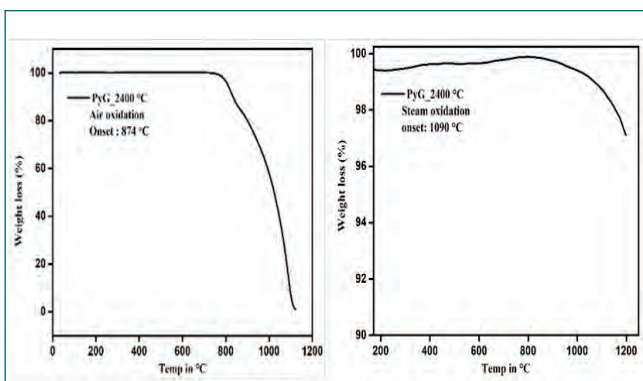


Fig. 1 Dynamic TGA of PyG synthesized at 2400 °C in air and steam

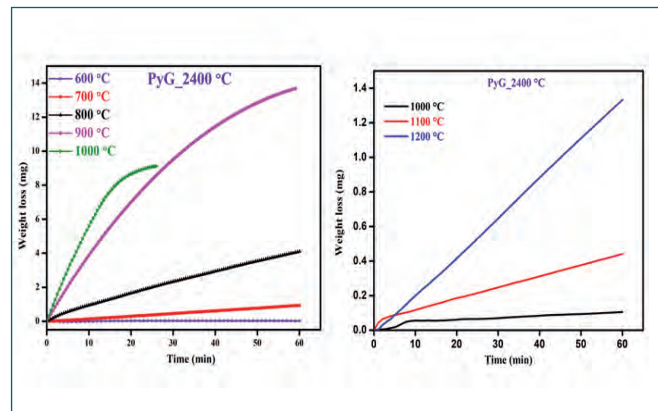


Fig. 2 Isothermal TGA of PyG in air and steam

inflection point 874 °C. The 600, 700, 800, 900 and 1000 °C isothermal TG plots showing the weight loss (mg) versus time (min) for PyG are shown in (Figure 2a). The linear oxidation rate constant (K) values exhibit strong temperature dependence, increasing with increasing oxidation temperature (Table.1). Furthermore, at 600 °C isothermal temperature, the PyG exhibited zero oxidation kinetics.

The dynamic oxidation of PyG synthesized at 2400 °C from 160 to 1200 °C under steam (58 wt% H₂O) atmosphere with 10 °C/min heating rate are shown in the (Figure 1b). By the end of the dynamic TGA, the PyG has shown a maximum of 3% weight loss. The PyG exhibited higher thermal stability and superior oxidation resistance in steam with inflection point at 1090 °C. The 1000, 1100 and 1200 °C isothermal TG plots showing the weight loss (mg) versus time (min) for PyG are shown in (Figure 2b).The PyG shown monotonous increment in rate constant values with increasing the oxidation temperature. Based on the above trends it clearly implies that PyG oxidation kinetics in steam is slower than that in open air atmospheres.

Table 1: Calculated linear rate constant values of PyG under open air atmosphere

Temp. °C	700	800	900	1000
K (mg/min)	1.54×10 ⁻²	8.7×10 ⁻²	0.399	0.626

Table 2: Calculated linear rate constant values of PyG under steam atmosphere

Temp. °C	1000	1100	1200
K (mg/min)	0.1×10 ⁻²	0.64×10 ⁻²	2.2×10 ⁻²

IV.13 Design, Fabrication and Commissioning of Precipitator Column for Ammonium Diuranate Precipitation

In fast reactor fuel reprocessing, both depleted uranium and plutonium are recovered from the spent fuel. After the separation of these precious actinides through solvent extraction, nitric acid solutions of uranyl nitrate and plutonium nitrate are obtained. The uranyl nitrate product is received as the feed in the uranium reversion laboratory through an appropriate transfer. A precipitate of ammonium diuranate (ADU) is obtained by treating this solution with ammonium hydroxide in a precipitator column. The precipitation is carried out in batches and at the end of each bath operation the slurry is filtered to get the precipitate, and the latter is subsequently washed. The ADU cake thus obtained is calcined in air to get U_3O_8 powder and stored. The filtrate obtained after the precipitation is neutralized upto a pH of 1 and assayed to ensure the absence of precious actinides, and then disposed appropriately.

In order to carry out the ADU precipitation process, an indigenously designed precipitator column has been fabricated. A photograph and a schematic are shown in the figures. The precipitator column consists of a Borosil glass column at the top and bottom of which flanges made out of high density poly ethylene (HDPE) polypropylene (PP) are fitted. Over the top HDPE flange there is another steel flange which houses two nozzles to let in the feed and ammonia. Another nozzle has been provided for draining the slurry. All the three nozzles are in turn connected to appropriate process receptacles

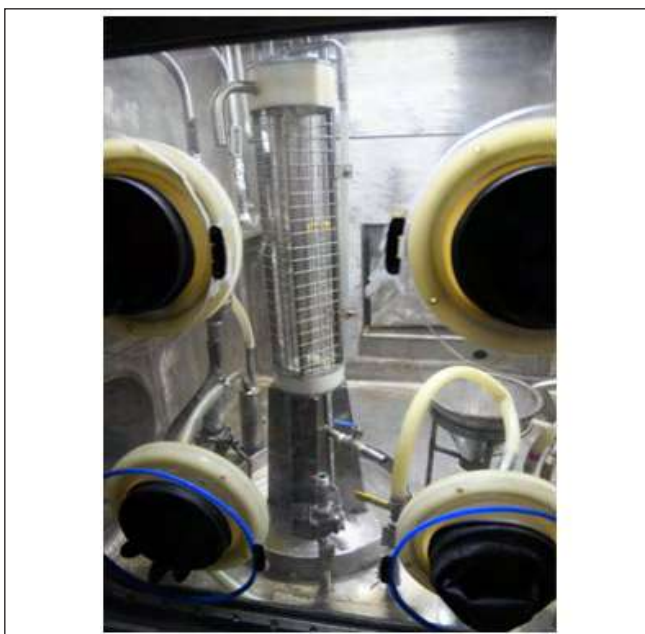


Fig.1: Photo of Precipitator column

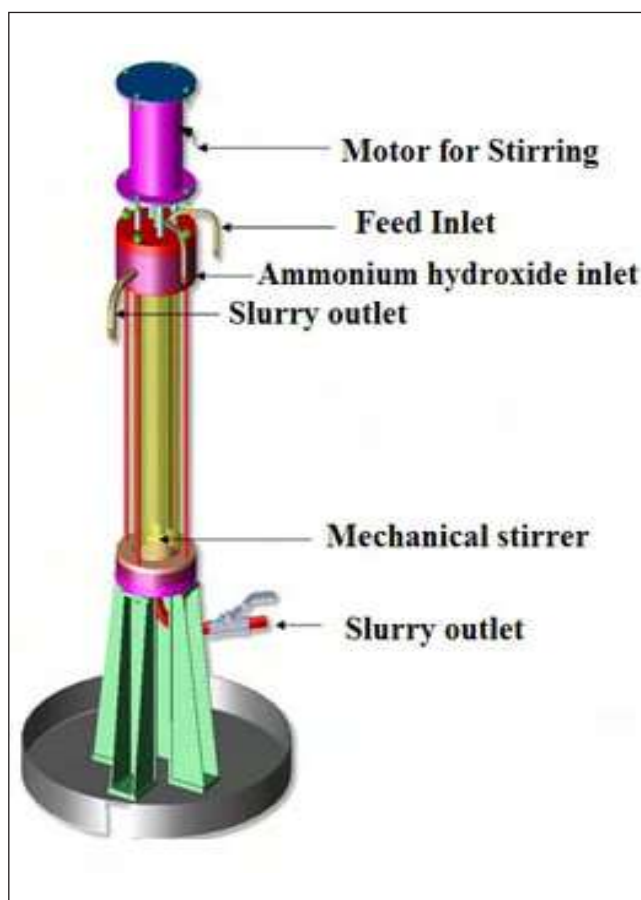


Fig.2: Schematic diagram of precipitator

through pipes. Feed and ammonia nozzles penetrate into the column. A pipe positioned at the center of the column all along its length and fitted with the blades at its bottom serves as the stirrer. The entire set up is supported on circular SS tray.

Testing of the precipitator column had been successfully accomplished by testing its efficiency with ferric hydroxide precipitation. The latter was carried out by pumping ferric nitrate and ammonium hydroxide solutions through appropriate feed points into the precipitator at varying flow rate by using valve less metering pumps. The precipitate was obtained through vacuum filtration. The filtrate was assayed for its residual iron content. The process was optimized by controlling the volume ratios of the feed and precipitant such that the filtration proceeds to completion with no significant loss of iron in the supernatant. Thus the performance of the column was assessed to be satisfactory and the process had been optimized. This column had been commissioned in the plant for carrying out the actual operations.

IV.14 Development of Remote Handling Equipment for Fuel Reprocessing

Remote handling equipment are vital components for material handling as well as for carrying out remote operations within the hot cell. In the fast reactor fuel reprocessing plants customized equipment need to be deployed at different steps of the process and these need to be remotely operated and maintained. Thus there is a need for indigenous development of these equipment. Also these equipment need to be tailored to suit the requirements of the operations pertaining to process sample retrievals, sample aliquoting and sample bottling. Customized equipments for remote replacement of bootings of different sizes mounted on to the master slave manipulators also had to be developed.

Booting Ejector: Bootings are used to cover the slave arm of the master slave manipulators in the hot side to prevent the manipulators from getting contaminated, in addition they ensure the leak tightness of the containment box. In rare instances, during the in cell operations in which the master-slave manipulators are used, the bootings might get damaged or ruptured. In such instances the damaged booting has to be replaced with a fresh one to rectify the breach of contamination. In order to facilitate this operation a special device to eject and re-install the booting called the, “booting ejector” was developed and the same had been successfully implemented at site. An image and the sectional view of a booting ejector are shown in the Figures.



Fig.1: Booting ejector long



Fig.2: Booting ejector long sectional view



Fig.3: Capper/ de-capper system

Capper/ de-capper system: In order to obtain analytical samples from the process streams special purpose nozzles and sampling circuits are provided within the containment boxes. The sample is drawn into bottles with the help of these nozzles and liquid transfers. The caps of these sample bottles need to be removed before sampling and replaced after the sampling remotely. A device called the capper-decapper had been developed in-house to accomplish the same. The additional cap provided on these bottles ensure that the liquid sample does not spill during its transit in the pneumatic fast transfer system. The assembled view of a capper/ de-capper system is shown in Figure-3. This system had also been successfully implemented in the plant.

Manual Aliquoting system: After drawing a bulk quantity of the sample from the process stream / tank, a small quantity (aliquot) of the same is quantitatively pipetted into the analysis vessel. In order to accomplish this a “remote manual aliquoting” system had been developed in-house and had been implemented **successfully in the plant**. It houses a pipette which on pressing takes a metered quantity of the sample solution and feeds it into the sample bottle. This is carried out with the help of the master-slave manipulators.



Fig.4: Manual Aliquoting system

IV.15 Development of Analytical Methods and Processes For Fast Reactor Fuel Reprocessing

In the facility for COmpact Reprocessing of Advanced fuel in Lead shielded cells (CORAL), spent fuels of high burn up (155 GWD/t) with a cooling period of more than two years discharged from FBTR is being reprocessed by PUREX process. In this process, 30 % V/V tri-n butyl phosphate dissolved in normal paraffin hydrocarbon is being employed as the organic solvent for the selective extraction of uranium and plutonium leaving bulk of the fission products into high level waste stream. Purified uranium and plutonium nitrate solutions obtained after the first cycle of extraction are further converted in to their respective oxides through ammonia and oxalate precipitation respectively followed by calcination. These oxide products would be subsequently used for fabricating the fresh (U,Pu) mixed oxide (MOX) fuel. The latter needs to be homogeneous and its composition needs strict control. In this context the precise and accurate determination of the uranium residue in the plutonium oxide is pertinent and important. The determination of trace level of U in samples containing large excess of Pu is quite challenging. Spectrophotometry comes in handy in addressing this issue for it is simple and facilitates the use of different chromogenic agents whose molar

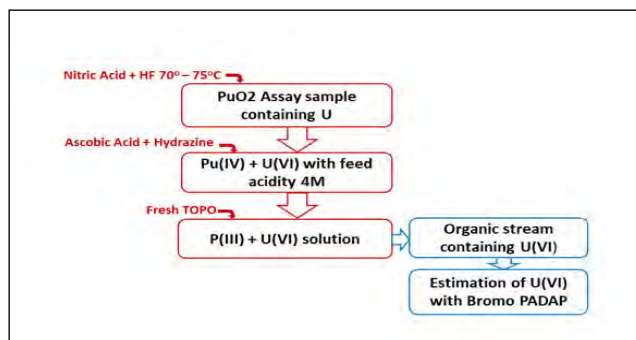


Fig.2: Graphical index of analytical method

extinction coefficients are quite different. In the method developed in our laboratory typically PuO_2 is dissolved in nitric acid and a resultant solution containing U(VI) and plutonium Pu (predominantly Pu(IV)) is obtained. As the distribution ratio of U and Pu between their aqueous solutions and a neutral organo phosphorous extractant, viz., tri-n octyl phosphine oxide (TOPO), are nearly rendering their mutual separation impossible.

However owing to its ionic potential (charge/radius) of Pu (III) possesses a lower distribution ratio as compared

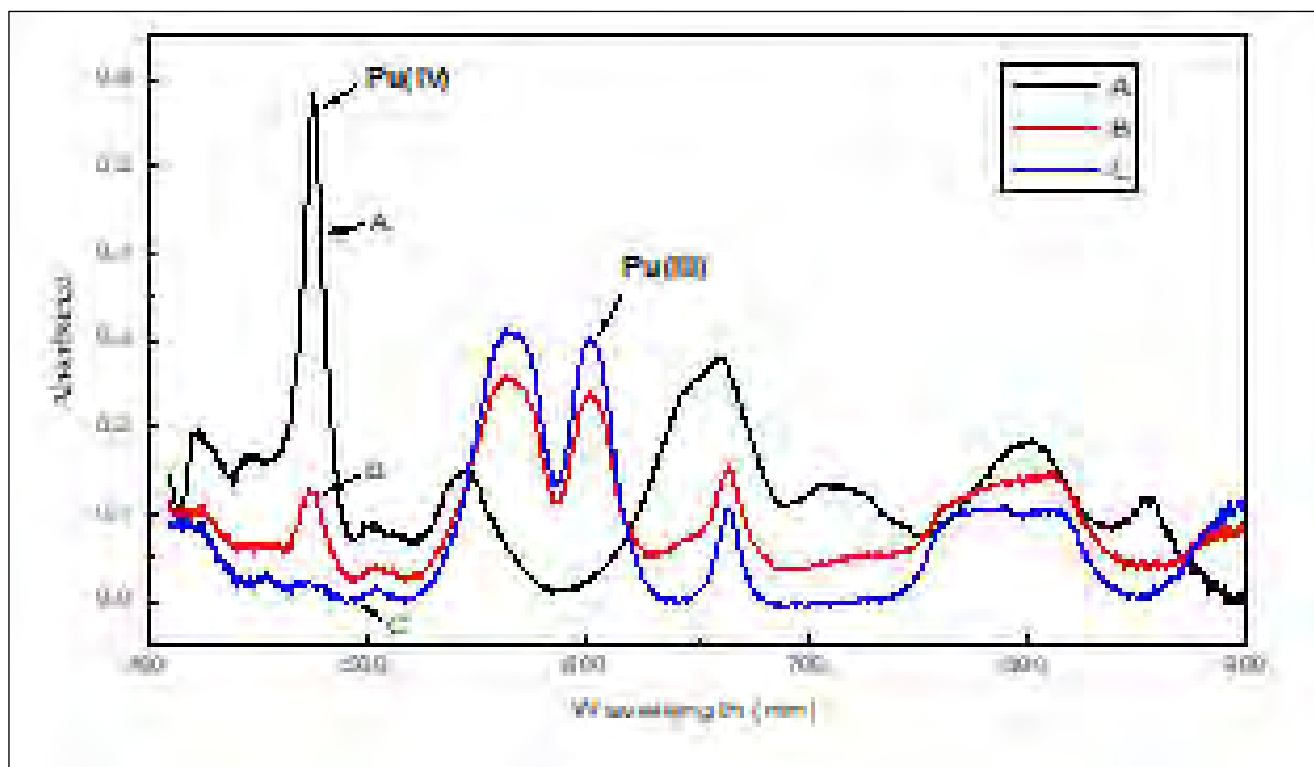


Fig.1: UV Visible absorbance spectra of plutonium nitrate solutions (A, Pu in 4 M HNO_3 in presence of hydrazine nitrate (0.01M) ; B, Pu in presence of ascorbic acid (0.01M) in 4 M HNO_3 ; C, Pu in presence of ascorbic acid (0.01M) & hydrazine nitrate (0.01M) in 4 M HNO_3 .)

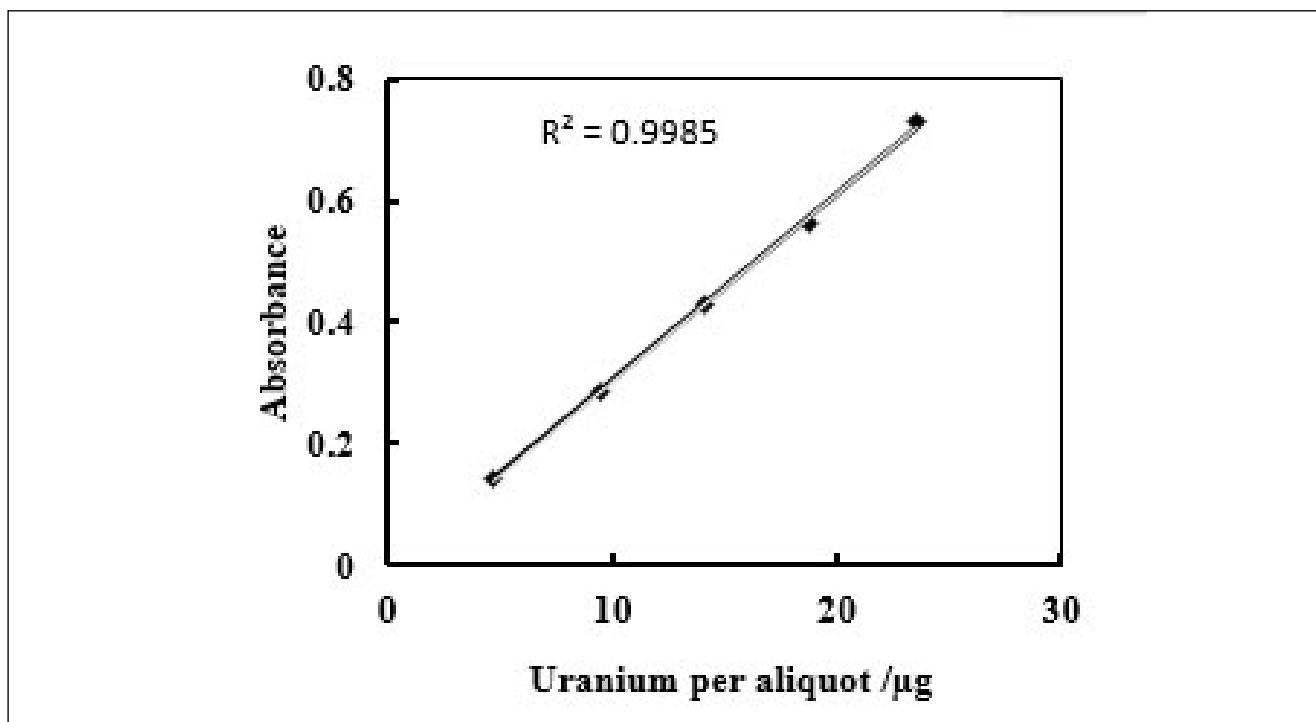


Fig.3: Uranium calibration curve

to Uranyl ion, when extracted from an aqueous solution into a neutral organo phosphorous extractant. Hence, it is possible to extract U selectively into the organic phase leaving the bulk of Pu in the aqueous phase, provided Pu in the aqueous phase is quantitatively reduced to Pu (III) by a suitable reducing agent.

An analytical method was developed in our laboratory based on the above principle. The experimental procedure was validated by using the following procedure. A known amount of PuO₂ was dissolved in concentrated nitric acid in the presence of a small amount of HF at 70-75 °C. The plutonium present in this solution was quantitatively reduced to Pu(III) by using hydrazine stabilized ascorbic acid. The absorption spectra of two solutions viz., the one as it is and another treated with the reducing agent mentioned as above, were recorded. The absorption maxima at 475 and 575-602 nm pertaining to Pu(IV) & Pu(III) respectively would confirm their presence (Figure.1). It was evident from our results that the hydrazine stabilized ascorbic acid brings about the quantitative reduction of Pu. This aqueous feed solution was then equilibrated with 0.1 M TOPO in o-Xylene. The aqueous phase containing pure plutonium nitrate solution was collected and stored while the organic phase was further scrubbed 4 M HNO₃.

The organic and aqueous phases were separated after centrifugation. The U concentration in the

Table. 1 U concentration in PuO₂ products

Sl. No	[U], (%) in PuO ₂ product	
	Spectrophotometry	IDMS
1	0.32	0.31
2	0.51	0.49
3	0.41	0.43

organic phase was determined by spectrophotometry method using Br-PADAP (2-(5-bromo-2-pyridylazo-5-diethylaminophenol)) as a chromogenic agent. A flow diagram showing the analytical scheme is shown in the Figure 2. The calibration curve was obtained by measuring the absorbance of standard solutions with different concentration of uranium which revealed linear dependence with a high correlation factor. As shown in Figure 3 the above procedure had been validated for solutions containing 2–30 µg of U per aliquot with a relative standard deviation of 5%. The concentration of U determined by this method had been successfully implemented for the determination of trace amounts of uranium in PuO₂ obtained are given in Table 1. The concentration values determined by this method are in close agreement with conventional method determined by using isotope dilution mass spectrometry (IDMS)

IV.16 Development of a Novel Speed Sensor for the Centrifuges in Fast Reactor Fuel Reprocessing

Centrifuges are used to clarify the feed solution in fast reactor fuel reprocessing. A high speed centrifuge is being used for removing the solid residue present in the dissolver solution. This centrifuge is operated with the help of an air operated turbine. The rotor of this centrifuge consists of a bowl with a shaft. A collet is attached to the shaft which acts as a metal target for speed sensing. The desired operating speed of the centrifuge is about 18000 rpm. The operating speed of the centrifuge is a critical parameter that needs to be monitored to ensure its proper and safe operation.

A novel customized non-contact sensor was developed in-house, which fulfils the following prerequisites. The sensor should withstand high radiation, should endure both acid and organic fumes prevailing inside the containment box and it should also be maintainable by Master Slave Manipulators. It should also work reliably from a distance of up to 8mm from the target.

The speed sensing system developed consists of two parts: a) a proximity sensor and b) the electronic unit. The sensor is a coil wound on a suitable former and housed with appropriate mechanical support. The coil senses the target material based on the induction principle. The target material is made up of a magnetically permeable material (SS430). The output signal from the sensor is pulsating DC. The electronic unit consists of circuits to sense the change in the coil inductance and generate



Fig.2: Sensor with pre-amplifier

the AC exciting voltage for the coil. It also has a human machine interface (HMI) as the operator interface and also generates output signals required for data acquisition and interlocking. The electronic unit is connected to the proximity sensor by RG 174 co-axial cable.

The sensor coil is excited by a high frequency oscillator. Excitation of the sensor coil generates a magnetic field that couples with the target. The strength of the magnetic coupling between the sensor and target depends on the distance of separation between them. The signal conditioning electronics senses the variation in inductance as the target moves when the centrifuge rotates and translates the inductance into a usable signal.

The pulsating DC output from the sensor is converted into standard voltage pulses and then counted using a counting system. The read-out electronics for the sensor was developed in-house to display the speed. The read-out electronics consists of an input filter board, a counter board and an HMI. The filter board eliminates the DC component of the signal. The counter board consists of a comparator and a nonretriggerable monostable multivibrator. The HMI is programmed to display the speed. The speed output is made available to the plant SCADA through Ethernet protocol. All the required interlocks were implemented using ladder logic programming in the plant PLC. The centrifuge speed sensors were installed and commissioned for all the centrifuges and were qualified for the process operating conditions.



Fig.1: Electronic unit

IV.17 Development of Vacuum Control System for Vacuum Based Liquid Transfer System in Reconversion

In fast reactor fuel reprocessing, the solutions containing uranium and plutonium separated from the spent fuel through solvent extraction, are independently subjected to chemical processing to obtain the oxides of uranium and plutonium. These processes are carried out in the reconversion laboratory. In this laboratory, vacuum transfers (VT) are used to carry out the transfer of liquids from one tank to another as well into the processing equipment. In a typical vacuum transfer operation, adequate vacuum is created in the destination tank with the help of an air ejector. The motive air pressure supplied to the air ejector is set at the required value by manually adjusting the Pressure Reducing Valve (PRV) provided in the main air header. The motive air supply for the ejector for each transfer is controlled by a Solenoid Valve (SV) provided in the air header. An interlock is also provided to cut off the SV based on the high level in the destination tank.

When the transfer is stopped by de-energizing the SV, due to the sudden loss of vacuum, liquid rushes into the air purge pipes that are immersed in the liquid of the destination tank. Significant time is taken for this entrained liquid to flow by gravity back to the tank and the resumption of normal air purge into the liquid. During this period, the level and density measurements of the destination tank yield erroneous values. Because of this error in the level measurement, the interlocks will also not function properly.

In order to overcome this difficulty in the level and density measurements immediately after the termination of the vacuum transfer, a control system has been developed which has been implemented by using a Programmable Logic Controller (PLC). The conventional PRV installed in the main air header is replaced by an electronic PRV to control the motive air pressure. Customized functional blocks are developed

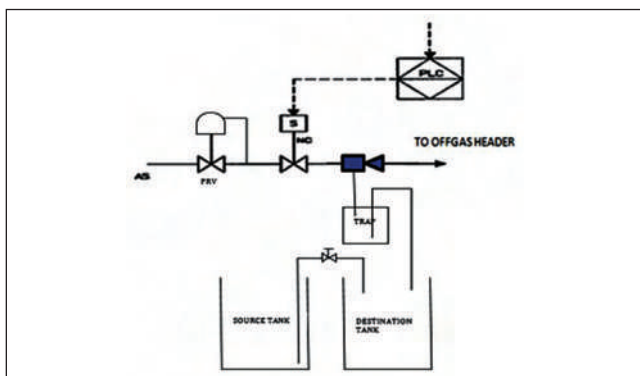


Fig. 1: Typical vacuum transfer schematic

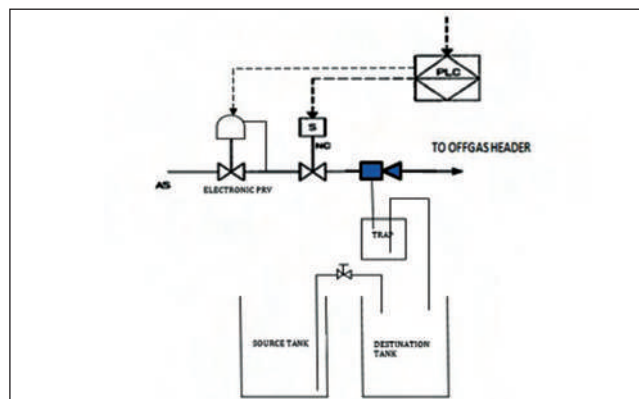


Fig. 2: Revised vacuum transfer schematic

in the PLC for this purpose. The analog output of the PLC is connected to the electronic PRV.

The PLC sets the initial air header pressure at 2.5 kg/cm². The intended liquid transfer from the source to the destination tank is initiated by energizing the SV from the operator screen in the control room. The liquid transfer by siphoning is initiated when the negative pressure is more than ~120" w.c. After 2 minutes from the start of SV, a ramp logic is initiated in the PLC to reduce the header pressure at a rate of 0.005 kg/cm²/second, till it reaches the target value of 1.2 kg/cm². During this period, the negative pressure in tank is gradually reduced up to ~70" w.c, below which it is observed that liquid transfer will not take place. When the destination tank reaches high level cutoff or if the transfer is switched OFF, the PLC reduces the vacuum by a finite step so as to stop the transfer while at the same time preventing the liquid in the purge pipe from going above the tank. Thereafter, the PLC ramps down the negative pressure in the tank to the minimum and then the SV is de-energized. The rate of decrement of header pressure, initial and final motive air pressure settings and the time to initiate the ramp are all determined and set by multiple trials. The flow rate in the purge rotameter is increased to 25 NLPH as against the normal rate of 20 NLPH, to speed up the restoration of the air purge through the liquid.

This control system has been commissioned and tested in the plant. It is found that by reducing the negative pressure in destination tank in a programmed manner, the effect on the purge measurement is significantly reduced and no liquid comes above the tanks though the purge probes. Due to this change in the control system, it is found that the functioning of all the vacuum transfers in the Reconversion Lab is satisfactory and thus safe operation has been ensured.

IV.18 Design, Installation and Commissioning of Averaging Pitot Tube Flow Meters with Wireless Communication for the Exhaust Ducts

Every radiological facility with a controlled ventilation system needs to monitor the flow through the exhaust duct in order to ensure that the relevant locations and systems within such a facility is maintained at an appropriate negative pressure with respect to the ambient. Thus the measurement of flow through the ventilation ducts connected to the stack gains prominence. Apart from measuring the flow, it also need to be remotely read and recorded for the exhaust ducts are usually at higher elevations not amenable for carrying out routine measurements manually.

In such instances the averaging pitot tube (APT) would come in handy to make such measurements for they are rugged, accurate, have no moving parts, have low permanent pressure drop and are easy to maintain. This flow meter works on the Bernoulli's principle. The pressure difference between the stagnation pressure and static pressure is measured by using a Differential Pressure (DP) transmitter. The stagnation pressure is averaged across the length of the duct by the APT using several taps. Where the availability of the straight lengths of the duct is less, three APTs are installed to obtain a more accurate average.

In order to overcome the difficulties in installing the long signal and power cabling at inconvenient locations, wireless signal transmission technology and in-built battery power were employed. Battery powered wireless adapters power the DP transmitter and converts the signal into a digital wireless signal which is transmitted to the Plant data acquisition system through the field wireless access point. All the wireless field devices communicate with the field wireless access point through

the industrial automation wireless communication standard ISA 100.11a, which in turn connects to field wireless management station through Ethernet interface and Modbus TCP/IP communication protocol. The ISA 100.11a protocol works in 2.4-2.48Ghz frequency with inbuilt 128 bit encryption and channel hopping algorithm for security. The wireless field devices are in a mesh network ensuring redundant paths of communication.

Calibration of the APTs was carried out at FCRI Palakkad considering the site requirements. The flow coefficient (k) was individually derived for the APT for each duct using a 1/3 duct model fabricated for each duct. The calibration was carried out using the wind tunnel as per ISO 3966 standard.

APT flow sensors have been installed in the plant exhaust ducts by drilling (Figure 1). Provisions were given at the site for access to facilitate their maintenance. The DP in the APT's are measured using draft range DP transmitters. The necessary impulse tubing with isolation valves was also installed. A temperature sensor was installed in the duct as well.

Battery powered wireless transmitters and field wireless access point were installed at site. The field wireless access point is connected to the wireless gateway which is connected to the plant SCADA LAN.

Software configurations of all the subsystems were carried out and integrated testing was done. The mathematical calculations for converting DP into flow rate have been done in the Plant SCADA for data logging and display in the Control Room. The measured flow rate is within $\pm 10\%$ of the theoretically expected flow rate.



Fig.1: APT in the plant exhaust duct along with wireless adapter fitted on DP transmitter

IV.19 Experimental Determination of Phase Equilibria in the system $U_{1-x}Cr_x$ ($x=0-55$ at.% Cr) by using DTA

With emerging interest of metallic fuelled fast reactor in India, it is important to study the phase equilibria of U-Cr system to develop the understanding of high temperature compatibility of U-Pu-Zr metal fuel with either austenitic or ferritic steel clad. In nuclear grade 9Cr-based ferritic-martensitic steel, Cr constitutes the second major element after Fe. From reactor safety point of view, it is also interesting to note that small additions of Cr in U-Pu-Zr based metal fuel results in a decrease of liquidus temperature of fuel matrix which is undesirable. To understand the multi component systems based on U and Cr elements, the solidus-liquidus and invariant equilibria data are very crucial as initial parameter since they are used in modeling the phase diagram by using many computational methods such as CALPHAD (CALculation of PHases Diagram) method. The information on the phase equilibria in this system (U-Cr) is a pre-requisite for modeling the quaternary system U-Pu-Zr-Cr.

The experimental data on the liquidus of U-Cr binary system are rather insufficient. High temperature liquidus data on only a few selected compositions have so far been reported in the literature. In view of the above, the liquidus temperatures, eutectic and eutectoid solid state phase transition have been investigated with 0-55 at.% Cr with 5 at.% interval by using DTA. Alloy samples of desired composition were prepared by arc-melting the appropriate amounts of U and Cr under ultra high purity argon atmosphere (4 ppm each of oxygen and moisture). A "triarc" furnace was used for this purpose. The residual oxygen from the arc-melting chamber was removed by melting zirconium metal sponge prior to the preparation of the alloy. In order to ensure homogeneity in alloy it

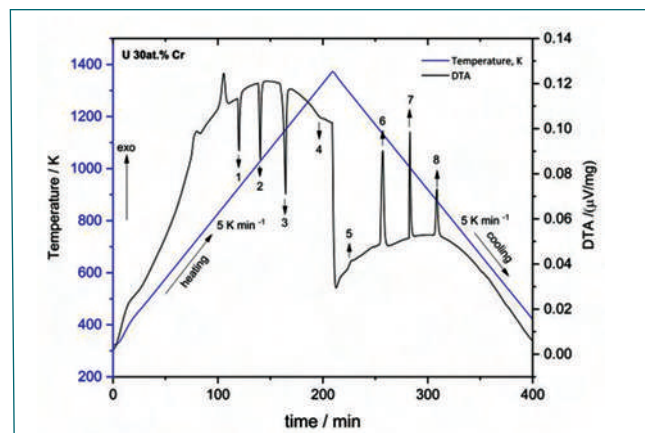


Fig. 2 Typical DTA profile obtained during slow heating and cooling of U-30at.% Cr alloy

was flipped and remelted at least thrice. No significant weight change was observed after the arc melting.

The differential thermal analysis (DTA) experiments were performed using small samples of 100 to 150 mg mass. Heating and cooling is done a 5 K min^{-1} under UHP Ar flow. Proper baseline compensation has also been carried out. The experimentally measured eutectic, eutectoid and liquidus in the U-rich region (0-55 at.% Cr) of U-Cr alloys are given in Fig 1. In Fig 2, a typical base line corrected DTA profile obtained on U-30at.%Cr alloy is shown. The four distinct peaks observed on heating are due to the following reactions:

1. $\alpha\text{-U} + \text{Cr} \rightarrow \beta\text{-U} + \text{Cr}$;
2. $\beta\text{-U} + \text{Cr} \rightarrow \gamma\text{-U} + \text{Cr}$;
3. $\gamma\text{-U} + \text{Cr} \rightarrow \text{liq.} + \text{Cr}$;
4. $\text{liq.} + \text{Cr} \rightarrow \text{liq.}$

From the data presented in Figure 1, it is evident that our results are in good agreement with literature data.

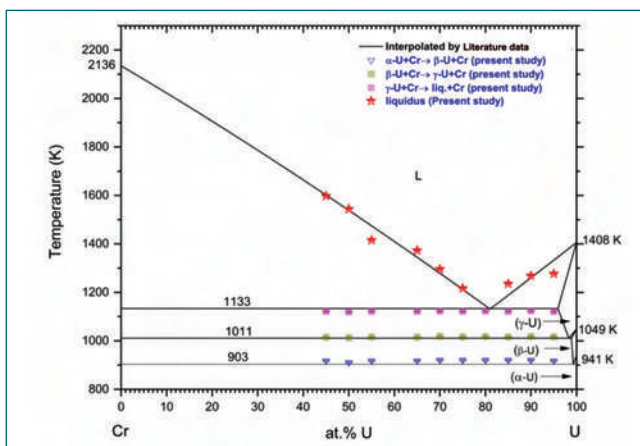


Fig. 1 Experimentally measured solidus and liquidus temperature of Cr-U system

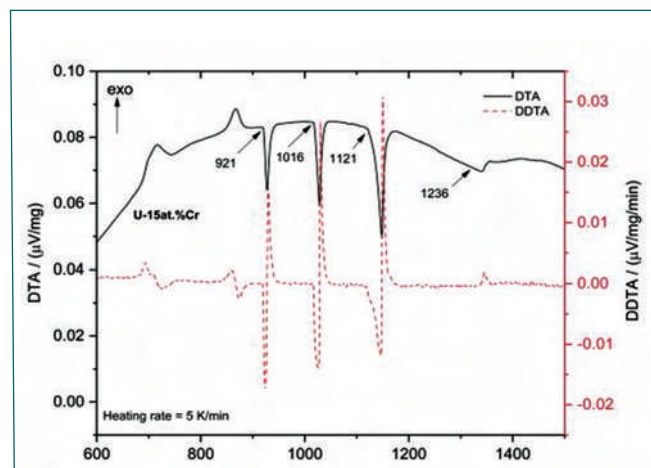


Fig. 3 Typical DTA & DDTA profile of U 15at.% Cr alloy

IV.20 Nd(III) Hypersensitive Peak as an Optical Absorption Probe for Determining Nitric Acid in Aqueous Solution: An Application to Aqueous Raffinate Solutions in Nuclear Reprocessing

In nuclear industry, the use of nitric acid is ubiquitous from the mining of the nuclear fuels to the reprocessing of irradiated spent fuels. PUREX process is widely used for the separation of U and Pu from the irradiated spent fuel. It involves the dissolution of fuel in concentrated nitric acid followed by the solvent extraction from the feed solution. The content of nitric acid needs to be determined in feed solution to minimize the loss of U, Pu and to decontaminate the fuel. The acidic waste (raffinate) solutions are treated before its safe disposal and hence, waste management operations which involve neutralization, ion-exchange, solvent extraction etc., wherein measurement of acidity is necessary. In this report, a new method is proposed for the measurement of nitric acid concentration based on the optical absorption spectroscopy using Nd(III) as a probe. The absorption peak of Nd(III) at 575.1 nm is hypersensitive and its absorbance is found to be gradually enhanced with increasing nitric acid concentration. Enhancement response was found to be linear over a wide range of 0.5-15.5 M nitric acid concentration.

A fiber optic spectrophotometer, model AvaSpec-2048 (2400 lines per mm grating, maximum resolution 0.15 nm) was used to record UV-Vis spectra. A 10 mm path length fused silica cuvette was used as the sample cell. 100 μ L of 1 M Nd(III) was added as a probe in 5 mL sample before recording the absorption spectra. Accuracy of the method was verified with acid-base titration using phenolphthalein as an indicator.

Figure 1 shows the absorption spectrum of Nd(III) in aqueous medium over the spectral range 480-920 nm. The concentration of Nd(III) to record this spectrum was 0.02 M (2885 ppm). The spectrum contains seven narrow peaks correspond to the intra 4f transitions of Nd(III).

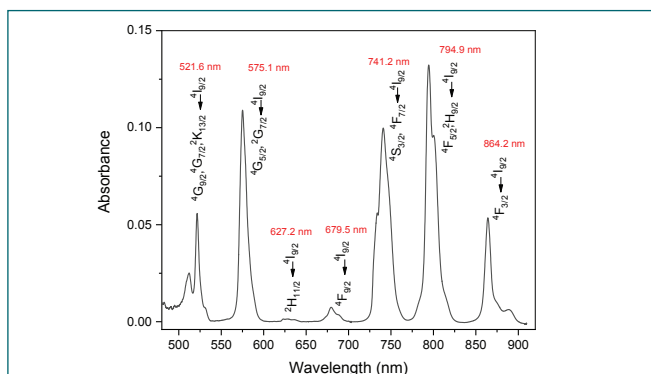


Fig. 1 Absorption spectra of 0.02 M Nd(III) in aqueous medium of HClO_4 (0.1 M).

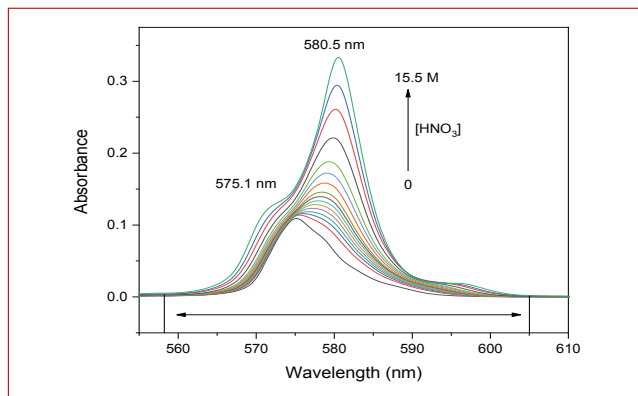


Fig. 2 Effect of nitric acid (0-15.5 M) on the Nd(III) absorption peak at 575.1 nm. The concentration of Nd(III) is 0.02 M. The arrow shows the spectral region (558-605 nm) of which integrated area was used for calibration

The intensities for all these peaks are modulated with nitric acid. A prominent variation in absorbance as well as in absorption wavelength (λ_{max}) is observed for the peak at 575.1 nm ($^4I_{9/2} \rightarrow ^4G_{5/2}, ^2G_{7/2}$) and hence this peak is used as a probe for the measurement of nitric acid concentration.

Figure 2 shows the gradual increase of absorption of this peak over 0.5 to 15.5 M of nitric acid. The absorbance at 580.5 nm (λ_{max} at 15.5 M nitric acid) as well as the integrated area over 558-605 nm vary linearly over 0.5-15.5 M of nitric acid. This variation based on measured integrated area is shown in Figure 3. This linear relationship provides a new and very simple method for the measurement of nitric acid concentration.

To apply the present method in the reprocessing solution, it is necessary to see the effect of other elements which

Table 1: Measurement of nitric acid (M) in various samples. Relative error in measured value is shown in parenthesis

Description of sample	Added HNO_3	Present method	Titration
Water	3.95	3.99(1.0%)	3.85(2.5 %)
Nd(III) solution (Nd-1000 ppm)	1.18	1.20(1.7%)	1.22(3.3%)
Uranium aqueous solution (U-10,000 ppm)	6.35	6.50(2.4%)	6.40(0.6 %)
Lanthanides aqueous solution (La, Ce, Pr, Nd, Sm, Eu; each 2000 ppm)	4.74	4.88(2.9%)	4.82(1.7 %)
SHLW	-	3.90	4.10

are likely to be present in these solutions. The elements which show significant spectral interference are Pr(III), Nd(III), Ru(III), Rh(III) and Pd(II). To address this interference problem, a unique background correction approach is used wherein sample solution for which nitric acid concentration needs to be estimated is itself treated as a reference. 0.02 M Nd(III) was then added as a probe to this sample solution and the absorption spectrum is recorded. This way the overall interference effect has been nullified.

The applicability of the present method was demonstrated by analyzing five unknown samples of different matrices (including SHLW, synthetic high level liquid waste). 5 ml of these samples were taken and 100 μ L of Nd(III) of 1 M was added as a probe in each of the samples. In order to check the reliability of the present method, the concentration of nitric acid in these samples was also measured by acid base titration and the values are compared (Table 1). From the table it is clear that the results obtained by the present method are in agreement

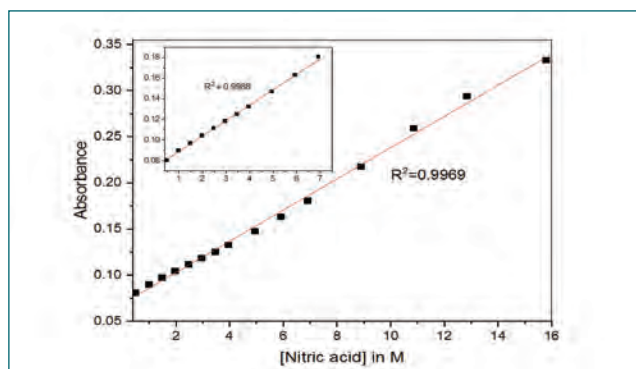


Fig. 3 Plot of integrated area (558-605 nm) of hypersensitive peak of 0.02 M Nd(III) as a function of nitric acid concentration. Calibration plot drawn over short range (0.5-7 M) is shown in the inset of this plot

with those determined by titration. The present method is simple and at the same time precise and accurate, which can be easily adopted to reprocessing streams. Another advantage is the use of fibre optic probe in the UV-visible technique wherein the whole process of measuring the acidity of the solution can be remotized.

IV.21 Pulsating Dielectric based Approach To Determine Tributyl Phosphate in Mixtures Containing TBP and Dodecane

Reliable determination of tributyl phosphate (TBP) in suitable diluents is indispensable in studies related to nuclear fuel reprocessing. At Innovative Sensors Section, a rapid and non-destructive dielectric based approach has been developed to determine TBP in mixtures of TBP and n-dodecane in the quality control as well as research laboratories associated with nuclear fuel reprocessing. The measurement is based on an in-house developed new class of sensors called pulsating sensors. The heart of the instrument consists of a three gate oscillator circuit that generates the first electronic response directly in digital domain in the form of digital pulses whose frequency is determined by the prevailing time constant of the circuit ($f \propto 1/RC$).

By using a parallel plate capacitor as the probe and using a resistor of fixed value in the oscillator circuit, the frequency output from the probe is made to depend solely on the dielectric of the probing medium ($f \propto d/R.e_0.k.A$). Here all the symbols retain their usual meaning. Both TBP ($k=8.34$ at 293.3 K) as well as dodecane ($k=2.01$ at 293.3 K) differ in their dielectric constants significantly. The overall dielectric of a mixture of TBP and dodecane is a function of the ratio of two solvents in the mixture. Sensitive and reliable monitoring of small changes in frequency due to the corresponding changes in the composition of the mixture forms the basis of the current technique.

With a single capacitive type probe and using a standalone embedded unit, two different ranges of TBP measurement

(1% v/v - 5% v/v and 5% - 35% v/v) can be covered. Figure 1 shows the photograph of the compact unit along with the probe. The probe consists of three mirror polished stainless steel electrodes arranged parallelly to each other with a distance of separation of 1 mm between the electrodes. The active sensing surface of each electrode is 65 mm x 17 mm (l x b). It takes less than a minute to take a measurement. The precision in measurement in the entire range varies from 0.15% to 8.75% RSD while the response time of the probe was found to be 4.5 s. Temperature is found to exert an influence on the probe output and hence measurements need to be carried out at constant room temperature. As compared to water, the presence of nitric acid in the organic phase exerts more influence on the probe output. In such situations, an alkali wash is recommended to remove the entrapped nitric acid along with other possible degradation products of TBP before taking the measurements.



Fig. 1 Photograph of the embedded unit along with the capacitive type probe

IV.22 Modeling and Validation of Solidification of Molten Salts

Reprocessing of spent fuel from future metallic fuelled FBRs is proposed to be carried out by Pyrometallurgical method which is based on molten salt electrorefining at 500°C. The important process steps in Pyroprocessing are electrorefining of uranium and plutonium from spent nuclear fuel using molten salt (eutectic mixture of 59% LiCl and 41% KCl) electrolyte, distillation of occluded salt and cadmium from cathode deposits and finally consolidation of actinides to form metal ingot. During the electrorefining process, fission products gets accumulated in the electrolyte along with some actinides as their chlorides. The fission products have to be removed from the molten salt periodically to minimize the decay heat loads and to decrease the contamination of salt in electrorefiner. Crystallization technique is used to recover pure molten salt from contaminated salt. Crystallization is a single step process to separate the fission products from the molten salt which uses the difference in solubility of the fission products in the solid phase and liquid phase. A solid phase containing pure eutectic salt mixture and a liquid phase containing dissolved fission products will be obtained at the end of this process. Crystallization involves purification of a chemical from a liquid mixture by solidification of the desired component. This reduces the waste volume remarkably compared to other techniques. The advantages of melt crystallization are relatively low

energy demand of freezing process and high selectivity of crystallization. Preliminary studies on crystallization was carried out using sodium nitrate as a simulant for LiCl-KCl. Theoretical modeling using ANSYS-Fluent and experimental studies to validate the model results was carried out.

The modeling of solidification of sodium nitrate was carried out using the commercial CFD software ANSYS-Fluent (19.2). Here, the energy equation with a source term enthalpy was solved over a finite volume in two dimensions. Enthalpy-porosity method is used to solve this problem, where the fluid is considered as a porous body. The fluid porosity is also the liquid fraction in the domain. At any given time, the domain would contain a solid region, liquid region and a solid-liquid mixture zone called the “mushy zone”. The geometry had an unstructured mesh with 8959 nodes. The entire domain at 308°C with liquid fraction 1 is the initial condition for the model. The top, bottom and side walls are the heat sinks. Both natural convection and radiative heat loss to ambient was considered for the boundary condition. A temperature monitor and a liquid fraction monitor were placed at the centre of the domain. The time step for the transient problem was 10s with 1320 time steps. This is a pressure based solver with no natural convection in the molten salt. During phase change, the liquid fraction in the domain decreases from ‘1’



Fig. 1 Experimental setup with data acquisition system

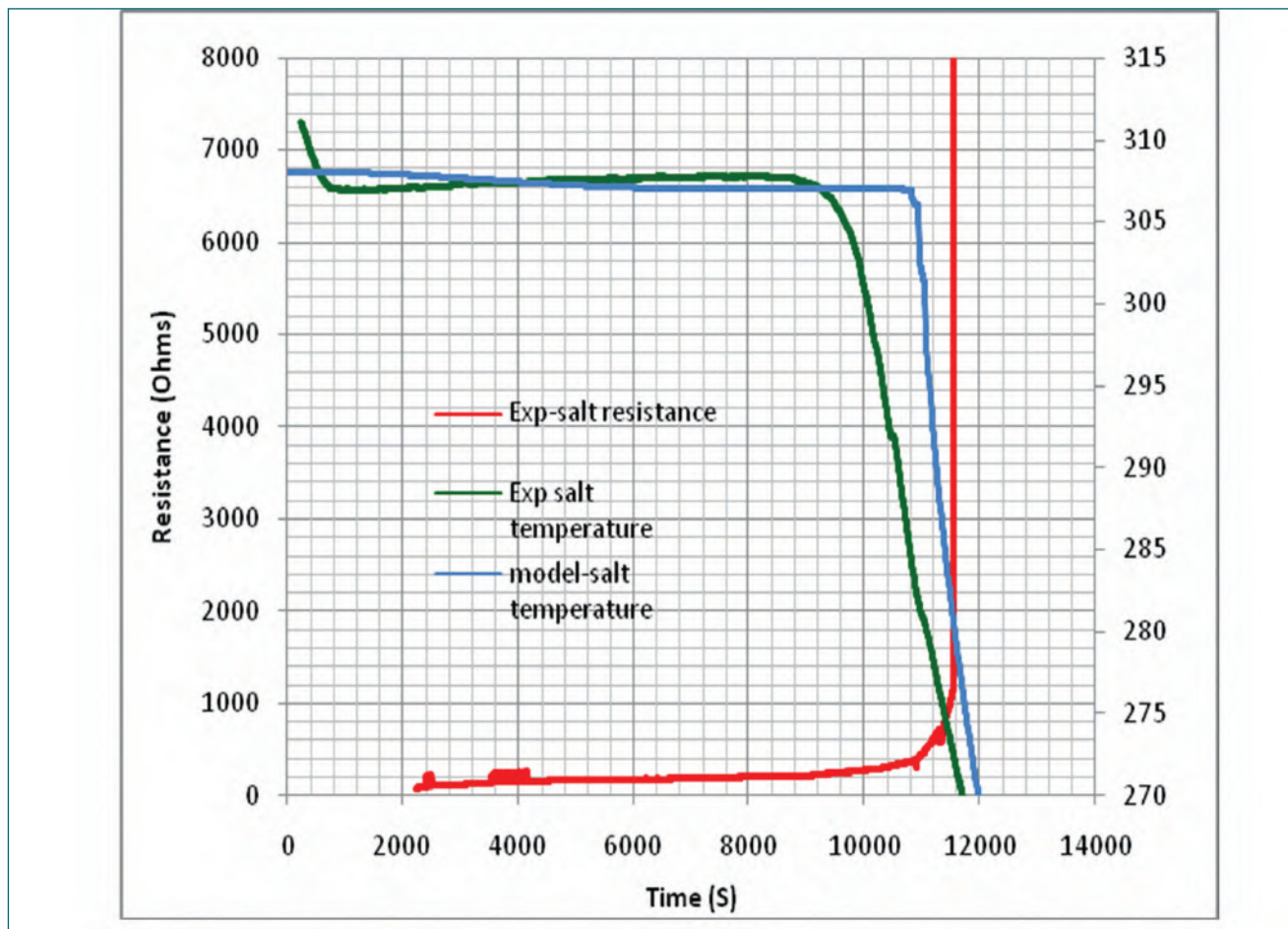


Fig. 2 Temperature and resistance variation in salt during phase change

at liquidus temperature and reduces to '0' when the domain reaches solidus temperature and solidification is complete. The experimental set up comprises of a test vessel of 4" dia and 420 mm length. The vessel is heated; salt is made molten and allowed to cool. During cooling, both temperature and resistance of the salt measured at central location using K-type thermocouple and Nickel wire respectively. Resistance measurement was done to identify phase change. In the Fluent model, salt temperature at the central location was monitored and plotted. It can be seen that during phase change the salt temperature is almost constant at $307 \pm 0.5^\circ\text{C}$. The duration of phase change as obtained from the model results is about 2.6 h. In the experimental plot,

the salt temperature remains almost constant at 307°C for 2.44 h. The phase change was also monitored by measuring the salt resistance at the same location. The salt resistance, initially at few hundred ohms at 307°C quickly rises to kilo-ohms at 306°C . The duration of solidification as predicted by model (2.6h) matches very closely with experimental result which is 2.44 h. The model can hence predict the solidification pattern of a molten salt with an error margin of 6%. Also, the concept of utilizing the resistance variation as a function of temperature to map the solidification front has been validated by these experimental runs. Fluent modeling of solidification pattern of molten sodium nitrate can now be extended to eutectic LiCl-KCl salt mixture.

IV.23 Conversion of 500 m³ Containment Box from Air to Nitrogen Environment and Achieving Required Purity using Purification System under Negative Pressure

Pyroprocess R&D Facility (PPRDF) is being set up for scaled up studies on alloys of natural uranium at 10 kg per batch scale, so that the experience will be generated for designing a Pyroprocess plant. This facility has an argon atmosphere Containment Box (CB) of 500 m³ volume. The CB houses several process equipments such as a High Temperature Electro Refiner (HTER) and an Automated Vacuum Distillation & Melting system (AVDMS) along with in-cell crane and power manipulator for enabling remote operation. The chemicals used in this process are highly sensitive to moisture and oxygen. Also uranium forms uranium nitride at high temperature in presence of nitrogen. Hence O₂ & H₂O concentration in argon should be kept below 50 ppm and Nitrogen below 20%. Also, as the pressure inside the containment box (CB) will be kept slightly negative to prevent outflow of radioactive aerosols this leads to ingress of air inside CB. Before starting any operation inside CB the environment has to be converted from air to Argon and maintain its purity, temperature and pressure throughout the operation. Conversion of air to argon atmosphere inside the containment box is to be done in three phases.



Fig. 1 PPRDF 500m³ containment box



Fig. 2 ARPS purification circuit

In first phase, air will be purged out by pure nitrogen to get oxygen concentration below 2000 ppm. In the second phase, the nitrogen will be further purified by using Argon Recirculation and Purification System (ARPS) to get oxygen and moisture concentration below 50ppm. In the third phase, the nitrogen will be displaced by argon to get nitrogen concentration below 20%. Figures 1 & 2 shows the photograph of CB and ARPS.

Conversion of CB from air to nitrogen environment and achieving required purity using ARPS was demonstrated under negative pressure condition. During this operation pure nitrogen from nitrogen generation system was first used to purge out air from CB. Pure nitrogen was passed

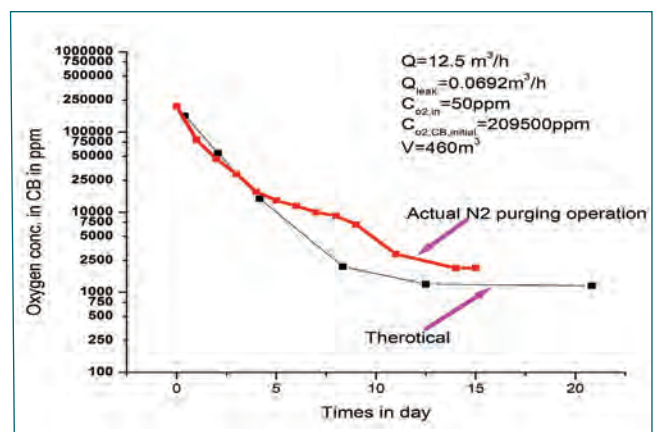


Fig. 3 Change in O₂ conc. in CB during N₂ purging operation

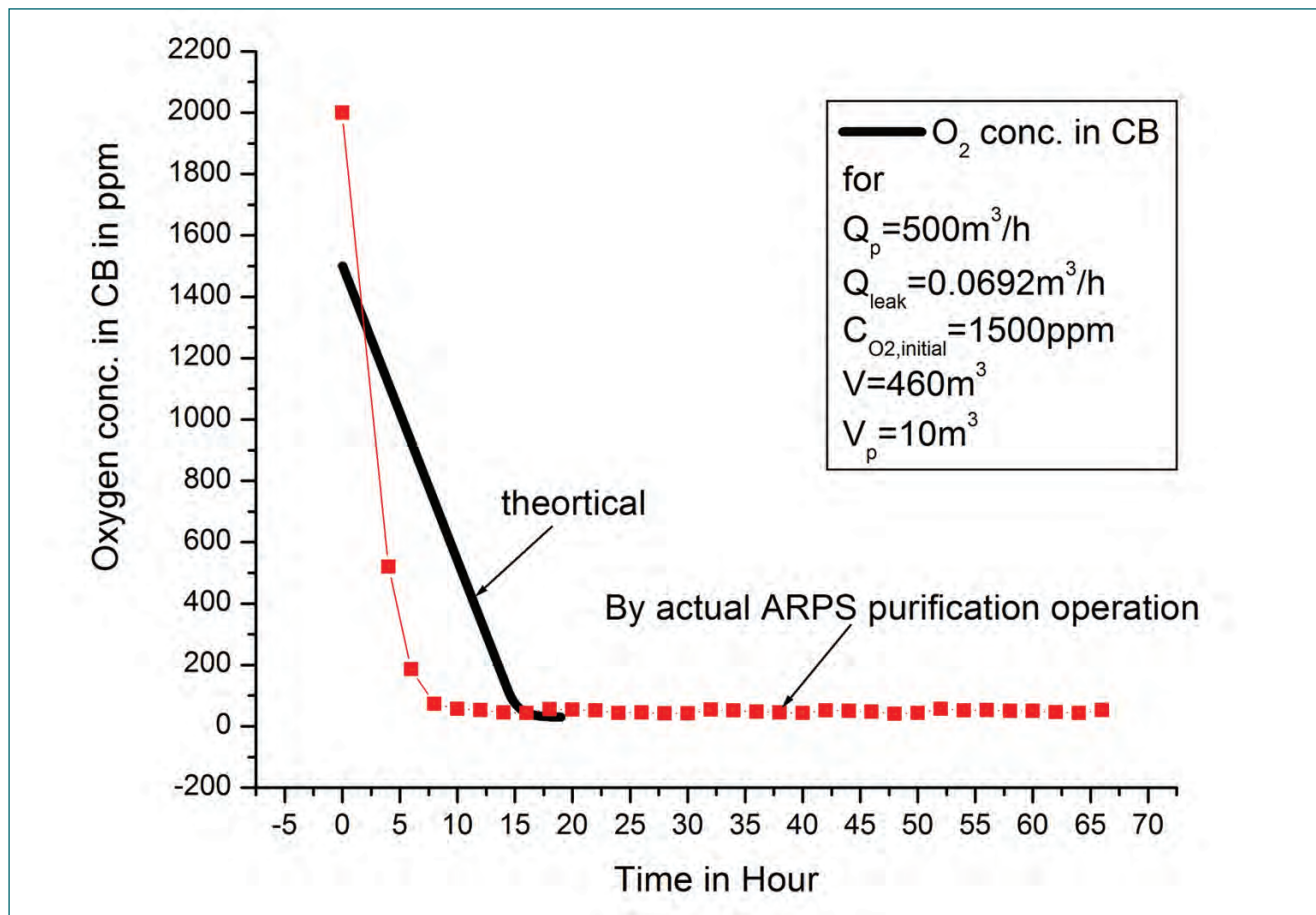


Fig. 4 Change in O₂ conc. in CB during N₂ purification operation using ARPS

at flow rate of 12.5 Nm³/h (average) and simultaneously the gas inside the CB was re-circulated using blower for proper mixing and distribution of purge gas. The oxygen concentration was continuously monitored. The temperature and pressure of gas inside the CB was continuously maintained at around 30 °C and between -20 to -40mmWC using heat exchanger in ARPS recirculation circuit and argon pressure control system respectively. During this phase the oxygen concentration in CB was brought from 209500 ppm to 2000ppm. The total duration taken for this operation was 15 days which was successfully matched with our theoretical prediction. Figure 3 shows the theoretical prediction and experimental data, of the change in the oxygen concentration with time during nitrogen purging operation. After achieving oxygen concentration below

2000ppm in CB, nitrogen purging was stopped and further purification of nitrogen inside CB was achieved by using Purification circuit of ARPS. The oxygen was removed by reacting oxygen with hydrogen in presence of Pd catalyst inside oxygen removal column. The moisture produced during the reaction and the moisture already present in nitrogen was removed by Molecular sieve beds. The temperature and pressure of gas inside the CB during this phase was also maintained around 30°C and between -20 to -40mmWC respectively. During this phase the oxygen concentration in CB was brought from 2000 ppm to 42ppm. The total duration taken for this operation was 10 hours which reasonably matched with the theoretical prediction. Figure 4 shows the change in the oxygen concentration with time during purification operation.

IV.24 Synthesis of Isoreticular Metal Organic Framework-3 for Recovery of Uranium from Aqueous Solutions

Metal Organic Frameworks (MOFs) are three dimensional coordination polymers possess the large surface area, tunable pore sizes, high porosity, thermal/chemical stability and reusability; thus they are outstanding candidates for solid phase extractants. In the present study, we report four post synthetically modified isoreticular metal organic frameworks from Isoreticular Metal Organic Framework-3 (IRMOF-3) namely, IRMOF-PC (2-pyridine carboxaldehyde), IRMOF-GA (glutaric anhydride), IRMOF-SMA (sulfamic acid), and IRMOF-DPC (diphenyl phosphonic chloride) via covalent grafting of organic functional moieties (amide, anhydride, sulphur, and phosphorous) by modifying pendant amino (-NH₂) group present in the IRMOF-3. The resultant MOFs displayed varying porosity, surface area, stability, and binding affinities compared to pristine MOF. As synthesized PSM MOFs were characterized by different characterization techniques namely, Fourier transform infrared spectroscopy (FTIR), powder XRD, BET surface area analysis, thermogravimetric analysis (TGA), NMR (13C, 1H and 31P), scanning electron microscopy (SEM), and energy dispersive X-ray spectroscopy (EDX). Post synthetically modified IRMOF-DPC showed enhanced thermal stability of about 450°C. The functionalized IRMOF-3 MOFs were subjected for recovery and sensing of U(VI) from aqueous medium and sorption studies were carried out using batch technique. Effect of solution pH on U(VI) sorption was investigated by varying the solution pH from 2 to 9. All the MOFs exhibit excellent sorption capacity towards U(VI) (>90%) and maximum sorption was observed at pH 5 (Figure 1). Sorption

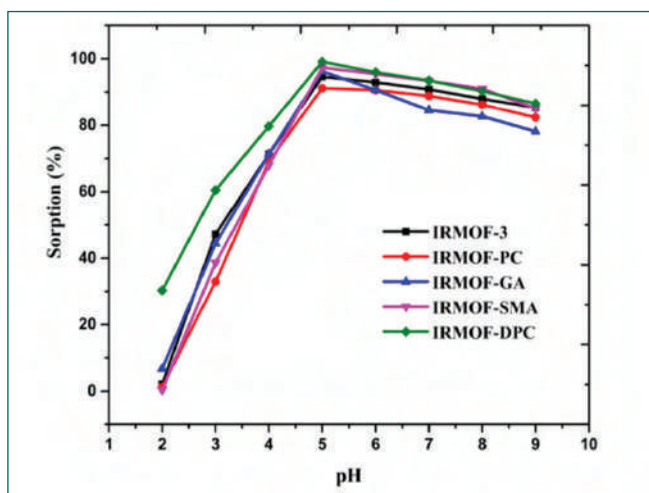


Fig. 1 Effect of pH variation on U(VI) sorption (%) onto IRMOF-3 and its PSM MOFs, $t=180$ min, $m_{\text{sorbent}}=10.0$ mg, $V_{\text{solution}}=3$ mL, $C_0=1000$ mg/L, $T=25 \pm 1^\circ\text{C}$

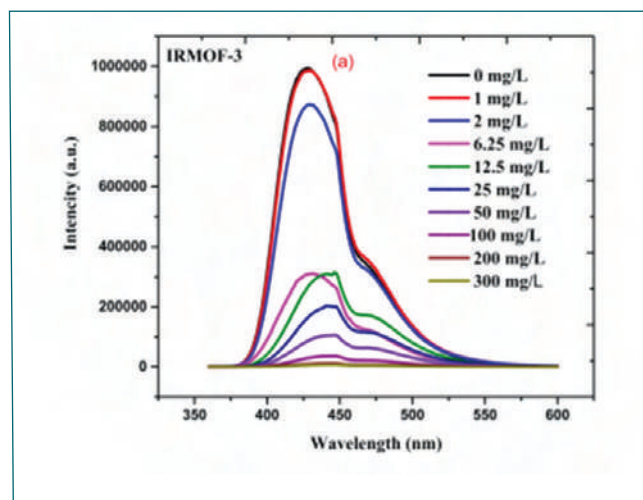


Fig. 2 The emission spectra of IRMOF-3 with increasing uranium (VI) concentration (0 to 300 mg/L)

capacity of MOFs is in the following order: IRMOF-DPC (300 mg/g) > IRMOF-SMA (275 mg/g) > IRMOF-GA (262 mg/g) > IRMOF-3 (256 mg/g) > IRMOF-PC (239 mg/g). IRMOF-DPC shows rapid sorption of uranium within in 5 minutes with excellent sorption of uranium >99%. Kinetic studies also performed to identify the saturation sorption of U(VI) and interestingly functionalized IRMOF-DPC exhibited very rapid extraction ability towards U(VI) from aqueous medium. In order to get back the sorbed U(VI) onto MOFs, desorption studies were carried out with different solvents and 0.01 M HNO₃ was found to be effective. Additionally, IRMOF-3 and PSM MOFs displayed excellent sensing studies for the detection of U(VI) from aqueous medium (Figure 2). Sensing studies revealed that, functionalized IRMOF-GA offered impressive detection limit (3.6 µg/L) out of five IRMOF-3 MOFs. These combined sorption and sensing results concluded the participation of organic functional groups in the sorption and fluorescence sensing of uranyl ions. And these functionalized MOFs could be used directly for detection of uranyl ions in less polluted sites, around mining and processing sites. Moreover, these MOFs furnished excellent selectivity via fluorescence quenching for U(VI) (~98%) over other lanthanide ions (La³⁺, Ce⁴⁺, Nd³⁺, Sm³⁺, Gd³⁺, and Eu³⁺) (~30-40%). This strategy is useful for studies seeking to synthesize highly stable solid state sorbents and sensors selective to U(VI) from aqueous media, within the context of nuclear industry as well as the ecosystem.

IV.25 Interaction of Uranium Ions with Moisture in LiCl-KCl Eutectic Melts

LiCl-KCl eutectic melt is the mainstay of pyroprocessing operations. Purity of melt is central to molten salt electrorefining as it is marred by problems due to corrosion of container material, high temperatures possibly leading to side reactions and loss of charge efficiency due to formation of loose deposit growths. One of the variables that is notably consequential both from cause and effect and scalability issues is content of moisture in the melt. The former is concerned with its effect on electrochemical performance of melt and the latter pertains to its influence on redox behaviour of actinide chlorides in melt in an actual electrorefining operation.

The first aspect can be represented by the following sequence of reactions involving formation of LiOH.



The latter aspect corresponds to hydrolysis of UCl_3 and PuCl_3 in melt containing moisture. In order to explore redox behaviour of melt in presence of moisture in the context of electrorefining, it is thus important to address both the above issues. Since moisture is known to be electro-active in the melt, it participates in a complex sequence of charge transfer reactions resulting in the formation of OH^- and O^{2-} ions that may further deteriorate the melt in terms of enhanced corrosion characteristics. These anionic species may lead to enhanced charging current at the electrode thereby increasing the residual current density of melt. Thus, presence of moisture could be qualitatively ascertained from residual current density. This is invariably captured in the cyclic voltammograms of different LiCl-KCl eutectic melts having varying degrees of moisture content (Figure 1).

In the potential range -0.5 to -2.0 V (vs. $\text{Ag}^+|\text{Ag}$ as ref.), which is the domain of electrorefining, a minor drifting of the baseline below the zero current in few

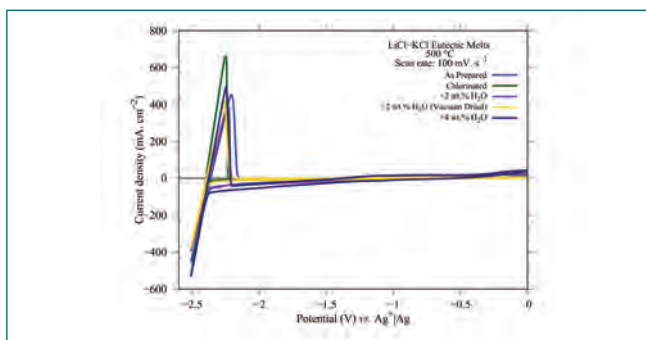


Fig. 1 Comparison of cyclic voltammograms of LiCl-KCl eutectic melts containing varying degrees of moisture content. $T=500^\circ\text{C}$

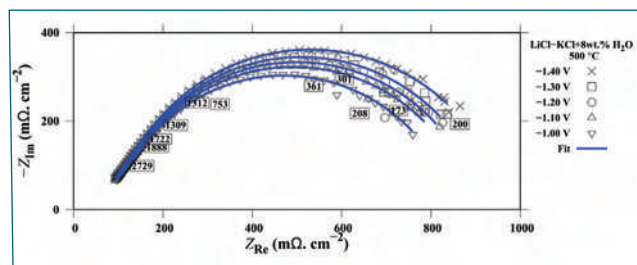


Fig. 2 Impedance response of uranium electrode in moisture containing LiCl-KCl eutectic melts. $T=500^\circ\text{C}$

voltammograms is the signature of finite charging current in the melt. A closer examination of the voltammograms reveals that adsorption of OH^- occurs at -1.25 V followed by its reduction at -1.65 V to O^{2-} . During anodic dissolution of uranium or uranium-based alloys at around -1.25 V, OH^- ions accumulate around uranium and imposes a resistance to the faradaic process of $\text{U}|\text{U}^{3+}$ couple. Thus, at -1.25 V, the forward reaction of U to U^{3+} is restricted due to the stability of OH^- film. This is reflected in the very prominent capacitive contribution in the impedance response of uranium electrode in moisture containing LiCl-KCl melt (Figure 2).

It is indicative from Figure 2 that a large semi-circle in the frequency dispersion plot is a reflection of formation of moieties and clusters of U^{3+} and OH^- that get complexed within the diffusion layer and subsequently they diffuse together into the melt. Evolution of the cyclic voltammogram of the melt containing both U^{3+} and OH^- shown in Figure 3 is in stark contrast to the familiar redox behaviour of LiCl-KCl- UCl_3 melts. Apart from $\text{U}^{4+}|\text{U}^{3+}$ and $\text{U}^{3+}|\text{U}$ couples, additional voltametric features in the potential region 0 to -1.80 V are representative of complexities arising due to presence of OH^- ion. Although it may not be practically possible to bring down the moisture content of the purified melt below 10 ppm, it is expected that about 50 ppm moisture may not severely impact the performance of the melt in electrorefining operations.

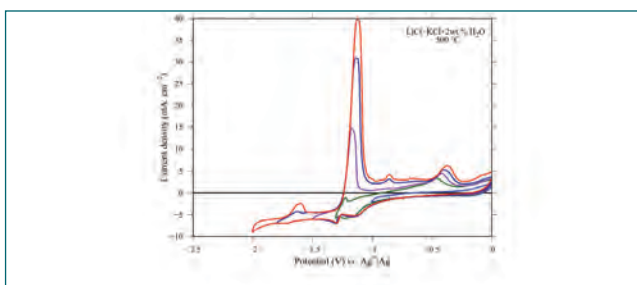


Fig. 3 Redox behaviour of U^{3+} in moisture containing LiCl-KCl eutectic melt after 72 h of anodic polarization of uranium electrode. $T=500^\circ\text{C}$

IV.26 Direct Preparation of Uranium – Titanium (U_2Ti) Intermetallic Compound by Direct Oxide Electrochemical Reduction Method

Uranium alloys are proposed as a fuel for liquid metal fast breeder reactors. Moreover, uranium alloys are considered as a potential candidate for storage of tritium in fusion reactors. In this context, U_2Ti intermetallic compound has gained considerable attention for the application of safe and high capacity storage material for hydrogen and tritium. This intermetallic is usually prepared by arc melting of a mixture of stoichiometric amount of uranium and titanium metals. The method involves two steps i) independent preparation of metals and ii) mixing of both metals by arc melting. Nevertheless, repeated arc melting and annealing is essential to achieve homogeneity of the sample.

Direct Oxide Electrochemical Reduction (DOER) is a promising technique in which metals or alloys can be prepared from the corresponding metal oxides or a mixture of metal oxides respectively. This single step process can directly yield alloys from its constituent metal oxides. The applicability of DOER towards the preparation of U_2Ti intermetallic from mixed UO_2 - TiO_2 oxides in $LiCl$ - Li_2O melt has been investigated. Mixed

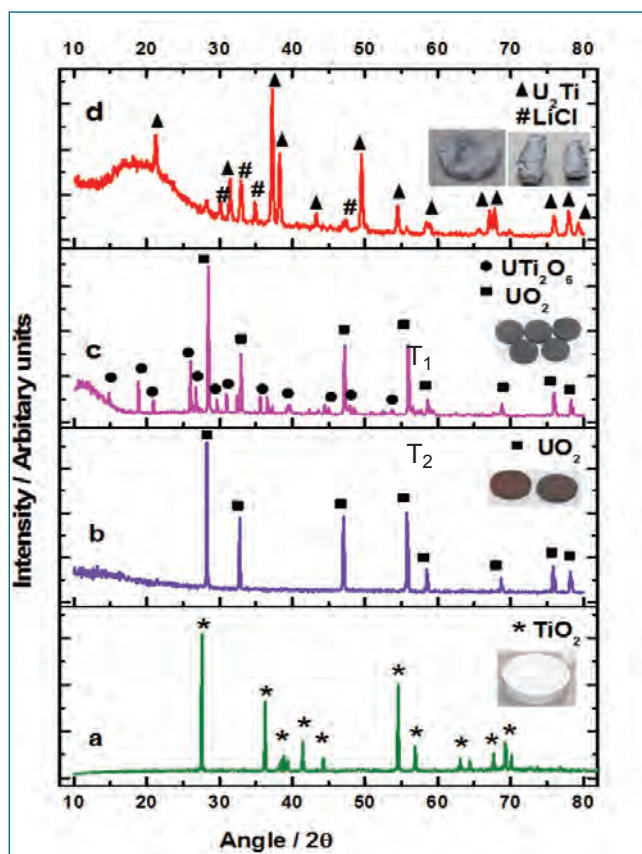


Fig. 1 XRD patterns of sintered a) UO_2 , b) TiO_2 , c) mixed oxide and d) reduced U_2Ti

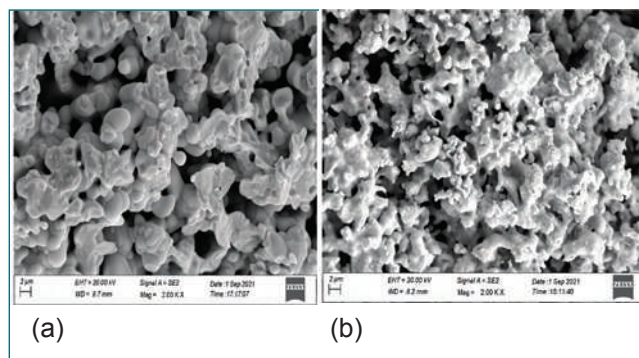


Fig. 2 SEM images of (a) mixed oxide and (b) U_2Ti

oxide pellet was prepared from the required quantity of UO_2 and TiO_2 and the pellet was sintered at $1500^\circ C$ under Ar - $8\%H_2$ atmosphere for 4h. The sintered pellet was characterized by XRD and SEM. It is noteworthy that TiO_2 can react stoichiometrically with UO_2 at high temperature and form UTi_2O_6 (Figure 1c).

Electrochemical reduction experiments were carried out in $LiCl$ - $0.5\ wt\% Li_2O$ melt at $650^\circ C$. $Ni|NiO$ was used as a reference electrode. Sintered mixed oxide pellet tied in a SS wire acted as the cathode and a Pt coil served as the anode. Prior to the electrochemical reduction experiments, cyclic voltammetry was performed to examine the redox behavior of UO_2 and TiO_2 . Reduction peak corresponding to UO_2 to U was observed very close to Li deposition potential ($\sim +150\ mV$ vs $Li^+|Li$) whereas reduction peaks corresponding to TiO_2 reduction were observed in the range of $+0.7$ to $+1.6\ V$ vs $Li^+|Li$. The cathodic onset potential of Li deposition and potential range of oxygen evolution were also determined by CV experiments. A constant current of 1 A was applied between the mixed oxide cathode and Pt anode for about 5 h. The electrolysis was interrupted periodically to allow the deposited lithium to react completely with the mixed oxide cathode. The corresponding anode reaction was the liberation of oxygen. The reduced product after electrolysis contained occluded and adhered $LiCl$ salt (about 20 - 30 wt%). It was characterized by XRD, SEM-EDX and oxygen analysis. XRD pattern of reduced product showed the diffraction peaks of U_2Ti and residual $LiCl$ (Figure 1d). Scanning electron micrographs of mixed oxide and U_2Ti intermetallic are shown in Figure 2a and 2b respectively. A typical nodular structure was noticed in the reduced product (Figure 2b). EDX of the reduced product also confirmed the formation of U_2Ti (U – 90.6 wt% and Ti- 9.1 wt %). The residual oxygen was found to be less than 100 ppm.

IV.27 Extraction and Monitoring of Uranyl Ions in Aqueous Solutions using Gel Immobilized Microgel Photonic Crystals

Monitoring and extraction of uranium from aqueous solutions in nuclear industrial waste water/ sea water is crucial towards its collection for further utilization as well as for decontamination of the solutions. Uranyl ion (UO_2^{2+}) is a stable form of uranium commonly present in nuclear waste solutions. To extract UO_2^{2+} from solution, adsorption is known to be an efficient method due to its high affinity to coordinate with different functional groups. There are various functional materials based on hydrogels, metal-organic frameworks, and nanoparticles reported for adsorption/detection of uranium in aqueous medium. However, the materials used for extraction cannot be analysed directly to detect and determine the uranium adsorbed on to them. Therefore the solution remaining after extraction is usually analysed by other techniques like inductively coupled plasma mass spectrometry, radio spectrometry etc. which needs pre-processing of solutions causing delay in the analysis. Thus, in situ information on adsorption of uranium during extraction has always been lacking. We have prepared a novel photonic hydrogel which can enable in situ monitoring of uranium during extraction by exhibiting a change in its optical properties. The photonic hydrogel consists of microgel photonic crystal immobilized in a hydrogel matrix. First the microgel particles of poly(N-isopropyl acrylamide)-co-poly(acrylic acid) in a pregel solution are made to order in a crystalline state and then it is exposed to UV-radiation which forms gel around microgel particles and immobilizes the microgel crystal. Optical reflection spectra of gel immobilized microgel crystal exposed to different uranium concentrations are shown in figure 1. All the spectra show a peak due to Bragg diffraction from microgel photonic crystal. In the

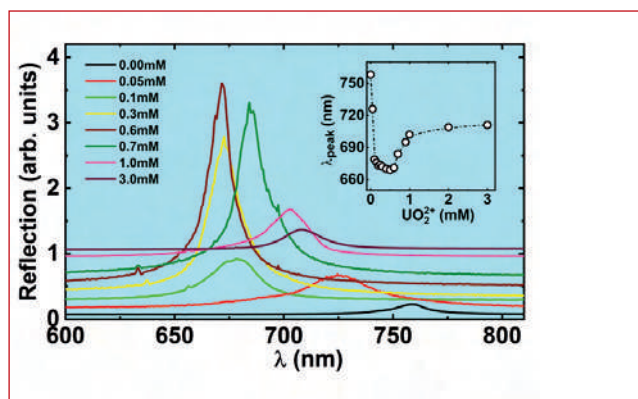


Fig. 1 Reflection spectra of immobilized microgel crystal at different uranium concentration. Inset shows variation of peak position with uranium concentration

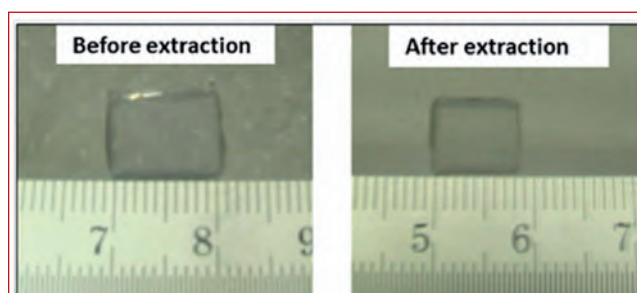


Fig. 2 Photographs of immobilized microgel photonic crystal before and after extraction of uranium

low concentration regime, increase in uranium content leads to a blue shift of the diffraction peak whereas at higher uranium content it leads to a red shift. There exists a threshold uranium concentration at which blue shifting peak changes to red shifting one. The blue shift /red shift of the diffraction peak occurs due to shrinking (Figure 2)/ swelling of the photonic hydrogel which in turn is effect of chelation of uranyl ions with ligands on photonic hydrogel / osmotic imbalance of uranyl ions inside and outside photonic hydrogel respectively. The change in optical spectra of photonic hydrogel upon uranium adsorption can be readily monitored and thus it provides a way for in situ monitoring of uranium during extraction. The uranium extraction capacity (at 0.6 mM) of the photonic hydrogel analysed using optical absorption (Figure 3) of Arsenazo-Uranium complex is found to be ~ 192 mg/g. These studies suggests that the gel immobilized microgel photonic crystals are good candidates for extraction cum monitoring of uranium in aqueous solutions and will be helpful for further research towards similar applications for other heavy metal elements and ionic impurities.

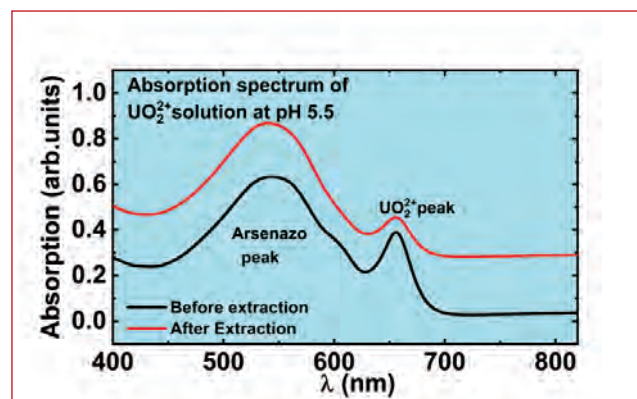


Fig. 3 Absorption spectra of UO_2^{2+} -Arsenazo-III complex before and after the extraction

IV.28 High Temperature Corrosion Evaluation of 2.25Cr-1Mo in LiCl-KCl Molten Salt by Electrochemical Technique

High temperature molten salt corrosion is one of the key issues that need to be addressed for structural materials required for high temperature environments. The understanding of high temperature corrosion of materials for reliability, economy, quality, safety and profitability of any industrial sector associated with high temperature process using molten salts is of utmost importance. The molten salt corrosion evaluation is generally studied by carrying out immersion experiments, salt deposit coatings experiments, and using electrochemical techniques. Electrochemical methods are rapid, economical and a suitable technique for evaluating the corrosion behavior of alloys in-situ than the conventional corrosion evaluation methods. The spent metallic fuel from the future sodium cooled Fast breeder reactors will be reprocessed through pyrochemical methods. The key separation process of the pyrochemical reprocessing. The electrorefining vessel contains LiCl-KCl eutectic salt as the electrolyte at 500 °C. Materials such as 2.25Cr-1Mo, 9Cr-1Mo steel and SS410 are being investigated for the electrolytic vessel to contain molten salt. In the present study, the 2.25Cr-1Mo has been evaluated for the molten salt applications using electrochemical techniques for about 200 h during immersion.

The open circuit potential (OCP) versus time plot of 2.25Cr-1Mo exposed to LiCl-KCl salt is shown in (Figure 1a). The OCP value was found to be more negative during the initial exposure periods. As the duration of exposure proceeds, the OCP value changes to a less negative/more positive value. The OCP fluctuate throughout the exposure, as evidenced from the plot, which indicates the instability of the alloy in molten salts.

The Linear Polarization Resistance (LPR) plots of 2.25Cr-1Mo steel recorded at different intervals of exposure to molten salt are shown in (Figure 1b). The polarization resistance (R_p) values obtained from the slopes of LPR plots found to be decreasing continuously over the entire duration of exposure, indicating more corrosion of the alloy and the non-protecting nature of the formed oxide film. As Cr amount is significantly less in the alloy, the formation of the protective chromium

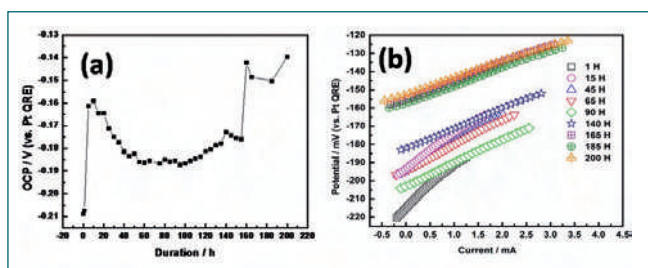


Fig. 1 (a) Open circuit potential & (b) LPR plots of 2.25Cr-1Mo steel exposed to molten LiCl-KCl salt at 500°C

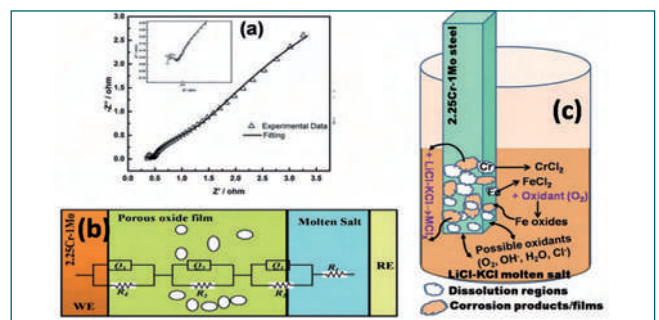


Fig. 2 (a) Nyquist plot & (b) equivalent circuit used for fitting EIS data and (c) corrosion mechanism representation

oxide films is not anticipated, and also no oxide film form is stable in molten salts due to the fluxing effect. The corrosion current density (i_{corr}) obtained using Stern-Geary equation, indicates the increase in corrosion rate with the duration of exposure to molten salt, which further ascertains that the formed oxide film, if any, is not protective.

The Nyquist plots (EIS measurements) recorded for 2.25Cr-1Mo exposed to molten salt at various intervals, one of the plots along with the fitting is shown in (Figure 2a) and the equivalent circuit used for fit is also shown in (Fig 2b). The Nyquist plot showed two semicircles starting from the higher frequency range and an incomplete semicircle at the lower frequencies. The incomplete semicircle reduces in size with the duration of exposure. This trend in impedance indicates the formation of some intermittent oxide films on the alloy surface. It was also found that the total impedance decreased with the increase in the duration of exposure. As shown in (Figure 2b), three time constants portray the 2.25Cr-1Mo alloy/oxide film interface, porous oxide film, and the porous oxide film/molten LiCl-KCl salt interface, respectively. Further analysis of the sample after corrosion evaluation in molten salt by optical microscopy and laser Raman spectroscopy revealed the formation of intermittent oxide layers comprised of α -Fe₂O₃ and Fe₃O₄.

The pictorial representation of the mechanism of molten salt corrosion is given in Figure 2c. The oxide films formed over the 2.25Cr-1Mo alloy surface is attributed due to the impurities/oxidants present in the molten salt, and those oxides are further fluxed by reacting with molten salt and dissolves in the molten salt.

The corrosion behaviour of 2.25Cr-1Mo steel in molten LiCl-KCl salt exhibited the formation of intermittent oxide film. The corrosion resistance of materials in LiCl-KCl molten salt is strongly related to composition of materials, the nature of oxides formed and the molten salt composition.

IV.29 High Temperature Mass Spectrometric Studies on <GdAl₂(cr)+GdAl(cr)> Two Phase Region of Gd-Al System

Thermodynamic properties of Gd-Al intermetallic compounds are of significance to the process of pyrochemical separation of actinides from lanthanides present in the molten chloride/fluoride salt electrolyte medium by employing the electrorefining process. In the present investigation, high temperature vaporisation thermodynamic studies over <GdAl₂(cr)+GdAl(cr)> two phase region of Gd-Al system were performed by employing in-house developed Knudsen Effusion Mass Spectrometer (KEMS) in the temperature range 1158-1323 K. This KEMS, comprises two vacuum chambers arranged one over the other, one of which houses an electron bombardment (EB) furnace and the other accommodates Quadrupole Mass Spectrometer. During the KEMS experiments, each chamber was maintained at the vacuum of the order of ~1 x 10⁻⁷ Torr by using a turbo molecular pump backed by a rotary pump.

The samples with the compositions $\chi_{Al} = 0.61$ and 0.63 and pertaining to <GdAl₂(cr)+GdAl(cr)> were prepared by arc melting appropriate amounts of high pure Gd and Al metals. The arc melted sample buttons were wrapped in tantalum sheets and sealed under vacuum in quartz tube at a residual pressure of 10⁻⁶ Torr under high pure argon atmosphere. These samples were initially heated at 473 K for 24 h and then annealed at 950 K for 720 h. They were phase characterised by using XRD and found to consist of the above two phases.

Two lots (Lot-1 and Lot-2) of samples from each composition ($\chi_{Al} = 0.61$ and 0.63) with approximately ~250 mg in each lot were used for the vaporisation studies. Samples were taken in Zirconia Knudsen cell covered with a lid having a knife edged orifice of 0.5 mm in diameter at its centre and the cell was placed in another tantalum outer cup having a black body hole at its bottom. Heating of the samples were accomplished by EB furnace. Disappearing filament pyrometer was used for measuring temperature of the sample by focusing

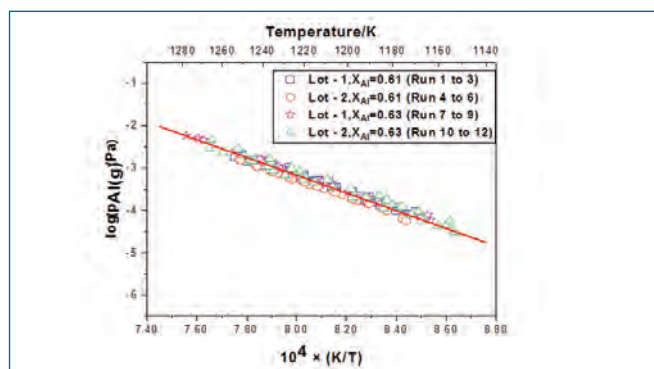


Fig. 1 Combined plot of $\log(p_{Al}(g)/Pa)$ Vs $1/T$ K⁻¹

$\Delta_f H^\circ_{m, 298.15}$ kJ mol ⁻¹	Method	Reference
-83.8±11.8	KEMS	Present study
-78.3±18.7		
-85.8	Modelling	L. Jin et al.
-81.0	Calphad calculation	H. Bo et al.
-97.2	Modelling	Cacciamani et al.
-82.5	First principle calculation	M.C. Gao et al.
-85.8±2.6	Liquid Al calorimetry	Colinet et al.
-78.8±6.0	Liquid Al calorimetry	Sommer and Keita
-137.4	Miedema's model	Niessen et al.

on to the black body hole. The molecular beam of equilibrium vapour effusing out of the orifice was ionised (cross beam ionisation) in the ion source region using electrons of energy 13.8 eV (at an emission current of 100 μ A) emitted from oxide coated iridium filaments. The ions thus produced were mass analysed by Quadrupole triple filter and detected by secondary electron multiplier (SEM) operating in pulse counting mode. was the only ion observed in the mass spectrum of equilibrium vapour and Al(g) was found to be the corresponding neutral precursor.

Subsequently, temperature dependence of ion intensity of ²⁷Al⁺ was carried out in the range 1158-1323 K. Totally 12 temperature dependence runs were carried out. The pressure calibration constant required for converting the measured ion intensity data of ²⁷Al⁺ into partial pressure of Al(g) was deduced from the experiments carried out over the liquid region of pure aluminium in the temperature range of 1140-1225 K. The recommended p-T relation for Al(g) (1158-1323 K) was deduced by least-squares fitting the logarithmic values of all the partial pressure points from the individual runs (159 points) against the reciprocal of temperature and is given as (Figure 1),

$$\log(p_{Al}/Pa) = (-20282 \pm 260)/T + (13.06 \pm 0.21)$$

From the p-T relation of Al(g), standard enthalpy change, at 298.15 K, of the reaction (GdAl₂(cr) = GdAl(cr) + Al(g)) was evaluated by second law method. $\Delta_f H^\circ_{m, GdAl(cr), 298.15 K}$ was deduced to be - 83.8±11.8 kJ mol⁻¹. Also the expression for standard molar Gibbs energy of formation of GdAl(cr) derived is given as, $\Delta_f G^\circ_{m, GdAl(cr), \tau} = (-101.7 \pm 6.6) + (0.00667 \pm 0.00560)T$ kJ mol⁻¹. Table 1 shows the comparison of $\Delta_f H^\circ_{m, GdAl(cr) 298.15 K}$ obtained in the present study with the literature data.

IV.30 Design and Development of Machine Vision based Slug Inspection System

Sodium bonded metallic fuel pins containing U-Pu-6wt.%Zr ternary alloy as fuel slug and U-6wt.% Zr as blanket slug in T91 clad tubes as fuel pins are being developed for future fast breeder reactors in India. Design and development of the Machine Vision (MV) surface inspection system is towards inspecting metal fuel slugs cast in the Injection casting system. Qualification of cast metal fuel slugs by three-dimensional scanning and defect analysis is achieved through image processing. The objective of the MV system is to inspect and analyze surface discontinuities due to casting defects such as cracks, voids/cavities, scratches, grooves, and pores that greatly influence the material's properties and impair the quality of slug. Therefore, these defects have to be within the design limits so that the slug can be used for fabrication of fuel pin for metal fuel for fast reactors.

Manual slug inspection and defect measurements are prone to observational errors like parallax, random and measurement errors. Non-contact, automated visual inspection using machine vision system for metal rod inspection is sought to eliminate the observational errors. MV surface inspection system acquires images of the slug material, analyses the images for defects, classifies the defects, interprets the defect information and displays the results to the user as shown in Figure 1.

This system involves the use of optical non-contact sensing to acquire and interpret images in order to obtain features of the part being inspected. Then a suitable image processing technique is used to develop a customized algorithm and vision system to identify and quantify the surface defects. Vision based surface inspection system consist of the following main elements – a mechanical positioning system to feed and traverse the rod (slugs) and imaging system as depicted in Figure 2.

Major components of the system are - Vision system with Line scanner machine vision camera, Laser 3D

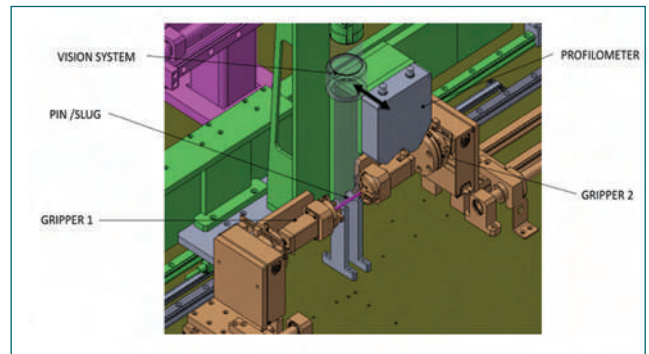


Fig. 2 Layout of MV surface inspection system

profilometer, Linear Servo motor drive to scan the slug surface along the length, Position controlled rotary gripper for rotating the slug 360 degrees in a mechanical inspection bench and an image processing algorithm to inspect, analyze and categorize the defects identified.

Steps involved in image processing is depicted in Figure 3 and a typical dimension measurement of a void defect (LxWxH – 1.18x0.86x0.29mm)is represented in Figure 4.

A brief overview on computer based MV based slug surface inspection systems highlighting the salient features of various automated subsystems and its features has been presented. Vision system has been developed and implemented for inspection of surface defects on the cast metal fuel slugs. The MV system surface defect measurement capabilities are in order of $\pm 0.01\text{mm}$, as is required for the slug quality inspection system for meeting the slug design specification.

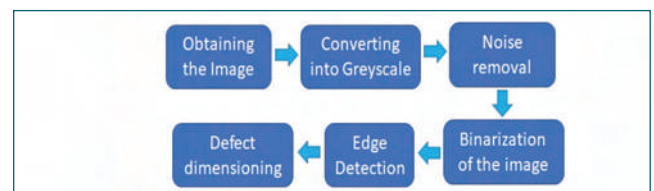


Fig. 3 Steps in Image processing

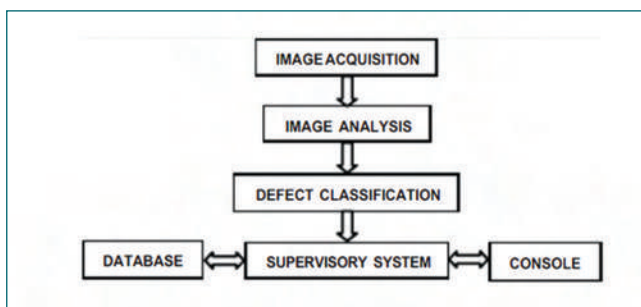


Fig. 1 Functional subsystem

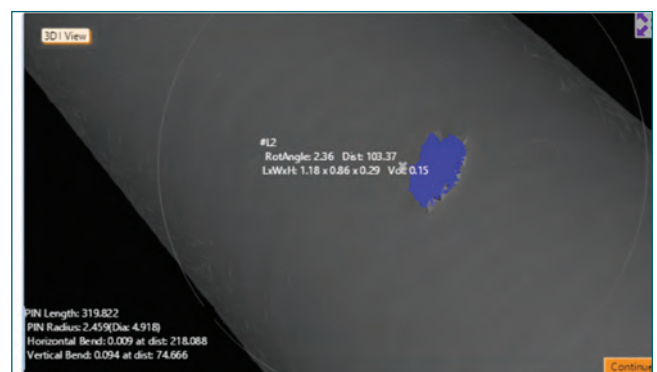


Fig. 4 Defect dimensioning – typical measurement

IV.31 Seismic Integrity Assessment of Free-Standing Lead Wall Assembly using a Shake Table Facility

All the operations carried out in the fast fuel reprocessing plants are carried out in shielded facilities which are qualified to handle radioactive materials. The hot cells usually have a special grade concrete in which the containment boxes would be housed. Certain other hot cells use only a wall made by a stack of lead bricks as the shielding. These are free standing stable stacks. However, these need to be qualified for their stability in the unlikely event of their disruption due to a seismic event. The influence of such an excitation due to earthquake on the structural integrity of this free standing lead wall is of paramount importance in preventing the damage to the associated systems in the plant. The integrity has to be ensured under design level of earthquake loading as per safety regulatory bodies. Hence, it was proposed to carry out experimental investigations that are more reliable for such nonlinear systems as compared to mathematical models.

The main objectives of this study are:

- Characterization of the dynamic feature of free standing lead wall assembly and predicting the acceleration response at different locations.
- Estimation of the transient structural response under combined excitations simulating the actual site conditions.
- Generation of design guide lines for using lead bricks as free standing wall without seismic structures.

A systematic series of experiments were designed and developed to identify the range of parameters governing the dynamic behavior of this lead wall. These experiments

were carried out under different simulated ground motions with and without intermediate plate in order to analyze the dynamic behavior of the lead wall. Displacement and acceleration time histories were monitored. Figure 1 shows the photographs of lead wall assembly captured at a particular instant of time, corresponding to the cases with and without the intermediate groove plates, respectively. Nodes A and B denotes the extreme ends of the wall on front side. Dotted green lines indicate a typical mode shape of the wall for each configuration. The encircled areas represent the portion of wall that is likely to have a significant deformation during the oscillations. The effect of including the groove plate on the seismic integrity performance is presented by highlighting these effects at the appropriate locations. In addition this lead bricks arrangement was enclosed in a steel structure only to safeguard the shake table, by using which this experiment was carried out.

Based on the results from these investigations, the following conclusions were drawn:

- A peak brick displacement of 40 mm was observed under tri-axial seismic ground motion of USNRC spectra with peak ground acceleration value of 0.3 g.
- Lead wall, stacked to a height of 1.5 m has been seismically qualified and doesn't require any additional support even under an equal ground motion of USNRC with PGA of 0.3 g.
- Lead wall stacked up to a height of 2.5 m with intermediate groove plate provided that were at an interval of 1m is qualified for floor response spectra (FRS) at +4.75 m elevation of the plant.

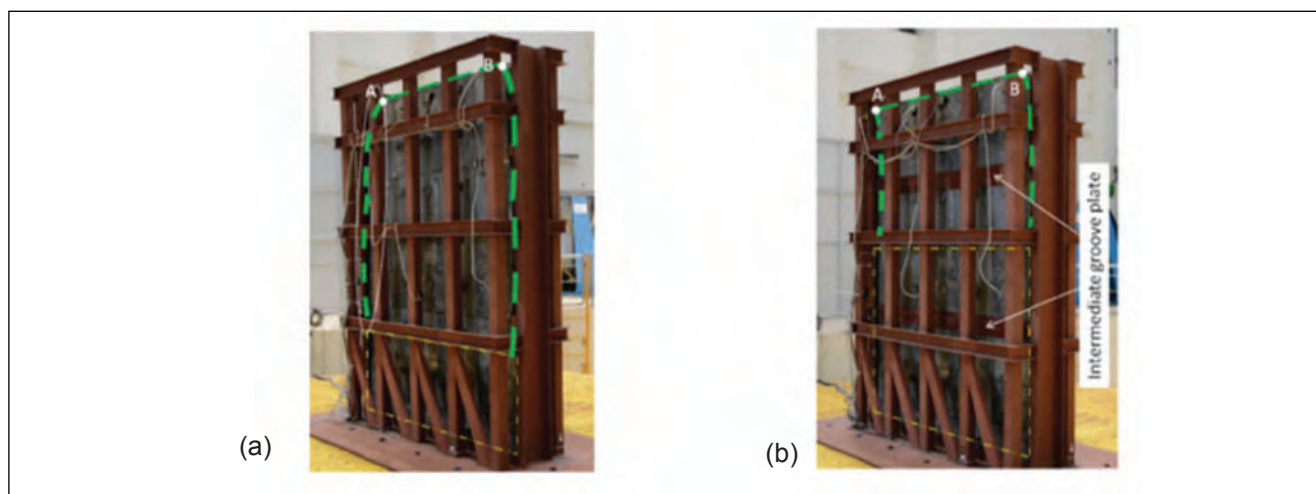


Fig. 1: Temporal snapshots of lead wall with superstructure (a) without intermediate plate and (b) with intermediate plates under UNSRC ground motion of PGA value of 0.6 g

IV.32 Confirmatory Leak Testing and Qualification of Containment Boxes

In Fast Reactor Fuel Reprocessing Plants solvent extraction equipment viz., centrifugal extractors, mixer settlers and its associated piping are located inside specially designed SS304L containment boxes surrounded by concrete/lead walls. The containment box (CB) acts as a barrier for the radioactive material handled inside. Leak testing of such large volume integrated containment boxes were undertaken in our Centre for the first time in a first of its kind fast reactor fuel reprocessing plant. This containment box had provisions for installation of viewing windows, lighting windows, manipulators, apart from several pipe and duct penetrations. Specially designed glove boxes were integrated into the containment box for housing in-cell crane drives, material and waste transfer, maintenance of components, etc. Two process cells each having a containment box of about 100 m³ volume were tested for their leak tightness.

Confirmatory leak testing of these containment boxes along with their glove boxes were carried out by installing all seals in place, to ensure the leak tightness under actual plant conditions. All the lighting and viewing windows were fixed with radiation resistant glasses. All the manipulator openings were fixed with bootings. For preventing over pressurization of containment box,



Fig. 1: View of part of the containment box



Fig. 2: View of incell crane drive glove box

safety features such as interlocks were provided for the air supply cut off at 50 mmWC g. In addition water seal provision was also given, as a failsafe mechanism, to release the excess pressure of the containment box in case pressure exceeds 50 mm wc g. The view of part of the containment box closed with radiation resistant glass and manipulator bootings is shown in Figure 1. The view of incell crane drive glove box closed with glass panels and gauntlets is shown in Figure 2.

Leak detection was carried out on all glass seating locations by soap bubble and smoke test method and the observed leaks were arrested by tightening SS frames, modification of glass seating frames, applying sealant at temporary locations, changing the defective glove box gauntlets and glove ports etc. After ensuring no observable leaks by soap bubble method, smoke test was carried out to identify the fine leak points by visually observing the smoke pattern in a dark environment. Leaks observed during smoke test were arrested and ensured that no observable leaks are there in smoke test. After arresting all the identified leak points, leak testing was carried out by pressure decay method. Pressure and Temperature readings were recorded and average leak rate was calculated. Leak rates within acceptable levels were successfully achieved and the containment boxes were thus qualified for handling radioactive material.

IV.33 Ultrasonic De-Choking Studies on Centrifugal Extractor Bowls

In fast reactor spent fuel reprocessing, centrifugal contactors are employed to extract U(VI) and Pu(IV) from radioactive spent fuel dissolver solution. These centrifugal contactors are susceptible to choking due to the deposition of the insoluble materials present in the dissolver solution. In order to resolve this issue, it was proposed to develop a method and equipment for in-cell dechoking of the CE bowls. In this context, a simulated solution of zirconium molybdate was prepared and deposited in the centrifugal extractor rotating bowl. The CE bowl was then cleaned using ultrasonication in a specially designed vessel and probe. The experimental setup and a view of the chamber fabricated for cleaning the bowl are shown in Figure 1.

A bath was designed and fabricated in stainless steel 304L for accommodating the ultrasonic probe (40 kHz), which was a custom-made unit that fits into the available plant space. Passive solution draining was provided in the bath for easy removal of waste liquid and suspension. Suspension of Zirconium molybdate in water was used for choking of centrifugal contactor bowl. A slurry of zirconium molybdate was prepared by mixing zirconyl nitrate and ammonium molybdate in the ratio of 2:1 in demineralized water. The average particle size (d50) of zirconium molybdate was determined to be 3.5 μ m. This suspension was passed into the centrifugal extractor bowl by pumps. The bowl was removed from the choking setup once it was completely choked. The choking setup consisting of CE, pumps and variable frequency drive is shown in Figure 2.

De-choking experimental setup consisted of a controller and stainless steel chamber in which the ultrasonic



Fig.2: Experimental setup for choking of centrifugal contactor bowl

probe was kept. The temperature of the bath liquid was monitored using a separate thermocouple. The de-choking of zirconium molybdate was studied as a function of time, ultrasonic frequency, power of the probe, etc. The choked bowl was assembled in the chamber containing distilled water and de-choked in the setup shown in Figure 1. The de-choking studies showed that the removal of particles from the bowl was fast in the initial stages and gradually decreased with time. Figure 3 shows the change in the weight of particles with time brought about by ultrasonication of the chamber.

The present ultrasonic probe removes 80 to 90% of the insoluble deposited in the bowl in 2 -3 hours, and more than 95% gets removed within 10 hours, irrespective of the amount of choking or air drying. The promising results established the possibility of employing this ultrasonic probe for de-choking of solid particles from the CE bowls in hot cells.



Fig. 1: Equipment for ultrasonic cleaning of centrifugal contactor bowl

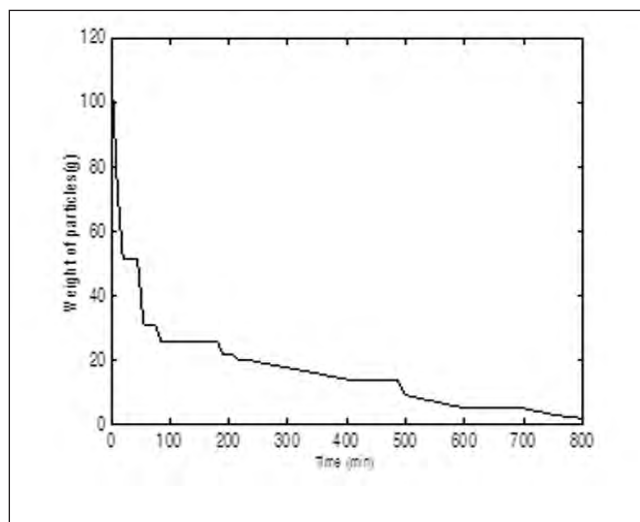


Fig.3: A plot of the variation in particle weight deposited in CE with time due to ultrasonication

IV.34 Radiolytic Degradation Behavior of Tri-Iso-Amyl Phosphate/N-Dodecane System Upon Cyclic Irradiation

Traditionally, 1.1 M tri-n-butyl phosphate (TBP) in n-dodecane (n-DD) has been used as the solvent in the PUREX process for reprocessing the spent nuclear fuel arising from thermal reactors. However, TBP exhibits third phase formation and undergoes severe degradation during the reprocessing of plutonium rich FBR spent fuel. In view of this, its higher homologue namely the tri-iso-amyl phosphate (TiAP) has been considered. As the FBR fuel is discharged usually at a much higher burnup, the fission product content and the radioactive dose associated with it are usually very high. Hence, the organic phase undergoes severe hydrolytic and radiolytic degradation, which leads to the poor recovery of actinides. The retention of actinides and the presence of degradation products in the organic phase reduces the recycling ability of the solvent largely. The present study deals with the radiolytic stability of TiAP/n-DD under metal loading as well as acid loading condition to assess the recycling ability of the solvent. The extent of degradation of the organic phase was quantified by its uranium retention and the change in its concentration upon radiolysis.

Two sets of organic solutions comprising of 1.1 M TiAP in n-DD equilibrated with 4 M HNO₃ (Set-I) and 1.1 M TiAP/n-DD equilibrated with 0.25 M UO₂(NO₃)₂ solution in 4 M

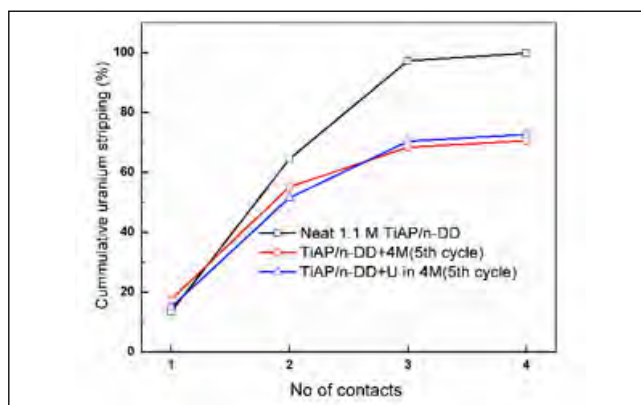


Fig. 2: Comparison of U(VI) retention of recycled organic phase with neat solvent

nitric acid (Set-II) were prepared. Both these organics were subjected to cyclic irradiation to a cumulative absorbed gamma dose of 500 kGy in five cycles with an absorbed dose of 100 kGy in each cycle in a ⁶⁰Co gamma irradiator. After each cycle, the irradiated organic phase was contacted with 0.01M HNO₃ for stripping of U(VI) followed by sodium carbonate and 0.01 M HNO₃ wash. The physicochemical properties (density, viscosity and interfacial tension), concentration of extractant in the organic phase were measured. These results were compared with that of the neat solvent after each cycle. Upon cyclic irradiation, the change in density and

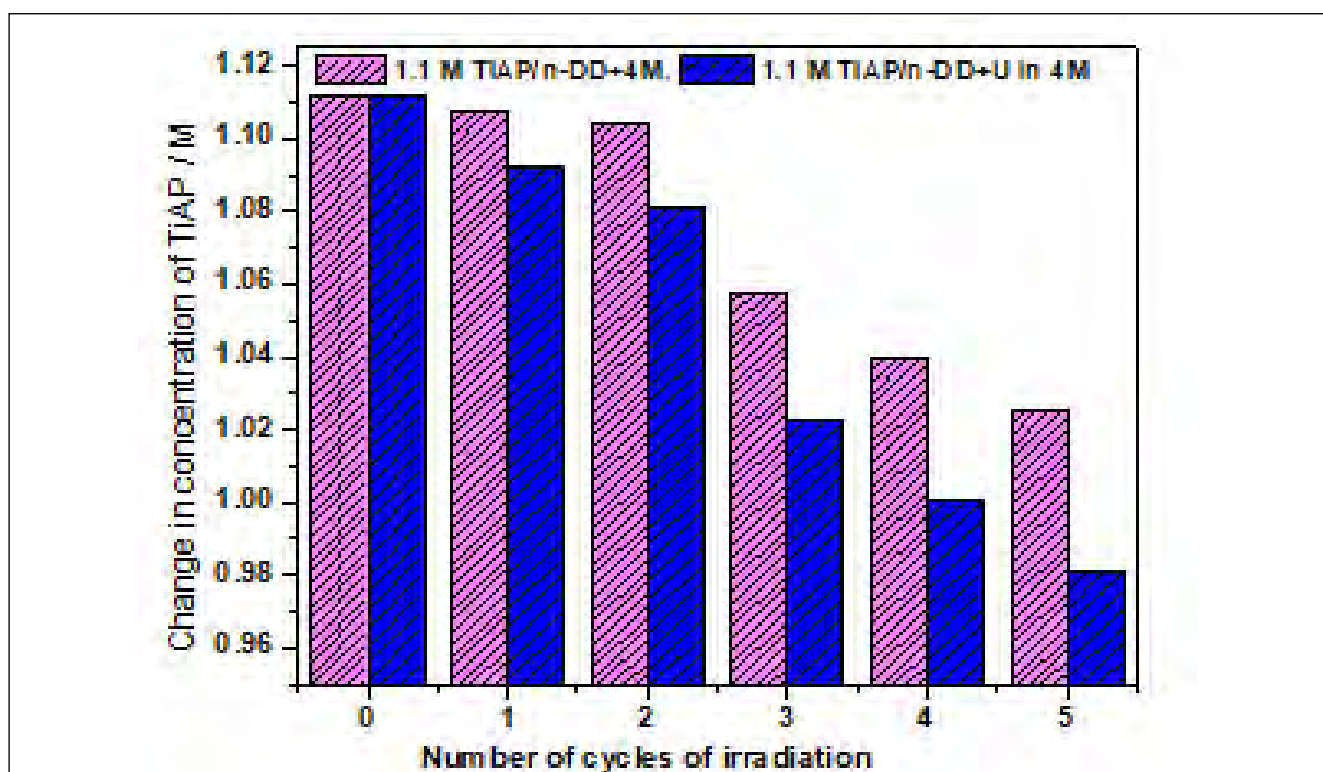


Fig. 1: Change in concentration of the extractant TiAP up on cyclic irradiation

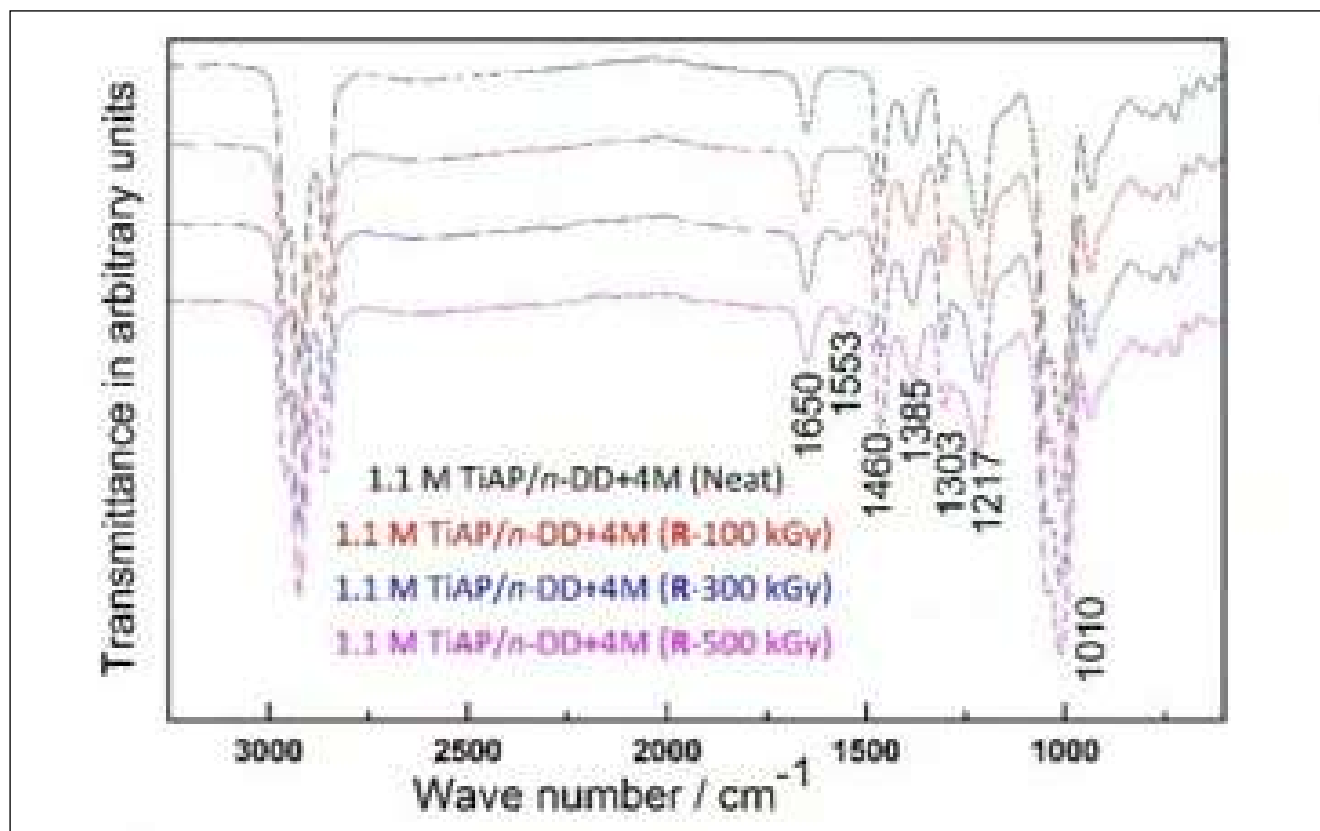


Fig. 3: Comparison of FT-IR spectra of recycled organic phase *TiAP/n-DD+4M* with neat solvent

viscosity of the recycled organic phase was marginal. But significant variation was observed in the measured IFT value as comparison with the neat solvent. For recycled organic phases Set-I and Set-II, reduction in IFT up to 16% and 20% respectively were observed as compared to neat solvent after 5th cycle of irradiation and recycling.

The degradation behaviour was assessed by determining the concentration of *TiAP* in the recycled organic phase by gas chromatography. The results are compared in Figure 1. It could be seen that irradiation under metal loading condition leads to a higher degree of degradation of the extractant *TiAP*. Up to 2 cycles of recycling after irradiation, there is a minor change in the extractant concentration beyond which the extractant degrades appreciably. The recycled organic phases after each cycle of irradiation were subjected to metal (uranium) retention to assess their performance compared to neat solvent. A typical behaviour of uranium retention test in recycled 1.1 M *TiAP/n-DD* after 5th cycle of irradiation is shown in Figure 2. For the neat *TiAP/n-DD*, more than 97% recovery of uranium could be achieved within three contacts of the loaded organic phase with 0.01 M nitric acid. After the fourth contact of the loaded organic almost complete recovery (> 99%) of uranium was achieved. However, for the recycled organic phases of *TiAP/n-DD*, the cumulative stripping of uranium gradually decreases after each cycle of irradiation, though the change is not significant.

From the above trend in Figure 2 it can be concluded that some of the degradation products except the acidic degradation products of *TiAP* (*HDiAP* and *H₂MiAP*) which are not washable have a high affinity towards the metal and their accumulation in the solvent up on each cycle increases which leads to a gradual decrease in the recovery of uranium from the loaded organic phase during stripping. Also it was observed that, the recycled solvent under metal loading condition has a better stripping performance than the recycled solvent under acid loading condition which is similar to the result obtained earlier that revealed decrease in the concentration of the extractant up on radiolysis.

The FT-IR spectra of 1.1 M *TiAP/n-DD+4M* organic phase prior to recycling up on degradation is compared with that of the recycled organic phases after 1st, 3rd and 5th cycle of irradiation in the absence of metal loading in Figure 3. The strong transmittance bands observed at 1010, 1217, 1303, 1385, 1460 and 1650 cm^{-1} are the characteristic frequencies of *TiAP* and acid protonated *TiAP*. All the transmittance bands are common in the recycled organic phases except a weak band at 1553 cm^{-1} . But the band gets prominent with increased intensity in the recycled organic phase after each cycle of irradiation. The N-O asymmetric stretching vibrations of nitro alkane occurs around 1550 cm^{-1} which indicate the formation of nitro derivatives in the recycled organic phase which are not washable with alkali and gradually get accumulated in the solvent.

IV.35 Performance Assessment of Some In-Cell Equipment for Reprocessing

The used nuclear fuel is chopped and the fuel meat is brought into solution by treating it with nitric acid in the dissolver. This “dissolver solution” would contain insoluble residue that need to be separated before further processing. These particles lead to choking of the liquid transfer lines and also create operational difficulties in solvent extraction step. The solid residue comprises particles with their ranging 0.5 to 500 μm . A high speed centrifuge (Figure-1) is used in order to separate these solid particles from the liquid solution.

These devices need to be constructed out of a material that would be compatible with 9 M nitric acid. Two such centrifuges were fabricated and operated at a speed of 18000 RPM. Their speed of rotation was measured by using a custom-made non-contact eddy current sensor. Since these centrifuges are housed in the hotcell that also houses other equipment, it was ascertained that the vibrations from these high-speed centrifuges are not transmitted beyond the permissible level to the structure and other components within the cell.

The coast down and run up plots was made and the results were found to be quite satisfactory. No major resonance build-up was observed during the crossing over of critical speeds by the flexible rotor. During the operation of the centrifuge at its rated speed of around 18000 rpm, vibration velocity spectra were taken from the centrifuge top bearing and bowl region as shown in Figure-2. The operation of the centrifuge was smooth and the overall vibration amplitude was as low as 0.45 mm/s and 0.39 mm/s respectively from the top bearing and centrifuge bowl. Both the process and mechanical performances were satisfactorily verified.

The centrifugal extractors (CE) are the key equipment in fast reactor fuel reprocessing. Since these equipment operate at high speeds, it is necessary ensure that the

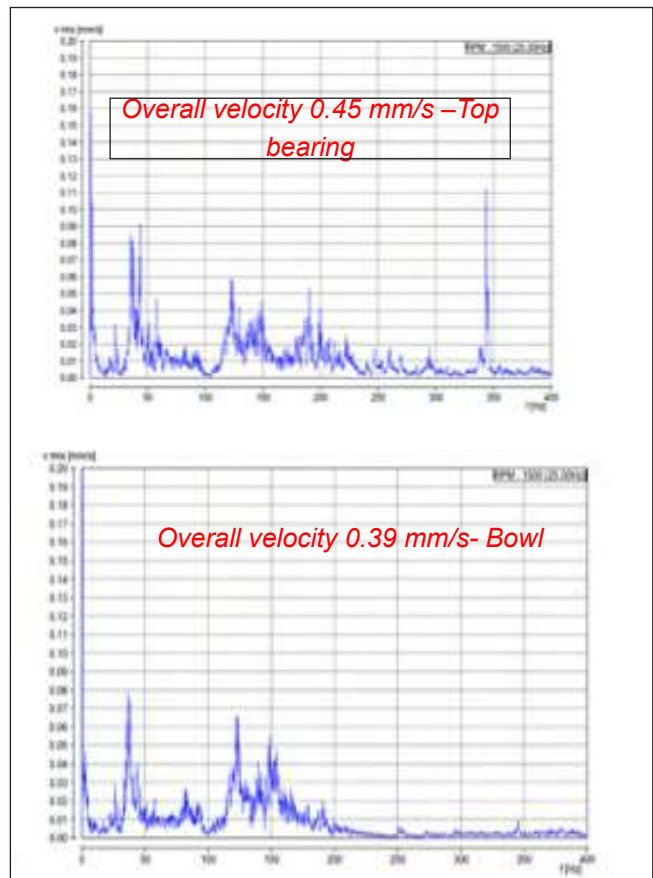


Fig.2: Overall RMS velocities on Centrifuge top bearing and bowl location

vibration of the operating CEs does not adversely affect the other equipment as well as the structural components in the containment boxes. Hence, it is necessary to ascertain the same by carrying out the analyses of the characteristics of the transmitted vibration. It is also important ensure that the vibration transmitted to the glass viewing panels mounted on the containment boxes are brought down to a minimum. High vibrational amplitudes might induce differential tightening loads on the bolts used in fastening the glass panels and could



Fig. 1: Centrifuge assembly with support structure



Fig.3: CE stage with 22 bank

initiate cracks in the glass panels and lead to breach of containment.

In order to investigate the source and severity of these vibrations, accelerometers were placed at different locations where high vibrations were expected, and the RMS velocities, amplitudes and frequency spectra were recorded. In order to minimize these vibrations, the supporting structure of CE and the containment box were modified and stiffened. After these modifications, the RMS velocities and amplitudes on the window flanges

were significantly reduced to -1.7mm/s on the window flange. The maximum value of displacement measured on the window flanges was insignificantly low and was found to be less than deformation thickness of the elastomer seals placed on these glasses.

Thus, it was ensured that the elastomer seal would accommodate any displacement of the window flange on either direction of the glass and no load would act even on the glass panel during normal and even abnormal running condition.

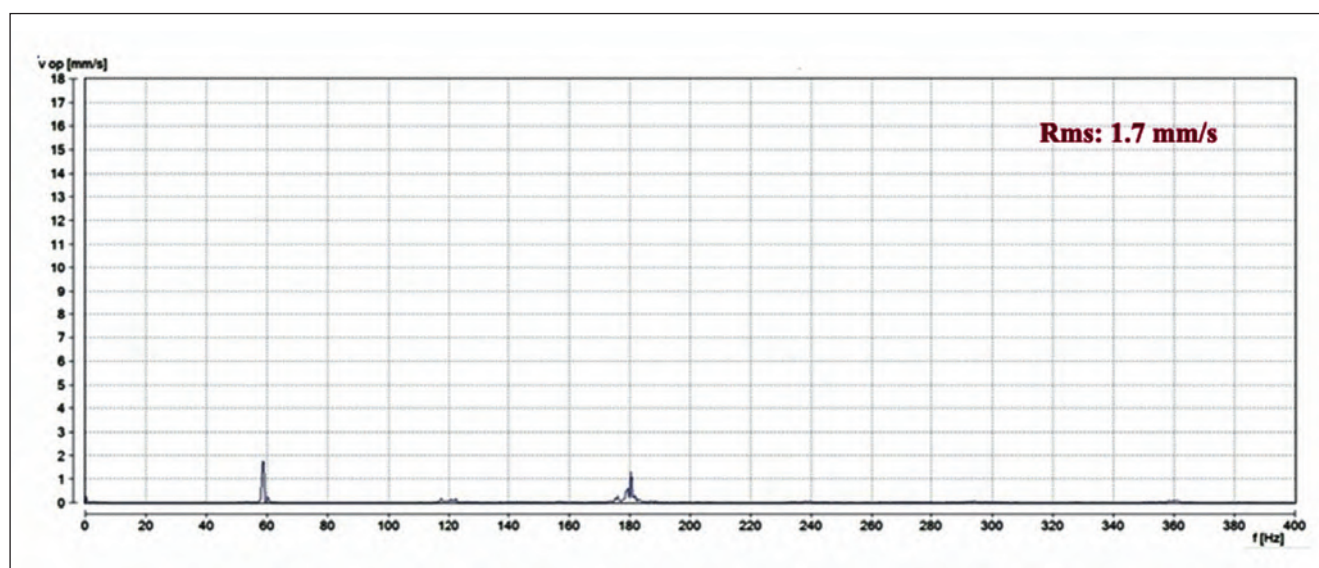


Fig.4: Frequency spectra on window flange

IV.36 Testing of Grease for In-cell Application

In nuclear industry many of the moving components like control drive mechanisms, coolant pumps, valves, fueling machines and other auxiliary equipment for handling spent fuel elements require lubrication. These lubricants are exposed to intense radiation. Further in the reprocessing plants lubricants are exposed to both radiation and oxidizing chemicals such as nitric acid. Selection of a grease with reasonable chemical and radiation stability is an important aspect in this regard. These also need to meet the requirements with respect to their endurance and lubrication of the rotating and moving parts of the in-cell equipment.

Greases are multi-phase systems, which are often a complex mixture of several components. The chemical and physical properties of the grease originate from the co-existence and interaction between various components. Greases range semi-fluid to solid systems originating from the dispersion of a thickener in oil. A commercially available grease was selected for testing the suitability of its application in Reprocessing Plants. The selected grease has hydrocarbon as the base oil, Li as thickener, solid lubricants and has a consistency value of 2. In order to study the suitability of this grease it was irradiated and tested for its compatibility with pertinent chemicals.

For evaluating the suitability of the grease for application in the plant, grease samples were exposed to gamma radiation to the dosage of 5 MGy in a gamma chamber in atmospheric air environment and at ambient temperature. The gamma chamber contains Co-60 as the source having a dose rate of 4.11 kGy/h. These samples were also exposed to vapours of 6 M nitric acid and the effect of radiation and nitric acid vapour on the properties of this grease was tested.

Drop point and worked penetration measurement of the selected grease was carried out in accordance with ASTM D 566 and ASTM D 217 respectively.

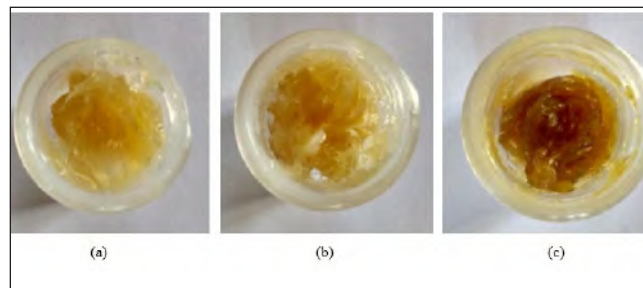


Fig. 1: Pictures showing a) un-irradiated grease, b) 1 MGy irradiated and chemically exposed grease and c) 5 MGy irradiated and chemically exposed grease

This grease was found to undergo degradation in radiation and chemical atmosphere. Upon irradiation and exposure to chemicals radicals are formed. These radicals can cause chain scission or cross linking. Generally both chain scission and cross linking have been observed in which one mechanism is predominant depending on prevailing conditions. The degradation of drop point and worked penetration properties of the grease due to both radiation and chemicals (vapours of 6 M nitric acid) was studied. Figure 1 (a to c) show the photograph of un-irradiated and irradiated grease as well as a grease that was exposed to chemicals.

It was evident from the experiments that up to 1 MGy there is no appreciable degradation. On further irradiation at 5 MGy mild degradation was observed leading to dark colouration. The grease properties; viz., drop point and worked penetration were measured for this grease before and after irradiation and chemical exposure and are given in table 1. Degradation in drop point and worked penetration was found to change by about 10 % or less at a dose of 5 MGy. Our trials demonstrated that the present grease could be used in the plant up to a maximum cumulative dose of 5 MGy. Radiation resistance could be further increased by incorporating an aromatic or an inorganic thickener.

Table 1: Drop point and worked penetration for grease before and after irradiation and chemical exposure.

Property	Un-irradiated grease	1 MGy irradiated and chemically exposed grease	5 MGy irradiated and chemically exposed grease
Drop point (°C)	160	160	170
Worked penetration (10 ⁻¹ mm)	230	225	215

IV.37 Development of a Novel Hydroxyacetamide based Extractant for The Preferential Separation of Zirconium from Simulated High Level Liquid Waste Through Liquid-Liquid Extraction and Extraction Chromatography Methods

Aqueous reprocessing of U-Pu-Zr based metallic fuels would generate high-level liquid waste (HLLW) solutions containing the major fraction of zirconium in the fuel, after recovery of uranium and plutonium. Based on a rough estimation, the zirconium content of HLLW solutions from metallic fuels shall vary from 4 g/L to 8 g/L, based on the dissolution conditions employed for the fuel. As the concentration of zirconium is more than the total concentration of all other fission products and activation products in HLLW, any further treatment of such HLLW solutions from metallic fuels would require a pre-treatment step for selective removal of zirconium. The extraction of zirconium from acidic feeds has been studied by solvent extraction as well as ion exchange methods using various extractants. The aqueous chemistry of zirconium is rather complex, especially at higher concentrations, and only a few extractants have been identified for the separation of zirconium from HLLW solutions.

In the solvent extraction processes for the spent nuclear fuel zirconium has been identified as a troublesome element due to its tendency for the formation of polymeric species leading to the undesirable crud formation at the aqueous-organic interphase. The high polarity and

polymerisation of zirconium complexes limit the loading of zirconium in most of the organic solvents commonly employed for the treatment of HLLW solutions. A novel amide based ligand, *N,N*-Di-octyl-2-hydroxyacetamide (DOHyA) was identified as a suitable extractant for the preferential extraction of zirconium from simulated HLLW (SHLLW) feeds in our recent studies. Compared to the other common extractants based on phosphine oxides or diglycolamides, DOHyA showed better extraction capacity for zirconium due to its lower aggregation tendency in non-polar diluent, *n*-dodecane. A solvent extraction scheme (Figure 1) was studied and proposed for the selective removal of zirconium from SHLLW solutions from metallic fuels.

In the first step, all the zirconium from the waste feed was extracted to an organic phase containing DOHyA in *n*-dodecane. The concentration of DOHyA employed in this step was decided based on the concentration of zirconium in the feed, so as to allow the maximum stoichiometric extraction of zirconium with minimum extraction of other fission products. Under such conditions, it was possible to extract nearly 99% of zirconium in the feed solution along with all the molybdenum in the waste feed. In the second step, all the co-extracted fission products and activation products were selectively scrubbed from this loaded solvent phase using 0.5 M nitric acid. Only zirconium and molybdenum remained in the organic phase, and these were stripped from the organic phase using a suitable aqueous phase in the third step. A stripping formulation of 0.2 M oxalic acid in 0.5 M nitric acid was found to be useful for the selective stripping of zirconium at lower concentrations (< 2 g/L). But prior stripping of molybdenum was essential for the selective recovery of zirconium in this step, when zirconium loading is more than 2 g/L. In all the cases, selective removal of zirconium up to 8 g/L in the simulated HLLW solution was found to be feasible with the use of DOHyA using the proposed scheme (Figure 1).

Solid phase extraction (SPE) was also studied for the separation of Zr(IV) from the feed originating from metal fuel dissolver solution. In SPE, a known amount of the metal selective ligand was attached to a solid phase support (mainly neutral polymeric resins) by solvent impregnation technique.

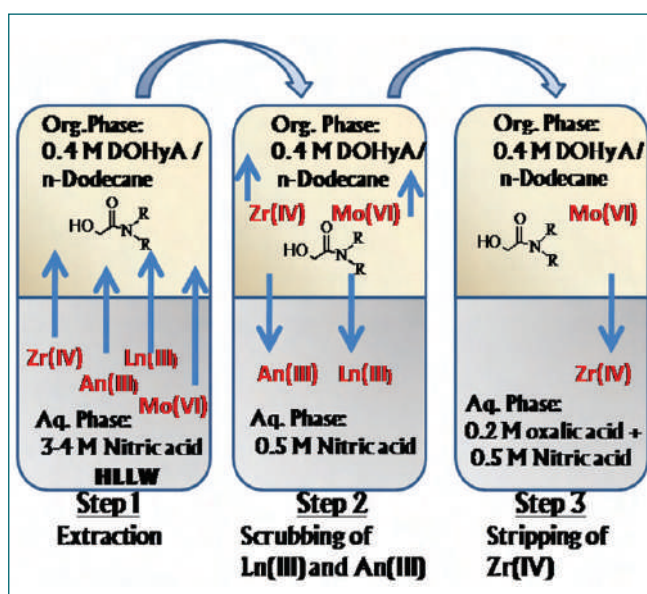


Fig. 1 Proposed solvent extraction scheme for the preferential separation of zirconium from simulated HLLW solutions from U-Pu-Zr alloys

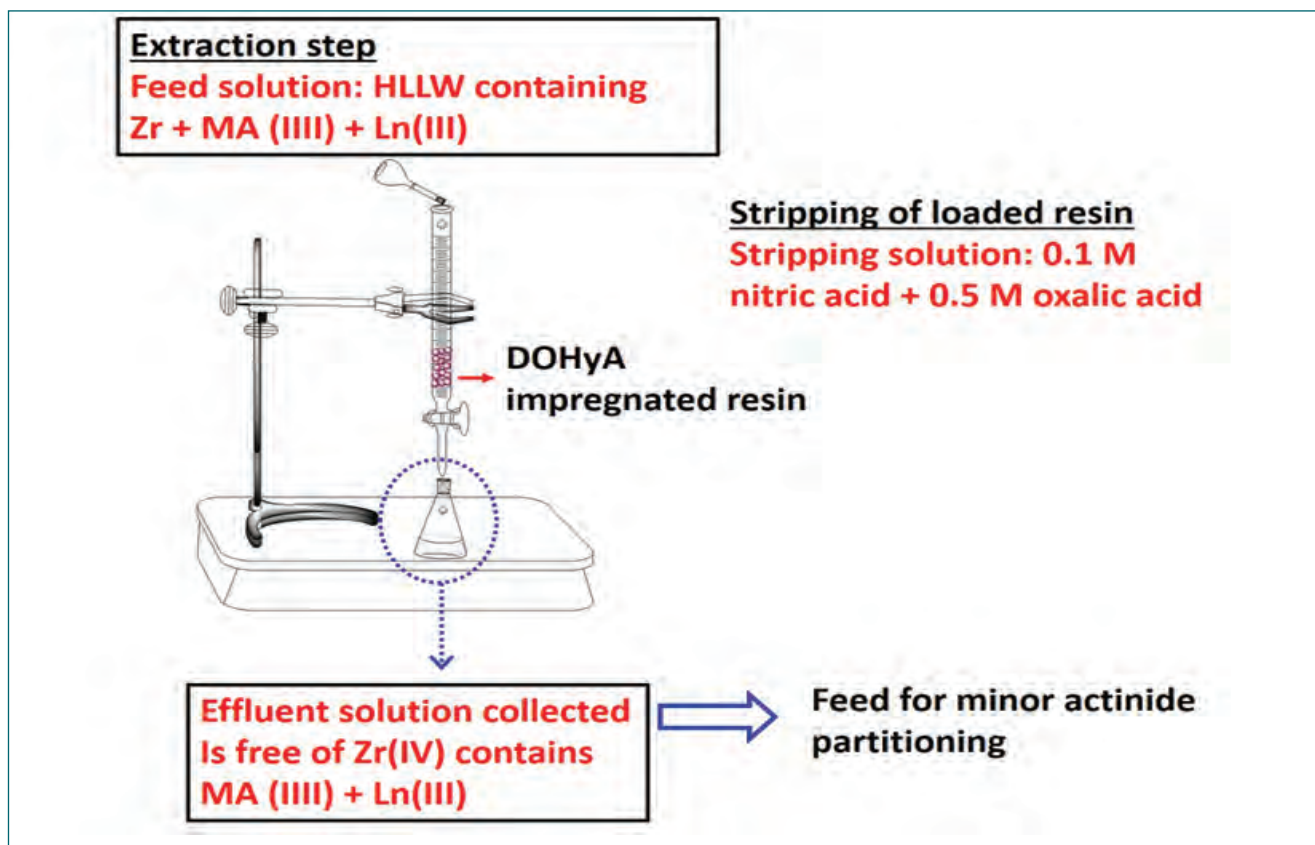


Fig. 2 Proposed Zr extraction scheme from HLLW generated from U-Pu-Zr alloys

Solid phase extraction has merits over liquid-liquid extraction in terms of enhanced selectivity and separation, and there is not issue of third phase or crud formation. DOHyA was impregnated to a polyacrylic resin, commercially available under the brand name Amberlite XAD-7, and was studied for the adsorption of zirconium and other fission products from nitric acid medium. Based on the liquid-liquid extraction and column experiments, a flow-sheet for the selective removal of zirconium from the feed solution was developed, so that the resultant high-level waste would be amenable for further processing.

Adsorption of Zr(IV), Nd(III) and U(VI) at different acidity (nitric acid) present in the aqueous feed indicates that the uptake of Zr(IV) to resin (DOHyA/XAD-7) phase is very high (~ > 99 %) at all the concentrations ranging from 0.5 to 4 M, whereas lesser amounts of Nd(III) and U(VI) were adsorbed to resin phase. The separation factors achieved at 4 M nitric acid for the separation of Zr(IV) from Nd(III) is approximately 1000 and for the separation of Zr(IV) from U(VI) is approximately 800. Recovery of the loaded Zr(IV) was investigated by employing four different aqueous phases: 0.1 M nitric acid, 0.1 M oxalic acid + 0.1 M nitric acid, 0.2 M oxalic acid + 0.1 M nitric acid and 0.5 M oxalic acid + 0.1 M nitric acid. Among these 0.5 M oxalic acid + 0.1 M nitric acid showed quantitative stripping of Zr(IV) in minimum stages.

Extraction behavior of Zr from SHLLW containing 2 g of the resin was studied by column (glass column of 8 mm (inner) diameter) chromatography. 200 mL of SHLLW containing 500 mg.L⁻¹ of Zr(IV) was passed through the packed resin at a flow rate of 1 mL/min. 10 mL of effluent fractions were collected, which were subsequently analyzed for concentrations of Zr(IV) and lanthanides by ICP-OES analyses. Zr(IV) extraction was above 99 % in first four fractions, which corresponds to 40 mL of the effluent collection. During the first two stages, some amount of U(VI) and lanthanides such as Eu, Sm, Nd, Dy and Pr were extracted to a smaller extent: U(VI) was extracted up to 68 % during the first stage (10 mL), Nd(III) was extracted up to 23 %. However, lighter lanthanides such as La and Ce were extracted to a smaller extent, even in first stage. The better extraction observed for loading of Zr(IV) during initial stages should be due to the enhanced selectivity of DOHyA towards Zr(IV) over other lanthanides. The extraction of Zr(IV) decreases after 10 stages due to saturation. Quantitative recovery of the loaded Zr(IV) was achieved by employing 0.1 M nitric acid and 0.5 M oxalic acid + 0.1 M nitric acid. Based on the selective separation of Zr(IV) over trivalent elements, a modified approach for processing HLLW obtained out of U-Pu-Zr was devised and is shown in Figure 2.

IV.38 Design and Structural Analysis of Large Capacity High Level Liquid Waste Storage Tank and Aid on Components for its Handling, Safe Transportation and Installation at the Underground Farms

Fast reactor fuel Reprocessing Plant (FRP) at the Fast Reactor Fuel Cycle Facility (FRFCF) will generate large quantities of high level liquid wastes. Large volumes of these radioactive wastes need to be stored underground in large capacity waste storage tanks to be housed at the Waste Tank Farm of the FRP. These tanks need to be designed to last for about 40 years and more and should hold their integrity, in a highly radioactive and corrosive environment throughout this period. In view of these stringent requirements, utmost care was taken at every stage viz. design, material procurement, manufacturing, transportation, installation and preservation, which are all challenging tasks. The detailed engineering design of these tanks were analyzed for the effect of internal / external pressure, thermal loading, hydrostatic and hydrodynamic loading on these tanks. A 3D model of the one such tank shown in Figure 1 was generated to check the interference of internal components.

The structural integrity of these tanks were ensured for sustained load as well as for any Design Basis Accidents (DBA) namely PCW failure, buoyancy in case of flood or a seismic event. Towards this, a finite element model of this tank was developed and analysis was carried out considering different loads and their combinations as shown in Figure 2 and qualified as per ASME Sub section NC.

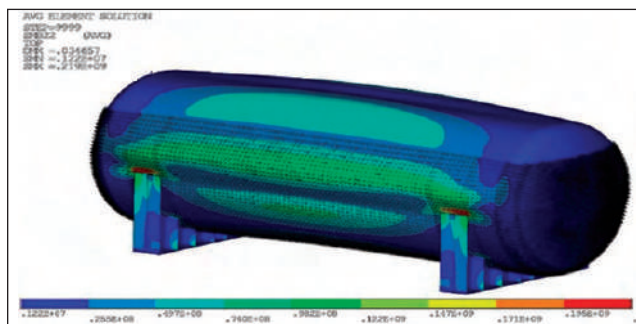


Fig.2: FE analysis of HLW Tank

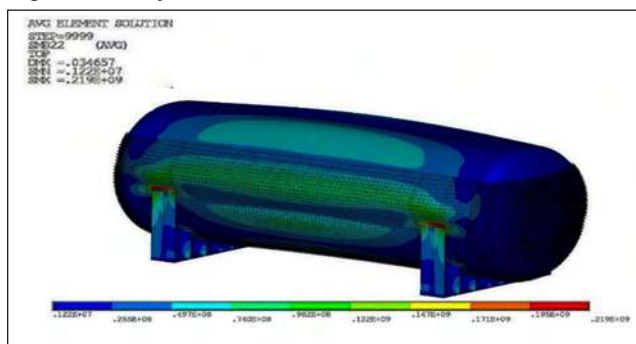


Fig.3: FE analysis of spreader beam and tank lifting lug

During the transportation and installation, these tanks are handled using the lifting lugs, which are a critical part of this system. The positioning and orientation of the lifting is important to minimize the induced stresses. The design and analyses of the lifting lugs were carried

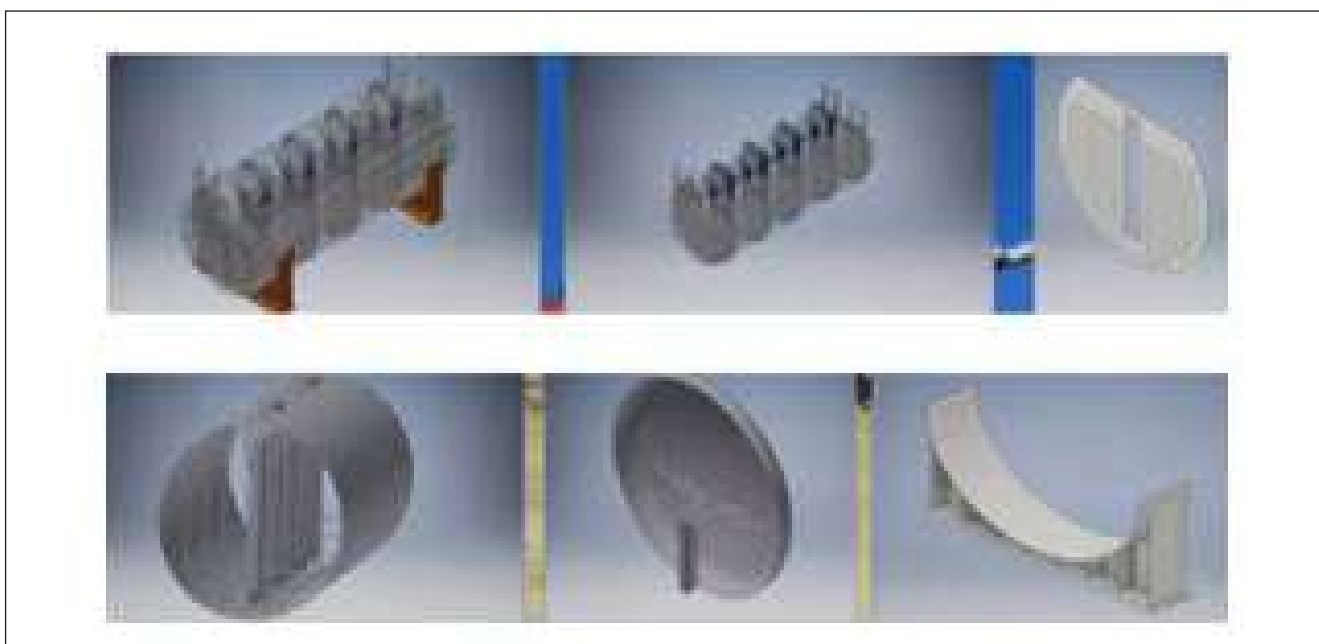


Fig.1: 3D model of HLW tank with internal component

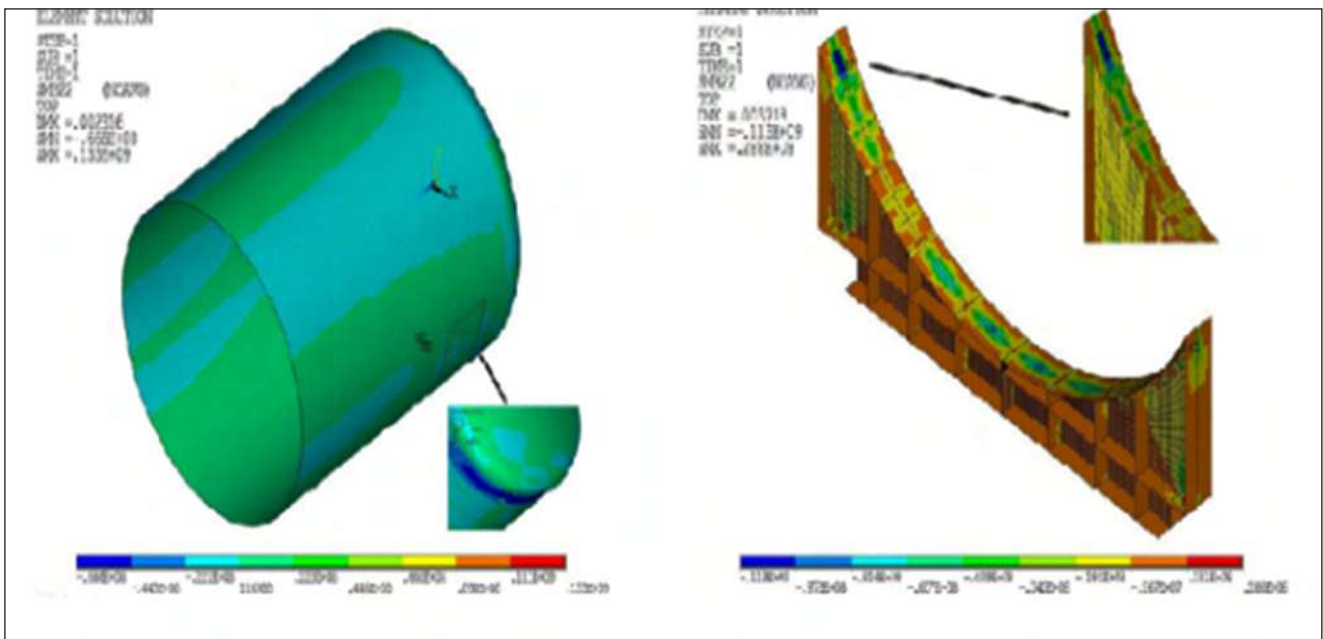


Fig.4: Analysis of Temporary saddle and tank assessment

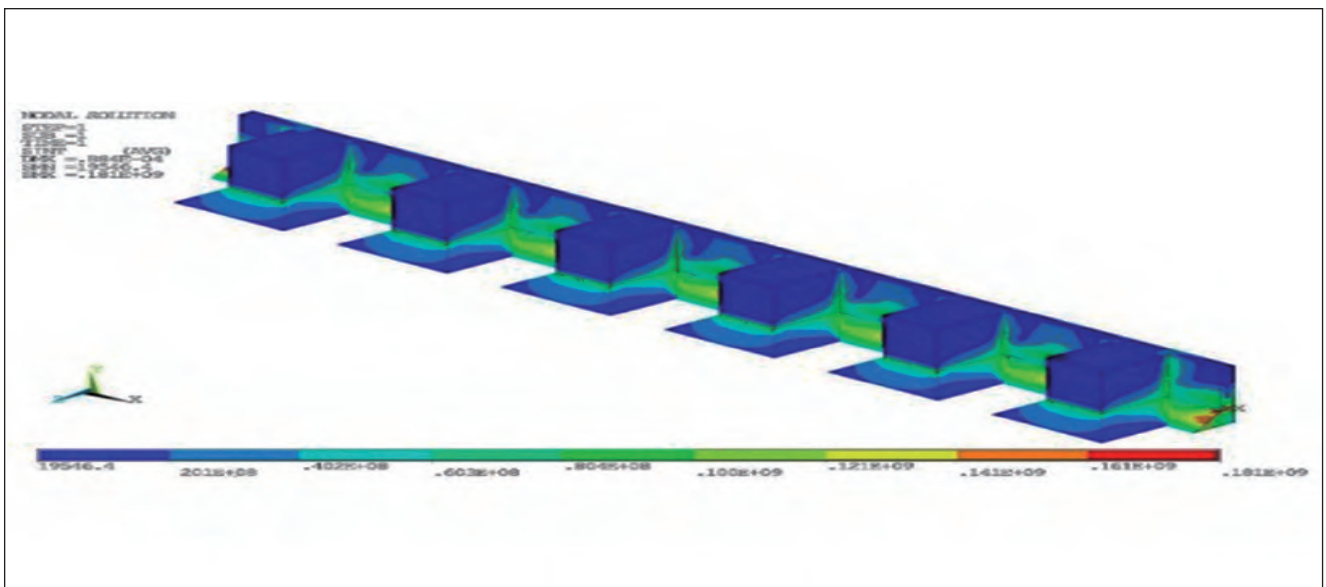


Fig.5: Analysis of saddle fixtures

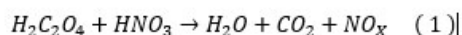
out paying due consideration to the impact load as per the design code requirement and were implemented. In order to distribute the load evenly over the lifting lugs while lifting and handling, a spreader beam was designed and the FE analysis of the same was carried out. The FE analyses results are shown in Figure 3. During the installation of these tanks in WTF at -10.5m level, these tanks had to be lifted / lowered with the help of a special strand jack system, skidded to their respective locations by skid track system. The alignment of the tank saddle to the EP pedestal is done by providing a temporary saddle. Hence, the FE analysis of these Over Dimensional Component (ODC) tank was done to assess the suitability of the use of a temporary saddle. In addition, to check the structural integrity of temporary saddle under the load of the ODC

tank, a preliminary design of the temporary saddle was conceptualized, and an iterative FE analyses was carried out. Thus the temporary saddle design was finalized and implemented (Figure 4)

The WTF tanks were designed with the saddle support connection with foundation, of which one is fixed while the other sliding to accommodate thermal expansion. The support connection between the pedestal and fixed/ sliding saddle were designed, their structural analyses had been carried out under seismic loading as shown in Figure 5. The multidisciplinary task involved in the design and analysis of the tank and aid on components, manufacture, transportation and installation at -10.5m level of WTF/FRP/FRFCF have been successfully accomplished.

IV.39 Catalytic Denitration Process for Treatment of High Level Liquid Waste in Fuel Reprocessing

Spent nuclear fuel generated from the nuclear reactors has been reprocessed by employing Plutonium Uranium Recovery by Extraction (PUREX) process. The raffinate of PUREX process is called as high level liquid waste (HLLW) and contains uranium & plutonium residues, minor actinides and long lived fission products. This HLLW having more than 95% of the total radioactivity of spent nuclear fuel and 2-6 M of nitric acid concentration. Such composition makes it one of the most undesirable corrosive wastes generated in any reprocessing plant. The HLLW from reprocessing plant is transferred to the waste immobilization plant (WIP) for final disposal. The final disposal process includes nitric acid killing followed by vitrification. The acid killing in HLLW can be achieved in a multiple ways but the chemical denitration process which uses a reducing agent is most suitable. Among many reducing agents like sugar, formaldehyde and formic acid, formaldehyde is widely used for denitration due to the good reaction rate it offers as well as lack of precipitates. However the formaldehyde based process suffers from excessively rapid reaction, high exothermicity and build-up of formic acid and foam in the reaction mixture. In order to overcome these issues an alternate process that employs oxalic acid is being contemplated.



Even though the reaction between oxalic acid and nitric acid is thermodynamically feasible its kinetic is very slow. The reaction (1) would proceed at a significant rate only if the reaction is performed by refluxing the concentration with nitric acid (>9M). However this mixture is highly corrosive. Alternatively the reaction rate could be enhanced by using a catalyst, so a Mn²⁺

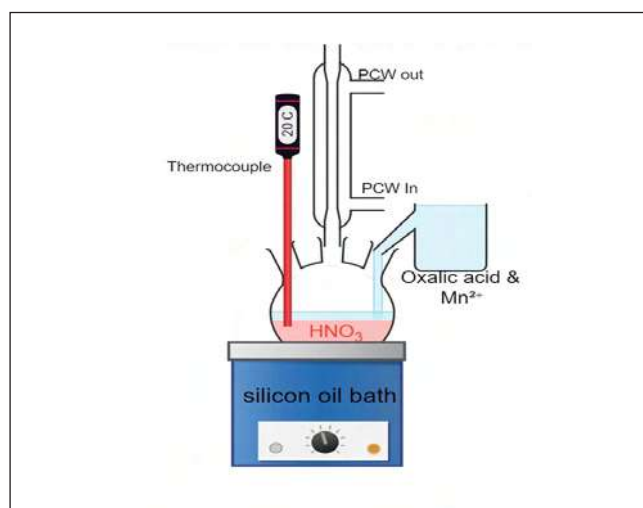
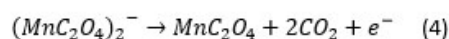
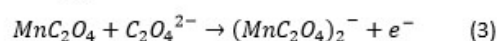
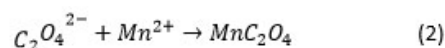


Fig. 1: Photo of precipitator column



Fig. 2. Equipment set up for catalytic denitration

based catalytic denitration was tested at laboratory scale with simulated HLLW. The autocatalytic mechanism of Mn²⁺ is explained in equation (2 - 4).



The Simulated HLLW is heated upto 375 K using a silicon oil bath. When the required temperature (375 K) is reached, oxalic acid along with catalyst was added. Figure 1 & 2 show the experimental set up. The sample from reaction mixture was drawn at regular intervals of time and analyzed for oxalic acid and nitric acid concentration. These concentration profile as a function of time is graphically presented in Figure 3. The result indicates that nitric acid concentration decreases by almost 40% within 3 h without the formation of any foam or precipitate. The catalytic denitration method offers all the advantages of the formaldehyde based process while it is also free from the inherent shortcoming of formaldehyde. The newly developed method is simple, safe and has the ease of operational and process control. It can be a potential alternative for formaldehyde based denitration process.

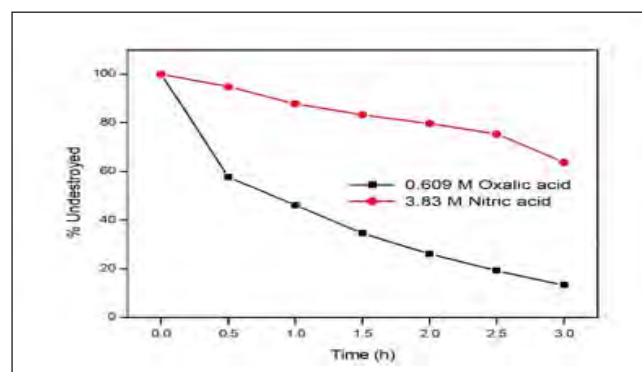


Fig.3: % Undestroyed oxalic acid and nitric acid v/s time at 375 K

IV.40 Quality Assurance and Non-destructive Examination for Rotating Bowl of Centrifugal Extractor used in Reprocessing Plant

Annular centrifugal extractor (CE) is used in reprocessing of spent fuel from fast breeder reactor. Many advantages such as low residence time, high efficiency of mass transfer and quick attainment of steady state etc. supports this option. Extraction process is carried out from a mixture of fluid containing organic compound, fission products and high concentration nitric acid using centrifugal action provided by rotating bowls (RB). Good dynamic and surface properties of RB are required for harmless vibration and corrosion levels. Good quality surface conditions and reasonable geometrical parameters particularly cylindricity of fabricated RB is needed to achieve the same. The level of quality control of circumferential closing seam weld joints (Figure 1a) between thin parts of RB cylinder is the main factor to achieve this. Gas tungsten arc welding (GTAW) using specially designed fixture with guided type joint design (Figure 1b) and sequential welding has been utilised to obtain weld joints with acceptable surfaces and geometry. The outer surface of welded structure are maintained minimum at surface finish N8 with a cylindricity (run out) of 0.1 mm by machining. It has been observed by examination (visual, LPE and radiographic) of cut sections of RB (Figure 2a,2b &2c) that irregular inside surface profiles particularly due to lack of penetration in circumferential weld joints predominantly affect the dynamic balancing (DB) of fabricated RB. This often leads to rejection of completely fabricated RB. However, complete examination of internal surfaces is difficult due to lack of approach

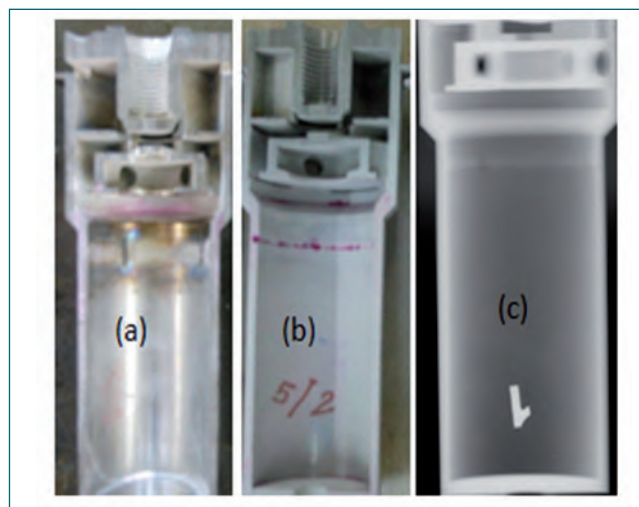


Fig. 2 internal surface examination of cut section of fabricated RB (a) visual examination showing complete penetration, RB qualified dynamic balancing requirement, (b) LPE showing lack of penetration in root and (c) X-ray showing lack of fusion at junction of guided faces, couldn't qualify the dynamic balancing as per ISO 1940gr.G2.5

and difficult to obtain meaningful radiograph of circumferential weld joints due to abutting surfaces of internal structural components.

The concern has been addressed in welding procedure qualification (WPQR) test, by augmenting the test requirements. The WPQR was carried out using similar joint design and fixture. Welding sequence, heat input and other variables have been identified based on the test results of the transverse tensile and bend test,

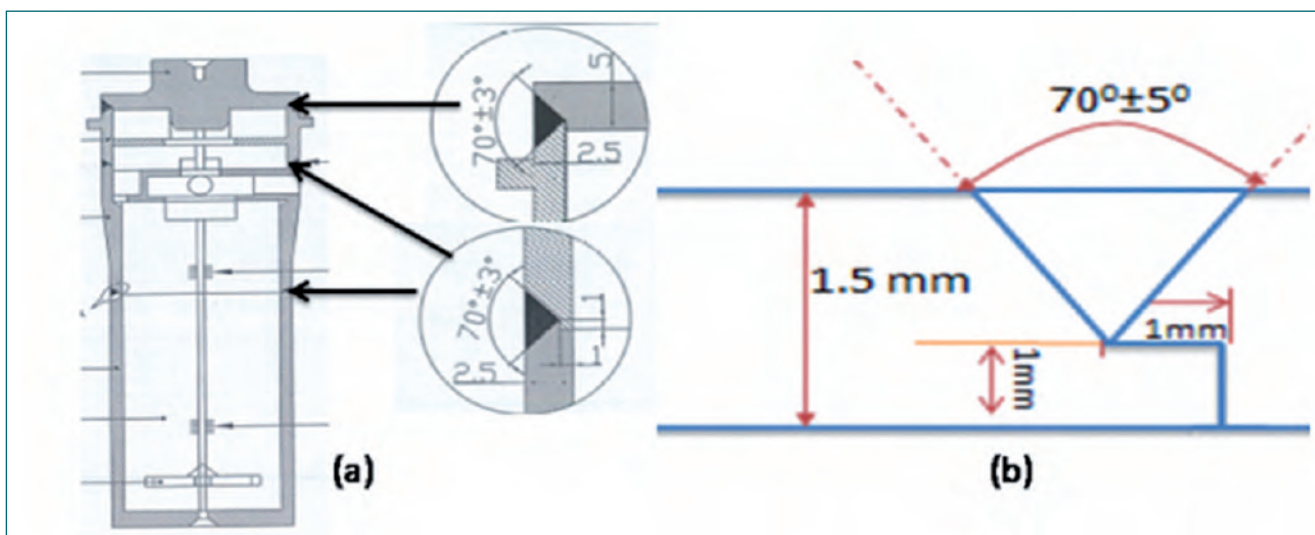


Fig. 1 Rotating bowl (a) weld map showing location and detail of circumferential weld joints (b) detailed view of guided type joint design

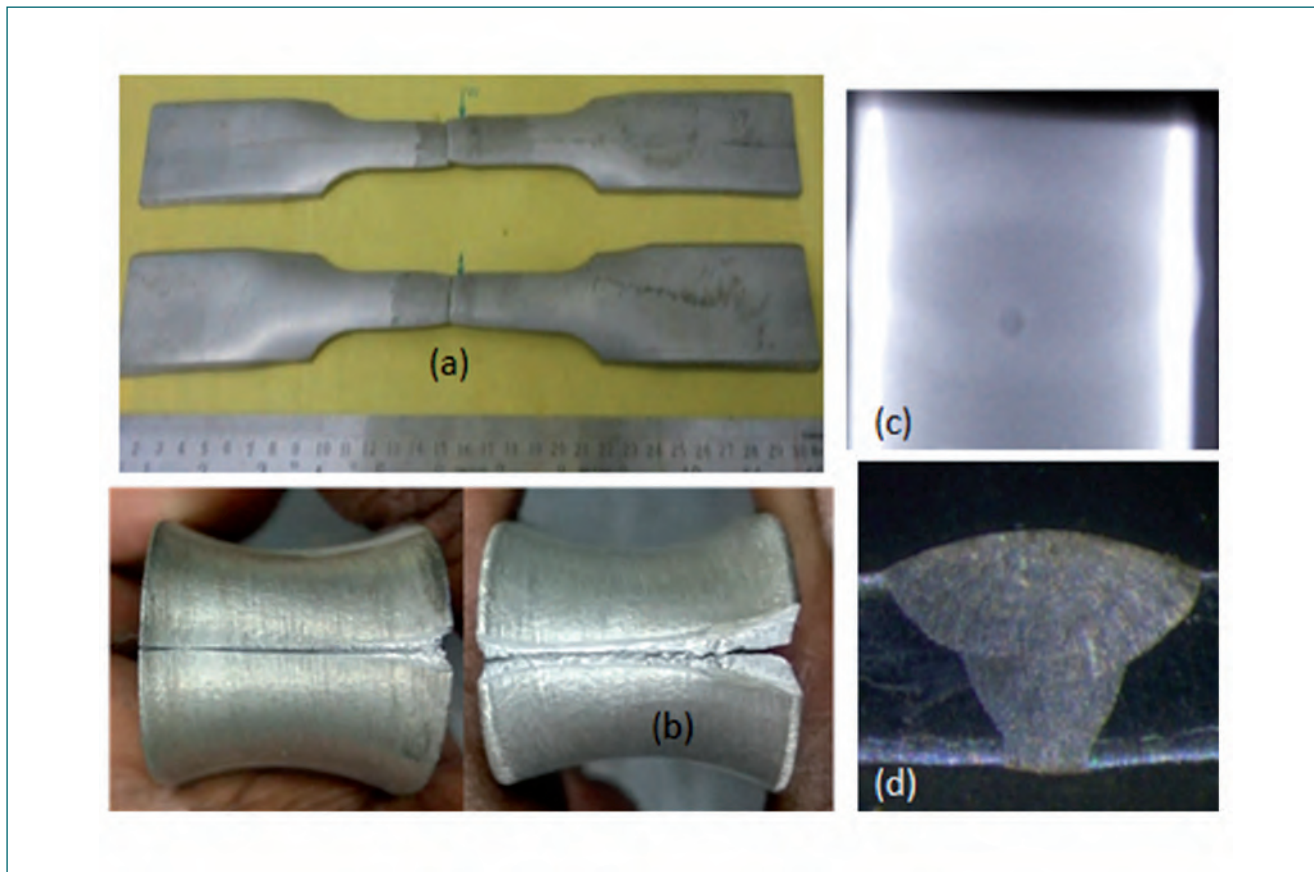


Fig. 3 Test results of WPQR (a) transverse tensile test , failure can be seen on base metal (b) initially lack of fusion observed in root bend test, after changes in heat input acceptable results are observed, (c) porosity observed initially, due to faulty unclean fit up (d) macro examination showing complete penetration in given joint design

Table 1: Recommended essential variables	
Variable	Address the concerns related to RB
Joint design	Helps in providing even internal surface with optimum penetration and distortion control.
Heat input	Corrosion ,distortion control
Position and welding sequence	Welding uniformity, even mass distribution and distortion control
Clean fit-up	Porosity, mass distribution
Radiography test	Any detectable defect
Macro-examination	optimum penetration

radiography, LPE, visual and macro examination of weld cross section. The IGC practice C of ASTM 262 has been carried out with maximum exposure of HAZ to ascertain corrosion rates at par with base metal. Figure 3 shows few test results during WPQR.

Table 1 shows the summary of the recommended welding variables to be kept as essential apart from the recommendations of ASME sec IX for GTAW.

The rejection of fabricated RB reduced drastically during dynamic balancing by the use of given welding procedure specification.

IV.41 Feasibility Studies on use of Single Piece Bottom Closure for geometrically Safe Annular Tanks for Reprocessing Plants

Annular tanks are used in nuclear reprocessing plants for storing fissile solution in an annular space of 60 mm formed between inner and out shell vertically. A typical annular tank is fabricated by closing annular space between concentrically and vertically positioned inner and outer shell by means of upper and lower flanges with full penetration corner joints as shown in Figure 1a. The corner joint may be regarded as a butt joint which is used to join two plates at right angles to each other as shown in Figure 1b. Corner weld joints are difficult to assemble and also to maintain correct alignment particularly due to slender thickness shells, welding of lug plates welding and distortion due to high heat input. The aforementioned problems to some degree, to produce the lack of root weld penetration and root undercut (crevice) during welding.

Distortion of flanges associated with nozzles welding makes misalignment with inner and outer shells which in-turn results in indication during Ultrasonic inspection from weld root geometry. Moreover weld root reinforcement favored to beam angle also produces spurious indications at root side as shown in Figure 1c. Since the scanning only at shell side (single side only), discrimination of spurious indications from defect signals at weld root is tedious and sometimes misleading too.

It has been decided, for the purpose of alleviating the aforementioned problems to some degree, to produce an annular tank using single piece bottom enclosure by machining route to facilitate the full penetration butt weld joint with inner and outer shells. To demonstrate fabrication and NDE feasibility study, single piece bottom enclosures of 120° segment is machined from solid bar



Fig. 2 Machined single piece bottom enclosure

by using CNC vertical Milling machine (2 Nos of 60° segments) as shown in Figure 2.

The Residual stresses, both in axial and hoop directions are measured on the ID and OD sides location of machined component, using X- ray diffraction technique within the depth of 10 μm from surface. Both the axial and hoop stresses on the ID and the OD sides of enclosure were compressive as shown in Figure 3. The compressive residual stress at the surface of a component is tends to increase fatigue strength and fatigue life, slow crack propagation, and increase resistance to environmentally assisted cracking.

Single piece bottom enclosure avoids corner weld joint and facilitates butt weld joints between flanges and shells which in-turn ensures good root weld penetration and 100 % weld volume inspection by radiographic examination in-lieu of ultrasonic examination. X-Radiography of welds were performed using equivalent to double wall double image techniques with suitable offset to cover the outer and inner shells welds of 60 mm annular gap in single exposure as shown in Fig 4. The radiographic examination of welds are successfully completed with 2% equivalent sensitivity and meeting the ASME section III division I subsection NC class 2 components requirements.



Fig. 1 (a) Annular tank assembly (b) shell with flange corner joint and ((c) UT signal from weld root

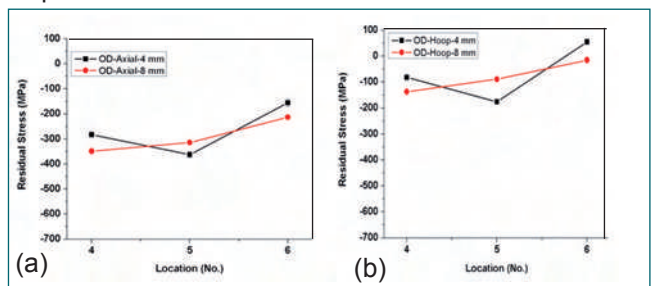


Fig. 3 Residual stress measurement in (a)axial and (b) hoop directions

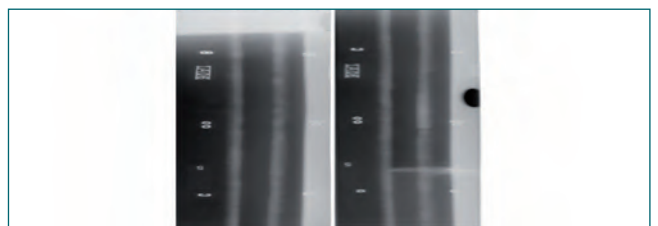


Fig. 4 RT image of weld joints

IV.42 Establishment of Fabrication Sequence during Manufacturing of Jacketed Cylindrical Tanks for Back End Fuel Cycle Facility

Jacketed vertical cylindrical tanks, as shown in Figure 1a, are used for storing high level radioactive liquid waste in shell surrounded by cooling water jacket for removing radioactive decay heat. Austenitic Stainless Steel 304L has been used as the work horse material. The tank is fabricated from a 12 mm thick plate and welded with torispherical dish ends at both ends and surrounded by jacket made of 6 mm thick plate connected with top and bottom rings of 8 mm thick as shown in Figure 1b. Typical dimensions of a jacketed cylindrical tank are: Inner diameter of shell 1030 mm, Outer diameter of jacketed shell 1154 mm and overall height 1922 mm.

Weld joint connecting cooling water jacket flange with main shell is of 'T' joint with Single bevel limited to access only from face side of the weld as shown in Figure 1b. Code of construction being followed for fabrication of such tank is ASME Section III Division 1 NC. Code calls for 100% volumetric examination of all T joint welds by suitable non-destructive technique. Radiography and ultrasonic examination are the widely used and codified NDT techniques. Due to weld joint configuration and accessibility, Volumetric NDT by radiographic examinations is precluded as it is not possible to achieve the required quality parameters (optical density & Sensitivity) due to the access limitations. So the conventional ultrasonic examination using the 45° and 60° contact angle beam technique is used to scan

the weld from flange side with 2 mm side drilled hole as reference reflector as shown in Figure 1c as a measure of sensitivity.

Due to dissimilar thickness of shell and flange along with single bevel at shell side, controlling heat input and producing full penetration sound welds during welding is a real challenge. During the scanning of the weld joints at the top and bottom rings, continuous indications which crossed the 50% and 100% of DAC and spotted at shell root side of weld joint were reported. Since 'T' weld joints are not accessible for any root visual weld examination, it is a real challenge to discriminate the flaw from spurious indications produced from weld root geometry as shown in Figure 1d.

To validate the defect indication from spurious indication, 'T' weld joint mock up piece, as shown in Figure 1e, simulating the actual production conditions has been fabricated. The same weld joint is visually examined and observed for the lack of penetration (LOP) at shell side as shown in Figure 1f. UT signals of production and mock up weld joints are compared. It has been observed that both the signals are similar in nature based on beam path and depth from surface. Based on the UT results, the tank is opened and observed for the LOP at shell side as shown in Figure 1g. Fabrication sequence has been changed to facilitate double sided welding of flanges with shell and deposited the sound weld as per the codal requirements.

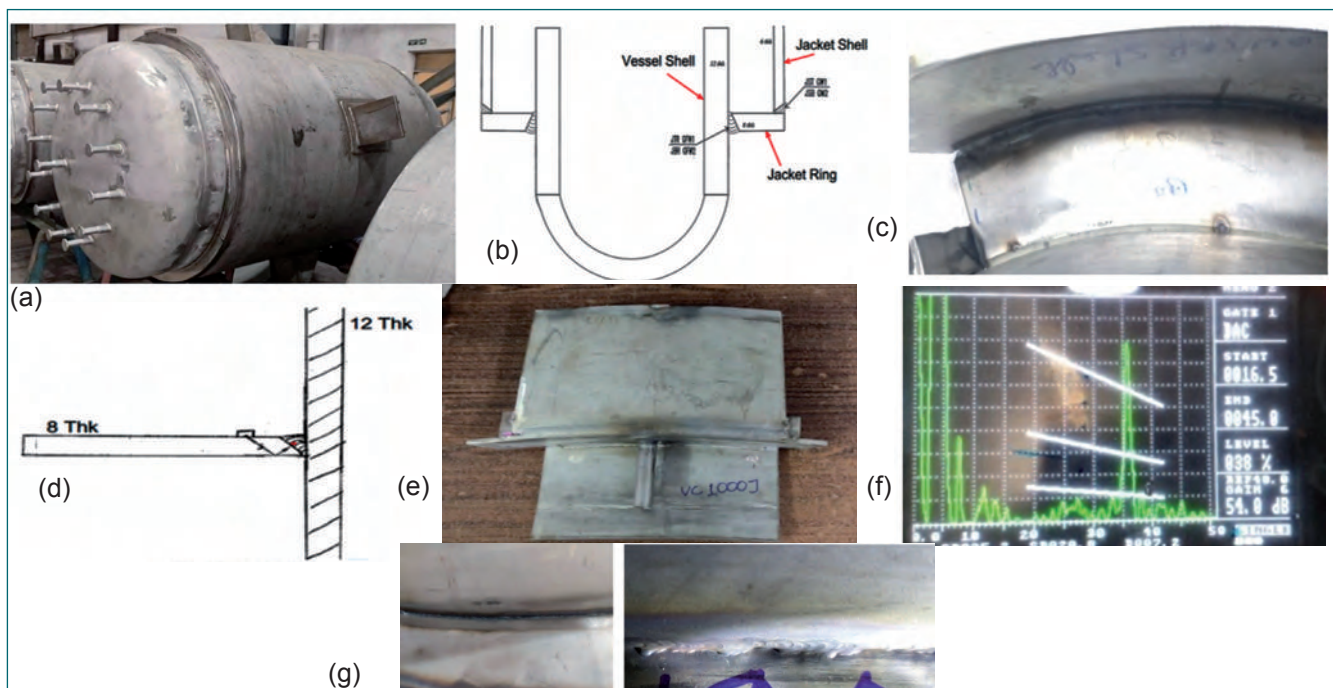
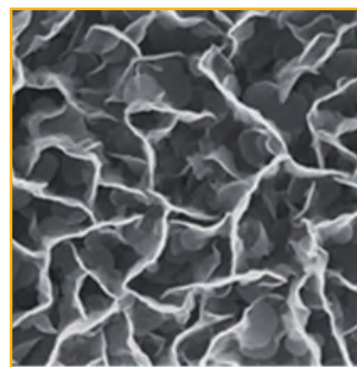
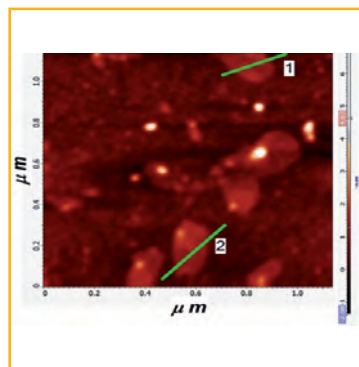
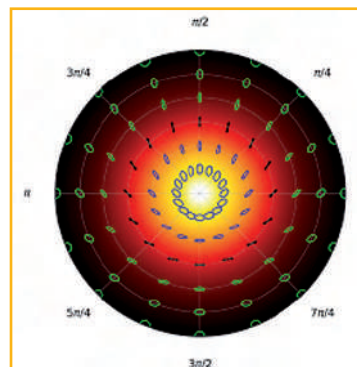
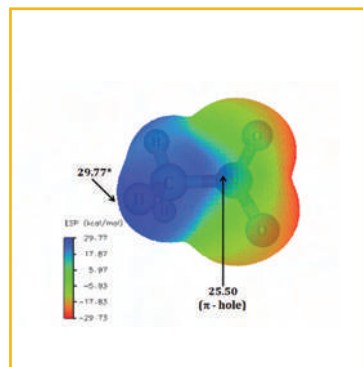


Fig. 1 (a) Jacketed cylindrical tank VC 1000J (b) Schematic diagram of VC 1000J (c) UT reference block (d) Main shell with flange 'T' weld joint (e) 'T' weld joint mock-up weld (f) UT signal from LOP and (g) Lack of weld penetration at shell side of 12 mm thickness



Basic Research

CHAPTER V

V.01 Development of Portable Cadmium Zinc Telluride based Gamma Radiation Detector

Research and development of sensor element used in radiation detectors is very important to achieve self-sufficiency in indigenization of different radiation monitoring devices used by nuclear facilities and reactors. Silicon and high purity germanium (HpGe) based detectors, with high energy resolution are being successfully used for radiation monitoring. However, one of the major drawbacks in these detectors is the requirement of cryogenics for operation. In this connection, IGCAR has envisaged to indigenously develop portable room temperature Cadmium Zinc Telluride (CZT) based gamma spectrometer.

CZT based detectors with wide bandgap (~1.57 eV), high atomic number, high resistivity (~ 10^{10} Ω -cm) and high electron mobility-lifetime product ($mt \sim 5 \times 10^{-3}$ cm^2/V) are ideal candidate for room temperature radiation detection. However, the growth of high-quality CZT single crystals involves several challenges due to inherent materials properties.

Travelling heater method (THM) is the most common techniques used for growing detector grade CZT crystals. The schematic of the indigenously designed and fabricated THM system is shown in Figure 1. A photograph of a typical grown CZT single crystal with optimized growth parameter is shown in the inset of Figure 1. The cut wafers from the crystal boule were lapped and then polished with progressively decreasing Al_2O_3 particle size from 5 μm to 50 nm. The wafers were properly etched and passivated. Gold electrodes were



Fig. 1 Schematic of THM setup and photograph of a typical grown CZT crystal

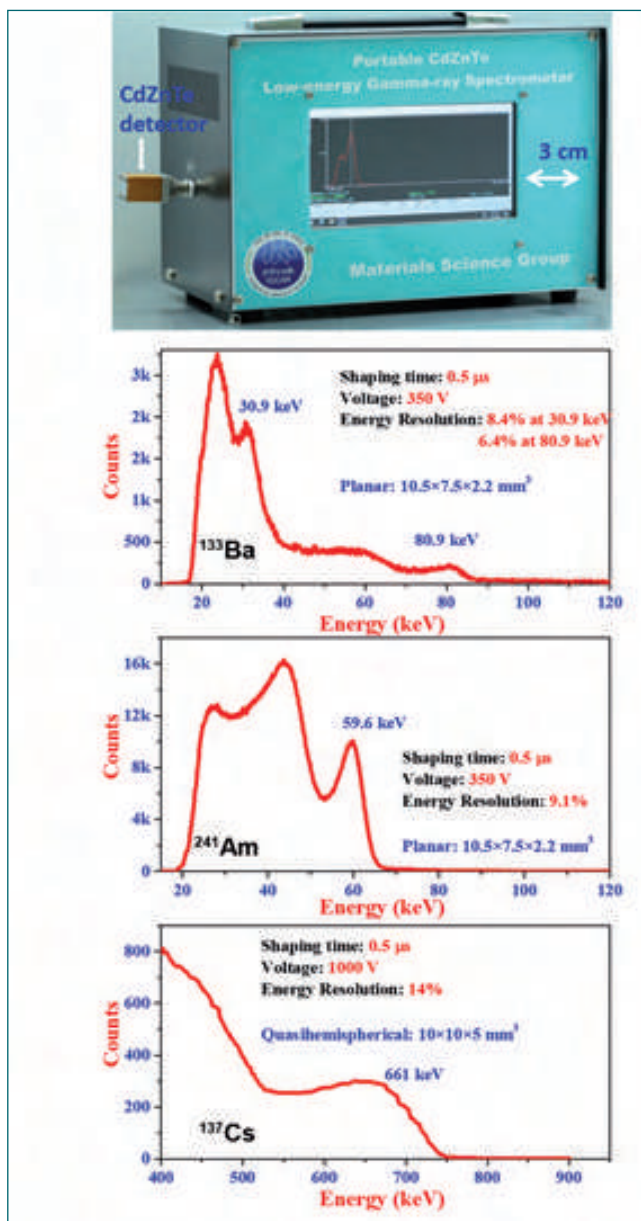


Fig. 2 The crystal housing attached to the in-house developed portable gamma-spectrometer. Acquired Gamma spectrum of ^{133}Ba , ^{241}Am and ^{137}Cs and its energy resolution

deposited using electroless process. The CZT crystals was housed in aluminum casing with BNC connector and attached to an in-house developed portable gamma spectrometer as shown in Figure 2.

The photo peak of ^{241}Am and ^{133}Ba at 59.5 keV and 81 keV were resolved with an energy resolution of 8-9% whereas, ^{137}Cs was resolved at a resolution of 14%. Further developments in growing high-quality single crystal, device fabrication process and signal analysis electronics are in progress to improve the sensitivity and resolution.

V.02 Understanding the Darkening of White Amorphous TiO₂ under X-ray Irradiation

Amorphous TiO₂ powders when exposed to x-rays, turned darker with increasing exposure time while the highly crystalline forms of TiO₂ (anatase and rutile), showed no color change as shown in Figure 1. To understand the difference between the defect states generated and the process involved in defect generation during x-ray irradiation and ion sputtering, Ar⁺ ion beam irradiation was carried out on different phases of TiO₂ (amorphous, anatase and rutile). In this process, all the phases turned to grey color irreversibly (Figure 1) on exposure to air. This indicated that the surface chemistry in both the cases is different. The colors of the powders after sputtering were identical (grey), suggesting that the modified surfaces are identical irrespective of their phases.

The valence bands of the x-ray exposed amorphous TiO₂ powders showed a single broad band structure while that of the crystalline TiO₂ powders showed a dual-lobe structure. The valence band maximum (VBM) of the amorphous TiO₂ powders was at ~ 3.3 eV below Fermi level while that of the anatase phase was at ~ 2.8 eV (Figure 2), suggesting that the amorphous TiO₂ has a larger band gap, and thus the insulating behavior, as compared to the anatase phase. The absence of additional states in the region between the Fermi level (0 eV) and VBM in all the three TiO₂ powders suggest the absence of the lower oxidation states of Ti, especially the Ti³⁺ (3d) states. The Ar⁺ ion sputtered anatase phase of TiO₂ showed sputter induced amorphization of crystalline TiO₂ surface. The band also shows an increase in additional states beyond the VBM till the Fermi level, peaking at ~ 1 eV, due to the creation of Ti³⁺ and Ti²⁺ states. These additional states are found to be responsible for the conducting nature of the sputtered TiO₂ powders.

These results suggest that oxygen vacancies (V_Os) and Ti³⁺/Ti²⁺ defect states in TiO₂ are found to be responsible

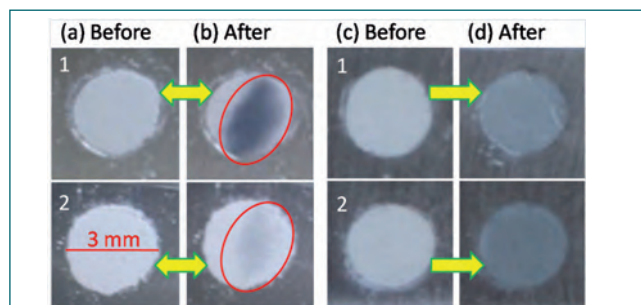


Fig. 1 Photographs of different TiO₂ powders (a) before x-ray exposure, (b) exposed to x-ray, (c) before sputtering and (d) sputtered with Ar⁺ ions. Legends: (1) White amorphous TiO₂ formed at room temperature. (2) Anatase TiO₂

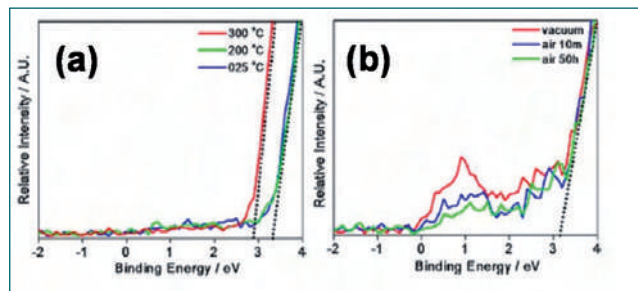


Fig. 2 XPS valence band spectra (Valence band maximum - Fermi level region) of amorphous TiO₂ (a) at room temperature, calcined at 200 and 300 °C after x-ray exposure, (b) calcined at 300 °C after Ar⁺ ion sputter and air exposure for different time periods

for the darkening (blackening or graying) of TiO₂ on x-ray irradiation and sputtering, respectively. The V_Os are highly unstable on air (oxygen) exposure, while the Ti³⁺/Ti²⁺ states are relatively stable as compared to the V_Os. The presence of Ti³⁺ or Ti²⁺ states in the surface or bulk of a TiO₂ particle can form a stable black TiO₂, whereas in the case of V_Os, the black TiO₂ can be stable only in air if the V_Os are present in the bulk. These results indicate that x-ray induced blackening of TiO₂ in ultrahigh vacuum is caused by the lower V_O formation energy and the insulating nature of amorphous TiO₂. The approximate thickness of the modified oxide layers over the TiO₂ particles surface was estimated and was in the range of 0.5-0.9 nm. The ultrathin surface layer (~1 nm) of TiO_{2-x} due to V_O creation on x-ray irradiation was responsible for the “reversible switching” of color in TiO₂ powder which is schematically shown in Figure 3. The reversible darkening of amorphous TiO₂ may have potential applications in the controlled tuning of resistive switching in metal–insulator–metal structures for nanoscale nonvolatile memory devices, nanoionic switches, adaptive electronic components, and watermarking security.

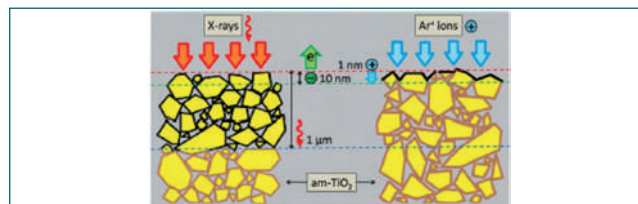


Fig. 3 Schematic of the x-ray and Ar⁺ ion exposed amorphous TiO₂ powders. The region between red and green dashed lines represents the XPS analysis depth; the region between the red and blue dashed lines represents the x-ray penetration depth. The yellow particles with brown borders represent the unaffected TiO₂ particles by either x-ray or Ar⁺ ions; the yellow particles with black borders represent the surface modified TiO₂ particles in both cases.

V.03 Damage and Recovery by Ion Irradiation in 3C-SiC

SiC is an ideal candidate material for devices operating at high power, high frequency and high temperature conditions due to wide band gap and its electrical and thermal properties. Further, due to low neutron absorption cross-section, SiC is a proposed structural material for fusion reactor and used as a diffusion barrier to retain the fission products in fuel kernel of TRISO fuel. In nuclear reactor and space applications, SiC would be exposed to ionizing and non-ionizing radiation. These radiation induced defects can affect the properties of SiC. In the present study, the damage accumulation by 200 keV Si⁺ ion irradiation and followed by, recovery of damage associated with 14 MeV Si⁺ ion irradiation in 3C-SiC was studied. Damage accumulation and recovery is extensively studied with a non-destructive Raman scattering technique and Rutherford backscattering spectrometry(RBS)/ion chaneling.

Figure 1 show the Raman scattering of pristine 3C-SiC epilayer(1.9μm) on Si substrate. Raman spectrum of epitaxial 3C-SiC/Si(111) show LO phonon mode at 971 cm⁻¹ and weak TO phonon mode at 795 cm⁻¹. In the high wave number regime, upon ion irradiation, C-C bonds were observed. Total disorder is calculated as $1 - A_{norm}$ where A_{norm} is total area under LO mode of ion irradiated sample normalized to corresponding area of pristine SiC. Chemical disorder (short range order) is defined as ratio of C-C bonds to C-Si bonds. Variation of total disorder is plotted with chemical disorder and shown in Figure 2a. The curve is divided into three stages, Ist stage, only total disorder increases (upto 0.05 dpa), IInd stage, both total and chemical disorder increases (0.1 dpa to 0.2 dpa) and IIIrd stage, total disorder attained saturation but chemical disorder increases. In Ist stage, there is lack of translational invariance or long range order due to formation of point defects and defect clusters at lower ion doses. In IInd stage, defect clusters coalesce to form amorphous zones but crystalline structure of Si-C

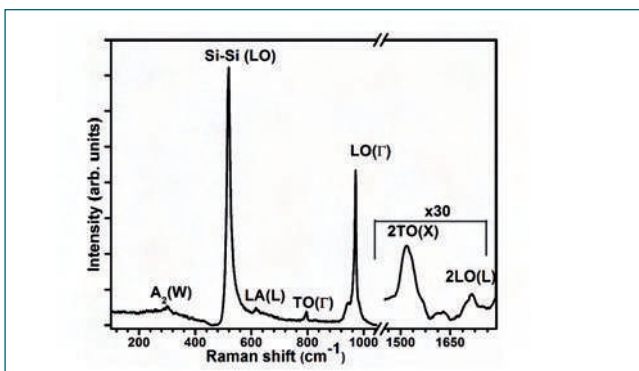


Fig. 1 Raman scattering of pristine 3C-SiC/Si sample

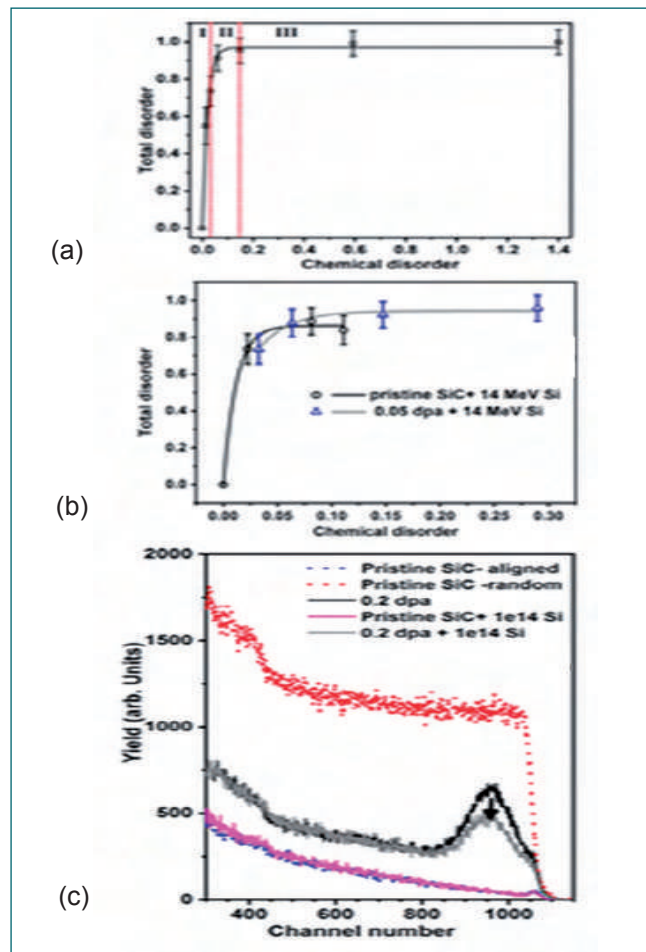


Fig. 2 Total disorder versus chemical disorder for (a) 200 keV Si⁺ ion irradiated and (b) sequentially irradiates 3C/SiC. (c) RBS/ion channeling result of ion irradiated 3C/SiC samples

remain. In IInd stage, the transformation of crystalline to amorphous state was evident from C-C bonds, which form chainlike structure of C (mixed sp^2/sp^3) surrounded by Si-Si and Si-C networks. From Figure 2(b), the presence of amorphous domains is observed in the samples irradiated with sequential ion irradiation (0.05 dpa of 200 keV Si⁺ ion and ion fluence of 5×10^{14} ions/cm² of 14 MeV Si⁺ ion) because the χ value is ~ 0.15 . In the case of 0.2 dpa (200 keV Si⁺ ion) sample, after 14 MeV Si⁺ ion irradiation (1×10^{14} ions/cm²), the backscattering yield has reduced significantly (as marked in Figure 2(c) with arrow). It proves that the partial recovery of defects is observed due to electronic energy loss (4.9 keV/nm) of 14 MeV Si⁺ ions.

The present experimental results show that when the pre-existing damage (caused by low energy ion) is less (< 0.05 dpa), the recovery of damage occurred upon high energy Si⁺ ion irradiation and it is mainly due to ionization induced annealing of defects.

V.04 Atomistic Simulations of Grain boundary Effects on the Crack Growth Behavior in BCC Fe

The rapid progress of computational capability and the availability of reliable inter-atomic potentials has made the molecular dynamics (MD) simulations a major tool to understand the deformation mechanisms at atomic scale. In this work, we utilize MD simulations to understand the effect of twin boundaries (TBs), which are special grain boundaries on the crack growth behavior in BCC Fe. The growth of an atomically sharp crack against the TBs has been studied under mode-I loading (Figure 1). The specimen had the dimensions of $1.6 \times 17.3 \times 17.3 \text{ nm}^3$. Single and multiple TBs were introduced perpendicular to the direction of crack growth (Figure 1). The periodic boundary conditions were applied only in the crack front direction, i.e., $[110]$ (Figure 1). MD simulations were carried out in LAMMPS package employing Mendeleev EAM potential for BCC Fe. AtomEye is used for visualization of atomic snapshots.

Figure 2 shows the stress-strain behavior of pre-cracked perfect BCC Fe along with that of specimen containing one and three TBs perpendicular to the crack growth direction. During elastic deformation, the stress-strain behavior in all the samples is almost similar up to the peak value of stress. Following this, flow stress varies from sample to sample mainly due to their different internal microstructure, i.e., TBs. Finally, the sample without any TBs fails at a strain value of 0.07 and this failure strain increases with increasing the number of TBs. In order to understand this correlation, the atomic snapshots were analyzed for all the cases and presented in Figure 3. In a specimen with no TBs, the crack propagates rapidly on $\{110\}$ planes leading to early brittle failure (Figure 2 and Figure 3a). However, in specimen containing a single TB, the propagation of brittle crack is arrested temporarily at the boundary

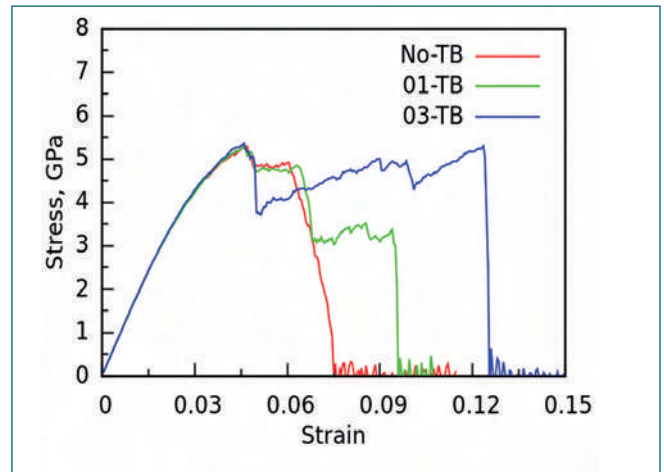


Fig. 2 Stress-strain behavior of pre-cracked perfect BCC Fe along with that of BCC Fe containing one and three TBs

leading to significant plastic deformation (Figure 3b) and increase in failure strain (Figure 2). Once the strain reaches certain critical value, the crack penetrates the TB and grows rapidly on a symmetric $\{110\}$ plane leading to final failure (Figure 3c). Similarly, in sample containing three TBs, the plastic deformation is amplified by each TB (Figure 3d) leading to an increased plastic deformation and failure strain as compared to the specimens with single and no TBs. With increasing deformation, void nucleation, growth and its merging with preceding crack (void coalescence) lead to the final failure as shown in Figure 3d. These results suggest that the presence of TBs increases the amount of plastic deformation leading to better crack resistance and high failure strain as compared to samples without TBs.

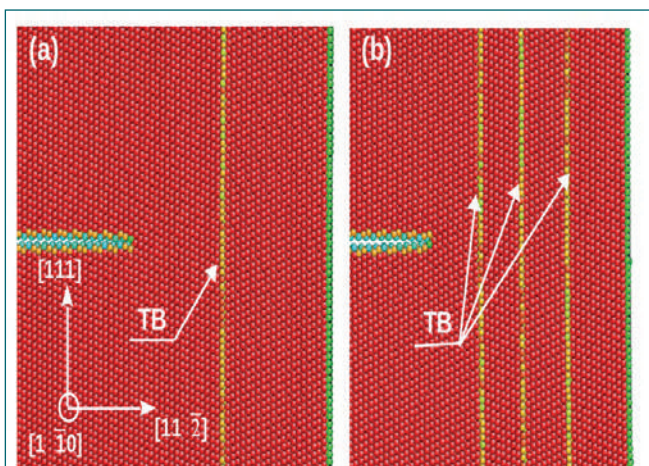


Fig. 1 Initial simulation models considered in this study. The atomically sharp $(111)\langle 110 \rangle$ crack in a sample containing (a) single TB and, (b) multiple TBs

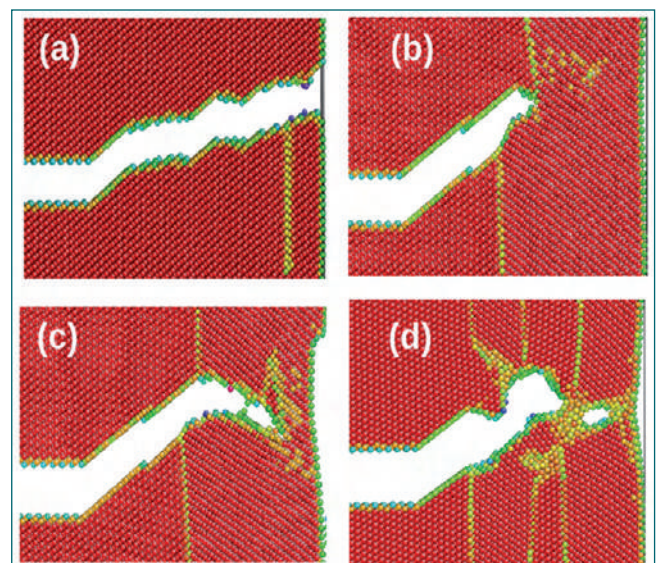


Fig. 3 MD simulation snapshots showing the growth of crack in sample containing (a) no TB, (b-c) single TB, and (d) three TBs

V.05 Bandgap Opening in Monolayer Graphene by Low Energy Argon Ion Impacts

Over the past several decades, ion bombardment modification of solid surfaces has been of academic and technological interest. Graphene is one of the interesting 2D materials and ion irradiation has been shown to produce structural modification, transition from sp^2 to sp^3 hybridization, defects and doping effects. The ballistic electron transport properties (mobility $\sim 105 \text{ cm}^2/\text{V-s}$) along with its outstanding thermal conductivity ($\sim 5000 \text{ W/m-K}$) and the ability of a graphene network to reorganize its structure near a defect site, make graphene an interesting system for ion irradiation studies. Graphene being a semimetal has zero bandgap and it limits its applications. An electronic bandgap in graphene can be opened by processes like uniaxial strain, breaking of the translational symmetry, by breaking the equivalence between the A and B sublattices of its honeycomb lattice, introduction of vacancy defects in the sublattice, doping with boron or nitrogen, chemical bonding to the substrate, quantum confinement by formation of graphene nanoribbons, graphene-BN hybrids, etc. We have devised a new process of opening the bandgap in graphene by irradiation with low fluence Ar-dimer ions. When the fluence of ion irradiation is less, ion impacts do not overlap and they can produce surface defects like craters or hillocks with the size, depth and number density dependent on the ion species, energy, energy loss and the type of target material.

Monolayer graphene is grown on copper foil by CVD process with methane and hydrogen as precursor gases at a substrate temperature of $1000 \text{ }^\circ\text{C}$. Ar monomer and Ar-dimer ions are irradiated with 35 keV/atom and atomic fluence of $1 \times 10^{12} \text{ ions/cm}^2$. Figure 1 shows the scanning tunneling microscopy (STM) images of pristine and irradiated graphene samples. Pristine graphene is smooth while craters have been observed in irradiated samples at the ion impacts which are indenting into copper substrate, which pull down the graphene layer conformally and introduce disorder into graphene. The number density of craters per atom produced by Ar-monomers is higher than that of Ar-dimer ions.

Raman measurements show that graphene is of monolayer thickness from I_{2D}/I_G ratio. I_D/I_G ratio shows

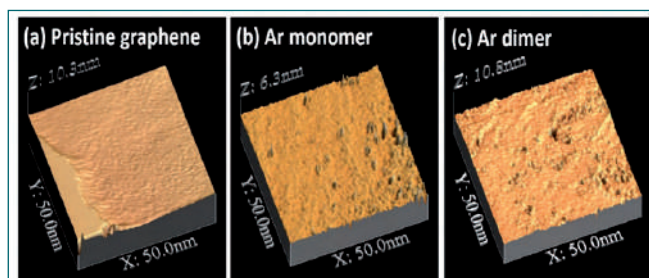


Fig. 1 STM images of (a) pristine (b) 35 keV Ar^+ and (c) 70 keV Ar_2^+ ion irradiated Graphene

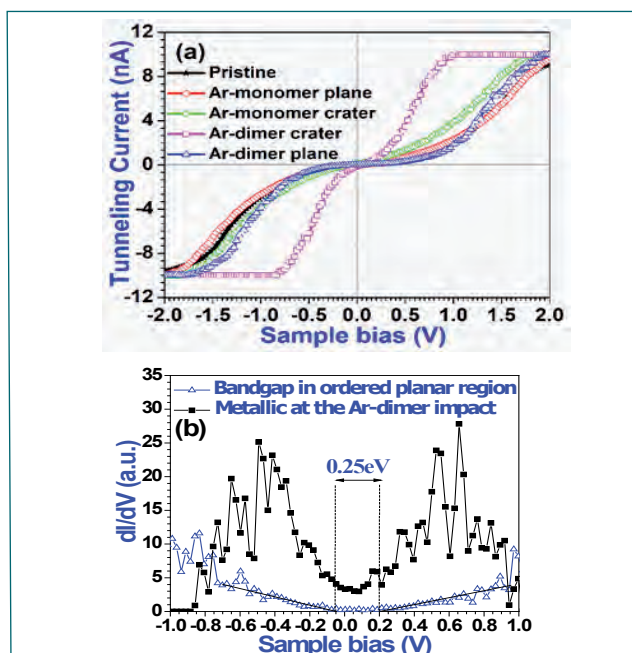


Fig. 2 STS images of (a) pristine, 35 keV Ar^+ and 70 keV Ar_2^+ ion irradiated Graphene, (b) Differential Conductance versus bias voltage from ion impact and planar regions

that defect density is less in the case of Ar-dimer irradiation compared to Ar-monomer irradiation. Due to vicinage effect in electronic energy loss of Ar-dimer ions, defects have annealed out, leading to lesser defects and preserving the long range order in graphene to a larger extent. There is blue shift in G and 2D peak positions with 2D peak shift almost twice that of G peak, which implies the presence of compressive strain. The strain in the case of Ar-dimer ($\sim 0.09\%$) is more compared to Ar-monomer ($\sim 0.06\%$) irradiated graphene. X-ray absorption near edge spectroscopy measurements show additional peaks upon irradiation around around 287 eV , indicating the presence of vacancy defects in graphene. Scanning Tunneling Spectroscopy (local I-V curves) and the corresponding conductance versus bias voltage curves show that semimetallic graphene is metallic at the ion impacts in both Ar-monomer and dimer irradiation. In Ar-dimer irradiated graphene, at the ion impact region, local density of states is higher and there is a shift in Dirac point position by $+0.07 \text{ eV}$ indicating p-type doping. In addition, at the ordered region $\sim 15 \text{ nm}$ away from the ion impact, there is a bandgap opening of 0.25 eV as obvious from Figure 2(b). The presence of compressed strain cannot give rise to this bandgap. The observed vacancy defects can break the equivalence between A and B sublattices of graphene and can give rise to the observed band gap. This process can be used to make a 2D super crystal of metallic quantum dots on semiconducting matrix with applications in low energy switching devices.

V.06 First Report on Growth of 2D Van der Waals Bonded Bi-layer V_2O_5

Vanadium pentoxide (V_2O_5) is a semiconducting metal oxide well known for its 2D layered structure connected by van der Waals bond between two consecutive layers. It is a technologically interesting material with several applications such as in batteries, catalysis, sensors, etc. Reduction in size from bulk to few layers have shown augmented performance such as in improving cyclic stability and performance in battery applications and increased aerobic oxidation processes in catalysis. However, growth of a true 2D bi-layer of V_2O_5 has not been attempted by researchers due to challenges in surface reconstruction arising out of instability compensation pertaining to strong ionic nature prevalent in metal oxides. Chemical exfoliation technique has been adopted in this study and bilayer thickness has been achieved by optimizing the concentration of bulk V_2O_5 in formamide.

Figure 1a shows the schematic of the exfoliation process. Upon intercalation with formamide molecules, the bulk V_2O_5 powder swells up. After ultrasonication, the layers are set free, delaminating the swelled crystal into thin 2D nanosheets. The samples made with concentrations of 6 and 1 mM are designated as A1 and A2, respectively. The crystal structure of V_2O_5 comprises of corner and edge-sharing VO_5 square pyramidal units. The thickness

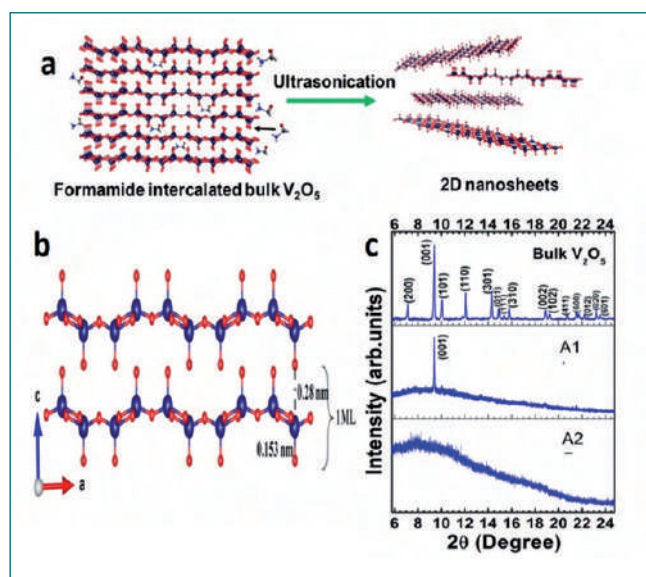


Fig. 1 (a) Schematic diagram showing the exfoliation of α - V_2O_5 using formamide as the intercalating agent. (b) Schematic of one monolayer of V_2O_5 , shown as the sum of bond lengths of $V-O_1$ and the van der Waals bond, i.e. 0.43 nm. (c) X-ray diffraction pattern of bulk V_2O_5 precursor and the exfoliated samples A1 and A2 prepared at 6 mM and 1 mM concentration, respectively

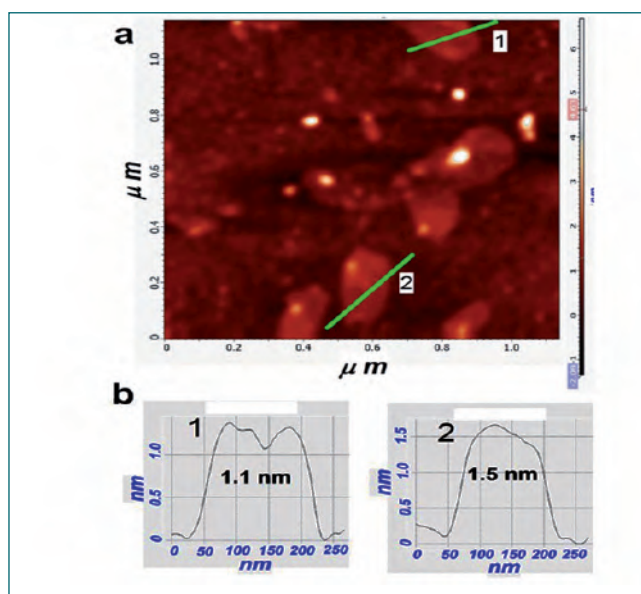


Fig. 2 a) AFM image of exfoliated ultrathin layers of V_2O_5 . b) Line profile of height measured across the nanosheets, labeled as 1 and 2

of a monolayer 2D- V_2O_5 can be estimated as the sum of bond length of the $V-O_1$ π -bond and the Van der Waals bond between them (Figure 1b). The thicknesses of monolayer, bilayer, trilayer and quad-layer 2D- V_2O_5 are calculated from theoretical modeling as 0.43, 0.87, 1.3 and 1.74 nm, respectively. XRD pattern for the exfoliation of V_2O_5 is shown in Figure 1c with comparison against bulk powders. Exfoliated layers in sample A1 exhibited a prominent peak corresponding to (001) reflection, indicating a massive reduction in the thickness of the V_2O_5 layer in the direction of the c-axis. The absence of any peaks in the exfoliated layers in sample A2 indicates a further reduction in thickness.

In order to measure the thickness of nanosheets in sample A2, AFM topograph is recorded. Figure 2a shows an AFM image of the well-dispersed layers. The standard deviation of the measured step height is ~ 0.1 nm. Since a typical bilayer V_2O_5 should have a thickness of about 0.87 nm, and a trilayer should have a thickness greater than 1.3 nm (Figure 2b), the observed thickness is concluded to be from bilayer. Statistical average of ensembles obtained showed a higher percentage of bilayer as compared to tri-layer or above.

The formation of bilayer 2D- V_2O_5 nanosheets is further confirmed using FESEM, XPS and atom-resolved STEM characterizations. This novel bilayer 2D V_2O_5 would open up efforts in synthesizing true bilayer metal oxides for more promising applications.

V.07 Pnictogen Bonding with Nitrogen: Matrix Isolation Infrared Spectroscopic and Computational Studies

The significance of weak intermolecular interactions in determining the 'bulk-phase' properties of materials is quite well-known. Perhaps the most popular of such manifestations would be the role of hydrogen bonding in causing the anomalously low density of ice relative to that of water. Hydrogen bonding has been known and studied for a century and more. When a covalently bound H-atom (bound to D) plays the electron acceptor, in sustaining a weak/strong interaction with the electronegative atom of another molecule (A) (or of the same molecule, to which said hydrogen is not bound covalently), the interaction $D-H\cdots A$, forms a hydrogen bond. Polarization of the D-H bond by the electronegative atom D induces a localized anisotropy of positive polarity, in the electrostatic potential (ESP) surrounding hydrogen, along the extension of the D-H bond. This is termed as a σ -hole. The location of the σ -hole is said to cause the characteristic linearity of the H-bonds. Atoms of the p-block elements, covalently bound within molecules, have also been observed to possess features such as the σ -hole on their respective ESP isosurface. The presence of these positively polar anisotropies, impart a counter-intuitive electrophilicity to such atoms (which are generally presumed to be electronegative, and thus nucleophilic). The corresponding weak interactions, $D-X\cdots A$, are named after the group to which 'X' belongs. When X is of an element of group 14, $D-X\cdots A$ forms a tetrel bond, while those of group 15, 16 and 17 would be termed as pnictogen, chalcogen and halogen bonds, respectively.

Of these, pnictogen bonding has been a point of interest and could be relevant to the nuclear reprocessing industry because of the extensive usage of phosphorus containing extractants. Pnictogen bonding by phosphorus,

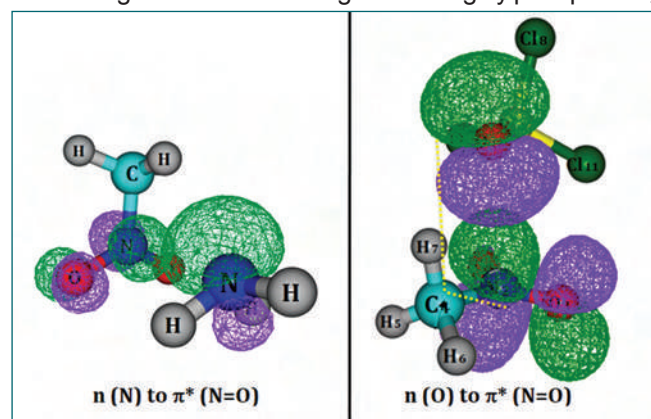


Fig. 1 Charge transfer interactions corresponding to the $O=N\cdots N$ and $O=N\cdots O$ pnictogen bonds in NM-AM (right) and NM-PO (left) dimers respectively

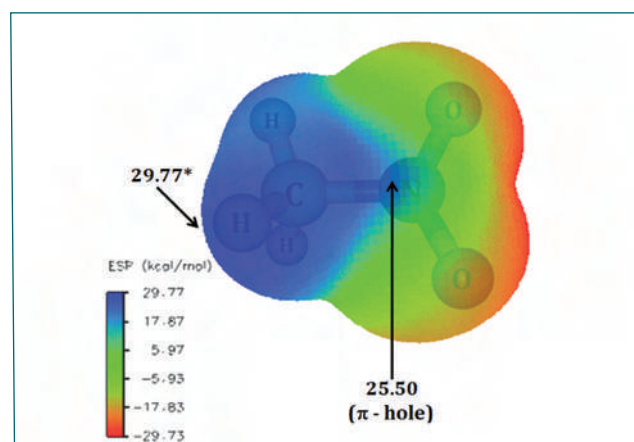


Fig. 2 Electrostatic Potential (ESP) map of nitromethane (CH_3NO_2), displaying the π -hole over nitrogen in the $O=N=O$ moiety. The ESP is projected on the van der Waals isosurface of electron density (0.001 a.u.)

in its trivalent and pentavalent states, have been explored quite extensively by matrix isolation infrared spectroscopy and ab initio computations. As mentioned before, pnictogen bonding is a direct consequence of the presence of localized anisotropies in the ESP surrounding the pnictogen atom in a molecule. The polarizability of the pnictogen atom is directly related to the prominence of the anisotropy, which would in turn determine the strength of the respective pnictogen bond. Nitrogen being the smallest of pnictogens is known to have the lowest polarizability due to which pnictogen bonding involving nitrogen as the electron acceptor has been quite elusive. Also, the ubiquity of nitrogen as a Lewis base in the multitude of molecules in which it occurs, adds to the intrigue of a possible electron accepting nitrogen. Nitromethane, CH_3NO_2 , a popular polar solvent, contains a nitrogen atom, which is deprived of its electron density, so as to facilitate a resonating π -bond with the twin oxygen atoms. Correspondingly, the ESP of CH_3NO_2 reveals a localized region of positive potential over nitrogen in the otherwise negative potential over the $O=N=O$ moiety. This anisotropy, termed as π -hole, is observed to facilitate a pnictogen bond involving the nitrogen of CH_3NO_2 as the electron acceptor. $O=N\cdots N$ and $O=N\cdots O$ pnictogen bonds have been discovered experimentally, within matrix isolated heterodimers of CH_3NO_2 with NH_3 (NM-AM) and $POCl_3$ (NM-PO), respectively.

The structures of these heterodimers have been optimized computationally using state-of-the-art post

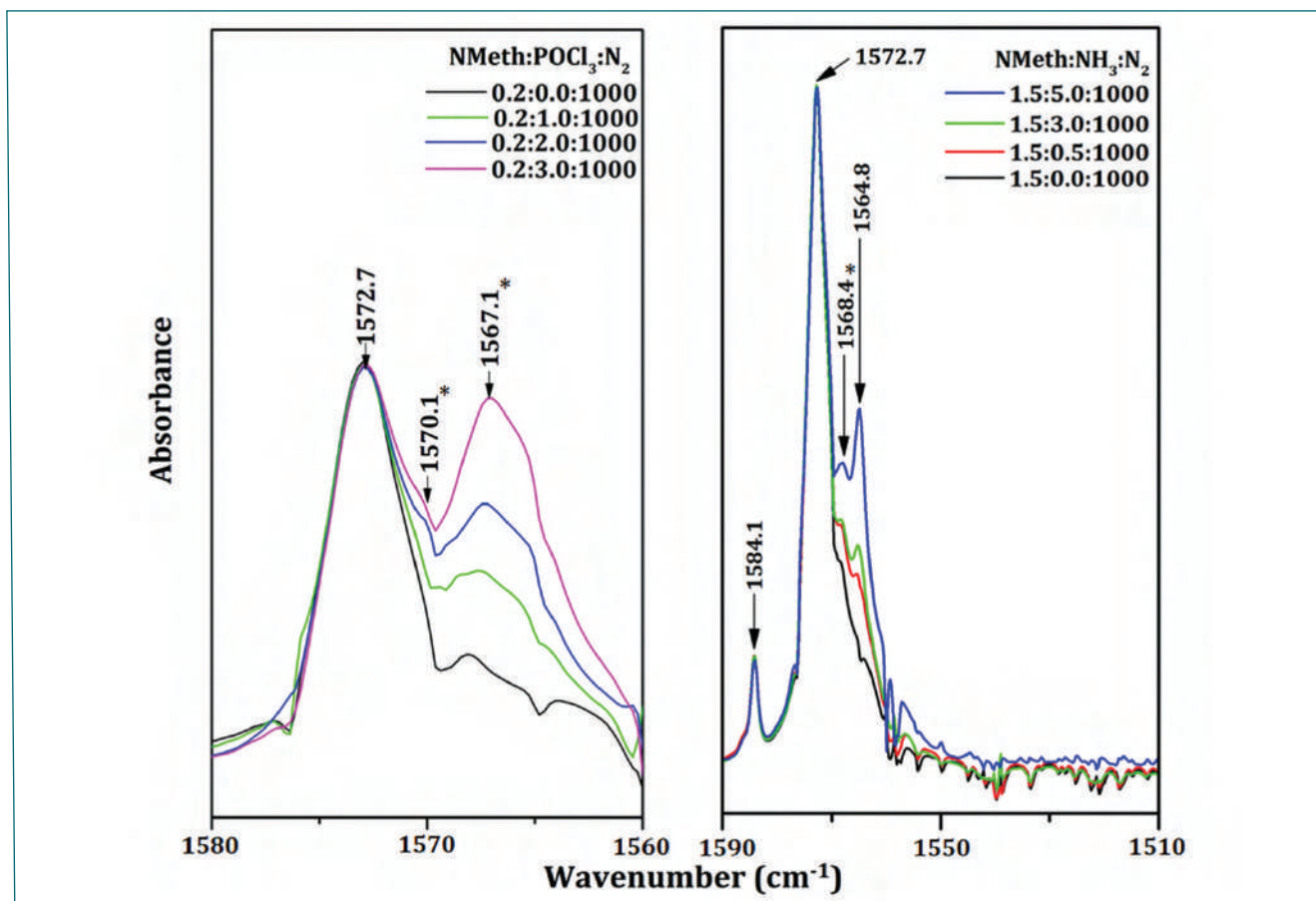


Fig. 3 The O=N=O stretching regions of the IR spectra of matrix isolated mixtures of nitromethane with POCl_3 (right) and NH_3 (left), displaying the appearance of new absorptions (marked with *), evidencing the formation of NM-PO and NM-AM, respectively

Hartree-Fock treatments and density functionals. The pnictogen bonded heterodimers form the most favored structures, on the respective potential energy surfaces (PES) of the NM-AM and NM-PO, in terms of energy. The formation of heterodimers causes perturbations in the signature modes of vibration within the sub-molecules. These manifest as shifts in the characteristic frequencies associated with these modes namely: the O=N=O stretching in CH_3NO_2 , the N-H bending in NH_3 and the P=O stretching in POCl_3 . These shifts are small due to the weak nature of non-covalent interactions binding the heterodimers. However, the enhanced resolution offered by matrix isolation infrared technique allows the capture of these shifted features, thus evidencing the formation of the heterodimers. The observed shifts are found to be in good correlation with those predicted by harmonic frequency calculations performed on the respective geometries of NM-AM and NM-PO, thereby revealing the structure of isolated heterodimers. The characteristic directional determinism, caused by the π -holes driving O=N \cdots N/O=N \cdots O pnictogen bonds, manifests in the perpendicular location of the donor atoms, relative to the O=N=O plane. The geometries are subjected to Quantum Theory of Atoms in Molecules (QTAIM)

analysis, which affirm the presence of the pnictogen bonds, by means of intermolecular Bond Critical Points (BCPs). Natural Bond Orbital (NBO) analysis proves the Lewis acidic role of nitrogen within NM-AM and NM-PO with NH_3 and POCl_3 as the Lewis bases, respectively. The binding energies associated with NM-AM and NM-PO, have been fragmented into contributions from electrostatic, dispersion and charge transfer effects, alongside Pauli Repulsion. The dominant role of electrostatics is revealed by the results which fit with the primary role of π -hole an electrostatic phenomenon, in sustaining the O=N \cdots N/ O=N \cdots O pnictogen bonds NM-AM/NM-PO respectively. Non-Covalent Interactions (NCI) analysis, which characterizes the intermolecular electron density in terms of the descriptors: Reduced Density Gradient analysis has been performed on NM-AM and NM-PO dimers, which enables the fragmented analysis of the different interactions sustaining the heterodimers namely: O=N \cdots N pnictogen and C-H \cdots O hydrogen bonds in former and O=N \cdots N pnictogen, Cl-P \cdots O phosphorus and C-H \cdots O hydrogen bonds in latter. In short, the possible participation of covalently bound nitrogen in non-covalent interactions, as an electron acceptor (pnictogen i.e) is firmly affirmed using the combination of experiment and theory.

V.08 Phonon Instabilities and Symmetry Breaking in Uranium Intermetallics: U, U₂Ti and U₂Mo

Uranium and its compounds show a rich variety of interesting phenomena like Mott insulator, heavy fermions, antiferromagnetism and charge density wave etc. Along with the important applications in the nuclear industry they are also of interest for evaluating the theories of condensed matter physics and have been studied both experimentally and theoretically. The variety of properties shown by these compounds is because of 5f electrons of uranium atoms which are on the verge of delocalization. Whenever they are localized they give rise to the Mott insulating behaviour or the magnetic behaviour and when they are delocalized they lead to heavy fermions and charge and spin density waves. Understanding these properties is a must to predict the behaviour of these compounds. In the present study three intermetallic uranium compounds are studied using density functional theory (DFT) based calculations and the observed instabilities are found to be related to the symmetry breaking of the structure and the existence of charge density waves in these compounds.

The DFT calculations are carried out for α -U metal, U₂Ti and U₂Mo using plane waves Vienna *ab-initio* simulation package. The known room temperature structures of these are orthorhombic for α -U, hexagonal for U₂Ti and rhombohedral for U₂Mo. The calculated electronic density of states is plotted in figure 1 which shows that the 5f electrons of Uranium are found to be participating in bonding in these compounds. The calculated elastic constants are in very good agreement with experimental data and they obey the Born stability criteria. But the calculated phonon dispersion shows phonon instability corresponding to $(\frac{1}{2} 0 0)$ point in α -U, $(0 0 \frac{1}{2})$ in U₂Ti and $(0 \frac{1}{2} 0)$ in U₂Mo as shown in figure 2 with their corresponding modes. These modes when allowed to

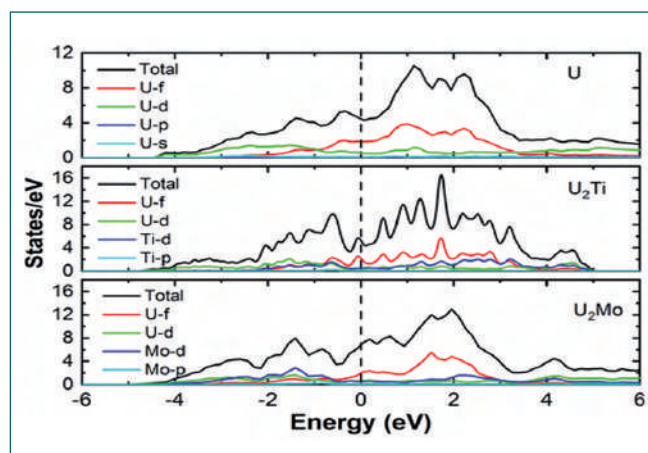


Fig. 1 Electronic DOS for α -U, U₂Ti and U₂Mo

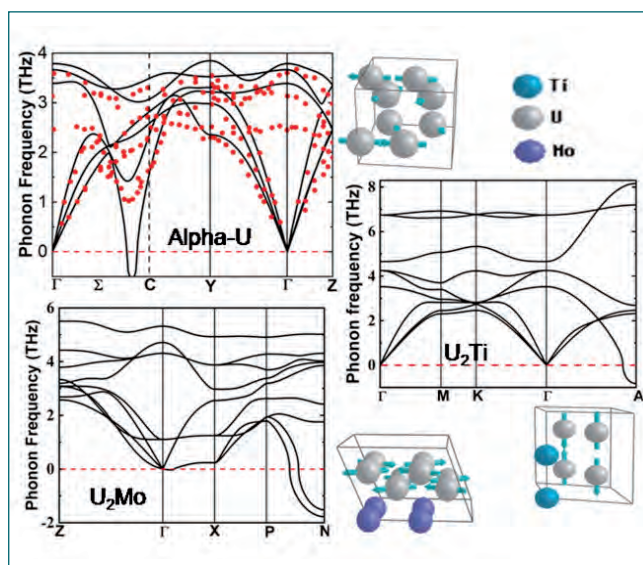


Fig. 2 Calculated phonon dispersion for U (red dots: exp. data), U₂Ti and U₂Mo and unstable phonon modes

relax lead to symmetry breaking in these compounds and the U-U bond become unequal in different directions. The charge densities for the distortions led by these modes show the symmetry breaking for linear chains of U and U₂Ti and zig zag chains in U₂Mo. There is a correlation between the symmetry breaking and U-U bond length in these systems. In the direction of symmetry breaking, the U-U bond distances are 2.79 Å, 2.80 Å and 2.78 Å for α -U, U₂Ti and U₂Mo resp. The symmetry breaking can be corroborated with charge density wave existence in U metal at lower temperatures which is also known from experiments. In case of U₂Ti and U₂Mo due to lack of experimental data this instability could not be verified and future experiments may confirm these findings. The special relationship between the U-U bond lengths and the dimerization of U atoms is summarized in Table 1.

Table 1: Summary of the symmetry breaking in α -U, U ₂ Ti and U ₂ Mo			
Compd.	U-U (Å) (Original)	U-U (Å) (Distorted)	Facts
α -U	2.79	2.61, 3.13	CDW confirmed in experiments
U ₂ Ti	2.80	2.58, 3.18	A cusp is seen in low temperature Expt. resistivity curve.
U ₂ Mo	2.78	2.70, 2.99, 2.67	No data available at low temperatures

V.09 Tailoring the Polarization and Complex Amplitudes of Light Beams

Monochromatic light beams are characterized by three components: a polarization vector indicating the instantaneous direction of the electric field in the transverse plane, the phase distribution indicative of the shape of its wavefront, and the electric field amplitude profile which specifies the intensity variation across its transverse plane. Of these, the polarization state of a light beam is altered by sending it through specific anisotropic materials called waveplates. Such plates have a unique direction in them such that the electric field components along and perpendicular to this unique travel with different velocities and therefore acquire different phases. The thickness of these plates are chosen so as to introduce specific amount of phase difference between these orthogonal components. Waveplates are therefore characterized by this scalar phase difference introduced between the two components called the retardance and a unit vector characterizing the unique direction. Apart from changing the polarization by introducing a relative phase difference between two orthogonal components, these waveplates also impart a global phase whose origins are geometric in nature. While standard light beams have a uniform state of polarization in all of its transverse plane called the scalar light beams, one could also design a light beam with polarization, phase and electric field amplitude varying in its transverse plane. Such beams are called structured light beams and have found increased attention in recent years in diverse fields like optical trapping, materials processing, quantum information and quantum communication. Generation of such structured light beams require

waveplates which have a spatially varying fast-axis orientation and/or retardance. Such waveplates are termed singly-inhomogeneous (s-plates) or doubly-inhomogeneous (d-plates), depending upon whether the spatial variation is in one of the parameters or both, respectively. The familiar q-plate employed for imparting orbital angular momentum to light beam is an ubiquitous example of the former. These q-plates are s-plates with constant retardance but whose fast axis orientation varies linearly with the azimuthal angle. While multiple techniques have been available for generating these kind of s-plates, fabrication of d-plates still appears to be a difficult task. The work presented here is in this context. We have theoretically demonstrated that a d-plate can be equivalently realized using a gadget comprising of three collinearly placed s-plates, with the outer two being identically oriented quarter-wave s-plates (QW-s-plates) and the central one being a half-wave s-plate (HW-s-plate). We call this arrangement of s-plates as the QHQ-s-plate. In this arrangement, the effective fast axis is determined by the fast axis of the outer QW-s-plates while its effective retardance is determined the relative orientations of the fast axis of the HW-s-plate and the QW-s-plates. The equivalence between the d-plate and the QHQ-s-plate established by us is not just with respect to the polarizations transformations, but also with respect to the associated phase change. Further, our method of realizing d-plates using QHQ-s-plate has an important advantage in that several d-plates can be realized by a single set of s-plates by changing the relative orientations, ensuring the outer quarter-wave q-plates are identically oriented.

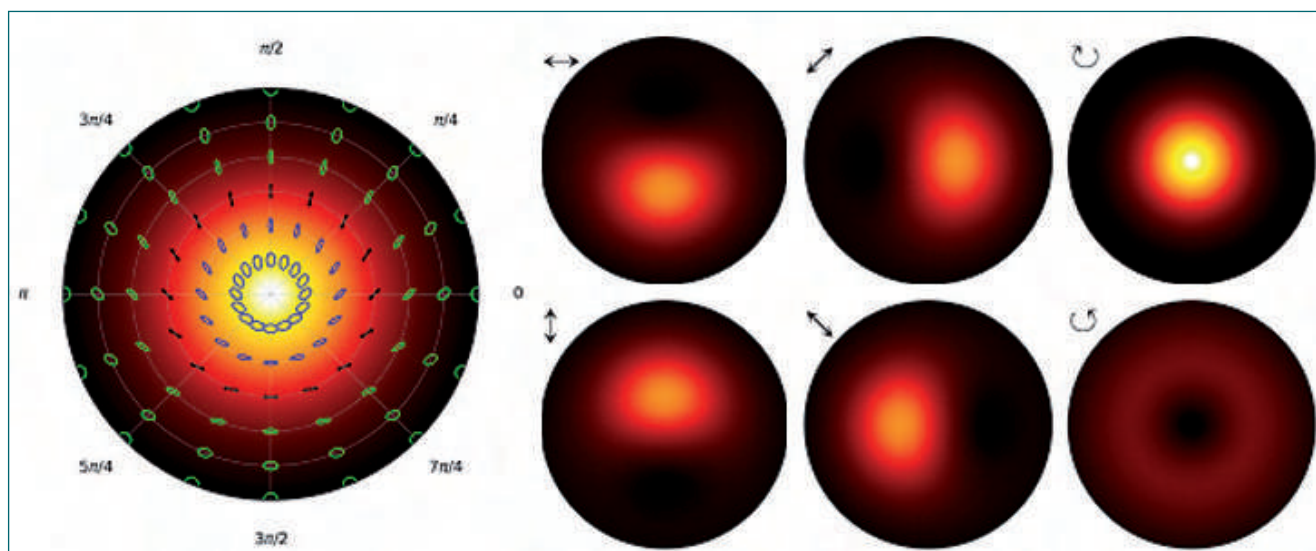


Fig. 1 Full Poincare beam generated using the QHQ-s-plate gadget. The background color-coding indicates the intensity while ellipses depict the local polarizations. The subsequent six smaller images depict the intensities along three mutual unbiased bases. In the colorbar, the brighter colours indicate higher intensity, while darker colour indicates lower intensity. The six projections are necessary so as to completely reconstruct the state.

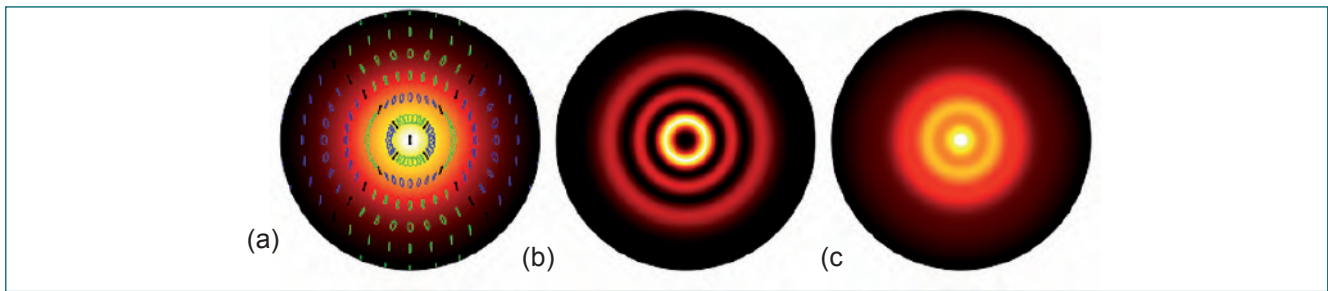


Fig. 2 (a) Intensity and polarization distribution of the vector beam emergent from the QHQ-s-plate set for generating the LG(2,2) mode. (b) Intensity in the horizontal component and (c) Intensity in the vertical component.

An extreme class of vector beams that can be envisaged is the so-called "full Poincaré beams", which are vector beams which consist in their transverse plane every possible state of polarization. Early applications of FPBs have been in generating flat-top beams, in using their optical curl forces towards trapping sub-micron size particles, for studies of atmospheric turbulence, beam propagation in non-linear media, Mueller polarimetry etc. In the d-plate we have designed for generating full Poincaré beams, the retardance and fast-axis variation are decoupled from each other. At every radius, the d-plate has a uniform retardance, and a fast-axis orientation linearly varying with the azimuthal angle. In other words, this d-plate functions as the above mentioned q-plate, at every radial distance. For a circular polarization input, the emerging beam will be such that at its centre the polarization is same as the input. At a distance equal to the half of the extent of the waveplate, the polarization is plane polarized, whose direction varies with the azimuthal angle. At the radial distance equal to the extent of the waveplate, the polarization is again circular, but now with opposite helicity of that of the input. The independent and simultaneous variation in both retardance and fast-axis orientation of the d-plate ensures that every elliptical polarization state is available at some point with the finite extent (defined by the size of the plane). The left most image of Figure (1a) depicts the transverse plane of the it is evident that all possible polarization states are present in the output vector beam. In this image the local polarizations are depicted in terms of polarization ellipses. The plane polarizations are depicted as a double-headed arrows, with circular polarizations are depicted as circles and elliptical polarizations as depicted as ellipses. The colour of the ellipse indicates the helicity of polarization: blue standing for left and green indicating the right. The six figures following it depict the intensities along six cardinal projections: horizontal, vertical, diagonal, anti-diagonal, left and right circular. Further, this d-plate is capable of producing distinct full Poincaré beams for different input polarizations. The quality of full Poincaré beams generated by this method depends on the ability of fabricating d-plate with simultaneous variation in both retardance and fast-axis orientation. However, this

d-plate can be realized as a QHQ-s-plate in a straight forward manner. The required QW-s-plate in case is just a quarter-wave q-plate and the required HW-s-plate is also like a q-plate but with an offset angle that varies with the radius. This example illustrated the application of d-plate and the corresponding QHQ-gadget for polarization manipulation. Waveplates, homogenous or inhomogeneous, alter only the polarization and global phase of light beams without altering their intensity. Therefore they cannot by themselves be used for shaping the intensity of light beams. In this context, we show that using d-plates together with standard polarizers, it is possible to do any complex amplitude shaping of scalar light beams. The idea here is to unitarily transform the input scalar light beam into a vector beam, which is a superposition two components of orthogonal polarizations. We import the desired component complex electric field distribution into one of the components and project the remanent electric field onto its orthogonal polarization component. Now, using a standard polarizer we purge the orthogonal component from the emerging vector beam so that what remains is a scalar light beam of desired amplitude distribution. Once a d-plate is designed it can be implemented using the QHQ-s-plate gadget. We demonstrate this idea by showing how the higher order LG beam, the LG(2,2) mode can be extracted from the standard Gaussian LG(0,0) mode.

Figure (2) shows the transverse plane intensity profile as the beam propagates through the QHQ-s-plate gadget set for generating this mode. The left-most figure shows the vector beam at the exit plane of the QHQ-s-plate gadget, ignoring the diffraction effects as the beam propagates inside the s-plates. The subsequent two figures depict the intensity profiles of the desired and remanent components. It is evident that the desired component, depicted in Figure 2b, is LG(2,2) mode, which is of-course of reduced intensity and beam waist. This component can therefore be extracted from the vector beam using a standard polarizer or a polarising beam splitter. To summarise, it is possible to generate any vector beam or to sculpt any higher-order mode of light beam, from the ubiquitous fundamental Gaussian mode, using only the QHQ-s-plate and a standard polarizer.

V.10 Virtual Instrument Automation of Ion Beam Analysis and Ion Implantation Experiments for Accelerator Based Materials Research

Manual conduct of ion implantation and analysis experiments without much beam induced effects and with optimized ion beam utilization involve many complex tasks like precise sample positioning, fluence control, various backscattering spectra acquisitions. These tasks are not only challenging processes but also tedious and time-consuming. Hence, we have developed and established virtual instrument automation of ion beam analysis experiments like standard Rutherford Backscattering spectrometry (RBS), Hi-RBS and multiple sample ion implantation experiments for use with the 1.7MV tandetron and other accelerators operating at MSG,IGCAR. A personal computer (PC) based indigenous instrumentation developed for this include various signal conditioning circuitry, isolation amplifiers, and transistor drivers along with cost-effective and off-the-shelf commercial components like a general purpose, multifunction data acquisition card.

The automation has several precision and key tasks including control and measurement of ion beam fluence, particle selection by back scattered energy screening, controlled collection of backscattered yield using single and multi-channel analyzers. Handling multiple samples, controlling their positions with a 0.01 mm linear and an angular 0.01° resolution using a five axis goniometer are also automatically done.

Based on our in-house expertise and experience in various experimental automations, we have developed various virtual instruments based on LabVIEW for automation of the ion implantation, standard RBS and Hi-RBS experiments. The prime goals for the automation include obtaining the ion implantation, standard RBS and Hi-RBS energy spectra of the samples in the minimum possible time with the least human intervention, low dose and low beam damage effects.

In a typical automated standard RBS experiment, the sample positioning, ion beam current and fluence

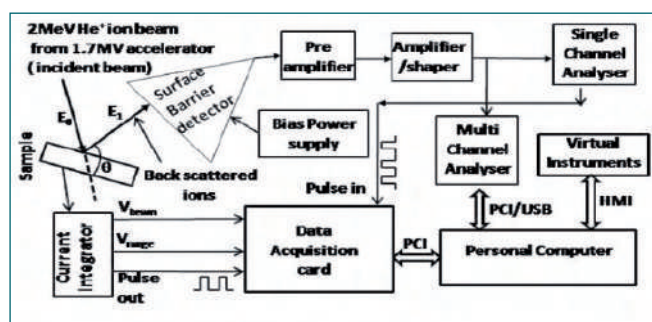


Fig. 1 Block diagram of automated standard RBS measurement system

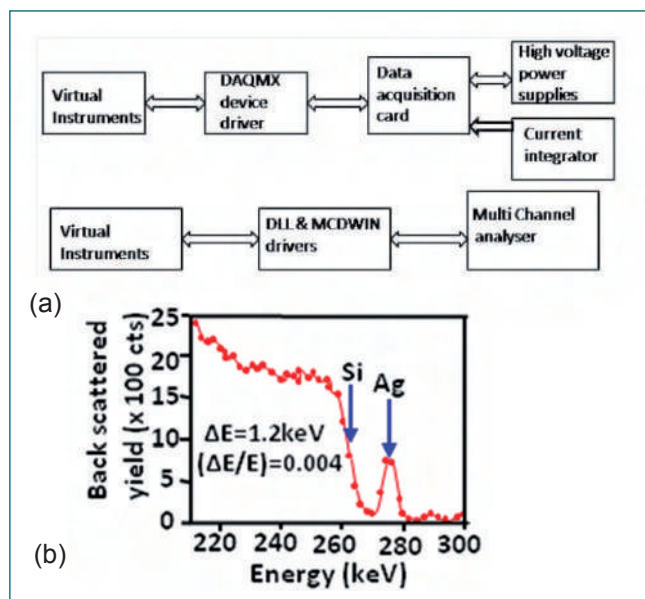


Fig. 2 (a) Hierarchy levels of virtual instrument automation software (b) Hi-RBS from a 3nm thick Ag film taken with 300kV H⁺ ion beam

measurements, Faraday cup control, and backscattered yield data collection from the multi channel analyser(MCA) for the preset dose counts are done in a sequence of steps. The programs interface with the ion beam current integrator, obtains, computes and displays the ion beam current, the current range, accumulated dose counts besides comparing with the user input irradiated dose count. An on-line plot of region-of-interest counts obtained from MCA versus dose/fluence is updated and the data are auto stored in a text file. Also these processes are repeated at 100Hz. Integrated tests showed the satisfactory performance of the automatic conduct of ion implantation, standard RBS and Hi-RBS experiments. The satisfactory field performance of the automated system was observed using 1–2 MeV H⁺ and He⁺ beams. A close agreement of <3% between the fluence obtained from the standard RBS analysis and the fluence recorded by the automated system was observed for a set of Si samples for various ion beams and fluences.

Using the virtual instruments based automation, we could drastically reduce not only the experimental time (from many hours to tens of minutes) but also the efforts required for completion of a single experiment. Thus the automation has had a huge impact on our work load, improved efficiency and provided a better performance in experiments involving both single sample and sample batches.

V.11 Evaluation of Spatial Resolution of Gamma Ray Computed Tomography System

Computed tomography (CT) is proven to be an excellent tool for identifying the location and internal features of the complex object including its dimensions. Performance of CT system depends on spatial resolution and contrast sensitivity of the CT image. Spatial resolution is the ability to image the fine structure and it can vary with sampling interval, spatial accuracy of the sample and effective beam width. The spatial resolution of the WACT system has been evaluated using in-house developed CT phantom.

Waste Assay Computed Tomography (WACT) system is the first generation single source single detector CT system (Figure 1) meant for radioactive waste assay of nuclear waste drum. A two-axis manipulator system is placed between source and detector to perform the CT scan for a particular layer. Source and detector are collimated and placed in-line & face to each other and can move vertically to scan the object. Reconstruction of CT images are done by using in-house developed Convolution-based Filter back-projection algorithms.

To measure the spatial resolution and dimensional accuracy of the CT image, a slit phantom (100 mm dia and 10 mm thick SS disk) is designed and fabricated

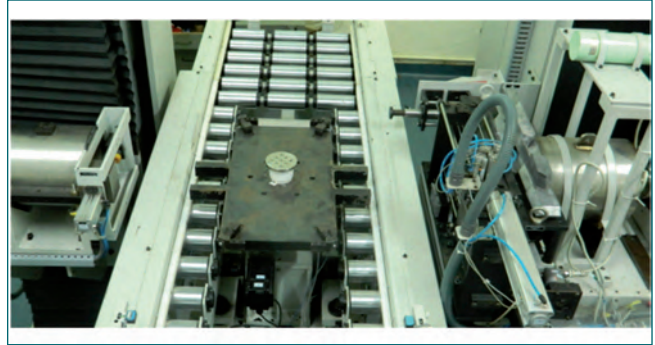


Fig. 1 WACT system



Fig. 2 Slit phantom

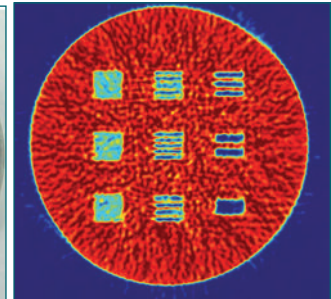


Fig. 3 Reconstructed CT image

at Central Workshop (Figure 2). This phantom has nine sets of square wave pattern slots and each slot has a specific number of slits of different widths but uniform length (10 mm).

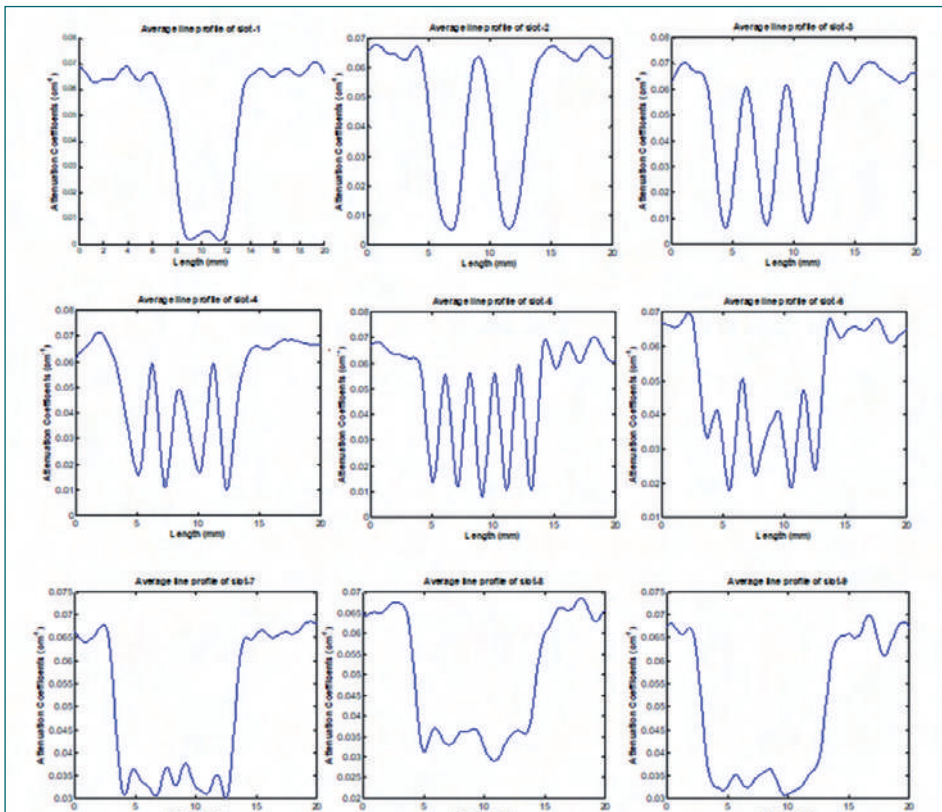


Fig. 4 Line profile of reconstructed image

Three sets of CT scan were taken with 121 parallel rays per projections (180 projections) using Cs-137 (1 Ci) gamma source. The slit phantom was scanned at various beam widths (3.2 mm, 2.8 mm and 2.1mm) by adjusting the source and detector collimators. In all the three scans, presence of nine slots was clearly seen in the reconstructed images. It is observed that the slits are well resolved with lower beam width than with higher beam width (Figure 3). For the lowest beam width (2.1 mm), 5 slits could be resolved and hence, it's resolution is 5 line pair per cm (Figure 4). It was observed that error in dimensional measurement increases beyond 5lp/cm.

V.12 The Role of Alkyl Chain Length in Phosphoryl Oxygen Basicity

Metal-ligand complexation is one of the significant steps in the extraction process, and due to this reason, the strength of a metal-ligand bond is often correlated to the extraction ability of a ligand. It is observed that the extraction ability of phosphorus-based ligands increases across the series: phosphates, phosphonates, phosphinates and phosphine oxides. This was often attributed to the increased basicity of the phosphoryl oxygen upon structural modification. However, the spatial arrangement of the ligands, which is crucial in determining the stability of the complex, is also an essential factor in understanding the increased extraction behaviour. In this context, we have applied quantum chemical calculations to verify whether there is a direct correlation between phosphoryl oxygen basicity and alkyl chain length by focusing on the phosphate class of compounds. Eight ligands were considered starting from the simplest molecules, phosphine oxide (PH_3O), phosphoric acid (H_3PO_4), and their alkyl-substituted derivatives, trimethyl phosphate (TMeP), tri-ethyl phosphate (TEtP), tri-propyl phosphate (TPrP), tri-butyl phosphate (TBP), tri-pentyl phosphate (TPeP) and tri-hexyl phosphate (THeP).

Our quantum chemical calculations indicated no evidence to support the hypothesis ‘phosphoryl oxygen basicity increases with alkyl chain length’ in phosphate ligands. The electronic charge at phosphoryl oxygen remains the same in all the ligands (Mulliken: 0.52 – 0.55, NBO: 1.03 – 1.10, AIM: 1.47 – 1.52), indicating that the basicity of phosphoryl oxygen is unaffected by the alkyl chain length (Table 1). We have also identified a

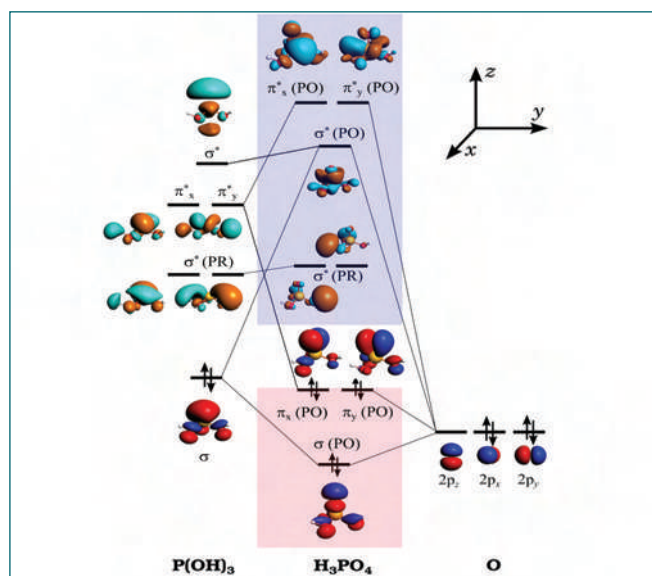


Fig. 1 The orbital interaction diagram for H_3PO_4 with fragments $\text{P}(\text{OH})_3$ and O ..

Table 1: The calculated electronic charge for P and O in various ligands at B3LYP/def2-TZVP level

Ligands	Computed electronic charges on oxygen and phosphorus (parenthesis) atoms of P=O group		
	Mulliken	NBO	AIM
H_3PO	-0.5 (+0.4)	-1.0 (+1.3)	-1.5 (+3.1)
H_3PO_4	-0.5 (+0.8)	-1.1 (+2.5)	-1.5 (+3.8)
TMeP	-0.5 (+0.9)	-1.1 (+2.5)	-1.5 (+3.8)
TEtP	-0.5 (+0.9)	-1.1 (+2.5)	-1.5 (+3.8)
TPrP	-0.5 (+0.9)	-1.1 (+2.5)	-1.5 (+3.8)
TBP	-0.5 (+0.9)	-1.1 (+2.5)	-1.5 (+3.8)
TPeP	-0.5 (+0.9)	-1.1 (+2.5)	-1.5 (+3.8)
THeP	-0.5 (+0.9)	-1.1 (+2.5)	-1.5 (+3.8)

negative hyperconjugation interaction between the filled π ($\text{P}-\text{O}$) to vacant $\sigma^*(\text{PR})$ molecular orbitals (Figure 1), with a substantial charge transfer, *i.e.* 0.24 e, in all tri-alkyl phosphate ligands.

In summary, no direct correlation is observed between the elongation of alkyl chain length and the basicity of phosphoryl oxygen. The electronic charge at phosphoryl oxygen (or phosphoryl group) is an essential parameter in determining the basicity of the ligand as it is directly responsible for the electrostatic metal-ligand interaction. However, other parameters such as steric repulsion, charge transfer, dispersion interaction, etc., also contribute to metal-ligand interaction. Our results indicate that multiple factors affect the extraction behavior, and it does not solely depend on the net electron density of phosphoryl oxygen. Therefore, we propose that it is more appropriate to define basicity as ‘affinity’, which includes all the contributing factors of metal-ligand interaction.

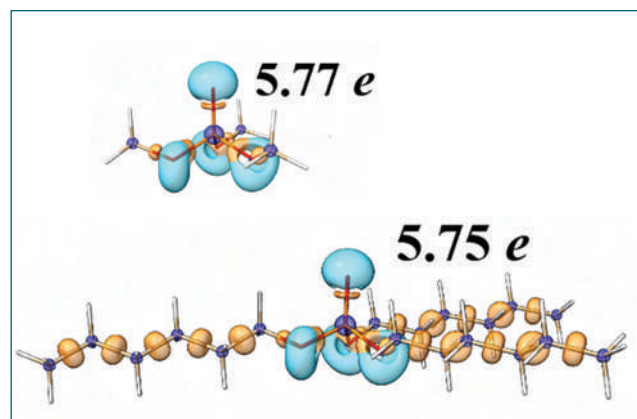


Fig. 2 The electron localization function (ELF) isosurfaces for TMeP and THeP ligands (electron population phosphoryl oxygen is indicated in figure)

V.13 Correlation Between Anion Related Defects and Ion Beam Induced Luminescence in $Y_4Zr_3O_{12}$

The oxygen deficient fluorite compounds, pyrochlore, disordered fluorite, monoclinic pyrochlore, and δ -phase are capable of surviving extreme radiation environments at elevated temperatures without amorphization which makes them potential hosts for the immobilization of high level nuclear waste. Many of these oxides: especially $Y_2Ti_2O_7$, $Y_4Zr_3O_{12}$, and $Y_4Hf_3O_{12}$, are also commonly found as homogeneously dispersed nano-precipitates in oxide dispersion strengthened (ODS) steels containing Ti, Zr, and Hf.

In general, luminescence in fluorites and related structures due to excitation from ions (Ionoluminescence, IL), electrons (Cathodoluminescence, CL), or photons (Photoluminescence, PL) are attributed to anion vacancy related defects. The luminescence occurs when a strongly localized, electron-deficient vacancy readily accepts an electron and recombines radiatively. Ion beam induced luminescence (IBIL or IL)-the photon emission caused by excitation using ion beams is a sensitive, yet relatively unexplored tool for gathering information about the native and irradiation-induced electronic band structure and the defect states of the target. The ionoluminescence spectra usually range from ultraviolet to infrared, with an intensity proportional to the number density of defects and usually interpreted using crystal band structure and defect levels within the bandgap.

The luminescence spectra produced by irradiation by light (He) ions in $Y_4Zr_3O_{12}$ can be interpreted using hybrid functional based density functional theory calculations to understand the nature of native and irradiation induced defects in $Y_4Zr_3O_{12}$. The $Y_4Zr_3O_{12}$ used in this study is prepared from Y_2O_3 and ZrO_2 precursors by ball milling

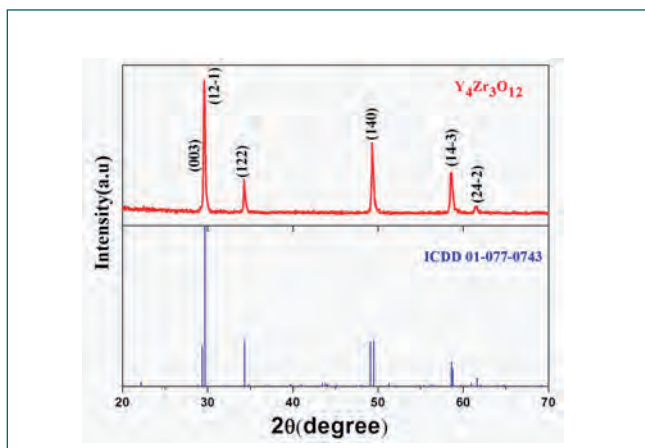


Fig. 1 XRD of as prepared $Y_4Zr_3O_{12}$

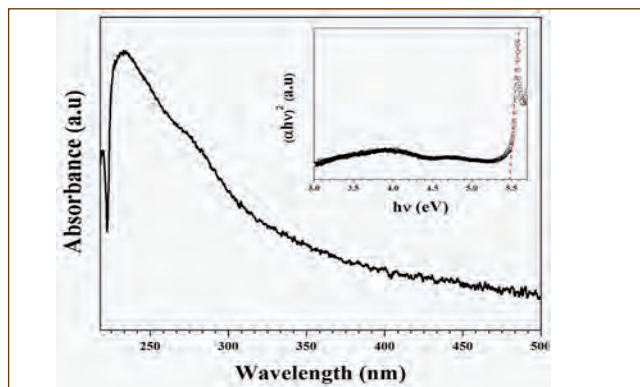


Fig. 2 UV-vis spectra of as-prepared $Y_4Zr_3O_{12}$, with Tauc plot depicting bandgap

(8h) followed by sintering (1300°C, 120h). The phase formation is confirmed using powder-XRD (Figure.1), Bandgap being a pivotal parameter in explaining any luminescence property of a material, we proceeded to measure the bandgap energy of as-prepared $Y_4Zr_3O_{12}$ using UV-vis absorption spectroscopy. Band gap energy value determined from the Tauc plot (Figure 2) is 5.47eV. Further DFT calculations are performed to estimate the bandgap of $Y_4Zr_3O_{12}$.

The calculations using HSE06 hybrid functional provide a bandgap value of 5.27 eV, which is close to the experimentally measured value.

The ionoluminescence spectroscopy estimate the nature

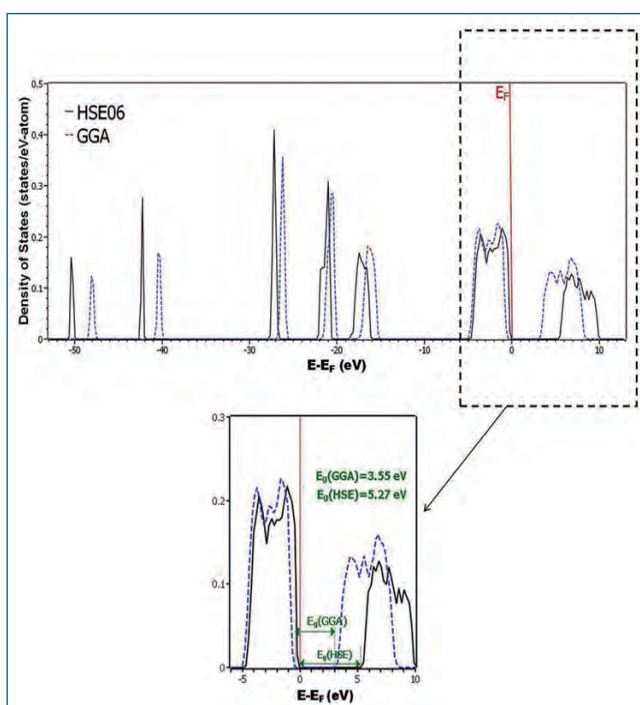


Fig. 3 DFT-HSE06 simulation of bandgap in $Y_4Zr_3O_{12}$

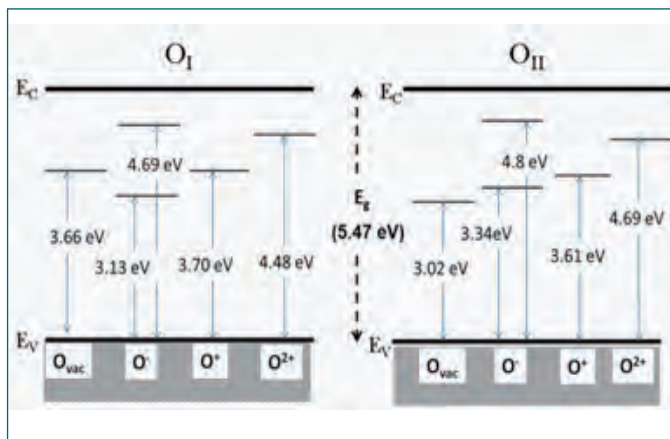


Fig. 4 The defect levels in $Y_4Zr_3O_{12}$, of O_I and O_{II} in different charge states, calculated using HSE06

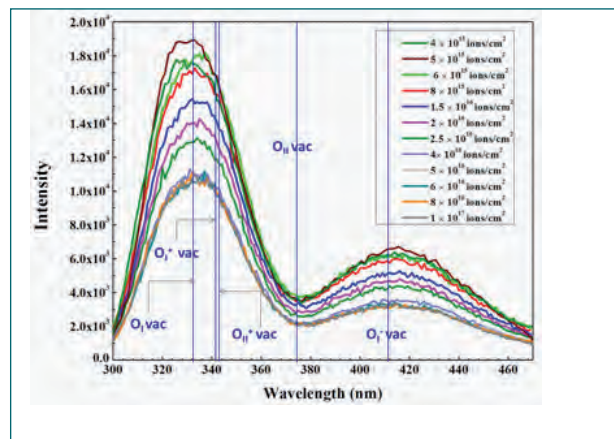


Fig. 5 Frenkel pair formation energies of $Y_4Zr_3O_{12}$ for different Frenkel-pair configurations

of irradiation induced defects was carried out in the in situ IL facility at IGCAR, Kalpakkam. The as-prepared $Y_4Zr_3O_{12}$ pellet is irradiated by He^+ ions of energy 100 keV, and luminescence during irradiation is recorded at definite intervals, until maximum fluence of 1×10^{17} ions/cm² is achieved at a constant current of 1 μ A.

The IL spectra of $Y_4Zr_3O_{12}$ pellet acquired for various fluences (Figure. 4) consist of two major bands centered at 330nm (3.72 eV) and 415nm (2.98 eV), respectively. The intensity of the first band is nearly three times the intensity of the second one. After an initial increase, the intensity of bands decrease with an increase in fluence. At a fluence of 4×10^{16} ions/cm², the intensities of the bands drop by 40% and remain the same up to 1×10^{17} ions/cm². It is obvious that IL bands are far away from the band edge, and therefore, they can only be due to deep level emission (DBE) from the native defect levels or the defect levels created by irradiation. The native and irradiation-induced defects and color-centers produce defect levels within the bandgap, the optical transitions involving which are responsible for ion beam induced luminescence.

In order to find the origin of IL peaks in $Y_4Zr_3O_{12}$, first-principles calculations of different luminescence centers to determine corresponding defect levels are carried out using HSE06 hybrid functional. The simplest oxygen vacancy defects created are F-centers, anion vacancies filled by $2(O_2^- \text{ or } F_2^-)$, $1(O^- \text{ or } F^-)$, or 0 (O-vacancy or a-center) electrons. The defect states associated with an O_I vacancy create a localized state at 3.51 eV above the valence band maximum (VBM) within the bandgap. The defect levels in $Y_4Zr_3O_{12}$, of O_I and O_{II} in different charge states, calculated using HSE06 functional, are summarized in Figure. 4. From the defect levels computed, it is evident that the energy gap between valence band and energy level positions of O_I^- (339nm),

O_I^+ (335nm), and O_{II}^+ (343nm) vacancies fall on the wavelength range of the first band (centered at 330nm) of IL spectra. A free electron captured by these levels will undergo recombination and simultaneous photon emission of energy ~ 3.7 eV. Similarly, the radiative recombinations associated with O_{II} (413nm) and O_I (371nm) vacancies will

be contributing to the second band at 415nm. In addition to this, there might be contributions from polarons associated with the thermal activation energy of trapping of the defects. The initial increase in IL intensity with fluence is due to the irradiation induced defects. As the irradiation proceeds, the native defects as well as the irradiation induced defects undergo clustering or modified into non-luminescent defects. The decrease in intensity with increase in fluence is due to the quenching of luminescence centers by forming defect clusters during irradiation.

In summary, the $Y_4Zr_3O_{12}$ oxide synthesized by solid-state route showed well-resolved peaks in XRD, which are in exact agreement with previous reports. Further, the bandgap measured using UV-vis spectroscopy and hybrid-functional based electronic structure calculation is 5.27 and 5.47 eV, respectively. Here, the shortcomings of conventional DFT techniques on estimating the bandgap are compensated by selecting a suitable hybrid exchange-correlation functional. The ionoluminescence spectra acquired during 100keV He ion irradiation show two bands, centered at wavelengths 330 and 415nm, respectively, which can be attributed to radiative electronic transitions involving anion-related defect levels within the bandgap. The defect levels calculated using DFT-HSE06 simulations are in-line with the bands observed in the IL spectra. The O_I , O_I^+ , and O_{II}^+ vacancy defects contribute to the band at 330nm, and neutral O_{II} and O_I vacancy defects contribute to the band at 415nm.

V.14 Colorimetric Detection of Nano-molar Oxalic acid at Room Temperature

The simple dicarboxylic acid, oxalic acid (OA) found widely in plants, animals, microorganisms, and commonly in spinach, ginger, tomato, and chocolate tends to form less soluble salts as oxalates with alkali and alkaline metals. and causes often drainage of Ca to affect the physiological activities of the heart and neural system. It may distress kidney function. However, OA is an industrially important chemical in production of celluloid and rayon, lather and dressing, extraction of rare earths from monazite. Additionally, OA resulting from industrial processes such as phenolic derivatives becomes a serious concern for water pollution. Therefore, the monitor of OA within a permissible level is important, for instance, limit of OA content in spinach is preferred to be 9.7 mg/1g. Monitor of OA is also necessary for organic fuels e.g. ethylene glycol-based fuels. The electrochemical platforms are prevalent for OA sensors and the non-enzymatic electrochemical sensors with nanomaterials have shown attractive advantages like high stability, ease of processability, cost-effectiveness, and sensitivity. However, its performance depends strongly on the presence of noble metals such as Pt nanoparticles. So efficient but simple, cost-effective, and environmentally friendly method is required for selective detection of sub-micro-molar OA for an early alarm. It is noteworthy that oxalic acid with $pK_{a1} = 1.25$ and $pK_{a2} = 4.2$ is prone to interact with sulfur to make sulfide bond or form a less soluble H_2S in an aqueous medium to exit as gas. Furthermore, OA can act as surface capping ligand for nanostructures and can influence the optical absorption sufficiently and thus offers a way for its determination. In this context, large

surfaces of NPs with an effective reaction centre can be excellent probe when it offers a measurable change in optical response for the detection

Considering above analogy ZnS is synthesised without a capping agent in the sunlight. Thus green synthesis of ZnS NPs is found to be cubic Zinc blende phase with a band gap value (E_g) of 4.3 eV (Figure 1a). The blue shifted E_g from a bulk value of 3.67 is indicative of quantum dots formation. Notably, ZnS NP shows a significant broad band in the visible region of the absorption spectrum. This feature is due to presence of vast surface defects, mainly from elemental type 'S' (E_s) defects as supported by PL studies (Figure 1b). Moreover, it is also observed that OA interacts with ZnS NPs strongly with Es and alters the PL spectrum. The UV-visible absorption of 0.25 mg/ml solution of ZnS NPs and results from the addition of different concentrations of OA are shown in Figure 1c.

The absorption band quenches on the addition of OA and this feature is favourably used for OA detection and estimation by recording each spectrum from different concentrations of OA. The response is thus straight forward. The method is quick and offers nM detection. Typical smell of H_2S was found during the initial addition of OA to the ZnS NPs confirming an interaction between S and OA. Notably, the solubility of H_2S is almost 100 times less than NH_3 . Thus, subsequent decrease in the absorption intensity due to the loss of S, mainly from surface defects is justified. Interaction with S of ZnS NPs is supported by the chemical formation of Ag_2S from Ag^+ . Interaction of ZnS NPs with organic solvents like methanol, ethanol, acetone, other metal ions and oxalates was studied (Figure 1d). For selectivity study, the absorption peak intensity was recorded and the response after OA addition was defined as, $R = (ZnS_{ab} - X_{ab})/ZnS_{ab}$. Here X_{ab} is the absorbance at 500 nm on the addition of OA to ZnS NPs and ZnS_{ab} is reference absorbance of ZnS NPs. For understanding the comparative performances, the optical response of OA is taken as 100% response for micro-molar concentration and then it is compared with other analytes which do not interfere significantly (Figure 1d). However, citric acid and acetic acid provide almost 28 and 24% responses. The PK_a values for OA, citric acid, and acetic acid are 1.25, 3.13, and 4.756 respectively and thus provide a self-explanatory for proportionate variation with acid strength of organic acids. Thus, nM to mM detections of OA in a single step is realized in a selective and environmental friendly way.

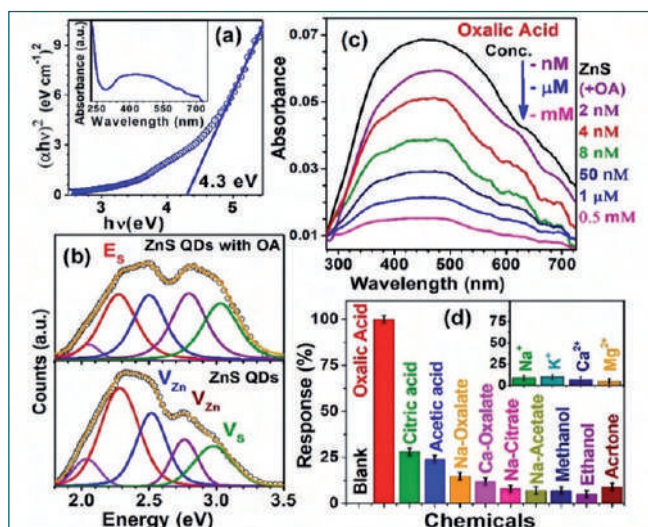


Fig. 1 (a) Absorption and Tauc's plot, (b) PL spectra (c) colorimetric OA detection, (d) selectivity study

V.15 Investigation of Magnetic and Magnetocaloric Properties of DySe₂

Magnetocaloric effect (MCE) is a magneto-thermodynamic effect in which a magnetic material subjected to changing magnetic field experiences a change in temperature. It is characterized by two parameters viz., adiabatic temperature change (ΔT) and isothermal entropy change (ΔS). Materials which have large values of MCE parameters are suitable for MCE based refrigeration applications. Rare earth metals (RE) based binary compounds are found to be promising in this regard; however, many binary compounds are still unexplored. The study of magnetic behavior of unexplored binary RE compounds is important to search for potential working materials with improved MCE parameters over a wide temperature span. Magnetic and MCE behavior of hitherto unexplored DySe₂ compound is reported for the first time in this article.

DySe₂ sample was synthesized by solid state reaction. XRD indicates the structure as tetragonal with lattice parameters $a = 4.0093 \text{ \AA}$ and $c = 8.2300 \text{ \AA}$. The structure belongs to the space group $P4/nmm$ with the constituent elements occupying Wyckoff coordinates: Se1 (0, 0, 0), Se2 (0, 0.5, 0.3666) and Dy (0, 0.5, 0.7265). Se1 atoms occupy the centers and corners of two square bases along the top and bottom basal planes of unit cell

as shown in Figure 1a. The Dy atoms occupy the apex positions of square pyramids whose Se1 square bases are at angle 45° to the basal Se1 squares. The Se2 atoms form square bases of inverted square pyramids with apex positions occupied by the Dy atoms. The square bases of both the pyramids do not contain the central Se atoms as shown in Figure 1a. Temperature (T) dependent magnetization behavior for DySe₂ at 100 Oe field is shown Figure 1b. The system exhibits paramagnetic (PM) to antiferromagnetic (AFM) phase transition at $T_N \sim 4.7 \text{ K}$. Hysteresis is not observed between cooling and heating measurements. The PM behavior above T_N is analyzed using Curie-Weiss law. The effective magnetic moment (μ_{eff}) and Curie-Weiss temperature (q_{CW}) are found out to be -11 m_B and 10.8 K . The negative value of q_{CW} indicates the presence of AFM interactions in the sample. The Neel temperature T_N systematically decreases with increase in field as shown in inset of Figure 1b. The randomization of AFM order in the presence of applied field is responsible for decrease in T_N .

Isothermal magnetization (M) measurements with field (H) at different temperatures are shown in Figure 1c. Magnetization traces the same path for ascending and descending field directions exhibiting zero coercivity at all temperatures. Below T_N , the system exhibits a change of slope in M at low fields. The signature is clearly seen as a peak in dM/dH versus H plots as shown in Figure 1d. This may be due to field induced meta-magnetic transition from AFM to ferromagnetic/canted AFM phase. Though temperature dependent hysteresis is not observed, system exhibits negative slopes on H/M axis close to T_N as shown in Figure 1e. This indicates the PM to AFM transition is of first order type. System also exhibits additional negative slope change for $T < T_N$ indicating the meta-magnetic transition is also a first order transition. Maxwell's thermodynamic relation was used to extract magnetic entropy change (ΔS) from MH measurements. The variation of ΔS as a function of T for field change DH in the range 10-70 kOe is shown in Figure 1f. ΔS exhibits nonmonotonic behavior with a peak (ΔS^{max}) for all DH . The magnitude of peak increases with increase in DH . For $DH = 10 \text{ kOe}$, ΔS is positive at $T = 3 \text{ K}$ and the magnitude decreases with increase in T , passes through zero at $\sim 4 \text{ K}$ and becomes negative above this temperature. For $DH > 10 \text{ kOe}$, ΔS is negative in the entire range. The value of ΔS^{max} is found to be $\sim 11.7 \text{ J/kg-K}$ for $DH = 70 \text{ kOe}$. The observed values of ΔS^{max} are moderate as compared to envisaged potential RE based MCE systems at low temperatures.

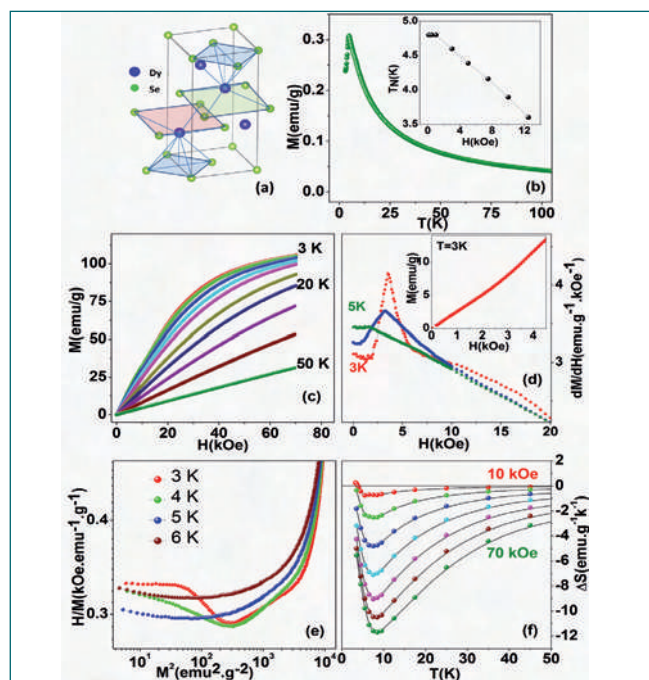


Fig. 1 a) Unit cell of DySe₂; Selenium atoms from the adjacent unit cells are shown to depict the square pyramids (b) Magnetization M versus temperature T ; inset: Neel temperature T_N versus applied field H (c) M versus H (d) dM/dH versus H ; inset: M versus H at $T = 3 \text{ K}$ (e) H/M versus M^2 plots (f) Entropy change (ΔS) versus T

V.16 Metal Oxide / Vertical Graphene Nanosheets Hybrid Electrodes for Energy Storage Applications

Ever growing impetus in renewable, green energy sources and the identification of sustainable energy storage device has gained copious attention. Of late, the electrochemical capacitor (or) supercapacitor (EC or SC), emerged to be a promising energy storage device, propelled the energy research to meet clean energy challenges of twenty-first century. The SC's have high power density with moderate energy density, bestows them fast charge-discharge (order of 10 sec) and prolonged cycle life (around 10^5 cycles). Thus, SC's are considered to bridge the gap between conventional high-energy batteries and high-power capacitors.

Transition metal/metal oxides, nitrides, hydroxides, oxynitrides and conductive polymers are the common pseudo supercapacitor electrode materials, possess high capacities with moderate cycle life, yet carbon materials like carbon nanotubes, carbon fibers, and graphene have drawn more attention due to their excellent electrical conductivity and superior electrochemical stability. Additionally, the graphene and metal oxides composites exhibit the combination of the excellent cycle stability of graphene and the high-capacity properties of metal oxides. Further, the development of vertical graphene Nanosheets (VGN) a 3D interconnected graphene network based electrode in combination with metal oxides remarkably enhance the comprehensive properties of nanocomposites. The current developments of metal oxide decorated Vertical graphene (MOx/VGN) hybrid electrodes for electrochemical capacitors at IGCAR are elucidated here.

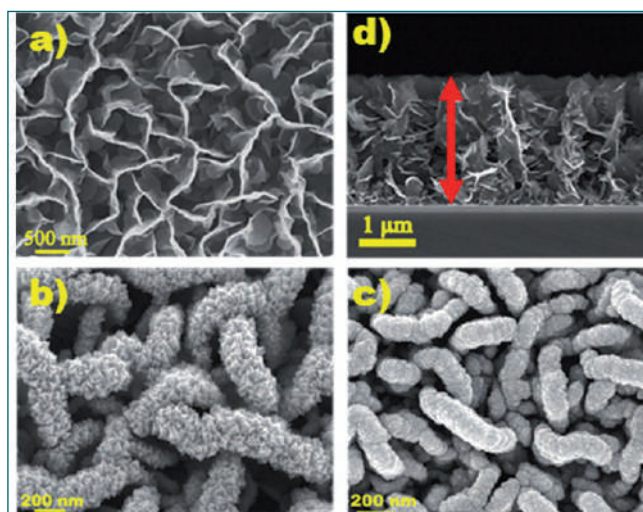


Fig. 1 FESEM morphology of (a) as-grown VGN, (b) CuO/VGN, (c) NiO/VGN and (d) cross section height of VGN

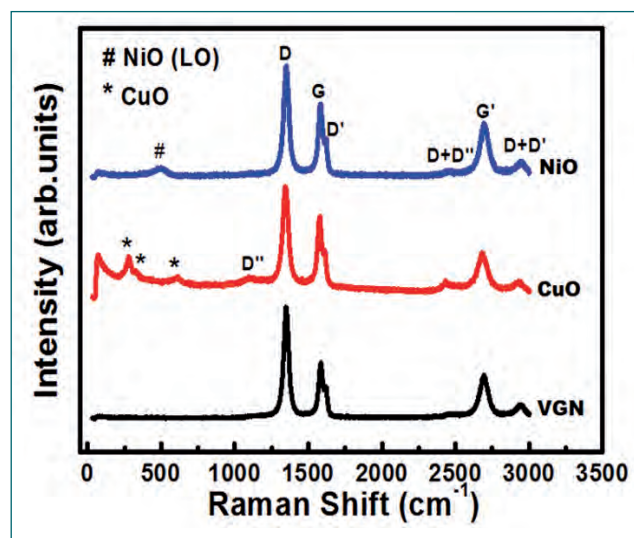


Fig. 2 Raman spectra of as-grown, CuO and NiO/VGN

Herein, the VGNs are grown by using plasma enhanced chemical vapor deposition (PECVD) technique using high pure Ar, CH₄ gas mixture. On the other hand, both CuO and NiO are deposited onto VGN using pulsed laser deposition technique (PLD) using high pure CuO and NiO targets, respectively.

Figure 1(a-c) illustrates the FESEM morphology of as-grown and CuO, NiO decorated VGN. The 3D interconnected porous networked morphology of VGN is evident in Figure 1(b,c). Decoration of VGN with CuO and NiO nanoparticles is shown in Figure 1b and 1c. Cross sections FESEM image in Figure 1d confirmed the vertical growth of interconnected graphene sheets of VGN.

Figure 2 depicted the Raman spectra of as grown and CuO, NiO decorated VGN. The Raman spectrum for as-grown VGN shown characteristic carbonaceous peaks D (1348 cm^{-1}), G (1581 cm^{-1}), G' (2690 cm^{-1}) of VGN and are observed in all the three spectra. Additionally, the characteristic peaks of CuO and NiO in lower frequency regions confirm their decoration on VGN.

The cyclic voltammetry measurements are performed in 3 electrode configuration with KOH electrolyte and Pt counter electrode. The Figure 3 (a-c) showed CV curves of as-grown, CuO and NiO VGN, respectively. The VGN possess near rectangular CV curve affirmed their electric double layer capacitance nature. On the other hand, CV curves of CuO and NiO decorated VGN are dominated by redox peaks due to their pseudo capacitance nature. The measured areal capacitance

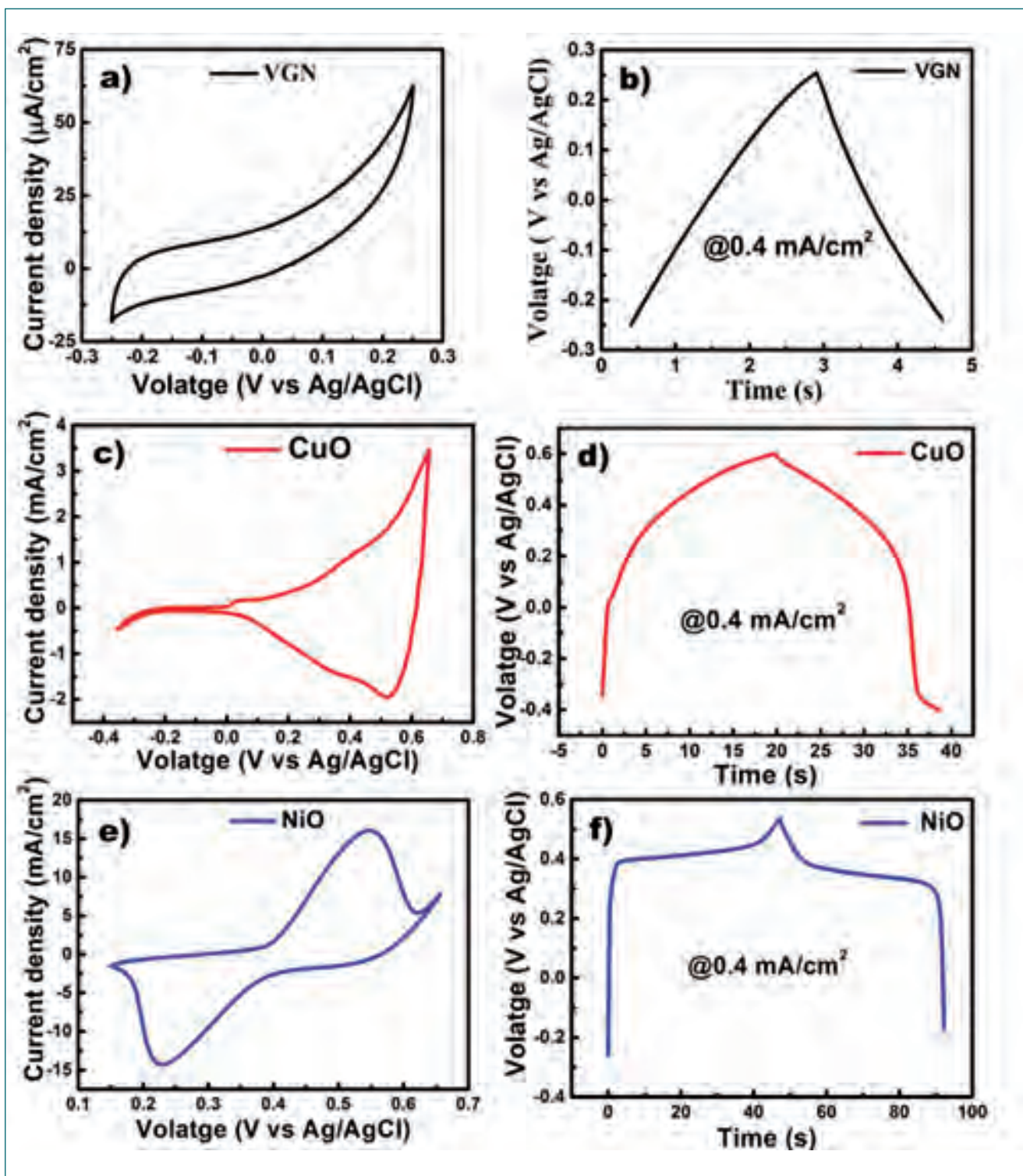


Fig. 3 (a) to (c) CV profiles and (d) to (f) CD profiles of as grown, CuO and NiO decorated VGN, respectively

values are $150 \mu\text{F}/\text{cm}^2$, $20 \text{mF}/\text{cm}^2$ and $80 \text{mF}/\text{cm}^2$ for as-grown, CuO and NiO VGN, respectively. The corresponding charge-discharge profiles are depicted in Figure 3(d-f). The triangular CD profile of as-grown VGN affirmed its EDLC nature. In contrast, bell-shaped CD profile of CuO represents its pseudo capacitive nature and NiO/VGN showed a battery type CD profile. Also,

these electrodes are subjected to 2000 charge-discharge cycles and found that the capacitance retention is 90%. These results substantiated the potential usage of metal oxide (CuO, NiO)/VGN hybrid electrodes for the fabrication of supercapacitor devices towards energy storage applications.

V.17 Effect of Electric Dipolar Interaction on Inter-Droplet Force Profiles in Magnetically Polarizable Pickering Nanoemulsions

Oil-water emulsions are thermodynamically unstable systems, where kinetic stability is imparted by functionalization of the oil-water interfaces using suitable moieties, such as surfactants, polymers and nanoparticles. Despite the immense progress made on the preparation and applications of nanoparticle stabilized Pickering emulsions, the knowledge of the exact nature of colloidal interaction forces is still in its infancy and requires further attention. For electrostatically stabilized Pickering emulsions, the presence of asymmetric image charge cloud at the oil-water interface, due to the strongly attached charged nanoparticles, makes the total repulsive force profile complex owing to the combined contributions from the screened Coulombic and electric dipolar interactions. With an objective to probe the nature of colloidal force in Pickering nanoemulsions, inter-droplet force measurement studies were carried out using the magnetic chaining technique.

In the present study, starting from a polydisperse sodium dodecyl sulfate (SDS) stabilized emulsion, monodisperse SDS stabilized nanoemulsion was obtained using a fractionation technique, from which γ -Al₂O₃ nanoparticle (hydrodynamic diameter \sim 12 nm) stabilized oil-in-water magnetic nanoemulsion (MNE) of average hydrodynamic diameter \sim 253 nm and containing superparamagnetic nanoparticles in the oil phase, was prepared using a solution exchange route. Under the exposure to a static external magnetic field, the MNE droplets undergo disorder-to-order transition and form linear chain-like structures along the direction of the external field. Exploiting this phenomenon, inter-droplet force profiles were measured using the in-house developed magnetic chaining technique, where

prominent Bragg's reflection peaks were observed when the incident wavelength matched with the inter-droplet spacing, which was tuned by varying the strength of the external magnetic field. The inter-droplet force measurements were carried out at different pH and salt concentrations and the role of mono, di and trivalent salts on the inter-droplet force profiles was systematically probed. The repulsive force components due to the screened Coulombic (single decay length Debye-Huckel model) and electric dipolar interactions were theoretically calculated and compared with the experimental force magnitudes at varied inter-droplet distances and salt concentrations.

Figure 1a shows the experimental inter-droplet force profiles for the MNEs, in the presence of 1.65 mM monovalent (NaCl) salt concentration, as a function of normalized inter-droplet spacing $[\kappa_D(d-2r_e)]$, where κ_D is the inverse of Debye screening length, d is the center-to-center separation between the MNE droplets and r_e is the radius of the MNE droplets. Figure 1a also shows the theoretically calculated inter-droplet force profiles, considering the individual electrostatic (screened Coulombic interaction), electric dipolar (long range asymptotic form) interactions, as well as the combined interaction. It can be seen from Figure 1a that the experimental force magnitudes differed by orders of magnitude from the theoretical values, considering the screened Coulombic interaction alone. The presence of strongly adhered charged nanoparticles at the oil-water interface, for the Pickering MNEs, resulted in the formation of asymmetric image charge cloud in the vicinity of the polar/non-polar liquid-liquid interface, which caused a stronger electric dipolar interaction that invariably modified the nature of the interaction forces. It was further observed from Figure 1a that, incorporating the contributions from electric dipolar interaction, the theoretically calculated force profiles were in good agreement with the experimental data. Figure 1b shows the surface plot of the theoretically calculated force profile, surrounding a single Pickering MNE droplet (NaCl concentration \sim 5.45 mM). The developed theoretical model was also experimentally validated for divalent and trivalent salts.

The findings clearly show the importance of electric dipolar interaction for charged particle stabilized magnetic nanoemulsions and offer deeper insights into the nature of colloidal force between the interacting MNE droplets.

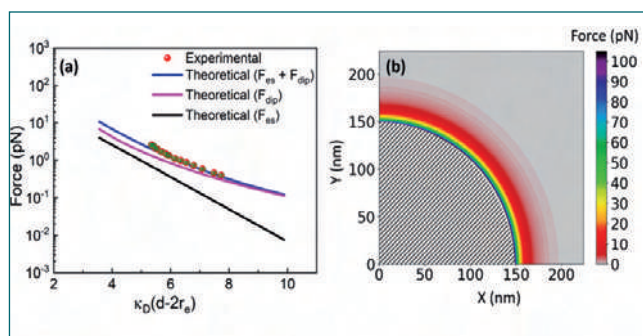


Fig. 1 a) The experimental and theoretical inter-droplet force profiles for the pickering MNE, in the presence of 1.65 mM NaCl salt concentration, as a function of $\kappa_D(d-2r_e)$. (b) The surface plot of the theoretically calculated force profile, surrounding a single pickering MNE droplet.

V.18 Depth-resolved Microstructural Response in He-ion Implanted FeCrCoNi

High entropy alloys (HEAs) are novel alloys having multiple elements in near/equiatomic proportions and yet forming simple solid solutions owing to their high configurational entropy. These alloys are bestowed with excellent material properties such as good thermal stability, high temperature strength, good resistance against oxidation, corrosion. Recently, many studies have focussed on the irradiation resistance in Fe-based HEAs in order to assess the applicability of these alloys as nuclear structural reactor materials, using a variety of techniques such as Rutherford backscattering, transmission electron microscopy (TEM). In the present work, the radiation response of FeCrCoNi to helium ion implantation (energy- 130 keV, fluence – 1×10^{16} ions/cm²; 3×10^{-2} dpa) in terms of the formation and growth of helium bubbles is investigated using the variable low energy positron beam by post annealing the room temperature implanted sample in the temperature range from 373-1373 K.

Monoenergetic positrons are implanted starting from surface up to a depth of a few hundreds of nm by varying the energy of the positron beam. For each positron beam energy, the Doppler spectrum resulting from electron-positron annihilation is obtained using the HPGe detector. The defect-sensitive S-parameter expressed as ratio of counts in peak region to the total counts under the 511 keV peak is deduced from each Doppler profile. In presence of vacancy defects, the S-parameter increases, and therefore a plot of S vs. E_p (positron beam energy) represents the depth profile

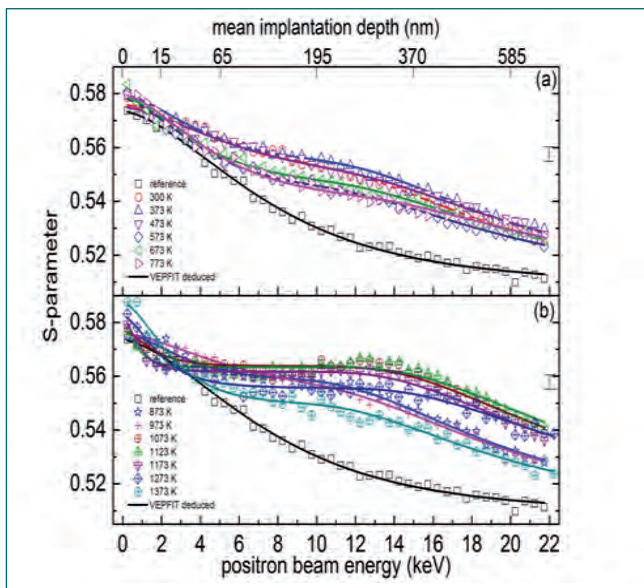


Fig. 1 S-parameter vs. E_p in the temperature range 373-1373 K. The solid lines through the data points are the result of VEPFIT analyses

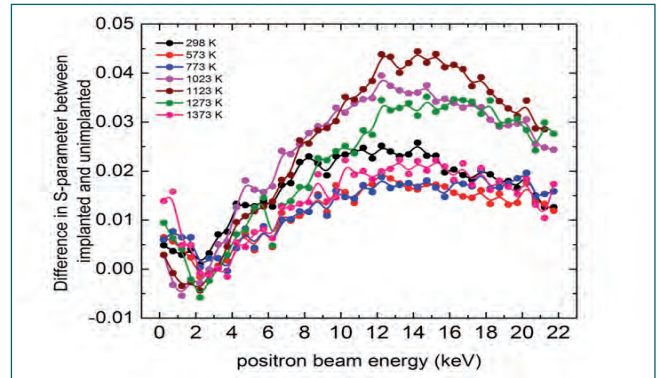


Fig. 2 Difference in S-parameter vs. E_p in the temperature range 373-1373 K

of implantation-induced defects. The variation of S vs. E_p is shown in Figure 1. Different stages of the defect microstructure such as the defect annealing (up to 573 K), nucleation of helium bubbles beyond 673 K and the growth of bubbles at higher temperatures are observed. Figure 2 shows the difference data in S-parameter between the isochronally annealed implanted sample and the unimplanted sample. The difference data shows a peaking around 15 keV (~ 370 nm) and the peaking is maximum for the 1123 K annealed sample. This is the temperature where there is maximum growth of the He bubbles in FeCrCoNi. The difference data in S-parameter has been averaged between 12 and 18 keV for all the anneals. Upon comparing the results of the present study with that of the reported data obtained for He ion-implanted in Ni, it is very clear that the difference data in S-parameter is higher for Ni than in FeCrCoNi (Figure 3). The difference in S-parameter is 0.04 in FeCrCoNi, whereas it is 0.08 – two times high in Ni at 1123 K. This means that the bubble growth in FeCrCoNi is less than that of Ni implying that FeCrCoNi has better resistance to bubble growth.

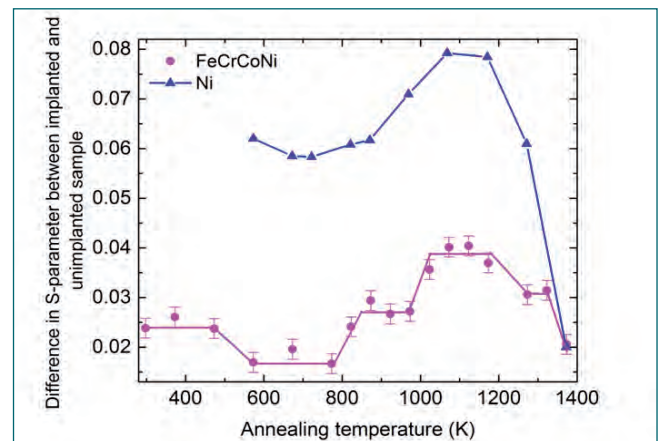


Fig. 3 Comparison of difference data in S-parameter of Ni to that of FeCrCoNi

V.19 Structural, and Mechanical Properties of $Y_2Ti_2O_7$ Single Crystal

The pyrochlore rare earth titanates have attracted much attention of researchers because of their superior structural characteristics and exotic physical properties. Yttrium titanate ($Y_2Ti_2O_7$) is one of the important members of the pyrochlore family. It has a strong electron-phonon interaction and high oxygen vacancy concentration which results in large defect concentration. The $Y_2Ti_2O_7$ compounds also have high tolerance to high energy radiations and they are useful as host material for immobilization of nuclear waste. Moreover, the ultrafine $Y_2Ti_2O_7$ nanoclusters is one of the strengthening additives which provides the mechanical strength and radiation resistance in oxide-dispersion-strengthened alloys. Hence, the fundamental properties (elastic constants) of $Y_2Ti_2O_7$ single crystal is very much needed, which are directly related to crystal structure and the chemical bonding.

$Y_2Ti_2O_7$ compound seed rods were synthesized by power metallurgical route from high pure materials and annealed at 1400 °C for 24 h. Due to non-availability of single crystal seed, growth was initiated using a polycrystalline rod by Optical Floating Zone technique having four mirrors. Figure 1 shows the $Y_2Ti_2O_7$ single crystal, XRD pattern of powdered yttrium titanate single crystal for phase purity along with rocking curve for the single crystal quality. The absence of secondary phases related to Y-Ti-O complex structure confirms the phase purity of the grown $Y_2Ti_2O_7$ crystal (JCPDS:00-42-0413). Further, it is known that the pyrochlore structure undergoes an order-disorder transformation into defect fluorite structure when the cation antisite disorder increases. The degree of cation antisite disorder estimated (I_{331} / I_{400}) ratio of our single crystal is 0.76 which is very close to the theoretical value (0.71) for

Table 1. Mechanical properties of $Y_2Ti_2O_7$ single crystal as compared with Y_2O_3 , TiO_2 , and $Y_2Ti_2O_7$ polycrystalline ceramics

Physical Properties	Y_2O_3 (literature)	TiO_2 (literature)	$Y_2Ti_2O_7$ Poly-crystalline (literature)	$Y_2Ti_2O_7$ single crystal (This work)
Hardness (GPa)	6.9 - 9.1	11.0	12.1	16.4 ± 0.4
Elastic Modulus (GPa)	188	270	253	321.1 ± 6.9
Bulk Modulus (GPa)	158	152.5	170	243.3 ± 5.2

an ideal and fully ordered pyrochlore structure. The orientation of the grown crystal is found to be $\langle 111 \rangle$. The FWHM of the rocking curve is 695 arcsec, which shows the quality of the crystal (Figure 1 inset). Hence, the analysis of the XRD pattern confirms that this yttrium titanate crystal has highly ordered pyrochlore structure with minimal cation antisite disorder. Detailed Raman studies (not shown in figure) are also performed in order to confirm absence of secondary phase.

Table 1. presents the measured Indentation Hardness (H), Indentation Modulus (E) and Bulk modulus (B) using nano-mechanical characterization and also these values are compared with the literature values of Y_2O_3 , TiO_2 , $Y_2Ti_2O_7$ polycrystalline ceramics. The mechanical properties of the yttrium titanate single crystal is higher than its polycrystalline counterparts and its constituent metal oxides, Y_2O_3 and TiO_2 .

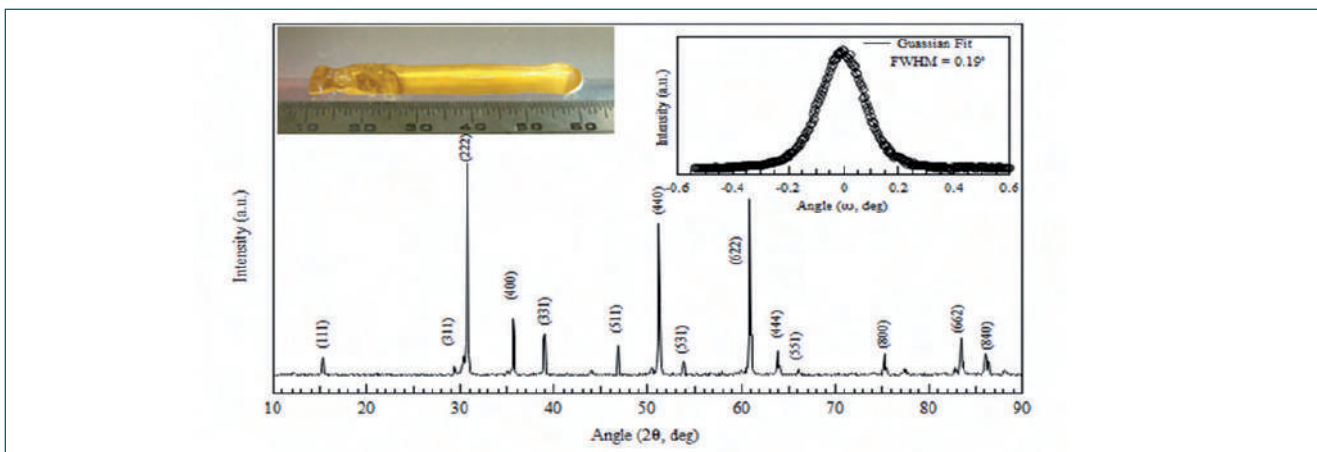


Fig. 1 XRD profile with in sets single crystal and its rocking curve

V.20 Blue Luminescence of SnO₂ Quantum Dots for Selective Trace Ammonia Detection

Tin oxide (SnO₂) nanostructures are highly used in key technological applications, e.g., gas sensors, optical devices, catalysis, energy storage, biosensors. The resistive sensors based on defects chemistry of SnO₂ are well investigated and established in contrast to contactless optical sensors like photoluminescence (PL). In fact, the later is though demanding application but remains elusive so far as it needs comprehensive understandings on the role of cationic and oxygen defects as well as their creation in abundant quantity so as to provide a reasonable PL signal. Notably SnO₂ is a dipole forbidden wide band gap (3.6 eV) *n*-type semiconductor. Its rich defects chemistry related to Sn interstitial and O vacancies, mainly in nanostructures provide PL signal. The wide variations of defects offer opportunity in tailoring optical property and can act as an optical probe. So, for a selective ammonia sensor, Sn defects along with O vacancies in SnO₂ are focused, in particular, with reference to the blue emission (BL) PL sensor. To achieve the goal, prerequisite is the creation of vast surface area along with effective defects such as cationic and oxygen. This is realized in the form of SnO₂ nanoparticles (NPs).

SnO₂ NPs of ~ 2.5 (S-1), 4 (S-3), 9 (S-5) and 25 nm (S-8) sizes are synthesized and characterized. The rutile tetragonal phase is verified by the X-ray diffraction and HR-TEM. The PL spectra are acquired using 325 nm as an excitation source. A broad band observed around 2 eV for all NPs is displayed in Figure 1(a). This peak is attributed to various oxygen vacancies. The peaks at 1.84, 1.96, 2.11, arise due to bridging type oxygen vacancies (V_B) and other transitions at 2.28 and 2.45 eV are from in-plane oxygen vacancy (V_I). Earlier reports show that V_I and V_B create shallow and deep donor levels, respectively. The inset indicates two obscured peaks at 2.77 and 2.96 eV which are referred to blue emission PL. The distribution of various defects is established by using temperature dependent PL as well as synchrotron based EXAF measurements. The related

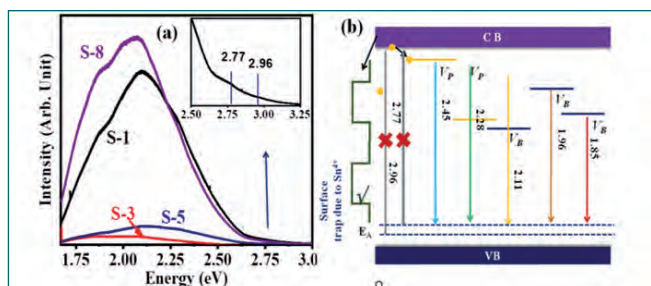


Fig. 1 (a) PL spectra (b) band diagram of SnO₂ NPs

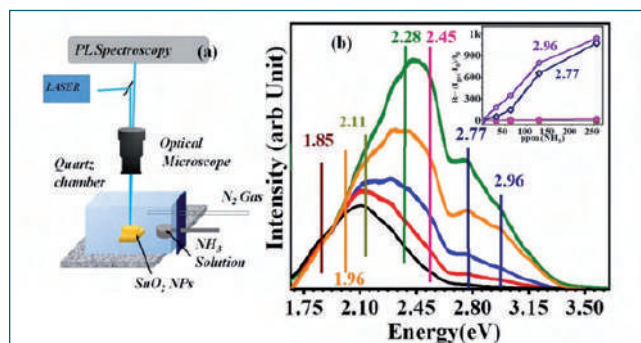


Fig. 2 (a) Sensor chamber set up (b) PL spectra on ammonia exposures and inset for sensor responses

band diagram is shown in Figure 1b. A comprehensive understanding is gained with a plausible explanation for the observation of the obscured peaks theoretically by DFT calculations. The PL sensor experiment is conducted at atmospheric conditions. A schematic diagram of the used sensor set up is shown in Figure 2(a). The different volumes of NH₄OH act as a source of ammonia. Then, PL from various SnO₂ NPs was recorded and a typical result is shown in Figure 2(b) for SnO₂ NPs (S-1) which is smaller than the Bohr exciton radius of 2.7 nm.

Strong change in PL intensity is clearly observed around 2 eV. Importantly, an increase in intensity is observed for both BL peaks on gradual increment of NH₃ concentrations. N₂ is passed to get rid of NH₃ and to understand the recovery process. The recovery is obtained within minute. The difference in intensity before and after exposure is then recorded as sensor response which is shown in Figure 2b as inset. Very high response is obtained for BL peaks. Possible interferences from other vapours like acetone, alcohols do not show noticeable change in BL intensity. Thus, selective nature for ammonia sensor is achieved for a wide range of concentrations of ammonia (30 to 250 ppm).

The underlying mechanism for the enhanced BL intensity is established. The presence of cationic and low coordinated Sn is found to be most crucial component for BL transitions. The acidic sites act as interacting sites for Lewis base NH₃. Before, exposing NH₃, surface defect state created by under-coordinated Sn traps the photo excited carrier to prohibit BL observation. Sn⁴⁺ trap states increases the probability of transition of photo-excited electron back to the valance band on adsorption of ammonia. This enhances intensity of BL. Preferential adsorption site is also verified by DFT calculation. Thus, contactless NH₃ sensing using SnO₂ QDs is realized in selective manner by using PL as a probing tool.

V.21 Structure–Compressibility Correlation among MoB_x

Diamond is the hardest naturally occurring material known. The search for new hard materials has provided three classes of materials: carbonaceous materials like diamond, diamond-like carbon and nano diamond; covalent compounds formed by low-Z elements such as BN and SiC; and transition metals (TMs) forming intermetallic compounds with C, B and N. The first two classes require extreme conditions for their synthesis, i.e. high pressure and high temperature. The third class of materials can be synthesised by a number of methods such as sintering, hot pressing, arc melting and chemical synthesis. Among them, TM borides readily form compounds because of high valence of TMs and electron deficiency of B. The TM borides are used across industries for their chemical inertness, refractory nature and hardness. Molybdenum forms a large number of borides with various stoichiometries, i.e. Mo₂B, MoB, MoB₂, Mo₂B₅ and MoB₃. Here we report synthesis of MoB₃ by arc melting and study its compressibility behaviour. Also, systematic computational studies on molybdenum borides (Mo₂B, MoB₂, MoB and MoB₃) are carried out to establish the structure–compressibility correlation.

High-pressure XRD experiments were carried out using a Mao–Bell-type diamond anvil cell. A stainless-steel gasket of 200- μm thickness was used to contain the sample between the two opposed diamond anvils. Methanol ethanol water mixture was used a pressure transmitting medium. Silver was loaded along with the sample for pressure calibration inside the DAC. A Genix3D micro X-ray generator with Mo as the target was used for generating X-rays with wavelength 0.711 \AA . The diffracted X-rays were collected onto the image plate of mar345. First-principles calculations were performed on MoB_x as implemented in VASP code. The PAW formalism with the GGA of PBE to the exchange correlation functional was favoured. The maximum plane wave cut-off energy was set at 550eV.

The MoB₃ was synthesised by arc melting Mo and B in the atomic ratio of 1:4. The excess B was used to compensate for the B loss that occurred while arc melting. The powder XRD pattern was compared with all known phases of Mo–B. The XRD pattern agreed with that in ICDD PDF card 04-007-1054 and could be indexed to the Mo_{0.8}B₃ structure. The Rietveld refinement of the ambient XRD pattern was carried out using the GSAS

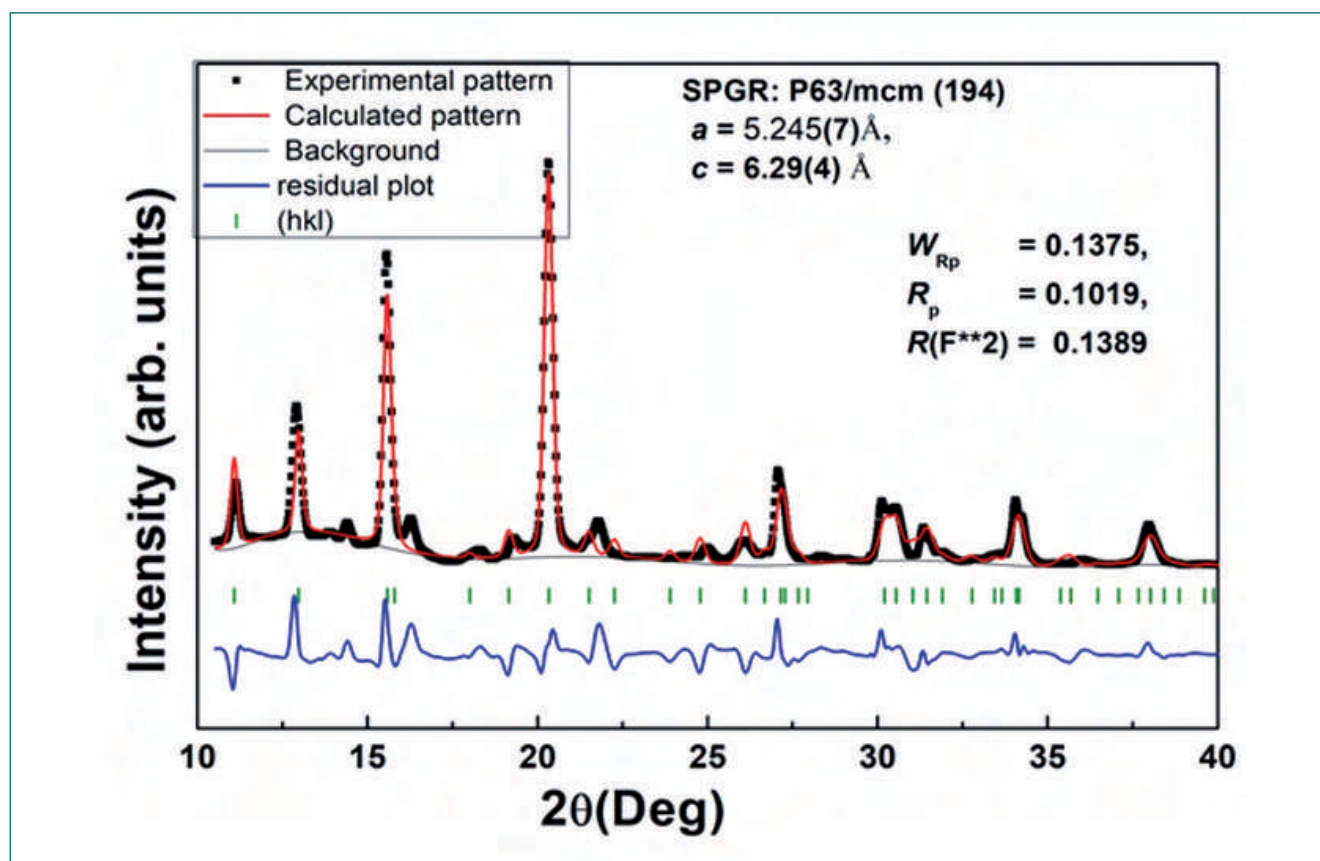


Fig. 1 XRD pattern of MoB₃

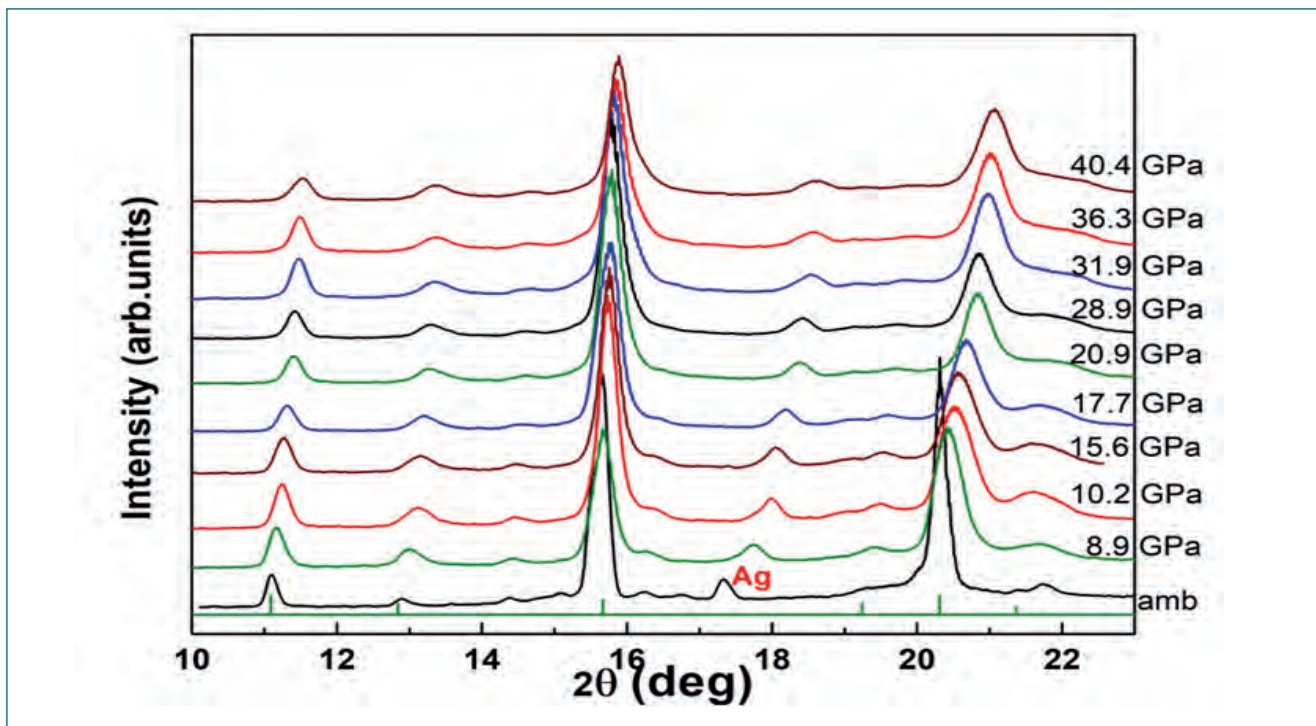


Fig. 2 XRD patterns of MoB₃ at various pressures along with a stick plot of ICDD PDF 04-007-1054 showing (hkl)

+ EXPGUI software package (Figure 1). The obtained lattice parameters were $a = 5.245(7)$ Å and $c = 6.29(4)$ Å. The refined parameters were $W_{Rp} = 0.1375$, and $R_p = 0.1019$, and the reduced $\chi^2 = 0.1389$ indicated that the synthesised sample was Mo_{0.8}B₃, which is referred to from here on as MoB₃.

The in-situ HPXRD studies were carried out on MoB₃ up to a pressure of 40 GPa. The collected XRD patterns at various pressures after integration were plotted (Figure 2). The silver 2q peak corresponding to the (200) plane (Figure 2) was used to estimate the pressure inside

the DAC. The XRD patterns showed no significant change, indicating that the hexagonal structure was stable up to the highest pressure studied. The unit cell volumes were obtained at different pressures and fitting the P-V data yielded a bulk modulus of 254 (9) GPa in good agreement with 258 GPa obtained from DFT calculations. Bulk moduli of other borides of Mo as functions of B are shown in Figure 3a. The variation of bulk modulus as the ratio of Mo to B showed interesting behaviour. It is generally understood that the addition of a low-Z element into the TM lattice enhances the

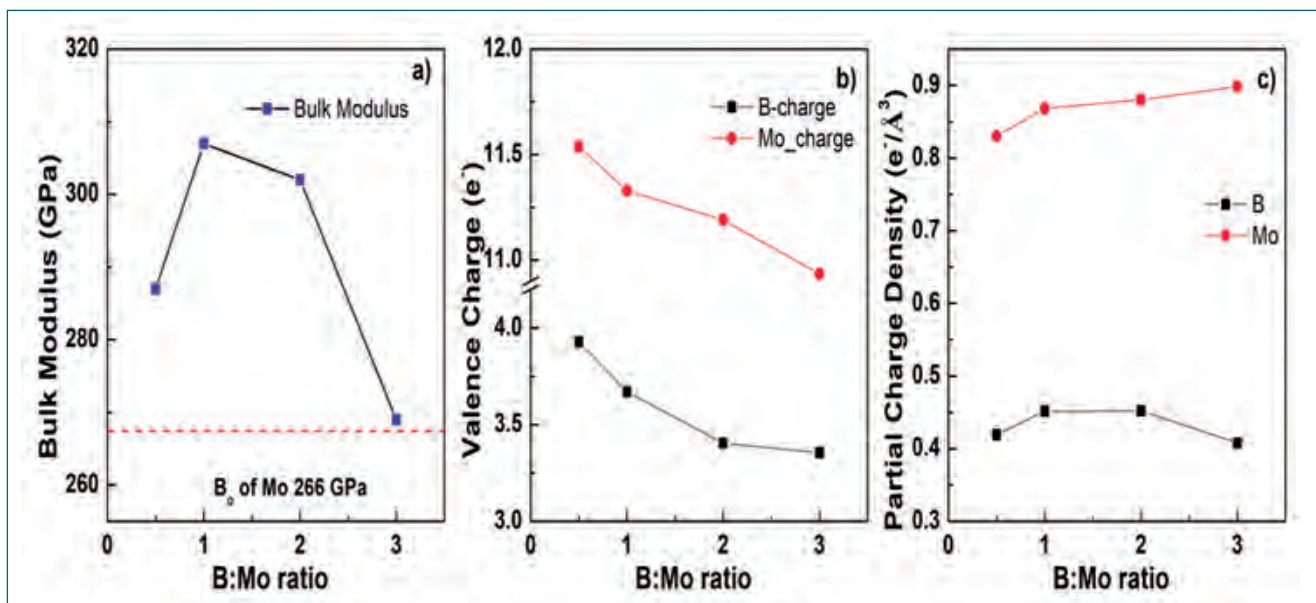


Fig. 3 Comparison of properties of Mo borides as functions of B to Mo ratio: (a) bulk modulus, (b) valence charge on B and Mo and (c) partial charge density on Mo and B

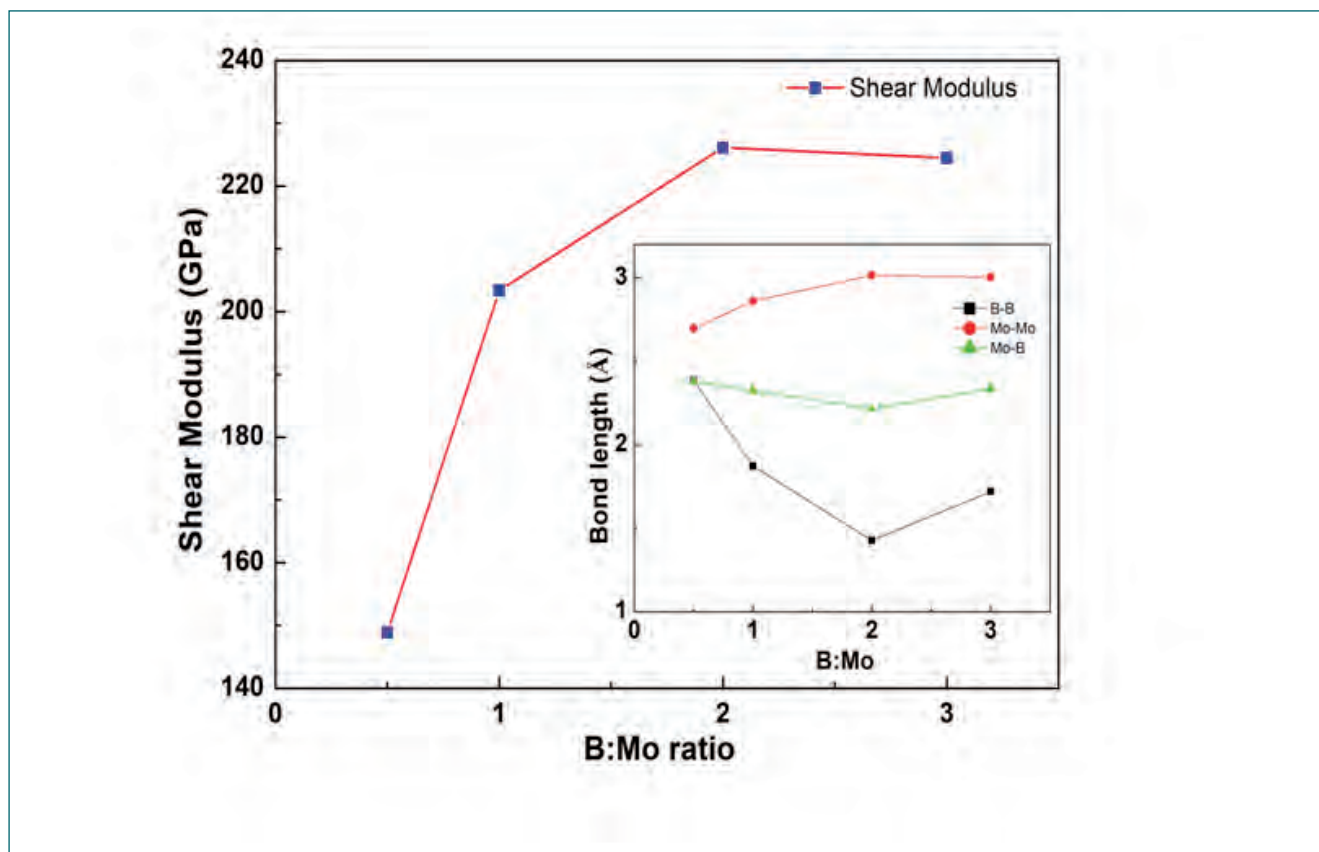
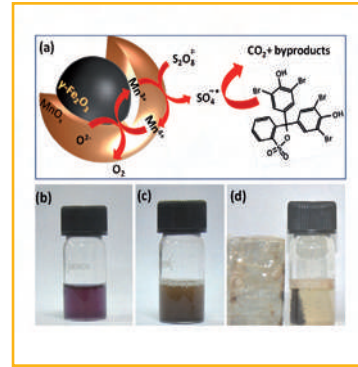
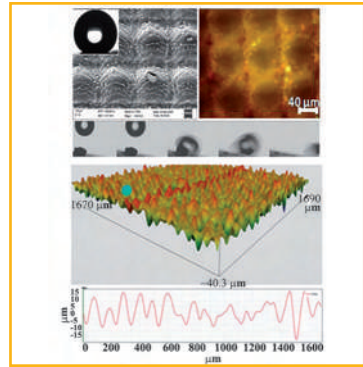


Fig. 4 Variation of shear modulus in MoB_x ; inset shows bond lengths of B–B, Mo–Mo and Mo–B

mechanical properties of the TM. In its pure form, Mo has a bulk modulus of 266 GPa. On addition of B to the TM, the bulk modulus increased but did not increase linearly – it saturated at MoB – MoB_2 and then decreased below that of Mo for MoB_3 . Compressibility of any compound essentially depends upon the valence charge density of the compound. To investigate this, Bader charge analysis was carried out on the MoB_x system to understand the charge distribution. On incorporating B into the metal lattice there was valence charge transfer from Mo to B. As the B ratio increased in the TM lattice, the amount of valence charge transfer from Mo atom also increased (Figure 3b). Although the valence charge transfer increased from Mo to B, the charge transfer was now shared among a higher number of B atoms and hence the valence charge on B also decreased with increase in B ratio. With the increase in B ratio, valence charge was transferred from Mo to B and so the volume of the charge contained surrounding Mo declined, leading to an increase in partial charge density at Mo site. Partial charge density of B increased from Mo_2B ($0.419 \text{ e}^-/\text{\AA}^3$) to MoB ($0.452 \text{ e}^-/\text{\AA}^3$) and remains same for MoB_2 ($0.452 \text{ e}^-/\text{\AA}^3$) and then decreased for that of MoB_3 ($0.408 \text{ e}^-/\text{\AA}^3$) (Figure 3c). Bulk modulus variation was closely related to that of the B partial charge density. The bulk modulus increased from 288

GPa for Mo_2B to 307 GPa for MoB and 302 GPa for MoB_2 , which were very close, and then decreased to 269 GPa for MoB_3 . Shear modulus obtained from the computed elastic constants as given by Voigt-Reuss-Hill approximation is shown in Figure 4. Interestingly the shear modulus increased with addition of B into the metal lattice and peaked at around 2:1 of the B:Mo ratio and remained almost constant with further addition of B. The bond length and more particularly bond strength were dominating factors in the shear modulus. Bond length variation among the nearest atoms in MoB_x is shown in the inset of Figure 4. The B–B bond length decreased from Mo_2B to MoB_2 and then increased for MoB_3 . There was a similar trend in bond length of Mo–B. The Mo–Mo bond length increased from Mo_2B to MoB_2 and slightly reduced for MoB_3 . In MoB_x , beyond MoB_2 the bulk modulus decreased very rapidly and the shear modulus was nearly unchanged. Our first-principles calculations showed that the shear modulus and bulk modulus tapered near MoB_2 .

HPXRD studies on MoB_3 and the computational studies on MoB_x reveals that compressibility behaviour of MoB_x ($x = 0.5, 1, 2$ and 3) exhibits a parabolic trend and is understood in terms of electronic structure and mainly arises due to the partial charge density of boron.



Directed Basic Research

CHAPTER VI

VI.01 Quantitative Recovery of Boron as Boric acid from Enriched Boron Carbide by Pyrohydrolysis

Recovery of enriched boron from spent radioactive control rods is necessary considering the cost of enriched boron and also to minimise the waste. Recovery of boron from materials using various methods such as pyrohydrolysis and electroextraction has been studied. Pyrohydrolysis procedure does not require dissolution of boron carbide and also results in pure boric acid. Optimisation of pyrohydrolysis conditions for the recovery of boron from boron carbide was standardized and the purity of the boric acid was evaluated by Inductively Coupled Plasma-Optical Emission Spectrometry (ICP-OES).

A photograph of the pyrohydrolysis setup established is given in Figure 1. Quartz pyrohydrolytic tube with proper attachment to carry out pyrohydrolysis was used. B_4C was loaded in alumina boat for the recovery studies. Experimental conditions such as furnace temperature, flow rate of air and moisture, weight of sample and collection method were optimized to get complete recovery of B. The recovery of boric acid was also investigated for oxygen as carrier gas. Both powder and pellet forms of boron carbide samples were used for the separation studies. Recovery of boron was assessed by analyzing the collected boric acid solution by mannitoboric titration. Concentration of impurities in boric acid was determined by analyzing the boric acid by ICP-OES.

Studies of varying furnace temperature revealed 873 K as the optimum temperature since further increase of temperature resulted in the attack of alumina boat. Therefore, all the recovery studies were carried out at

S.No.	Weight of enriched B_4C (g)	Carrier gas	Recovery of boron
1	0.1	Air	99 %
2	0.2		99 %
3	0.3		98 %
4	0.5	Oxygen	97 %
5	1.0		96 %

873 K. After the experiment, to facilitate collecting the condensed boric acid in the connecting bend tube, it was melted by heating using hot air gun. B recovery of nearly 100% was obtained up to 0.3 g by using air as carrier gas (Table 1). Higher amount such as 0.5 g in air does not result in complete recovery even after 15 hours of collection. Use of oxygen as carrier gas resulted around 97% recovery of boron up to 1 g of enriched B_4C for 10 hours of collection. The collection time to get complete recovery was also found to depend on the particle size of boron carbide. All the impurities W, Fe, Mg, Ca and Al in the collected boric acid were found to be below the detection limits of ICP-OES. The complete recovery of boron was also demonstrated for various enriched boron carbide samples.

Complete recovery of boron as boric acid from boron carbide by the pyrohydrolysis method was demonstrated. The high purity of the collected boric acid was established by the analysis of boric acid using ICP-OES.

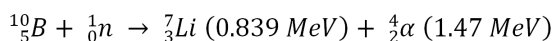


Fig. 1 Pyrohydrolysis facility for boron recovery

VI.02 Boric acid as Converter Material for Semiconductor Neutron Detectors - A GEANT4 Simulation

Neutron detectors find applications in a wide range of fields including in homeland security, detecting special nuclear materials, space exploration and power level monitoring in nuclear power plants. Currently, gas based He^3 detectors are being employed for the above applications owing to their high neutron detection efficiency (η). However, acute shortage of He^3 has compelled scientific community to look for alternatives including solid state detectors. Semiconductor solid state detectors have inherent advantages such as miniaturized size, bulk manufacturing capability, insensitivity to microphonics and requirement of low voltage for operations. The simplest configuration of a semiconductor neutron detector pertains to that of a planar geometry which consists of a neutron sensitive converter material coated on a semiconductor p - i - n diode. The interaction of thermal neutrons with converter material results in the generation of charged particles which is detected by the diode. The challenge lies in the design of converter material in terms of choice of material, thickness, coating on diode, integrity of the coating etc.

Conventionally, ^{10}B , ^6Li and ^{157}Gd containing converter materials are employed for detection of thermal neutrons. Amongst the three, ^{10}B is a natural choice for integration with electronic devices such as p - i - n diodes as it possesses neutron interaction cross section of 3840 barns, moderate Q-value along with good gamma discrimination and thermal stability. The interaction of thermal neutrons with boron results in Li and alpha as per relation .



However, the simplest boron containing material, viz., boric acid (H_3BO_3) is still unexplored although it is non-toxic in nature, easy to handle and can be directly spin coated using a suitable binder. Fabrication being both capital and time intensive, it is prudent to optimize various material and geometrical parameters related to boric acid. The optimizations of parameters have been carried out using GEANT4 (GEometry And Tracking) package, which is a Monte Carlo based method.

A systematic simulation study was undertaken to optimize critical geometric parameters, including the number of detector units (DUs) for boric acid coated Si p - i - n diodes in two dimensional (2D-planar stack) and three dimensional (3D-spherical, cylindrical and cuboidal) configurations to estimate η .

The results of a typical configuration, namely 2D detector (Figures 1a and 1b) stacks are presented here. The simulations carried out for different thicknesses (0.25 μm to 10 μm) of boric acid coating and Boron enrichments (B_E) revealed (Figure 1c) the existence of a critical thickness at which η showed a maximum. Typically, at a critical thickness of $\sim 3.5 \mu\text{m}$, the η for 100% B_E content in boric acid was found to be 15.96% for 30 DUs. Apart from efficiency calculations, histogram plots were generated using G4Analysis Manager, which clearly shows two resolved peaks pertaining to the energy deposited by charged particles ($^7\text{Li} = 0.839 \text{ MeV}$ and $\alpha = 1.47 \text{ MeV}$) in Si detector (Figure 1d). These results indicate that boric acid is a natural choice of converter material for detection of thermal neutrons owing to its non-toxic nature, ease of handling and amenability to fabrication indifferent configurations.

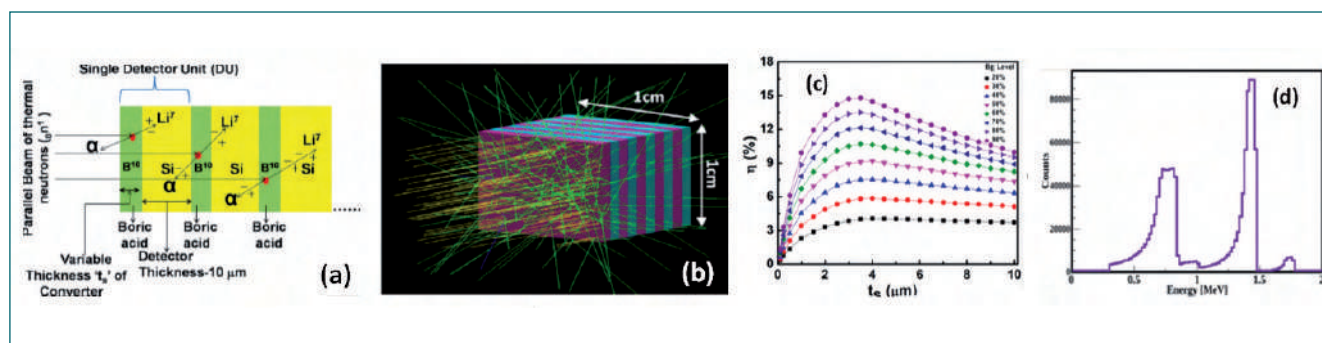


Fig. 1 Planar stack detector configuration consisting of boric acid as a converter material and Si as a detector material (b) Typical snapshot of GEANT4 simulation (c) Variation of efficiency η with thickness t_s for planar stack configuration with Variable B_E (d) Histogram plot of the energy deposited by charged particles (^7Li and α) in Si detector region for stack configuration at $t_s = 0.25 \mu\text{m}$

VI.03 Comprehensive Analysis of Evolving Serrated Hysteresis Loops of Alloy 617M in low Cycle Fatigue Under Dynamic Strain Ageing Range

One of the fatigue-life limiting phenomena operative during service at high temperature is dynamic strain ageing (DSA). Under monotonic loading, the occurrence of DSA is quite well understood but under cyclic loading, the DSA phenomenon is only grossly reported through a few of the manifestations such as inverse strain rate sensitivity of the half-life stress, limited ductility and reduced fatigue life. Currently our understanding on DSA effects under cyclic loading gets limited because of the complexity involved in the manual analysis of the evolving serrated hysteresis loops. The present report is on the DSA phenomenon in Alloy 617M forging by analysing the hysteresis loops of select low cycle fatigue (LCF) tests conducted using total strain amplitudes of ± 0.25 , ± 0.4 , ± 0.6 and $\pm 0.8\%$ at 573, 773 and 973 K at a constant strain rate of $3 \times 10^{-3} \text{ s}^{-1}$. As analysis of serrated flow behaviour during LCF through manual method is cumbersome, a software package was specifically developed in LabVIEW for automated analysis and mapping of stress drops occurring in the hysteresis loops as a function of the imposed strain

cycles. The magnitude of the evolving serrations both within a cycle and through the entire fatigue life, was extracted automatically from the loops and the results in the form of 2D-DSA stress drop maps are shown in Figure 1. Critical stress, strain and normalized strain hardening rate (NSHR) are indicated in the 2D-DSA plots. The stress drops change at every moment of fatigue life which is indicative of the dynamic nature of the underlying phenomenon of DSA under cyclic loading. Unlike monotonic loadings, the critical parameters for the initiation of serrations (such as critical strain and work-hardening) do not remain constant as the fatigue event progresses and hence warrants a more comprehensive analysis. The most conducive temperature for the occurrence of DSA in the alloy is found to be 773 K, as evidenced by the minimum critical total strain, large magnitude stress drop and a high density of serrations. Serrations disappear from the hysteresis loops after few cycles that is indicative of in-situ precipitation as the dominant feature at 973 K.

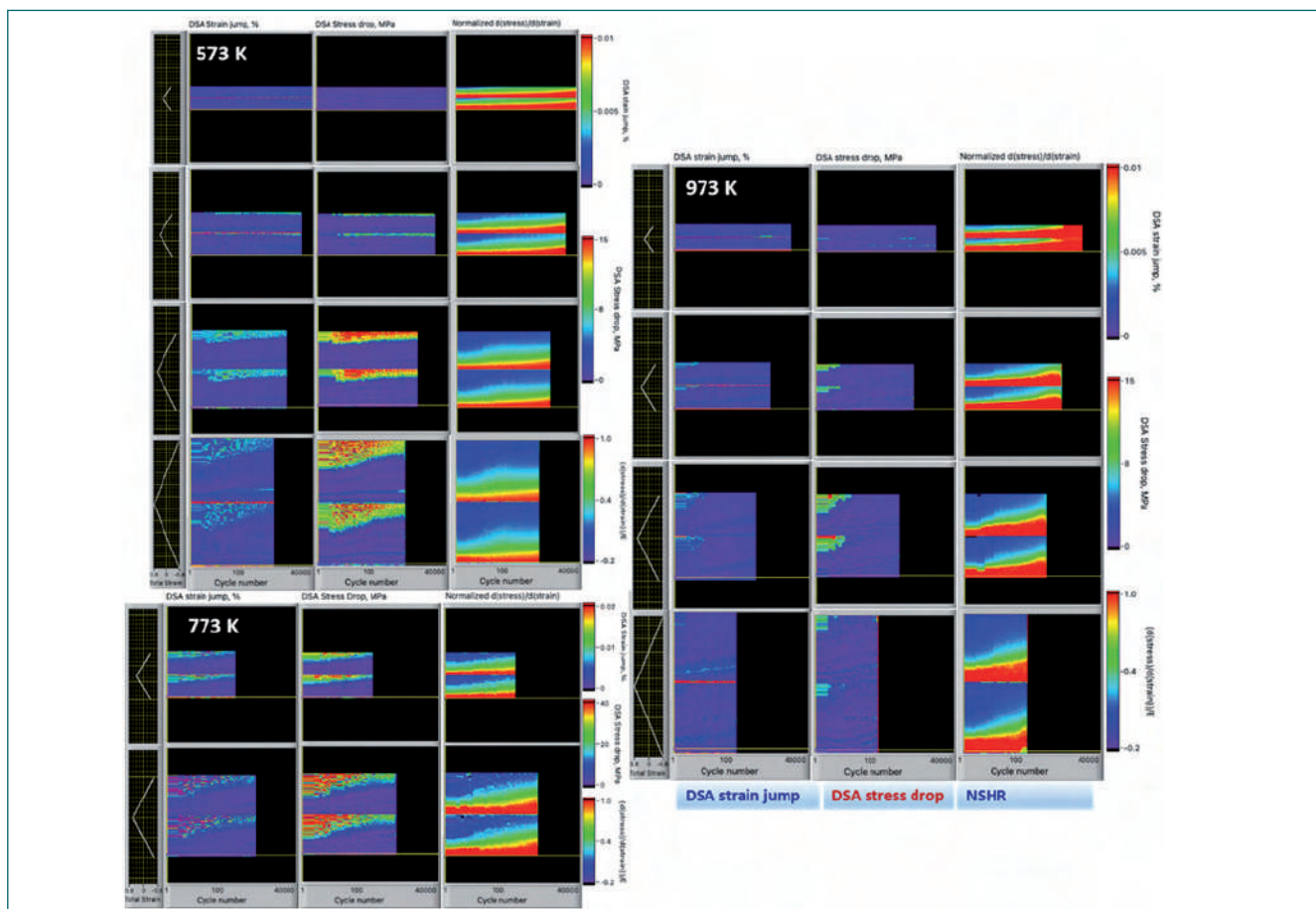


Fig. 1 Depiction of 2D DSA strain jump, stress drop and strain hardening maps in the strain-cycle frame obtained at 573, 773 and 973 K

VI.04 Development of Tools for Enhanced Detection of Flaws in Metallic Materials using Pulse Phase Thermography

Infrared thermography (IRT) is a non-destructive technique used for detection of flaws in metallic and non-metallic materials. The advantage of IRT as compared to other NDT techniques is its wider area coverage and non-contact measurements in a short span of time. In active thermography, external heat is applied to the specimen and the decay of the surface temperature is studied which are influenced by non-uniform heating and surface conditions. However, pulsed phase thermography (PPT) overcomes these limitations of conventional active thermography by adopting pixel by pixel analysis of data sequences in Fourier domain. Figure 1 shows the principle of pulse phase thermography. Generally, flash lamps are used to heat the specimens and the data acquisition is carried out in synchronous manner by IR thermal camera. The temporal evolution of temperature at each pixel location is Fourier transformed to obtain the magnitude and phase at each pixel location which is analyzed for defect detection. The inspection of metals demands data acquisition at higher frame rate as compared to composite materials due to higher thermal conductivity. An analysis tool has been developed in-house for extracting the amplitude and phase information from the sequence of thermal images. The two dimensional maps of the amplitude and phase at optimum frequency values are generated for detection of defects.

In this study, flash lamp was used to heat stainless steel specimen of dimension 95 (Length) x 95 (Width) x 12 mm (thickness) with sixteen artificially fabricated circular flat bottom holes (FBH). The diameters of the circular holes are 12, 10, 8 and 6 mm which are located at a depth of 0.75 mm to 1.7 mm from the surface. The photograph of the specimen with artificial flaws is shown in Figure 2, in which the depths of four FBHs are also indicated.

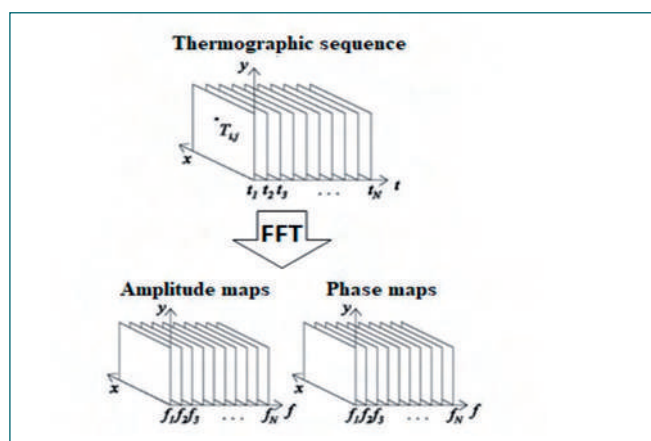


Fig. 1 Principle of pulse phase thermography (PPT)

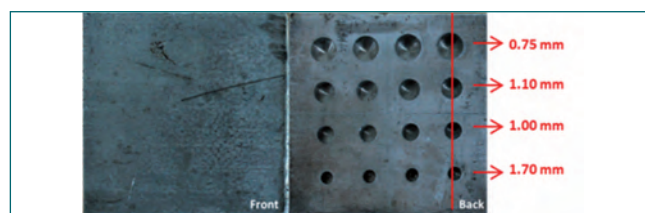


Fig. 2 Photograph of the front and back side of the specimen. The thickness values of the four flat bottom holes are indicated

The thermal images were acquired at a frame rate of 400 Hz. The temporal evolution of temperature with time was extracted and Fourier transform was performed at each pixel location using in-house developed routines. The amplitude and phase maps generated at a frequency of 0.4 Hz are shown in Figs. 3 (a-b). The phase image shows higher sensitivity for detecting deeper flaws, which is highlighted by a dashed rectangular box in the phase image. The better flaw detection capability of phase images stems from the insensitivity of phase to surface conditions and non-uniform illumination. The line profiles of the amplitude and phase at the pixel locations covering the four flaws whose depths are provided in Figure 2 are shown in Figs. 3(c-d), respectively. The observed change in phase is consistent with the increase in the defect depth and the full width at half maximum (FWHM) can be used for estimating the diameter. The application of PPT for quantitative flaw sizing in metallic materials is demonstrated. Analysis of raw thermal image data using in-house developed routines has opened up the possibilities of developing and implementing advanced signal/image analysis algorithms not readily available in the commercial software.

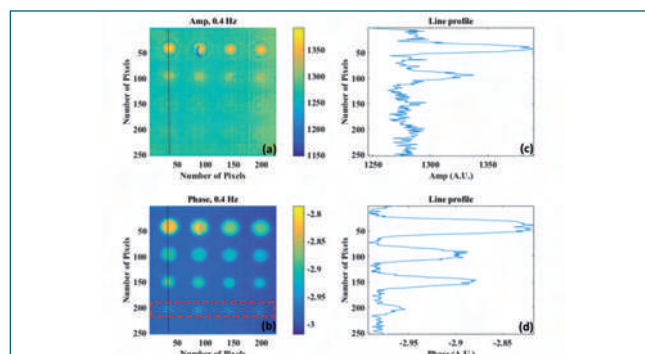


Fig. 3 (a-b) Amplitude and phase images corresponding to 0.4 Hz obtained by processing the thermal image sequences. The line profile of amplitude and phase pertaining to the lines indicated in (a-b) are shown in (c-d), respectively. The thickness values indicated in back surface of the specimen in Fig. 2 correspond to the location of the line profile. One pixel is equal to 0.37 mm x 0.37 mm

VI.05 Synthesis of Silicon Carbide Capped Cobalt Ferrite Nanoparticles for Organic Dye Removal

We synthesized CoFe_2O_4 nanoparticles (CFUC) by the co-precipitation of 1:2 ratio of CoCl_2 and FeCl_3 solutions using NaOH as a precipitating agent. Thus prepared particles were capped with a uniform, stable, ultrathin (~ 1.4 nm) layer of SiC (CFSi) using sonochemical decomposition of di-chloro-di-methyl silane (DCDMSi) as capping agent, without compromising much of its magnetic properties and investigated for organic dye adsorption ability of these capped particles.

The prepared SiC capped CoFe_2O_4 nanoparticles were hydrophilic in nature and exhibited excellent colloidal stability with hydrodynamic size of ~ 16 nm and zeta potential of ~ 32 mV. Crystallite size was analyzed using X-ray diffraction analysis (XRD) as ~ 12 nm (Figure 1a) for both CFUC and CFSi. Thermogravimetry-Differential scanning calorimetry (TGA-DSC) analysis confirms the thermal stability and coating characteristics of the adsorbed silica layer. Fourier transform Infra-red spectroscopy (FT-IR) for both CFUC and CFSi (Figure 1b) confirm the bonding characteristics of the silicon carbide over the CFSi nanoparticles, where, the peaks related to Si-C in the frequency range of $\sim 1265 - 803$ cm^{-1} were masked by the oxide reststrahlen band, while the minor sharp band at ~ 3750 cm^{-1} confirm the presence of isolated silanol groups along with the extensively hydrogen bonded vicinal silanol groups on the CFSi. VSM analysis showed a saturation magnetization of ~ 66 emu/g with a narrow hysteresis loop, whereas at low temperature (4K) showed a higher magnetization of ~ 85 emu/g with larger hysteresis and remanance for CFSi particles. In addition to these the morphology and the chemical composition of the synthesized silica

coated cobalt ferrite particles were also analyzed using TEM, HRTEM and EDX techniques.

The synthesized CFSi nanoparticles were investigated for organic dye adsorption ability using organic dyes (methylene blue (MB), Brilliant blue R (BBR), bromophenol blue (BPB), Rhodamine B (RB) with different functional moieties for their removal from water medium. Possible mechanism for the adsorption of different dyes on SiC capping and the mode of interaction of different functional moieties were analyzed. The dye adsorbing capability of SiC coated CoFe_2O_4 nanoparticles showed that the anionic dyes bind over these nanoparticles electrostatically. CFSi showed the highest binding tendency towards BPB in comparison to that of the uncapped CFUC (Figure 1c). The maximum adsorption capacity (q_t) after 5 min of incubation for CFSi is ~ 120.5 mg g^{-1} with adsorption efficiency (q_e) of ~ 96.4 % for the initial concentration (C_i) of 2500 mg/l of BPB, while the values were 4 mg g^{-1} and 80 % respectively for CFUC for C_i of 100 mg/l.

The unique benefit of this approach is sonication aided synthesis of SiC capped CoFe_2O_4 nanoparticles without using of metal catalysts and exogenous initiators with hazardous chemicals, high temperature, pressure or long reaction time. This method provide straight through channel for dye removal under a magnetic field without the need of centrifugation, precipitation, filtration, washing and ultrasonication without degrading the dyes irreversibly. The new process of dye removal using CFSi is quite fast and requires only a small external magnetic field to separate dyes.

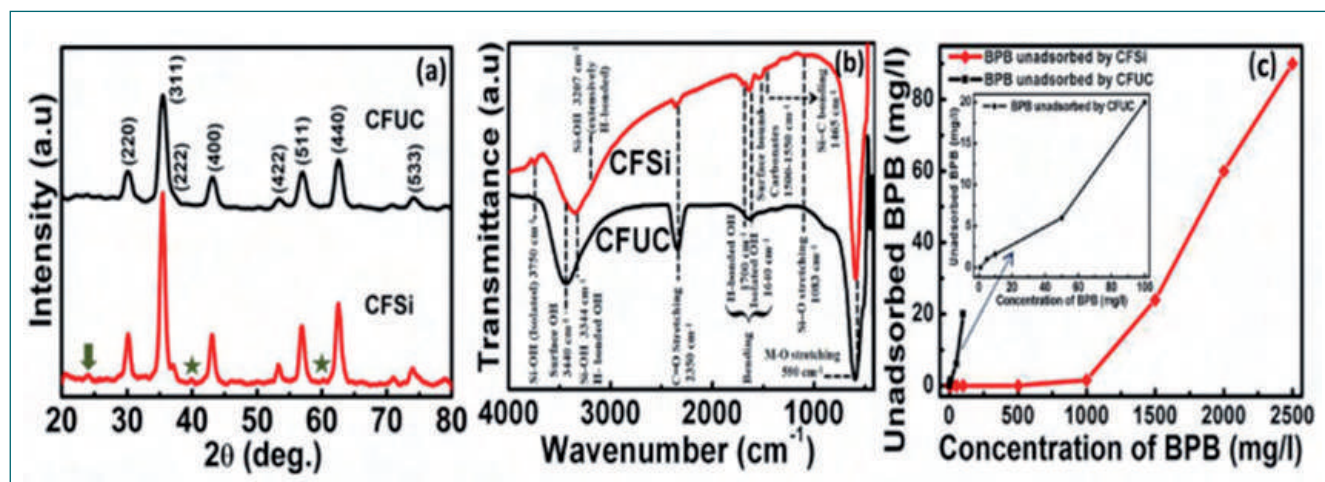


Fig. 1 (a) XRD pattern of CFUC and CFSi (b) FT-IR spectra of CFUC and CFSi and (c) Un adsorbed BPB by CFSi as a function of concentration of BPB (inset (c) unadsorbed BPB by CFUC as a function of concentration of BPB)

VI.06 New Ways of Fabrication of Superhydrophobic Titanium and Aluminum Surfaces with Superior Antibiofouling and Self Cleaning Abilities

Superhydrophobic (SHP) surface modification of metals has been an area of interest during the last few decades because of improved wetting characteristics, corrosion resistance and antifouling properties. The long-term stability and durability in aggressive service conditions are the major concerns for the current SHP coatings. The non-uniform and loosely adherent coating is often counterproductive. Single-step surface modification provides robust and durable SHP surfaces that are advantageous for practical applications. In this context, laser surface patterning was found to be effective for SHP surface modification of titanium and its alloys and other engineering materials such as copper and steel. High processing rate, low material wastage and permanent surface modification are some of the advantages of this single-step laser patterning process. The main objective of the present work is to

develop a robust superhydrophobic titanium surface with antibiofouling property by employing direct laser patterning without using low surface energy materials such as fluorocarbons or silane. Moreover, the use of nanosecond lasers ensures faster processing, and scalability besides cost-effectiveness for practical applications. Superhydrophobic titanium surfaces with four different line spacing of 20, 50, 80 and 100 μm were fabricated by employing a nanosecond laser surface patterning. The samples showed superhydrophobic behavior with an average water contact angle (WCA) of $162.7^\circ \pm 2.2^\circ$, $168.7^\circ \pm 3.1^\circ$, $162.2^\circ \pm 1.5^\circ$ and $161.7^\circ \pm 2.3^\circ$ for 20, 50, 80 and 100 μm line spacing samples, respectively. The sliding angle for 20 and 50 μm line spacing samples was $\sim 6^\circ$ and that of 80 and 100 μm line spacing samples was $\sim 5^\circ$. Some of the laser patterned titanium samples showed WCA as high as 170°

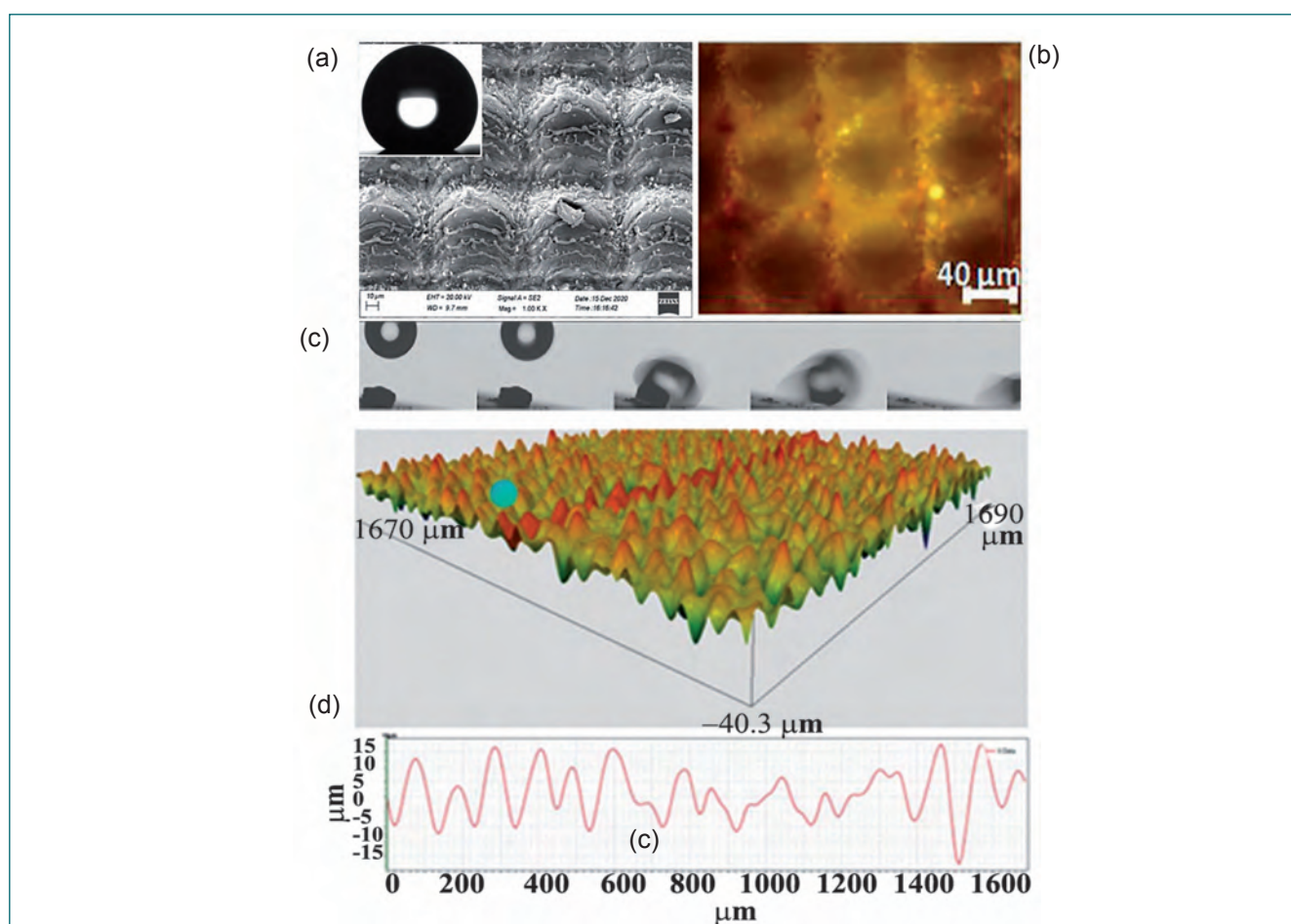


Fig. 1 (a) FESEM image of laser patterned titanium surfaces with 80 μm line spacing. Inset shows the water contact angle on the laser patterned titanium surface, (b) Epifluorescence image of 80 μm line spacing sample exposed in *Pseudomonas sp.* culture for 6 h, (c) Demonstration of self-cleaning property on a laser patterned titanium surface. The sample was inclined at an angle of 8° with water droplet impinging on the surface from a height of 6 mm and (d) Surface topography image and the corresponding surface profile of laser patterned surface with line spacing 80 μm

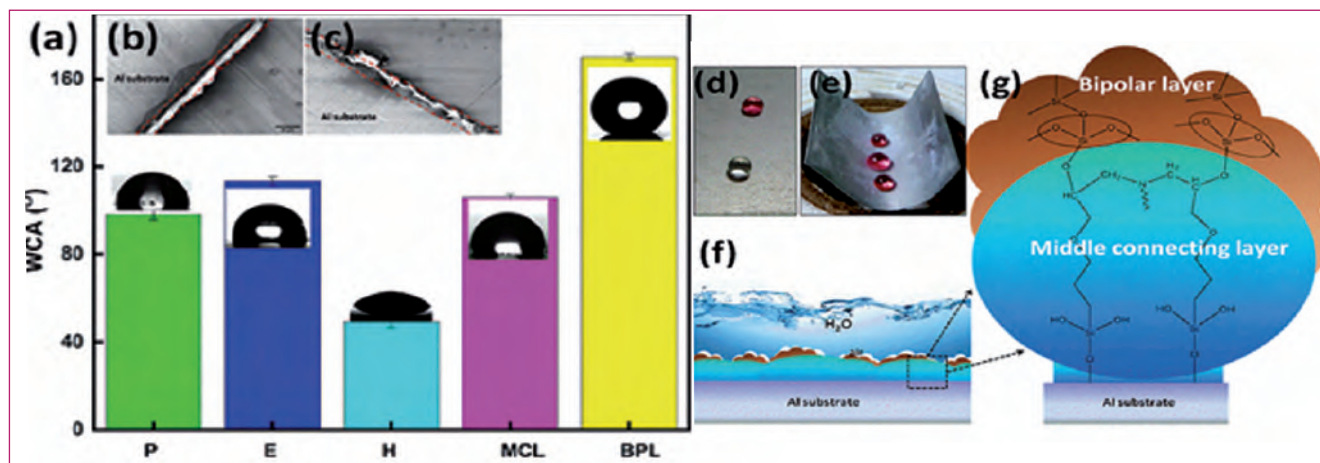


Fig. 2 (a) Water contact angle (WCA) of polished (P), etched (E), hydroxylated (H), middle connecting layer (MCL) and bipolar layer coated Al sheet (BPL). FESEM cross section images of (b) MCL coated Al sheet (c) SHP Al sheet. Photographs of (d) planar and (e) folded SHP sample with colored water droplets. (f & g) Schematics showing the chemical structure of the coating

with free rolling of the water droplets from the surface without any tilting. The surface morphology (Figure 1a) and roughness parameters indicated the dual structure on the laser patterned samples. An average water contact angle of more than 160° (Figure 1a) was obtained on prolonged aging for all the laser patterned samples in an open atmosphere due to the accumulation of hydrocarbon from the atmosphere. The non-polar carbon-containing species adsorbed on the surface due to longer storage duration in ambient conditions contributed to the superhydrophobic effect. The presence of an organic carbon-based layer over the laser patterned samples was confirmed by various analytical techniques. The patterned samples exhibited excellent repellence to *Pseudomonas sp.*, (Figure 1b) and 4 order reductions in bacterial adhesion as compared to control titanium samples. In the present study, better antimicrobial property of the laser patterned surface is attributed to the micro-nano features along with the photocatalytic activity of the titania surface. Laser patterned titanium surfaces also exhibited water repellency in chloride solutions of 5 M ionic strength and remarkable mechanical durability. Self-cleaning effect was observed in the laser patterned titanium samples inclined at an angle of 8° with a water droplet impinging on the surface from a height of 6 mm (Figure 1c). The impinging water droplets picked up the contaminants and rolled off the surface under gravity and tangential impact force. Since the adhesion between the water droplets and SHP laser patterned titanium surface was minimal, the water droplets rolled off the surface at a low sliding angle. The micro-nano topography (Figure 1d) of the SHP laser patterned surface causes the contaminants to make contact only with the peak of the hierarchical structures, resulting in a lower Van der Waals attractive

force between the contaminants and the surface. The laser patterned titanium samples are found to regain the superhydrophobicity by replenishing the carbonaceous layer (denuded in organic solvents) on exposure to an open atmosphere for 14 days. Immersion in organic solvents led to desorption of physically adsorbed carbonaceous layer over the laser patterned surface resulting in the transition from superhydrophobic to hydrophobic behavior. Thus, storage in the open atmosphere in ambient conditions led to the replenishing of the carbonaceous layer on the laser patterned surface. This study provides new avenues to engineer the wetting properties of surfaces by varying laser patterning conditions.

Superhydrophobic (SHP) coatings have received enormous attention in recent times because of their unique properties such as water repellency, anticorrosion, antifouling, self-cleaning, anti-wear and antifriction. The key challenge in the fabrication of SHP coatings is the ability to fabricate mechanically robust SHP surface. Therefore, the main objective of this work was to develop a mechanically robust superhydrophobic coating on an Al substrate with self-cleaning ability, reduced corrosion, and bacterial adhesion. Durability is achieved by the introduction of a covalently bonded middle connecting layer between the substrate and low surface energy material. The coating consists of a top hydrophobic layer of hexamethyldisilazane modified nano-silica (low surface energy material) and a middle connecting layer of hydrolyzed glycidoxypropyltrimethoxysilane. FESEM images of etched and hydroxylated samples showed a coarse flaky hydrated oxide layers on the surface, due to the oriented growth of boehmite to form a layered structure.

The polished Al surface was hydrophobic with a WCA

of $97.9 \pm 2.2^\circ$. The surface became SHP with a WCA of $170 \pm 1.5^\circ$ after the formation of bipolar layer (BPL) coating (Figure 2a). On the coated surface, the droplet starts rolling off the surface even when the surface was perfectly horizontal. This clearly demonstrates that the sliding angle (SA) is less than 10° . Figures 2b and 2c shows FESEM cross section images of middle connecting layer (MCL) coated SHP Al samples with thickness $\sim 10 \mu\text{m}$ and $\sim 12 \mu\text{m}$, respectively. Figures 2d and 2e are the photographs of planar and folded SHP sample with colored water droplets which suggest that surface folding do not affect the superhydrophobicity (i.e. maintains the high WCA and low SA even under folded conditions). The schematic depicting the chemical structure of the coating is shown in Figure 2f & 2g.

A two order decrease in the corrosion current density and $\sim 99\%$ corrosion inhibition efficiency was achieved (Figure 3a) in SHP aluminum samples. The SHP sample also showed poor adhesion to gram-negative

and gram-positive bacterial strains (Figures 3c and 3d). Antimicrobial studies revealed that the presence of micro nano features and plastron in the Cassie Baxter state of the SHP Al surface provided an unfavorable situation for the bacteria to attach. Superhydrophobicity of the surface was retained even after folding, shear abrasion test, cross-hatch tape adhesion test, and 3 days immersion in 0.1 M NaCl solution (Figures 3b and 3e-3g). Less than 5% detachment of the coating (4B) after cross-hatch tape adhesion test (ASTM D3359-09) and the retention of superhydrophobicity up to 150 cm in the abrasion test (ASTM D4060), confirmed the mechanical robustness of the fabricated superhydrophobic surface. Durability studies confirmed that the presence of microstructures and covalent bond formation between the substrate and low surface energy material through MCL enhanced the durability of the coating. This work provides a framework to develop mechanically robust SHP coating with enhanced corrosion resistance, and antifouling capabilities.

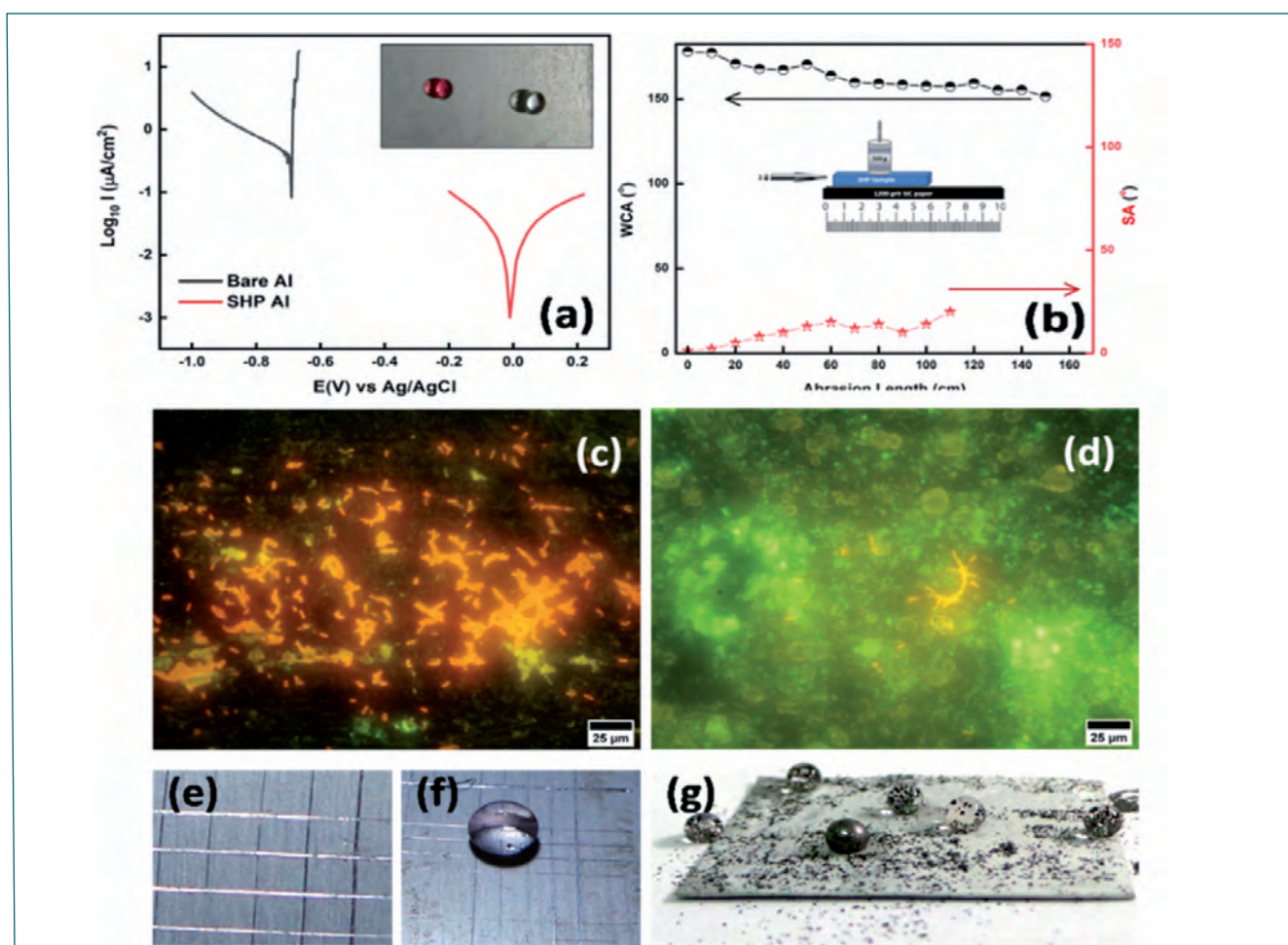


Fig. 3 (a) Tafel plots of bare and SHP aluminum samples (inset is photograph of SHP sample with colored water droplets), (b) Variation in WCA and SA with abrasion length (inset is schematic of experimental set-up), (c & d) Epifluorescence micrographs of *Pseudomonas sp.* biofilm formed on bare and SHP Al samples, (e & f) Photographs of SHP sample without and with droplet after cross-hatch tape adhesion test and (g) Photographs of water droplets on the SHP surface contaminated with hydrophobic graphite

VI.07 Development of Multi-Mode Plane Wave Imaging Methodology for Mapping of Planar Defects

Multi-mode plane wave imaging (PWI) is an advanced phased array ultrasonic (PAUT) imaging methodology. The PWI principle consists of sweeping plane wave ultrasonic beam at multiple angles during transmission, using the wide aperture (multiple elements) of a phased array transducer. Thereafter, the backscattered / reflected signals are received by all elements in the aperture for each transmission sequence and the individual A-scan signals are stored individually for further post processing using total focusing method (TFM). PWI-TFM provides focusing at every pixel points (i.e. at all depths) in the region of interest. As all A-scan signals are stored individually, multiple reflected and mode converted signals may also be utilized for full face mapping of planar defects oriented close to the vertical plane. Such defects are sized using weak tip diffracted signals only in conventional PAUT. Moreover, as multiple elements in the phased array probe are excited together and the plane wave exhibits minimal divergence, the ultrasonic signal amplitude in the medium is high and results in good SNR even at larger depths in highly attenuating materials.

A comprehensive software is developed in-house at NDED for generation of multi-mode PWI images from the data acquired using a commercial phased array equipment. Nine different PWI modes viz., LdL, LdLL, LdTT, LLdLL, LLdL, LLdT, LLdLLL, LTdL and LTdT (L: longitudinal, T: transverse and d: interaction with the defect) are explored. The propagation and interaction

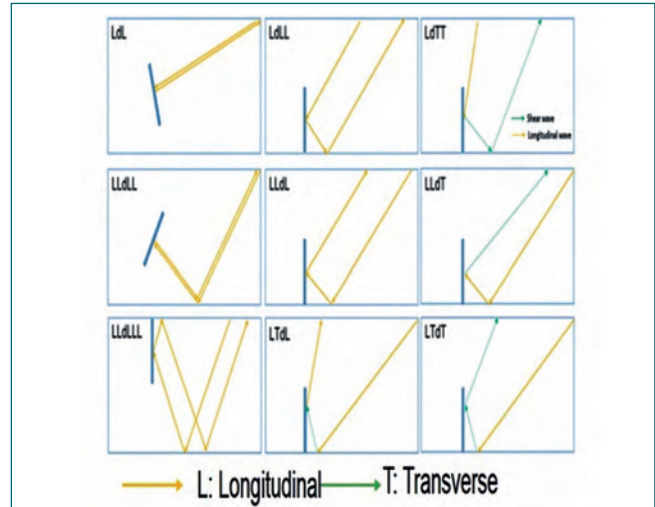


Fig. 1 Schematic of nine different modes employed in generating the PWI images

of ultrasonic waves with the defect for the nine modes are illustrated in Figure 1. Plane waves at 87 different angles (0° to 86°) were generated using a 2 MHz, 64 elements, 0.75 mm pitch phased array transducer. For each transmission at a specific angle, the reflected signals were received with all 64 elements. As a result, a total of 87×64 A-scan signals were acquired in a single measurement and stored for post-processing using the in-house developed software. Different modes highlight the characteristic features of defects of different types more specifically according to the position of the defect and their orientations with respect to the incident beam. To provide an overall idea of the presence and

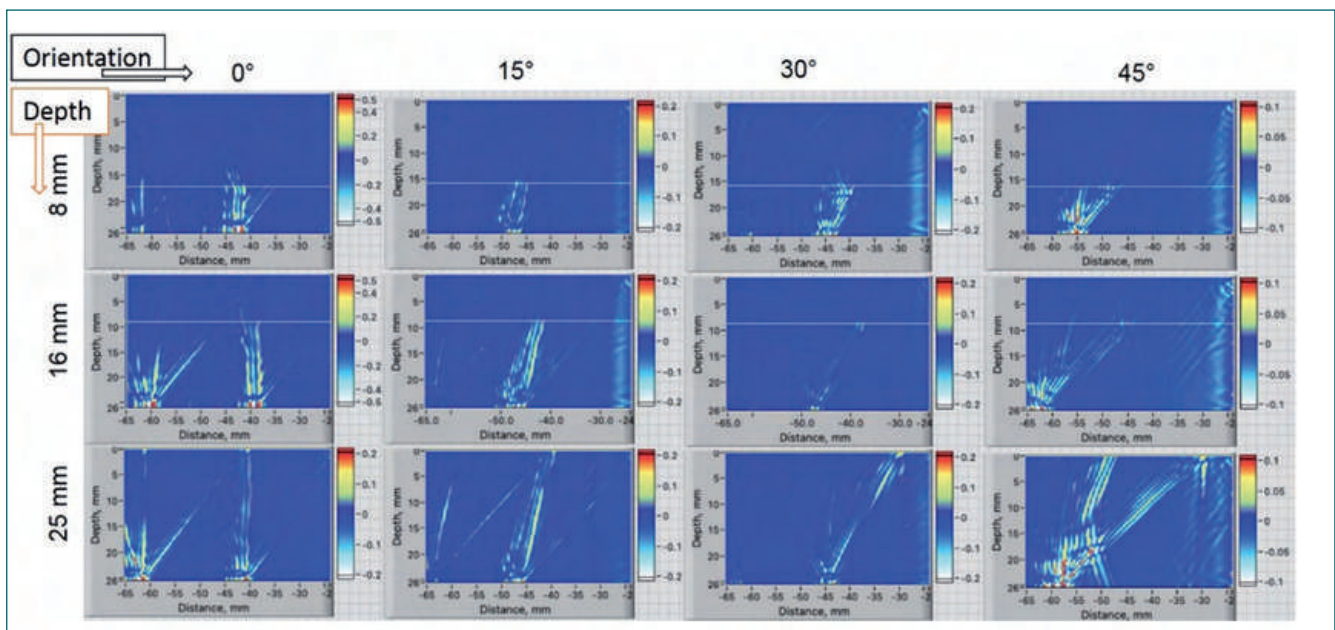


Fig. 2 Multi-mode PWI composite images of planar defects of various through wall dimensions (8 mm, 16 mm & 25 mm) and orientations (0° , 15° , 30° & 45°).

characteristics (size and orientations) of defects, a composite image is generated by the summation of all the nine mode images using suitable weighing factors. Figure 2 shows multi-mode PWI composite images obtained from reference planar defects (bottom side) with depth varying from 8 to 25 mm (edge) and the defect orientation varying from 0° to 45° in 25 mm thick aluminum calibration samples. Data were acquired at similar probe position and the same processing is performed on all the data. Composite images provided direct visualization of planar defects at various depths and orientations.

Multi-mode PWI has specific advantages during in-service inspection of weld joints due to beam directionality. Further, direct visualization of the face of planar defects helps differentiating planar defects with isolated individual defects, which may be misinterpreted in conventional tip diffraction based approach. The developed multi-mode PWI based PAUT is employed by NDED, IGCAR to characterize inter-granular stress corrosion cracks (IGSCC) in the recirculation line weld joints at Tarapur Atomic Power Station (TAPS 1&2).

VI.08 Efficient Degradation of Organic Effluents using Core-Shell Iron Oxide-MnO_x Nanoparticles via Advance Oxidation Process

Organic-pollutants released into water bodies pose serious concerns because of its detrimental effects in aquatic biota, environment and economy. Among various water treatments, advanced oxidation processes such as Fenton, photochemical, electrochemical, ultrasonic, persulfate based oxidation, ozonation, gamma ray/electron beam etc. are efficient approaches in oxidizing or degrading organic effluents from industrial wastes. Persulfate based oxidation is found to be more economical due to the lower material cost, availability of a wide variety of metal oxides suitable for persulfate activation, higher yield and less stringent operational parameters. Among the metal oxides, dual functional

magnetic nanomaterials offer the unique advantage where the iron oxide core is used for imparting magnetic property for the easy separation of particles after use without secondary pollution while MnO_x is used for activation of persulfate.

In this context, Iron oxide capped MnO_x core-shell type nanoparticles(S0) were synthesized using oxidation-precipitation followed by hydrothermal synthesis and demonstrated its efficient dye degradation via persulfate activation at 30 °C. Further, transition metal ions such as Ag⁺ (SA) and Zn²⁺(SZ) were doped in MnO_x to achieve better dye degradation efficiency through increased oxygen activity. The iron oxide core

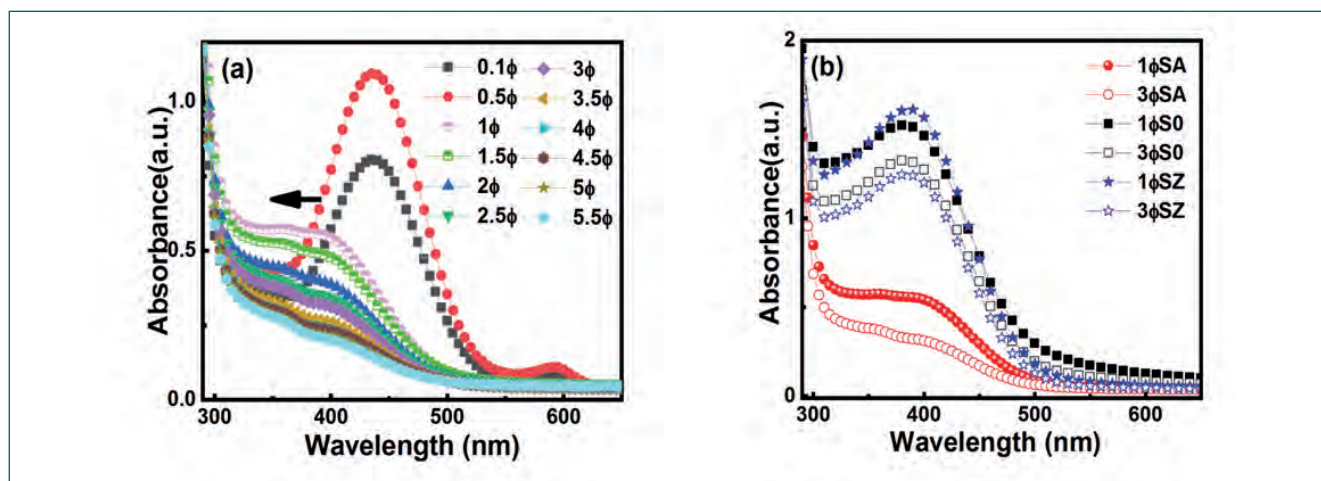


Fig. 1 (a) Absorbance of BPB containing different wt% of SA ($\phi = 0.33$ wt %) where the maximum absorption peak was shifted to a lower wavelength ~ 400 nm (hypsochromic shift), due to the breakage of the BPB structure (b) Absorbance spectra of S0, SA and SZ at 1 and 3 ϕ

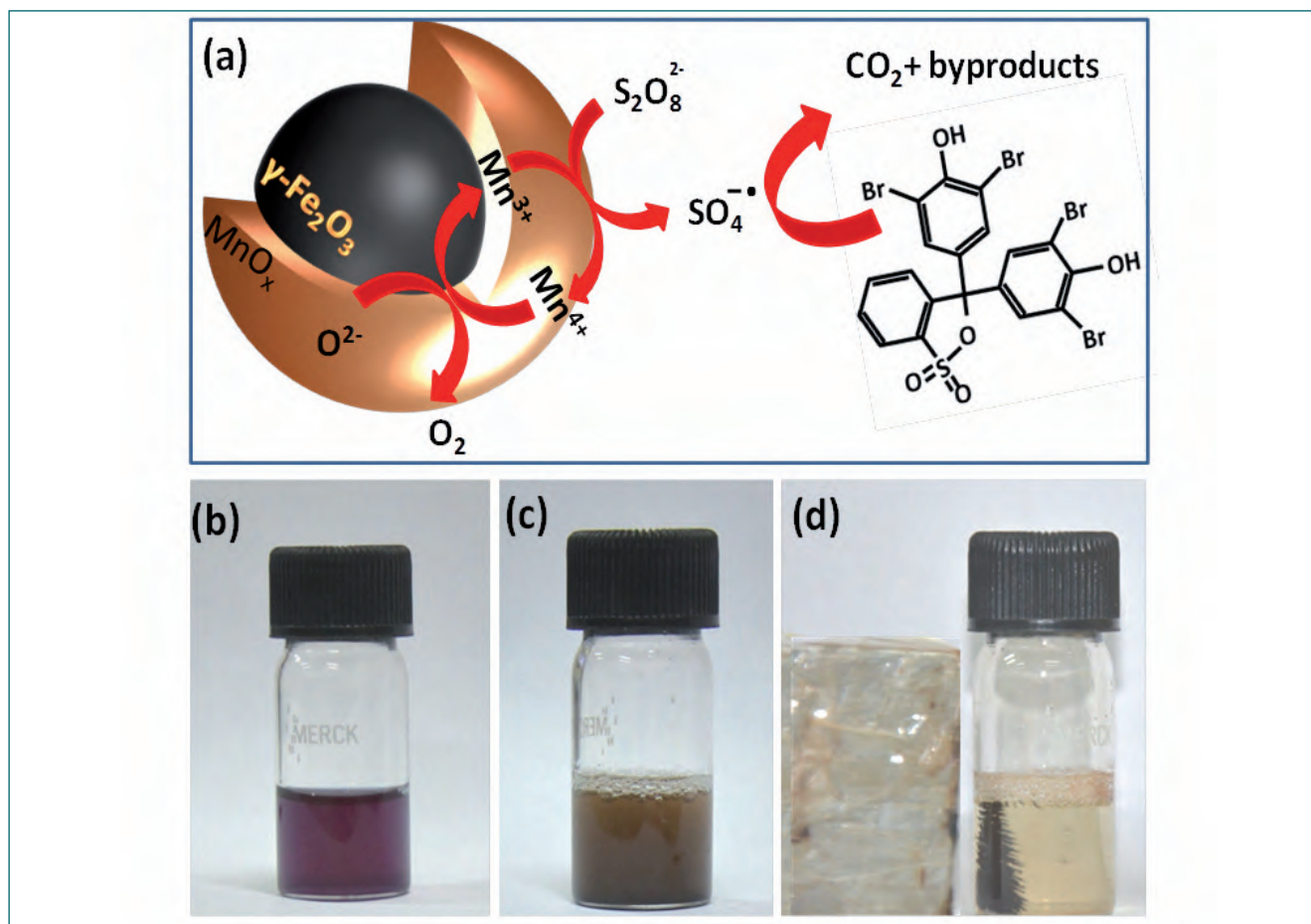
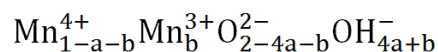


Fig. 2 (a) Schematic depicting the core-shell structure and the dye degradation mechanism. Photographs showing different steps involved in the dye degradation: (b) BPB solution alone (c) dispersion of SA nanoparticles and persulfate into dye solution (d) separation of SA after dye degradation using a magnet

with diameter of $\sim 25\text{--}29$ nm with an amorphous MnO_x shell of ~ 2.9 nm is prepared using this approach. XPS analysis revealed that doping of transition metal ions caused the change in the ratio $\text{Mn}^{3+}:\text{Mn}^{4+}$ with the order $\text{S0} < \text{SA} < \text{SZ}$, where SZ showed only Mn^{3+} state. All the nanoparticles showed superparamagnetic behavior with saturation magnetization values $\sim 58 \pm 0.6$, 49 ± 0.5 and 59 ± 0.6 emu/g for S0, SA and SZ, respectively making them ideal for magnetic separation. The dye degradation and removal capability of S0, SA and SZ were studied using bromophenol blue BPB dye shown in Figure 1. The loss of 592 peak and hypsochromic shift followed by decolorization unambiguously confirm the successful degradation of BPB. SA, S0 and SZ showed degradation percentage of 91, 61 and 51% with 1.8 wt% of nanoparticles. The XPS analysis revealed an enhanced reactivity and mobility of lattice oxygen activity O_{latt} in SA as compared to SZ and O_{ad} corresponding to surface adsorbed oxygen (O_2^- or O^-), OH groups and oxygen vacancies in SA, (3.9% as compared to 2.4%) in SZ shown in Table 1. This indicates that surface oxygen species in the vicinity of Ag–O–Mn entities are more active than those near Zn–O–Mn entities. The above

findings suggest the possible mechanism of activation of persulfate is that in the nanoparticles, Mn^{3+} oxidizes to Mn^{4+} and transfer the electron to persulfate ion as shown schematically in Figure 2. The peroxide bond and the hydroxyl bond of persulfate is cleaved to form and radicals. To maintain the charge balance, the lattice oxygen converts to O_2 by donating electrons to two Mn^{4+} to form Mn^{3+} . This results in decrease in O_{latt} , formation of vacancy or OH, which is described by the equation ,



where 'a' corresponds to fraction of Mn^{4+} missing in the lattice and 'b' is the fraction of Mn^{4+} replaced by Mn^{3+} . This causes an increase in the O_{ad} site, which is in agreement with the XPS results.

Table 1 : Results of XPS analysis of peak $\sim 529.8\text{--}530.1$ eV. The percentage of lattice oxygen O_{latt} (O_2^{2-}), O_{ad} (~ 530.9 eV), percentage of $\text{Mn}^{3+/4+}$ of SA and SZ, before and after dye degradation are given

Catalyst	Pristine nano-particles (%)				After dye degradation (%)			
	O_{latt}	O_{ad}	Mn^{3+}	Mn^{4+}	O_{latt}	O_{ad}	Mn^{3+}	Mn^{4+}
SA	64.8	21.2	63	37	58.5	25.1	72	28
SZ	63.3	21.5	100	0	60.3	23.9	79	21

VI.09 Determination of Carbon in Primary Sodium by Distillation-Combustion Followed by Infrared Spectroscopic method: A Feasibility Study

Determination of impurities especially carbon in primary sodium, a coolant in Fast breeder reactors, causes adverse effect in the structural material of the coolant system as the presence of this impurity can induce carburization or decarburization at the sodium-clad interface at elevated temperatures, which leads to possible degradation of mechanical properties of stainless steel. Furthermore, sodium can get contaminated with carbon from the pump oil used for running the sodium loop. Owing to the high purity requirement of primary sodium as coolant, it is essential to monitor and establish a method to determine carbon in the primary sodium. The combustion method is a potential method that can determine very low carbon content at ppm level in the sodium using a minimum quantity of samples. This report describes a new stainless steel manifold facility commissioned inside a fume hood to estimate microgram level of carbon in primary sodium by converting carbon into CO_2 by combustion reaction followed by quantification using infrared (IR) spectroscopy.

The carbon estimation facility consists of an alumina reaction tube, copper oxide catalyst trap (BASF), activated charcoal (AC) trap, pressure gauge and vacuum pump. UHP Oxygen/Argon gas inlet line is connected through BASF and AC traps to remove the trace level CO_2 and moisture impurities.

A modified new stainless steel (SS) manifold system was designed, fabricated, and commissioned inside the



Fig. 2 CO_2 gas sampler placed inside the sample compartment of IR spectrometer

fume hood. Figure 1 illustrates the photograph of the entire combustion system. To simulate a combustion reaction using low-level of carbon in sodium and to validate the proposed method, initial experiments were carried out using glucose as a surrogate material under similar experimental conditions. For these studies, ~60 mg of glucose was diluted to 500 mL with water. Each mL of this solution is equivalent to ~450 ppm of carbon dioxide which corresponds to ~46 μg of carbon. About 1 mL of glucose sample was taken in a weight basis in a quartz crucible and was dried using vacuum method. Subsequently, the dried quartz crucible was transferred to a ceramic reaction vessel attached with KF end connection and Swagelok valves and the entire system was evacuated through rotary pump. UHP



Fig. 1 Photograph of the carbon analysis combustion system established

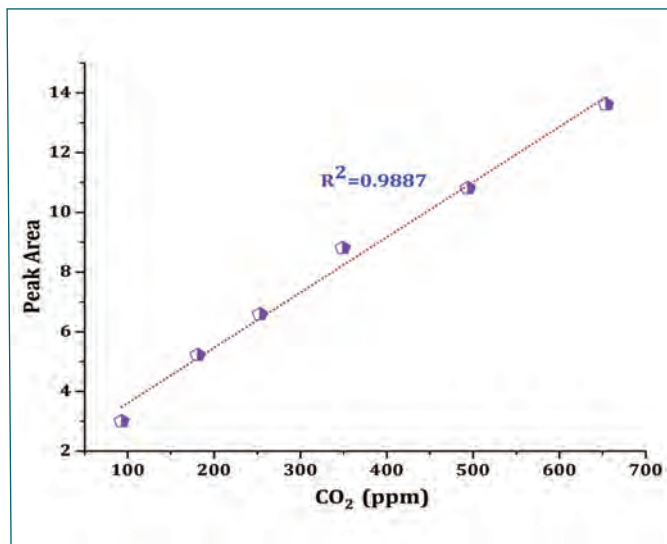


Fig. 3 Calibration plot for CO₂ gas using IR gas cell

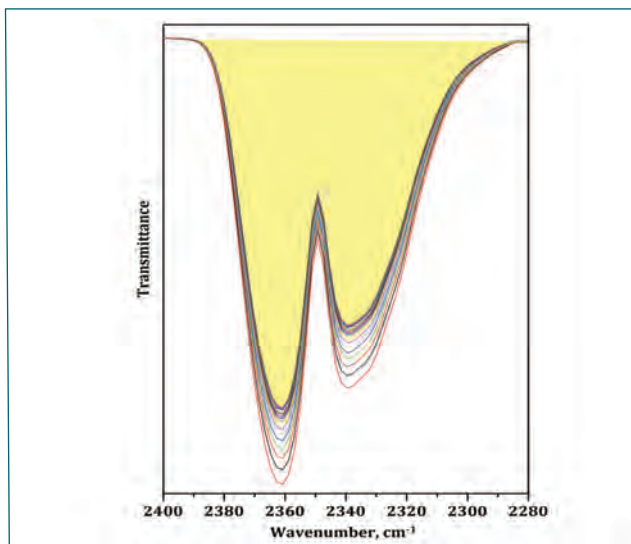


Fig. 4 Typical IR spectra of CO₂ gas recorded as a function of time

oxygen gas was allowed to purge the sample and an excess amount of oxygen for combustion reaction was filled in the reaction tube. The reaction tube was heated up to 1000°C with a rise in temperature of 8°C/min in static condition. The increase in pressure in the closed system was continuously monitored using the pressure gauge. Once the reaction vessel reaches 1000°C it is maintained at this temperature for 2 hrs to ensure the complete conversion of carbon to CO₂. The reaction vessel was cooled to room temperature and UHP argon gas was filled to make the overall pressure of 760 torr. Subsequently, the reaction vessel was removed from the system and was connected to another manifold attached with IR gas sampler connected to diffusion pump backed by rotary pump. Around 50 torr of argon and CO₂ gas mixture from the reaction vessel was filled in an evacuated IR gas sampler and was diluted up to 760 torr using UHP argon.

The resultant CO₂ was analyzed using gas phase IR spectroscopy. At the outset, a calibration plot was established by filling known concentrations of CO₂ (in terms of pressures) in gas cell (Figure 2) and by recording the IR spectra at 4 cm⁻¹ resolution using Bruker Vertex 70 IR spectrometer. The area under the doublet peak at

2362 cm⁻¹ and 2337 cm⁻¹ were measured and is plotted for different composition of CO₂ in Ar in the gas cell. The typical calibration plot in the region of 100-700 ppm of CO₂ is shown in Figure 3. Since, the atmosphere around the sample compartment also contains CO₂; the complete removal of CO₂ was achieved by continuous purging of the compartment using dry N₂. The IR cell along with the sample compartment of IR spectrometer is shown in Figure 3. A sequential recording of infrared spectrum ensured continuous decrease of the transmittance corresponding to atmospheric CO₂. The IR scanning was continued for a minimum period of thirty minutes until the transmittance becomes constant as shown in Figure 4. Before every experiment, blank run with crucible without glucose/sodium was accomplished to discern the background values.

By using the combustion method the carbon was estimated in glucose and bath sodium and the results are listed in Tables 1 and 2. The results of vacuum drying indicated a recovery in excess of 90 % in glucose. Similar, methodology was adopted to estimate carbon in bath sodium and the results showed 48 and 61 ppm of carbon. Experiments are in progress to use this method for determining the carbon content in primary sodium.

S No.	Wt of glucose (mg)	Expected carbon (mg)	Experimentally determined carbon (mg)
1	0.25	0.092	0.091
2	0.13	0.048	0.047

S No.	Wt. of bath sodium taken (g)	Experimentally determined carbon in sodium	
		µg	µg/g
1	2.25	108	48
2	2.00	123	61

VI.10 Enhanced Magnetic Fluid Hyperthermia in Copper Ferrite Nanoparticles due to Near-Resonant Relaxation Dynamics

Magnetic fluid hyperthermia (MFH) is being developed as an alternate cancer therapy, where a dispersion of magnetic nanoparticles (MNPs) is delivered to the tumour tissues and exposed to a radio frequency alternating magnetic field (RFAMF), which causes magneto-thermal energy conversion due to Neel-Brown relaxation of the MNPs. This results in an increase in fluid/tissue temperature, which is therapeutically beneficial. One of the primary challenges in practical applications of MFH is the restrictions imposed on the MNP dosage and RFAMF parameters, considering biological safety. Hence, studies are being conducted for optimizing the magneto-structural properties of the MNPs to enhance the heating efficiency.

Among various types of MNPs, superparamagnetic iron oxides (Fe_3O_4 and $\gamma\text{-Fe}_2\text{O}_3$) are the most widely used materials for MFH-based cancer therapy due to their high saturation magnetization, long-term stability and good biocompatibility. Of late, significant MFH efficiency has been reported for several other types of mixed spinel ferrites. Among these, CuFe_2O_4 MNPs exhibit ferrimagnetism below ~ 728 K and shows several unique magnetic properties due to the predominant presence of Cu^{2+} ions at the octahedral site, which is a typical Jahn-Teller ion (d^9 electron configuration leads to doubly degenerate ground state) and results in cubic-tetragonal distortion, depending on the Cu^{2+} concentration and heat treatment. The anisotropy field of Fe_3O_4 MNPs is higher than the biologically relevant field amplitudes used in MFH applications and hence, alloying with magnetically soft copper ions reduces the effective anisotropy energy barrier, thereby allowing significant magnetization reversal at comparatively lower RFAMF amplitudes. Further, CuFe_2O_4 MNPs have been

reported to exhibit good anti-microbial properties and comparatively lower differential cytotoxicity. Hence, with an objective to evaluate the suitability of CuFe_2O_4 MNPs for MFH applications, the RFAMF induced heating efficiency was systematically probed in the present study.

Polyethylene glycol coated CuFe_2O_4 MNPs were prepared using solvothermal (CFPG, size $\sim 13.4 \pm 0.9$ nm) and hydrothermal (CF, size $\sim 8.4 \pm 0.8$ nm) methods. Temperature dependent magnetization measurements indicated the presence of superparamagnetic phase at room temperature. The saturation magnetization for CFPG MNPs (~ 32.7 emu/g) was found to be ~ 31 % higher than the CF MNPs due to nearly collinear Neel type alignment of the magnetic moments in the tetrahedral and octahedral sites with a low Yafet-Kittel angle of $\sim 6^\circ$, as compared to $\sim 23^\circ$ for the CF MNPs, which exhibited triangular spin alignment with splitting of the octahedral sub-lattice. The magnetic core-shell structure was confirmed from the low-temperature in-field Mossbauer spectra and the spin canting angles were found to be higher for the magnetically disordered shell region. The thickness of the magnetically disordered shell was found to be significantly lower for the CFPG MNPs, which also contributed to the higher saturation magnetization for this system.

MFH studies were conducted at a fixed frequency of 126 kHz and under four different RFAMF amplitudes. The maximum heating efficiency for CFPG MNPs was found to be $\sim 192 \pm 7$ W/g, which was significantly higher than the previously reported values for copper ferrite MNPs and the intrinsic loss power was found to be comparable to several commercially available ferrofluids. The heating efficiency was also theoretically estimated from the high frequency hysteresis loops shown in Figure 1 a & b for CFPG and CF MNPs, respectively, where it was observed that the hysteresis loop areas were larger by ~ 65 % for the CFPG MNPs, indicating higher magneto-thermal energy conversion for the solvothermally prepared CuFe_2O_4 MNPs. The higher heating efficiency of CFPG MNPs was attributed to the near-resonant relaxation dynamics ($\omega\tau = 0.97 \sim 1$, where ω and τ indicate the angular frequency of the applied field and effective relaxation time, respectively). The observed high heating efficiency along with negligible room temperature coercivity indicated the suitability of the solvothermally synthesized polyethylene glycol coated CuFe_2O_4 MNPs for MFH.

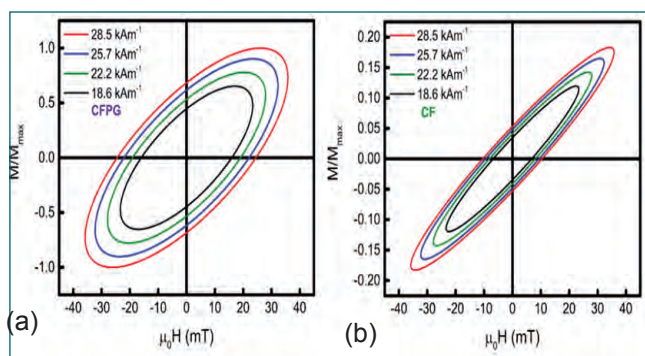


Fig. 1 Theoretically calculated dynamic hysteresis loops for the (a) solvothermally and (b) hydrothermally synthesized CuFe_2O_4 MNPs, during varied RFAMF amplitudes

VI.11 A Novel Method for Thickness Measurement in Conducting Materials by Apparent Conductivity Calculations Through Transient Eddy Current NDE

A novel method for thickness measurement in conducting material has been established by combining the measurement of the decaying induced eddy current and its associated apparent conductivity calculations. In conventional frequency domain NDE (Non-destructive Evaluation), the skin depth is the limiting factor due to the single frequency excitation. In contrast, with a pulsed excitation, the induced eddy currents decay with time and the decay of the eddy current consists of continuum of frequencies and hence the entire thickness of the conducting material could be investigated in a single shot. The time at which the decay of the eddy current is maximum is called diffusion time “ t_m ” and the corresponding calculated value of apparent electrical conductivity “ σ_{app}^m ” both of which can be directly correlated to the thickness of the material (Figure 1 (c) and (d)). Since the induction of the eddy current and its associated secondary magnetic field measured by using suitable magnetic sensors ($h_z \propto (\sigma t)^{3/2}$ for B-field and $V_z \propto (\sigma^{3/2}/t^{5/2})$ for an induction coil) is directly related to the conductivity of the materials, one can calculate the apparent conductivity $\sigma_{app}(t)$ as a function of decay time. Apparent conductivity calculations have been made for aluminum plates based on the thin conducting sheet model in which the applied magnetic field is uniform throughout the thickness. Subsequently, transient eddy current NDE measurements have been performed with stacks of aluminum plates by using pickup coils in the form of an absolute (probe A) as well as differential configuration (probe B). From this, it has been shown that the square root of the ratio of the maximum diffusion time, t_m and the corresponding apparent conductivity, σ_{app}^m called as maximum diffusion depth, δ_m which is proportional to the plate thickness (Figure 1 (e)). The diffusion depth is a parameter derived from standard electromagnetic equations is analogous to the skin depth in the frequency domain.

$V_z \propto (\sigma^{3/2}/t^{5/2})$ for an induction coil) is directly related to the conductivity of the materials, one can calculate the apparent conductivity $\sigma_{app}(t)$ as a function of decay time. Apparent conductivity calculations have been made for aluminum plates based on the thin conducting sheet model in which the applied magnetic field is uniform throughout the thickness. Subsequently, transient eddy current NDE measurements have been performed with stacks of aluminum plates by using pickup coils in the form of an absolute (probe A) as well as differential configuration (probe B). From this, it has been shown that the square root of the ratio of the maximum diffusion time, t_m and the corresponding apparent conductivity, σ_{app}^m called as maximum diffusion depth, δ_m which is proportional to the plate thickness (Figure 1 (e)). The diffusion depth is a parameter derived from standard electromagnetic equations is analogous to the skin depth in the frequency domain.

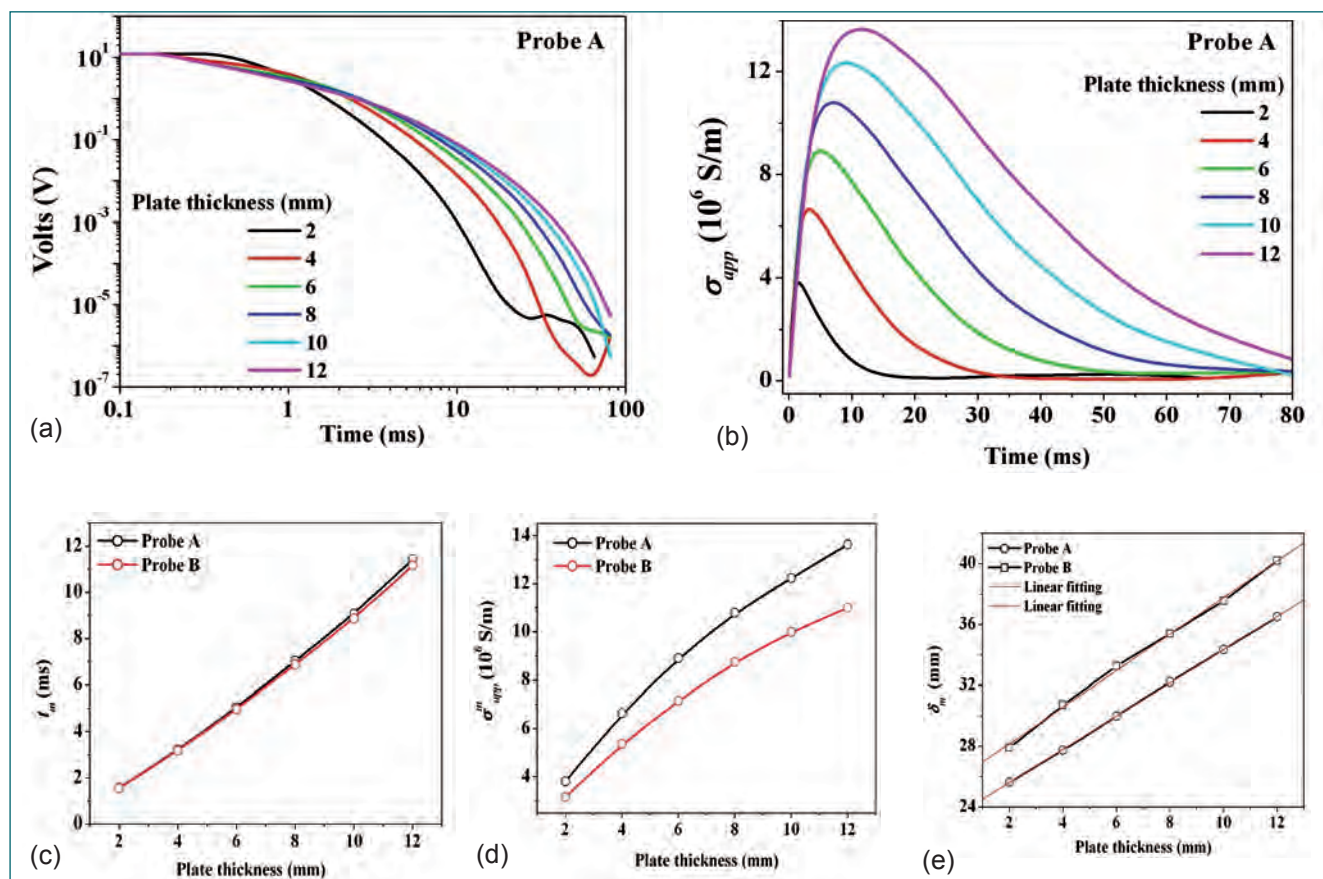


Fig. 1 (a) and (b) are the decay of the secondary magnetic field recorded with time for the stacked aluminum plates by the probe A and the corresponding calculated apparent conductivities respectively. (c) The diffusion time, t_m and (d) maximum apparent conductivity, σ_{app}^m obtained from the apparent conductivity calculations for aluminum plates with different thicknesses. (e) The maximum diffusion depth, δ_m obtained from (c) and (d) for aluminum plates with different thicknesses

VI.12 Depth Measurement of Surface Discontinuities by Ultrasonic Testing Technique in Diaphragm compressor of Additional Up-Gradation Facility

A diaphragm compressor is being used for helium gas pressurization in Additional Up-Gradation Facility (AUGF), BARCF. Helium gas leakage was observed between diaphragm and diaphragm head during compressor operation. The dimension of diaphragm head is 535 mm outer diameter, thickness of 110 mm and made from EN19 steel. The aim of this study is to find the depth of discontinuity on surface of diaphragm head as shown in Figure 1.

As Conventional Ultrasonic method using Normal or Shear waves is not possible in the present context as the discontinuities are limited only to surface. Surface wave ultrasonic inspection has been used to characterise the surface discontinuities. Typical equipment details for evolving procedure is as shown in Table 1. Reference reflector (Notches) of various depths as shown in Table 2 are used for this study. Totally Six notches with a depth of 0.05, 0.10, 0.15, 0.20, 0.25 and 0.30 were made by EDM machining process on 120X120X18 mm carbon steel specimen as shown in Figure 2.

The variation of attenuation properties between diaphragm head material and reference block was compensated by a correction factor using same depth

Table 1: Equipment details	
Equipment	Olympus make, Model Epoch 650
Technique	Pulse-Echo, Surface wave
Probe	Panametrics, 5X5 mm Crystal, 5MHz, 90°
Range (mm)	0 – 50

Table 2: Reference block detail	
Material	Carbon steel
Dimension	120X120X18 mm
Notch dimensions (mm)	Length: 10 & Width: 0.5
Depth of notches (mm)	0.05, 0.10, 0.15, 0.20, 0.25 & 0.30



Fig. 1 Photograph of top flange of diaphragm compressor

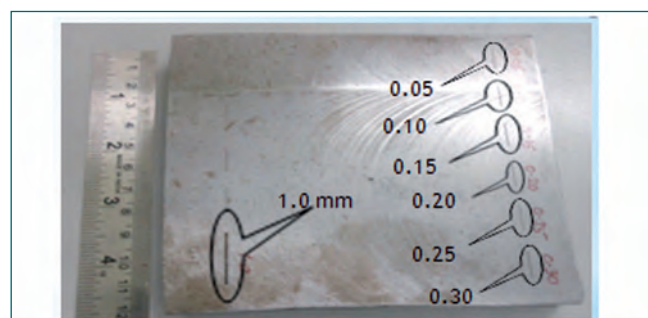


Fig. 2 Carbon steel specimen (120X120X18 mm) with 0.06, 0.10, 0.20, 0.3 & 1.0 mm depth notches

(1 mm) of groove on diaphragm head and notch on reference block respectively. The amplitude (50.5dB) from 0.30 mm depth notch was set as reference zero and the amplitudes drop (dB) for other depth notches were recorded as given in Table 3. The gain for all the notches and discontinuity were recorded by positioning the probe at a distance of 10 mm.

The amplitude for the discontinuity was noted in the chart. It is observed that amplitude from the discontinuity falls between 0.05 and 0.20 mm notches as shown in Figure 3.

Ultrasonic examination by surface wave technique has been developed and validated by carrying out on discontinuity location of diaphragm head sealing surface. Surface wave technique was successfully applied to find the depth of surface discontinuity.

Table 3: Reference gain settings						
Gain (dB) for 80% FSH at a dist. of 10 mm						
Notch depth (mm)	0.05	0.10	0.15	0.20	0.25	0.30
Gain (dB)	50.5	42.6	39.3	38	35.7	33.1



Fig. 3 Indication from discontinuity from diaphragm head

VI.13 Ultrasonic Testing Methods for Inspection of Large Diameter Bearing Balls

Ball bearings are used in many kinds of machines and devices with rotating parts. The purpose of a ball bearing is to provide a relative positioning and rotational freedom while transmitting a load between two structures. The size of the ball bearing will vary depends upon the load requirement and dimensions. The large bearings are more critical compared to small bearings from maintenance point of view. The steel balls are the vital part in ball type bearings. The failure of balls can affect the functionality of the bearing. The large diameter bearing balls are prone to encounter forging defects if not manufactured with due care. These defects may affect the load bearing capabilities of the balls and may lead to failure of bearing.

A typical bearing ball is manufactured from the high carbon steel forged bars in spheroidized annealed condition conforming to ASTM A295 - AISI 52100 or IS: 4398 Grade 104Cr6. It shall be free from defects such as pipes, seams, laminations, excessive inclusion of non-metallic impurities and any other internal defects. Forged bars should generally qualify the requirements of product

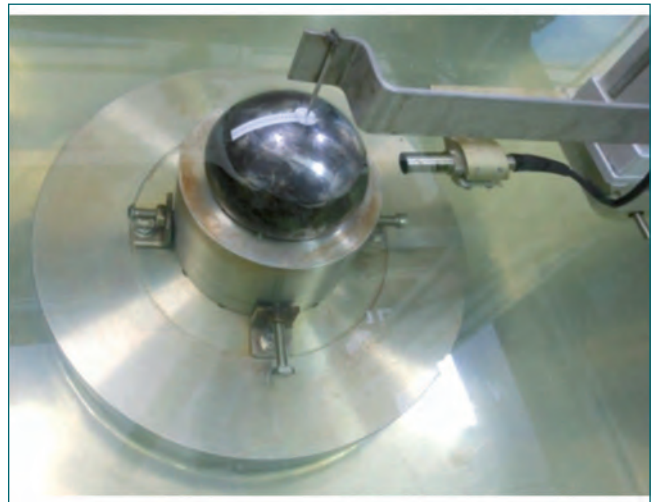


Fig. 2 Steel ball scan set up

Table 1: Testing parameters	
Equipment	Six axis immersion manipulator
Probe	Ø 0.5" crystal, 5 MHz, 50 mm focused probe
Water column distance	25 mm
Scan axis	Theta (Table rotation) 3600
Index axis	Z (Scan length of 2 mm with 0.2 mm index)
Scanning resolution [mm]	0.5
Scanning speed [mm/s]	10 mm/sec
Sampling frequency	125

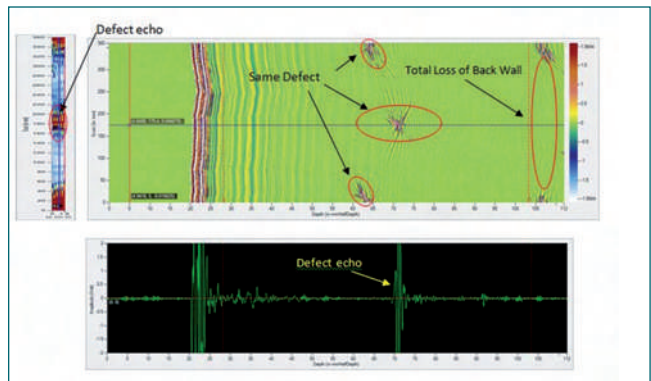


Fig. 3 A, B and C-scan images showing defect indication with total loss of back wall echo

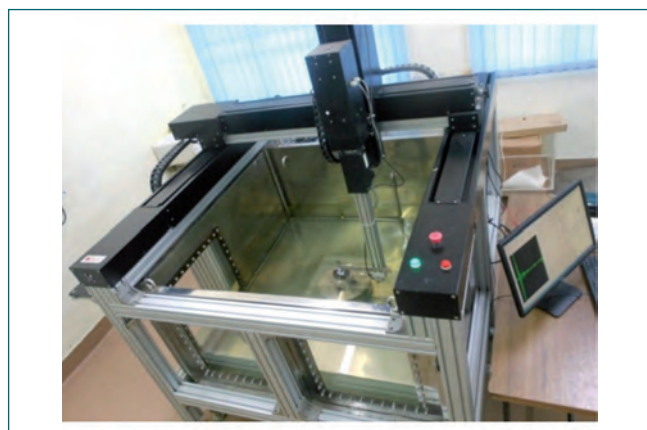
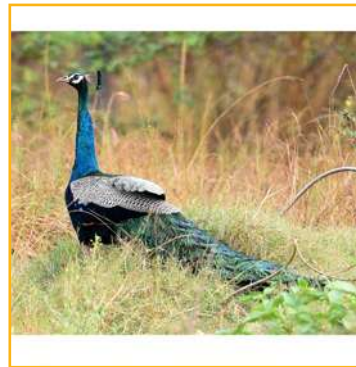
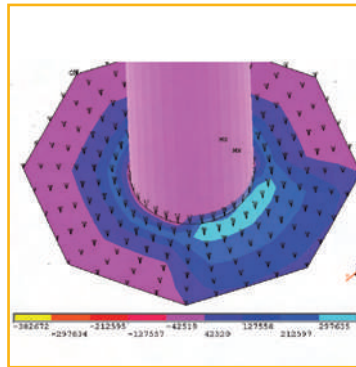
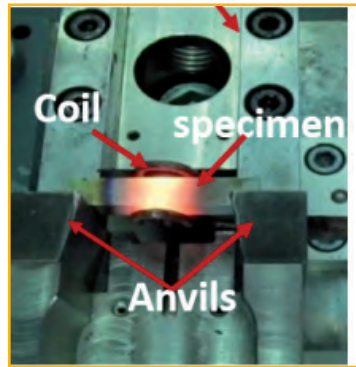


Fig. 1 Six axis immersion manipulator with Large Diameter Bearing ball set up

analysis, dimensional tolerances, microstructure, grain size, hardness, inclusion content, decarburization, surface defects and failure test. The non destructive examination of the bearing balls can be done either by using radiography testing or ultrasonic testing.

The Six axis motorized robotic ultrasonic inspection manipulator along with data acquisition and data analysis software have been used to inspect the steel ball. The test set up is shown in the Figures 1 and 2.

Immersion ultrasonic testing was successfully applied using optimized scan procedure. The B and C scans obtained from immersion UT gives defect indication information in image format, which can be analyzed for precise depth measurement as shown in Figure 3. The B and C scan data can be further used for cartography of defective specimen. The results of immersion UT were validated with radiographs and found complementing each other. The commonly occurring shrinkage defects in steel bearing balls can be easily evaluated and mapped with high depth accuracy by using immersion UT.



CHAPTER VII

Infrastructure, Resource Management & Biodiversity

VII.01 Development and commissioning of an In-Situ Heating System for Elevated Temperature Impact Testing

Impact testing determines the amount of energy absorbed by a material deformed at high strain rates to fracture. In Charpy V Notch (CVN) impact test, a notched rectangular specimen of 10 x 10 x 55 mm (full size) positioned on the anvil of the test machine is deformed by pendulum striker at a velocity of about 5 m/s. The data from impact tests performed over a range of temperatures (from sub-zero to above ambient) are used to evaluate the ductile-brittle transition temperature and fracture toughness parameters of structural steels. Conventionally, the CVN specimen is heated or cooled to the desired temperature in an environmental chamber external to the test machine and the specimen is placed on the machine anvils manually using self centering tongs or through an automated device fitted with a set of synchronised actuators or using a robotic arm.

Radiometallurgy laboratory is equipped with a 450J capacity instrumented impact test machine for testing full size as well as sub size CVN specimen (5 mm x 5 mm x 55 mm). As per ASTM standards, the specimen after temperature conditioning needs to be positioned on the machine anvils with an accuracy of ± 0.25 mm (of notch center) and within 5s for standard CVN and within 3s for sub size CVN specimen to minimise heat loss. Impact testing at sub-zero and elevated temperatures is challenging for irradiated specimens as they have to be handled remotely using manipulators and more so for sub size specimens to meet the ' ± 0.25 mm' positional accuracy and '<3s' test standards criteria.

With the objective of completely eliminating the transfer of specimen from environmental chamber to the machine and the associated uncertainties due to heat loss and specimen centering, an in-situ, non-contact induction type heating system has been developed and integrated with the existing 450J impact test machine. The induction heater system consists of a 10kW power source, pyrometer, temperature controller, water chiller, a coil and a coil movement system. After manually placing the CVN specimen on the machine anvils, inductor heater coil mounted on a pneumatically actuated cylinder is positioned close to the specimen to uniformly heat the specimen volume extending up to 10 mm on either side from V-notch. The tempering of specimen is controlled with feedback from the pyrometer which measures the temperature around the V-notch. Upon achieving the desired test temperature ($\pm 1^\circ\text{C}$) followed by soaking, the system is programmed to switch off the heating

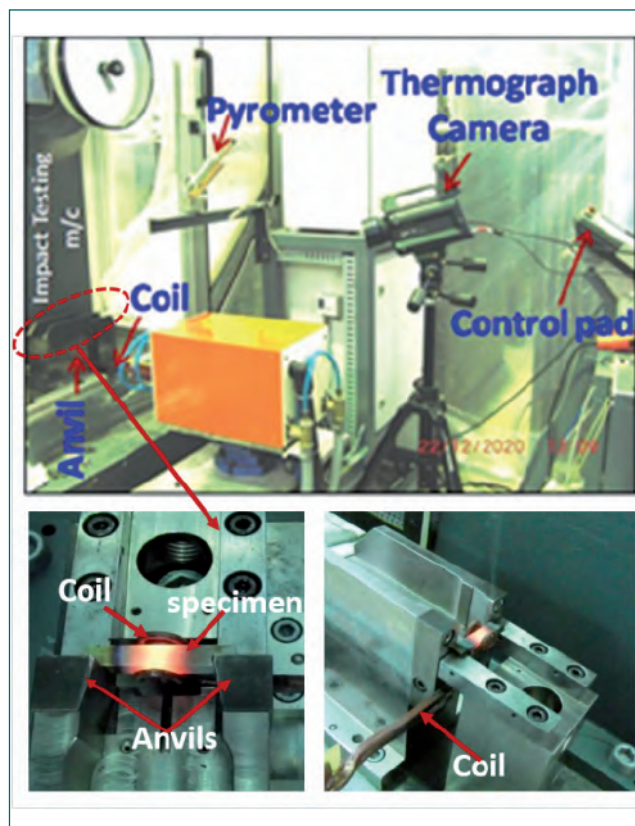


Fig. 1 Photograph of the in-situ heating system for elevated temperature impact testing

and to actuate the inductor coil system to slide down to the space (100 mm height x 50 mm width) below the specimen support within 2s, making way for the swinging pendulum at 5 m/s to strike the conditioned specimen.

The temperature distribution at various locations on the steel specimen and machine parts such as anvils, specimen support, etc., during heating for various temperatures (100-600°C) was measured using a thermography camera with an accuracy $\pm 1^\circ\text{C}$. For a set temperature of 600°C, heating time of 15-20s and soaking time of 3 minutes, the specimen temperature across 10 mm on either side from V notch was within 2°C and the anvil temperature was maximum $\sim 130^\circ\text{C}$. Figure 1 shows in-situ heating system and a typical specimen at high temperature. There was no electromagnetic interference between induction heating system and controller of impact test equipment during test period.

To conclude, an in-situ heating system has been developed and standardized for carrying out impact testing of both standard and sub size CVN specimens at temperatures above ambient up to 600°C.

VII.02 Design and Development of Standing Wholebody Monitor

During radiological emergency, a transportable whole body monitoring system is required for rapid screening of workers as well as public for the internal exposure of fission products. An easily transportable standing whole body monitor has been indigenously designed and developed at HISD, IGCAR. The system consists of a subject chamber and a detector chamber of outer dimensions 212 x 125 x 63 cm and 212 x 41.5 x 52 cm respectively. The whole system is supported on a carbon steel platform of dimension 150 X 125 X 2 cm. The system is provided with 49 cm opening for the subject for entry. The distance between the left side shield of subject chamber and detector chamber is 10.5 cm. The inner width of detector chamber is designed according to the diameter of detector assembly (including PMT). The detector chamber is lined with copper to stop characteristic X-rays from lead. The system consists of four cylindrical NaI(Tl) detectors of dimension 7.5 cm X 7.5 cm, 20 cm X 10 cm, 12.5 cm X 10 cm & 10 cm X 7.5 cm and placed at various heights (150 cm, 125 cm, 85 cm and 54 cm) from the bottom platform (Figure 1). The detector at the top has a provision to move vertically by 5 cm based on height of the subject. The detectors are assembled in a linear vertical array and their locations are optimized to cover neck, chest, pelvis and thigh of

Indian reference man/women. Height and width of the subject chamber is designed in such a way that the subject (maximum size of reference man in India) can comfortably move into the chamber.

Both detector and subject chambers are shielded on all three sides using 227 numbers of interlocking lead bricks of 5 cm thickness and are lined with SS plates. SS plate provided at inner side is 3 mm thick and the outer side SS plate is 6 mm thick. Thickness of lead shielding is arrived based on MCNP calculations to attenuate photons with energies upto 3 MeV. Each lead brick weighs about 20 kg. All the lead bricks are numbered for easy assembling. The shielding effectiveness is evaluated by radiometric technique and found to have background reduction of 85% in ^{137}Cs and 65% in ^{40}K regions. The overall weight of the standing whole body monitor is about 4.5 tonnes.

All the detectors are configured as individual gamma spectrometers. Calibration is carried out using uniformly filled BOMAB phantom (Figure 2) and the efficiency values are 61 CPS/kBq and 40 CPS/kBq for ^{137}Cs & ^{60}Co respectively. Monitoring of a subject using this monitor is shown in Figure 3. The minimum detectable activity for the system is 20 -30 Bq for ^{137}Cs and ^{60}Co for a counting time of 1 min.



Fig. 1 Detector chamber with detectors



Fig. 2 Monitor with BOMAB phantom



Fig. 3 Monitor with subject

VII.03 Health Physics Surveillance at IGCAR during Special Operations

Radiological surveillance to all nuclear facilities in IGCAR is continuously being provided by Health Physics Unit stationed at each facility. Health physicists carry out radiation survey, radioactivity monitoring and measurement of radiation exposure on day-to-day operation to meet the regulatory requirements. During Covid-19 lock down period, uninterrupted round the clock shift HP services were provided to all the operation and maintenance works assuring radiological safety at all times.

In Fast Breeder Test Reactor (FBTR), few of the devices inside the primary purification cabin at B cell were taken for maintenance to rectify the sensors and faulty signal circuitry. The primary hot argon line connecting the storage tank and over flow tank was observed to be blocked due to sodium aerosol deposition. The above works were executed during reactor shut down with minimum radiation exposure from radioactive primary sodium to the employees.

In B6 Cell, the radiation level varies between 1.4 mGy/h and 5.5 mGy/h. Dose budget was estimated in pre-job ALARA meeting and a micro schedule was prepared suitably for rectification works. The collective dose incurred in the work was monitored using TLD and electronic pocket dosimeters to ensure adherence to monthly, quarterly and annual dose limits. Radiological work permits were cleared on day-to-day basis by monitoring the radiological status inside the cell and individual exposures. Personal protective equipments and lead aprons were provided to individuals during the work. Temporary shielding was provided at few locations to reduce the background radiation level. The collective dose incurred for the work carried out in B6

cell was 20.8 P-mSv, which is only 60% of the estimated collective dose. During radiography work performed in hot argon line at B4 cell (Figure 1), the incurred collective dose was 16.6 P-mSv which is 56 % of the estimated collective dose.

At CORAL, three fuel reprocessing campaigns (FBTR fuel) were successfully completed. The collective dose expenditure is 137 P-mSv. As a part of dose reduction activity, radioactive wastes from Active Analytical Laboratory, Blister Box, Partition Box and Plutonium Reconversion Glove boxes were periodically cleaned and shifted to Alpha Solid Waste Storage area. Replacement of (i) exhaust filter in Pu Reconversion Laboratory, (ii) CORAL cell light assembly and (iii) aviation lights of Stack were executed under the surveillance of HP. Remote Regulatory Inspections under independent supervision was carried out. Requalification and Relicensing of plant personnel and health physicist were conducted. As part of Radiation Protection Training to plant personnel and Cat I & II trainees, online classes were conducted in batches.

As part of commissioning activities of Demonstration Fuel Reprocessing Plant (DFRP), all the radiation monitors installed in the plant were periodically tested and their performance was evaluated. Consequent to change in the layout of DFRP, zoning and access control were reviewed and monitors were installed at exit point. For effective monitoring of Stack duct, an indigenously developed iso-kinetic probe (shrouded probe) was installed at DFRP. The shielding efficacy of flexible radiation shielding material was evaluated for using in pneumatic active liquid sample bottle transfer lines.



Fig. 1 Hot argon line (insulation removed) in B4 cell

VII.04 Safety Management During COVID-19 Pandemic - Prevention of Virus Spread

In IGCAR, preventive and protection measures are taken aiming to minimize the probability of being exposed to SARS-CoV-2. At workplace, Standard Operating Procedure (SOP) followed to control spread of the virus. Strict adherence to these guidelines by each and every individual (both department/contract employees) is essential in controlling and eliminating this pandemic. Various technologies were implemented *through various engineering controls* at the workplace of IGCAR to avoid human contact during the pandemic situation (Figure 1a).

Hand sanitizer with auto dispensing unit was installed at the entrance of all the buildings. All employees sanitize their hands before proceeding to work spots. Auto dispensing units are filled with in-house prepared alcohol based hand sanitizing liquid twice a day. Foot operated hand sanitizer dispensing machines were installed at radioactive laboratories.

The rooms were sanitized by fumigating dilute hydrogen peroxide solution (1%). Necessary Personal Protective Equipments such as Face Mask-N95, Covid-19 Suits, Gloves, Face shields, Full face and half face respirators were procured and provided to front line workers.

Employees entering the office were monitored at the entry gates for temperature by using non-contact thermal imaging camera and IR based thermometer. Non-contact thermometers were installed at the entrance of each building (Figures 1b and 1c).

Facilities were sanitized of by using dilute sodium Hypochlorite solution through Fire tender. Meeting rooms were sanitized by fumigating alcohol based disinfectant (Figure 1d).

To avoid human contact, foot operated taps were installed in wash basins at all toilets of IGCAR (Figure 1e).

To avoid human contact for the operation of lift buttons, foot operated control unit was provided for the passenger lift at both inside and outside the lift at each elevation (Figure 1f).

Bio metric machines meant for monitoring the attendance of employees installed at each building of IGCAR were modified by installing finger proximity sensors near IN and OUT buttons. This will help to avoid human contact without touching the hands-on biometrics machine (Figure 1g).



Fig. 1 (a) Automatic & foot operated hand sanitizer dispensers (b) thermal imaging and IR scanning of employees (c) non-contact thermometers (d) sanitization of buildings and meeting room (e) foot operated taps for wash basins (f) foot operated lever at outside of the lift (g) modified biometrics machine with finger proximity sensor

VII.05 Water Quality Monitoring System using Pulsating Sensors for Applications in Various Water Reservoirs in IGCAR

A Water Quality Monitoring System (WQMS) was developed for continuous monitoring of; conductivity, temperature, and pH in water bodies at different locations in IGCAR. The project was executed in collaboration with Computer Division as per the request received from CIVIL, ESG. The system is entirely in-house developed and interfaced with wireless nodes to remotely log measured parameters from different locations and represent through a GUI (Graphical User Interface). In this project, the scope of ISS was the design and fabrication of the sensors and data acquisition system. The sensors are designed based on pulsating sensor transduction technique, constructed with a pair of sensing electrodes and logic gate oscillator (LGO) for signal generation. The mechanical design and the electronic configuration of sensors are customized according to the field application.

In the first phase (at the RCL sump), leak-tight immersible sensors were designed and deployed at 4 m depth in the water column for continuous quality monitoring. The field requirements such as operation location, probing medium, measurement range, and environmental conditions were evaluated to optimize sensor performance. The geometry of probing electrodes, housing, and mounting of sensor electronics was standardized accordingly.

The conductivity sensor consists of two electrodes fixed

in a PTFE - based mechanical structure with a logic gate oscillator mounted on the probe head. The geometry of the sensing electrodes is decided based on the range of measurement. The output signal generated is interfaced with the data acquisition system using a 5m multi-core signal cable with a multi-pin round DIN connector. The cable is routed through a strong PVC pipe to hold the sensor immersed to the desired depth of 4m inside the sump.

Transducer boards (LGO) for sensors were designed, assembled, tested, and calibrated along with the sensing electrodes for 25 - 1000 μ S/cm range of measurement. The sensing probes and transducer electronics (LGO) were molded and integrated with mechanical support for deployment at the site (RCL sump). An in-house developed multi-point calibration methodology was followed to calibrate the conductivity sensor using standard KCl solutions. The nonlinear regression method establishes a relation between the sensor output, primary signal frequencies and the standard conductivity of different KCl concentrations. A second-degree curve fitting algorithm is used for generating calibration coefficients.

The temperature sensor is an RTD element-based probe with logic gate oscillator-based read-out circuit. The temperature sensor is also molded and interfaced with the data acquisition system like the conductivity

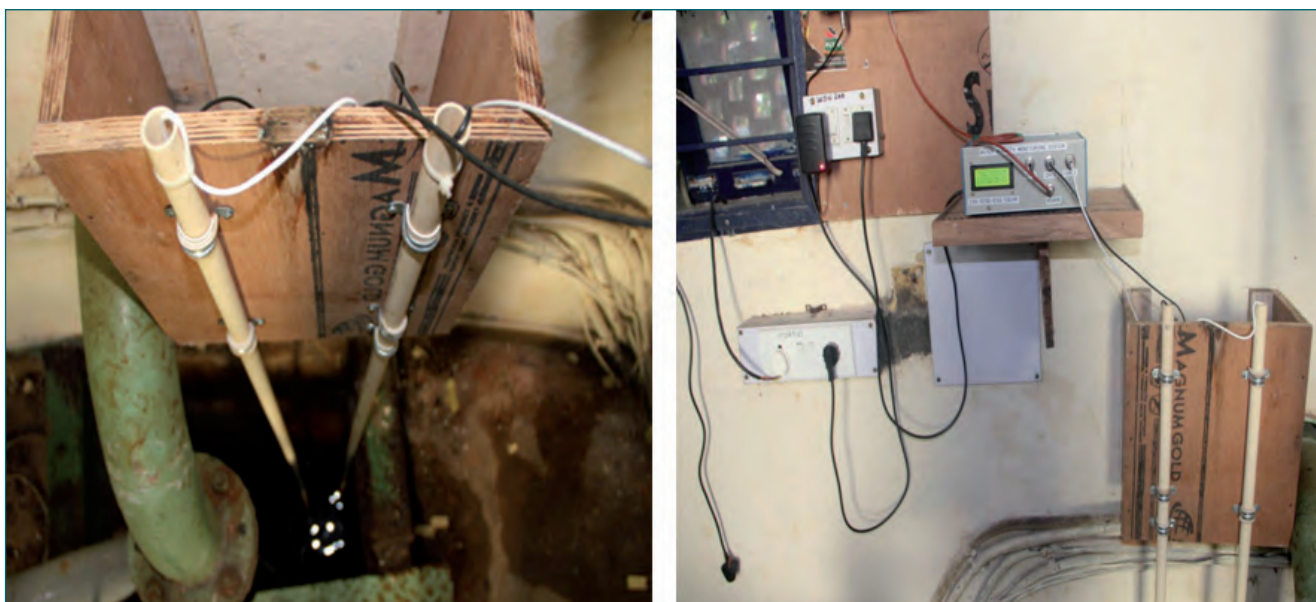


Fig. 1 WQMS consisting of conductivity probe, temperature probe installed at RCL site



Fig. 2 Fibre float testing at fabrication site,(B) float assembled with the probes,(C) leak test of float with probes in RCL sump

sensor. A thermostat controlled water bath was used to calibrate the temperature probe in the range of 20–55 °C. A commercially available electrode was used for pH measurement. The potential difference generated at the electrode is converted to digital pulse output using a V to F converter. The pH probe is calibrated using three standard buffer solutions.

The data acquisition system (DAS) is a micro-controller based embedded 3 channel unit, and it measures the frequency of the primary digital signal from sensors and converts it to the corresponding parameter. The measured values are displayed on an Alphanumeric LCD, and it is sent to wireless nodes. The MODBUS/RTU communication protocol is used to interface wireless nodes using the RS485 link. The DAS act as a slave with a fixed address for master queries from wireless nodes. The measured parameters are transmitted in fixed point format to wireless nodes upon a valid MODBUS query. The measurement unit and sensors are powered up using isolated dual 5V DC power supply. The actual sensing probes are calibrated using the final measurement unit assembled for the specific site. The DAS was configured with corresponding calibration coefficients, threshold values, and measurement settings using RS485 to USB converter at ISS electronics lab. The measurement of conductivity, temperature, pH was demonstrated at the RCL site. The WQMS consisting of

a conductivity probe, a temperature probe, with cabling and mechanical support installed in the RCL sump is shown in Figure 1.

Deployment of WQMS in the IGCAR reservoir was taken up as phase II activity. As the water level fluctuation is unexplored in this large reservoir site, a fiber float is designed to hold and immerse all three sensors on the surface level (Figure 2A and 2B). The electronics for all the sensing electrodes are mounted on the probe head, and the pulse output from each sensor is routed to DAS fixed at an elevated platform. The DAS is interfaced with the wireless sensor and transceiver nodes to transfer the measured parameters using routers to the receiver unit at Central display station. The display station exhibits and logs the data received at desired intervals using the customized GUI. Solar panels with battery management circuit are used to power the entire system in this remote site. Leak test of the fiber float assembled with all the three probes carried out in RCL sump is shown in Figure 2C. The testing of WQMS assembled for the IGCAR reservoir site (inclusive of calibration of probes, all types of interruptions) and the plot of the data logged from all the sensors (pH, temperature and conductivity reported as TDS) for a period of one month at ISS lab is shown in Figure 3. The system is ready for deployment at the IGCAR reservoir.

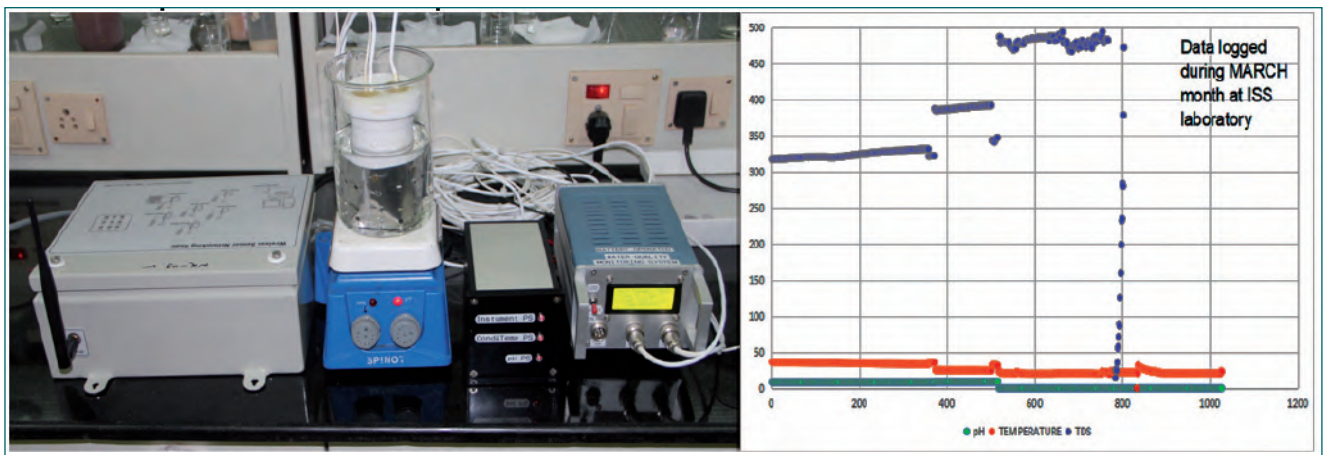


Fig. 3 WQMS assembled for IGCAR reservoir site being tested at ISS laboratory

VII.06 Development of Face Recognition Based Attendance Recording System

Biometric attendance recording system currently installed in DAE Kalpakkam complex utilizes hand geometry template. One of the social challenges posed by COVID – 19 is to authenticate employee without any contact. Face recognition is considered for contactless recognition of employees. Computer vision application effectiveness depends heavily on computing power available with System on Chip(SoC). Thanks to graphical processing units embedded with processor.

Face recognition system consists of three modules namely face detection module, key point identification module and matching module. It also consists of 5 megapixel camera that generates high resolution images.

Face detection scans group of pixels for faces. It is implemented using convolution neural network trained using imageNET dataset. Contrary to conventional processing, this neural network is run on GPU cores rather than CPU. The trained neural network is accelerated using 128 Maxwell cores available on Jetson Nano. The detected faces are then passed on to key point identification module.

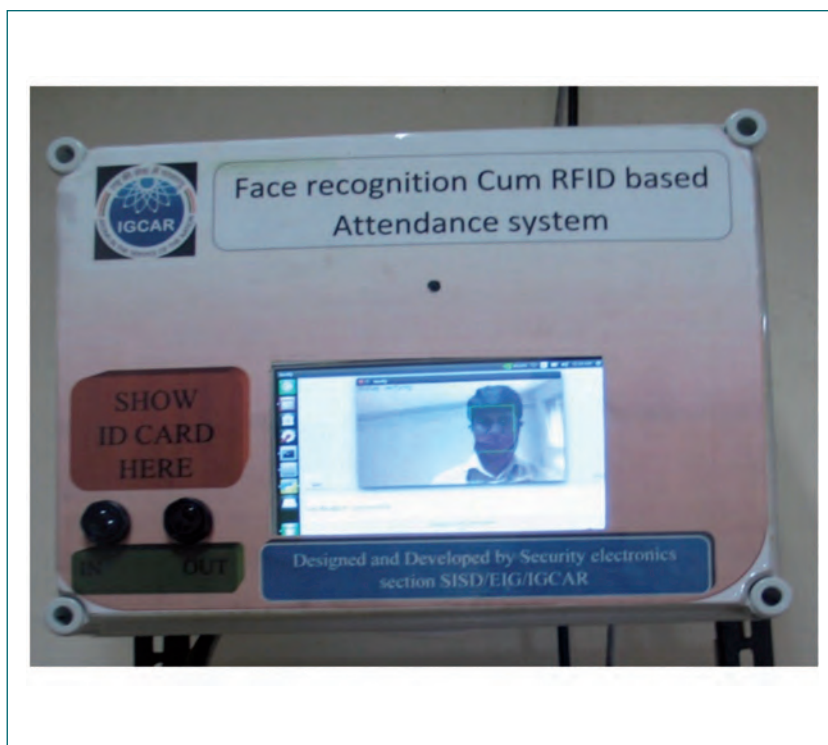


Fig. 1 Face recognition in Security Electronics Section

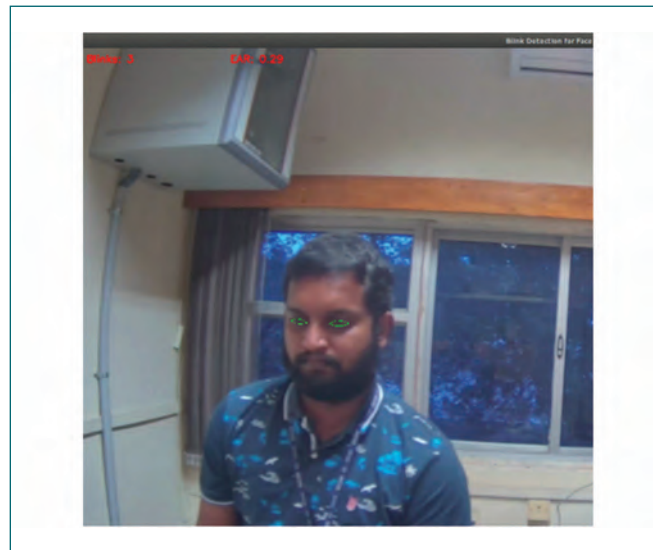


Fig. 2 Blink detection in face recognition

Face comparison is carried out using Euclidean distance between stored template and live template. Face recognition is shown in the Figure 1.

To improve robustness of the system, liveness detection is also incorporated in the current system. Liveness detection in face recognition helps to detect if face projected to a camera is real or not. In face

recognition system, it is implemented using calculation of aspect ratio of eye. Eye landmarks are derived from existing facial landmarks of a detected face. Aspect ratio is calculated from eye landmarks using eye width and height. Aspect ratio approaching zero is treated as a blink.

Average human blinks 15 to 20 times a minute. Accordingly face recognition duration is increased to 7 seconds from 1 second to perform blink detection at least one time during recognition interval. Blink detection is shown in Figure 2.

The system is integrated with existing attendance system and deployed in Security Electronics Section.

VII.07 Commissioning of Private Cloud for providing On-demand Computing and Storage Services at IGCAR

Cloud computing is a modern computing paradigm that delivers computing resources (processing power, storage, network and software) as services over a network. It offers flexibility, scalability, high availability and effective utilization of resources with lower operating costs.

Private clouds are clouds whose operation is limited to a single organization. A private cloud solution for IGCAR is designed to provide a reliable, flexible and secure hosting platform for providing service delivery models of Infrastructure as Service (IaaS) and Platform as Service (PaaS). Our private cloud solution is based on open source software tools and commodity hardware. Several important services such as Email servers, Intranet web servers and storage servers are being hosted in the platform.

The private cloud setup of IGCAR is provisioned using Open stack, a collection of open source tools that controls large pools of compute, storage and networking resources. The following services are configured for the smooth operation of cloud:

a) Identity service for managing authentication and authorization,

- b) Image service for users to upload and discover data assets such as images and metadata definitions,
- c) Block storage service to present storage resources to end users,
- d) Network service to manage network interfaces,
- e) Compute service to manage hypervisors and deploy instances and
- f) Dashboard to manage the entire cloud.

The private cloud is supported by a high performance, reliable, scalable and self-managing storage deployed using commodity hardware and an open source software defined storage platform called Ceph. The storage has a usable space of 200 TB and provides a completely distributed operation without a single point of failure. The following functional modules are configured for the Ceph based storage:

- a) Monitors that keep track of cluster nodes, cluster configuration, data placement and global cluster state,
- b) Managers that provide additional monitoring and keep track of runtime metrics and current state of the cluster,



Fig. 1 Smart cooling racks hosting the private cloud

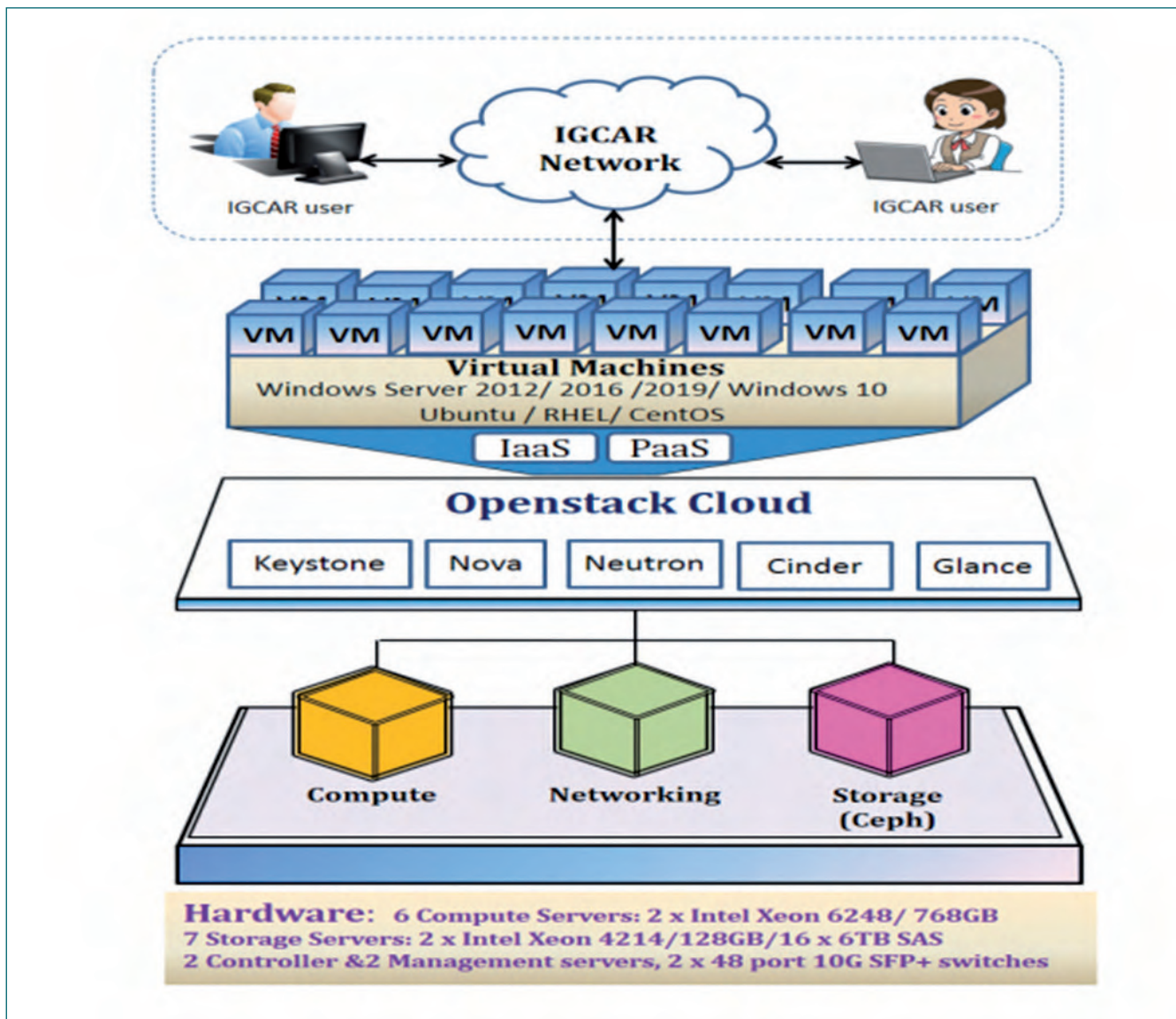


Fig. 2 Block diagram of the private cloud setup

- c) OSD (Object Storage Daemon) that stores data and handles data replication, recovery and rebalancing,
- d) MDS (Metadata Server) which is needed to create the Ceph File System and stores its metadata.

The private cloud of IGCAR is configured using 7 storage servers, 6 compute servers, 2 controller servers and 2 management servers. The storage servers are configured for Ceph cluster. Controller servers control the entire cloud infrastructure by running cloud services in high availability mode. Compute servers host user Virtual Machines (VMs) and management servers run scripts for servers are configured for Ceph cluster. Controller servers control the entire cloud infrastructure by running cloud services in high availability mode. Compute servers host user Virtual Machines (VMs) and management servers run scripts for provisioning and monitoring the entire cloud. The whole setup is hosted at Computer Centre using smart cooling racks having

modularized design to support the high-availability and redundancy (Figure 1). A block diagram of the cloud infrastructure is presented in Figure 2.

Open source tool, Metal as a Service (MAAS), is used for installation, commissioning and deployment of operating system on the servers. Another open source tool, Ansible, is used for configuration management and deployment of cloud services. Zabbix, an open-source software tool, is used to monitor the entire infrastructure - networks, servers, virtual machines and cloud services.

The servers are connected over 10Gbps networks for storage & VM connectivity and 1Gbps networks for monitoring & management. The solution is designed to host more than 100 virtual servers and supports multiple versions of Ubuntu, RHEL, CentOS, Rocky Linux, Windows Server 2012/2016/2019 and Windows 10 operating systems.

VII.08 Development USB Access Control System for Desktops

USB Access control software is developed to secure the user's data from unauthorized access and monitor the usage of USB devices on personal computers & thin-clients. The USB application continuously monitors the end user machines and sends the information about the connected removable devices to a centralized server. The centralized server verifies the authenticity of the removable device and prevents mounting of unauthorized devices. The following are the sub modules developed and commissioned as part of USB Access Control System.

USB Client Service

The software service was developed in C# to detect the removable devices of the desktop whenever it is attached. It fetches the information like Vendor ID, Hardware ID from the removable device and generates a unique id with predefined configuration. The generated unique id is verified against the centralized server, if the device is registered the client software allows the access of the device and if it is not registered the software un-mounts the removable device from the desktop.

Desktop Monitoring Client Module

The module's mandate is to fetch essential information related to the end system like IP address, MAC address, OS details, Antivirus details etc. The software generates a unique identifier to the desktop using the fetched information with a predefined scheme. The details are forwarded to centralized monitoring & control server to check against the registration details. The software displays the registration status and registration in the GUI and it also provides a link to register the desktop if the desktop is not registered. Figure 1 shows the GUI of client software.

Centralized Monitoring & Control Server(CMCS)

A web based CMCS server monitor & control the systems connected to campus LAN and removable

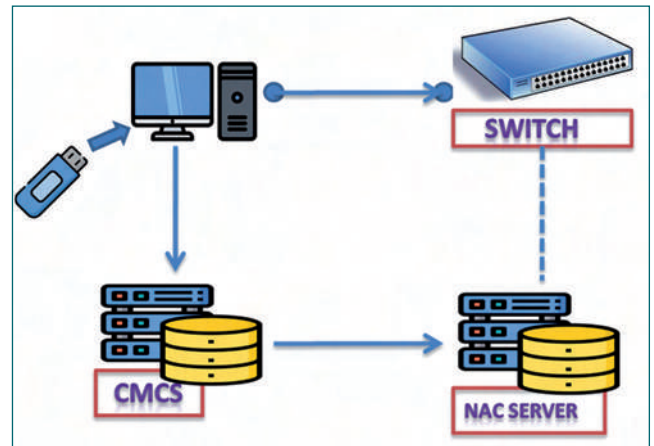


Fig. 2 Network & system connectivity flow chart of USB access control system

devices connected to end systems. It collects the system information from desktop client software and provides the registration status to NAC to allow/restrict the desktop connection to Campus LAN. It also provides access permission to USB client software if the connected USB is already registered.

The CMCS system provides a facility for the registration of new removable device with proper approvals.

The system also generates various analytic reports like: No. of active desktops in campus LAN, No of USB devices/hard disks registered etc.

Integration with NAC

A software module is developed to integrate the CMCS with NAC. This module provides the registration & antivirus information of a connected desktop to the NAC. The NAC then allows/prevents the desktop connection to campus network.

The USB access control system software has been developed and commissioned in computer division LAN. Figure 2 shows the Network & system Connectivity flow chart of USB Access control System.

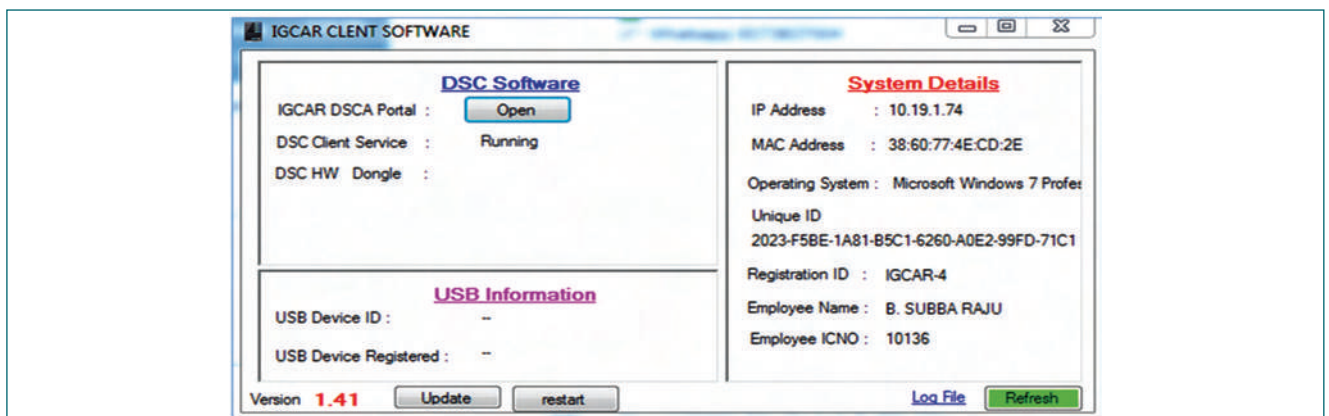


Fig. 1 GUI of client software

VII.09 Analysis of Intze Type of Overhead Water Tank for Hydrodynamic Effect

Overhead water tank is a life line structure and its basic purpose is to secure constant water supply with sufficient flow to wide area by gravity. The height of the elevated tank depends on the area and height of the building to be covered for the water supply. Elevated water tank will be subjected to hydrodynamic pressure (during earthquakes) and hence modal analysis and response spectrum analysis are performed incorporating fluid structure interaction effects. The new water tank at North Plant site of IGCAR having a volume of 554 m³ and caters to the requirement of all facilities. The tank is of Intze type and is supported on cylindrical concrete shaft. The tank is analysed for earthquake considering hydrodynamic effect using Finite element method (FEM). Design earthquake is considered as per IS 1893 2016 with the following parameters: Zone III, Importance factor 1.5 and Response reduction factor 3.5. Impulsive pressure distribution is shown in Figure 1.

Intze Tank

Intze tank is generally preferred for inward radial thrust of the bottom conical part to balance an outward radial thrust of the lowest components. The Intze tank made of inverted conical portion (roof), the cylindrical shaped wall (middle) is supported on bottom conical part and base slab. The proportions of base part and conical part are arranged to balance the outward thrust with bottom part to the internal thrust due to conical part.

Intze tank has three ring beams at every junction of the walls to resist the horizontal thrust and hoop tension. Top ring beam is provided to resist the thrust from top conical part. The middle ring beam at the bottom of cylindrical wall will remain in hoop tension and bottom ring beam will receive inward horizontal thrust from conical part as

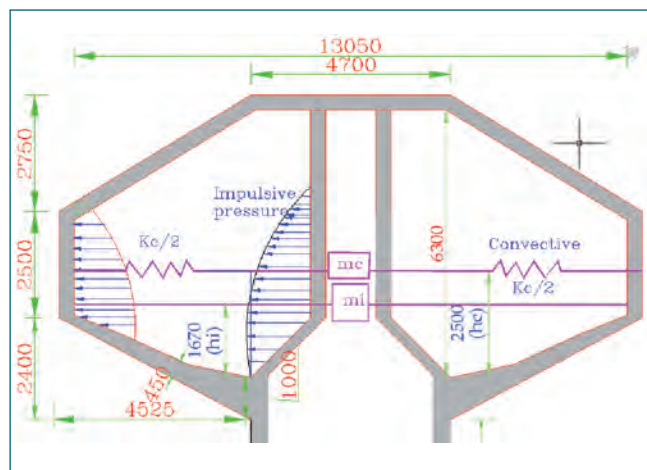


Fig. 1 Impulsive pressure distribution

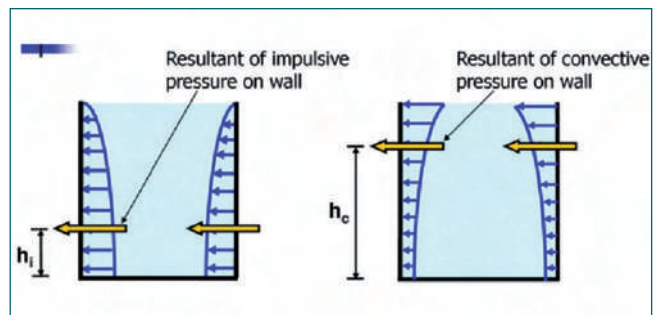


Fig. 2 Hydrodynamic pressure distribution

well as outward thrust from bottom part. During seismic base excitation, liquid exerts additional pressure on wall called hydrodynamic pressure which has curvilinear variation along wall and its direction is opposite to base motion. Summation of pressure along entire wall gives net hydrodynamic force which is non zero.

Procedure for Hydrodynamic pressure & force:

When tank is partially full and subjected to ground motion, it undergoes two types of dynamic fluid pressures (Figure 2). Liquid in bottom portion of the tank moves with wall is called impulsive mass/liquid. Liquid in top portion undergoes sloshing and moving relative to wall is called convective or sloshing liquid. Impulsive liquid moves with wall rigidly attached have same acceleration as wall. Convective liquid moves relative to wall as it is attached with springs and has different acceleration than wall. Both Impulsive and convective liquid exert pressure on wall but their nature is different. Housner's graphs for impulsive mass (m_i) & convective mass (m_c) and their height are used to calculate the impulsive and convective forces. The values are shown in Table 1 below. From the graphs, the hydrodynamic forces are calculated as,

$$\text{Impulsive force} = \text{acceleration} \times m_i$$

$$\text{Convective force} = \text{acceleration} \times m_c$$

Table 1 Details of Mass and centre of Impulsive and convective

S no	Description	Mass in kg	Height in m
1	Total mass	553700	5.3
2	Convective mass	332200	2.3
3	Impulsive mass	207600	1.67

It may be noted that 37.5% of liquid is excited in impulsive mode while 60% participates in convective mode. Sum of impulsive and convective mass is about 2.5% less than total mass of liquid.

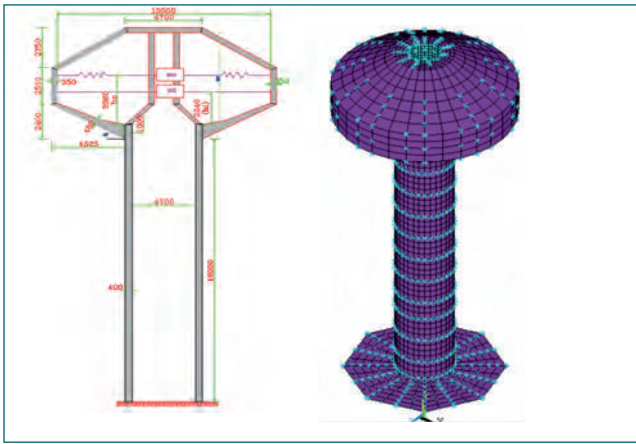


Fig. 3 (a)Geometry of Intze tank and (b) FEM lumped mass model

Seismic Analysis of Intze tank

Dimensional geometry and FE model are shown in Figure 3.

For the analysis of Intze type elevated water tank following are the dimensions and parameters. Concrete having Elastic Modulus $E = 27.4 \times 10^6$ kPa, Poisson ratio = 0.2 and Density = 2500 kg/m³. The Intze tank has been modelled using four noded shell element, 3-D beam element and spring element for boundary condition. Geometrical specifications and shell property details are shown in Tables 2 and 3.

Modal Analysis Results:

Mode shapes for the Intze water tank structure are shown in Figure 4.

Results from Seismic Analysis:

Base shears and time period for both impulsive and convective are shown in Table 4 below.

Table 2: Geometrical specification for shaft supported water tanks						
Capacity (m ³)	H (m)	D (m)	d s (m)	h(m)	h/D	t(mm)
554	18	13	4.7	6.3	0.48	400

D = Internal diameter of the tank, H =Height of shaft from Ground to tank bottom, ds=diameter of the shaft ,h=height of the tank and t=thickness of shaft



Fig. 5 Deformed shape under seismic excitation in X direction

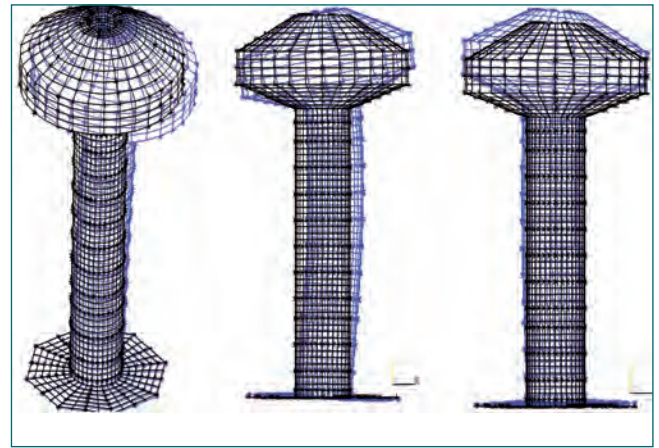


Fig. 4 Predominant mode shapes (a)Mode1=0.859Hertz (1.16 sec), (b) Mode3=4.3Hertz (0.23 sec) and (c) Mode4=4.6Hertz (0.22 sec)

Shell results are shown in Figures 6 through 11.

Total lateral base shear is about 18.3% of total seismic weight of tank out of which contribution of structure with Impulsive mass is 11.5 % & convective component base

Table 3: Shell property		
S.No	Members	Sizes(mm)
1	Top conical portion	300
2	Cylindrical wall	300
3	Top ring beam	300x450
4	Bottom ring beam	300x600
5	Conical slab bottom	350 to 600
6	Bottom slab	400
7	Bottom ring beam (near to shaft)	1000x1000

Table 4: Seismic analysis results		
Description	Tank structure with Impulsive	Convective
Base shear	1891.6 kN	1100 kN
Sloshing Height	-----	783 mm
Time period	1.16 sec	4 sec
Horizontal seismic coefficient(A _h)	0.047	0.02
<i>Total Base shear (Impulsive & convective) = 2144 kN</i>		

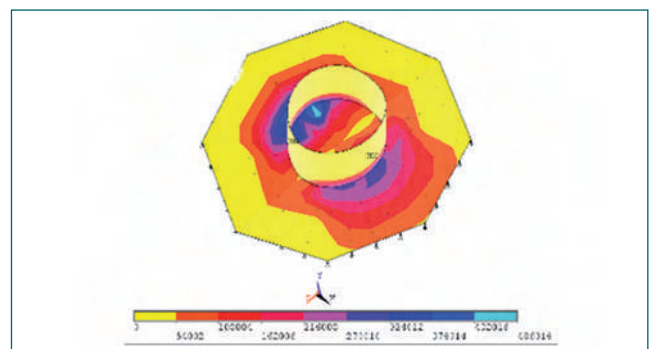


Fig. 6 Moment (M_θ) in raft foundation under seismic X direction in Nm

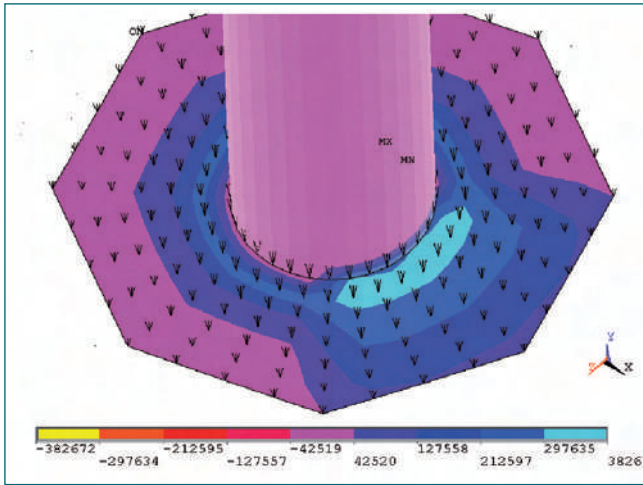


Fig. 7 Moment (M_{θ}) in raft foundation for static load case in Nm

shear is 6.8%. Maximum displacement under seismic excitation is 42 mm which is less than permissible deflection of 110 mm (height / 250). Maximum value of vertical membrane force 516kN (N_y) formed at

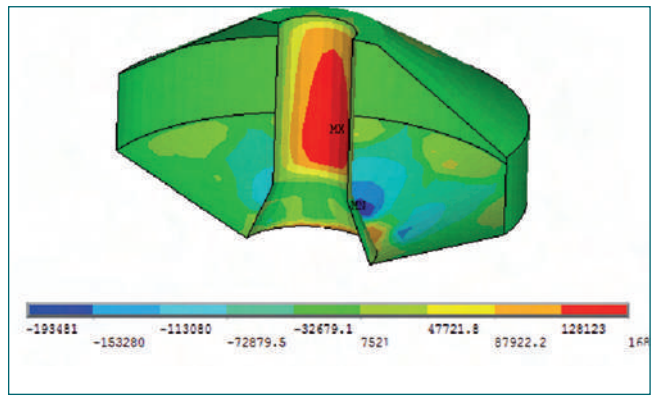


Fig. 8 Vertical membrane force(N_y) in Nm for convective case

bottom conical portion for impulsive & 1052kN (N_y) for convective cases (sloshing). Slosh height was found to be 783mm which is within the provided free board of 1m. Figure 12 indicates the picture of completed Intze Tank after construction.

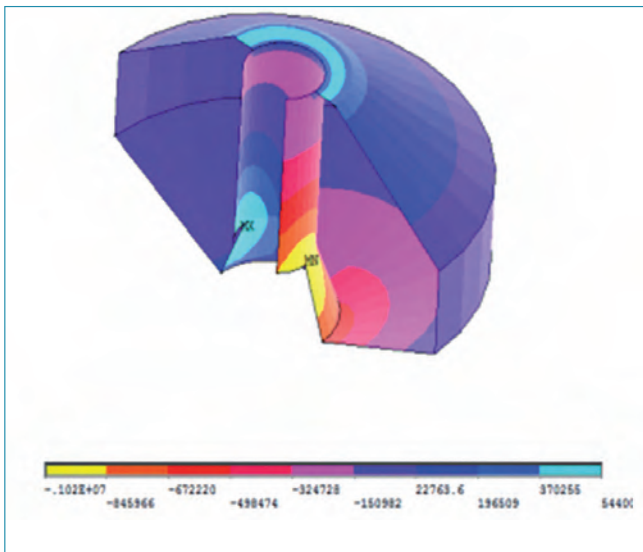


Fig. 9 Shell membrane force (N_{xy}) for seismic load case in X direction in N

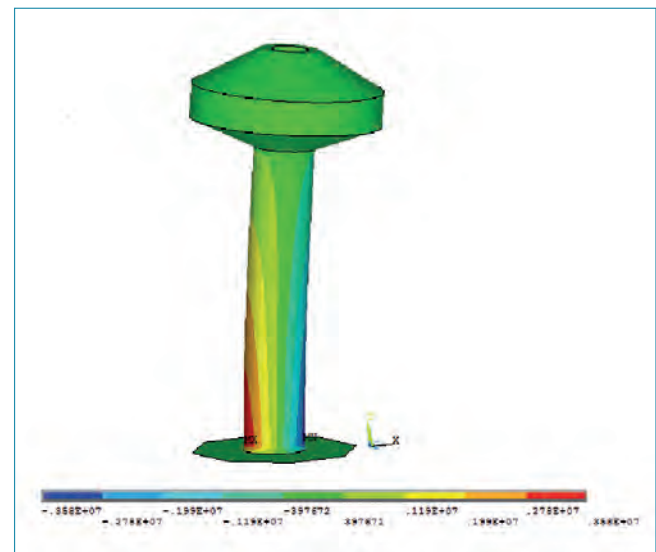


Fig. 10 Vertical membrane force (N_y) for seismic load case in X direction in N

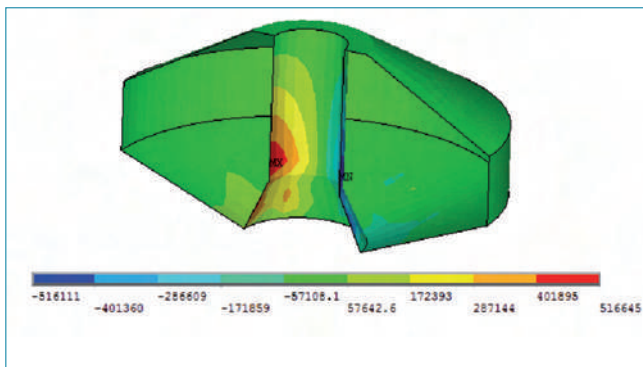


Fig. 11 Vertical membrane force(N_y) for seismic load case X direction in N



Fig. 12 Picture of completed Intze Tank

VII.10 Infrastructure Development at DAE Nodal Center, Chennai

The Department of Atomic Energy (DAE) has various constituent units and these units carry out various tasks since all these activities take place at different places, the department has felt need for setting up of a nodal facility in Chennai city area to co-ordinate its various activities. Accordingly it is proposed to set up a nodal center in the land acquired from Ministry of Defense at Pallavaram Chennai. The site of 6.13 acres, roughly pentagonal in shape is divided by road belongs to Tamilnadu State Government as indicated in Figure 1. As per site layout given in Figure 2, accommodation categorised buildings like training hostels, guest house and service buildings like substation /sump are grouped in one side (plot-B) and office buildings are grouped in another side (plot-A) based on functional requirement.

The infrastructure facilities located in this DAE nodal center are (Site plan indicated in Figure 3):

- Common infrastructure facilities like transit DAE guest house, IMSc training hostel and post doctoral fellowship (PDF) flat lets for Institute of Mathematical Science (IMSC) and integrated office building complex for various DAE Units.
- Land development works and associated service facilities
- Internal & external electrical services & air conditioning facilities

Training Hostel-IMSC: This is the hostel facility, located in plot B, designed for IMSC scholars and the plans are organized according to simple management and maintenance. Rooms are arranged one side of corridor with central courtyard design to give good ventilation and privacy. The hostel facilities are provided around the multi-functional courtyard which will be used as indoor games area as well as the meeting places of students. It's planned as single occupancy rooms with all facilities like bed, study table, walk in wardrobe with attached toilet and individual



Fig. 2 Site layout

balcony. It is a ground plus two floors structure with all modern amenities like lift, music room, reading room and television hall. The building comprises of 35 numbers of rooms in all floors with dining facility at first floor of 60 person capacities, entrance lobby with spacious waiting area and reception office. Considering the barrier free design ramps, physically challenged toilet in all floors and one hostel room in ground floor is totally designed for wheel chair movement. Figure 4 and 5 indicate ground floor plan and exterior view of training hostel respectively. Rooms are provided with individual AC system with 24 hrs wi-fi. For fire safety, smoke detectors are provided in the corridor and fire alarms are provided in all rooms. The buildings has total built up area of 2700 square meter. On completion, the hostel building is handed over to IMSC for occupation.

PDF flat lets-IMSC: This facility is meant for married scholars of IMSC and visiting scholars, which located in plot-B, opposite to IMSC hostel, by sharing the common facilities like dining facility, indoor sports room, gym, etc. Individual amenities like music room, reading room and common hall arranged in first and second floors above ground floor lobby. Total numbers of flat lets are 21, which are in ground plus two floors. Second floor is provided with bigger flat by combining two flat lets. Total building



Fig. 1 Location plan



Fig. 3 Site plan

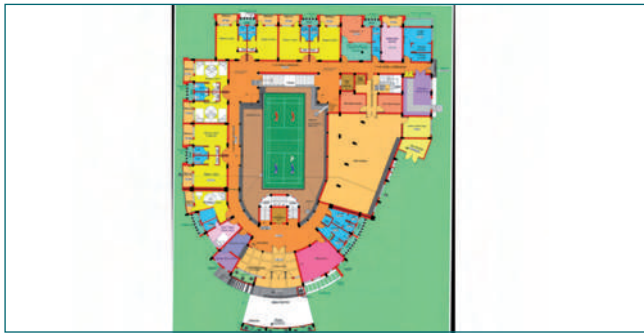


Fig. 4 Ground floor plan of training hostel



Fig. 5 Exterior view of training hostel

has built up area of 1704 square meter. Figure 6 and 7 indicate ground floor plan and exterior view of PDF flat let respectively. Total cost of construction for training hostel and PDF flat let is INR 1325.47 lakh. On completion, the building is handed over to IMSC for occupation.

DAE Guest House: Site proximity to Chennai airport is given a thought to plan transitory guest house to facilitate the officials coming and going to the other DAE units. The state of art guest house is planned with single, double and suite rooms. The impressive double height entrance lobby, reception and dining hall is planned. Double rooms are planned in ground floor (Figure 8) and single rooms in first and second floor. Suites of 4 numbers are planned in second floor with conference room. Single & suites are finished with high end materials like UPVC windows, polished wooden finish full body vitrified tiles and balconies with glass hand rails. Each room provided with amenities like bed, study table, walk in wardrobe with attached toilet and balcony. Rooms are provided with individual AC system with 24 hrs wi-fi. Figure 9 & 10 indicate exterior & interior

view of the DAE guest house respectively. For fire safety, smoke detectors are provided in the corridor and fire alarms are provided in all the rooms. Total area is 2037 square meter. Total cost of construction for DAE guest house is INR 878.87 Lakh.

Substation: To meet power requirements of DAE nodal center an 11 kV Substation is commissioned by drawing power from Tamilnadu Electricity Power Generation and Distribution Corporation Limited (TANGEDCO) through a ring main to improve reliability. It is designed to feed upto 2.5 MVA with 1 MVA DG back up. Capacity is planned to raise in a phased manner. Presently normal supply is of 1.25 MVA & DG 500 kVA capacities. Dry type transformers are provided to enable space above panel room and transformer bays to be used as an office space to make maximum utilisation of space. Lobby, staircase, lift, physically challenged toilet & other utilities are provided to cater the first floor office area. Figure 11 shows exterior view of the substation. The total built up area is 1704 square meter and first floor is presently occupied by NPCIL- MAPS.



Fig. 6 Ground floor plan of PDF flat let



Fig. 7 Exterior view of PDF flat let



Fig. 8 Ground floor plan of DAE guest house



Fig. 9 Exterior view of DAE guest house



Fig. 10 Reception counter of DAE guest house



Fig. 11 Exterior view of substation

VII.11 Establishment of Central Water Chilling Plant – II

Air-Conditioning and Ventilation System Division (AC&VSD) is responsible to fulfill air-conditioning, precision cooling, process cooling and ventilation requirements of various office buildings, data centers, R&D laboratories and radioactive facilities of IGCAR. The air-conditioning requirements of the IGCAR is presently met by Central water chilling plant (CWCP-I), standalone AC plants with screw and reciprocating chillers, package air-conditioners, variable refrigerant flow system, unitary air-conditioners like window and split ACs. Proposal to establish CWCP-II was conceived in XII plan envisaging additional chilled water required for upcoming facilities, extension of existing facilities and for replacement of R-22 based package units and standalone chillers in a phased manner to satisfy environmental protocol, reduce number of small units, reduce operation and maintenance cost and for energy saving.

A taskforce was constituted by Director, IGCAR to assess the present and future AC loads on CWCP-I and CWCP-II. Based on the recommendation, CWCP-II is designed to optimally house 4 Nos. of 750 TR water cooled chillers (3 working + 1 standby mode) and 3 Nos. of 375TR air cooled chillers (2 working + 1standby mode). The piping system is designed to take up an operating air-conditioning load of 3000 TR in the future. The total AC load of IGCAR will be shared by CWCP-I and CWCP-II in the next 5-10 year span. Presently two 750 TR capacity centrifugal chillers (fig:1) are installed and commissioned with chilled water pumps, condenser cooling water pumps, cooling towers and associated piping network. At present, the new plant will cater to the air-conditioning demand of Training School and Training Centre, Material Science Laboratory (MSL), Material development laboratory (MDL), Condensed Matter Physical Laboratory (CMPL), Particle Irradiation Facility (PIF), Electronics and Instrumentation Laboratory (EIL), Homi Bhabha Building (HBB).

Figure 2 & 3 shows the views of pump room with associated piping and cooling tower. Additionally 2 Nos. of 375 TR air-cooled chillers will be installed shortly to meet essential load requirement.

The highlights of equipments selected for CWCP-II are as follows:

Table 1: Major technical specification of chiller	
Type of chiller: Centrifugal, dual stage, water cooled chiller	
Type of motor: Semi-hermetic, refrigerant cooled, 6.6 kV, 3 Ph, 50 Hz.	
Rated capacity	750 TR
No. of Impeller stages	Dual stage
Refrigerant	R-134a
Chilled water supply temperature	7.2 °C
Chilled water return temperature	12.7°C
Chilled water flow	115 lps
Condenser water inlet temperature	32.8 °C
Condenser water outlet temperature	37.3 °C
Condenser water flow	165 lps
Motor rating	497 kW
Specific power consumption	0.605 kW/TR

- 750 TR capacity dual stage, eco friendly, energy efficient centrifugal chillers with low specific power consumption i.e., 0.605 kW/TR.
- Dual stage impeller with economizer (flash chamber) in centrifugal chiller is less prone to surging and capable to unload up to 50% at 35.0°C (95.0°F) condenser entering water temperature.
- Energy efficient chilled water and condenser water pumps with premium efficiency IE3 motors as per IEC 600034-30-1, suction diffuser and triple duty valves.
- FRP cross flow type cooling towers with film type fills used for efficient condenser cooling with closer approach.
- Pre-insulated pipes used for chilled water system for better insulation properties
- Implementation of VVVF drives for pumps and cooling towers for better controls and energy optimization.

The total specific power consumption of newly commissioned chillers along with pumps and cooling towers is about 1 kW/ TR, which is approximately 15% lower than the existing system. The savings in energy will be realized in a phased manner with replacement of system at the user end. The main technical specification of chiller is given in Table 1.



Fig. 1 CWCP-II high-bay with chillers and associated piping network



Fig. 2 View of pump room with piping in CWCP-II



Fig. 3 View of cooling towers with piping in CWCP-II

VII.12 Green Cover and Biodiversity at Kalpakkam

IGCAR has expanded over the years, building new facilities and infrastructure and stands out today for doing so without hindering the vast expanse of green cover and the delicate ecology of its environs.

IGCAR celebrates its Golden Jubilee this year (2021). This article is a pictorial tour of the buildings constructed amidst the extensive green cover and several water bodies housing a beautiful floral and faunal biodiversity.

The DAE Kalpakkam complex has many water bodies supporting an exceptional biodiversity encompassing myriad species of birds, mammals, reptiles, amphibians, fishes, etc. Birds & Butterflies indicate the quality of the ecosystems they thrive in, and they will work as one of the best early warning systems for any adverse changes

WIP marsh and Kunnathur marsh are freshwater bodies surrounded by multi-storied vegetation, dense scrub vegetation, and open wooden country. Many nesting, breeding, and fledging are documented in these marshes. The secluded wetlands have played a significant role in attracting rare avian visitors as well.

More than one hundred and eighty-two species of birds, over 75 species of butterflies and, fifteen varieties of mammals have been spotted and recorded on our campus.

The aerial view of three prominent buildings in IGCAR in 2010 and a decade later gives an idea of the greenery maintenance at IGCAR Campus (Figure 1-3)



Fig. 1a IGCAR Aerial View in 2010



Fig. 1b IGCAR Aerial View in 2021

in their environment. With the help of water birds, we can quickly identify the general condition of wetland habitats. The seclusion zones in the campus with scarce human activity attract many migratory birds and butterflies.

IGCAR, in association with Tamilnadu Forest Department, has planted more than 10,000 trees in 2021 inside the DAE Kalpakkam campus.

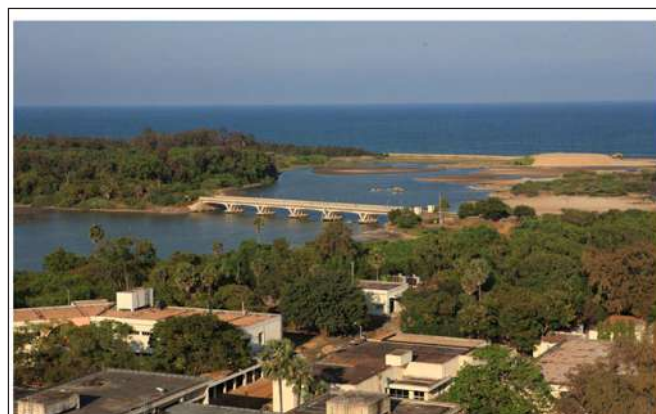


Fig. 2a Edaiyur Bridge in 2010

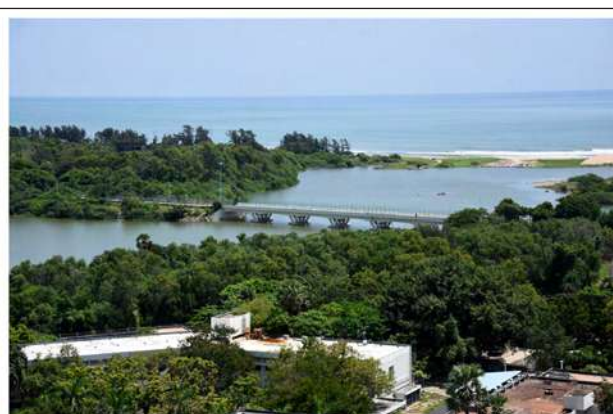


Fig. 2b Edaiyur Bridge in 2021



Fig. 3a Hall V in 2010



Fig. 3b Hall V in 2021

Mangrove vegetation

The Sadras backwater is a natural backwater system, and small Mangrove vegetation acts as a roosting place for many wetland birds (Figure 4). The large availability of fishes, mollusks, crustaceans, and aquatic plants attracts many wetland birds.

in IGCAR campus (Figure 5). The above mentioned locations are all office premises where people move about a lot and the owlets have accustomed to it. The owlets are observed throughout the year and are very active at dawn and dusk.



Fig. 4 Mangrove vegetation at Kalpakkam township

Spotted Owlets

IGCAR campus has many old trees with holes. This year, it was observed that the number of Spotted Owlets has increased in the vicinity of Homi Bhabha building, CDO building, Backside of Admin & Accounts, helipad area, around HASL building and many other regions

Indian Peafowl

Indian Peafowl is the national bird of India and is widely distributed all over the Indian Subcontinent. There is a sudden abundance, from the last counted 15 birds to more than 30 Indian Peafowls inside the DAE campus, Kalpakkam (Figure 6). In the MS Swaminathan Research

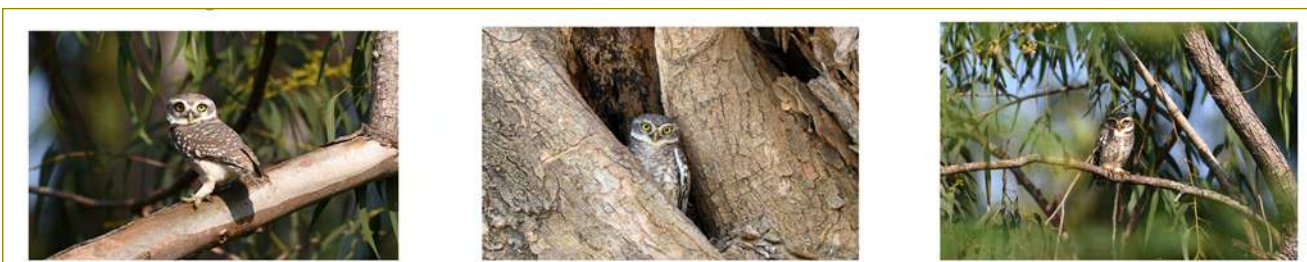


Fig. 5 Spotted Owlets Near CDO main gate, IDEAS building and Kokilamedu



Fig. 6 Indian Peafowl near Kokilemedu roadside, WIP Marsh and M S Swaminathan Plant

plantation, they eat the crops and breed. Peahens are identified by their loud calls and the males have long train-like feathers. They are found on the roadside of KKM gate and other IGCAR campus roads by early morning and late evening.

Red-necked Falcon

Falcons are rare in this part of the region. In 2020, SIRD documented two pairs of Red-necked Falcons nesting

bird species like brown-headed gulls, Caspian terns, lesser crested tern, palla’s gulls, and little terns. Recently SIRD recorded around 155 numbers of Pacific golden plovers along with marsh sandpipers and redshanks.

Some other species documented during 2021 are Indian Silverbill, White-eye Buzzard, Chestnut-winged cuckoo, and common hawk cuckoo.

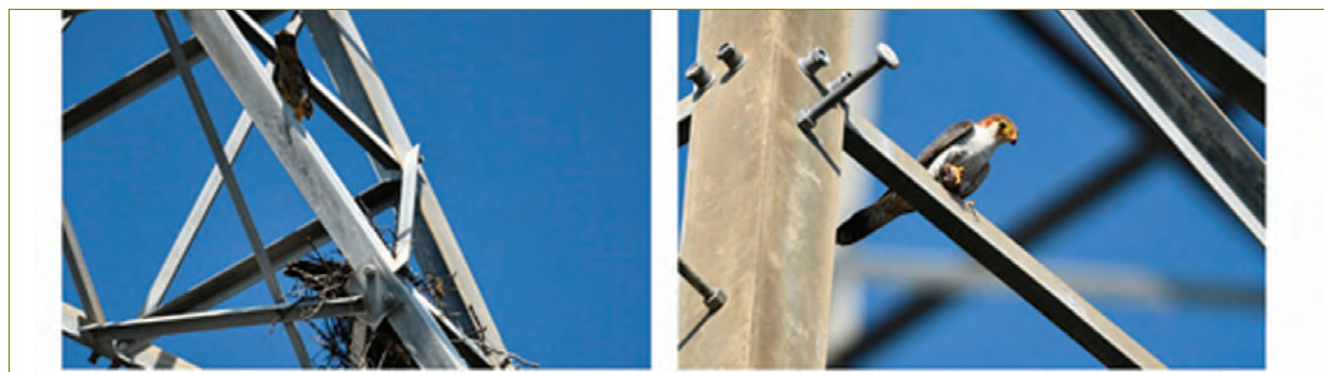


Fig. 7a Red-necked Falcon with Nesting

Fig. 7b Red-necked Falcon with Ashy Woodswallow kill

inside the IGCAR campus for the first time (Figure 7). These are very active in the dusk and are arboreal birds. They are found in pairs and can spot their prey from nearly two miles away.

Gulls, Terns & Plovers

Gulls and Terns were documented in Kalpakkam Township backwater and Edaiyur backwater (Figure 8). The mouth of the Edaiyur backwater is one of the most important stopover locations for many flocks of migrant

Biodiversity documentation

DAE Complex, Kalpakkam has a rich, thriving biodiversity and SIRD continuously documents new species of birds and butterflies spotted within the campus. The bird species documented this year include the Chestnut-winged cuckoo, Marsh Sandpiper, Common Hawk Cuckoo, White-eye Buzzard, Albino Myna, Flock of Pacific Golden Plover, Whimbrel, Little Tern, Barn Owl, Jungle Prinia, and Red-Necked Falcon. Twelve new butterfly species have also been recorded.



Fig. 8 Gulls & Terns @ Edaiyur Backwater

VII.13 Digitally Transformed Research Library

Scientific Information Resource Division (SIRD) is the second-largest research library in DAE, with an extensive collection spanning 65,000 books, 50,000 back volumes, 540 journals, 15,000 standards, and two lakh technical reports. SIRD caters to the information needs of more than 5000 scientists, engineers, research scholars, and students of various DAE Units at Kalpakkam.

Literacy development programmes

SIRD along with the Madras Library Association, Kalpakkam Chapter had organized a two day webinar on Emerging Trends in Digital Research Library during 16-17th June 2021. The webinar was streamed live through Webex platform and the official YouTube channel of IGCAR. More than 200 library professionals and students benefited by attending the webinar.

SIRD conducted an International Conference on Recent Advances in Information Technology (READIT) during November 24-25, 2021 at the Sarabhai Auditorium, IGCAR, Kalpakkam, in hybrid mode (Figure 1). The theme was “Innovative Technologies for Sustenance of Libraries”. This conference is the 12th in the biennial series since the inception of READIT in 1995. The lectures were released on the official READIT channel on Youtube.

The conference included invited talks by domain experts in the topics “Evolving information resources models, discovery tools, innovative technologies for future libraries, knowledge management techniques for libraries, and the role of Libraries in enabling scholarly communication”, to name a few.

A panel discussion was conducted on the theme ‘Future trends in scientific publishing and resource subscription models’. Discussion ranged from ‘One Nation One

Subscription, future trends in subscription models and scientific publishing to vendors in digital resources era’.

Author workshop was arranged for Springer LB Materials DB and the usage of Typeset tool. Typeset tool is subscribed by SIRD to facilitate scientific proof making of research articles for different publishers.

Publication of a book on Avian Fauna of the DAE complex

SIRD has published a book in 2021 titled “Our Feathered Friends @ DAE Kalpakkam Complex – A glance through the lens” with an ISBN. This authentic documentation of 155 avian varieties categorized as per the International Union for Conservation of Nature (IUCN) from Least Concern to Vulnerable was done with technical support from the professional ornithologist, Dr. P. Pramod, Senior Principal Scientist, Salim Ali Centre for Ornithology and Natural History (SACON), an institution under the Ministry of Environment, Forest and Climate Change. Further, the scientific name, habitat and feed of the bird species have also been recorded for each bird.

Award 2020

Ms Emerald Publishers has accorded IGCAR the ‘Real Impact Award 2020 : Library Commitment to Impact” due to the efforts invested by SIRD for providing extensive and reliable scientific information resources to enable research at IGCAR (Figure 3).

Digital Library Updates

Video streaming infrastructure of Sarabhai auditorium was upgraded with the latest streaming facilities which includes four HD cameras, enhanced storage, and networking facilities. Web conference has been integrated to the video streaming using HD cameras.



Fig. 1 Smt. S. Rajeswari, Convener READIT, Shri S. Ragupathy, Distinguished Scientist, Director, EIG & RTDG, Dr. G. Ravikumar, Head, SIRD, BARC, Prof. J. P Singh Joorel, Director, Infflibnet and Shri E. Soundararajan, Secretary READIT releasing the souvenir at the inaugural function READIT.

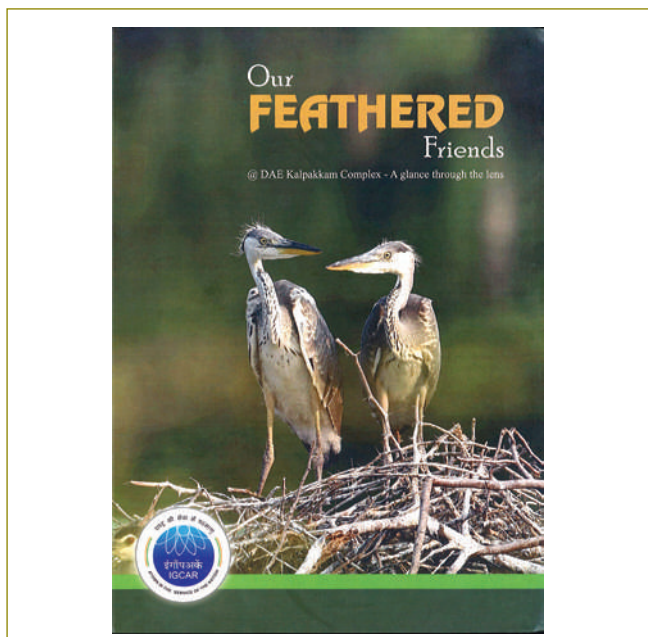


Fig. 2 Publication of a Book on Avian Fauna



Fig. 3 Library Commitment to Impact Award 2020

This has facilitated in conducting hybrid conferences in the Sarabhai auditorium and broadcast the audience, persons at the podium in high resolution. Convention Centre Auditorium was refurbished with digital audio conference facility, HDMI display systems, Laser projection facility, acoustically treated wall panelling, flooring and modernized control room system facilities. SIRD has published the IGC Annual reports and Newsletters in Flipping Book format to enhance ease of reading (Figure 4).

Citation reports were generated for award nominations from IGCAR, BARC and VECC using Scopus. Google Scholar Publications profiles were created (2010-2021) for all the groups in IGCAR. Academic performance reports for NAAC, HBNI, DAE PRIS were generated from Scopus & Web of Science.

In-house Publications and Photography

Designing and printing of certificates, brochures, souvenirs, pocket diaries, greetings are a part of SIRD services. IGC reports, IGC Newsletters and Annual report were published in time.

More than 10 short films were recorded and developed in-house. The 60th Coral Campaign, DFRP Sample handling robots, Covid-19 awareness, security guard selection trail, CF8, READIT conference and Graduation function were some of the events that were recorded on video.

SIRD continues its efforts to provide relevant information resources and services to enhance research activities of IGCAR and other DAE Units at Kalpakkam.

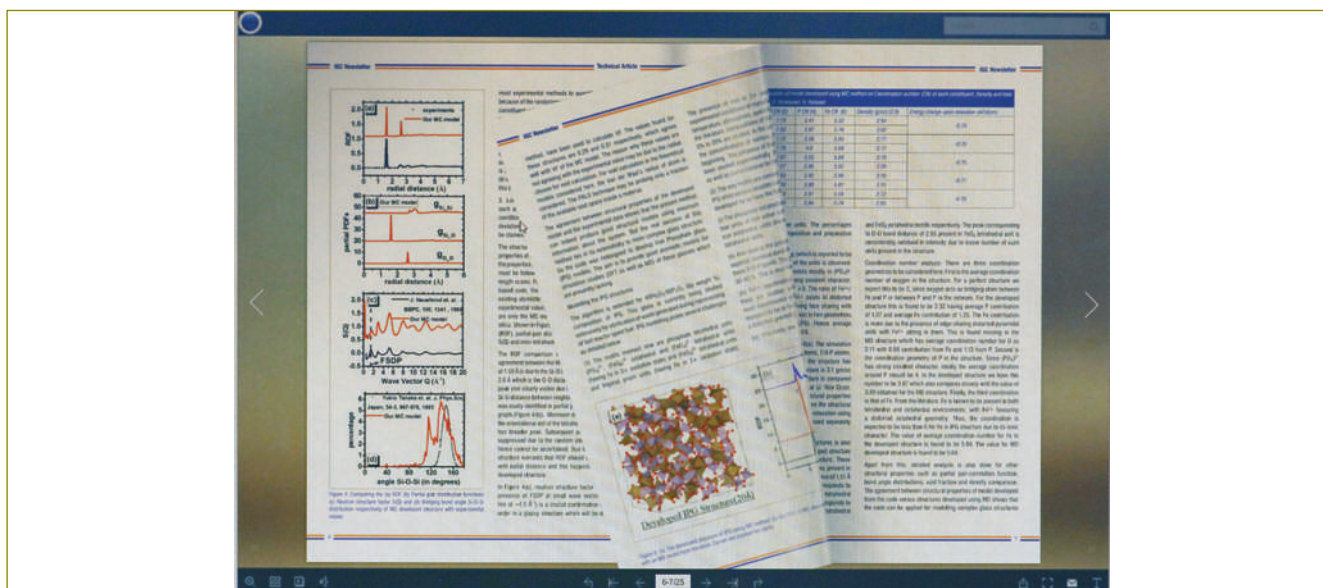


Fig. 4 In-house Publications as Flip Book

CHAPTER VIII

Awards/Publications/
Events/Organisation

Awards & Honours

Dr. John Philip, World's Top 2% Scientist in career ranking with a rank of 1,24,776 and listed as World's Top 2% Scientist in 2021 ranking with a rank of 56,477

Dr. M. Vasudevan, World's Top 2% Scientist in career ranking with a rank of 2,24,331 and listed as World's Top 2% Scientist in 2021 ranking with a rank of 1,16,119

Dr. Sandip Dhara, Materials Science Group is admitted as a Fellow of the Institute of Physics, England (October 2021) and listed as world's Top 2% Scientist in 2021 ranking with a rank of 2,30,595

Dr. Anish Kumar, Head, NDED has been selected as the Editorial Board member of journal Research in Nondestructive Evaluation (American Society for Nondestructive Testing)

Aritra Sarkar awarded Alexander-von-Humboldt Research Fellowship by AvH Foundation, Germany to conduct research at the University of Siegen, Germany and Institute of Physics of Materials Czech Academy of Science, Brno

Aritra Sarkar Selected as Member of "IN-YAS" for the period 2022-2026 by Indian National Young Academy of Sciences SIRD, IGCAR is **Winner of Real Impact Awards 2020 : Library Commitment to Impact**, by Ms Emerald Publishing, UK

Dr. Harish Chandra Dey, MMG has been awarded **Prof. Placid Rodriguez Memorial Lecture (2020) award** by IIW, India for "Development of Welding Procedures for Critical Applications in Nuclear and Fossil Power Plants" during National Welding Seminar 2020-21, April 8-10, 2021, Baroda

E. Premkumar, SIRD, SQRMG won the Bronze medal at Uganda Para-badminton International tournament 2021

Best Paper Awards

K. K. Madapu, C. Abinash Bhuyan, S. K. Srivastava, S. Dhara

The novel mechanism in understanding a strong enhancement of photoluminescence quantum yield in large-area monolayer MoS₂ grown by CVD (Best Paper IIM, Kalpakkam Chapter), J. Mater. Chem. C 9 (2021) 3578 doi: 10.1039/D0TC05263A

Nanda Gopala Krishna, R. P. George and John Philip

"Anomalous enhancement of corrosion resistance and antibacterial property of commercially pure Titanium (CP-Ti) with nanoscale rutile titania film" Corrosion Science 172 (2020) 108678 (awarded by IIM, Kalpakkam chapter)

Manali Nandy, B. B. Lahiri and John Philip

"Visual detection of defects in carbon steel using magnetic nanoemulsions effect of stabilizing moieties on the defect detection sensitivity"

Sensors and Actuators A: Physical Vol. 314 (2020) 112220

S. C. S. P. Kumar Krovvidi, J. Veerababu, Sunil Goyal, A.Nagesha, A. K. Bhaduri

Viscoplastic Constitutive Parameters for Inconel Alloy-625 at 843K

3rd Structural Integrity conference and exhibition (SICE-2020), IIT-Mumbai, December 11 - 13, 2020

S. C. Vanithakumari, Geetisubhra Jena, Sofia Solomon, C. Thinaharan, R.P. George and John Philip

"Fabrication of superhydrophobic titanium surfaces with superior antibacterial properties using graphene oxide and silanized silica nanoparticles" Surface and Coatings Technology 400 (2020) 126074 (awarded by IIM, Kalpakkam chapter)

S. C. Vanithakumari, R. P. George, John Philip

Development of Superhydrophobic Coating on Steel by Electrospinning

National Symposium on Electrochemical Science and Technology 2020 (NSEST-2020) held via online mode, Bengaluru, January 21-22, 2021

Best Poster Awards

G. Sainath and A. Nagesha

“Atomistic simulations of twin boundary effect on the crack growth behaviour in BCC Fe”.

8th International Conference on Creep, Fatigue and Creep-Fatigue Interaction (CF-8) held during August 24-27, 2021 at Indira Gandhi Centre for Atomic Research, Kalpakkam

Rangoli Hareesh, E. Vetrivendan, Ravikumar Sole and S.Ningshen

Steam Oxidation of CVD Synthesized Pyrolytic Graphite at Different Pyrolysis Temperature for High Temperature Application, CORCON - 2021, November 18 - 20, 2021 at NACE International Gateway India Section (Virtual mode)

B. K. Sahu, S. Parida, Gurpreet Kaur, Aji Kumar, S. Dhara, A. Das

Defect modulated visible light emission in 1-D SnO₂ nanostructure grown by graphene oxide assisted vapor solid process Intl. Conf. on Adv.Mater. and Mech. Characterization (ICAMMC-2021, Dec. 2-4), SRMU, Chennai

C. Abinash Bhuyan, Kishore K. Madapu, S. Dhara

Biodegradable ultrathin MoS₂ Photodetector

International Conference on Frontiers in Mater. for Technology Applications (FIMTA-2021, August 4-6), CSIR-IIMT, Bhubaneswar

Seminars, Workshops, Webinars and Meetings

- Hindi Fortnight Prize Distribution Function at Sarabhai Auditorium, Hindi Section on February 4, 2021
- “Scientific Writing for Journals” by Ms. Swati Meherishi, Editorial Director, Applied Sciences, Springer Nature Springer at Sarabhai Auditorium, SIRD on February 18, 2021
- Theme meeting on Innovative I&C concepts & Technologies for Nuclear Reactor (I2CT-21) at Sarabhai Auditorium, EIG, IGCAR on February 24-25, 2021
- Swatchhta Pakhwada at Raja Ramanna Auditorium, Admin Section, February 26, 2021
- “Balancing a Healthy & Happy life” by Smt. Ananthi Raghupathy, Founder and Director, Happy Motherhood, Chennai at Sarabhai Auditorium on March 17, 2021
- “Awareness of Laws & Accessibility of the Courts to Women in India” by Smt. Adhilakshmi Logamurthy, Advocate, High Court, Chennai on March 22, 2021
- “Courage or Comfort – Choice is yours” by Dr. S.A. Jemima Kingsley Director, Orbito Asia Diagnostics, Coimbatore Women’s day celebration by IWSA at Sarabhai Auditorium on March 22, 2021
- CSTD, Metallurgy and Materials Group, in association with the IIM, Kalpakkam chapter, organized a one day free Webinar on “Corrosion Science and Technology (COST 2021)” on May 12, 2021.
- Online Training programme on Reservation in services by ATI at Raja Ramanna Auditorium, June 23, 2021
- Online Training program on Stress Management by ATI at Raja Ramanna Auditorium on June 24, 2021
- Online training programme on National Pension Scheme by ATI at Raja Ramanna Auditorium on June 25, 2021
- Online Training program on Office procedure and record management by ATI at Raja Ramanna Auditorium on June 28-29, 2021
- Online Refresher programme on CCS (Pension) Rules, 1972 by ATI at Raja Ramanna Auditorium, June 30, 2021
- Online Training programme on Refresher programme on CCS pension rules 1972 by ATI at Raja Ramanna Auditorium on July 1, 2021
- Online Training programme on exercise of financial power (DAE) rules 1978 by ATI at Raja Ramanna Auditorium on July 2, 2021
- “e-Procurement under central public procurement” by M. Rama Amirtham, Senior Technical Director, NIC-HQ, New Delhi by EIG at Sarabhai Auditorium, July 7, 2021
- Online programme on 14th Generic Training on Cyber Security by ATI at Sarabhai Auditorium, July 9, 2021
- Lecture for Research scholars by Psychiatrist doctor by SQ&RMG at Sarabhai Auditorium on July 13, 2021
- Webinar series for sharing operating and regulatory experiences on safety significant events in Nuclear Power Plants by AERB at Raja Ramanna Auditorium on July 22, 2021
- Seaborg Memorial Lecture by Dr. K.L. Ramkumar, Retired Senior Scientist, BARC at Sarabhai Auditorium, September 3, 2021
- IGC Colloquium on Indian Space Programme by V.V Srinivasan, Outstanding Scientist, Director, ISTRAC/ISRO at Sarabhai Auditorium on September 7, 2021

- Hindi Fortnight Celebration at Sarabhai Auditorium, Hindi Section on September 14, 24 and 27 2021
- Dr Placid Rodriguez Memorial Lecture By Dr. B. Venkatraman, Director IGCAR at Sarabhai Auditorium on October 5, 2021
- Recruitment meeting at Sarabhai Auditorium, Recruitment Section on October 8-14, 2021,
- Online programme on 19th Generic Training on Cyber Security by ATI at Sarabhai Auditorium on October 21, 2021
- Vigilance Awareness Week by admin at Raja Ramanna Auditorium on October 28,2021
- 15th Batch (OCES-2020) BARC training school graduation day at Sarabhai Auditorium on October 28,2021
- Vigilance Awareness Week by admin at Sarabhai Auditorium on October 29,2021
- Online Training programme on pay bill register by ATI at Raja Ramanna Auditorium on October 29, 2021
- Vigilance Awareness Week by admin at Raja Ramanna Auditorium on November 1,2021
- Presentation/interaction sessions on GeM by Assitant purchase officers, MRPU at Sarabhai Auditorium on November 2,2021
- Curie Memorial Lecture by Dr. E. Prabhu, DRM, Advanced Nuclear Medicine Research Institute, Chennai at Sarabhai Auditorium on November 12, 2021
- READIT-2021 International Conference Organised by SIRD, at Sarabhai Auditorium on November 24-25, 2021
- Online Training programme on DPC proceedings and merit promotion scheme by ATI at Raja Ramanna Auditorium on November 26, 2021
- Online Training programme on Sexual Harrasment of women at work place (Prevention, Prohibition and redressal) Act 2013 by ATI at Sarabhai Auditorium on December 9, 2021
- Presentation/interaction sessions on GeM by Assitant purchase officers, MRPU at Sarabhai Auditorium on December 17, 2021
- Online Training programme on Accounts Experience on various subjects by ATI at Sarabhai Auditorium on December 22, 2021
- Webinar series for sharing operating and regulatory experiences on safety significant events in Nuclear Power Plants by AERB at Raja Ramanna Auditorium on August 6, 2021 to December 2021

DAE Awards



Department of Atomic Energy has instituted annual awards for excellence in Science, Engineering and Technology in order to identify best performers in the area of Research, Technology Development and Engineering in the constituent units (other than Public Sector Undertakings and Aided Institutions). The Young Applied Scientist, Young Engineer, Young Technologist, Homi Bhabha Science and Technology Award and Scientific and Technical Excellence Award fall under this category. Group Achievement awards for recognition of major achievements by groups have also been instituted. Life-time Achievement Award is awarded to one who has made significant impact on the DAE's programmes. They are the icons for young scientists and engineers to emulate. The awards consist of a memento, citation and cash prize.

The recipients of the Awards from IGCAR for the year 2019 were:

Homi Bhabha Science and Technology Award	: Sandip Kumar Dhara
DAE Scientific and Technical Excellence Award	: 1. Shri Rakesh Kumar Mourya, SO/F, SE&HD, RDTG 2. Shri Utpal Borah, SO/G, MDTD, MMG
Young Scientist Award	: Dr. G. Sainath, SO/E, MDTD, MMG
Young Engineer Award	: 1. Shri P. Lijukrishnan, SO/E, ETHD, RDTG 2. Shri E. Vetrivendan, CSTD, MMG
Meritorious Service Award	: Shri S. Palavesamuthu, GM, Canteen, Administration
Meritorious Technical Support Award	: 1. Shri I. Amir Abhas, FM/C, ROD, RFG 2. Smt. M. Padalakshmi, PIED, MMG

Group Achievement Awards:

"Life extension of FBTR Through an integrated Strategy"

Dr. P. Parameswaran (Group Leader)

Dr. S. Raju, Dr. V. Thomas Paul, Smt. T. Ezhilarasi, Shri R. Thirumurugesan, Shri A. K. Panda, Dr. S. Murugesan,

Smt. M. Jyothi, Dr. C. Sudha, Dr. Harapasanna Tripathy, Shri R. Sundar, Smt. M. Padalakshmi, Dr. R. Divakar, Dr. V. Karthik, Shri C. N. Venkiteswaran, Shri A. Vijayaragavan, Dr. C. Padmaprabhu, Shri V. Anandaraj, Shri V. V. Jayaraj, Shri Ran Vijay Kumar, Shri Ashish Kolhatkar, Shri M. Sakthivel, Shri Bhabani Sankar Dash, Shri L. Pandian, Smt. S. Gomathi, Shri Rabindra Nayak, Shri Panchanan Patra, Shri V. Murugan, Shri S. Anguraj, Shri S. Manimaran, Shri P Loganathan, Shri V. Rajendran, Shri B. S. Ramesh Babu, Shri K. Dinesh, Shri .S. Rama Rao, Shri G. Bhaskaran, Shri Shobit Verma, Shri R. Athisankaran, Shri G. Raghukumar, Smt. E. Radha , Smt. Neethu Hanna Stephen, Shri V. Velu, Shri V. Rajkumar, Shri P. K. Chaurasia, Shri M. Muthuganesh, Shri R. Ravikumar, Shri Rajesh Saxena, Shri Adish Haridas, Dr. D. Venkata Subramanian, Shri Rajeev Ranjan Prasad, Dr. D. Sunil Kumar, Shri R. Ramesh, Dr. S. Murugan, Shri G. Ramesh, , Smt. Alka kumari, Shri P. Ramesh, Dr. K. Chandran, Mrs. M. Lavanya, Dr. R. Raja Madhavan, , Dr. R. Sudha, Dr. Anthony

Group Achievement Awards:

"Development of welding and Inspection Procedures for Disimilar Metal Weld Joint between 10Cr Steel & Alloy 617M Welded Rotor for Advanced Ultra Super Critical (AUSC) Thermal"

Dr. Shaju K. Albert (Group Leader)

Dr. Arun Kumar Bhaduri, Dr Harish Chandra Dey, Dr. Anish Kumar, Shri Utpal Borah, Dr. K. V. Rajkumar, Shri S. Pongseenasan, Shri Arvinth Davinci Shri M. Arul, Shri D. Manokaran, Dr. C. Ravishankar from MMG. Shri S. Murugan, Shri V. Rajendran, Shri T. Saravanan, Shri C. Palani, Shri D. Mohan, Shri S. P. Jaisankar, Shri E. Gothandan, Shri B. Sathish Kumar, Shri B. Muhammed Shijas, Shri A. Ramanathan, Shri R. Manikandan, Shri S. Surendra Kumar, Shri E. Damodaran, Shri K. Punniyakotti, Shri Bhagaban Mohanty, Shri P. Karuppasamy, Shri V. Kodairasan, Shri A. Gunasekaran from ESG. Shri Navtresh Bajpai, Shri K. Krishna Chaitanya, Shri P. Azhagesan, Shri P. Narayana Rao, Shri R. Rajesh from SQRMG

Group Achievement Awards:

"Development of Robotic vehicle and Remotely Operated Devices for the Visual Inspection of Fast Reactor Fuel Reprocessing Facilities"

Shri C. Rajagopalan (Group Leader)

Dr. S. Murugan, Dr. Purna Chandra Rao B, Shri Joseph Winston, Shri R. Chellapandian, Shri G. Senthil Kumaran, Shri Saji Jacob George, Shri V. Rakesh, Shri Ashutosh Pratap Singh, Shri M. Murali, Shri K. Dhanapal, Shri Jobby C Johnson, Shri D. Ganesan, Smt Shanthi Rajendran, Smt. S. Saravana Priya from RDTG. Shri A. K. Sasi, Shri Shekhar Kumar, Shri M.S. Gopi Krishna, Shri Surajit Halder, Shri P. Varadharajan, Shri Abdul Muqtadir, Shri D. C. Thomson from RpG. Shri G. Ramesh from SQRMG

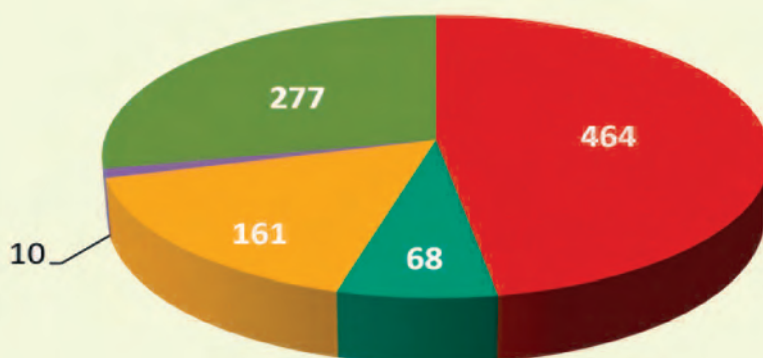
Group Achievement Awards:

"Indigenous Design, Development and Implementation of Electronics Security Systems and Computer Based Security Automation for DAE Kalpakkam Complex"

Shri G. Prabhakara Rao (Group Leader)

Shri P. Arumugam, Shri S. Krishnan, Shri M. Vincent, Shri Gyanendra Prasad, Shri S. Lakshmi Prasad, Shri Satya Rajesh Medidi, Shri I. Gowtham, Shri T. Sathishkumar, Shri M. Raja Sekhar, Shri P. Balaji, Shri J. Immanuel from EIG

IGCAR Publications during the Year 2021



- Articles in Journals
- Articles in Press
- Conference Papers
- Book Chapters
- Internal Reports

H-Index of IGCAR

Scopus : 114 | Web of Science : 106 | Google Scholar : 124

EVENTS

Webinar - International Conference on Light Matter Interaction (ICLMIN – 2021)

May 19-21, 2021



The webinar was attended by more than 800 leading scientists and students all over the world across six sub-continent of Africa, Asia, Australia, Europe, North and South America.

International Conference on Light Matter Interaction (ICLMIN – 2021) was organized by Indira Gandhi Centre for Atomic Research (IGCAR), Kalpakkam during May 19-21, 2021 in online mode [<https://sites.google.com/view/iclmin2021/home>; <https://iclmin2021.in/index.html>].

The conference focused on Light-Matter Interaction and its study using Optical Spectroscopy along with their applications in material sciences encompassing physical, and chemical sciences. The conference was inaugurated by Dr. A. K. Bhaduri, Director IGCAR with welcome address by both Dr. Shaju Albert, Director MSG and Dr. M. Kamruddin, Associate director, ANG. Chief Guest Prof. Chandrabhhas Narayana, Director, Rajiv Gandhi Centre for Biotechnology (RGCB), Trivandrum delivered the plenary lecture on "Application of Surface Enhanced Raman Spectroscopy for studying Bio-molecular interactions" for the opening session.

The conference focused on the utilization of conventional as well as advanced optical spectroscopy on novel low dimensional materials, along with specific sessions on phase transformations under extreme conditions, and single quantum emission. Localized techniques namely near-field scanning optical microscopy (NSOM) assisted, and surface and tip enhanced Raman spectroscopy (SERS and TERS) are another area of major interest. The webinar was attended by more than 800 leading scientists and student all over the world across six sub-continent of Africa, Asia, Australia, Europe, North and South America. Indian participants were spread all over the country. The scientific deliberations were conducted in eight technical sessions with invited and contributory presentations. The conference presented an opportunity for young researchers to interact with leading experts in the specialized field of research. There were 13 foreign speakers spreading over five sub-continent and 18 Indian speakers from IITs, National Universities and Research Institutes.

Conference was attended by 800 participants and was well appreciated by all.

Media Coverage: <https://pib.gov.in/PressReleasePage.aspx?PRID=1721373> (Please use google translator)

<https://www.chennaicitynews.net/news/tamilnadu/international-conference-on-light-matter-interaction-iclmin-2021/>

<https://kalaipoonga.net/business/international-conference-on-light-matter-interaction-iclmin-2021>

Reported by

Dr. Sandip Dhara, Materials Science Group

Webinar on Emerging Trends in Digital Research Library

June 16-17, 2021

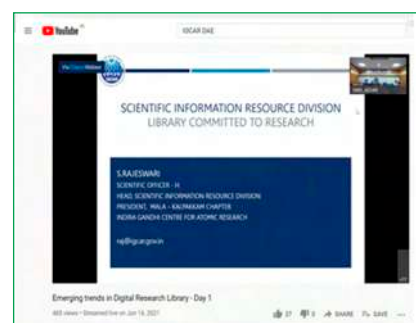


Presidential Address by Smt. S. Rajeswari, Head, SIRD

Scientific Information Resource Division (SIRD) in association with the Madras Library association, Kalpakam Chapter organized a two-day webinar on Emerging Trends in Digital Research Library during June 16-17, 2021. There were more than 300 participants for the webinar. The webinar was live streamed through Webex platform and official YouTube of IGCAR. The registered participants joined through YouTube. The speakers and dignitaries were on Webex platform. Shri. E. Soundararajan, Head, DRTS, SIRD welcomed the delegates of the webinar. The inaugural address was given by Dr. B. Venkatraman, Distinguished Scientist and Director SQRMG. Smt. S. Rajeswari, Head, SIRD delivered the presidential address. The webinar focused on the emerging technologies and trends for research digital library and highlighted the impact of library in R&D output of institutions. There were technical talks by eminent speakers from SIRD, Pondicherry University, Madras Library Association and NITTR, Chennai. The presentations ranged from emerging trends in digital library infrastructure, research and publication ethics, research data management and analysis through institutional repository and scientometrics to name a few. All the sessions were quite interactive. Participation Certificates were mailed to the registered participants in digital format. The YouTube link for the webinar is <https://www.youtube.com/watch?v=xAWGqnZPIMY> and <https://www.youtube.com/watch?v=3s5DLH6NL8w> for day 1 and day 2 respectively.



Indira Gandhi Centre for Atomic Research (IGCAR) Scientific Information Resource Division (SIRD) In association with Madras Library Association Kalpakam chapter (MALA-KC)		
Webinar on Emerging trends in Digital Research Library		
Day-1 (16-June-2021)		
Timing	Topic	Speaker
08:30 - 09:30	Welcome Address	Dr. B. Venkatraman Secretary, MALA-KC
09:30 - 09:45	Inaugural Address	Dr. B. Venkatraman, Distinguished Scientist Director SQRMG & IISG, IGCAR
09:45 - 10:15	Presidential Address	Smt. S. Rajeswari President, MALA-KC and Head, SIRD, IGCAR
10:15 - 10:30	Special Address-1	Dr. K. Sivasamy President, Madras Library Association
10:30 - 10:45	Special Address-2	Dr. K. Sivasamy Secretary, Madras Library Association
10:45 - 11:45	A glimpse of IGCAR with Publications	Dr. S. Sundaraman Head, LIS, SIRD, IGCAR
11:45 - 12:00	Emerging trends in Digital Library Infrastructure	Head, SIRD, SIRD, IGCAR



Reported by
Smt. S. Rajeswari, Head, SIRD

National Seminar on Welding Science and Technology (NSWEST 2021)

July 23 - 24, 2021



Inauguration function of NSWEST 2021 held on July 23, 2021 from Blue room, IGCAR

Shri G. Nageswara Rao, Chairman, Atomic Energy Regulatory Board (AERB) inaugurated the Two days seminar “National Seminar on Welding Science and Technology – Present Status & Future Direction (NSWEST 2021)” remotely on July 23, 2021 from Mumbai. This seminar was organized by the Indian Institute of Welding (IIW) – Chennai branch on virtual platform from IGCAR, Kalpakkam and about 200 engineers, scientists, research scholars and industrial personal attended this seminar. In his inaugural address, Chairman, AERB emphasized the use of advance welding process like, electron beam welding and acceptance of automation in welding. He highlighted the importance of dissimilar weld joint in industries and effect of residual stresses on the performance of the weld joint. He touched upon post weld heat treatment (PWHT) of weld joints, ASME codal guidelines on thickness, stress corrosion cracking (SCC) in heat affected zone HAZ of weldment, meeting leak before break (LBB) criteria for safety considerations and application of advanced non-destructive examination (NDE) techniques for quality assurance etc. He further emphasized on in-situ repair welding, in-service inspection, integrity assessment and life extension of nuclear components. He suggested to accepted prefabrication as a criteria in nuclear industries to avoid site fabrication due to limitation at the site.



Inaugural address by Shri G. Nageswara Rao, Chairman, Atomic Energy Regulatory Board (AERB)

A total of 129 technical lectures covering welding skill development, weld inspection, weld automation, consumables development, coating, fabrication, residual stress, corrosion, repair welding, creep, fatigue and high temperature materials & their weldability related to nuclear power plants, thermal power plants, defense and space sector were presented in 23 sessions, including 2 Plenary Talks, 29 Keynote, 10 Invited talks and 80 contributory papers.

Reported by

*Shri T. V. Prabhu, Head, CFED, MCMFCG
& Convener, NSWEST-2021*

Technology Transfer of “Portable High Volume Air Sampler”

August 25, 2021



Technology license and document on IGCAR's High Volume Air Sampler technology being handed over by Head, IC-IGCAR to Director of M/s First Source Impex Pvt. Ltd., Bengaluru

Portable high volume air sampler is a light-weight device, made of Fiber Reinforced Plastic (FRP) and has an inbuilt embedded controller to start, stop, log and to calculate the total volume of air sampled. This is employed to collect airborne particulates in a filter paper medium at desired flow rates up to 2800 lpm. The import-substitute technology has been developed at SQRMG, IGCAR as part of the 'Atma Nirbhar Bharat' mission of Government of India and devices have already been deployed for in-house air quality monitoring. The device finds applications in pollution control boards for collection of suspended particulate matter in monitoring environmental pollution and in industries discharging particulate effluents for the purpose of monitoring. This is used in nuclear installations for the collection of air samples to estimate air-borne radioactivity levels.

This technology was transferred to M/s First Source Impex Pvt. Ltd., Bengaluru on August 25, 2021 at a brief event coordinated by Incubation Centre-IGCAR. The meeting was attended by Dr. B. Venkatraman, Director SQRMG (IGCAR), Dr. N. Subramanian, Head, Incubation Centre-IGCAR, Dr. C. V. Srinivas, Head, EAD, SQRMG, Dr. V. Subramanian, Head, ATBS, RESD, SQRMG, Dr. S. Chandrasekaran, Head, EnAS, EAD, SQRMG, Dr. M. Menaka, Head, RAMS, RESD, SQRMG, Shri R. Rajesh Kumar (Director, First Source Impex Pvt Ltd., Bengaluru) and Shri B. Balakrishnan (First Source Impex Pvt Ltd., Bengaluru).

*Reported by
Dr. N. Subramanian
Head, Incubation Centre-IGCAR*

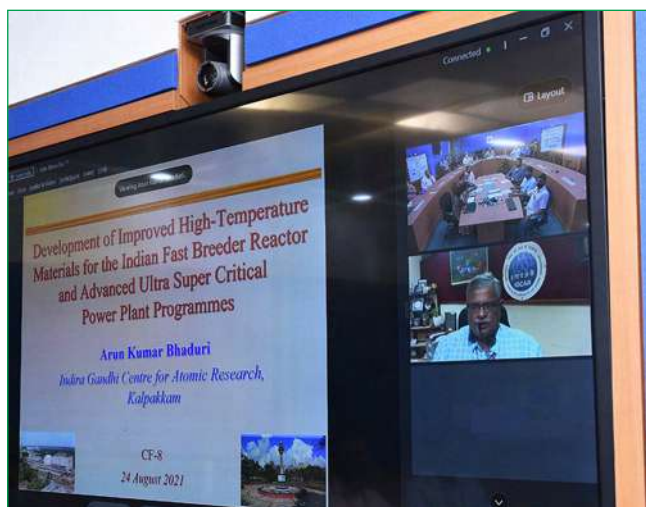
Eighth International Conference on Creep, Fatigue and Creep-Fatigue Interaction (CF-8) [Web Conference]

August 24-27, 2021



Dr. R. Divakar, Associate Director, MEG, IGCAR, Dr. M. Vasudevan, Head, MDTD, IGCAR, Dr. B. Venkatraman, Director, IGCAR and Dr. Shaju K. Albert, Chairman, Local Organizing Committee, CF-8 and formerly, Director, MMG, IGCAR during the inaugural session of CF-8

The Eighth International Conference on Creep, Fatigue and Creep-Fatigue Interaction (CF-8), jointly organized by Indira Gandhi Centre for Atomic Research (IGCAR), Kalpakkam and the Metal Sciences Division and the Kalpakkam Chapter of the Indian Institute of Metals (IIM) was conducted as a Web Conference between 24.8.2021 and 27.8.2021. The conference was conducted in collaboration with the Japan Society of Mechanical Engineers (JSME) and was attended by about 150 scientists and engineers from India and abroad, specializing in the areas of creep, fatigue and their interaction. The inaugural address of the conference was delivered by the Chief Guest Sri. S. C. Chetal, Senior Scientific Advisor, Bharat Heavy Electricals Limited and former Director, IGCAR and Indian Mission on AUSC programme. He observed that high temperature design codes lay strong emphasis on the strength of materials whereas ductility does not directly enter into the analysis, adding that a proper balance between the two is essential to ensure structural integrity and safety of components subjected to high temperatures and high stresses during service. He also suggested that emphasis should be given in the areas of creep-fatigue interaction, unification of design factors among various codes, mechanical properties of weldments before and after repair welding, component testing, etc. from the viewpoint of long-term safety and integrity of components and structures. A total of 102 technical lectures covering creep, fatigue and their interaction aspects of various structural materials of interest to nuclear and fossil-fuel power plants, defence and aerospace sectors were presented in 23 sessions including 24 keynote and 6 plenary lectures by leading experts on the core theme of the conference. The concluding session of the conference identified several potential areas that could be included in the scope of the next conference of the CF-series.



Plenary lecture being delivered by Dr. A.K. Bhaduri, the then director, IGCAR on August 24, 2021.

Prominent among them were testing under simulated environments, condition monitoring of ageing plants, testing requirements for strategic applications, miniaturization of specimen testing and thrust for physics-based modelling. Dr. Shaju K. Albert, Chairman, Local Organizing Committee, CF-8 presented a summary of the proceedings with a brief overview of the papers presented during the four days.

A total of 45 presentations delivered by Students and Young Scientists were included for consideration of best presentation awards. Three best presentations in each category were honoured with the awards comprising of citations and cash prizes.

*Reported by
Dr. R. Divakar, Associate Director, MEG, IGCAR,*

4th AC & Refrigeration Service Program - ACRESERVE 2021

October 08, 2021



Shri V.Rathnakumar, Convener- ACRESERVE, Shri VijayaBhaskaran, RD South -2, ISHRAE HQ , Dr. K. Ananthasivan, Director, RpG, Shri Kesavan Nair, AD, TSG, ESG, Shri Biswanath Sen, Head, ACVSD and Shri V. Suresh Kumar, President ISHRAE Kalpakkam Chapter during inaugural function

Air-Conditioning & Ventilation System Division (AC&VSD), IGCAR in association with Indian Society of Heating Refrigerating & Air-conditioning Engineers (ISHRAE) - Kalpakkam Chapter organized the 4th AC & Refrigeration Service Program at Conference room, ESG Annex building, IGCAR on October 08, 2021. ACRESERVE is a training programme in Air conditioning and Refrigeration - Service conducted for technicians and contractor workers engaged in operation, Maintenance and service of HVAC equipments and systems. About 60 delegates (Technicians & Contract workers) from DAE units at Kalpakkam and ISHRAE Kalpakkam chapter members attended the training Programme in batches following safety protocols.

The conference started with the warm welcome address by Shri Biswanath Sen, Chairman ACRESERVE & Head, AC&VSD, ESG. Shri V. Suresh Kumar, President ISHARE Kalpakkam & Head, RFS, CFED addressed the gathering and briefed about ISHRAE and its activities. Shri K.P. Kesavan Nair, AD, TSG indicated about the necessity of such a training program. Shri V. Rathnakumar Convener, ACRESERVE and Head, ACMS, ACVSD highlighted about ACRESERVE. The chief guest of the inaugural function was Dr. K. Ananthasivan, Distinguished Scientist and Director, RpG, IGCAR. In his keynote address, Dr. K. Ananthasivan emphasized the importance of air quality in human life. He also enlightened on requirement of proper ventilation in buildings including radioactive facilities.

Shri Vijayabhaskaran, RD South-2, ISHRAE HQ delivered a useful talk on “Best Practices in Maintenance and Operation of HVAC system for energy efficiency”. Other topics covered in the training programme include Basics of AC & Refrigeration, ISHRAE COVID -19 guidelines for offices and Residents, Electrical Safety for operation of HVAC, Introduction to Radioactive Ventilation – Operation & Maintenance of Systems, Good practice of Erection, testing & commissioning of Split & Window Air conditioners, Best way of Operation & Maintenance of Centrifugal Chillers and Basic understanding of Instrumentation. The talks were delivered by in house experts from ESG, RpG, and MCMFCG. Additionally, a Workshop demo on operation was organized on different types of compressors and Brazing Techniques.

During the valedictory function, Participation certificates were distributed to the delegates and the training programme facilitated good interactions among delegates and experts in the area of HVAC. Shri M. Ravi, President (Elect) ISHRAE Kalpakkam proposed the vote of thanks.

*Reported by
Shri Biswanath Sen, Head, AC-VSD-IGCAR*

Dedication of 750 TR Capacity Centrifugal Chiller at Central Water Chilling Plant – II

October 13, 2021



Dr. B. Venkatraman, Distinguished Scientist & Director, IGCAR along with Senior Colleague dedicated during the first 750 TR capacity Centrifugal Chiller at CWCP - II to the centre

Central Water Chilling Plant-II [CWCP-II] is established by Air-Conditioning & Ventilation System Division [AC&VSD] to augment the central air-conditioning infrastructure of IGCAR. CWCP-II is designed to house four 750 TR capacity water cooled chiller and three 375 TR capacity air cooled chillers. The piping system is designed to take up an operating air-conditioning load of 3000 TR considering the future requirement. The new plant will cater to the air-conditioning demand of existing buildings - Training School and Training Centre, Material Science Laboratory (MSL), Material Development Laboratory (MDL), Condensed Matter Physical Laboratory (CMPL), Particle Irradiation Facility (PIF), Electronics and Instrumentation Laboratory (EIL) to name a few. The plant will also be useful in replacing the standalone packaged and unitary AC systems in various buildings which are at the end of their useful life. As phase I of the project, two 750 TR capacity centrifugal chillers are installed and commissioned with chilled water pumps, condenser cooling water pumps, cooling towers and associated piping network.

Dr. B. Venkatraman, Distinguished Scientist & Director, IGCAR dedicated the first 750 TR capacity Centrifugal Chiller at CWCP - II to the Centre in a ceremony organized by AC&VSD. Senior officials of the Centre, Dr. S. Raju, Director, MSG & MMG; Shri K. R. Sethuraman, CAO, IGCAR and Shri V. Sivakumar, IFA, IGCAR graced the occasion. Serving & retired colleagues from Engineering Services Group were also present in the memorable occasion. Shri Biswanath Sen, Head, AC&VSD has briefed regarding operational features and highlights of 750 TR centrifugal chiller and future plan of Central Water Chilling Plant-II. Shri K.P. Kesavan Nair, AD, TSG congratulated ACV, Civil and Electrical colleagues for completing the works within shortest possible time observing all the COVID protocols. Director, IGCAR has appreciated the efforts of AC&VSD in developing air-conditioning infrastructure to mitigate air conditioning problems.

As a customary, Dr. Venkatraman has recorded his invaluable remarks quoted as "A good initiative completed in time. Appreciate the entire ESG for this and request them to continue excellent and selfless services being rendered to the Scientific and Engineering cum Admin & Acct. community. Jai hind." on the equipment log book. Director, IGCAR has also planted a *Mimusopselengi* (Magilam) plant at CWCP-II premises to mark the remembrance of the event.

*Reported by
Shri Biswanath Sen, Head, AC-VSD-IGCAR*

One Day Theme Meeting on SQUID Sensor and Its Applications

November 16, 2021



Some photographs of the event

A one day theme meeting on the applications of Superconducting Quantum Interference Device (SQUID) sensors for biomedical and geomagnetic research was conducted on November 16, 2021. With the welcome address by Dr. N. V. Chandra Shekar, Associate Director, MSG the meeting was inaugurated by Dr. S. Raju, Director, Materials Science Group. An introduction to the theme meeting was given by Mr. R. Baskaran, Head, SQUIDS and Applications Section. Dr. T. S. Radhakrishnan, Former Head, MSD, IGCAR gave the key note address. There were three technical sessions respectively dedicated to Biomagnetism, Time domain electromagnetic (TDEM) system and presentations by research scholars on recent developments in SQUID based applications. The first session on biomagnetism was chaired by Dr. M. Vineetha, Head-Pediatrics, DAE Hospital, Kalpakkam. Dr. Sanjib Sinha, Head, Department of Neurology, NIMHANS, Bengaluru presented a talk on the clinical applications of magnetoencephalography (MEG). Dr. Goutham K. Bhargava a senior resident of NIMHANS presented his work on the use of advanced machine learning algorithms applied to MEG signals. Dr. Santhosh Satheesh, Professor, Department of Cardiology, JIPMER, Pondicherry, emphasized the importance of early diagnosis of cardiovascular diseases and highlighted the role of MCG from a diagnostic perspective. Mr. S. Sengottuvel, SAS, MSG, IGCAR presented an overview of investigations conducted using the 37 channel MCG facility at Kalpakkam in collaboration with hospitals and medical institutions in the neighbourhood. The second session was on the TDEM applications of SQUID chaired by Dr. K. Gireesan. Dr. Ijee Mohanty presented her work on the geophysical prospecting done at Tumallapally, Kadappa district, Andhra Pradesh using the TDEM system. Ms. Lata Bisht, SAS, CMPD, MSG, presented her work on transient eddy current based non-destructive testing to measure the thickness of metal sheets and demonstrated the accuracy of the technique using simulation and actual measurements. Dr. R. Nagendran, gave an excellent account of a specific research problem probed using SQUID based TDEM, namely the negative decay transients, which is poorly understood in the literature. The last session was exclusively devoted to presentation by students and was chaired by Dr. H. Anitha, Professor, MIT, Manipal, Karnataka. Mr. Pathan Fayaz Khan presented his work on the development of a complete biofeedback system for conducting MEG and EEG experiments. The technical session was followed by a discussion with senior members of the Group. Dr. M. Jayashree, Medical Superintendent (MS), DAE Hospital, Kalpakkam chaired the session. Ideas on taking the program forward towards clinical use of SQUID based MCG were discussed.

Reported by

Dr. N. V. Chandra Shekar Associate Director, MSG, IGCAR,

International Hybrid Conference on Recent Advances in Information Technology (READIT) November 24-25, 2021



Smt. S. Rajeswari, Convener READIT, Shri S. Ragupathy, Distinguished Scientist, Director, EIG & RTDG, Dr. G. Ravikumar, Head, SIRD, BARC, Prof. J. P. Singh Joorel, Director, Infflibnet and Shri E. Soundararajan, Secretary READIT releasing the souvenir at the inaugural function READIT.

Director Dr. B. Venkatraman, felicitating Smt. Prabhavathy Soundarajan, Head, LISS, SIRD.

The Scientific Information Resource Division of IGCAR in association with the Madras Library Association - Kalpakkam Chapter (MALA- KC) organized the 12th biennial Conference on Recent Advances in Information Technology (READIT) in hybrid mode during November 24-25, 2021 at the Sarabhai Auditorium, IGCAR, Kalpakkam, with the theme 'Innovative Technologies for Sustenance of Libraries'. For the first time since 1995, READIT was organized as an international event. International participants were from INIS group, IAEA Vienna, Institute of Physics UK, Springer Nature Singapore, along with research scholars from Sri Lanka and Nigeria to name a few.

About three hundred delegates from the academic and public Libraries, Publishers, Research scholars and Book exhibitors attended the conference in Hybrid mode. In the inaugural function, Smt. S. Rajeswari, Convener READIT & Head SIRD delivered the welcome address. The function was presided over by Shri. S. Ragupathy, Distinguished Scientist, Director, EIG & RTDG, IGCAR. Dr. G. Ravikumar, Outstanding Scientist & Head, SIRD, BARC delivered a special address. The Chief Guest of the inaugural event, Prof. J. P. Singh Joorel, Director, Infflibnet, Gujarat delivered the inaugural address. The Conference Souvenir was released by Prof. J. P. Singh Joorel. Shri E. Soundararajan, Organizing secretary READIT, proposed the vote of thanks. Dr. G. Ravikumar inaugurated the exhibition of Book stalls. The conference included 15 technical talks by domain experts in the field of Library and Information Science. A total of 15 presentations delivered by Students, Research Scholars and Librarians were considered for best presentation awards. Three best paper awards were announced to the paper presentations. Commercial presentations by Publishers were also arranged.

Dr. Nithyanandham and Smt S. Prabhavathy and Shri Ganesan from SIRD, IGCAR, were facilitated with Lifetime achievement award and significant contribution to Library awards by Dr. B. Venkatraman, Distinguished Scientist and Director IGCAR. Also, the contributions of Sri Premkumar, SIRD for representing India from DAE, who had received a Bronze medal in the international para badminton conducted in Uganda, was felicitated on READIT stage by Director, IGCAR, President MALA and President MALA-KC. A panel discussion was conducted on the theme "Future trends in scientific publishing and resource subscription models". An academic librarian, a scientist, a publisher, a vendor and a research librarian were part of the discussion. The conference facilitated good interactions among young researchers, students, professionals and well-known speakers in the area of future technologies for libraries. The conference was concluded with the valedictory function. Shri E. Soundararajan delivered the welcome address, Smt. S. Rajeswari presented the conference summary. The valedictory address was given by Shri Athmalingam, Associate Director, RESG, IGCAR. He also presented the best paper awards and honoured the sponsors of READIT 2021. Dr. V. S. Srinivasan proposed the vote of thanks. Conference was on Webex and YouTube simultaneously.

Reported by

Smt. S. Rajeswari, Convener READIT & Head SIRD

International Medal by Shri E. Premkumar of DAE in Uganda Para-Badminton International 2021

November 25, 2021



Honourable Chief Minister Shri M. K. Stalin along with Minister V. Meyyanathan and Shri E. Premkumar



Dr. B. Venkatraman, Director, IGCAR, has congratulated the extraordinary fete

Shri E. Premkumar, SA/E, is the official photographer of IGCAR. He has a keen interest in nature photography and is a dedicated badminton player. He regularly participates in Nationals and International Badminton events like All India Central Civil Services, All India Inter-Institutional Badminton Tournaments, Para-Badminton international etc. After he met with multiple injuries in his right leg, he concentrated in the Para-Badminton category. He got classified as Standing Lower 4 in the 2nd Fazza – Dubai Para-Badminton International in March 2019. Subsequently, he got selected through state and national para-badminton committees to represent India in International Para-Badminton tournaments. Shri E. Premkumar represented India in the Uganda Para-Badminton International held at Kampala from 15th to 21st November 2021. Other participants include Olympian Pramod Bhagat (Paralympic Gold Medalist), Manoj Sarkar (Paralympics Bronze Medalist), and other elite players who regularly represent India in International tournaments. Twenty-seven countries have participated in the Uganda Para Badminton International with 135 players and 265 entries. Shri E. Premkumar participated in three events, Men's Singles, Men's Doubles, and Mixed Doubles. In Quarter-Finals (Men's Doubles), he won the match against youth Asia champion Nehal Gupta & Sharadchandra Joshi (17-21, 21-14, 21-14) in a 35 minutes match.



Shri E. Premkumar in Uganda Para-Badminton International 2021

Sri E. Premkumar, for the first time from DAE, has won an International Para-Badminton Bronze Medal in the Uganda Para-Badminton International at Kampala on November 2021. Tamilnadu Government felicitated the para-badminton players. Dr. B. Venkatraman, Distinguished Scientist, Director, IGCAR, has congratulated the extraordinary fete during the international conference READIT held on November 25, 2021. Dr. Ananthasivan, Director, RPG, has honored Sri Premkumar with a souvenir

during their weekly IANCAS meeting. Many other sports councils like Thanjavur Badminton association, Para-Badminton association of Tamil Nadu, ACE badminton academy, NESCO etc have celebrated his fete.

Through this article IGCAR, DAE appreciate the young gentleman and record their appreciation for the achievement and the many laurels he would bring to DAE and India.



Shri E. Premkumar was felicitated by NESCO, Kalpakkam

Reported by

Smt. S. Rajeswari, Head SIRD

Technology Transfer of “Autonomous Gamma Dose Logger”

December 07, 2021



Transfer of IGCAR's Autonomous Gamma Dose Logger technology to M/s Ideal Sensors, Chennai on December 07, 2021. (From L-R): Shri S. Athmalingam (Associate Director, RESG, SQRMG), Dr. N. Subramanian (Head, Incubation Centre-IGCAR), Shri A. K. Gowri Ponraj and Ms. R. Krithika (both from M/s Ideal Sensors).

Autonomous Gamma Dose Logger (AGDL) is a radiation monitor developed at SQRMG, IGCAR to measure environmental radiation in a wide range from 100 nGy/hr to 5 Gy/hr. The AGDL uses Geiger-Muller tubes to measure the environmental gamma dose rate. It transmits the data through wireless communication and backs up the data in a portable data logger. The radiation monitoring system is powered by solar power system with battery backup, and it can be easily installed at any site with a mechanical structure. This system can be used for both routine and emergency radiation field monitoring purposes in nuclear installations and as a general environmental radiation monitoring equipment in other places. IGCAR's AGDL has distinct features such as wireless (RF) communication, off-line local data logging, rapidly and remotely deployable even across rough terrains and seamless expansion of networking. Valuable inputs for Emergency Decision Support System can be provided by the AGDL. Currently ~28 numbers of in-house made AGDL systems are operating successfully at DAE Kalpakkam site and connected to the Decision Support System for real-time radiation field inputs.

The AGDL technology, developed to meet the Atma Nirbhar Bharat goals of our government, was transferred to M/s Ideal Sensors, Chennai on December 07, 2021. In a brief event arranged by Incubation Centre-IGCAR, the technology license documents were handed over by Shri S. Athmalingam, Associate Director (RSEG, SQRMG) to Ms. Krithika Rajagopalan and Shri A. K. Gowri Ponraj from M/s Ideal Sensors, Chennai. Dr. N. Subramanian, Head, Incubation Centre-IGCAR, Dr. C. V. Srinivas, Head, EAD, SQRMG, Dr. S. Chandrasekaran, Head, EnAS, EAD and other colleagues from SQRMG and IC-IGCAR attended the event. For more information on this technology and various other technologies developed at IGCAR, IC-IGCAR can be contacted at the email id: incubation@igcar.gov.in.

*Reported by
Dr. N. Subramanian, Head, Incubation Centre-IGCAR,*

IGC COUNCIL



Chairman

Dr. B. Venkatraman

Distinguished Scientist & Director, IGCAR

Dr. B. Venkatraman, is from the 27th batch of Bhabha Atomic Research Centre Training School. With a research career spanning 36 years, he has specialised in application of ionizing and non ionizing radiations for non-destructive evaluation of materials and processes. During the last ten years, he has focused on enhancing, existing and establishing newer facilities as part of broad based radiation and environmental research programs at IGCAR.

He is a Member of AERB, SARCAR Committee and Convenor of BIS CHD 30 Sub Committee on Radiation Protection. He was a visiting scientist at Fraunhofer Institute of NDT Saarbrucken, Germany 2006-2007, has served as an expert for IAEA in Digital Radiology. He has more than 200 publications, is the recipient of Homi Bhabha Science and Technology Award 2007, INS Gold Medal 2005, seven Group Achievement Awards of DAE, D & H Schereon Award of IIW 1993, ISNT-NDT Man of the Year Award (R & D) 2001, IIW sharp tools award 2011, ISNT international recognition award 2013, and has won more than 10 best paper awards. He has been invited to deliver keynote, plenary and invited talks in international and national conferences . He is the Honorary Fellow of Indian Society of NDT and Fellow of Chennai Academy of Sciences. He is the President of Indian Society for NDT (ISNT) and President, Indian Association for Radiation Protection (IARP). He has guided about 6 students for their Ph D and is presently guiding 6 students. He is presently Distinguished Scientist and Director, Safety, Quality and Resource Management Group and Director, Engineering Services Group at IGCAR

Members



Dr. A. K. Mohanty, Dr. A.K. Mohanty born in 1959 at Odisha is a well-known nuclear physicist, completed his Bachelor's degree in 1979 from MPC College, Baripada and Master's degree in Physics in 1981 from Ravensshaw College, Cuttack which was at that time under Utkal University, Bhubaneswar. Dr. Mohanty graduated from the 26th batch of the BARC Training School and joined Nuclear Physics Division of Bhabha Atomic Research Centre in 1983 and got his PhD degree from Bombay University later on. He has taken over as Director, BARC on 12th March 2019. Before his appointment as Director, BARC, Dr. Mohanty has held the position of Director of Saha Institute of Nuclear Physics, Kolkata from June 2015. During the past 38 years, Dr. Mohanty has worked in several areas of nuclear physics covering collision energy from sub-Coulomb barrier to relativistic regime. It includes experiment using Pelletron accelerator at TIFR, PHENIX and CMS experiments at Brookhaven National Laboratory (BNL), USA and CERN, Geneva respectively. Dr. Mohanty has held several honorary positions. To name a few, he served as Secretary and Member Secretary of BRNS Basic Science Committee from 2004-2010, General Secretary of India Physics Association (IPA) 2012-2016 and later on President of IPA 2018-2020, India-CMS Spokesperson (CMS Experiment at CERN Geneva) 2013-2015, Dean, Academic, Physical & Mathematical Sciences, BARC, Homi Bhabha National Institute. Dr. Mohanty has been recipient of several awards and recognitions during his illustrious career. Some of Dr. Mohanty's awards and recognitions are: Gold Medal in Graduation (1979, Radha Gobinda Trust, Mayurbhanj), Young Scientists Award of Indian Physical Society (IPS, Kolkata, 1988), Young Physicist Award by Indian National Science Academy (INSA, New Delhi 1991) and DAE Homi Bhabha Science & Technology Award (2001) by Department of Atomic Energy, Mumbai. He was also conferred the CERN Scientific Associate position at CERN, Geneva from 2002-2004 and thereafter again from 2010-2011.



Shri S. Raghupathy, is currently heading Reactor Design & Technology Group and Electronics & Instrumentation Group as Group Director. He is a mechanical engineer and had graduated from A.C. College of Engineering & Technology, Karaikudi. After graduation, he joined the 29th batch of BARC Training School and completed the Nuclear Engineering course in 1985. He joined IGCAR in 1986 and was associated with the design of reactor assembly components and later with the design of fuel handling systems for PFBR & future FBRs. He is one of the Directors on the Board of BHAVINI and a member of several task forces for design, development and testing of fast reactor components. He has several national & international publications to his credit. He has received the DAE Science Technical Excellence Award and several group achievement awards. He has participated in many IAEA meetings & international conferences on FBRs. His field of interest include design of pressure vessels, regulatory codes & standards, heat & mass transfer, in-service inspection, non-destructive testing and reactor safety & economics.



Dr. N. Sivaraman, Joined Indira Gandhi Centre for Atomic Research (IGCAR), Kalpakkam in the year 1987. He is from the 30th Batch of BARC Training school. Dr. Sivaraman's research interest includes actinide chemistry, fuel chemistry, pyrochemical process, lanthanide separations, sodium chemistry & sensors, solvent extraction of heavy metals, high performance liquid chromatographic separation of radioactive species, burn-up measurements on nuclear reactor fuels, Supercritical fluid extraction of actinide complexes and development of extraction chromatographic techniques for recovery of actinides, etc. He is recipient of INSA-Royal Society, UK Fellowship(1997), Indian Nuclear Society Medal(2007) & Homi Bhabha Science and Technology Excellence Award(2008). He is also Professor of HBNI and supervising PhD scholars. He is presently Outstanding Scientist and Director, Materials Chemistry & Metal Fuel Cycle Group.



Dr. B. K. Nashine, FNAE, an Outstanding Scientist is B.E. in Electrical Engineering from GCE&T, Raipur, M.E. from VJTI, Bombay University, Ph.D from HBNI, Mumbai. He is from 31st batch of BARC Training School and presently Director Engineering Services Group and Associate Director Sodium Facility Group, RDTG. His research career spans for 34 years and he has specialized in the design of electromagnetic pumps, power system for Sodium loop and sodium loop operation for conducting experiments in support of R&D for sodium cooled Fast Reactors. The electromagnetic pumps designed by him have been tested successfully and employed in the Prototype Fast Breeder Reactor (500 MWe). He has developed sodium submersible electromagnetic pump which can withstand 5500C ambient temperature without any external cooling. He has served as Secretary in professional body like Institution of Engineers, Kalpakkam chapter, Indian Society for Non Destructive Testing, Kalpakkam chapter and Indian Nuclear Society, Kalpakkam chapter.



Dr. T. S Lakshmi Narasimhan is from 31st batch of BARC Training School and joined IGCAR in 1988. He completed his Ph.D. from University of Madras in the year 2001 and did his post doctoral research at Forschungszentrum, Juelich Germany (2004-2006) under Indo-German collaboration. His main area of research has been in the field of high temperature mass spectrometry which include fuel-clad chemical interaction studies related to fast reactors, vaporization thermodynamic studies on U-Pu-Zr, Metal- tellurium and Metal –tellurium- oxygen systems, alloys, boron, fullerenes etc., He has also been associated with Burn up measurements of thermal and fast reactor fuels. He has delivered many invited lectures in India and abroad and has about 55 Scientific publications in reputed International journals and about 70 papers in national and international conferences.

In July 2017 he became Associate Director, Resource Management Group. He served as Dean, Student Affairs under Homi Bhabha National Institute, a deemed university. He also served as Professor in the same University and guided two Ph.D. Students. He was heading the Technology transfer cell of IGCAR and coordinated the filing of patents and technology transfers and in October 2020 was designated as CEO of Incubation Centre at IGCAR to look after incubation and technology transfer activities. He is a mentor for the INSPIRE program of Department of Science and Technology for School Students and also actively involved himself in the spread of scientific awareness amongst educational institutions. Currently he is the Regional Director of Madras Regional Purchase Unit (MRPU), DPS which caters to the purchase and stores activities of IGCAR and other DAE units at Kalpakkam, HWP, Tuticorin and NFC, Pazhayakayal.



Shri K. V. Ravi, Distinguished Scientist & Chief Executive, Nuclear Recycle Board is a Mechanical engineer (Mysore University) from the 28th Batch of BARC training school. Shri K.V. Ravi joined Reactor Projects Division of BARC in 1985 and he has worked in the areas of Design, Construction, Commissioning and O&M of compact LWR at Kalpakkam till 2015. He has specialized in the field of Nuclear Fuel, Core assembly and fuel handling systems. He has also set up several Test/Experimental facilities for development of LWR components and contributed in development testing and qualification of several improved/indigenous versions of reactor components like, Control rod drives Hydraulic operated valves, feed and steam controllers. He also has hands-on experience in operation and maintenance of the compact LWR. In 2015, he was transferred to NRB as Project Director for Nuclear Recycle Projects at Kalpakkam and completed construction and commissioning of several Nuclear Reprocessing and High level Waste Management facilities at Kalpakkam. He has contributed in several design improvements and up gradation of plants which have resulted in continuous and reliable operation of the technologically complex Reprocessing and Waste management plants. He gained hands-on experience in Operation and Maintenance of Reprocessing and Waste management plants and large scale civil constructions in this assignment. He has been Functioning as Chief Executive, NRB, since 2017 and currently involved in managing the Major projects and operating facilities of NRB. He has also served as Facility Director BARCF in the period 2016-17 and presently holding the post of Facility Director as additional Charge. He has been a member of several committees including BARC safety council. He has been recipient of DAE Awards seven times and has number of journal publications, papers and technical reports to his credit.



M/s. Sushma Taishete joined as Joint Secretary in the Department of Atomic Energy, Government of India on 08-04-2020. She is a post graduate in Medical Microbiology from Haffkine Institute, Parel, Mumbai. She is the In-charge of Research and Development wing of the DAE handling Bhabha Atomic Research Centre (BARC), VECC, Kolkata, RRCAT, Indore, IGCAR, Kalpakkam and all aided institutions (eleven) in the Department. International Projects such as, ITER, LiGO, also fall under R & D Division. She has served in various capacities in Ministry of Defence, Ministry of Health & Family Welfare, National Health Systems Resource Centre, Ministry of Petroleum and Natural Gas and Department of Justice, Ministry of Law & Justice, Government of India during 1991 - 2020.



Shri V. Sivakumar, I.R.S joined IGCAR as a Internal Financial Advisor, he is also IFA for FRFCF/ GSO. He joined the Govt. Service as Central Secretariat Service officer and then selected for Indian Revenue Service in 2004., Shri Nair has worked in different place Delhi, Kolkatta, Chennai, Trichy, Tuticorin. in the field of Administration of Customs Act in sea-ports and Airport as an Anti-smuggling operations in coastal areas of Tamil Nadu, Handling of narcotic drugs cases and GST Intelligence.



Shri K. R. Sethuraman joined the Department on 02/02/1988 with a degree in commerce from Bangalore University. After joining the Department, he was sponsored by the Department for Diploma in Public Policy and Management course from the Management Development Institute, Gurgaon (2010-2012). He has completed 34 years of service in the Department serving in various capacities in different Units like AMDER, DAE Secretariat, BARC Facilities, RRCAT, BRIT and IGCAR thus gaining vast experience in all matters relating to administration. He is holding the post of Chief Administrative Officer from 15/02/2018. As administrative head of the Unit his mandate for administration is to provide service, advice and support with the highest level of professionalism valuing rules and procedures as a tool to achieve the objectives of the Organization and the desired outcome, contribute towards smooth internal functioning of the organization through dissemination of information, extensive use of automation and information technology, updating and simplifying procedures and instructions to the changing environment, proper record and data management systems, developing standard process sheets to ensure procedural compliance, periodical training of Officers and staff to enhance the knowledge and skill, secure better focus and ownership of task and increase their yield, monitoring delays, identifying bottlenecks and implementing remedial measures, promoting transparency and accountability in decision making process, mentor subordinates and build teams, promote harmonious relations and secure maximum amount of cooperation from the employees.

Organisation and Activities of Various Groups

Electronics and Instrumentation Group



Shri S. Raghupathy
Director, EIG



Dr. D. Thirugnanamurthy
AD, E&CG



Shri A. Venkatesan
AD, RC&IG



Shri R. Jehadeesan
Head, CD



Shri N. Sridhar
Head, ED



Shri M. Sakthivel
Head, I&CD



Shri R. P. Behera
Head, RTSD

Electronics and Instrumentation Group is focused on design and development of indigenous technology in the areas of Electronic Instrumentation & Control systems for fast breeder reactors and reprocessing plants that include Development of Distributed Digital Control System, Safety Critical and Safety Related Systems, Safe & Secure PLC, Virtual Control Panel based Control Room, Full-scope Operator Training Simulator, 3D modeling, animation & visualization of FBR subsystems and VR walkthrough of structures, Cyber Security Management for IT and I&C systems. Design and Development of advanced equipment and technology such as, indigenous Wireless Sensor Networks for nuclear facilities, strategic and societal applications, Time Domain Electromagnetic for Deep Seated Atomic Minerals Exploration, Plutonium Condition Air Monitoring System for reprocessing plants, Test Instrument for Steam Generator Tube Inspection, Radar Level Probe for Liquid Sodium Level Measurement, radiation resistance MEMS based sensor for nuclear applications and innovative sensors and instruments for nuclear facilities have been completed. Considerable expertise exists in designing, building and maintaining state-of-the-art high-performance supercomputing facility that continues to meet large scale compute- and data-intensive requirements in multi-disciplinary domains. Implementation of IT-enabled Nuclear Knowledge Management system for Fast Reactors and associated domains, computational intelligence systems, cryptography, cyber security solutions, knowledge management and development and deployment of modern security systems for access control and physical protection of nuclear complexes are initiated.

Engineering Services Group



Dr. B. K. Nashine
Director, ESG



Shri B. Harikrishnan
AD, CEG



Shri K.P. Kesavan Nair
AD, TSG



Shri Utpal Borah
Head, CWD



Shri N. Suresh
Head, CED



Shri Sudipta Chattopadhyaya
Head, CM&MWD, A&SED



Shri Biswanath Sen
Head, AC&VSD



Shri L. Subramanyam
Head, ESD

The Engineering Services Group (ESG) has a very important mandate of infrastructure development for all units of the Department of Atomic Energy located at Kalpakkam. It spans from planning, design, engineering, execution, testing and commissioning of Civil, Electrical, Mechanical, Air-conditioning and Ventilation works for the Laboratories, township including housing, schools, hospitals, hostels, roadways and various public utilities and facilities. This Group was also responsible for commissioning, operation and maintenance of various services for the Atomic Energy installations at Kalpakkam. Over a period of time when the facilities are grown, the responsibilities are limited mainly for IGCAR infrastructure. ESG comprises of two sub-groups: Civil Engineering Group (CEG) and Technical Services Group (TSG).

Civil Engineering Group (CEG) is primarily created with the intention of developing all the required infrastructures for mission of IGCAR. Mandate of CEG is construction of several laboratories, buildings and services beginning with the conceptual design to construction and its associated maintenance, for IGCAR's mission of 'Fast reactor development and its associated fuel cycles'. CEG undertakes in-house and collaborative research projects in civil engineering aspects of Fast Breeder Reactor (FBR). CEG has been keeping pace with progress in engineering, design and construction with technical advances. Engineering, analysis and design have undergone remarkable changes with computer codes developed by the group to solve complex problems. Concrete production and delivery systems have been improved, with automated mixing plants and stringent quality control. Special types of concretes have been developed and now the group has proved itself in providing technical support in design of major projects like PFBR and associated fuel cycle facilities. The group has developed expertise in characterization of site for safety related structures including geotechnical investigation. As the plant site has crossed 50 years, CEG has taken a mandate of structural assessment and ageing management of existing radiological facilities, major laboratories and conventional buildings. The present mandate of CEG is to sustain the present infrastructure as envisaged in the Vision -3 and augment

it during coming plan periods, continue the support for coordination and commissioning of PFBR related civil works, focus in the preparation of DPR for MFTR, RML-Phase II, CORIUM facility and for architectural & structural design, execution and quality control of civil infrastructure works for other unit works in DAE Kalpakkam along with development of the associated township works. With IGCAR South Plant site getting saturated, the focus is in developing north plant site for non-radiological facilities - AUSC, Doppler Weather Radar & Wind Profiler Building, RHIDS & SHIDS etc. to mention a few, and associated service corridor considering future requirements. Bearing in mind the land cost, it is planned to construct multistoried tower office complexes and laboratories with a view of conserving precious space. The Group has major plans of providing an aesthetic and sustainable green environment at the project site and also intends to introduce water management schemes to ensure uniform quality of water in all seasons through the years. CEG has recently completed structural assessment of FBTR, DFRP and other radiological facility buildings. The tasks are being steered by a team of senior civil engineers.

Technical Services Group (TSG) was established to take care of non-civil services of IGCAR. TSG comprises of three divisions: Air Conditioning and Ventilation Systems Division, Central Workshop Division and Electrical Services Division.

Air-conditioning and Ventilation Systems Division (AC&VSD) has a mandate of providing air conditioning and ventilation service to radioactive facilities and research laboratories of IGCAR. Presently, IGCAR has a total air-conditioning load of about 4500 TR, which is met by Central water chilling plant (CWCP-1) and standalone AC systems like package units (PAC), variable refrigerant flow (VRF) units, window and split air-conditioners. In view of increase of facilities at IGCAR and in order to sustain reliable air-conditioning services to the centre, a 2000 TR central Air-conditioning plant is (CWCP 2) being established near IGCAR gate as part of vision 3. The building is constructed and chillers of 2250 TR capacity have been commissioned. AC&VSD is also proposing to establish a hybrid central AC plant with combination of air and water cooled chillers for facilities coming up near KKM site. The division is also responsible for design, execution, testing and commissioning of material handling equipments like Electric overhead travelling (EOT) cranes, Electric wire rope (EWR) hoists for new facilities of IGCAR. Later, AC&VSD was entrusted with the responsibility of operation and maintaining of sea water desalination plant to provide potable water to IGCAR, BARCF and BHAVINI. It also looks after water purifiers for the facilities within IGCAR. The plant was commissioned in 2015. Since then, the plant is continuously supplying potable water to IGCAR reservoir as per the demand.

The need for dedicated workshop facilities was felt right during the days of conceptual formation of Reactor Research Centre (RRC). The Zonal Workshop at Hall-1 was established initially to meet the immediate requirements. Later, to meet the growing demand of manufacturing activities at RRC complex, Central Workshop Division (CWD) was established with the state of art machines and became operational in 1975. CWD has contributed for many technological development works in the manufacturing domain. The welding procedure for the PFBR SA in 2G position was developed CWD welders and first batch of Fuel/ Blanket sub assemblies was welded here successfully. CWD is continually extending its manufacturing support towards commissioning of PFBR. Recently two notable major works have been successfully carried out for PFBR, namely, Improved Guide and rails with Colomony hard faced coating for Transfer arm and Annular Linear Induction Pump (ALIP) duct assemblies. Both the works demanded expertise in PTA welding process, heat treatment and high precision and surface finish machining requirements. The large size Containment box (CB) system (Volume 500 m³) for pyro processing was fabricated in sections at CWD and finally assembled and welded at site. Achieving the high leak tightness of CB (< 0.05 vol % per hr) with 50 viewing and lightening windows was a challenging and critical task. To support reprocessing project activities, Annular tanks with varying size, Sampling, Vent and Multiple pots, Dissolver condenser, NO₂ generator were manufactured. CWD has maintained a high reputation in the production of quality products meeting stringent requirements of various codes. CWD is processing nearly 350 work orders every year to meet the demands of R&D, Labs in DAE also other units. DAE has conferred many meritorious service awards and Group awards to CWD officials for their excellence in machining, fabrication, inspection and maintenance fields.

Electrical Services Division (ESD) has a mandate to provide adequate, high quality, reliable and uninterrupted power required for various needs of the research activities and the infrastructural requirements of the centre. To meet this Electrical Services Division designs, construct, operate, maintain and upgrade Electrical transmission and distribution system keeping in mind the system reliability & safety. The division is also responsible for providing state of the art intercom telecommunication services to the plant site as well as for Energy conservation in the Electrical sphere through auditing and implementing various energy conservation measures. At present the Electrical demand is 29 MVA and which is catered by Electrical distribution network consisting of two numbers of 33 kV substations and 14 numbers 11 kV substations.

Thanks to the foresight of the earlier planners, MAPS has been providing adequate, safe, reliable and quality power to IGCAR, BARC Facilities and GSO till date. Starting from an operating load of about 1.5 MVA during 1977 fed by one number 33 kV substation and five number of 11 kV substations, the load on the power system has grown to a level of 29 MVA fed by two number 33 kV substations and 14 number 11 kV substations. The projections indicate that the load would grow to about 60 MVA by 2028. To meet the growing demand third power source with 230 kV/33 kV/11 kV, 50 MVA transformer at BHAVINI switchyard was commissioned in 2012. To evacuate this power along with this 33kV Indoor sub-station NCSS-2 was also commissioned in 2012. Main source for FRFCF is from NCSS-2. The electrical power system of FRFCF is conceived to meet the power requirements for the present phase as well as the envisaged expansion in the future. Moving further the 2nd IGCAR transformer at MAPS was upgraded to 35 MVA in 2019 to meet the growing power demand.

ESD has taken up many Energy Conservation activities over the years. One of the major activities being taken up under this is to establish a 2.4 MWp grid connected solar plant in the newly developed parking area in front of IGCAR new gate. Energy Conservation is a continuing activity and many innovative ideas are being implemented in the journey. ESD as a team is well set to take on the challenges pertaining to sustenance, augmentation and establishment of power systems at new projects of IGCAR. With a proactive approach all along, the division has initiated several augmentation measures at source end, receiving end and associated networks. With the steps that are being initiated, ESD will be able to meet the projected power requirements and is moving ahead with an objective to sustain the path of excellence.

Materials Chemistry & Metal Fuel Cycle Group



Dr. N. Sivaraman
Director, MC&MFCG



Dr. Kitheri Joseph
AD, MFRG



Dr. V. Jayaraman
AD, FMCG



Shri T. V. Prabhu
Head, CFED



Dr. S. Ghosh
Head, MFPD



Shri B. Muralidharan
Head, PPED



Dr. R. Kumar
Head, ACSD



Dr. A. Suresh
Head, FChD



Dr. Rajesh Ganesan
Head, MCD

The Materials Chemistry and Metal Fuel Cycle Group (MC&MFCG) is involved in Research and Development studies relating to metal fuel program, establishing pyrochemical processing of metal fuel, development of aqueous reprocessing methods, including reprocessing of metal fuels, sodium chemistry and development of novel chemical

sensors for detection of hydrogen, ammonia, NO_x etc. Some important current activities include installation of injection casting system for casting U-Zr slugs, augmentation of 10 kg injection casting system for the fabrication of U-6Zr slugs; fabrication and characterization of slugs for Delayed Neutron Detection (DND) applications for PFBR, Integrated operation of Argon Pressure Control System (APCS), temperature and attaining purity by Argon Recirculation and Purification System (ARPS), establishing the purity of 500m³ containment box for its purity and the requisite purity of O₂ and moisture (below 50 ppm each) in engineering test scale of pyroprocessing, pyroprocessing of irradiated U-Zr in hotcells at lab scale, direct oxide reduction of oxides of uranium to uranium metal, optimization of process parameters towards oxidation of metal fuel prior to its dissolution in nitric acid medium followed with extraction of heavy metals using TBP/n-DD, thermochemical properties and phase diagram studies on fuel materials and materials of interest for pyroprocessing, development of non-destructive methods for assay of plutonium, studies on the development of synthetic inorganic matrices for immobilization of waste from fast reactor fuel reprocessing, production of ⁸⁹Sr for societal applications, etc. Other important activity includes development of metal organic framework for sorption of actinides from aqueous medium, supercritical extraction and recovery of heavy metal ions; development of extraction chromatographic methods for recovery of actinides from lean aqueous waste streams, recovery of zirconium from aqueous waste and computational study on the structural aspects of actinide complexes. MC&MFCG also provides expert Analytical support and Radioanalytical services to various programmes in the Centre and for other DAE units. Some of these are development of analytical methods for assay of metal fuel and samples originating from pyrochemical process, measuring isotopic composition of boron and heavy metal ions e.g. actinides from reprocessing samples, assay of primary sodium samples for actinides and fission products. Besides these activities, some basic R&D studies are also undertaken for exploring intermolecular interactions using matrix isolation spectroscopy technique for the extractants of interest towards reprocessing application.

Materials Science Group



Dr. S. Raju
Director, MSG



Dr. N. V. Chandra Shekar
AD, A&NG, Head CMPD



Dr. Sandip Kumar Dhara
Head, SND



Dr. R. Govindaraj
Head, MPD

The Materials Science Group (MSG) comprises of Defects and Damage Studies Division, Condensed Matter Physics Division, SQUID & Detector Technology Division and Surface & Nano science Division. Scientists of MSG work on research problems spanning from the studies of irradiated defects in nuclear materials, developing thin film coatings for tribological applications, high pressure and temperature induced phase transitions in condensed matter systems and SQUID based MEG applications. Details of the research activities are as follows.

Defects and Damage Studies Division (DDSD) focuses on studies on defects, defect-impurity interactions in reactor structural materials, supplemented by computations. Ion beam radiation damage studies are carried out using a 1.7 MV tandem accelerator and a 400 keV in-house built linear accelerator either in single or dual

ion beam modes of irradiation to study defects and radiation response in materials of relevance for fusion and fission reactors. Defects, in particular open volume defects such as vacancies and their clusters are studied using positron annihilation spectroscopy. Positron beam based Doppler broadening studies have been used mainly for depth resolved defects studies in irradiated materials. Ion beam based characterization techniques such as high resolution RBS, channeling are being used extensively in addition to ion beam induced luminescence studies. Irradiation creep studies are being planned with proton beam of energy 2-3 MeV and high beam current. Various experimental results related to defects are analyzed using detailed computations with a variety of simulation and ab-initio codes. High speed cluster computers at IGCAR are being extensively utilized for computation of materials properties.

Surface and Nanoscience Division (SND) focuses on studies of monolithic and multilayered thin films and nanostructures using a variety of techniques such as secondary ion mass spectrometry, nanomechanical testing, Focused Ion Beam (FIB) based nanostructuring and nanopatterning, Scanning Probe Microscopy based characterization of various electrical and mechanical properties at nanoscale, nanospectroscopy with tip enhanced Raman spectroscopy (TERS) and Nanoscopy with near-field scanning optical microscopy (NSOM) imaging at sub-diffraction limit using polarized light. The division also specializes in high temperature tribological studies of structural materials as well as novel nano- and micro-crystalline diamond thin films. Furthermore, development of novel nanomaterials of 0D transition metal oxide (TMO), 1D noble metals and nitrides, 2D TMOs, and transition metal dichalcogenides (TMDs) for advanced sensor applications is being carried out. Research activities relating to sensors based on micromachined cantilevers are also being pursued.

Condensed Matter Physics Division (CMPD) pursues several theme based research programs: investigation of structure and physical properties of materials under extreme conditions such as high pressures, low temperatures, high temperatures and high magnetic fields. Further, over the years various facilities for the synthesis of novel, superhard materials have been established including a Laser Heated Diamond Anvil Cell (LHDAC) facility. The systems under investigation encompass nuclear materials, superconductors, strongly correlated systems, magnetocaloric materials, topological insulators, multiferroics, energetic materials, frustrated systems, f-electron based intermetallics and oxides, glasses and super hard transition metal borides. Research is also pursued to investigate emergent phenomena and proximity effects in heterostructures. Dynamic light scattering and confocal microscopy are utilized for studies on soft condensed matter. Optical trapping and manipulation of mesoscopic particles using holographic optical tweezers (HOTs) to study inter-particle interactions in colloidal suspensions/ biological systems are being pursued. Besides there is also an intense effort towards quantum metrology based research studies using entangled photons.

SQUID & Detector Technology Division (SDTD) focuses mainly on using SQUID based systems for applications. Magneto-Cardiography (MCG) and Magneto-Encephalography (MEG) have been successfully designed, assembled, standardized and used for clinical studies. Further, SQUID based measuring systems such as high field SQUID magnetometer, SQUID VSM, SQUID based set-up for Non- Destructive Evaluation (NDE) have been developed. SDTD also carries out intense research activities related to using SQUID based time domain electromagnetic measurements (TDEM) and geophysical explorations using TDEM. Another major thrust research area of this division is the development of gamma irradiation detectors. Towards this the researchers have grown highly resistive CdTe single crystals and developed a gamma detector for pulse height spectroscopic studies. This research activity is being actively pursued to develop compact semiconductor based detectors with enhanced efficiency, and technologically important single crystals for detector applications.

Metallurgy and Materials Group



Dr. S. Raju
Director, MMG



Dr. R. Divakar
AD, MEG



Dr. John Philip
Head, CSTD



Dr. Arup Dasgupta
Head, PMD



Dr. Anish Kumar
Head, NDED



Dr. M. Vasudevan
Head, MDTD



Shri Shaji Kurien
Head, PIED

The Metallurgy and Materials Group (MMG) of IGCAR, ever since its inception has been pursuing a vibrant research and development agenda, that is targeted to provide comprehensive and knowledge based solutions to a variety of materials related issues of India's fast reactor and associated fuel cycle programs. However, in the recent past, MMG has also contributed significantly to the cause of high temperature materials development towards India's advanced ultra supercritical power plant and fusion energy harnessing initiatives. Accordingly, the R&D activities of MMG are manifold. In scope, they pertain to the design, indigenization and accelerated field realization of new and indigenous material choices and process modifications, wherever these are mandated by the emerging demands on high design reliability. Amidst such setting, MMG has been spearheading a mix of basic and directed cross-disciplinary research activities under various themes. The human resource expertise of MMG is a diverse and balanced blend of experienced and energetic workforce, whose specialty touches almost all domains of materials engineering. The current portfolio of MMG includes:

- (i) Reactor & high temperature materials design & testing consultancy
- (ii) Advanced microstructure, mechanical & physical property characterization
- (iii) Novel component manufacturing initiatives for current and future FBR's. This include advanced materials fabrication & joining methods; special nuclear materials fabrication; Coatings & surface modification technologies for FBR and fuel reprocessing programs
- (iv) Nondestructive testing, inspection & qualification technologies
- (v) Post irradiation examination and component failure analysis etc.
- (vi) corrosion mitigation & materials protection solutions

It may be added that owing to the availability of quality technical expertise in combination with a wide range of advanced characterization tools, MMG has contributed to the development of three generations of nuclear structural materials, which are aimed at withstanding severe operating environmental conditions, typical of high flux fast reactors. Thanks to Internationally acclaimed expertise, MMG could also attract many young brains to pursue their research and post research careers at IGCAR, under the banner of Homi Bhabha National Institute (HBNI).

Reactor Design & Technology Group



Shri S. Raghupathy
Director, RDTG



Dr. B. K. Nashine
AD, SFG



Shri Jose Varghese
Head, CH&MD



Shri Sriramachandra Aithal
Head, RC&AD



Dr. K. Devan
Head, RND



Dr. A. John Arul
Head, RS&DD



Shri U. Parthasarathy
Head, SHTD



Dr. B. Babu
Head, DD&RSD



Shri V. A. Suresh Kumar
Head, RIOD



Shri V. Vinod
Head, ETHD



Shri Joseph Winston
Head, RH&IED



Dr. B. K. Sreedhar
Head, SE&HD



Shri S. Tanmay Vasal
Head, PPCD



Dr. K. Natesan
Head, THD

Reactor Design & Technology Group (RDTG) is responsible for the design, structural & thermal hydraulics analysis, core safety & plant dynamics analysis, structural mechanics including seismic testing, manufacturing technology development, engineering development, testing and qualification of Fast Breeder Reactor (FBR) components/systems. In addition, the responsibility of RDTG includes: Development of In service inspection devices & remote handling equipment for FBRs & FBR fuel reprocessing plants, Development of sensors & devices for sodium applications, Planning of irradiation experiments for testing of various fuel, structural and shielding materials

in FBTR, Design, development & fabrication of various irradiation devices for experiments in FBTR, Out-of-pile testing, precision machining and welding of miniature components and planning & execution of Shielding / Foil Activation experiments in KAMINI reactor. RDTG has expertise in design & engineering development of various systems/components of FBRs covering the Nuclear Steam Supply Systems (NSSS) and Balance of Plant (BoP) systems viz. Reactor Physics & Core Engineering, Reactor Assembly, Absorber Rod and Component Handling Mechanisms operating in sodium, Primary & Secondary Sodium Heat Transport Systems, Decay Heat Removal systems, Tertiary Steam Water Systems, Various Plant Auxiliary Systems, Electrical Power Systems, Plant Layout, Sodium Pumps, Electromagnetic Pumps, Cold Trap and Ultrasonic devices for use in sodium. RDTG has indigenously developed the design of Prototype Fast Breeder Reactor (PFBR) of 500 MWe capacity based on its design & analysis expertise, R&D program, technology development exercise and with the support from and in association with various other groups of IGCAR. The group is extending its technical support and design expertise to the PFBR project which is under commissioning by BHAVINI and is responsible for getting design safety clearances for PFBR from the Atomic Energy Regulatory Board (AERB). It also provides analytical support to other groups in the Centre. RDTG constantly provides the design and analytical expertise for the continuous enhancement of fuel & core performance of the Fast Breeder Test Reactor (FBTR) and operation at higher powers and higher operating temperatures focusing on the core engineering design, plant dynamics and core safety analysis. RDTG also plays a major role in the development of future Metallic fuel and has designed the metal fuel pins of different designs and fuel compositions for irradiation testing.

Design validation of critical components of FBRs are achieved through testing in sodium and in water using scaled down/full scale models. RDTG has acquired expertise in the development of sensors and devices for sodium applications, such as electromagnetic flow meters, level probes and leak detectors. Expertise has also been developed in handling of sodium and in the design, construction, commissioning & operation of various high temperature sodium test loops/facilities. The major sodium test facilities of RDTG include 5.5 MWt Steam Generator Test Facility (SGTF) for testing model steam generators of FBRs, SADHANA loop for experimentally demonstrating natural convection based safety grade decay heat removal system, Large Component Test Rig (LCTR) for testing critical full scale components, In Sodium Test facility (INSOT) for creep and fatigue testing of advanced materials, Sodium Water Reaction Test (SOWART) facility to study self wastage & impingement wastage of Steam Generator tubes and a state-of-art Sodium Facility for Component Testing (SFCT) for testing small and medium sized components and sensors. To meet the requirements of future FBRs, a new facility called Sodium Technology Complex is under execution.

Recent achievements of RDTG: Compression & flexure testing of enriched B4C pellets for FBTR poison rods, Hydraulic validation of Poison subassembly for FBTR, Decay heat measurements of structural material in KAMINI, Technical support towards rectification of LRP bearing, Evaluation of rotor dynamic coefficients of sodium pumps through CFD analysis, Simulation of pressure transient under turbine trip event, Performance and endurance testing of 50 m³/h Annular linear induction pump, Design and manufacture of additional nickel detectors for steam generator tube leak detection system of PFBR, Experimental verification of methodology in simulating neutron count rates with 0.1 cps/nv HTFC during initial fuel loading of PFBR, Seismic PSA study for PFBR, Study on the effect of orientation of PFBR fuel subassembly on response of gamma detector in FIZID system, Estimation of guard pipe compartment bellows, Vibration analysis of IHX downcomer, Stability analysis of secondary sodium pump, Vibration limits for ALIP in secondary sodium fill & drain circuit, Design and thermal hydraulic analysis of secondary sodium based decay heat removal system for FBR 1&2, Improved severe accident analysis in SFRs using slug-ejection model, Integrated steady and transient pool hydraulic analysis of primary sodium circuit, Numerical methodology for estimation of asymptotic crack size and comparison with A16 master curve prediction, Numerical analysis of hydrostatic bearing of large sodium pump using ARMD software, Numerical analysis of dynamic seals used in CSRDM, Testing of large sized bellows in sodium environment, Parametric studies to assess the bonding quality of sodium compatible ultrasonic transducers, Sensitivity evaluation of 100 NB permanent magnet flowmeters in sodium, Development and manufacture of 200 NB sidewall permanent magnet flow meter, Development of non-return valves for sodium service, Improvements in regeneration of sodium cold trap by altering geometry of wire mesh top plate, Simulation of gas entrainment phenomena inside FFLM, Finalisation of calibration scheme for eddy current flow meter of primary sodium pump, Performance evaluation of wire type leak detector layout for dished end test section in LEENA facility, Design & development of Reactor core viewing system (RCVS), Design, analysis and development of pressure decay method leak measurement system using mems based pressure sensor and Transfer & safe transportation of 3T of indigenously manufactured sodium from Baroda to Kalpakkam.

Besides providing technical support to PFBR, RDTG is currently engaged, in the development of future FBRs incorporating enhanced safety and improved economy. It has finalised the conceptual design of the future FBR and is currently undertaking the development of key systems and components and detailed engineering. Further, RDTG has evolved the preliminary conceptual design of a metal fuelled 100 MWt test reactor, planned to be

launched after FBTR. These apart, it has a modern design office with many advanced modeling and analysis softwares, experimental facility for testing major Reactor Assembly systems, Structural Mechanics Laboratory (SML) having state-of-the-art facilities for carrying out tests at component level to verify structural integrity at high temperature and a 100 t shake table with six degrees-of-freedom for seismic tests. The shake table is extensively used for the design validation of reactor systems and components of Nuclear Power Plants of NPCIL and other research projects undertaken by BARC.

RDTG also plays a major role in developing highly competent human resources by undertaking academic courses for the various science and engineering disciplines through the BARC Training Schools located at Mumbai, at IGCAR, Kalpakkam and at NFC, Hyderabad and provide guidance to many employees / students / JRF & SRF in their Post graduate, Ph.D and Research Programs.

Reactor Facilities Group



Shri K. V. Suresh Kumar
Director, RFG



Shri A. Babu
AD, OMG



Shri M. S. Chandrasekar
Head, THRDD



Shri K. Dinesh
Head, TSD



Shri G. Shanmugam
Head, RMD



Shri N. Manimaran
Head, ROD



Shri K. G. Subramanian
Head, QA&ISD

The Reactor Facilities Group (RFG) is responsible for safe operation of Fast Breeder Test Reactor (FBTR), KAMINI Reactor and Interim Fuel Storage Building (IFSB). Till recently, FBTR has been operating at a power level of 32 MWt. Towards raising FBTR power level to its design power level of 40 MWt with Mark-I subassemblies and poison subassemblies (to maintain the required shutdown margin), safety clearance has been obtained from AERB. Plant modifications and refurbishment works have been carried out and required core changes including addition of fuel are being carried out to operate the reactor at 40 MWt. Utilizing the reactor for irradiation of advanced fuels and structural materials for fast reactors and conducting safety related experiments form major goals of FBTR. KAMINI Reactor has been extensively used for neutron radiography, activation studies and testing of indigenously developed neutron detectors. RFG is also responsible for fabrication and safe storage of fuel, blanket, source and control subassemblies for PFBR. All the required number of assemblies for the first core of PFBR were already fabricated and stored safely in IFSB with all security surveillance measures and safeguards. The training division of the group is responsible for training the O&M staff of FBTR, PFBR and future FBRs. RFG also takes part in the operational safety review of PFBR project.

Reprocessing Group



Dr. K. Ananthasivan
Director, RpG



Shri Shekhar Kumar
Head, RPOD



Shri K. Rajan
Head, DFRPD



Dr. R. V. Subba Rao
Head, PRCD



Dr. K.A. Venkatesan
Head, RR&DD



Shri. M. Geo Mathews
Head, RpMD (M)



Shri. M. Dhananjeyakumar
Head, RpMD (EEI&C)

The Reprocessing Group at IGCAR has the primary mandate to establish advanced technology for the reprocessing of advanced fast reactor fuels. The major activities in progress in the Group include, design, construction, commissioning and operation of the fast reactor fuel reprocessing plants, development of novel processes & equipment and carrying out the R&D associated with the same. This group comprises the CORAL (Compact facility for Reprocessing Advanced fuels in Lead cells) facility, the Demonstration fast reactor Fuel Reprocessing Plant (DFRP), and a research facility for carrying out advanced research on fast reactor fuel reprocessing. The CORAL facility was commissioned in 2003 and continues to operate successfully, processing the mixed carbide spent fuel from FBTR. The facility continues to serve as a test bed and has provided valuable feedback for the design and construction of future reprocessing plants. CORAL has completed its original mandate of reprocessing of FBTR fuel sub-assemblies and closing the fast reactor fuel cycle and has been further relicensed by the regulatory body, after upgradation of the safety systems. The DFRP, whose mandate is to demonstrate the reprocessing of FBTR spent fuel at a plant scale and the initial spent fuel subassemblies of PFBR, is in an advanced stage of commissioning. The commercial scale plant, Fuel Reprocessing Plant (FRP), for processing the fuel discharged from PFBR is being constructed at the Fast Reactor Fuel Cycle Facility (FRFCF). The responsibility of design of FRP rests with RpG. In addition, the group also lends its expertise in procurement of long delivery items such as the optical glass slabs for radiation shielding windows, various types of master slave manipulators, lead bricks etc, for the FRFCF project. Concurrently focused R&D is being pursued to develop equipment, alternate processes and aqueous processing of metallic fuel.

Safety, Quality & Resource Management Group



Dr. B. Venkatraman
Director, SQRMG



Shri S. Athmalingam
AD, R&ESG



Dr. D. Ponraju
AD, H&SEG



Ms. S. Rajeswari
Head, SIRD



Dr. Vidya Sundararajan
Head, P&HRMD



Dr. R. Venkatesan HEAD,
RESD



Dr. C. V. Srinivas
Head, EAD



Shri Sanjay Kumar Das
HEAD, SED



Dr. N. Subramanian
Head, Incubation Centre

Safety, Quality & Resource Management Group (SQRMG) is responsible for Health Physics, Radiation Safety and Quality Assurance services, studies on Environment Impact Assessment, Severe Accident & Sodium Fire and management of resources like Financial (Budget), Human, Scientific Information services and conduct Academic Programmes of BARC Training School at IGCAR. Health and Safety Engineering Group (HSEG) comprises of Health & Industrial Safety Division (HISD) and Safety Engineering Division (SED). Radiological & Environmental Safety Group (RESG) comprises of Radiological & Environmental Safety Division (RESD), Environment Assessment Division (EAD), Quality Assurance Division (QAD) Planning and Human Resource Management Division (PHRMD) and Scientific Information Resource Division (SIRD).

HISD provides radiological protection and surveillance to all active plants, Bio assay and Whole body accounting services to all the occupational workers of the Centre and industrial and occupational health safety services to meet the mandatory requirements of AERB. HISD organizes training and awareness programmes on industrial, radiation and fire safety to occupational workers.

SED is carrying out studies on Severe Accident and Sodium Fire Safety. The major experimental facilities are THEME and SOFI for Molten Fuel Coolant Interaction studies, PATH facility for post accident heat removal studies, MINA and SOCA facilities for sodium fire studies and SFEF for large scale sodium fire and severe accident studies.

RESD focuses on R&D activities in the areas of sodium aerosol science and technology, radiation safety through modeling & simulation and societal applications of ionizing and non-ionizing radiations. RESD organizes public awareness programmes on radiation safety and nuclear energy. Technical Co-ordination & Quality Management Section (TC&QMS) is primarily responsible for quality control of several critical equipment for IGCAR manufactured

in the western region of the country and provides technical co-ordination services for the centre with BARC as well as the DAE, Mumbai. TC&QMS also participates in R&D activities which are being carried out at BARC towards meeting the mandate of IGCAR, FRFCF/NRB and PFBR.

EAD is responsible for providing radiation safety services such as TLD personal monitoring, luminescence dosimetry, retrospective dosimetry, bio dosimetry and focuses on R&D activities on atmospheric dispersion and modelling.

QAD is primarily responsible for catering quality assurance, inspection, Non-Destructive Testing (NDT) and quality audit activities during fabrication, construction & erection of System, Structure & Equipment for various Groups of our Centre in order to establish and implement an effective quality management system. QAD also extends its expertise to other DAE units and other strategic sectors.

The significant activities of PHRMD are planning and human resource management, conducting the academic programmes of BARC Training school at IGCAR and stipendiary trainees, formulating and monitoring capital projects towards budget planning and management, facilitating induction of Research Scholars, Research Associates and Visiting Scientists, coordinating the visits of important dignitaries and delegations to the Centre, formulating and facilitating collaborations and MoU including patents and piloting the activities relating to technology transfer.

Scientific Information Resource Division (SIRD) is the second-largest research library in DAE, with about 65,000 books, 50,000 back volumes, 540 journals, 15,000 standards, and two lakh technical reports. SIRD caters to the needs of more than 5000 scientists, engineers, research scholars, and students of various DAE Units at Kalpakkam. SIRD maintains the centralized institutional repository, the preprint server, and the RFID-based Library Resources databases. Dissemination of resources is through WebOpac, and remote access is through a mobile app. SIRD provides various services like photography, videography, reprography, content creation, auditorium, desktop design, and publication assistance. SIRD has played a vital role in documenting the biodiversity.

An Incubation Centre has been set up at IGCAR to promote and incubate the spin-off technologies from IGCAR. A team has been formed to meet the objectives, set up the necessary infrastructure and to interface with various Groups at IGCAR.

Administration & Accounts



Shri K.R. Sethuraman
CAO



Shri V. Sivakumar
IFA[FRFCF]

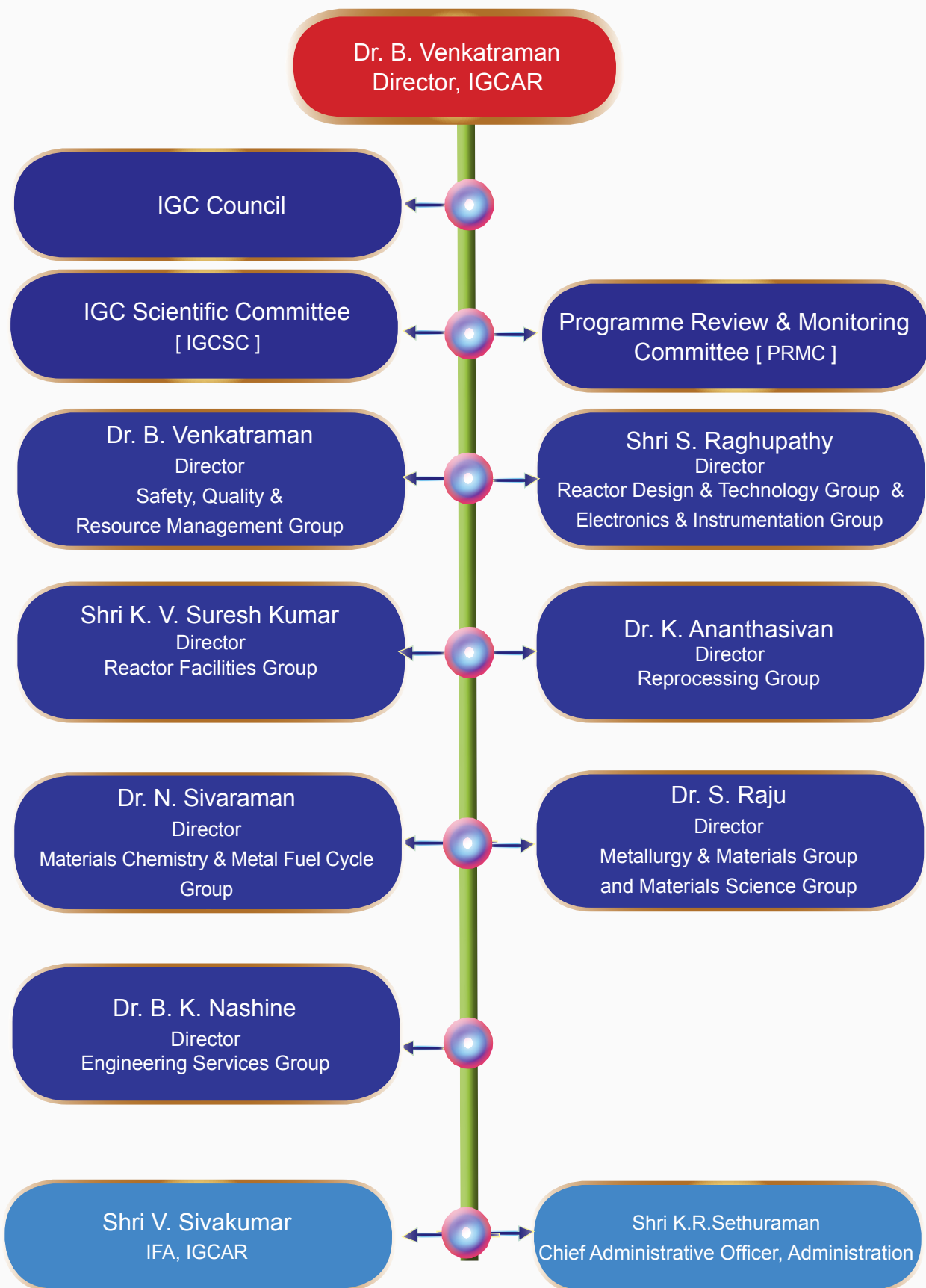


Smt Radhika Saikannan
DCA

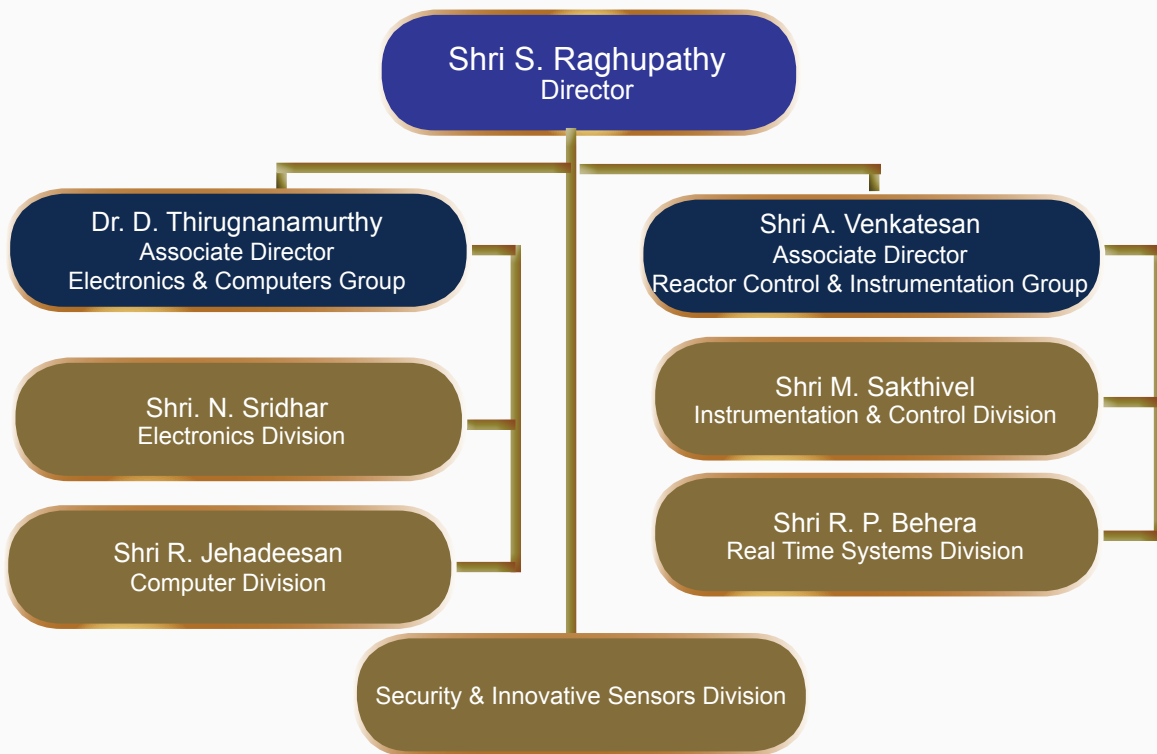


Smt S. Jayakumari
AO (E&V) & (L&G&R)

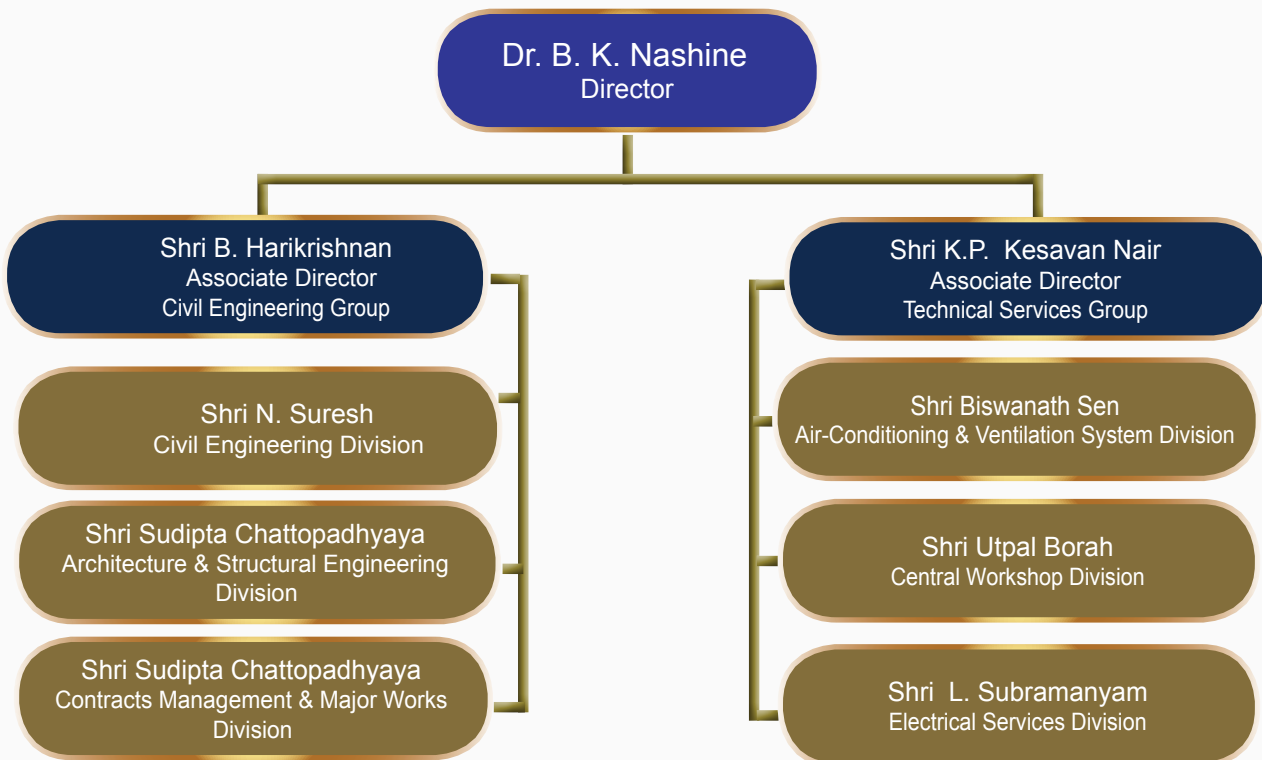
Organisation Chart - IGCAR



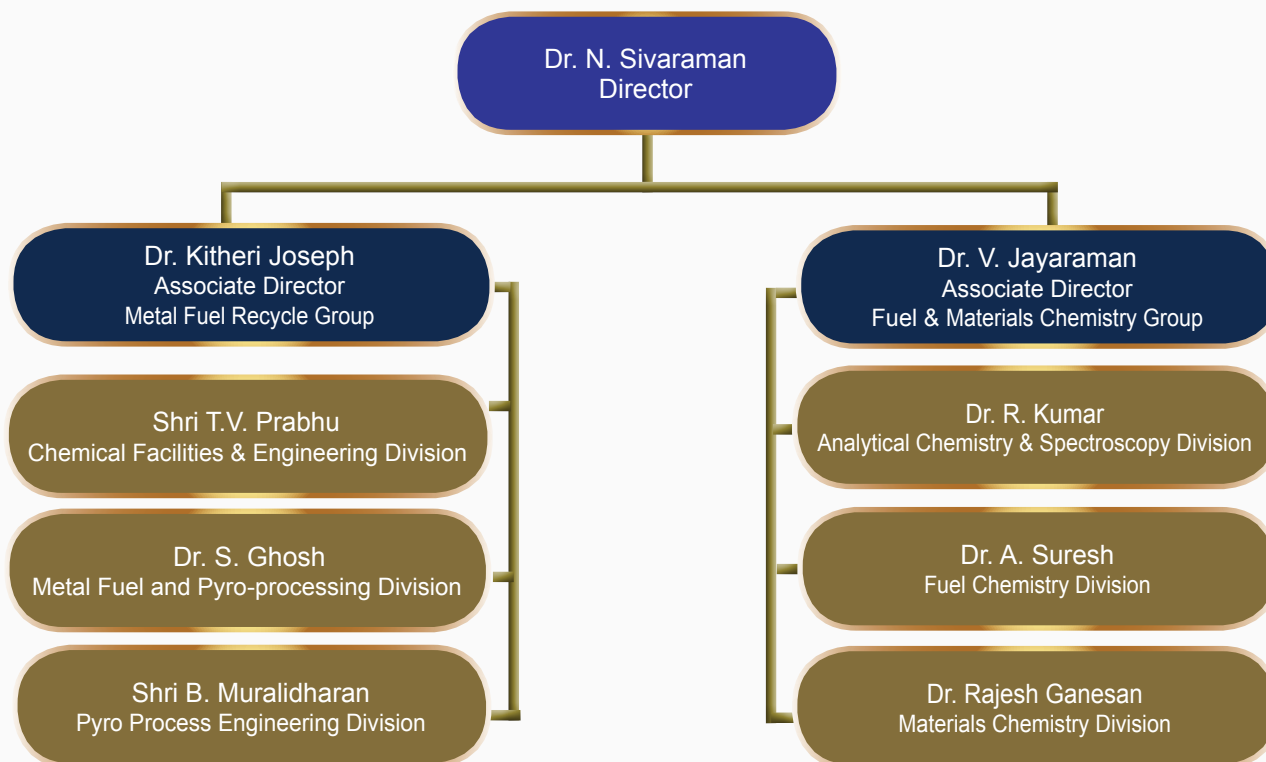
Electronics & Instrumentation Group



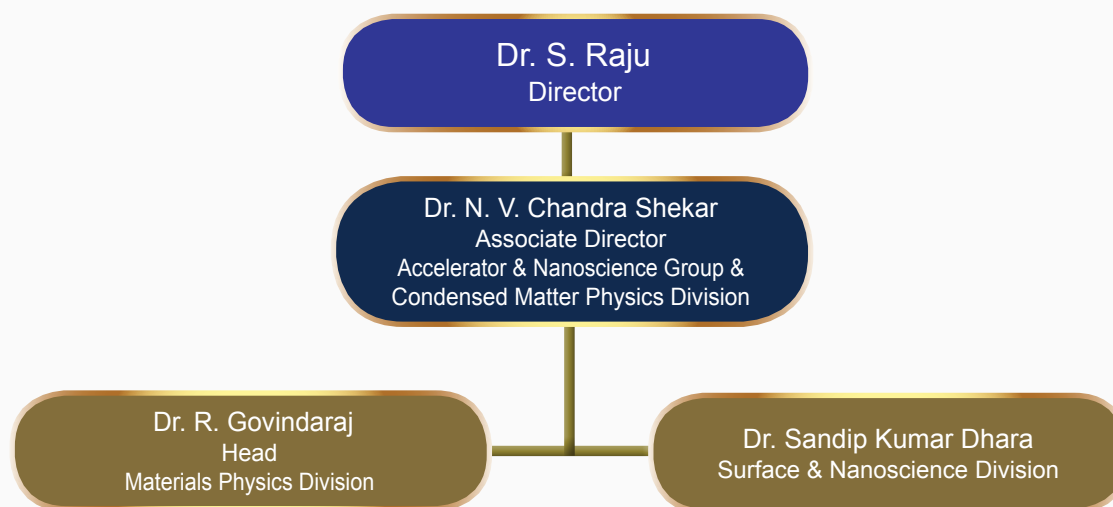
Engineering Services Group



Materials Chemistry & Metal Fuel Cycle Group



Materials Science Group



Metallurgy & Materials Group

Dr. S. Raju
Director

Dr. John Philip
Corrosion Science & Technology Division

Dr. Arup Dasgupta
Physical Metallurgy Division

Dr. R. Divakar
Associate Director
Materials Engineering Group

Dr. Anish Kumar
Non-Destructive Evaluation Division

Shri Shaji Kurien
Post Irradiation Examination Division

Dr. M. Vasudevan
Materials Development & Technology Division

Reactor Design & Technology Group

Shri S. Raghupathy
Director

Associate Director
Nuclear Systems Design Group

Dr. A. John Arul
Reactor Shielding and Data Division

Dr. K. Devan
Reactor Neutronics Division

Shri Jose Varghese
Component Handling & Mechanisms Division

Shri U. Parthasarathy
Sodium Heat Transport Division

Shri Sriramachandra Aithal
Reactor Core & Assembly Division

Shri V. Vinod
Experimental Thermal Hydraulics Division

Shri Joseph Winston
Remote Handling & Irradiation Experiments Division

Shri B. K. Sreedhar
Sodium Experiments & Hydraulics Division

Shri K. Natesan
Thermal Hydraulics Division

Dr. B. K. Nashine
Associate Director
Sodium Facility Group

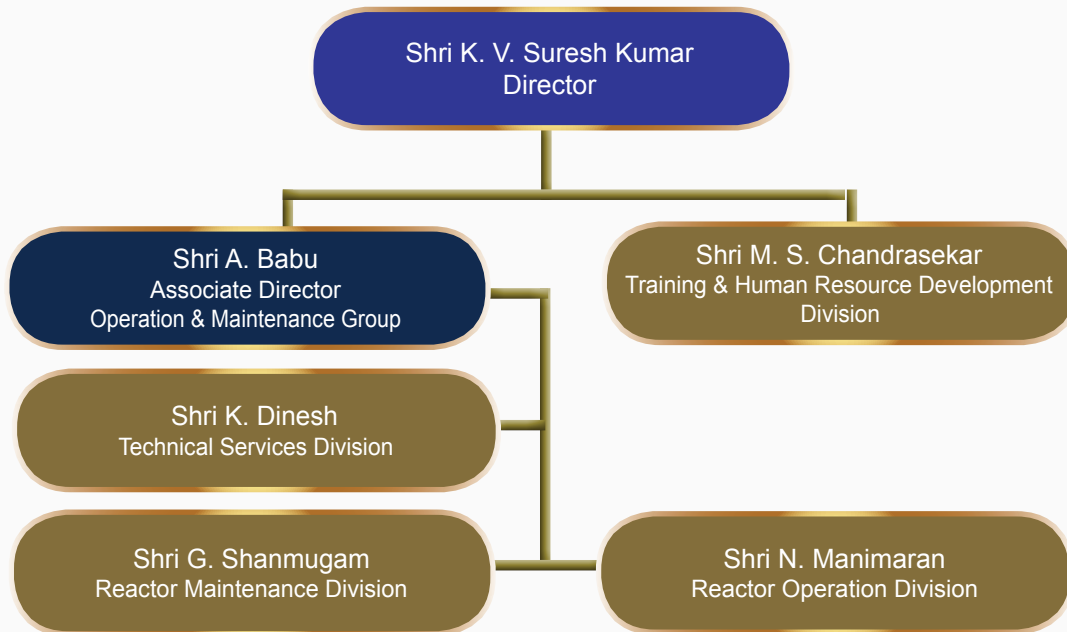
Dr. B. Babu
Device Development & Rig Services Division

Shri V. A. Suresh Kumar
Rig Operations Division & SGTF

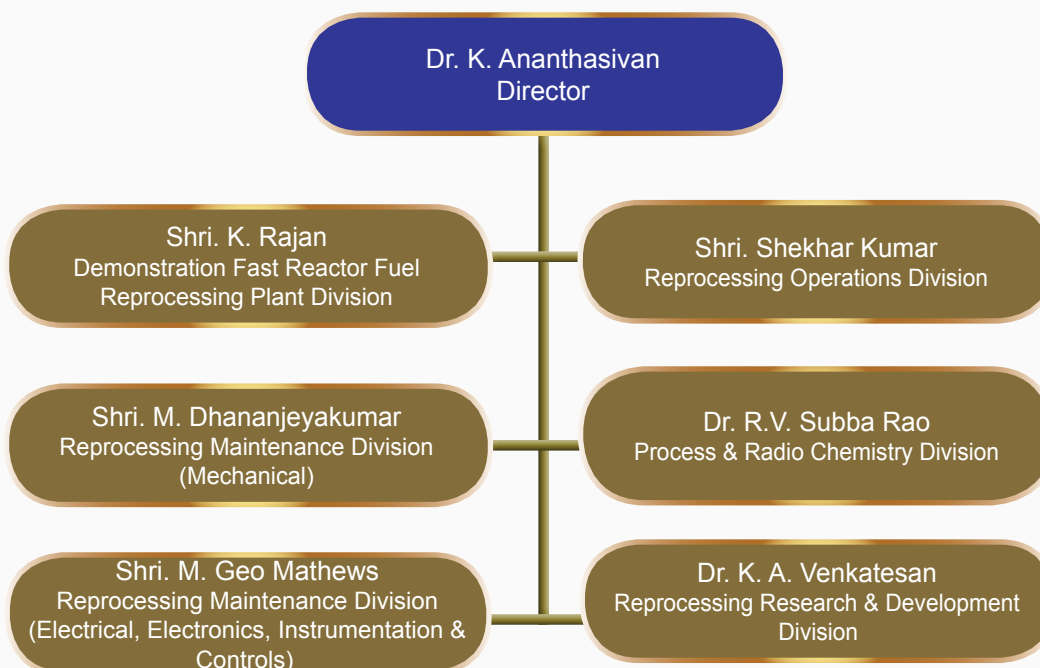
Shri S. Tanmay Vasal
Power Plant Control Division

S. Jalaldeen
Structural Mechanics Division

Reactor Facilities Group



Reprocessing Group



Safety, Quality & Resource Management Group

Dr. B. Venkatraman
Director

Shri S. Athmalingam
Associate Director
Radiological & Environmental Safety Group

Dr. D. Ponraju
Associate Director
Health & Safety Engineering Group

Shri S. Athmalingam
Quality Assurance Division

Dr. D. Ponraju
Health & Industrial Safety Division

Dr. C.V. Srinivas
Environmental Assessment Division

Shri Sanjay Kumar Das
Safety Engineering Division

Dr. R. Venkatesan
Radiological & Environmental Safety Division

Smt. S. Rajeswari
Scientific Information Resource Division

Dr. N. Subramanian
Head, Incubation Centre

Dr. Vidya Sundararajan
Planning & Human Resource Management
Division

Administration

Shri K.R.Sethuraman
Chief Administrative Officer

Smt. S. Jayakumari
Administration (Legal & General) &
Recruitment

Smt. S. Jayakumari
Administration (Establishment) & Vigilance

Accounts

Shri V. Sivakumar
IFA

Smt Radhika Saikannan
DCA

LIST OF IMPORTANT ABBREVIATIONS

AC&VSD	Air Conditioning and Ventilation System Division	MPD	Materials Physics Division
AERB	Atomic Energy Regulatory Board	MRPU	Madras Regional Purchase Unit
A&SED	Architecture & Structural Engineering Division	MSG	Materials Science Group
ANG	Accelerator & Nanoscience Group	NDED	Non-Destructive Evaluation Division
BARC	Bhabha Atomic Research Centre	NFC	Nuclear Fuel Complex
BARCF	Bhabha Atomic Research Centre Facilities	NICB	Nuclear Island Connected Building
BHAVINI	Bharatiya Nabhikiya Vidyut Nigam Limited	NPCIL	Nuclear Power Corporation of India Ltd.
CD	Computer Division	NSDG	Nuclear Systems Design Group
CED	Civil Engineering Division	OMG	Operation & Maintenance Group
CEG	Civil Engineering Group	PFBR	Prototype Fast Breeder Reactor
CF&ED	Chemical Facilities & Engineering Division	P&HRMD	Planning & Human Resource Management Division
CH&MD	Components Handling & Mechanism Division	PHWR	Pressurized Heavy Water Reactor
CMPD	Condensed Matter Physics Division	PIED	Post Irradiation Examination Division
C&MWD	Contracts & Major Works Division	PMD	Physical Metallurgy Division
CORAL	Compact facility for Reprocessing Advanced fuels in Lead cell	PPCD	Power Plant Control Division
CSTD	Corrosion Science & Technology Division	PPED	Pyro Process Engineering Division
CWD	Central Workshop Division	QAD	Quality Assurance Division
DDRSD	Device Development and Rig Services Division	RCAD	Reactor Core & Assembly Division
DFRFRPD	Demonstration Fast Reactor Fuel Reprocessing Plant Division	RD&TG	Reactor Design & Technology Group
DFRP	Demonstration Fuel Reprocessing Plant	R&ESD	Radiological & Environmental Safety Division
ED	Electronics Division	RESG	Radiological & Environmental Safety Group
EIG	Electronics and Instrumentation Group	RH&IED	Remote Handling & Irradiation experiments Division
ESD	Electrical Services Division	RMD	Reactor Maintenance Division
ESG	Engineering Services Group	RND	Reactor Neutronics Division
ETHD	Experimental Thermal Hydraulics Division	ROD	Reactor Operation Division
FBTR	Fast Breeder Test Reactor	RFG	Reactor Facilities Group
FChD	Fuel Chemistry Division	RpMD	Reprocessing Maintenance Division
FRFCF	Fast Reactor Fuel Cycle Facility	RpG	Reprocessing Group
HISD	Health & Industrial Safety Division	RpOD	Reprocessing Operation Division
HSEG	Health, Safety & Environment Group	RRDD	Reprocessing Research and Development Division
GSO	General Services Organisation	RSDD	Reactor Shielding and Data Division
IAEA	International Atomic Energy Agency	RTSD	Real Time Systems Division
IIT	Indian Institute of Technology	RC&IG	Reactor Control & Instrumentation Group
IMSc	Institute of Mathematical Sciences	SED	Safety Engineering Division
I&CD	Instrumentation & Control Division	SE&HD	Sodium Experiments & Hydraulics Division
MAPS	Madras Atomic Power Station	SFG	Sodium Facility Group
MCG	Materials Characterization Group	SHTD	Sodium Heat Transport Division
MC&MFCG	Materials Chemistry & Metal Fuel Cycle Group	SIRD	Scientific Information Resource Division
MCD	Materials Chemistry Division	SISD	Security and Innovative Sensors Division
MDTD	Materials Development & Technology Division	SMD	Structural Mechanics Division
MEG	Materials Engineering Group	SND	Surface and Nanoscience Division
F&MCG	Fuel & Materials Chemistry Group	SQRMG	Safety, Quality & Resource Management Group
MFFD	Metal Fuel Fabrication Division	THD	Thermal Hydraulics Division
MFPG	Metal Fuel and Pyroprocessing Division	THRDD	Training & Human Resource Development Division
MMG	Metallurgy and Materials Group	TSD	Technical Services Division
		TSG	Technical Services Group

Annual Report Editorial Team



Ms. S. Rajeswari
Chairman



Dr. V. S. Srinivasan
Secretary



Dr. John Philip



Dr. T. R. Ravindran



Dr. C.V.S. Brahmananda Rao



Shri A. Suriyanarayanan



Shri Biswanath Sen



Shri M. S. Bhagat



Shri G. Venkat Kishore



Dr. Girija Suresh



Shri M. Rajendra Kumar



Shri S. Kishore



Dr. N. Designan



Shri Gaddam Pentaiah



Shri K. Varathan

